Applicability of rock physics models in conjunction with seismic inverted data to characterize a low poro-perm gas-bearing sandstone reservoir for well location optimization, Bredasdorp Basin, SA

Jorge I. Adrian N.

Dissertation presented for the degree of Master of Science in the Department of Geological Sciences

University of Cape Town

April 2015

Supervisor: Mr. George Smith

I know the meaning of plagiarism and declare that all of the work in the dissertation, save for that which is properly acknowledged, is my own.

Signed by candidate

Signature Removed

Abstract

The primary focus of this dissertation is to develop a predictive rock physics theory that establishes relations between rock properties and the observed seismic and to present the results of different seismic characterization techniques to interpret a tight gas sand reservoir off the south coast of South Africa using as input rock physics analysis and inverted seismic outcomes.

To perform the aims and goals of this study a workflow that involves the execution of three main processes was implemented: (1) rock physics modelling, (2) a simultaneous seismic inversion, and (3) seismic reservoir characterization techniques.

First, a rock physics model was generated as a bridge between the seismic observables (density, Vp and Vs) and reservoir parameters such as fluid content, porosity and mineralogy. In situ and perturbational log-derived forward modelling was performed. Both in situ and perturbational forward modelling were used to generate synthetic seismic gathers, which were used to study the AVA attribute responses. Overall, the effect of fluid fill on this tight gas sand seismically is modest compared with the effect of porosity changes.

Second, there follows a detailed description of a workflow implemented to simultaneously invert P and S pre-stack seismic data. The derived elastic properties (acoustic impedance, Vp/Vs and density) were then used in combination with the rock physics analysis to characterize seismically the reservoir. The predicted acoustic impedance and Vp/Vs volumes show a good tie with the log data. However, the density outcome was of limited quality compared with the two mentioned above.

Finally, using outcomes from rock physics analysis and/or inverted data, four seismic techniques to characterize the reservoir were conducted. The techniques involved are: (1) AVO cross-plotting to generate a good facies property based on AVO attributes (intercept-gradient) and rock physics in the area of study, (2) rock physics templates (RPTs) to compute discrete rock property volumes (litho-Sw, litho-porosity) using a collection of curves that cover all possible “what if” lithology-fluid content-porosity scenarios for the reservoir and the inverted data, (3) a lithological classification to calculate litho-facies probability volumes based on a litho-facies classification using petrophysical cut-offs, multivariate probability functions (PDFs) and inverted data, and (4) an extended elastic impedance (EEI) inversion to derive rock property volumes (Vclay, porosity) based on AVO attributes (intercept, gradient).

Despite differences in the input and theory behind each technique, all outcomes share parallels in the distribution of good and poor facies or reservoir and non-reservoir zones.

Acknowledgements

I would like to express my gratitude to my supervisor George Smith for the useful comments, remarks and engagement through the learning process of this master thesis. Furthermore I would like to thank Sandro Borean, Andrew Dippenaar and especially Everton September to encourage me to take part in this exciting project.

I would like to thank PetroSA for the financial support and for providing the dataset to carry out this research.

Paola Vera, Robert Keirstead and Caroline Martinez for introducing me to the topics as well as for the tireless support and advice on the way. Also, I like to thank my fellow workers in PetroSA and Schlumberger for their friendship, dedication and advice: Omar El Saadi, Leonardo Santana, Alexis Carrillat, Abdullah Jawoodien, Erich Scholtz and Freddie Bowers. A special thanks to my friends Gervasio Robles for always having a reasonable answer, Alejandro Zabala by removing debris from my way and Javier Diaz for sharing his precious time during the process.

I would like to thank my loved ones (my family), who have supported me throughout the entire process, both by keeping me harmonious and helping me putting the pieces together. In this group an especial mention to my wife, Scarlet, and younger daughters, Vero and Saby. They understand my absences and have endless patience. Without their love, support, and encouragement, I could not finish. I will be grateful forever for their love.

Last but not least I would like to thank God for all his blessings and love.

Index

List of Figures

List of Tables

Chapter 1: Introduction

A reservoir is exposed to a great number of analyses in all stages of its active life (exploration, appraisal, development, enhanced recovery) in order to optimize the asset value and to reduce the uncertainty of geological and production factors. The use of seismic data has come to play an essential role in this process. However, seismic data alone is not sufficient to solve all the uncertainties related to different reservoir rock properties. On the other hand, rock physics seeks to establish relations between those reservoir rock properties such as porosity, rock type, fluid and pressure and the observed seismic response by developing a rock physics effective model. The rock physics effective models become the essential tool to improve the qualitative seismic interpretation process and therefore to reduce uncertainties and ambiguities in seismic interpretation, such as fluid/lithology, sand/shale and porosity/saturation.

Understanding the mineralogical, fluid and porosity behaviour and effects in a seismic context (elastic properties) is always a challenge in a low poro-perm gas sandstone reservoir. Different approaches based on (1) inclusion theoretical models such as the differential effective medium (DEM) and the self-consistent model (SCM), (2) contact theoretical models (unconsolidated and Hertz-Mindlin_Hashin-Shtrikman (HMHS)) and (3) Hashin-Shtrikman (HS) are evaluated by predicting the elastic properties in the interval of interest and comparing them with measured log data.

Rock physics can be used for many practical applications, including fluid-replacement models in well log data, assessing “what if” possibilities, cross-plotting well and seismic data, predicting and conditioning logs and seismic modelling.

This dissertation intends to prove the applicability of rock physics models in conjunction with seismic data to characterize a low poro-perm gas-bearing sandstone reservoir located offshore South Africa in the Bredasdorp Basin. A methodology was developed to determine a rock physics effective model to predict and understand the elastic response from the inverted dataset.

Once the rock physics model that best mimics the elastic properties of the real rock in a 1D analysis has been identified, reservoir characterization techniques (RPM template inverse modelling, EEI illumination, Bayesian classification, etc) are performed using that rock physics model in combination with 3D seismic inverted data. The ultimate objective of the reservoir characterization is to reduce risk in drilling outcomes and reduce operating costs. See Figure 1.1 illustrating the workflow suggested in this dissertation.

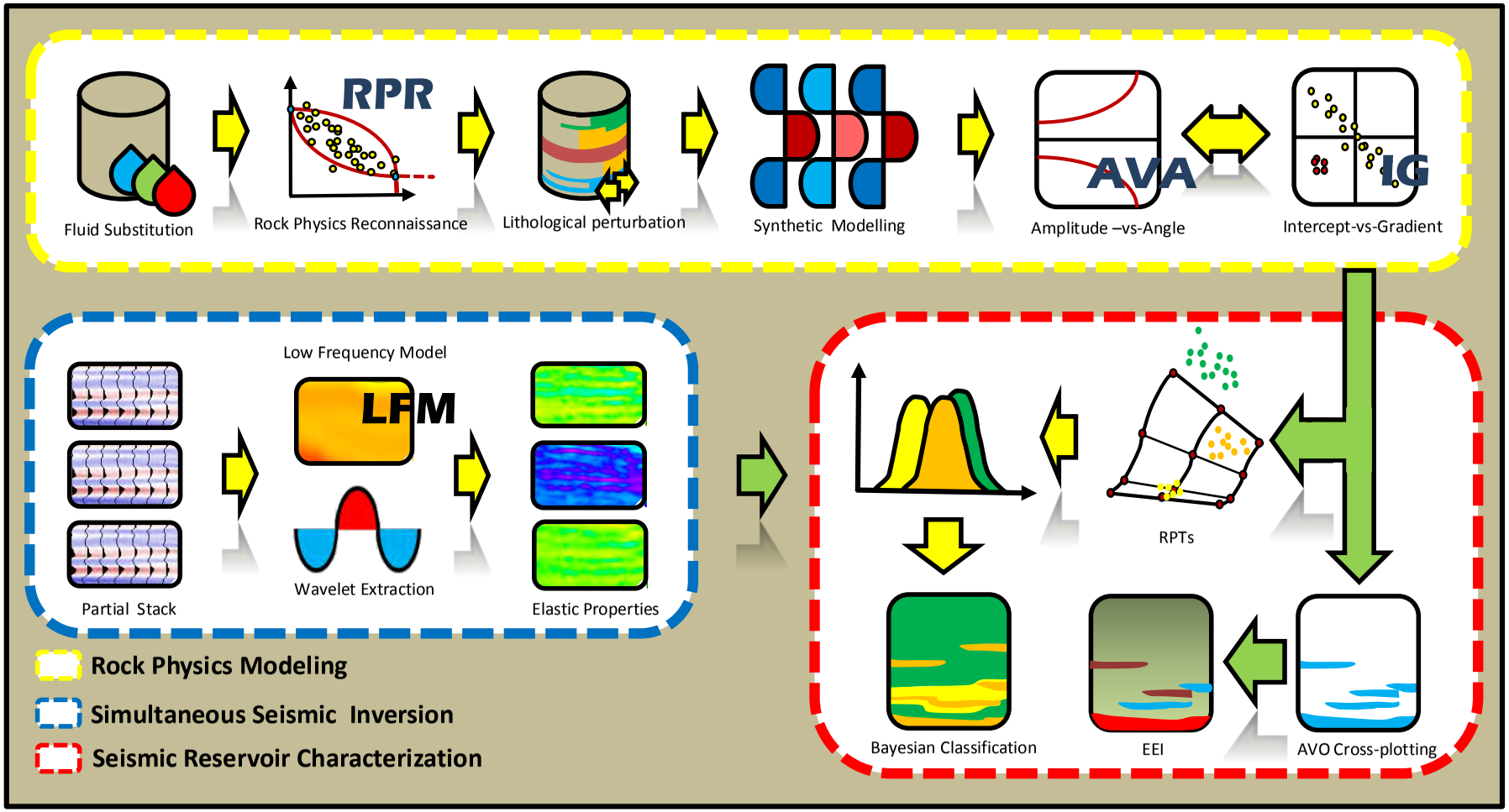

Figure 1.1: Workflow suggested on this dissertation involves three main steps; (1) a rock physics modelling to understand seismic response to changes on rock properties, (2) a simultaneous seismic inversion to transform seismic reflection (interface property) into rock properties and (3) a series of seismic reservoir characterization techniques combining rock physics model and inverted data.

Chapter 2: Theoretical framework

This chapter serves to introduce theoretical concepts and terms that were used throughout the development of this dissertation. Three main technical subjects are addressed in this chapter: (a) rock physics models, (b) pre-stack seismic inversion, (c) reservoir characterization techniques.

2.1 Rock physics models

Rock physics models aim to establish relations between rock properties such as porosity, water saturation, clay content, etc., and the observed seismic response, and to develop a predictive theory so that these properties may be estimated seismically.

Rock physics models fall within three general model classes: theoretical, empirical, and heuristic (Avseth et al., 2005). In this dissertation the main emphasis is on theoretical models.

Theoretical models are continuum mechanics approximations of the elastic properties of rocks. This category includes contact and inclusion models (unconsolidated, self-consistent, etc). Empirical models are based on experimental observations under specific physical conditions and with specific datasets. The last category, heuristic models, represents a non-mathematically rigorous way to relate parameters (Ruiz, 2009).

2.1.1 Theoretical models

Continuum mechanics approximations of the elastic, viscoelastic or poroelastic properties of rock are by definition theoretical models (Ruiz, 2009). One of the pioneers in this field, Biot (1956), formulated the coupled mechanical behaviour of a porous rock saturated with a linearly viscous fluid. At zero frequency, the Biot equations reduce to the Gassmann (1951) relations.

Elastic models may be classified into five kinds of models: (a) inclusion models, (b) contact models, (c) bounds, (d) transformation and computational models (Avseth et al., 2005). In this dissertation, we use different inclusion and contact effective medium models in different phases of the project. Figure 2.1.1 shows the granular rock (contact model) and equivalent elastic model, made of a continuous matrix and embedded elliptical inclusions with a fixed aspect ratio (see appendix 2.2.1)

2.1.2 Empirical models

Empirical models are mostly based on experimental observations under specific physical conditions and with specific data sets, but may also be derived from numerical experiments. The usual modelling approach involves a two-step process: a modelling step to determine

the functional form followed by a calibration step to determine the empirical coefficients (Avseth et al, 2005).

An example of the empirical models used in this dissertation is the Vp-Vs relations of Greenberg and Castagna (1992).

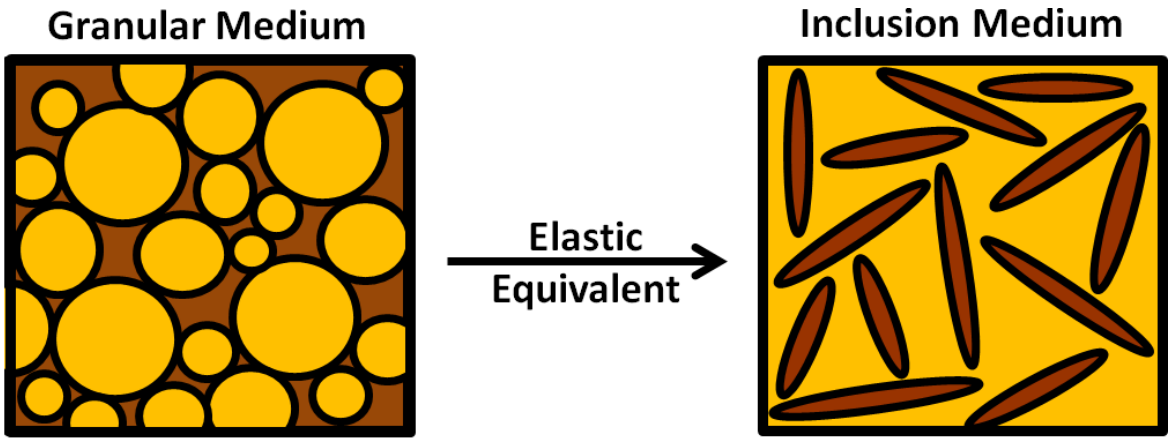

Figure 2.1.1: Two idealized equivalent physical kind of models. A granular medium, a random dense pack of spherical grains (Unconsolidated model and stiff model). A second model is the Inclusion medium model, a continuous matrix with isolated random distributed pores of a single aspect ratio (AR) (DEM model and Self-Consistent model).

2.1.3 Heuristic Models

A heuristic model is a non-mathematical, rigorous way to relate parameters. In heuristic models arguments are presented to justify why rock physics parameters should be related in a certain form (Avseth and Skjei, 2011). The Hashin-Shtrikman bounds are an example of those kinds of models.

2.1.4 Vs predictor models

Greenberg-Castagna model: Greenberg and Castagna (1992) developed a general method for predicting Vs in multimineralic, brine-saturated rocks based on empirical, polynomial Vp-Vs relations in pure monomineralic lithologies (Castagna et al., 1993). The method is based on an empirical Vs prediction in brine-saturated rocks whose solid phase consists of four minerals: quartz, calcite, dolomite and clay. If the rock is saturated with a different fluid, then an iterative scheme is used to substitute the original water with the new fluid. This method can be used in rocks composed of any combination of quartz, calcite, dolomite and clay (any or all) and in the medium to high porosity range.

Krief Model: Krief and Garat. (1990) observed a quasi-linear relation between the squares of Vp and Vs in multiple formations. Based on this observation, they gave the following relation between Vs and Vp:

$$Vs^2 = Vss^2 (Vp^2-Vpf^2)/ (Vps^2-Vpf^2)$$

where Vps *and* Vss are P- and S-wave velocities of the solid phase, respectively, and Vpf is velocity in the pore fluid. It is recommended for all consolidated lithologies and low to medium porosity ranges.

Mud rock model: Castagna et al. (1985) found the following relation between Vp and Vs in clastic silicate rock composed primarily of clay and silt-sized particles (mudrock):

Vp = 1.16 Vs + 1.36 km/s

This relation is based on in situ sonic and seismic measurements in water-saturated, Gulf Coast sands, so it is empirical and should not be expected to work well in all rock types. This model does not require any porosity or pore-fluid velocity information and is intended for water-saturated zones.

Vernik model: Vernik and Liu observed a relation between the squares of Vp and Vs in multiple formations. Based on this observation (Vernik and Liu, 1997), they gave the following relation between Vs and Vp:

$Vs = (a+bVp^2+cVp^4)^{0.5}$, (km/s)

Where,

Vp and Vs are P- and S-wave velocities of the rock,
in shale, a=-1.267, b= 0.372, c=2.84e-3,
in sand, a=-0.79, b=0.287, c=2.84e-3.

Since the Vernik model is applicable to under-saturated conditions, the model is modified by doing fluid substitution. The Vernik model is suggested for consolidated lithologies and low-to-medium porosity ranges.

2.2 Seismic trace inversion

By definition, seismic inversion is the process of transforming seismic reflection data into a quantitative rock property, generally by combining seismic and well data. Therefore, it helps to build static reservoir models for field development and to estimate probabilities for the presence of hydrocarbons.

Before delving deeper into the physical processes and techniques of seismic inversion, it is helpful to define forward modelling in order to gain a better understanding of the process itself.

Forward modelling refers to the algorithm, commonly the convolutional model, used to generate synthetic seismic data. In post-stack forward modelling, reflection coefficients are calculated from an impedance model and convolved with a wavelet. In pre-stack modelling, the forward model needs to be expanded to include AVO effects (Cooke and Cant, 2010). Seismic inversion is the reverse process of forward modelling.

In forward modelling, acoustic impedance is developed from a well log, combined with a seismic wavelet, and a synthetic seismic data trace is computed. Conversely, inversion

begins with a recorded seismic data trace and removes the effect of an estimated wavelet, computing values of acoustic impedance at each time sample and each CMP (see Fig 2.2.1).

The most basic and commonly used one-dimensional model for the seismic trace is referred to as the convolutional model (seismic model), which states that the seismic trace is simply the convolution of the earth's reflectivity with a seismic wavelet with the addition of a noise component. In equation form, where * implies convolution (Russell, 2004),

$$s(t) = w(t) * r(t) + n(t),$$

where $s(t)$ = the seismic trace,

$w(t)$ = seismic wavelet,

$r(t)$ = earth reflectivity and

$n(t)$ = additive noise.

The reflection coefficient series or reflectivity is the sequence of relative acoustic impedance changes within the earth, where acoustic impedance is defined as the product of compressional velocity and density. Acoustic impedance is converted to reflectivity by dividing the difference in the acoustic impedances by the sum of the acoustic impedances. The equation is as follows:

$$r(i) = \frac{\rho_{(i+1)}V_{(i+1)} - \rho_{(i)}V_{(i)}}{\rho_{(i+1)}V_{(i+1)} + \rho_{(i)}V_{(i)}} = \frac{Z_{(i+1)} - Z_{(i)}}{Z_{(i+1)} + Z_{(i)}}$$

where

r= reflection coefficient,

ρ= density,

V= velocity,

Z= acoustic impedance

and layer i overlies layer i+1.

A wavelet is a fundamental element in the seismic modelling; it produces the seismic trace via convolution with the reflectivity. A wavelet can be extracted through the autocorrelation of a real seismic trace or can be generated from equations which have parameters that describe the frequency content of the wavelet. Two types are Ricker wavelets, generated directly in the time domain and Klauder wavelets, generated in the frequency domain.

The Ricker wavelet is defined only by its dominant frequency, i.e. the peak frequency of its amplitude spectrum or the inverse of the dominant period in the time domain (the dominant period is found approximately by measuring the time from trough to trough).

In this dissertation, for synthetic generation the wavelets are extracted using the method of White, R.E (1980), which gives estimates of uncertainly in the amplitude and phase spectra (see Appendix 5.3).

Assuming that each wavelet on a seismic trace is an actual reflection from one or more lithological boundaries is ideal and simplistic; this is because many of the wiggles on a trace are not true reflections, but noise. Seismic noise can be grouped in two categories: (1) random noise, which is uncorrelated from trace to trace and is due mainly to environmental factors, and (2) coherent noise, which is predictable on the seismic (multiples), and noise which is less predictable, such as shot-generated near surface waves.

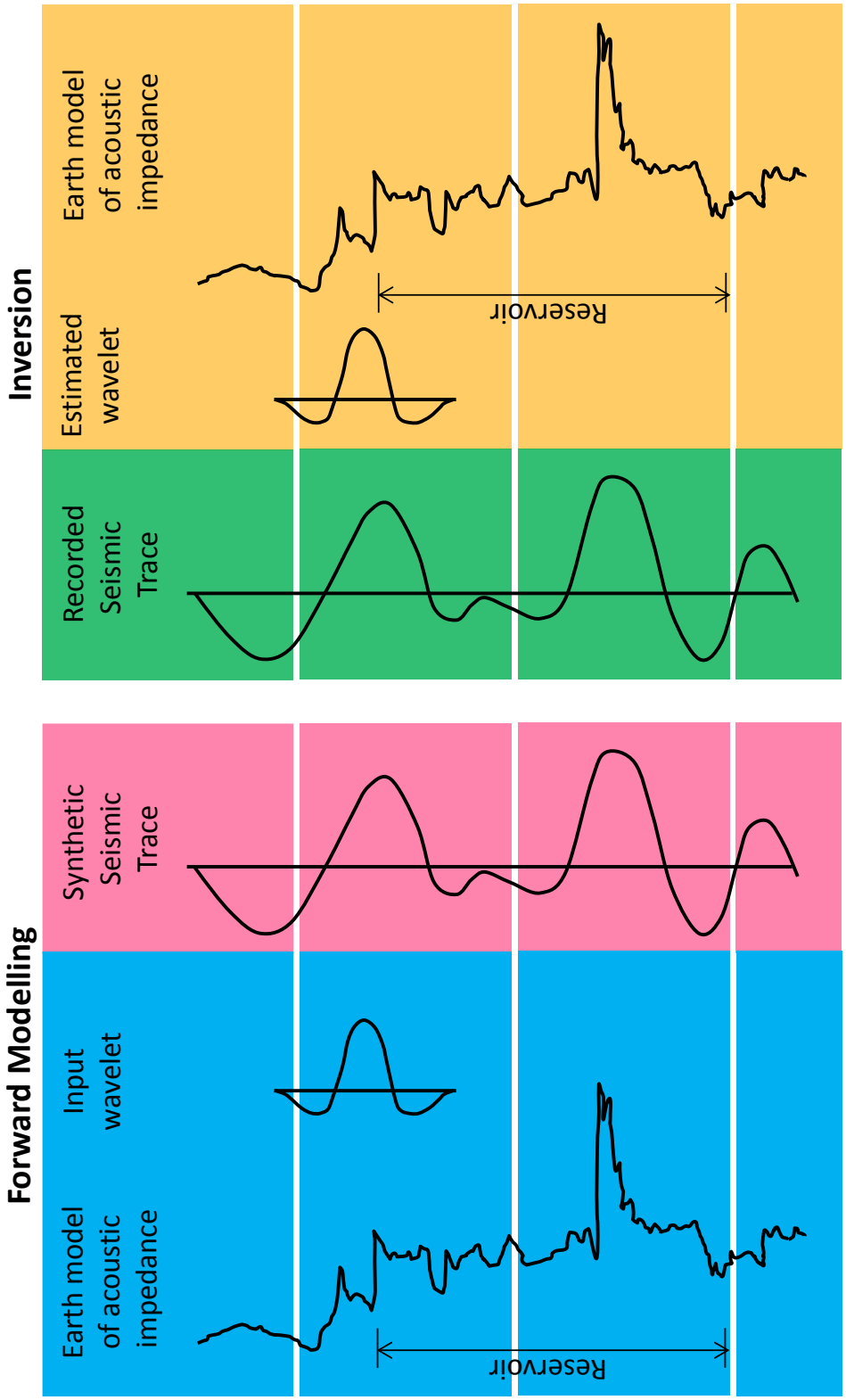

Figure 2.2.1: On the left, the common forward model for all inversions. Inversion model simply reverses the procedure (right side).

Rapid growth in technologies to characterize the reservoir, especially those related to seismic inversion techniques, has made it possible to pass from the analysis of reflection coefficients at acoustic interfaces to the analysis of elastic properties of formations (Avseth et al., 2005).

In seismic inversion there is no “one size fits all” approach. Each approach depends first of all on the available data and geological tasks.

(Filippova, K., et al, 2011) classified the seismic inversion technologies as follows:

(1) By the type of seismic data used for inversion (inversion of full stack seismic data or inversion of partial stack data).
(2) By the mathematical approach to the solution of the inverse problem: here we distinguish deterministic and geo-statistical approaches, which produce different levels of detail of estimated reservoir properties.

The classification above can be divided further into four major inversion techniques:

(a) Deterministic inversion of full stack seismic data
(b) Simultaneous deterministic partial stack inversion
(c) Geo-statistical inversion of full stack seismic data
(d) Simultaneous geo-statistical partial stack inversion

The inversion technique (b) applied in this study will be discussed in more detail in chapter V (see the workflow in figure 2.2.2).

2.3 Reservoir characterization techniques

2.3.1 AVO cross-plotting

Principles of AVO cross-plotting:

The variation in the amplitude of a seismic reflection with angle of incidence (AVO) depends on changes in velocity, density, and Poisson's ratio. AVO is often used as a hydrocarbon gas indicator because gas generally decreases Poisson’s ratio and often increases amplitude with incident angle/offset. However, other conditions can produce similar effects. The amplitude of an event is often plotted (see figure 2.3) against $\sin^2\vartheta$, where ϑ is incidence angle:

$$\mathrm{R}(\theta) = \mathrm{A} + \mathrm{B}\,\sin^2\theta$$

AVO cross-plots are a simple way of representing and to interpret amplitude-versus-offset data by cross-plotting AVO intercept (A) and gradient (B). Offset variations in amplitude for reflecting interfaces are represented as single points on a cross-plot.

Seismic reflections from gas sands can exhibit a wide range of amplitude-versus-offset (AVO) characteristics. A three-category classification based on AVO characteristics was

proposed by Rutherford and Williams, 1989 to describe the range of AVO effect that occurs at the top of gas sand. A fourth category was added by Castagna and Swan, 1997.

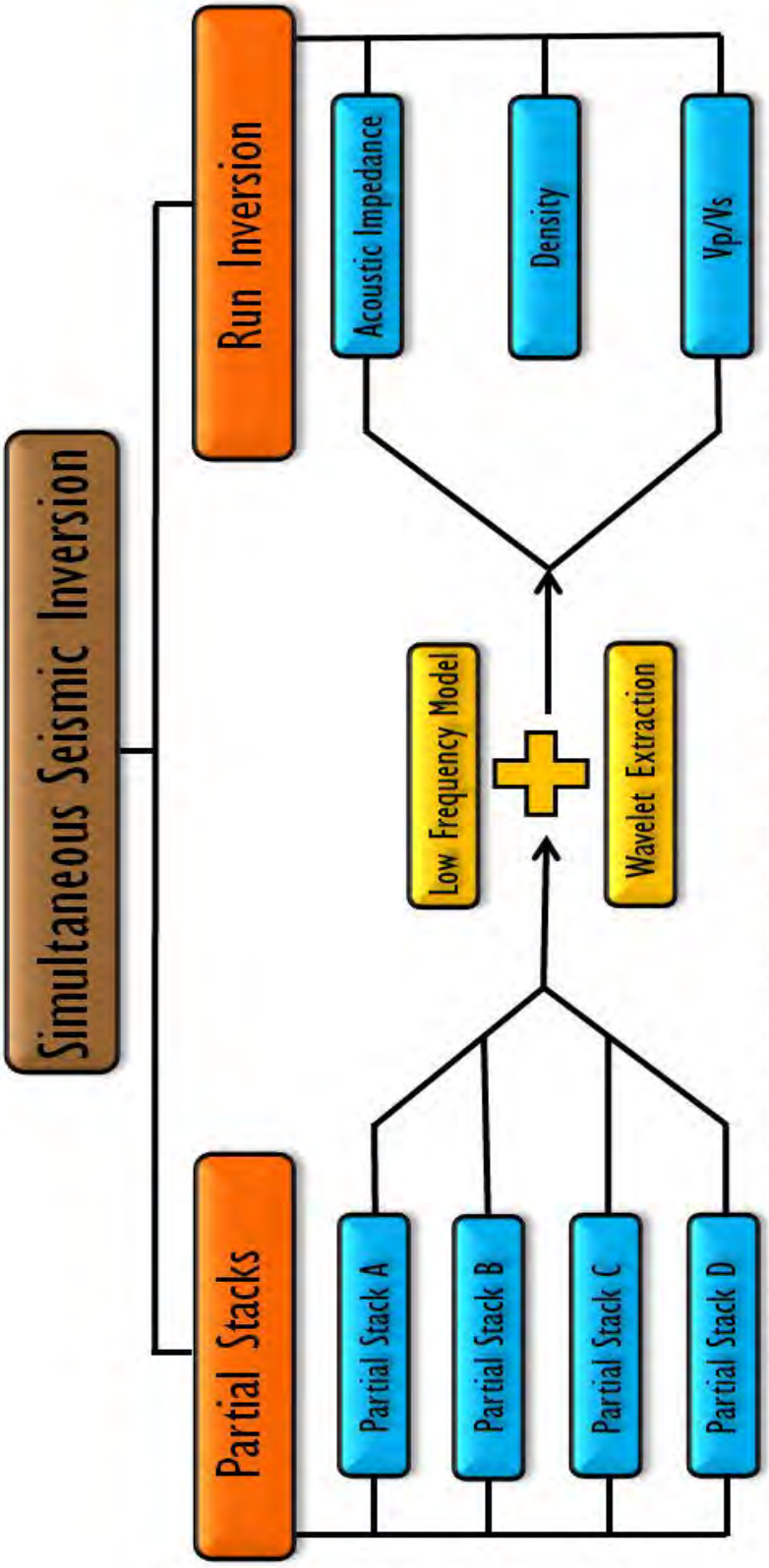

Figure 2.2.2: Simultaneous seismic inversion or AVO inversion method consisted on inverted partial stacks into elastic properties.

AVO classification:

Class I: reservoirs have higher impedance than the encasing shale with relatively large positive values for (A). The reflection coefficient of high-impedance sand is positive at zero offset and initially decreases in magnitude with offset.

Class II: reservoirs have nearly the same impedance as the encasing shale and are characterized by values of (A) near zero. The negative gradients associated with Class II sands are generally similar in magnitude to those for Class I sands (Rutherford and Williams, 1989). Class II is split in 2-sub categories based on the sign of the intercept value. If the intercept is a positive value near to zero it is Class IIp and if the intercept is a negative value near to zero it is called Class II by definition.

Class III: reservoirs have lower impedance than the encasing shale with negative, values for (A). The reflection coefficient of low-impedance sand is negative at zero offset and initially increases in magnitude with offset (Rutherford and Williams, 1989).

Class IV: This category was proposed by Castagna and represented by very low impedance gas sands for which the magnitude of the negative reflection coefficients decrease with increasing offset.

The reflection of the top of the gas sand of interest is classified (AVO response) depending on its position on an A versus B plane. Once identified the background trend (dashed line, see fig. 2.3) using well data, the top of gas sand reflections should plot below the background trend (Castagna and Swan, 1997).

Geobody extraction process:

A geobody is commonly defined as a 3D object extracted from a seismic volume. A geobody can be build up by repeatedly extracting several sub elements (Geoblobs).

Often the seismic anomalies (3D objects) that need to be isolated for further interpretation are located in a limited portion of the whole seismic volume. Hence, the seismic volume is cropped to the area of interest to enhance the performance on graphics cards and to optimize the CPU memory. The portion of seismic volume thus selected is called a “window”.

A window can be generated by cropping spatially the seismic volume constrained to a particular geometry or survey. There are 3 types of probes based on the geometry:

- Box window
- Well window
- Horizon/surface window

Box probe: The box window is a rectangular volume that can be resized and tilted. This window uses any available seismic volume survey as constraint to build the window.

Well window: The well window is a cylindrical volume following a well path that can be resized and prolonged.

Horizon/surface window: The horizon window is an irregular window that follows one or two horizon interpretations/surfaces. It is also referred to as “sculpting” in the industry.

The window can be manipulated to re-orient and reduce its size (similar to cropping a volume).

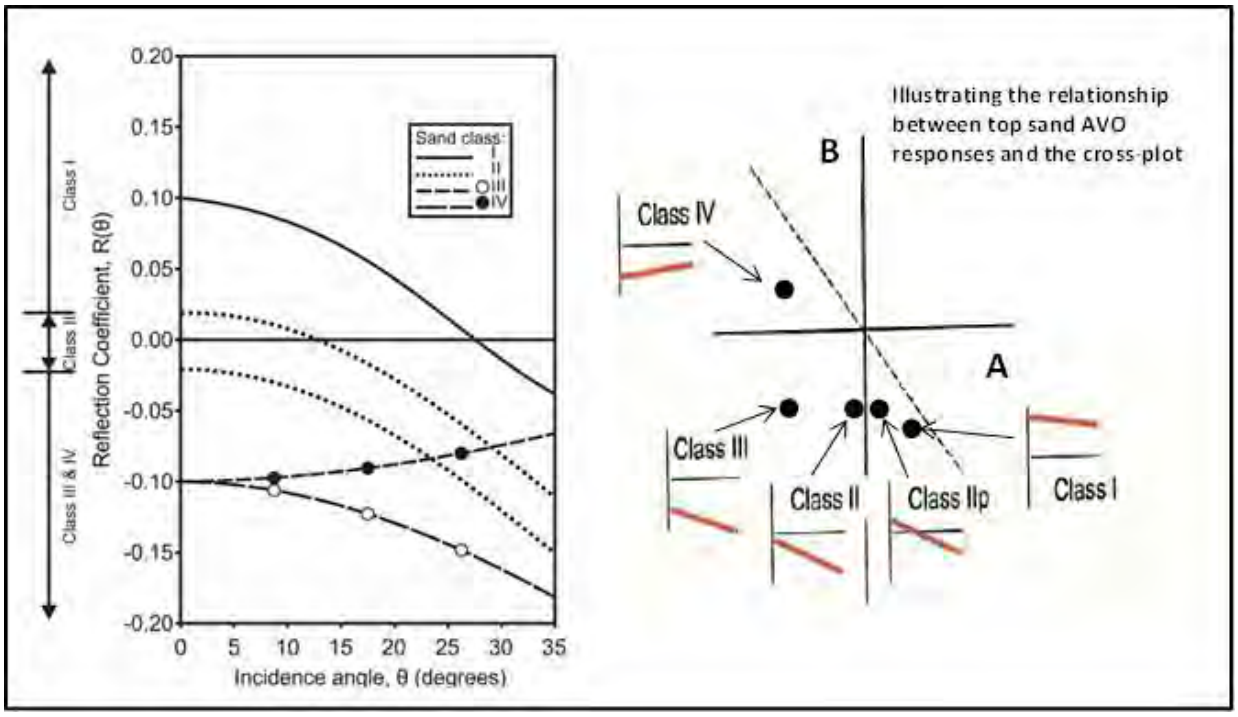

Figure 2.3: Amplitude variation with angle. The common three-category classification developed by Rutherford-Williams (1989) classification (q.v.) including a fourth category by (Castagna and Swan, 1998). Offset variations with amplitude are represented as single points on a cross-plot of intercept (A) and gradient (B). Modified from Simm, et al; 2000).

2.3.2 Statistical background

Probability Density Functions (PDFs):

A probability density function (PDF), is a function that describes the relative likelihood for a random variable to take on a given value.

The probability density function (PDF) of a continuous random variable X with support S is an integrable function f(x) satisfying the following:

(1) f(x) is positive everywhere in the support S, that is, f(x)>0, for all x in S

(2) The area under the curve f(x) in the support S is 1, that is:

$$\int_S f(x)dx = 1$$

(3) If f(x) is the PDF of x, then the probability that x belongs to A, where A is some interval, is given by the integral of f(x) over that interval, that is:

$$P(X \in A) = \int_A f(x)dx$$

Extracted from PennState, Eberly College of Science, Probability Theory and Mathematical Statistics, (STAT 414/415).

Bayesian theorem:

Bayes' theorem is a theorem of probability theory originally stated by the Reverend Thomas Bayes. It can be seen as a way of understanding how the probability that a theory is true is affected by a new piece of evidence.

Bayes' theorem is stated mathematically as the following equation:

$$P(A|B) = \frac{P(B|A)P(A)}{P(B)}$$

Here A and B are events,

P(A) and P(B) are the probabilities of A and B, and

P(A|B), the conditional probability, is the probability of A given B is true (Bayes and Price, 1763).

2.3.3 EEI illumination

Elastic Impedance (EI):

Post-stack inversion should not be applied to data with AVO effects, since changes in Vp/Vs are not explicitly accounted for. To extend the inversion to handle AVO data, algorithms like simultaneous seismic inversion (SSI) and Elastic impedance (EI) are used. The first will be addressed in chapter V and the latter is the foundation of EEI illumination.

The elastic impedance concept was originally developed by Connolly (1999). In contrast to the traditional AVO analysis, he formulated an elastic impedance approach where angle stacks for a range of incidence angles are inverted. He started with the Aki-Richards, 1980 equation which relates reflection amplitude to incidence angle:

$$R(\theta) = A + B\sin^2\theta + C\sin^2\theta\tan^2\theta$$

Where: $A = \frac{1}{2}\left[\frac{\Delta Vp}{Vp} + \frac{\Delta\rho}{\rho}\right]$ = intercept,

$$B = \frac{1}{2}\frac{\Delta Vp}{Vp} - 4\left[\frac{Vs}{Vp}\right]^2\frac{\Delta Vs}{Vs} - 2\left[\frac{Vs}{Vp}\right]^2\frac{\Delta\rho}{\rho}$$ = gradient,

$$C = \frac{1}{2}\left[\frac{\Delta Vp}{Vp}\right]$$ = curvature

For the zero-offset case:

$$R(\theta) = A = \frac{1}{2}\left[\frac{\Delta Vp}{Vp} + \frac{\Delta \rho}{\rho}\right] \approx \frac{1}{2}\frac{\Delta AI}{AI} \approx \frac{1}{2}\Delta \ln(AI)$$

By analogy, Connolly defined a new type of impedance such that:

$$R(\theta) \approx \frac{1}{2}\frac{\Delta EI}{EI} \approx \frac{1}{2}\Delta \ln(EI)$$

By mathematical manipulation, he showed that:

$$EI(\theta) = Vp^{(1+\tan^2\theta)} Vs^{(-8K\sin^2\theta)} \rho^{(1-4K\sin^2\theta)}$$

Where $K = \frac{Vs^2}{Vp^2}$

(Connolly, P., 1999)

Elastic impedance (EI) is a generalization of acoustic impedance for variable incidence angle. The key issue with EI is that it has strange units and dimensions and the values do not scale correctly for different angles (Whitcombe, 2002).

The Elastic Impedance (EI) method uses angle stacks for a range of incidence angles for the inversion. This approach to inversion also lets one use a different wavelet for each angle range (so the inversion becomes more accurate than using one wavelet for all angles in stacked data).

Extended Elastic Impedance (EEI):

Conventional EI is defined as a function of the reflection angle θ. Although EI is only valid as a model to predict recorded prestack seismic data over the 0-30° angle range, it is defined mathematically over a 0-90° angle range. Whitcombe et. al. (2000) extended conventional EI so that it is defined for all values of $\sin^2\theta$ between positive and negative infinity. This was achieved by replacing $\sin^2\theta$ with $\tan\chi$. The variable is now a new function called χ (chi angle or project angle) which varies between -90 to +90 degrees. The seismic data corresponding to EEI at a given χ angle can be constructed by performing a sample-by-sample linear projection of the recorded prestack amplitudes in $\sin^2\theta$.

Whitcombe et. Al. (2000) introduced Extended Elastic Impedance, EEI, as:

$$EEI(\chi) = [\alpha^p * \beta^q * \rho^r]$$

Where: $p = (\cos\chi + \sin\chi)$

$q = -8K\sin\chi$

$r = (\cos\chi - 4K\sin\chi)$

and K is a constant, usually set to the average value of $(\beta/\alpha)^2$ over the log interval of interest.

In Extended Elastic Impedance, the curvature term of the Aki-Richards equation was dropped.

χ and θ are related (Simm et. al., 2002) by the relationship:

$$\tan\chi = \sin^2\theta$$

Whitcombe (2002) refined the definition of EI to remove the dependence of its dimensionality on the angle θ, by using the normalization constants α_o, β_o, ρ_o, which are set to average values. This normalization can also be applied to EEI:

$$EI(\theta) = \alpha_0\rho_0 \left[\left(\frac{\alpha}{\alpha_0}\right)^p * \left(\frac{\beta}{\beta_0}\right)^q * \left(\frac{\rho}{\rho_0}\right)^r\right]$$

Gradient impedance is now the value of EEI at χ = 90 degrees. At this angle the exponents are:

p = 1

q = -8K

r = -4K

Chapter 3: Dataset and Geological Model

3.1 Geological Framework

The F-O field is located offshore South Africa, about 150 kms from Mossel Bay offshore in the Bredasdorp Basin (Fig 3.1.1). It was discovered in 1989 as a dry gas accumulation in an over-pressured very tight sandstone reservoir, and is characterized by low porosity (average: 9%) and low permeability (0.1 mD to 20 mD, av. 1 mD). The F-O structure was drilled by 6 vertical exploration and appraisal wells (F-O1, F-O2, F-O3, F-O4, F-O6 and F-O8) and there are another 3 wells in the vicinity of the structure (F-R1, F-S1 and F-J1). A gas-water contact at -3794m true vertical depth sub-sea (TVDSS) was identified only in F-O4. See Table 3.1.

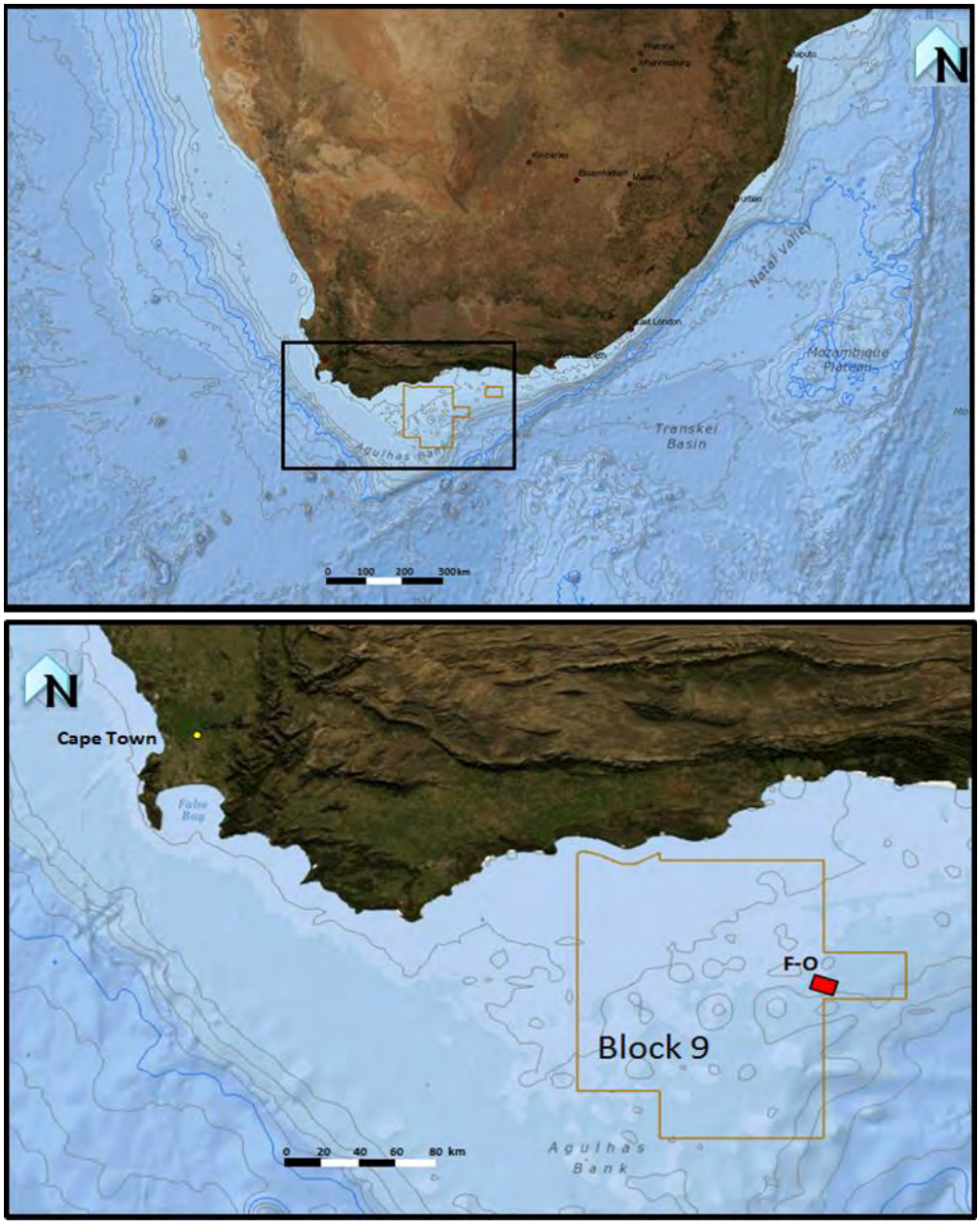

Figure 3.1.1: F-O Field general location map.

F-O is classified as a tight gas field. Tight is the term commonly used to refer to a low permeability reservoir. Many of the low permeability reservoirs worldwide that have been developed are sandstones, but significant quantities of gas are also produced from low permeability carbonates, shales and coal seams.

The F-O reservoir is in the diachronous synrift deposit of the upper shallow marine (USM) Sandstone (Valanginian) which is defined by the Top Upper Shallow Marine (TUSM) and the Base Upper Shallow Marine (BUSM) horizons. The USM varied in thickness between 66 - 153m in the wells drilled and represents a generally southward prograding marine clastic sequence sandwiched between continental deposits below and deep marine shales above.

The USM is overlain by the transgressive, deep-water Low Velocity Shale (LVS), in approximately the middle of which there is thought to be a regional unconformity (1At1). Over the FO field, however, TUSM coincides with 1At1 because of erosion. Figure 3.1.2 summarises the stratigraphy of the Bredasdorp Basin).

An extensive petrographic analysis over the F-O field by Hill (1994) shows that the main factor that controls reservoir quality is the abundant presence of intergranular clays (both detrital and authigenic). Clean, well-sorted sandstones, deposited under high-energy conditions, have the best quality, with all porosities (primary, secondary and micro-porosity) preserved. Porosity preservation in those sandstones was made possible by early calcite cementation and grain coating of chlorite. Sandstones deposited under lower energy conditions are generally more finely grained, less well sorted and more argillaceous than those deposited under high-energy conditions.

The Bredasdorp Basin was initiated during Late Jurassic rifting (major break-up of Gondwana), being affected by strike-slip movements related to the Agulhas-Falkland transform fault. In the context of the Agulhas/Falkland Fracture Zone (dextral strike-slip) activity, extensional faults are part of the suite of structures which were developed in the F-O field. Due to the Agulhas-Falkland Fracture Zone (AFFZ) activation, the stress field was re-oriented near the strike-slip fault, producing deformation of the pre-existing structures and possible local uplifts.

The F-O main structure is known to be only partly dip-closed. Fault sealing by a major east-west fault occurs along its northern margin probably due to fault gouge and/or cementation because this northern fault only partially displaces the reservoir. Many NW-SE trending faults also occur within the structural closure (see fig. 3.1.3).

The FO field is heavily faulted, and a limited number of these faults have cut into the LVS above. There is little evidence of faults extending through to the shallow section as far as 13At1 (see fig. 3.1.4).

The USM reservoir thickens markedly into the northern boundary fault and also into a north-south fault along the western flank of the main field. (PGS-Report, 2001)

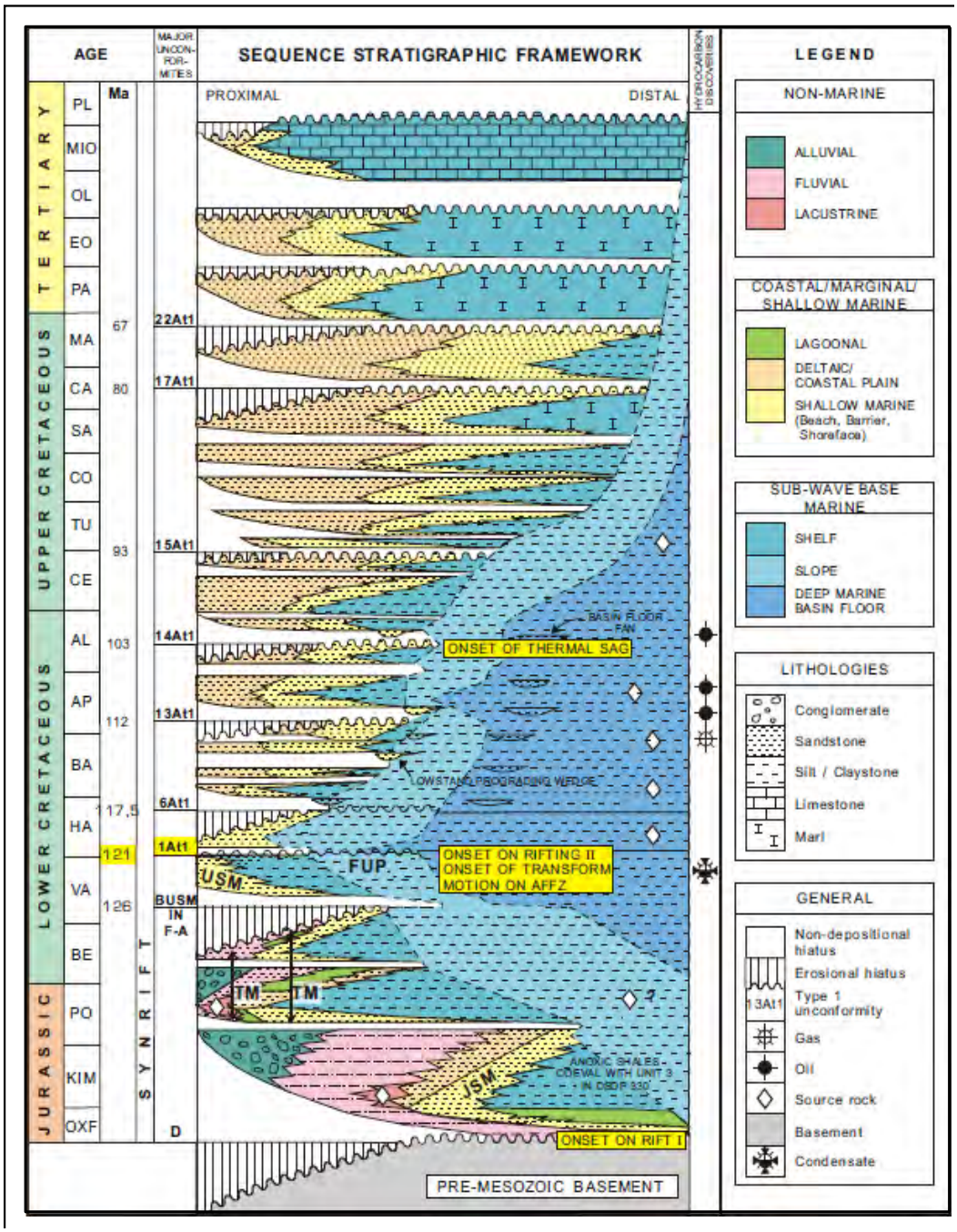

Figure 3.1.2: Summary stratigraphy, Bredasdorp Basin (after Jungslager,1996)

A smaller dip-fault closure (the F-O West structure) occurs 5 km west of the main field and similarly depends on sealing along the same northern fault as the main field (PGS Report, 2001) (see fig. 3.1.5).

The marker correlations are based on interpreted logs considering the gamma ray (GR) log shapes (coarsening-upwards (C-U) and fining-upwards (F-U) successions). These, with the identified para-sequence sets, allowed the reservoir to be divided into several zones (Zones A-G in upward order), which are different from those defined by Higgs (2007) mainly on the basis of the number of correlatable markers from log, biostratigraphy (only USM and 1At1) and dipmeter data (Robles, 2009) (see fig. 3.1.6 and Table 3.1.2).

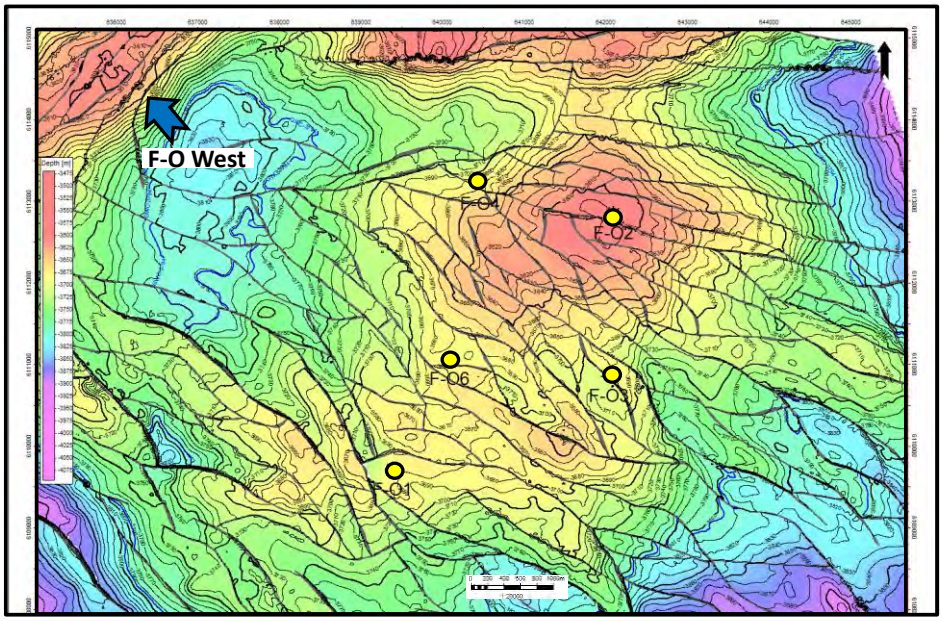

Figure 3.1.3: The top reservoir (TUSM) depth map illustrating the five well locations. A major fault system provides trap seal along their northern flanks.

3.2 Seismic data acquisition

A 3D survey based on deep interpolated streamer coverage (DISCover) of approximately 662 km² was acquired in 2011 offshore South Africa. The survey was conducted over Block 9 F-O, which is situated approximately 150 km SSW of Mossel Bay. Water depths were from 100 to 200 metres. The survey had a nominal 27 km average line length and was done in the E-W direction.

The field configuration was the following; 7 x 6000 m over streamers, 3x6000m (active length) under streamers. Over-streamer separation is 100 m at 8m depth, under-streamer separation is 233 m at 20 m depth. A dual source (flip flop) with a volume of 5085 cu in at 7m depth was used. The record length for this survey is 7 seconds and the shot point interval is 18,75 m (see fig. 3.2.1).

DISCover (Deep Interpolated Streamer Coverage) is a technique based on 3D over/under towed-streamer acquisition. The technique is designed to enhance bandwidth, providing increases in both low frequencies for deeper penetration and high frequencies for improved resolution. Therefore, it improves both geological mapping and the quality of any inversion for rock properties performed on the data.

The acquisition geometry and processing sequence can be found in appendix 3.2.

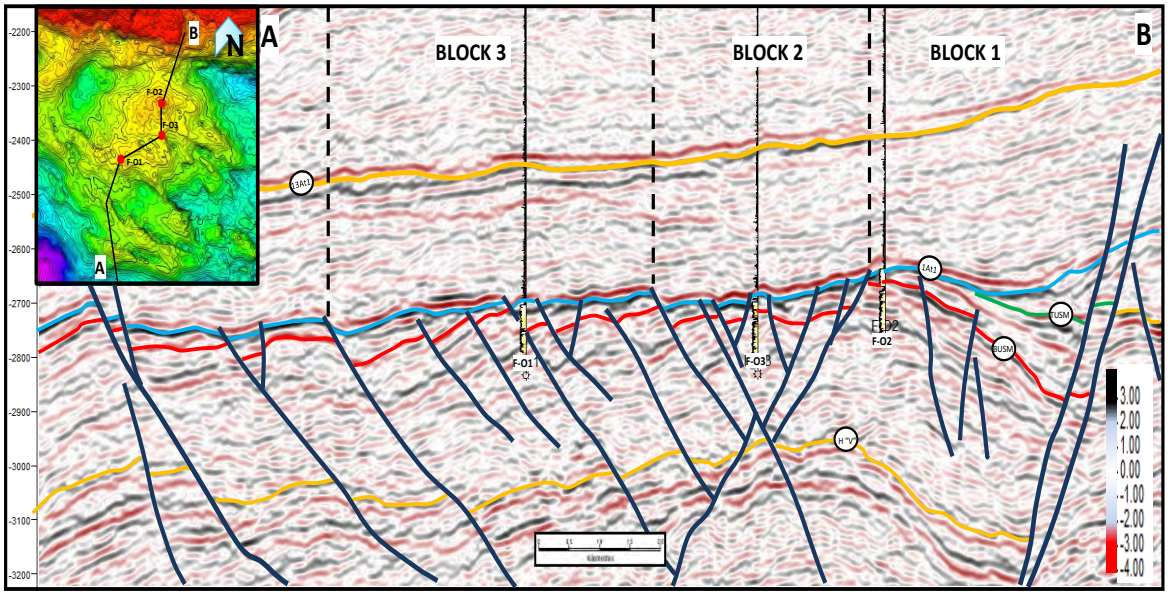

Figure 3.1.4: A longitudinal seismic line across the structural crest of F-O Field. Note the crestal erosion of the USM reservoir. The top of upper shallow marine (TUSM) is defined by the 1At1 seismic horizon. The BUSM is poorly defined seismically. Note also the USM thickening into the northern boundary fault which does not entirely displace the reservoir and therefore infers fault gouge, clay smear or diagenetic sealing along the fault.

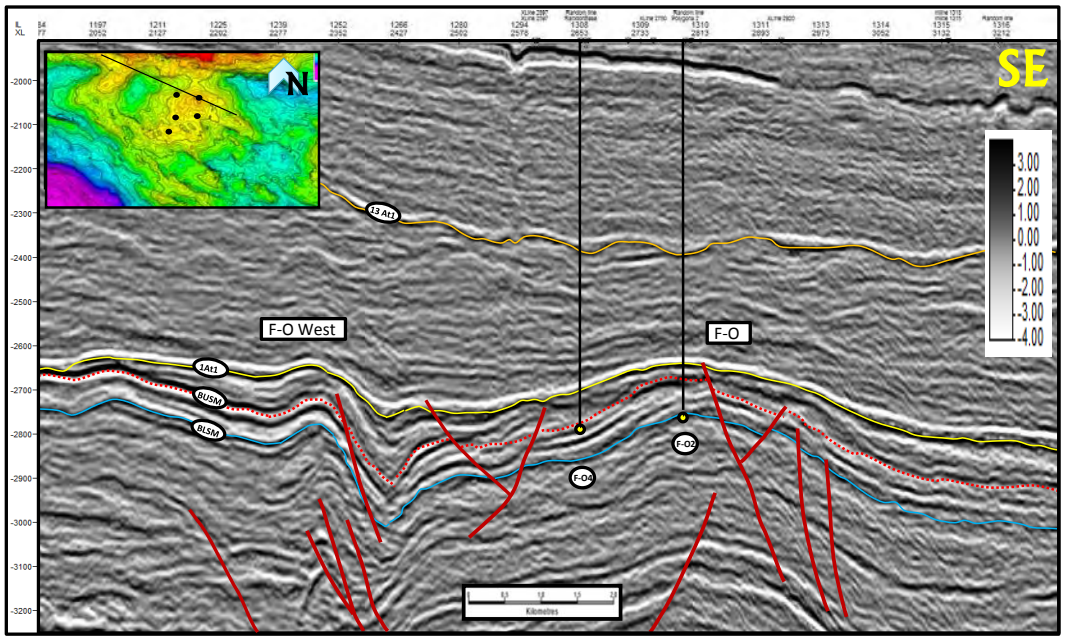

Figure 3.1.5: A transversal seismic line extending from F-O Main Field to F-O West structure. Note the total pinch-out of the USM to the extreme west.

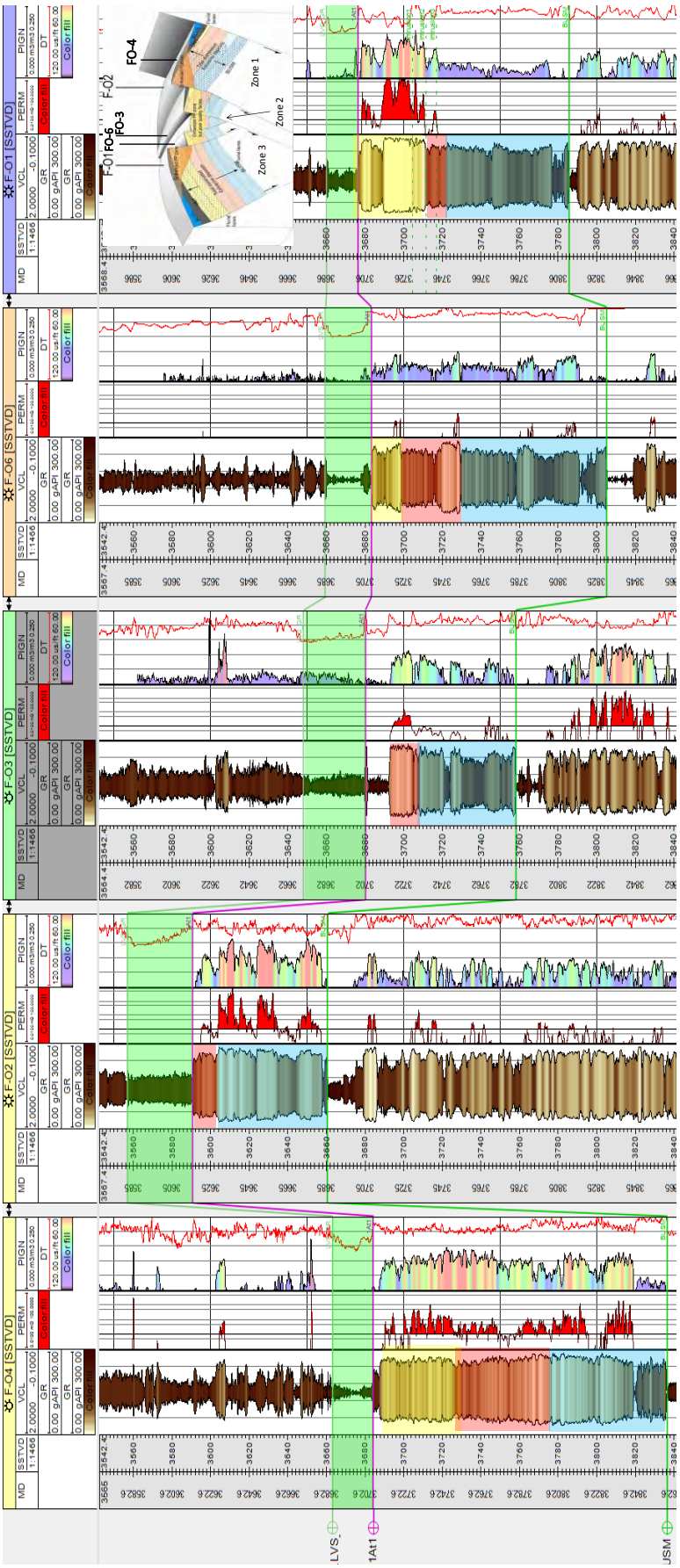

Figure 3.1.6: Roger Higgs' correlation modified by Robles,G.,(2009) and schematic block diagram with conceptual model.

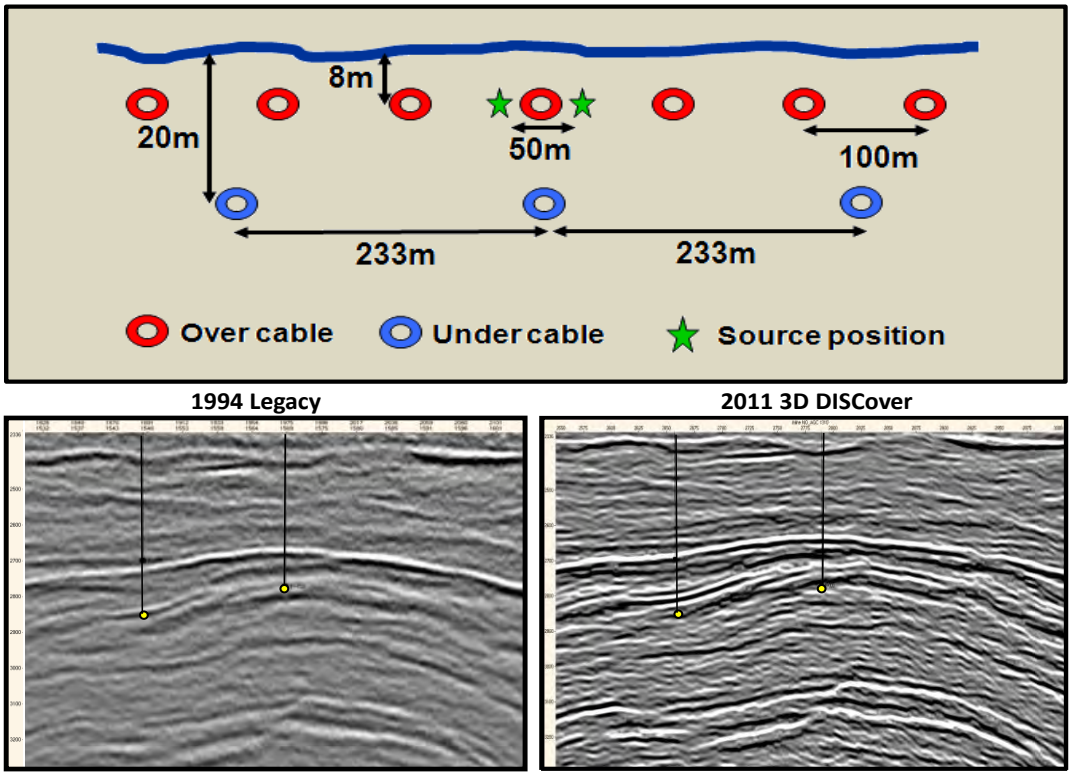

Figure 3.2.1: Acquisition parameters used (7 shallow cables at 8-m depth and 100-m separation and 2 deeper cables at 20-m depth and 233-m separation) in F-O field on the top. On the bottom, a comparative section between legacy vs DISCover survey. DISCover survey delivers enhanced continuity and much clearer large & small-scale features on seismic section, that cannot be clearly seen on conventional seismic (legacy).

3.3 Well Data

Six wells have been drilled in the field to date (F-O1, F-O2, F-O3, F-O4, F-O6 and F-O8). F-O8 was not considered for this study since it was very close to F-O1 (150 metres apart).

Conventional open-hole wireline logs were run across the reservoir section in all six wells. The main measurements acquired in all wells include (Table 3.3.1):

· Gamma ray, caliper, spontaneous potential

· Porosity logs: density, neutron, sonic

· Resistivity logs: dual laterolog, micro-spherically-focussed log (MSFL)

Of the following wells, additional log measurements were acquired across the reservoir:

· F-O1 – Deep induction, micro-spherically focused log (MSFL)

· F-O4 – Combinable magnetic resonance tool (CMR)

A formation micro-imager (FMI) tool was run in the vertical well F-O6, (8.5 inch section) over the interval 3100 to 3836 mMD

Conventional cores were cut in the reservoir in all wells for routine (grain density, fluid saturation, etc) and special core analysis (porosity and permeability at ambient and overburden conditions, resistivity index (RI) and air-water capillary pressure).

3.4 Seismic interpretation data

An extensive structural interpretation was performed on the area of interest using full stack 3D data (Table 3.4.1). Ten key horizons in total, from top to bottom (seabed, ref horizon, 22At1, 17At1, 16Bt1, 16At1, 13At1, 1At1, BUSM and BLSM) were interpreted to achieve three main goals; (1) velocity model and time-depth conversion, (2) reservoir structure definition and (3) seismic inversion. This dissertation will focus on goals two and three, for which only the last four horizons (13At1, 1At1, BUSM and BLSM) were used (Fig 3.4.1).

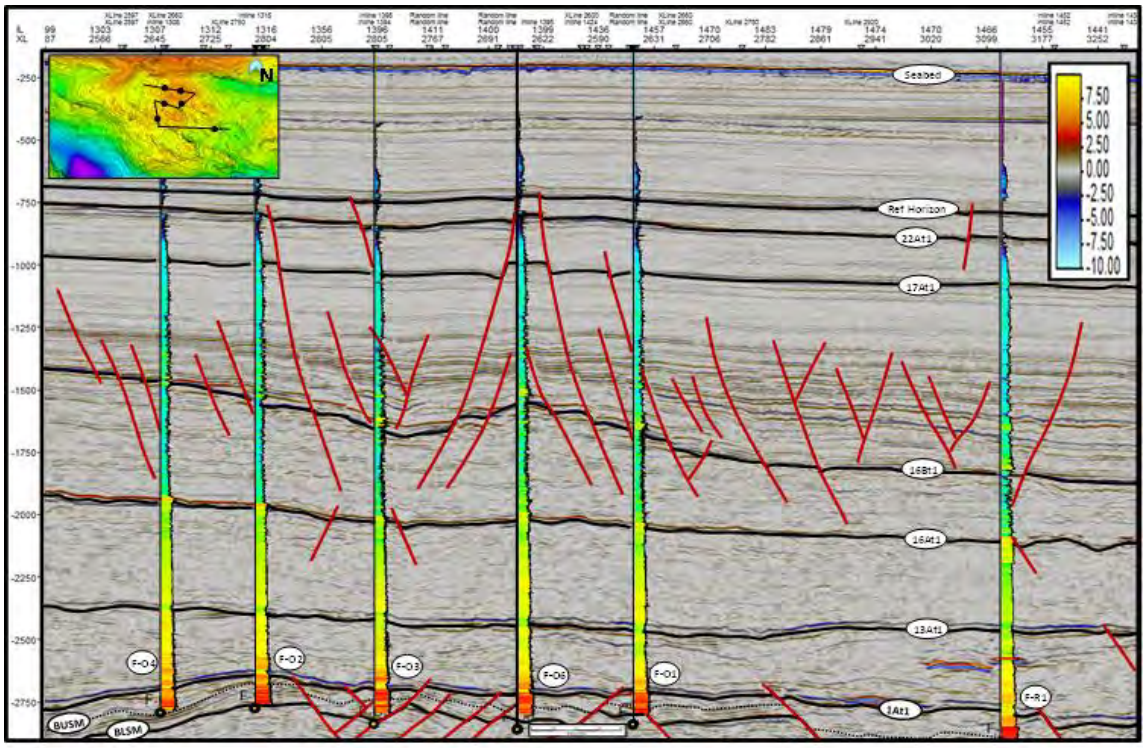

Figure 3.4.1: Horizons interpreted show a fair-to-good continuity reflector along the area of interest. The reservoir section thins over the crest of the structure as a result of erosion at the 1At1 unconformity. Above 1At1 shows variable thickness: local thinning and thickening. From 16At1 to 17At1, faulting resulted due to the gravitational forces affecting the paleo-slope combined with mechanical compaction of sediments (and dewatering of fine grained sediments), producing a polygonal fault pattern. The well logs are velocity logs.

Seismic-to-well ties for the six F-O field wells were conducted to establish the correspondence between seismic and well data. Most geological boundaries of interest are represented in the seismic as strong and continuous reflections, so the wells exhibit a mostly good well-seismic tie along the geological section (fig 3.4.2-3.4.8).

The 1At1 geological marker is an unconformity that represent the top of the reservoir at the F-O field, and its match with seismic varies between a peak and zero crossing seismic event on the synthetic seismogram of each well. The reflection is caused by the increase in impedance at the interface between low-velocity shale and USM, but this response is not always as simple as expected, owing to a combination of variables that compete to influence the seismic response (low velocity shale thickness, porosity, gas charge etc.). In chapter 4, a more extensive discussion of this behaviour is presented (see fig 3.4.9).

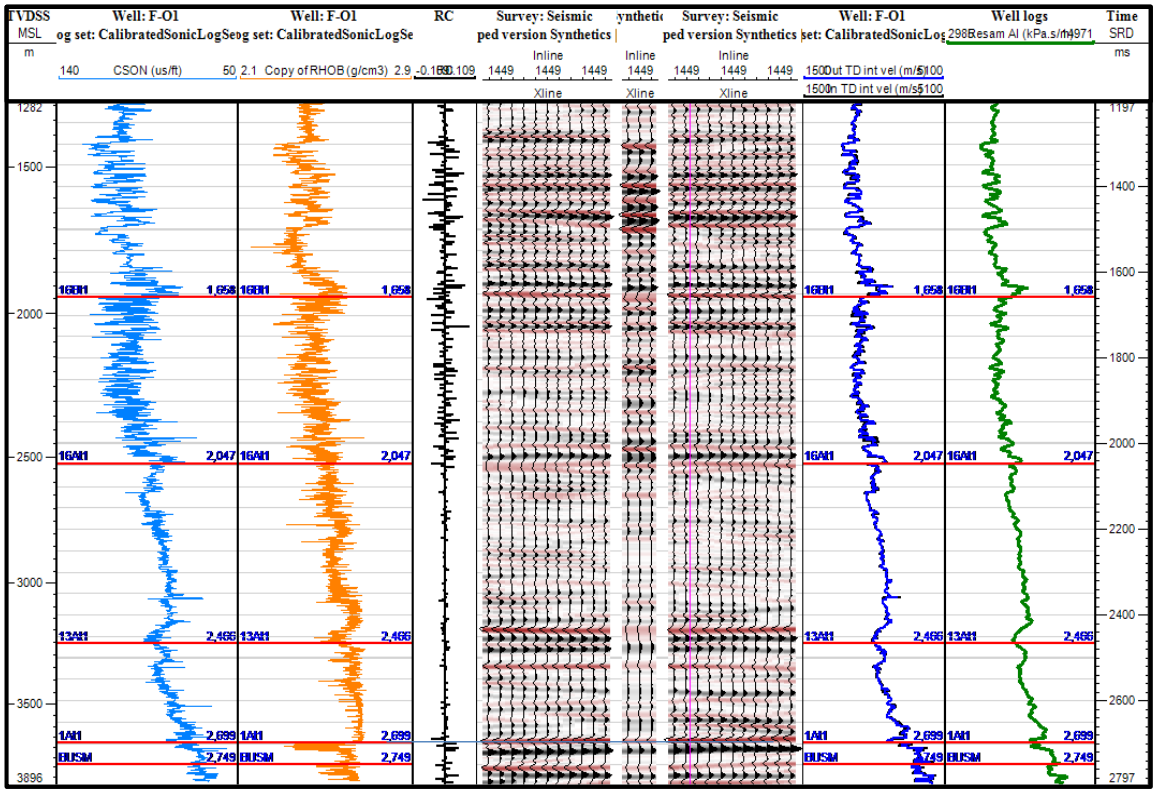

Figure 3.4.2: Well seismic tie at well F-O1.

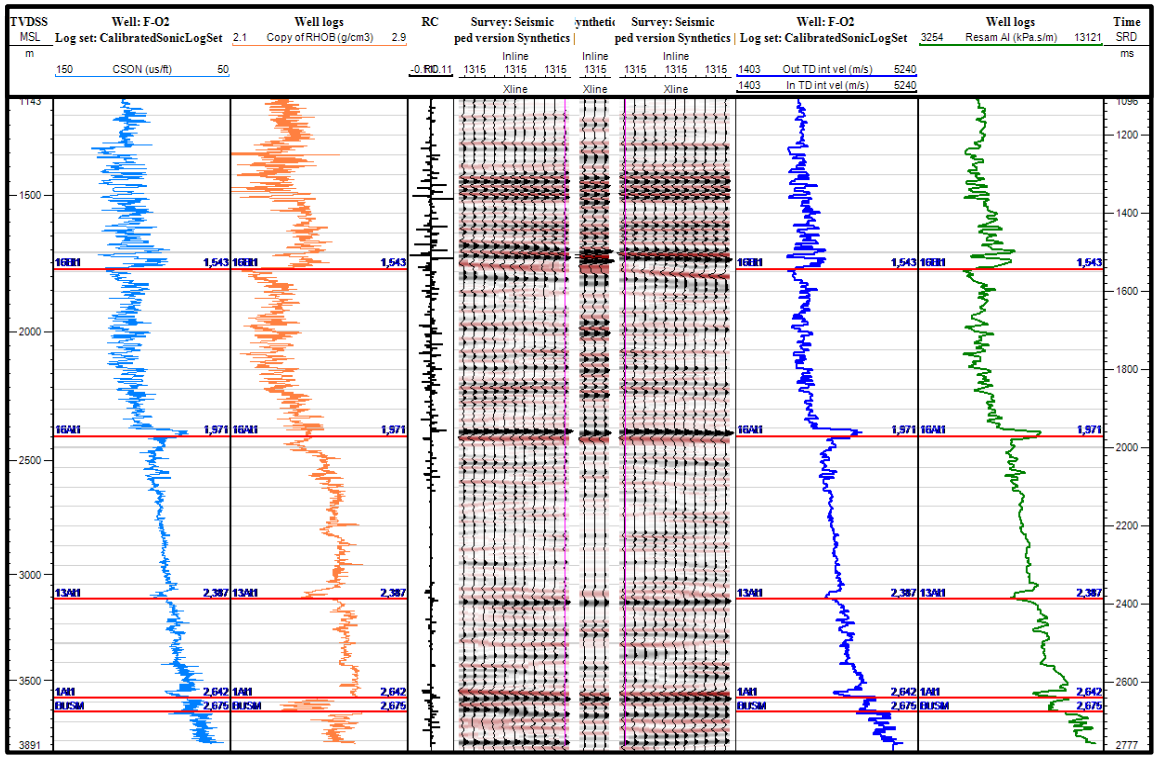

Figure 3.4.3: Well seismic tie at well F-O2.

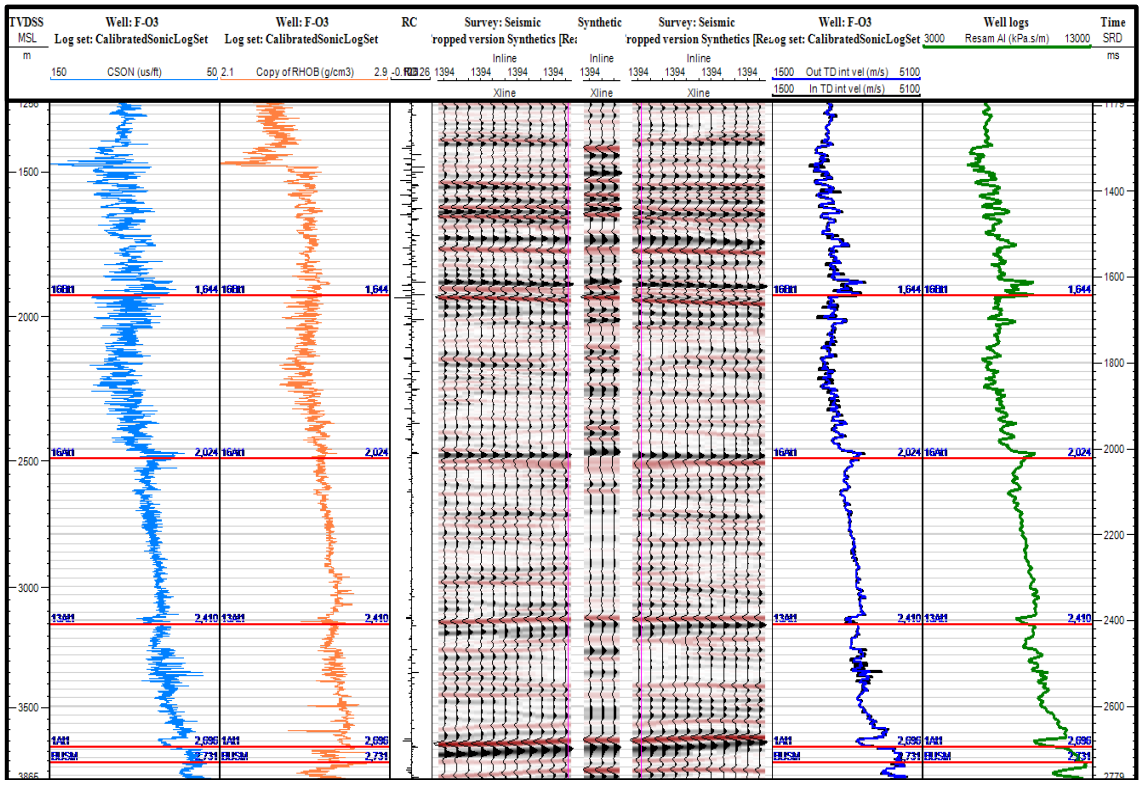

Figure 3.4.4: Well seismic tie at well F-O3.

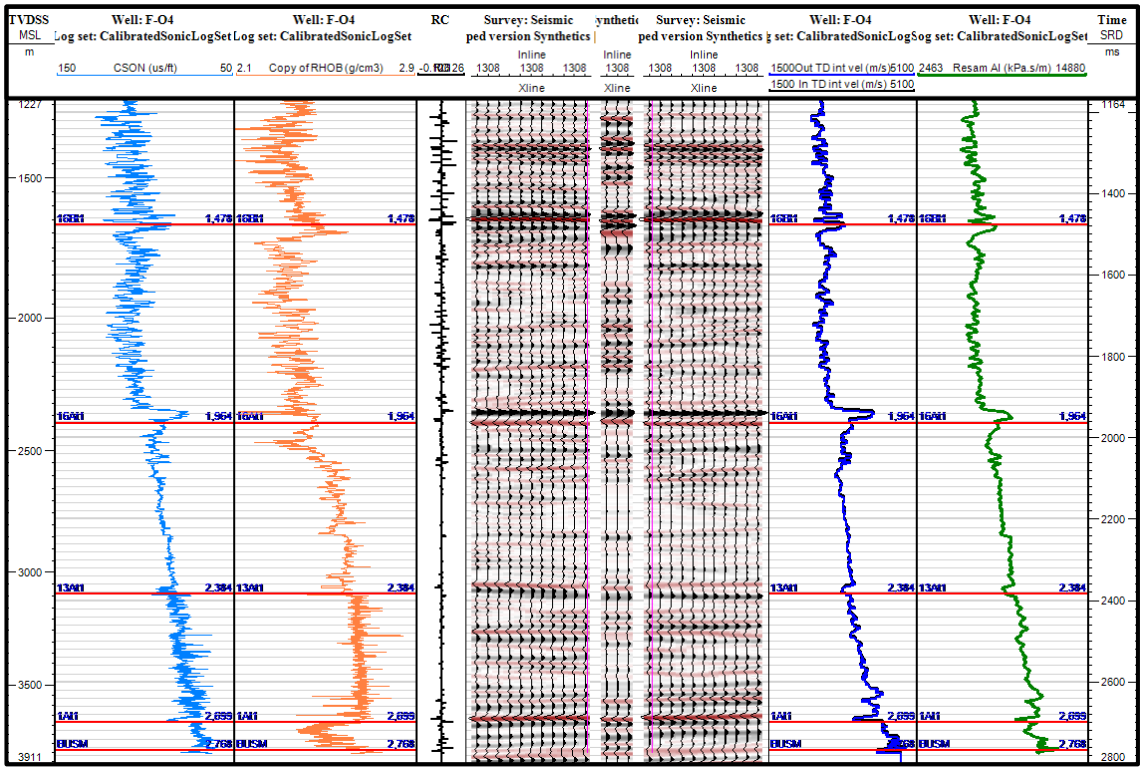

Figure 3.4.5: Well seismic tie at well F-O4.

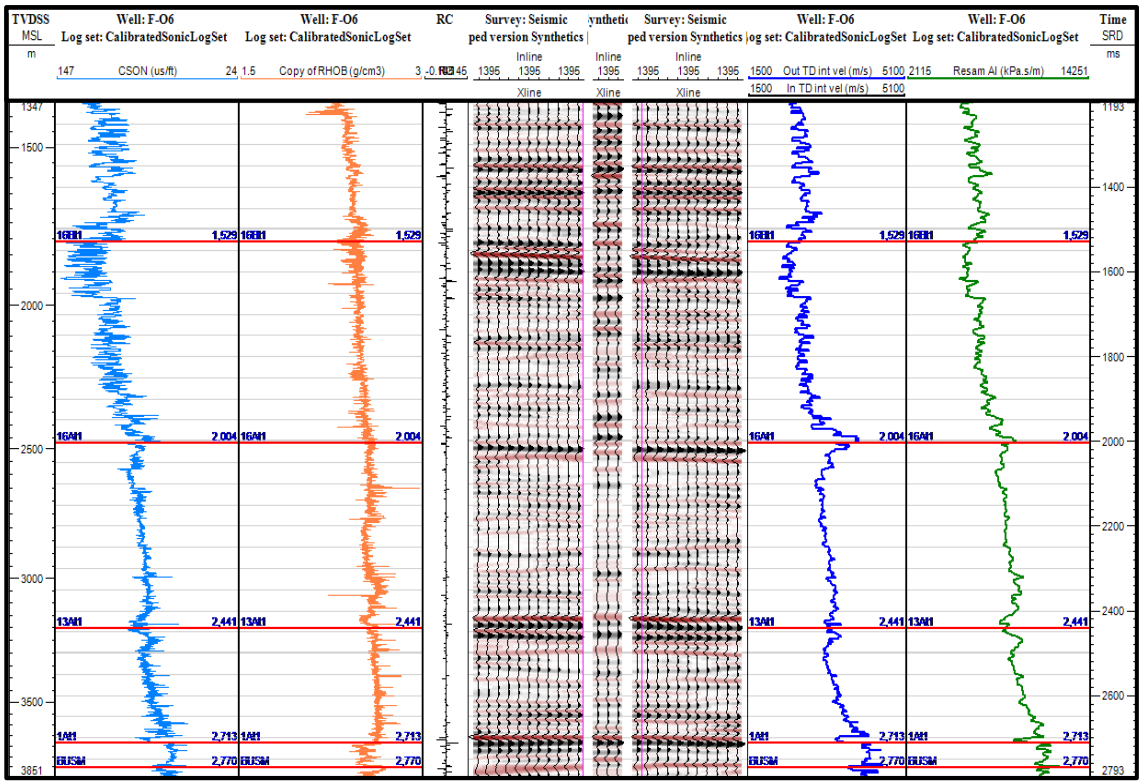

Figure 3.4.6: Well seismic tie at well F-O6.

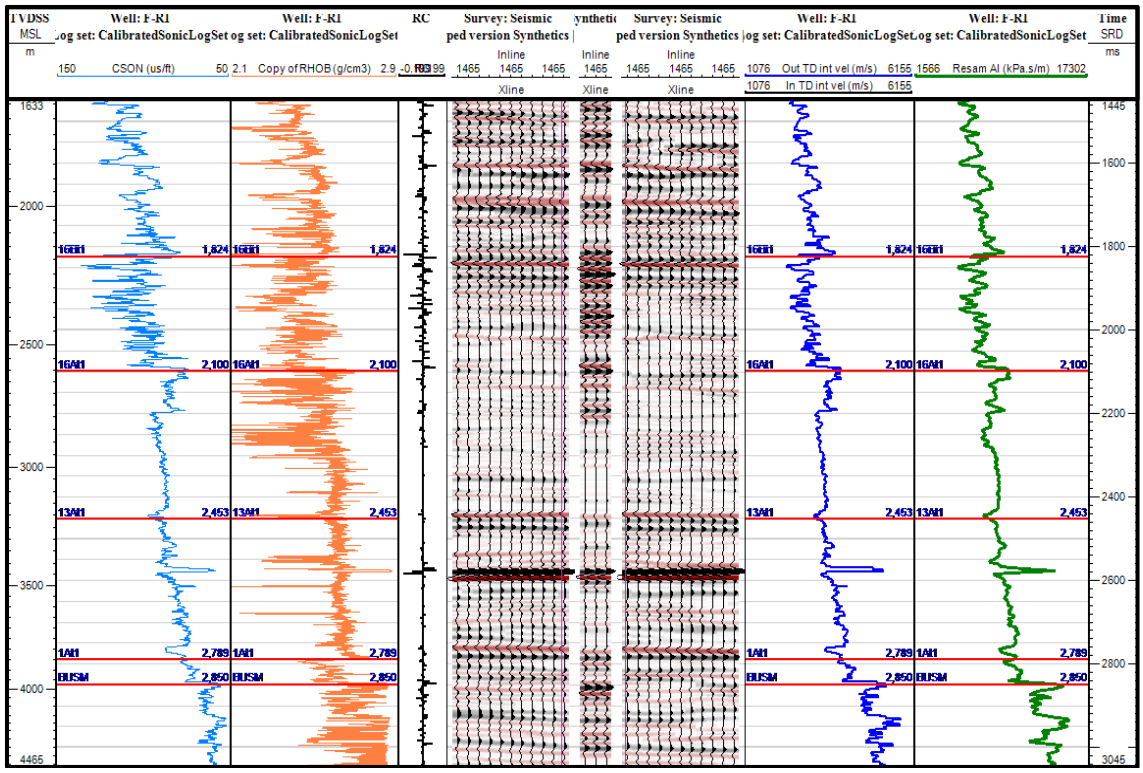

Figure 3.4.7: Well seismic tie at well F-R1.

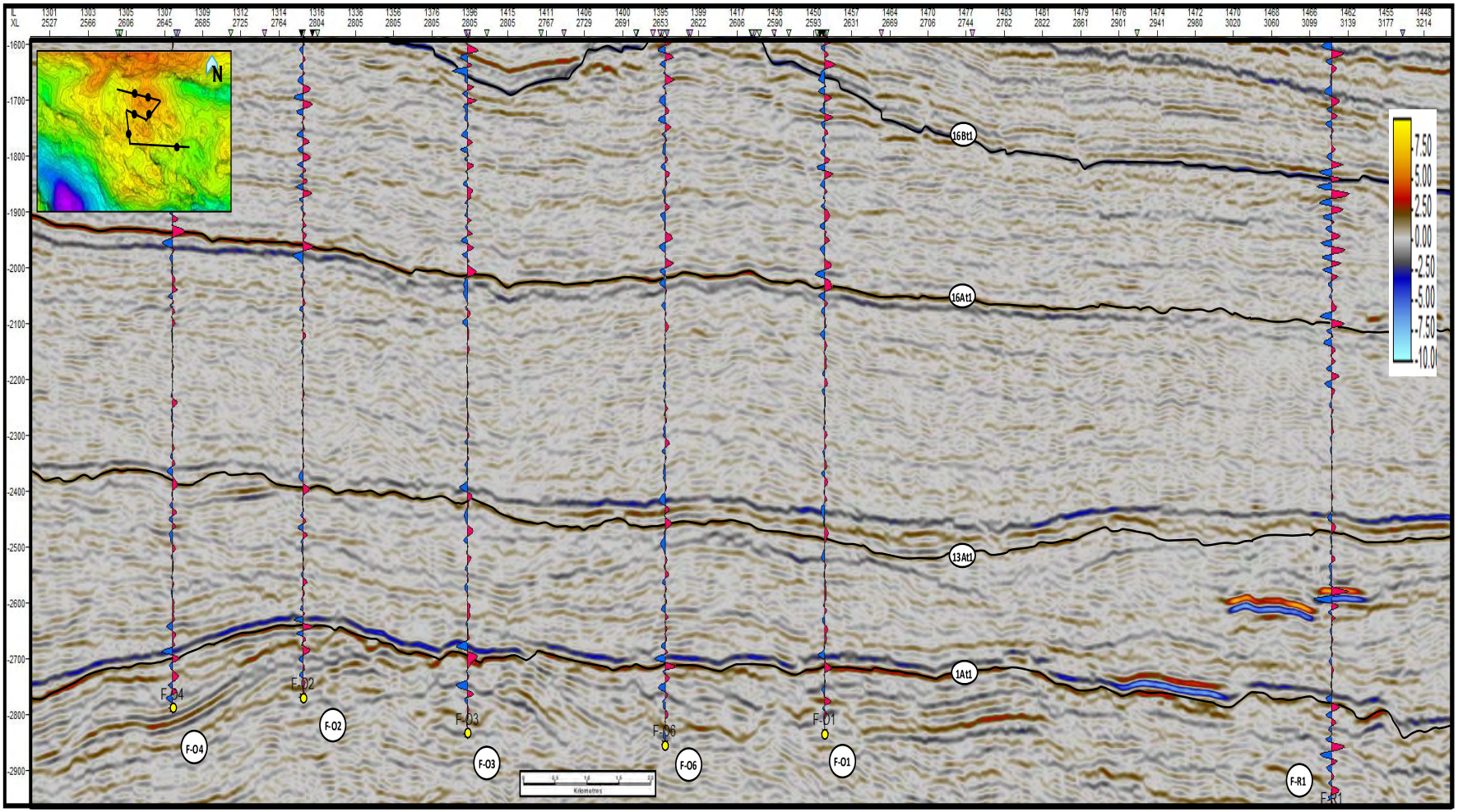

Figure 3.4.8: Random seismic section through all wells showing a good well-seismic tie on main geological boundaries.

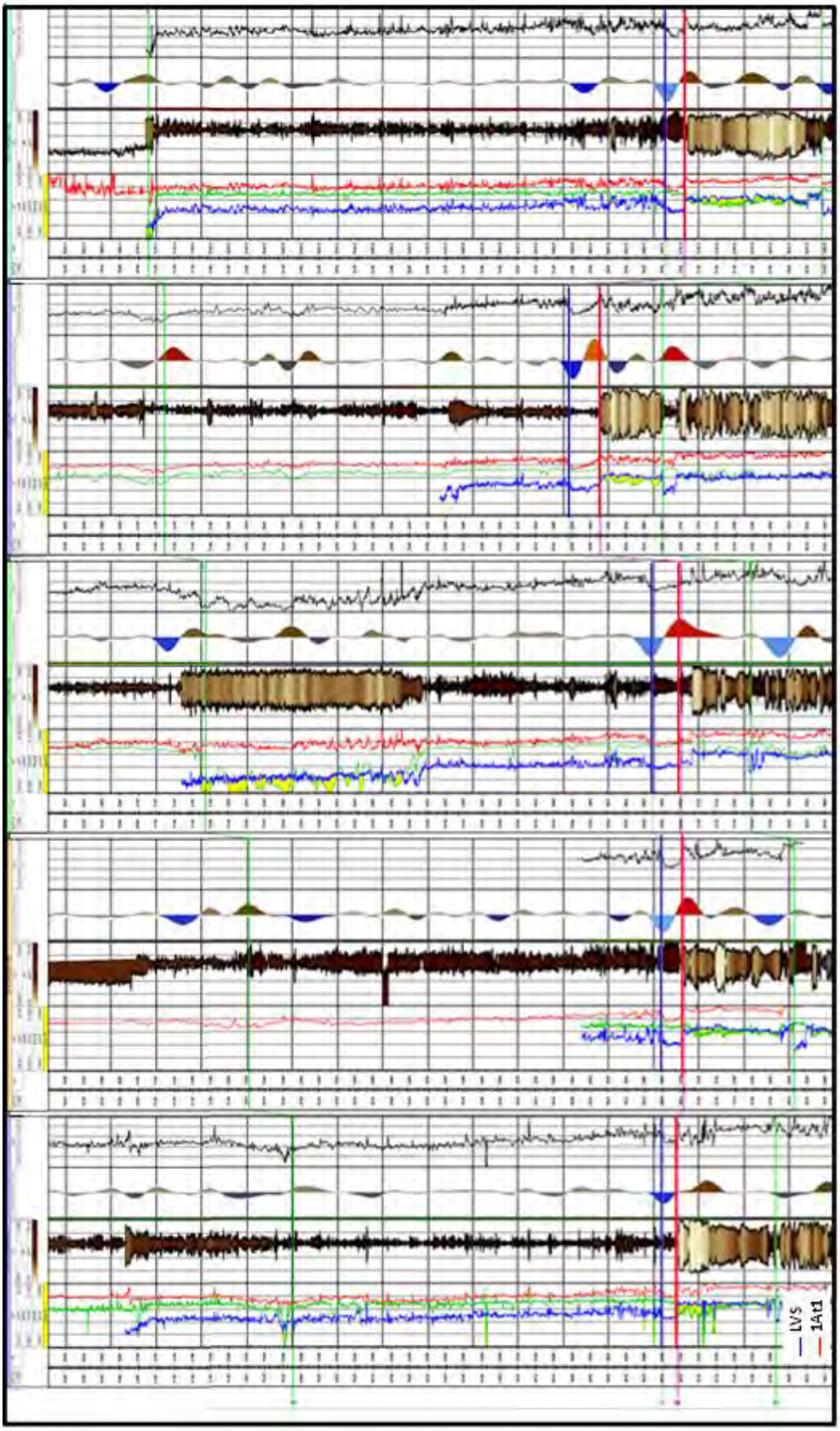

Figure 3.4.9: Well seismic correlation. The top of reservoir (1At1) represents the main seismic event to be correlated (red). However, the match vary from a peak to a zero-crossing event. The low velocity shale (blue) overlies this event contributing in the reflection expected in that interface.

Base of Upper Shallow Marine (BUSM) pick is a much lower confidence pick than any of the others, owing to its erratic behaviour and poor continuity. It is, however, a critical pick in determining the lateral reservoir distribution within the F-O field. To help solve this problem, a seismic reflector with greater continuity and amplitude below the BUSM, associated with the BLSM or Horizon V, was picked as a guide. This horizon was also a useful tool to improve the fault interpretation and as a constraint in the low-frequency model (LFM) generation to reduce uncertainty in the trace inversion process. Figure 3.1.4 shows the strong and continuous amplitude along most of the seismic section.

The seabed horizon was picked each 100 In-line/X-line. Horizons from ref. horizon to 13At1 were picked each 50 In-line and 50 X-line, 1At1-to-BLSM each 10 In-lines and X-lines and each 5 In-line and X-line in the area of interest, owing to their complex structural setting (table 3.4.2). The resulting maps seem of sufficient quality to be used to build the LFM and further reservoir characterization (see fig. 3.4.10-3.4.11).

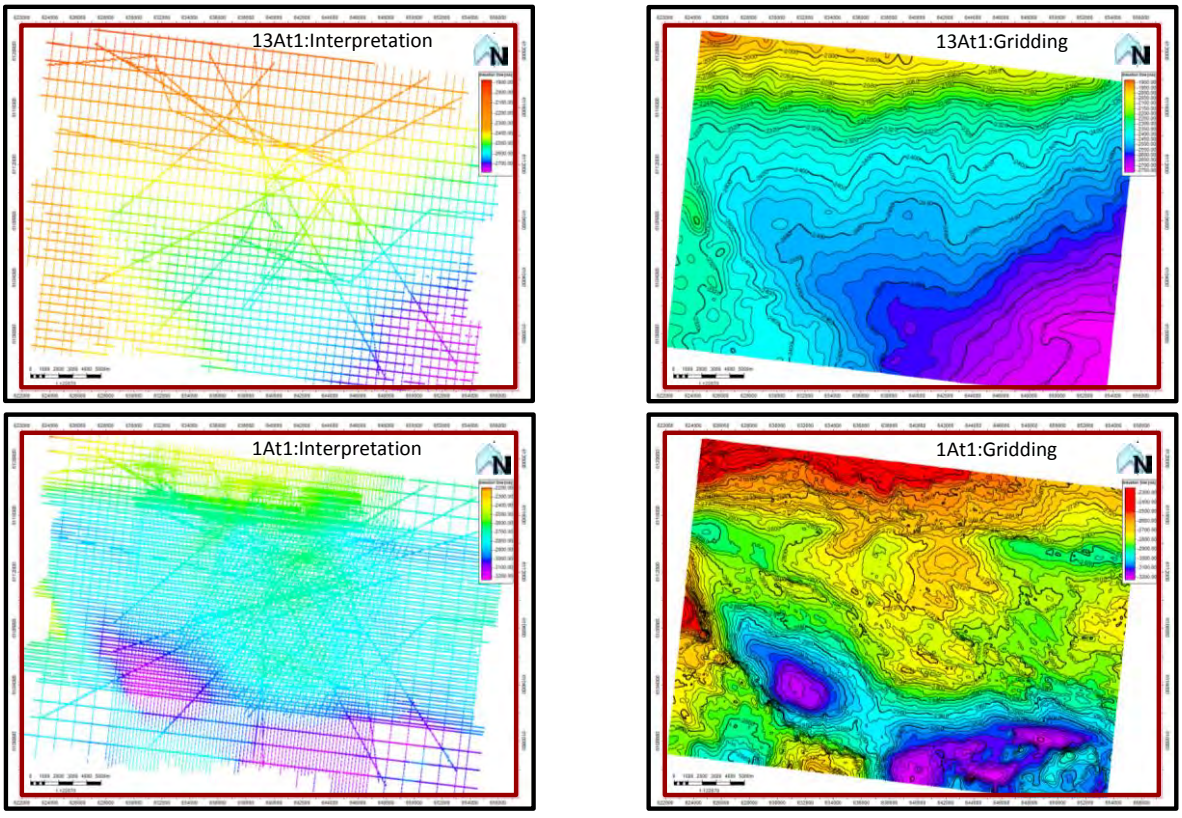

Figure 3.4.10:Horizon 13At1 was picked 25X50 lines in the area of interest and 50X50 in the vicinities. Note 1At1 was picked 10X5 lines , due the structural complexity and to represent the top of reservoir.

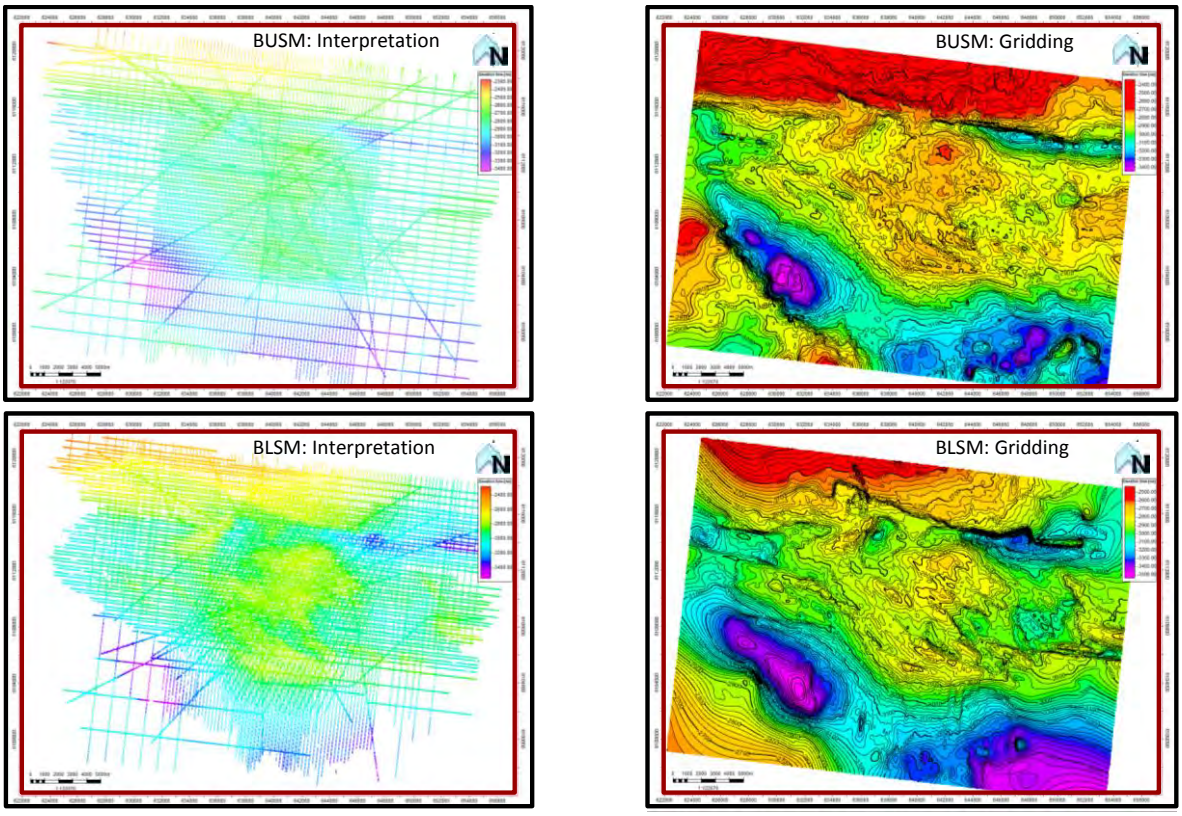

Figure 3.4.11: BUSM was interpreted each 10 In-line and 20 X-lines perhaps the poor continuity of seismic reflector. On the other hand, BLSM a reflector with strong amplitude response and continuity was interpreted each 10 and 5 In-line and X-l

3.5 Wedge modelling

A wedge model was used to understand vertical (thin bed) resolution by determining how much the bed could thin before its top and bottom reflections interfered with each other.

Changes in bed thickness are introduced into the model along with changes in acoustic properties (Vp, Vs, density). Using the full Zoeppritz solution for the synthetic response and a 25 Hz Ricker wavelet, the result is calculated for the “Gas Reservoir” (yellow) (see fig. 3.5.1).

The top left panel (fig 3.5.1) shows the maximum amplitude (0.096) of the wedge at the point of maximum constructive interference. This yields a tuning thickness (the bed thickness at which the boundary events constructively interfere) of +/- 40 m, which is equal to ¼ of the dominant wavelength.

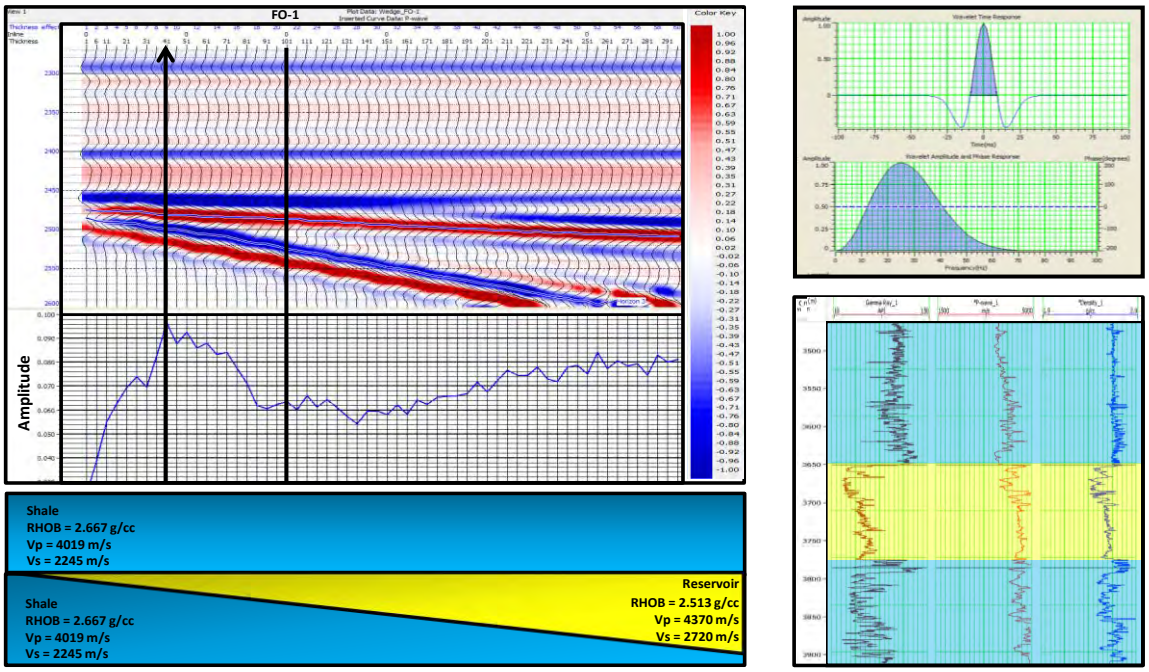

Figure 3.5.1: Wedge Modelling in well F-O1.

Chapter 4: Rock Physics Forward Modelling

The purpose of this rock physics analysis is to perform in situ and perturbational log-derived forward modelling for the five exploration wells that intersect the USM sandstone in the main structure on the F-O field. The primary goal is to understand the AVO/A response for the wells as logged, as well as to understand the effect of varying fluid fill, porosity, clay content and thickness.

Both in situ and perturbational forward modelling are used to generate synthetic seismic gathers, which are then used to generate and study the AVO/A attribute responses in order to help determine which, if any, AVO/A attribute pair or cross-plot products may be useful to:

a) Discriminate between gas sand and water sand

b) Discriminate between lower and higher porosity within the reservoir section

c) Discriminate between increases in clay volume

d) Discriminate between different reservoir thicknesses.

This chapter presents the different steps in the rock physics forward modelling workflow from data input preparation, best-fit effective medium model (inclusion and/or granular) to predict the elastic properties of the dataset, log data conditioning, perturbational modelling and synthetic/AVO analysis.

The workflow was as follows:

(1) Generation and set-up of the input parameters (gas-to-oil ratio (GOR), salinity, total porosity, etc) that are used in all of the modelling workflows, including fluid substitution, matrix modelling, Vs prediction, etc.

(2) Next, definition of the rock physics effective model that best fits the well data to analyse the effect of changing petro-physical properties and to correct bad data (wash-out, mud invasion) and/or predict a new property (shear velocity) if required. This sequence is called Rock Physics Reconnaissance.

(3) Then, fluid substitution using Gassmann's equation (Gassmann, 1951) to investigate the response of the elastic rock properties to changes in the fluid saturation of the reservoir.

(4) Then, perturbation of rock using the rock physics model in step 2 to investigate the response of the elastic rock properties to changes in the porosity, mineralogy and thickness of the reservoir.

(5) Lastly, creation of synthetic seismic gathers based on Zoeppritz's equations and using the perturbed elastic logs resulting from fluid substitution and petrophysical perturbation to understand how sensitive seismic is to different scenarios (see Figure 4.1).

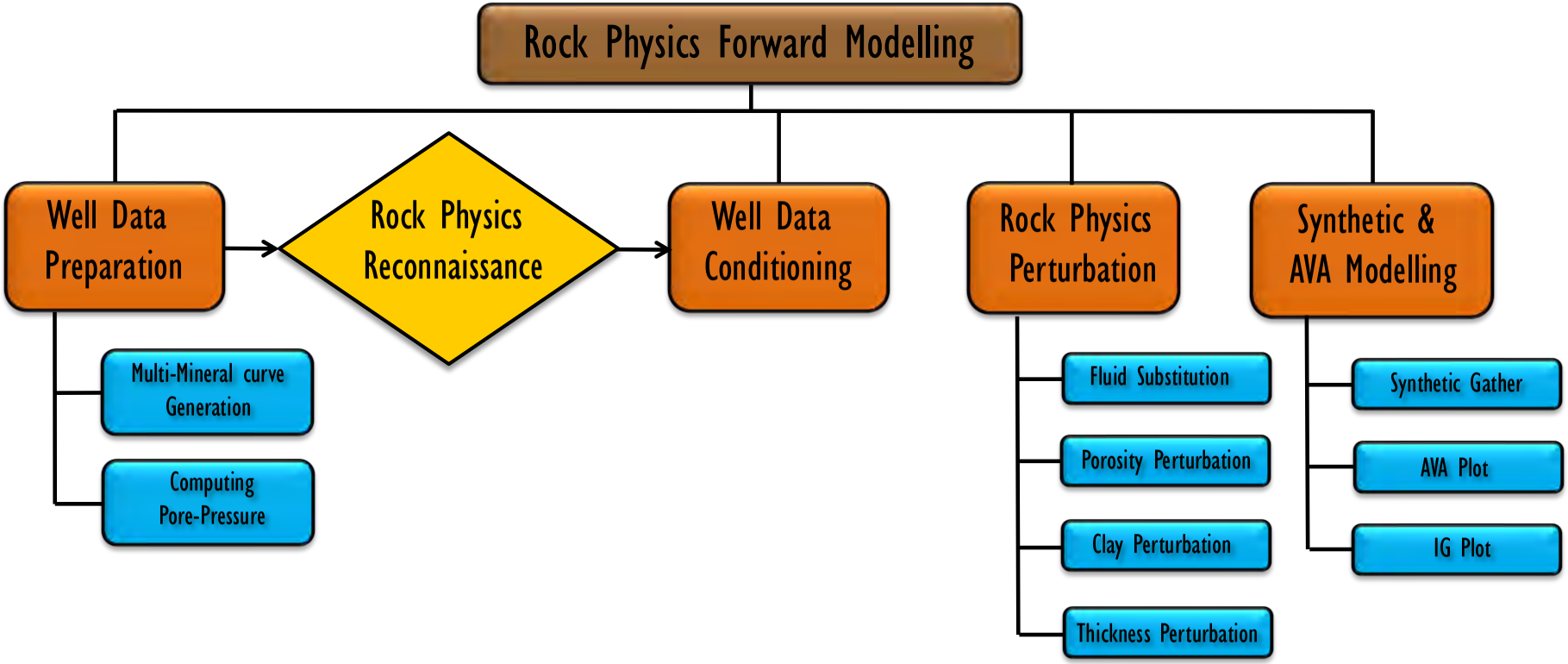

Figure 4.1:Rock physics forward modelling implemented on this project.

4.1 Well data preparation

The rock physics modelling process involves many mathematical expressions used to compute a vast number of parameters and curves (effective pressure, rock temperature, total porosity etc.), which, in conjunction with other input parameters (salinity, GOR, sand cut-offs etc.) and specific curves (Vp, Vs, density, etc.) are used to build different rock physics models and synthetic seismic responses. All this is possible by executing a sequence of logical routines following a particular order. Below is a list of much of the data input used for rock physics modelling:

Log data:

1. Sonic (Vp, as well as Vs, if available): Used for mineralogy and input into synthetic

2. Bulk density: input into synthetic, used for mineralogy and fluid saturation

3.- Gamma ray and/or SP: used for mineralogy

4.- Resistivity – deep, intermediate, and shallow: fluid saturations, invasion correction, mineralogy

5.- Caliper: used for hole condition. To determine the hole quality of shallow investigation devices (i.e. density & sonic)

Reservoir and other well and fluid data:

1.- Water resistivity or salinity: volumetrics and rock properties

2.- Oil API gravity and GOR: rock properties and acoustic behaviour

3.- Gas specific gravity: rock properties and acoustic behaviour

4.- Pore pressure information: rock properties and acoustic behaviour

5.- Bottom hole pressure and temperature: rock properties and acoustic behaviour

6.- KB, water depth and elevation for each well

7.- Mud log: used for mineralogy

8.- Tops to target zone and major formations

Additional data:

1.- Dipole shear: used for mineralogy and input into synthetic

2.- Core/cuttings reports: core-derived mineralogy (XRD, SEM, thin-section point count, etc)

3.- Interpreted curves such as porosity, water saturation and mineral volumes

4.- Petrophysical variables (m & n): volumetrics & rock properties

5.- Check shot and or time-depth information

6.- Wavelet parameters

7.- Base map

Data preparation provides a first inspection of available input. However, many times the information is raw data and needs to be processed into a different format by applying some operation or workflow. Furthermore, some datasets have more relevance than others because of the frequency with which they are used in the modelling workflows and operations, including fluid substitution, matrix modelling etc.

Petrophysical analysis for mineralogy, porosity and saturation, mineral composition and pressure-temperature information are examples of such datasets. A brief description of the procedure follows below:

a) Petrophysical analysis: Files of the current estimates of clay volume, effective porosity, water saturation and permeability were provided for each well. The procedure and results presented in appendix 4.1 were generated by PGS Reservoir Consultants (UK) Ltd during the reservoir evaluation in 2001.

b) Mineral composition: Mineral composition is an intermediate task in formation evaluation and also an input for building solid-rock properties (density, Vp, Vs, bulk-shear modulus and Poisson ratio). The goal of a lithology interpretation is to divide the bulk rock volume into total porosity and solid mineral components.

Mud logging is a detailed borehole mineral sample description obtained by examining the cuttings of rock brought to the surface by the circulating drilling medium (mud).

The volume of clay calculated in the petrophysical analysis mentioned above was the input to estimate the mineral composition. Mud logging informations, such a (1) gross lithology expressed as percentage from cutting column, and (2) lithology interpretation were used to compute the remaining constituents in the non-clay portion of rock.

Mineral rock component interpretation was carried out in each well over a depth interval which was significant in term of hydrocarbon presence (USM).

In terms of lithology, the reservoir section (USM) is primarily dominated by shale and sandstone. Occasional limestone stringers in the shale top seal and some authigenic mineral (calcite-chlorite) are rare among the wells; also some igneous intrusions are present in the southern part of the structure (FO1).

c) Pressure-temperature data: Pore pressure, temperature and effective confining pressure from depth are input to build fluid properties (density, P-velocity and bulk-modulus) for each fluid (brine, oil and gas) and solid properties (density, Vp, Vs and bulk-modulus).

All variables are involved in the generation of rock physics models.

Those parameters were computed based on the following relations and using the input parameters below:

Temp = surface temp, if depth ≤ water depth
Temp = surface temp + (depth - water depth)*GG/100, if depth > water depth
Ppore = (Ppore/D)* (depth - water depth) + (NW/D)*water depth
Peff = (OBP/D)*(depth - water depth) + (NW/D)* water depth – Ppore

where depth is the distance from the surface to the measurement point, water depth is the distance from the surface to the ocean bottom, GG is geothermal gradient, Ppore/D is pore pressure gradient, OBP/D is overburden gradient, and NW/D is the normal water pressure gradient, Ppore is pore pressure and Peff is effective differential pressure.

Pore pressure, water and overburden gradients were generated from the input data.

Variables GG, Ppore/D, OBP/D and NW/D were calculated based on follow expressions:

The geothermal gradient (GG) is the rate of increasing temperature with depth in the Earth's interior (see Table 4.1.1).

GG = 100 (BHT-Ts) / (TD-water depth)

Where:

GG= geothermal gradient (°/100 m)

BHT= bottom hole temperature

Ts= surface temperature

TD= final depth

The magnitude of OBP is found by integrating rock densities from the seafloor to the depth of interest, Z (Zoback, 2008). The overburden pressure (OBP) at a depth z is given by:

$$\int_0^z \rho(z) g dz$$

where:

ρ(z) is the density of the overlying rock at depth z (g/m3 or gm/cc)

g is the acceleration due to gravity

The overburden pressure gradient is:
(OBP/D) = OBP / depth below seafloor

The normal pressure gradient (NW/D) depends on the density of the fluid in the pores, integrated from the seafloor to the depth of interest. Fresh water with zero salinity will generate a pressure gradient of 0.433 psi/ft or 9.81 kPa/meter. Saturated salt water generates a gradient of 0.465 psi/ft or 10.4 KPa/meter. The normal water gradient or hydrostatic gradient is expressed as:

NW/D= pressure/unit height = density x conversion factor

The pore pressure gradient (Ppore/D) is the pressure gradient inside the pore space of the rock column from the surface of the ground down to the total depth (TD). The geopressure gradient may be described as high or low if it deviates from the normal hydrostatic pressure gradient of 0.433 psi/ft [9.8 kPa/m].

Eaton's method (Eaton, 1975) was used as follows:

Ppore/D = OBP/D - [OBP/D - NW/D] (Δtlog /Δt n) ^{3}

where

Ppore/D= the pore pressure gradient;

OBP/D= the overburden pressure gradient;

NW/D= the hydrostatic pore pressure; and the subscripts *n* and log refer to the normal and measured values of sonic delta-t (Δ*T*) at each depth.

Pore pressure, normal water and overburden pressure gradients were computed using the expressions referred to above.

Under normal pressure conditions, the sonic velocity increases with depth, so any deviation from this trend is an indication of possible abnormal pressures. Normal travel time (Δt n) is calculated using the sonic velocity log (Fig. 4.1.1).

The first step was to select the data point used to generate the normal compaction trend. The trend is built considering only shale, so If Vsh > 0.5 THEN DTsh = DT OTHERWISE DTsh = 0 (reddish interval is shale).

Then best fit or eyeball line to the DTsh data points (ignoring all zeroes) above the overpressure zone - this is the normal pressure trend line.

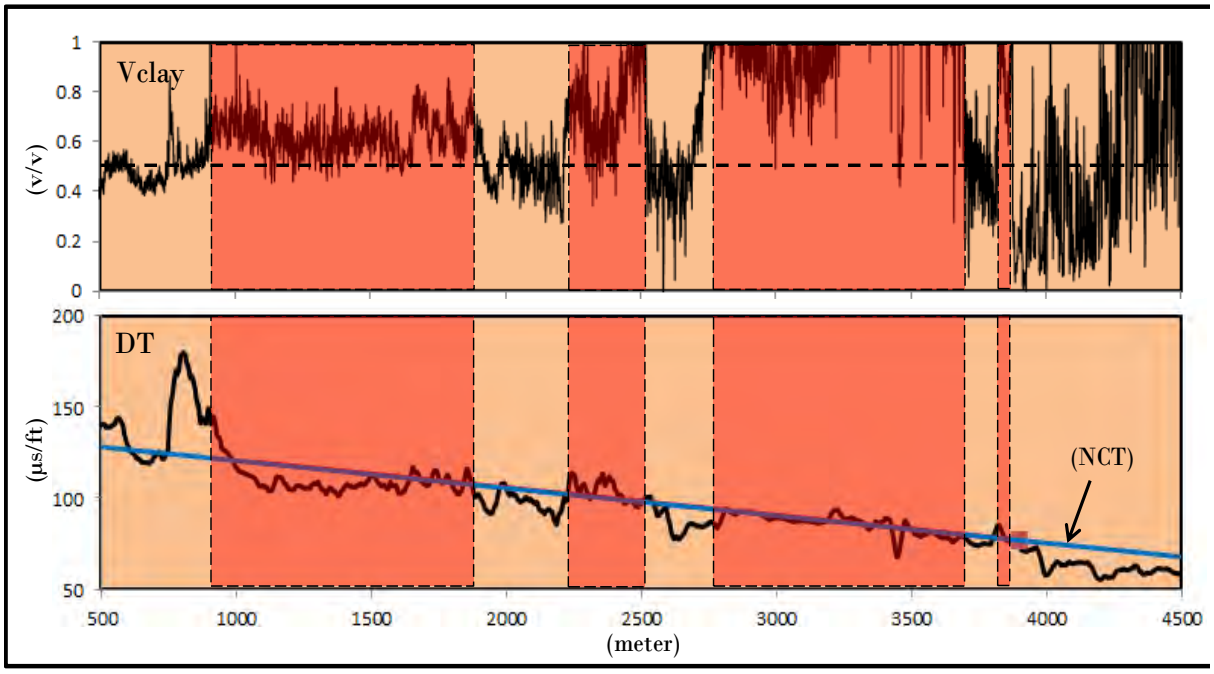

Figure 4.1.1: Illustration of the method using sonic ΔT. The normal compaction trend (NCT) is a straight line in log-linear space that has been fitted to the decrease in slowness as a function of depth where sediments are normally compacting.

4.2 Rock physics modelling

Six models, five theoretical models and one heuristic model were investigated to determine the one that best fit the well dataset. Theoretical models are split into two model sub-groups: (1) one group based on contact theory (Mindlin, 1949), which treats a rock as an aggregate of grains and estimates their stiffness from the contact stress between two spheres of equal size. In this group were used 3 models. The unconsolidated sand model (Dvorkin and Nur, 1996), also called soft-model (see figure 4.2.1), the Hertz-Mindlin_Hashin-Shtrikman model or stiff sand model and the intermediate stiff sand model; and (2) the inclusion models (Berryman 1980), which treat the rock as an elastic solid with cavities and accounts for the effects of shapes of multiple pores on elasticity. In this sub-group two models were investigated: the self-consistent approximation model (Budiansky 1965; Hill 1965; Wu 1966) and the differential effective model (Norris, 1985). An additional heuristical model (Raymer et al, 1980) was tested (see appendix 4.2).

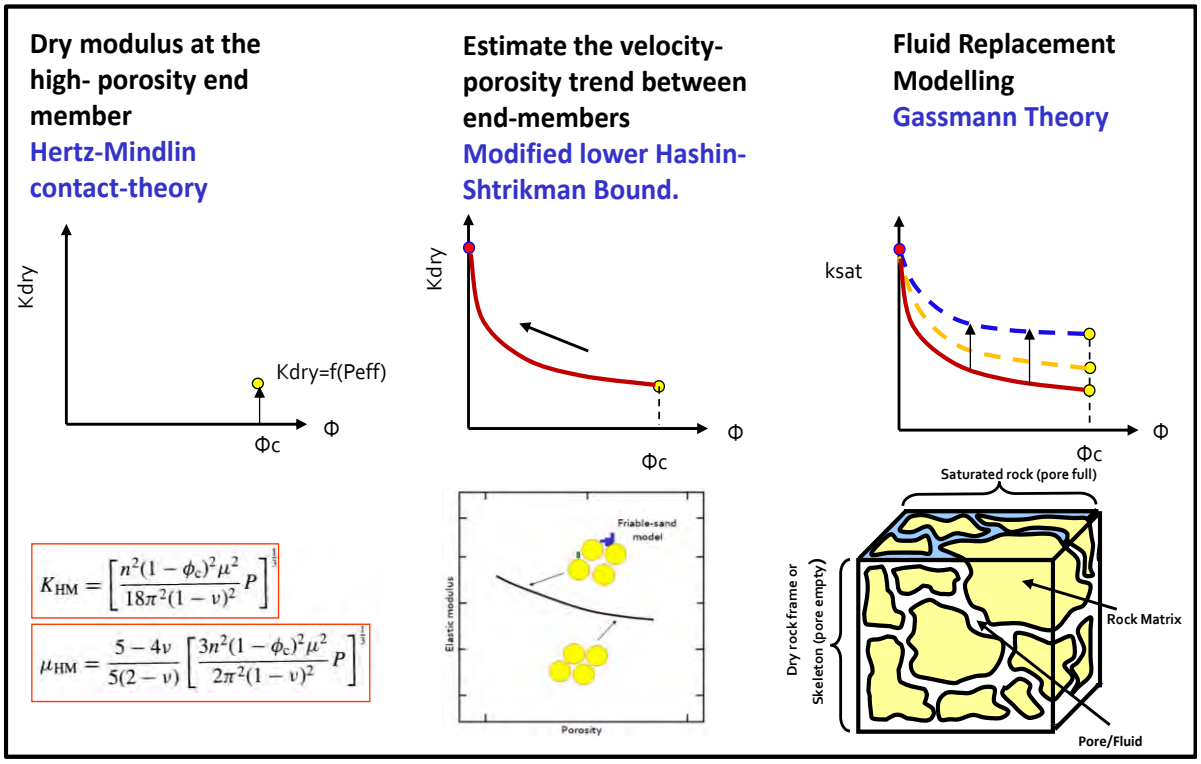

Figure 4.2.1: Unconsolidated-sand model sketch and the corresponding sedimentology variation modified. The dry sandstone is modeled by combining Hertz-Mindlin contact theory and lower Hashin-Shtrikman bound. (Courtesy of J. Dvorkin)

The procedure for rock physics reconnaissance implemented in this study comprises the following steps:

1) The basic parameters are defined for the wells, such as salinity, gas gravity, oil gravity etc.

2) Fluid and solid values are computed at in situ conditions, such as effective pressure (Peff), fluid density (DenFluid), fluid bulk modulus (KFluid), solid* density (DenSolid), solid bulk modulus (KSolid), solid shear modulus (GSolid) and total porosity (PhiT). Table 4.2.1 shows

the parameters chosen to compute the solid values (bulk modulus (K), shear modulus (G) and density) for each mineral included in the model.

3) Effective models have adjustable parameters such as critical porosity, coordination number (CN) or pore aspect ratio (AR) determined empirically from local data. At this point, model curves are built using as input the values in (2) and reasonable initial input parameter values (coordination number and aspect ratio, critical porosity) for the type of rock. Table 4.2.2 shows the CN, AR and critical porosity chosen for Vp and Vs in each well.

4) The Vp-density-Vclay cross-plot dataset is examined for each well, superimposing on it the different model curves computed in (3) (see figure 4.2.2 to 4.2.4).

5) The best fit model is determined visually; sand and shale model curves are adjusted by changing the coordination number for the granular model (unconsolidated, intermediate, stiff sand) and the aspect ratio for inclusion models (self-consistent, DEM) as many times as necessary to obtain the result desired. If model curves do not adjust to the dataset as desired, other parameters such as clay and quartz density, bulk modulus and shear modulus can be revisited.

6) Synthetic curves (Vp, Vs, density) from models are created once the optimal and consistent parameters have been obtained to best fit the sand and shale curves with the dataset in a cross-plot domain.

7) These synthetic curves are computed by applying a weighted average of sand-shale curves using the Vclay as a constraint. Nevertheless, it is not reasonable to expect a best fit on the whole borehole section if a single coordination number or aspect ratio value is used, so this involves a trial-and-error routine to calculate a coordination number or aspect ratio "curve" for the whole well by re-adjusting the parameter as required in each interval where the match between original and synthetic curves is not optimal.

8) Density, Vp and Vs synthetic log curves that come from the best model are iteratively used to edit erroneous measurements (wash-out, spikes, etc.) and to add data where it is missing data (shear velocity) on the original curves (see Fig. 4.2.5).

(*) Solid refers to the matrix.

Observations and Conclusions:

a) In the Raymer and HMHS model, Vp is overestimated and density is underestimated. A coordination number of 8 for P-velocity and 7 for S-velocity were considered.

b) Unconsolidated shale model curves plotted overlay shale data consistently in all wells.

c) An intermediate stiff sand model was adapted by using an exaggerated coordination number between 11 and 23 among the wells to simulate low-medium porosity sandstone successfully.

d) In both inclusion models (SC and DEM), the sand curves imitated with relative accuracy the well dataset for sand at the reservoir section. However, the intermediate stiff sand

model fits the compaction trend better in the five wells than in the other two inclusion models.

e) The intermediate sand model for sand and the unconsolidated shale model for shale were selected to perturb rock physics properties in this chapter.

Additionally, four Vp-Vs models (Greenberg-Castagna, Krief, mud rock and Vernik) were constructed to predict the shear velocity response when if was necessary. Observation and results are addressed in section 4.3.

4.3 Well log conditioning

This section illustrates the procedure and results of a well log data conditioning analysis using rock physics models. Reliable and good quality well log data (sonic and density) was essential for a successful quantitative seismic reservoir characterization, because any errors in the well log data are going to be propagated throughout the integrated proposed workflow and inconsistencies will remain within the final reservoir model.

In some cases well log sections are not appropriately conditioned for rock physics reconnaissance (RPR), and the logs may exhibit some problems (poor quality, inconsistency with surrounding wells and/or missing some data). Due to the small depths of investigation of sonic and density logging tools, measured logs are affected by borehole rugosity (washout), mud filtrate invasion in zones with high permeability and casing points. In some wells, particularly older ones, density and shear sonic logs were acquired in sections with limited depth or not at all, as in F-O4 and F-O1 respectively.

The tasks involved in this section are (a) editing the measured Vp, Vs, and density over the full wellbore to account for bad measurements from washouts or casing points or other problems (cycle skips, differential tension) and (b) predicting missing data via the rock physics reconnaissance (RPR) procedure.

The ultimate goal of well log conditioning is to correct these problems and to produce, for the entire wellbore, as complete a suite of elastic and electric log data as possible. Shear wave velocity prediction was also included.

Wash-out / Cycle skip correction

Borehole washout problems are frequent in the shales that overlie the main reservoir of the field, resulting in poor sonic and especially poor density log measurements. They are caused by an enlarged region of a wellbore. A wash-out in an openhole section is larger than the original hole size or size of the drill bit. Wash-out enlargement in F-O occurs mainly at the base of the 16At1 horizon and could be caused by soft or unconsolidated formations, in-situ rock stresses or even a mud density with lower density than the tensile strain, causing tensile failure on the rock. Cycle skips are commonly caused by the presence of enlarged boreholes (see appendix 4.3).

In the RPR process (see section 4.2) good measured log data is fitted to various rock physics models to predict Vp, Vs and density in order to patch those areas with bad measurements (wash-out / cycle skips) and/or to synthesize data in intervals in which it is missing (Vs) (see Figures 4.3.1).

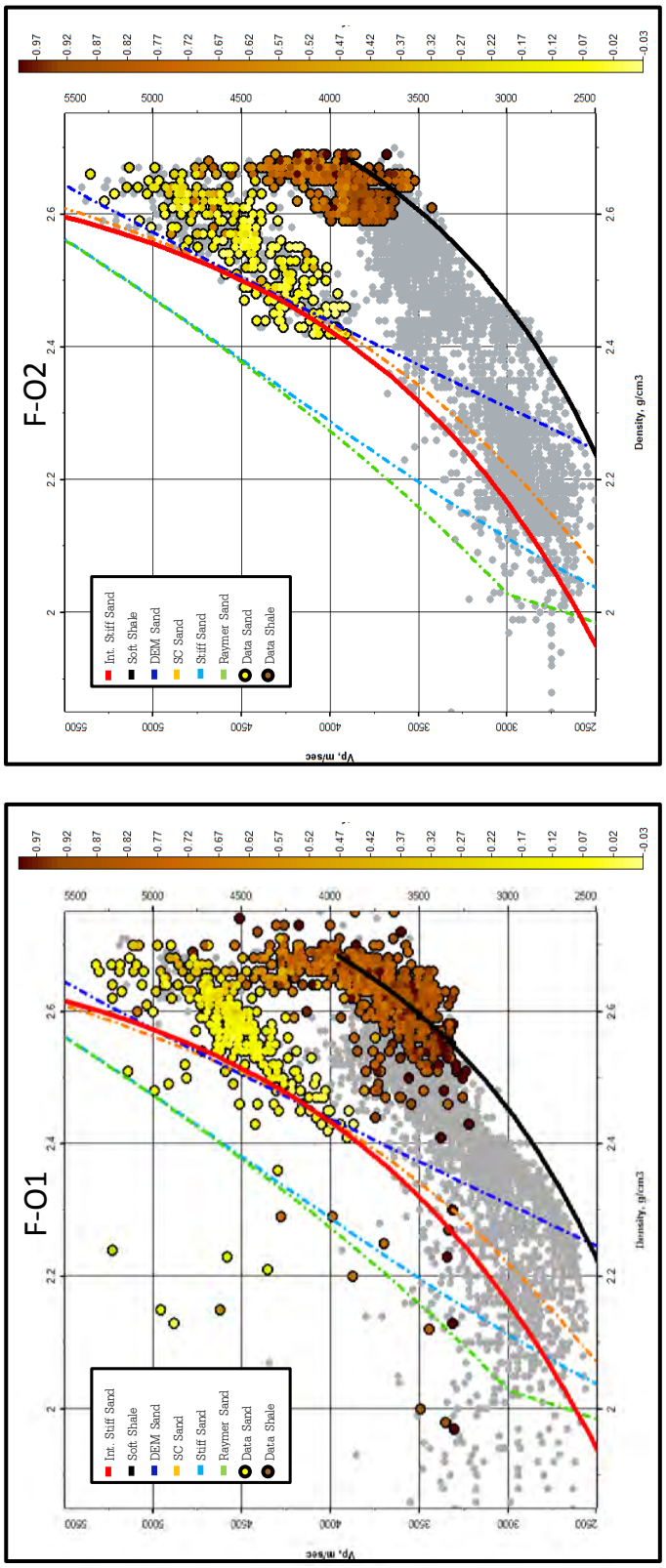

Figure 4.2.2: Bulk density (RHOB) vs P-wave velocity (VP) colour coded by VClay. Rock physics models are overlain to the data.

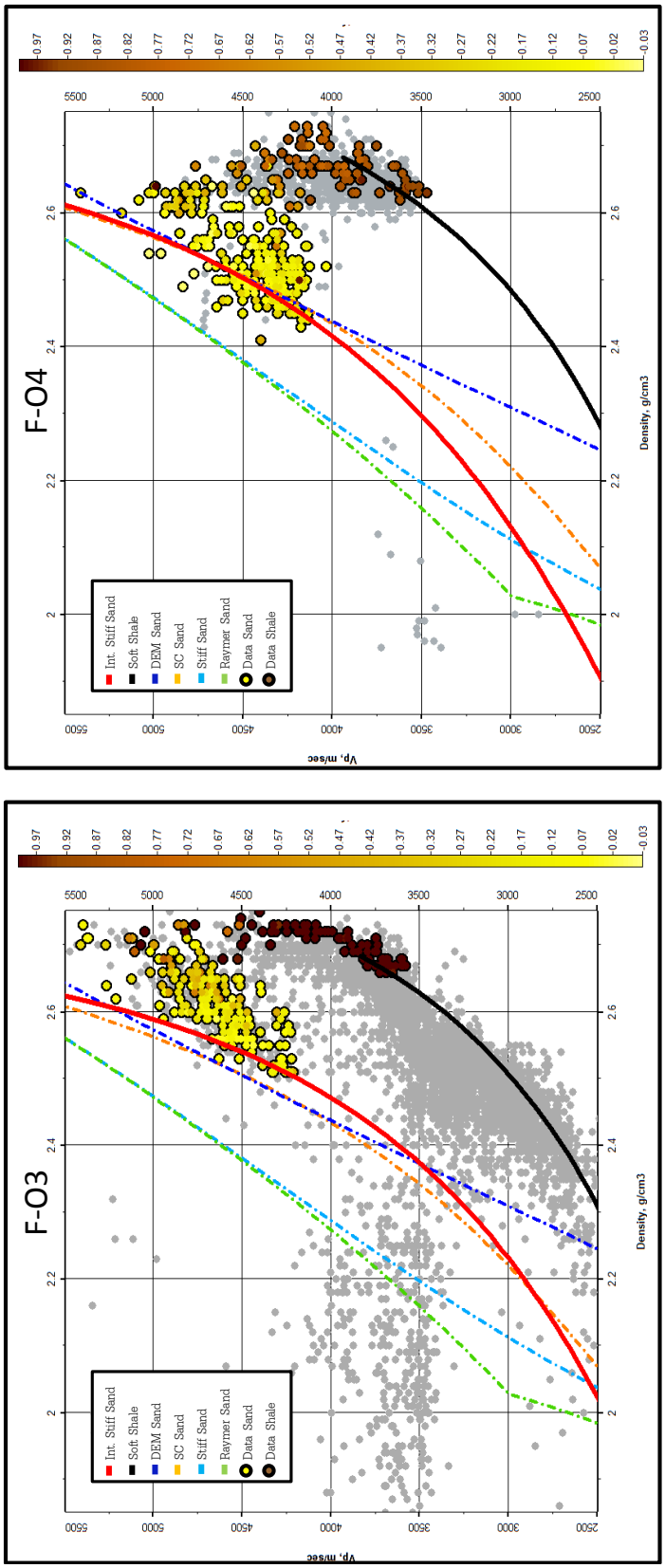

Figure 4.2.3: Bulk density (RHOB) vs P-wave velocity (VP) colour coded by VClay. Rock physics models are overlain to the F-O3 and F-O4 data.

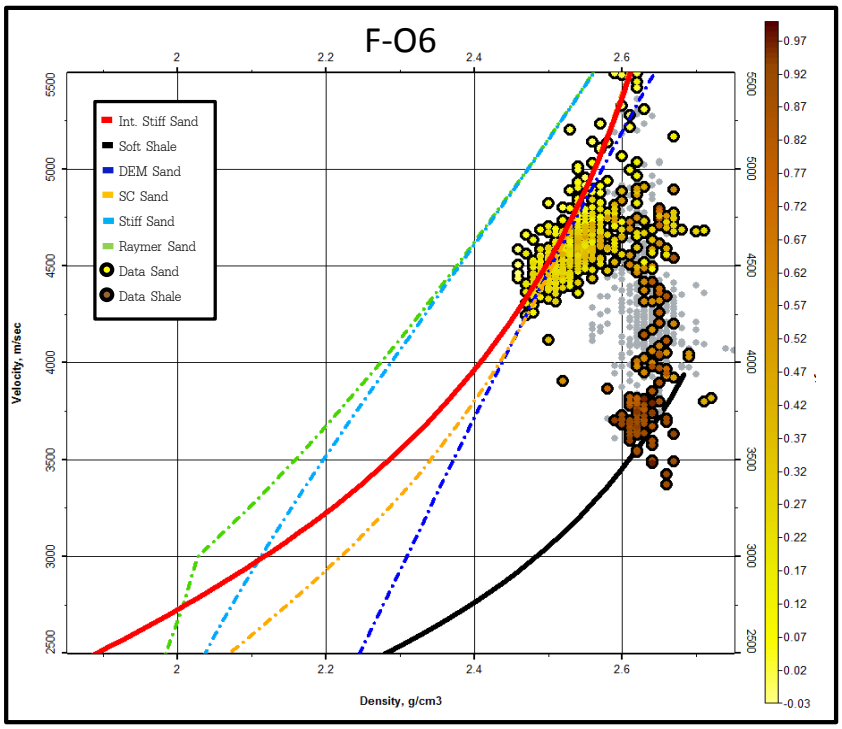

Figure 4.2.4:Bulk density (RHOB) vs P-wave velocity (VP) colour coded by VClay. Rock physics models are overlain to the data.

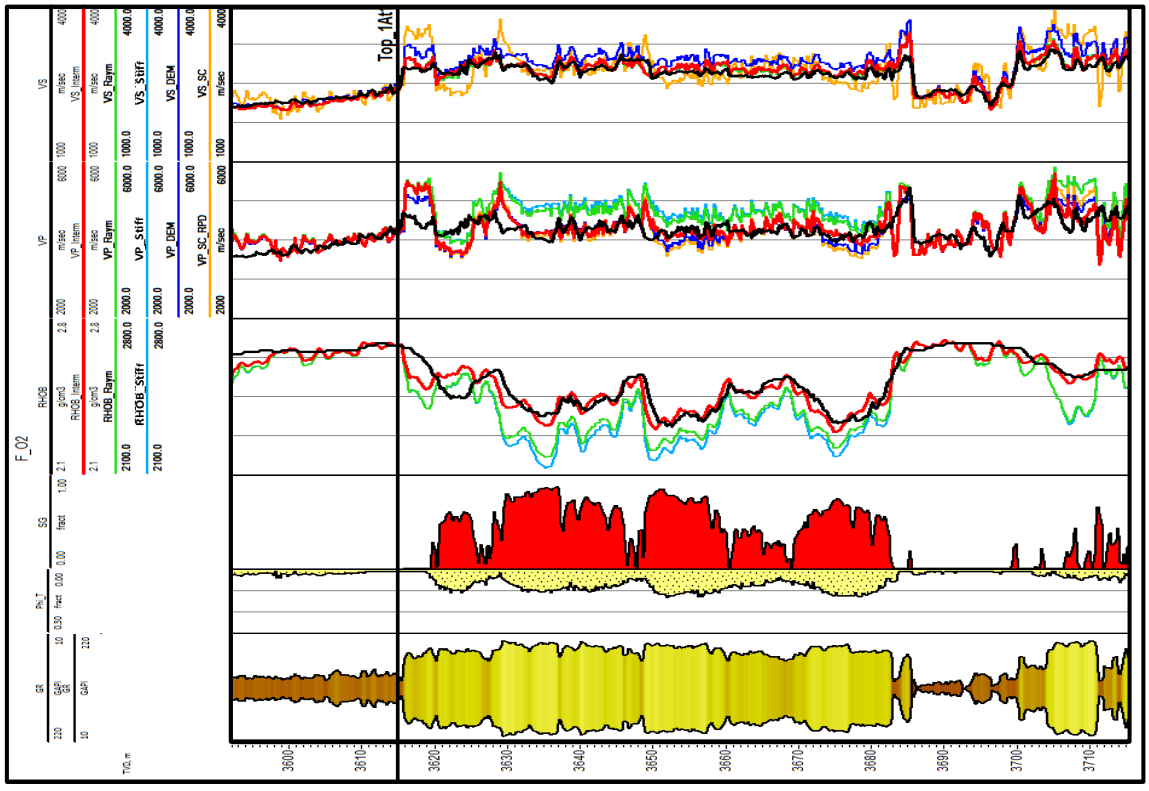

Figure 4.2.5:Rock Physics Reconnaissance Plot (Density-vs-Velocity -Vp) in well F-O2.

.

Mud invasion:

During the drilling process, muds of different compositions are used to support the wall and to remove the debris produced by the action of the bit. These muds invade the geological formations and modify the zones surrounding the well. Invasion often causes sonic logs to be too fast and density logs to be too high.

The elastic log correction for mud filtrate invasion was performed in a 3-steps procedure for all five exploration wells especially in the zone of interest (USM):

1) Assuming that zones with higher permeability are more susceptible to mud filtrate invasion problems, multiple depth reading resistivity logs were used to determine the depth of invasion. Conventional sonic and density tools have a depth of investigation of less than 10 inches so assuming that the invaded zone does not go beyond 60 inches, the cross-over between a deep resistivity/LLD (>60 in) and a shallow resistivity / LLS or MSFL (30-10 in) defines the invaded zone and degree of filtrate penetration in the formation.

2) Once the invasion depth has been defined, water saturations Sw and Sxw are computed from deep and shallow resistivity curves.

3) Lastly, the problem is reduced to computing Vp, Vs and density at true reservoir conditions beyond the invaded zone using fluid substitution based on the Biot-Gassmann theory.

Mud filtrate invasion started approximately between 1At1 (top of USM) to 10 metres below that mark in all wells where reservoir evidenced an enhancement of permeability, so less invasion was expected in wells F-O3 and F-O6 and more in F-O1 and F-O2, which had major exposure to Enhanced Poro-Perm (EPP) diagenetic process (leaching) (see figure 4.3.2-to-4.3.3).

Shear-wave velocity prediction

Shear-wave velocity (Vs) with compressional-wave velocity (Vp) are key for direct seismic identification of pore fluids using various seismic interpretation applications, including amplitude-versus-offset analyses (AVO). Measured shear-wave velocity logs are, however, often unavailable.

This study includes five wells of which only F-O1 has no shear velocity log as part of its suite of well logs.

The F-O8 well was drilled just 150 metres from F-O1 with the objective to test the pay sand that was not tested in F-O1 because of mechanical issues. This twin well was used to validate and control the quality of the different models constructed to predict the shear velocity response in F-O1. Four Vp-Vs relations (Greenberg-Castagna, Krief, mud rock and Vernik) were used to calculate the shear log.

The Krief, mud rock and Vernik relations are empirical equations predefined to lithologies with specific deposition and rock characteristics. These relations are expressed in terms of a few variables (compressional velocity (Vp), total porosity (PHIT)) that constrain the prediction.

The Greenberg and Castagna (1992) equations were built on the basis of a particular rock type, in which the empirical relations consider a more flexible rock system composed of quartz, calcite, dolomite and clay (any or all), in which each mineral in the solid matrix can be modelled separately using some regression coefficients representative of pure mono-mineralic lithologies in order to adjust the model to fit the well log data (see Table 4.3.1).

Initial Greenberg-Castagna regression coefficients were used as a first-pass to predict Vs in F-O1. Subsequently, sand and shale lithology coefficients were modified to obtain the best fit between empirical model and well data. Figure 4.3.4 shows at the top a Vp-Vs cross-plot with F-O8 data superimposed with Vs sand and shale model lines generated using customized coefficients from F-O data (solid line). The dashed line represents Vs model lines with the Greenberg-Castagna regression coefficients. Greenberg-Castagna regression coefficients clearly under-estimate Vs in slow sandstones and slightly over-estimate Vs in faster sandstones. At the bottom, the cross-plot includes all wells (F-O2, F-O3, F-O4, F-O6, F-O8) data and the different Vs model lines.

Synthetic Vs curves were generated in F-O8 as a blind test (quality control) using the different Vs models above (Figure 4.3.5). Vs model predictions show different outcomes. For instance, Vernik's relations significantly underestimate sandstones, but predict shales better. The mud rock's relation reproduces consolidated sand (tight) much better than more porous sands. However, the model overestimates the shale response. The Greenberg-Castagna and Krief Vs were effective in predicting both sandstones and shales in F-O8, but Greenberg-Castagna showed a slightly better effectiveness in predicting the shale data trend, especially in the low-velocity shale overlying the top of reservoir (1At1).

Based on these results, Greenberg-Castagna with customized relations were used to predict Vs log in F-O1.

Well log conditioning was performed over the entire well bore, resulting in a robust well log suite suitable for use in seismic reservoir characterization.

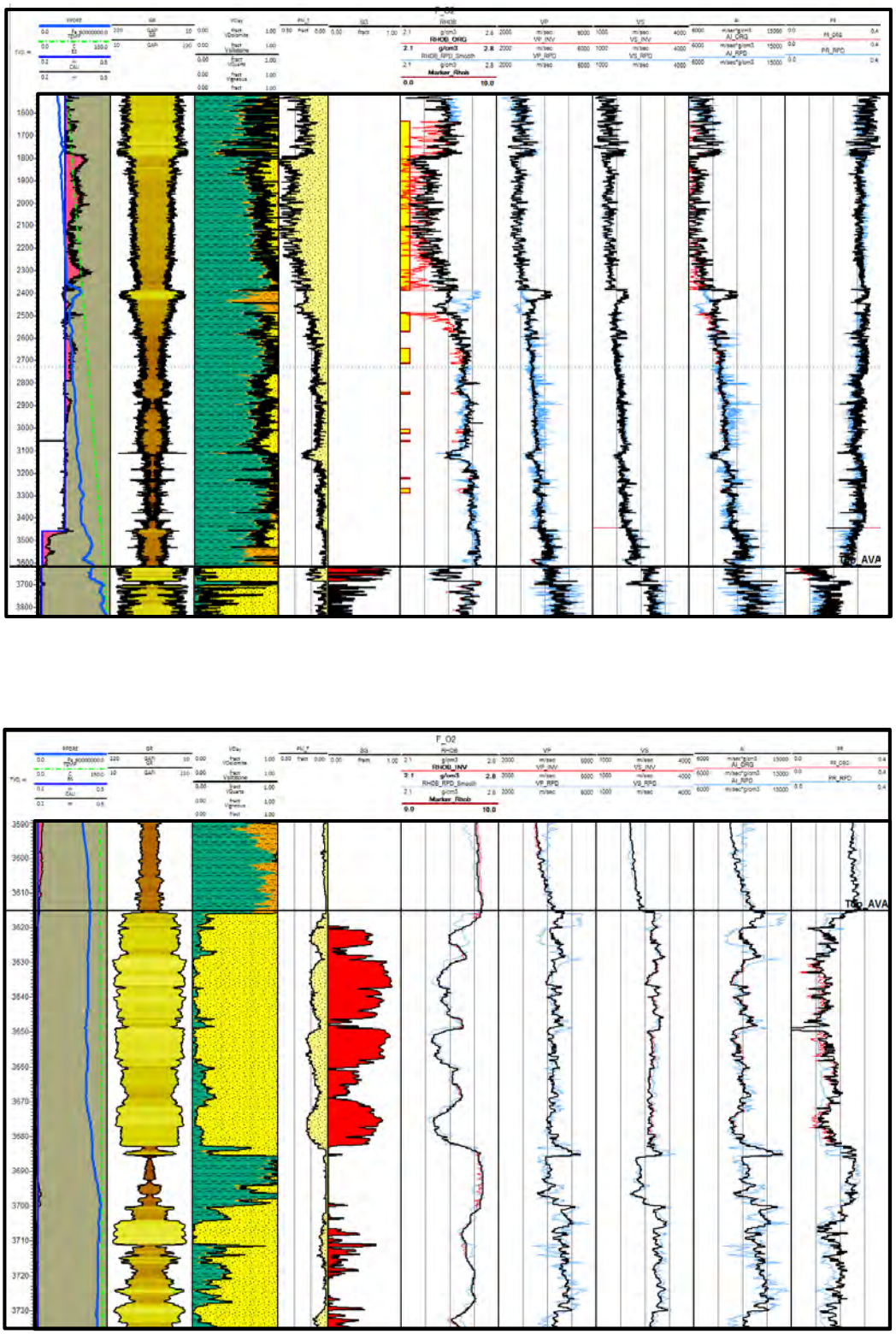

Figure 4.3.1: Plot template showing full well F-O2 on the top with rock physics model curve in light blue overlying. Vp model is estimated from density using intermediate sediment model for sands and unconsolidated for shales. Red curves are the original affected by wash-out and the black curve the original after correcting for the wash-out. These are the models that are used to perturb the elastic curves for porosity, mineralogy and thickness changes. On the bottom, a zoom-in of same plot.

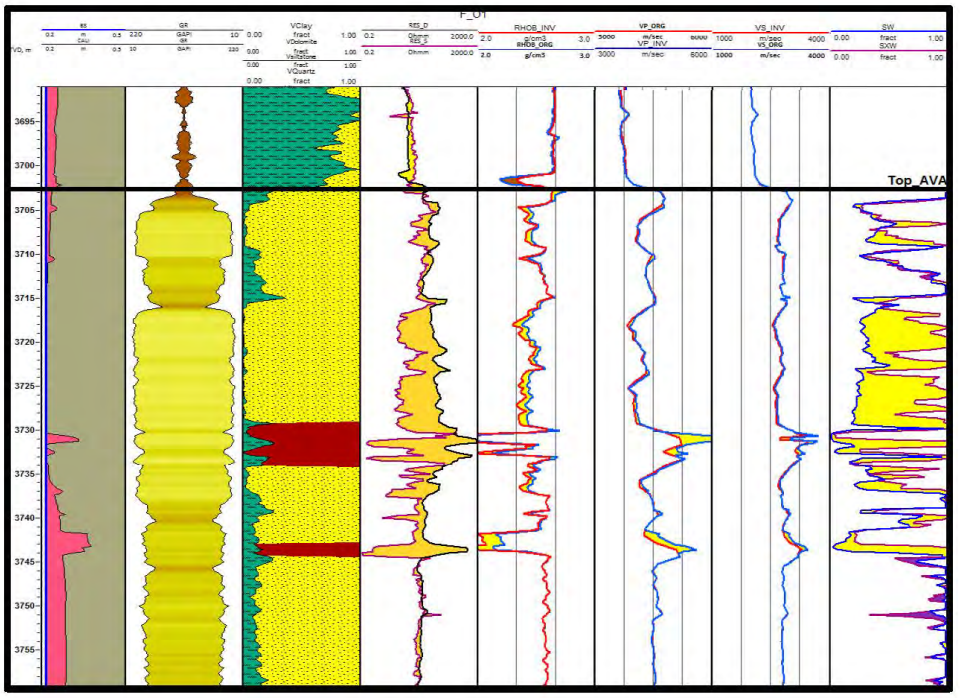

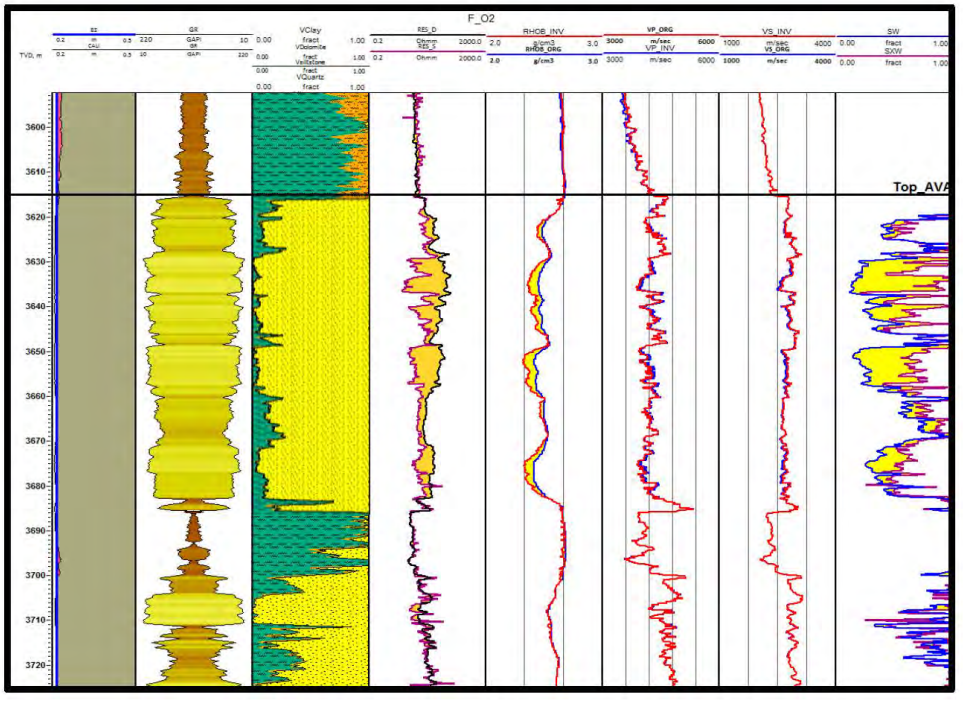

Figure 4.3.2: The original (blue) and corrected (red) Vp, Vs and density curves are shown for well F-O1 and F-O2

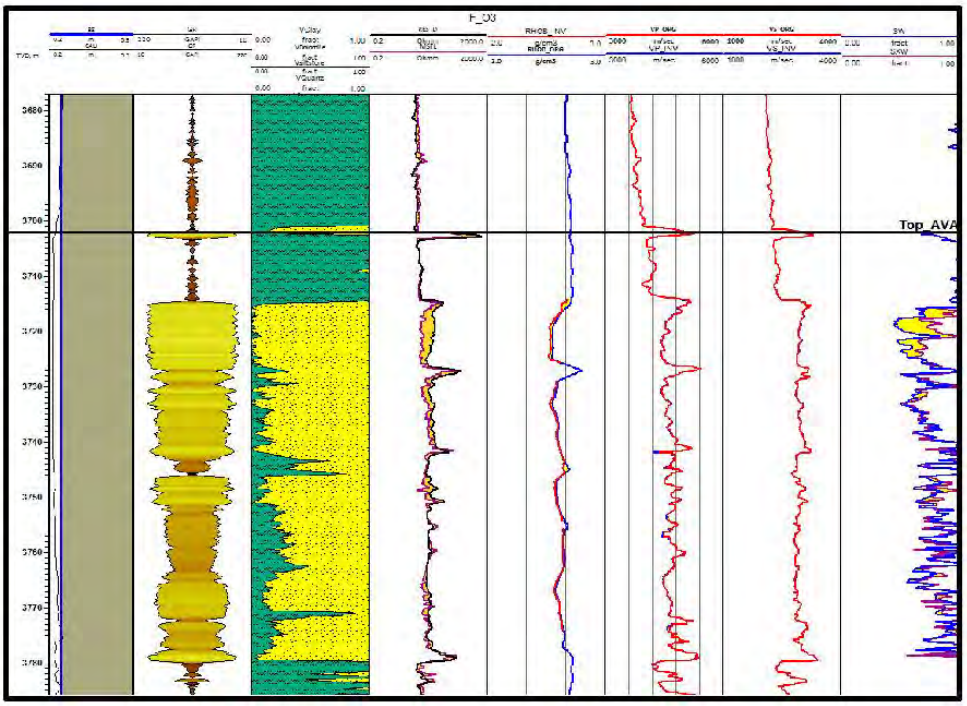

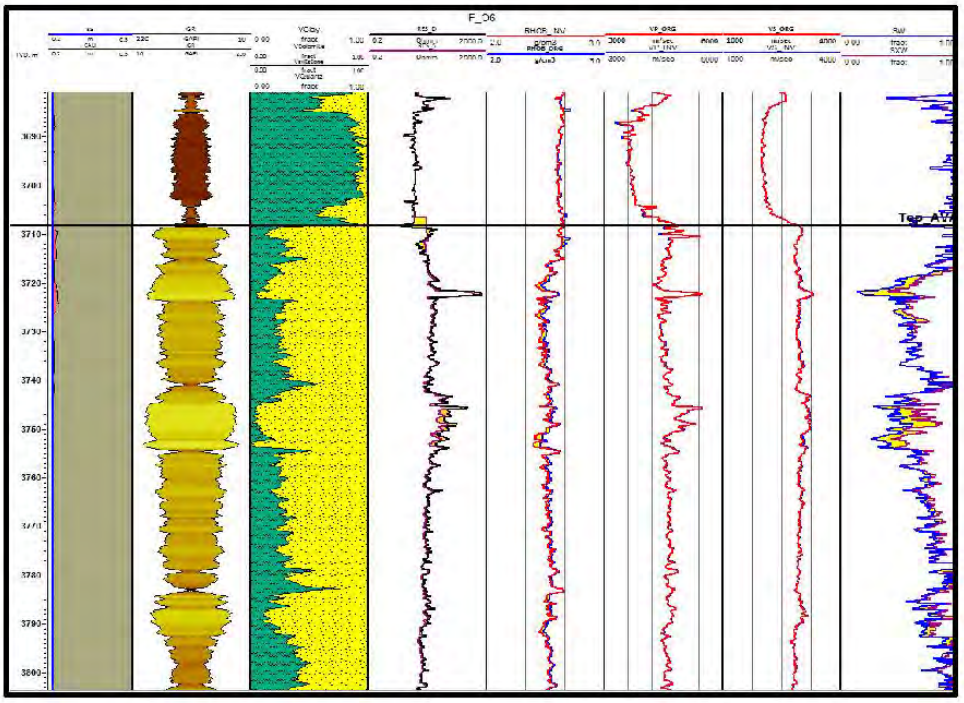

Figure 4.3.3: The original (blue) and corrected (red) Vp, Vs and density curves are shown for well F-O3 and F-O6

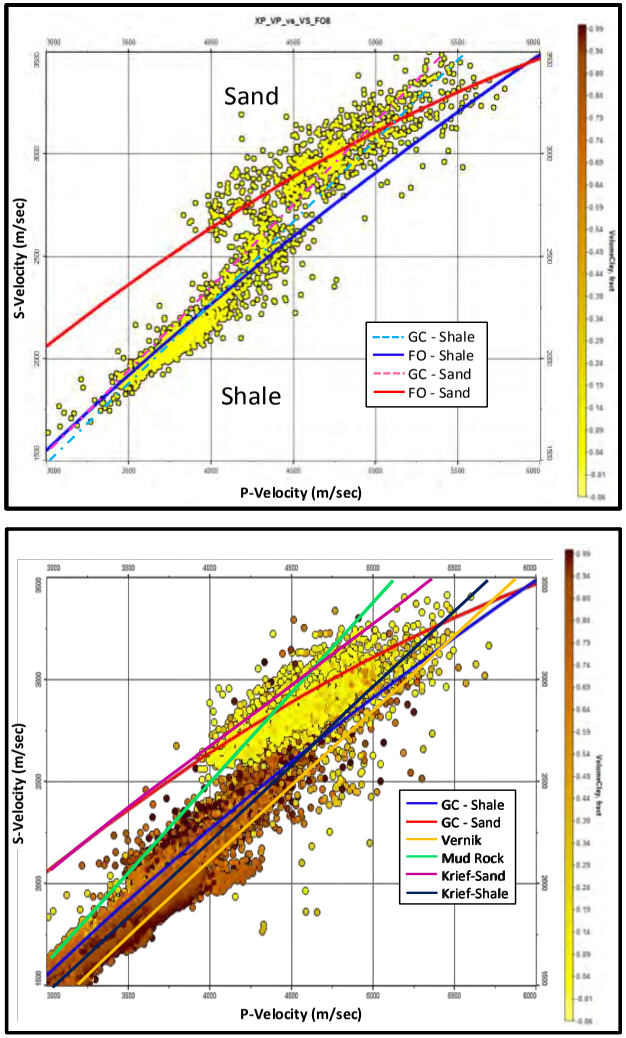

Figure 4.3.4: Greenberg-Castagna lithology coefficients were adjust to improve the model predictability , specially on sandstones. At the top a Vp-Vs cross-plot with F-O8 data superimposed with Vs sand and shale model lines generated using customized coefficients from F-O data (solid line) and greenberg-Castgna model lines in dashed lines. The figure in the bottom illustrate the match between data (F-O2, F-O3, F-O4, F-O6, F-O8) and different Vs model lines.

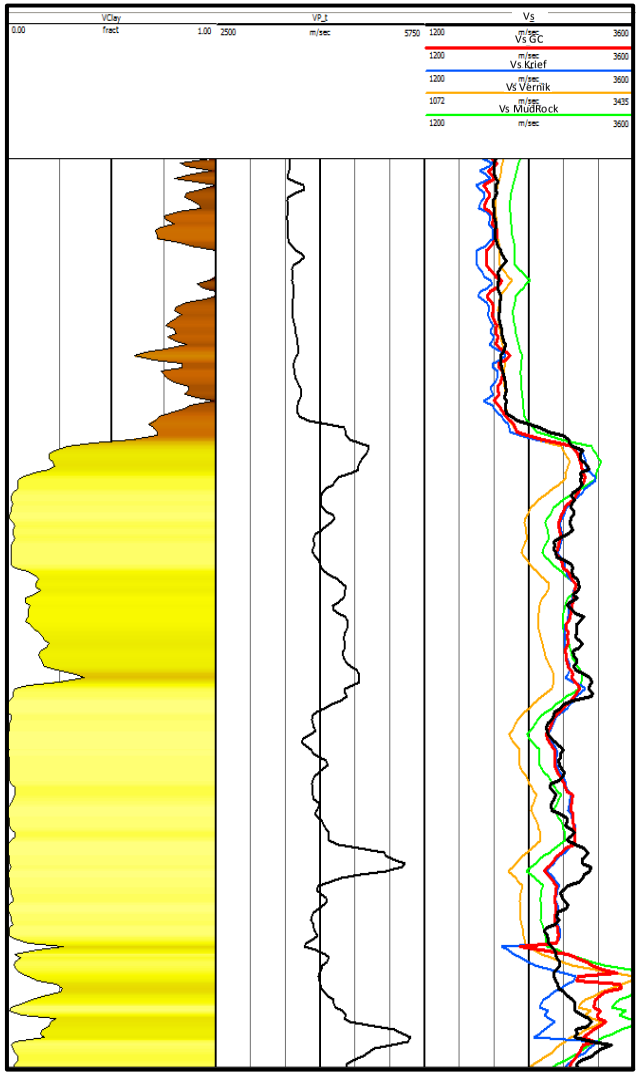

Figure 4.3.5: Synthetic Vs curves generated in F-O8 using all V s models as a quality control. Greenberg-Castagna resulted tin he most robust estimate.

4.4 Rock physics perturbation analysis

This section shows the results of perturbing the in situ properties in the wells using the Gassmann equations for fluid and rock physics modelling for porosity, mineralogy and thickness. The in situ reservoir properties and four sets of models were generated for the 5 wells.

(a)Gassmann was used for fluid substitution to perturb the in situ fluid to (Fig. 4.4.0.1):

- 100% water (water case)
- 80% gas; 20% water (gas case)
- 20% gas; 80% water (fizz case)

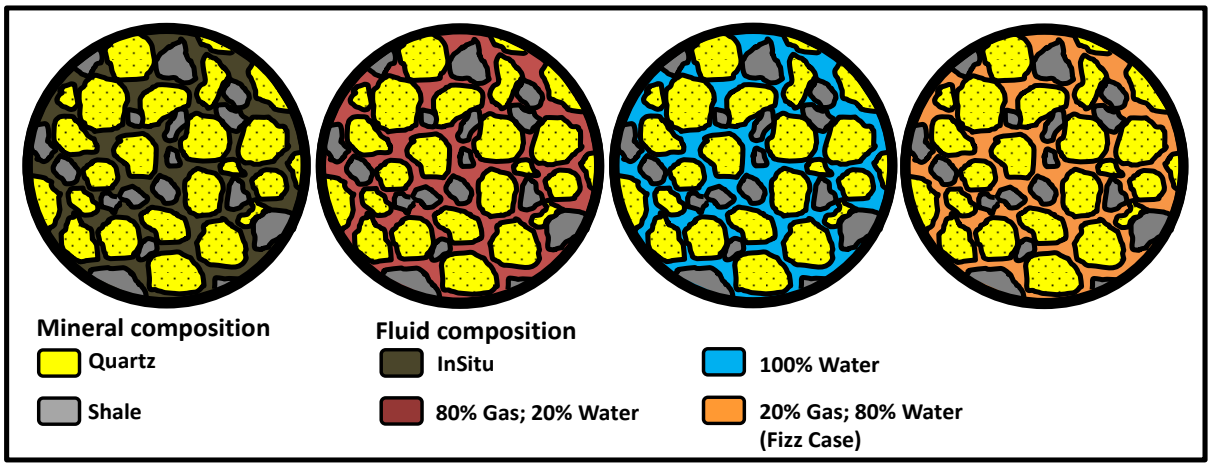

Figure 4.4.0.1: Fluid substitution cases.

(b)Porosity (Phi) models: The rock physics model resulting from RPR was used to perturb the porosity, keeping relative mineralogy volumes constant. Starting with in situ average porosity, the models were reduced and increased by 35%; four specific cases were analysed (Fig. 4.4.0.2):

- Reduced Phi, 20% gas, 80% water (fizz)
- Reduced Phi, 80% gas, 20% water (gas)
- Increased Phi, 100% water (water)
- Increased Phi, 80% gas, 20% water (gas)

(c)Clay models: The rock physics model resulted from RPR was used to increase clay volume, and reduce quartz volume by the same amount, keeping porosity constant. Four specific cases were analysed (Fig. 4.4.0.3):

- +20% clay volume, 100% water
- +20% clay volume, 80% gas, 20% water
- +40% clay volume, 20% gas; 80% water
- +40% clay volume, 80% gas, 20% Water

d) Thickness models: Four thickness models were analysed perturbing the reservoir in well F-O1 and F-O4. A methodology consists in removing a partial section from the log to simulate thinning in the section or to repeat a section from the log to simulate thickening via copy and paste:

• 2 models with decreasing thickness: 80% gas, 20% brine, in in-situ fluid conditions (*)

• 2 models with increasing thickness: 80% gas, 20% water & 100% water

(*) reducing partially the net pay section decreases even more the chances of any hydrocarbon fluid in the rock to impact on seismic response.

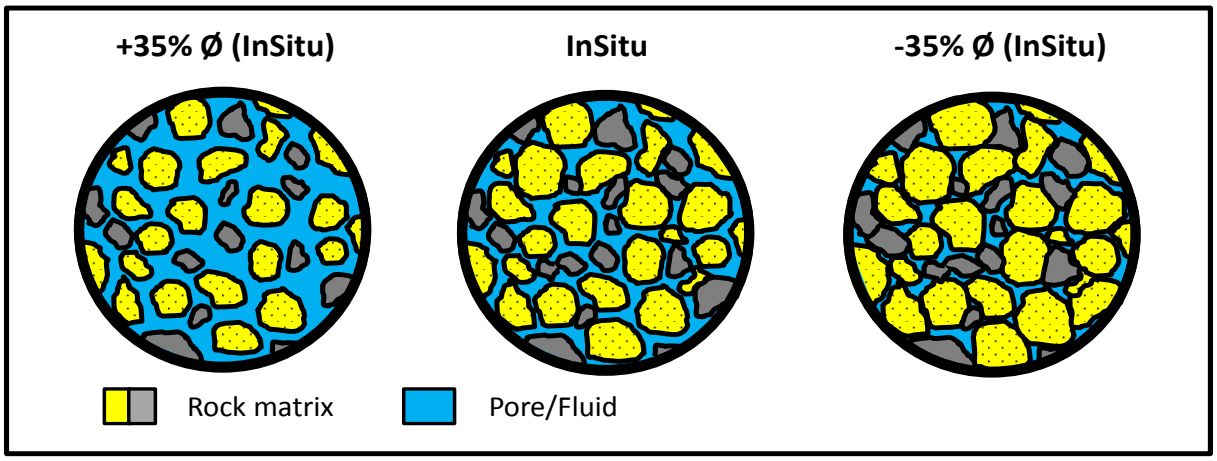

Figure 4.4.0.2: Model matrix to perturb porosity (Porosity cases).

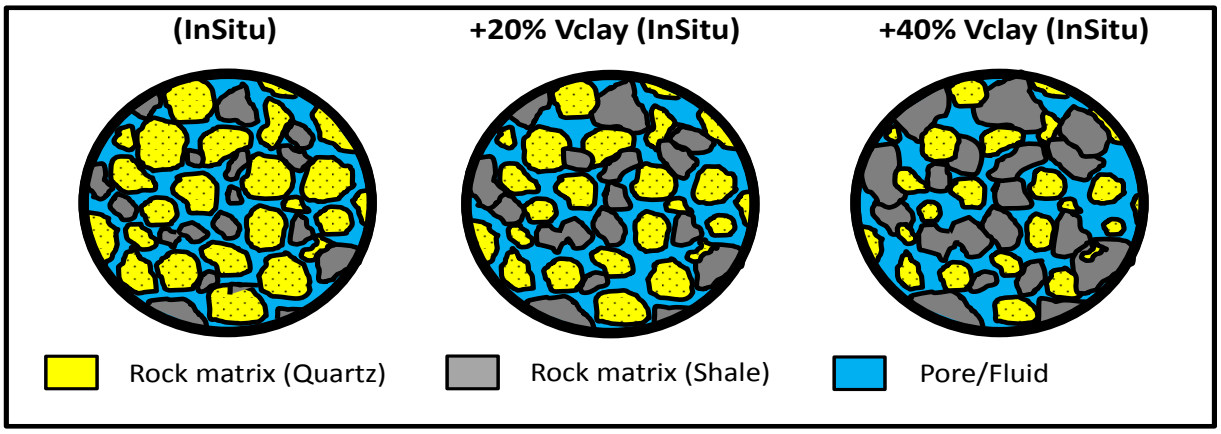

Figure 4.4.0.3: Model matrix to perturb Mineralogy (Vclay cases).

4.4.1 Fluid substitution

The effect of variations in fluid saturation in the reservoir sandstones was evaluated via fluid substitution using Gassmann (1951) relations (see appendix 4.4.1).

The values of the in situ case were perturbed to create “pseudo-wells” to account for possible inter-well differences (delta well modelling). The delta well modelling of three fluid substitutions represents the spectrum of variation of possible hydrocarbon saturation conditions that are likely to be found in the reservoir. The in situ fluid was substituted to a) 80% hydrocarbon gas, 20% water (red); b) 20% hydrocarbon gas; 80% water (orange); and c)

100% water (blue). The substitutions to partial hydrocarbon saturations occurred within select reservoir quality sands defined using cut-off characteristic of the good facies (VClay<0.35 & PHIT>0.06). The F-O hydrocarbon consists of light components, mostly methane (dry gas). Therefore, the hydrocarbon oil case was not considered in this exercise, because it is an unlikely scenario.

Figures 4.4.1.1, 3,5,7,9 show a log-plot with elastic curves (Vp, Vs & density) and derived properties (AI & PR) for each well in a depth window focussed on the pay target reservoir section.

Both P-velocity and density show a moderate sensitivity to hydrocarbon fluid changes when compared with the water case. Overall, the P-velocity shows the greatest effect to fluid changes as was expected. In the elastic domain, fluid effects are best seen in the Poisson's ratio and less in the acoustic impedance; there is moderate-to-good discrimination between gas and water and subtle discrimination between the gas and fizz cases.

Two classical cross-plot products are plotted: on the left Poisson's ratio (PR) vs acoustic impedance (AI) and on the right (lambda*rho vs. mu*rho) in order to identify the best combination, if any, for discriminating between pay and water target reservoir sections (figures 4.4.1.2, 4, 6, 8, 10).

Fluid cases are overlaid on the in situ data which is in black. The background trend is gray.

Both domains appear to have very similar sensitivity to fluid response. One main observation is: moderate to good separation between gas vs water case.

In the acoustic impedance-Poisson's ratio plot, a modest separation is seen between water and hydrocarbon cases in the acoustic impedance domain, but there is a significant improvement in the separation in Poisson's ratio domain. In the lambda-mu-rho cross-plot case, mu-rho shows a negligible to null separation in any combination, and lambda-rho shows good separation.

As the burial depth increases, compaction increases because the synrift reservoir is rather deep (+ 3500 metres). Consequently, porosity and the fluid sensitivity decrease. Therefore, the sensitivity in the elastic response to fluid in a reservoir can be attributed to how tight the rock is. Tighter sands (F-O3 & F-O6) will be less able to show good discrimination between fluid cases than softer sands (F-O2 & F-O1) whose porosity was enhanced by an Enhanced Poro-Perm (EPP) process (leaching).

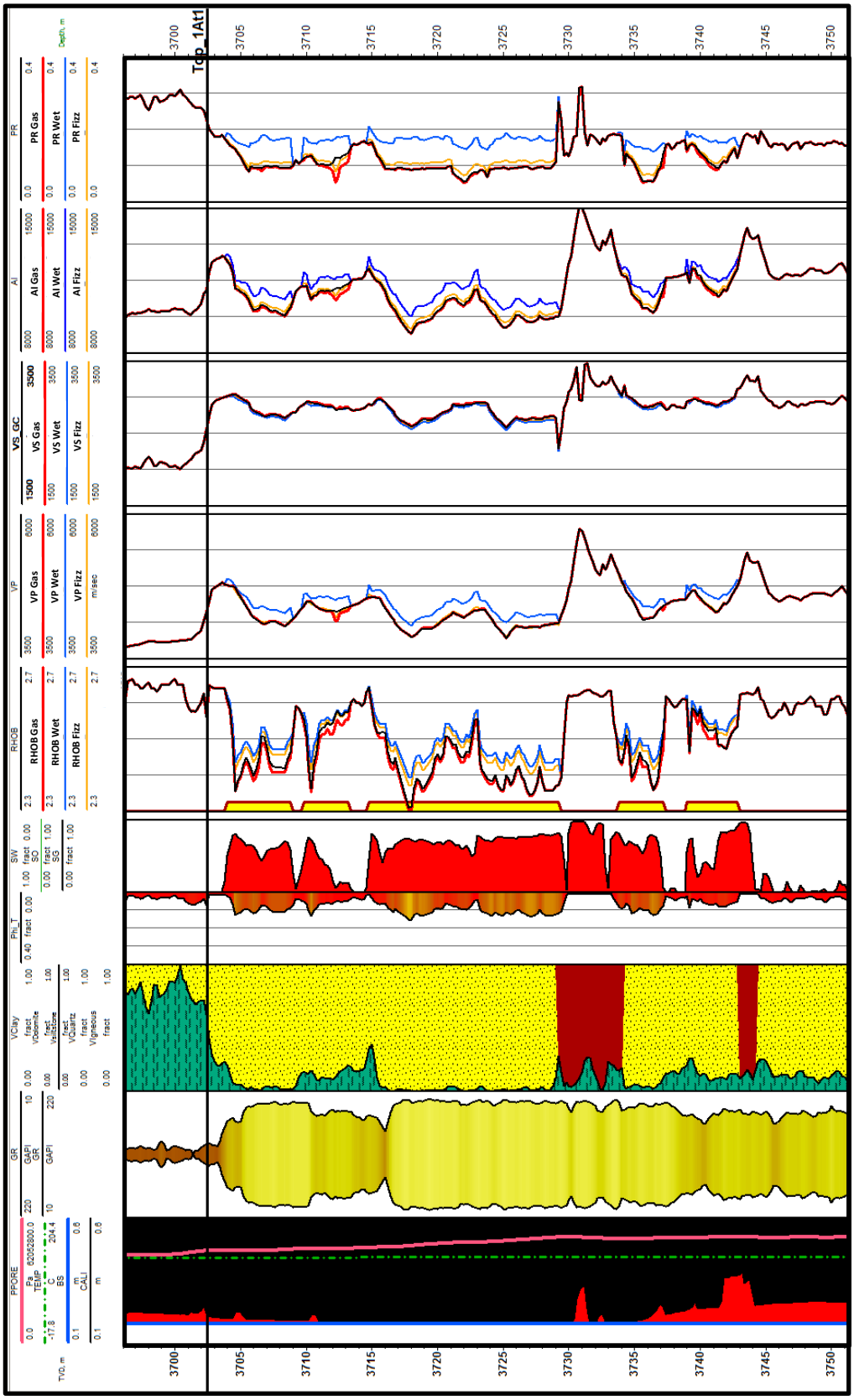

Fig. 4.4.1.1: Fluid Substitution_F-O1 (log-plot).

Acoustic Imp-Poisson ratio Plot

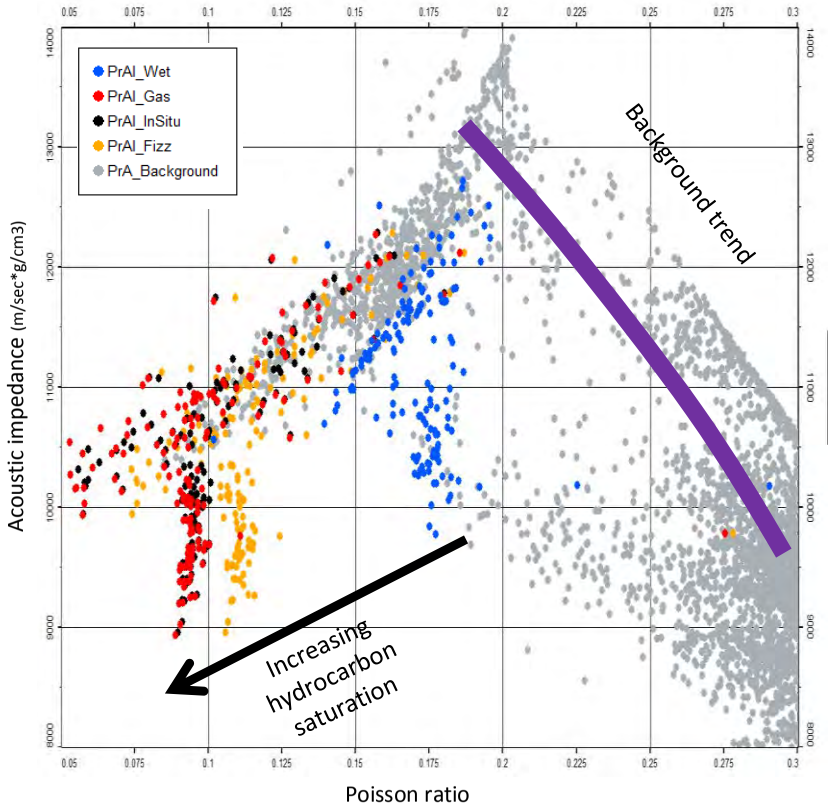

Lambda-Mu-Rho Plot

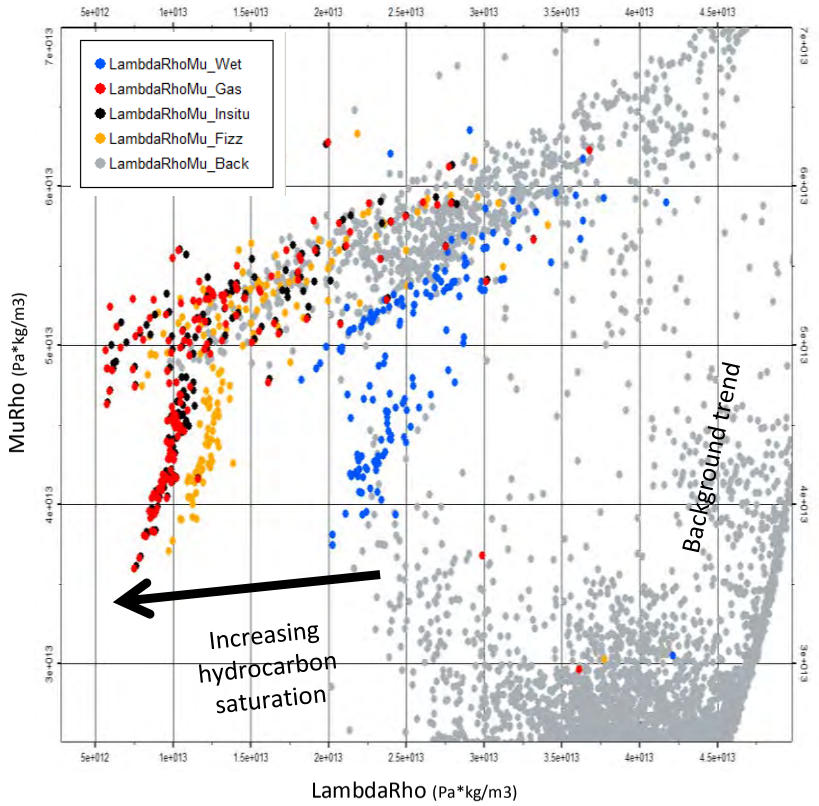

Fig. 4.4.1.2: Fluid Substitution_F-O1 (log-cross-plot).

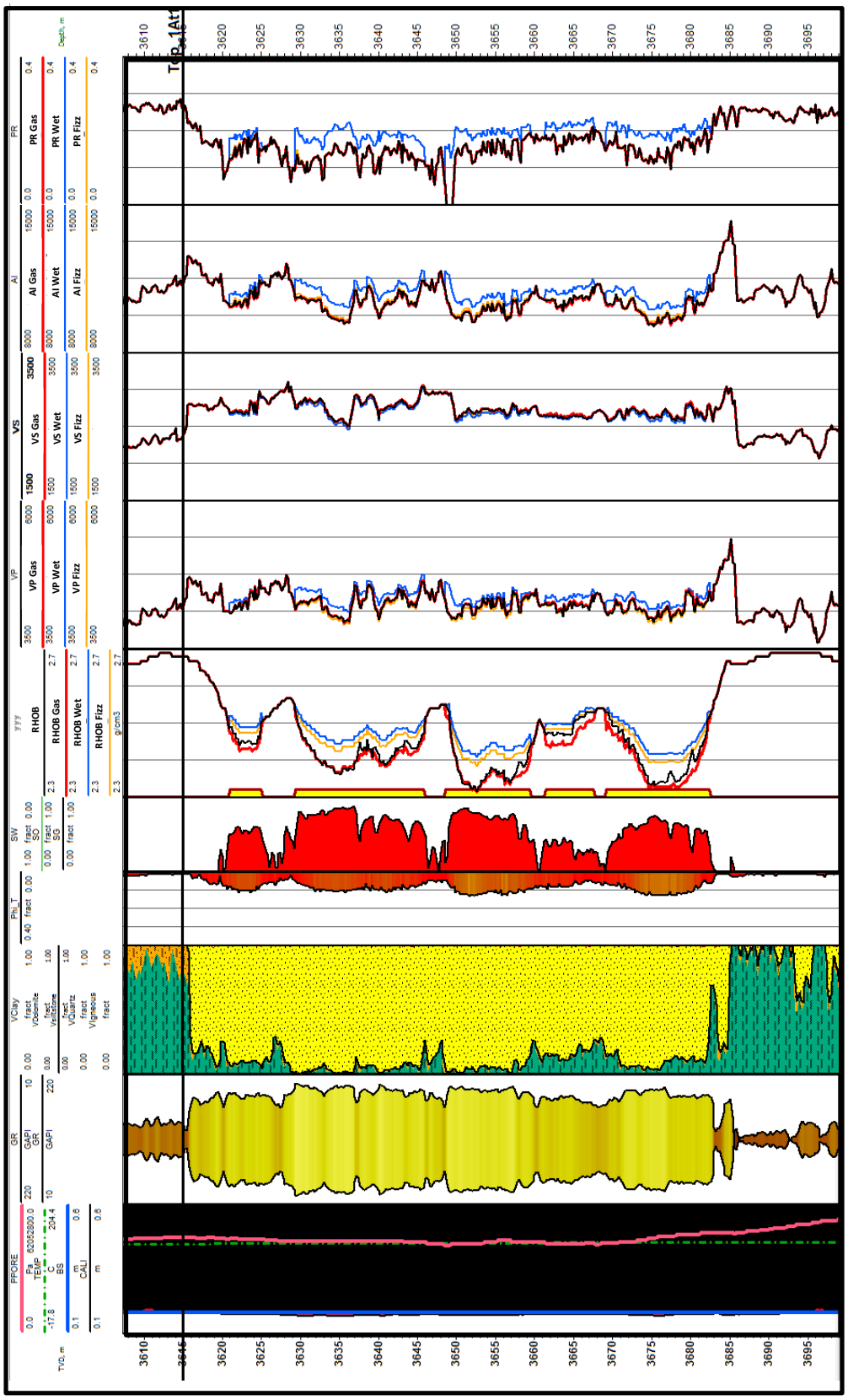

Fig. 4.4.1.3: Fluid Substitution_F-O2 (log-plot).

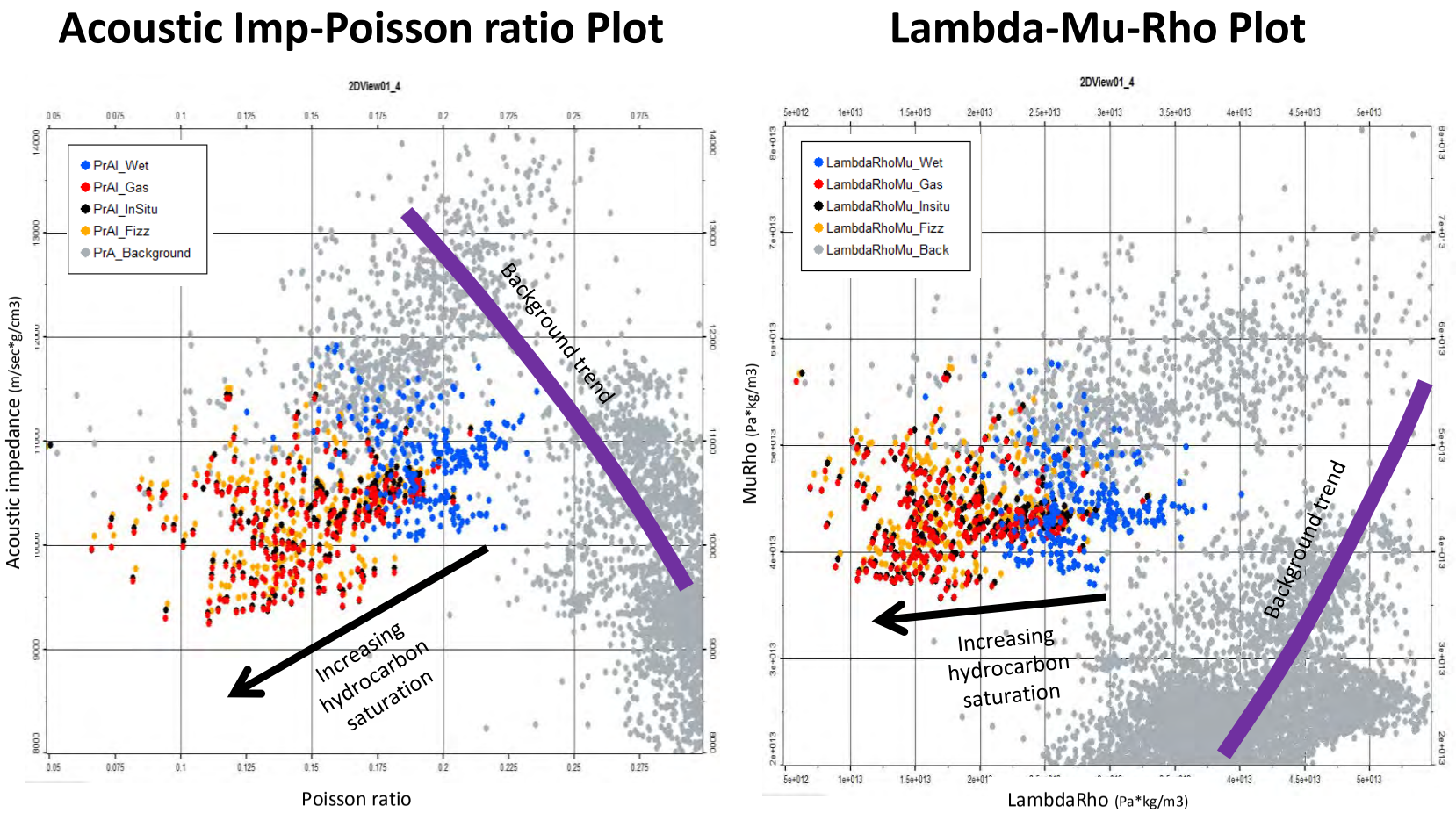

Fig. 4.4.1.4: Fluid Substitution_F-O2 (log-cross-plot).

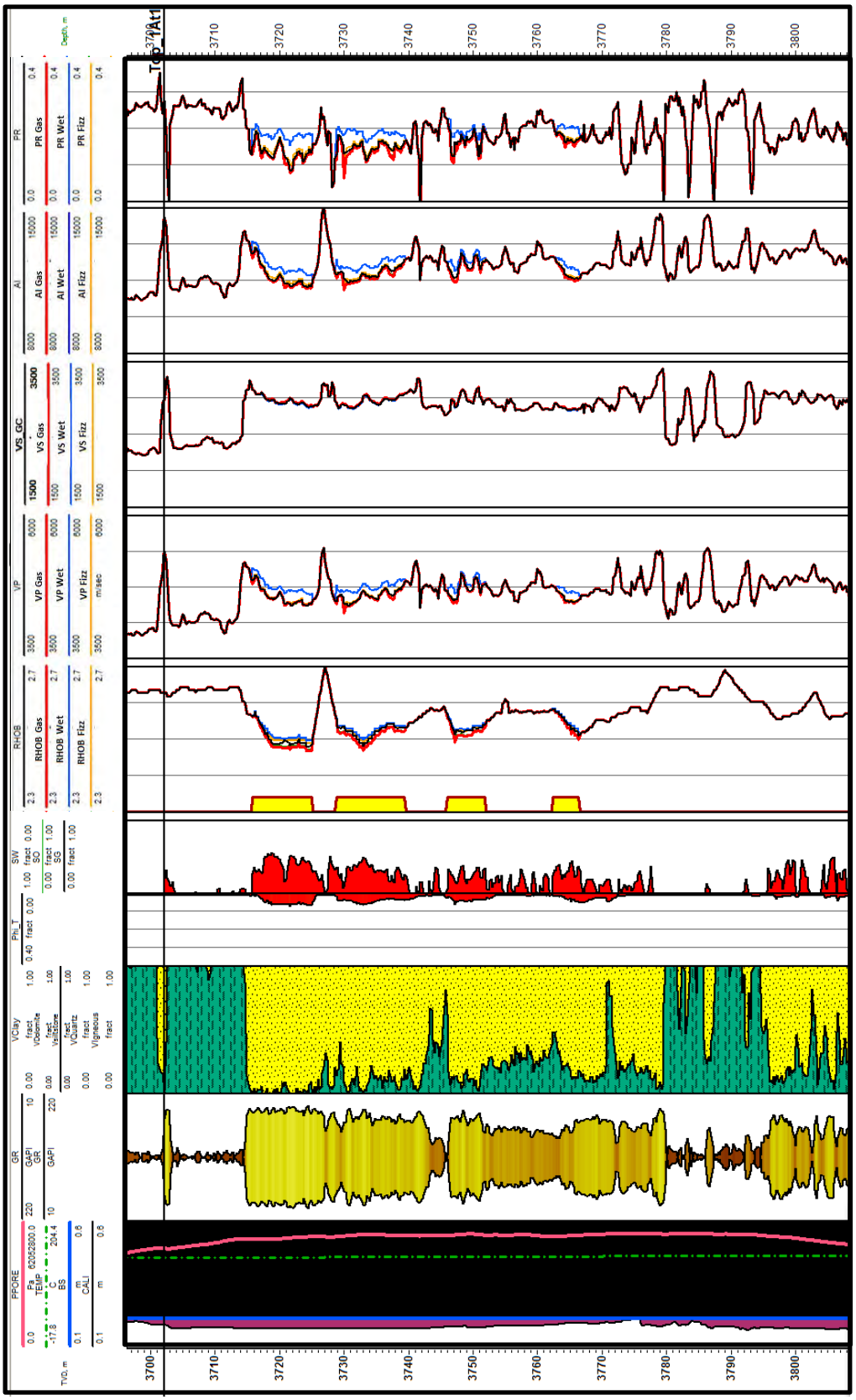

Fig. 4.4.1.5: Fluid Substitution_F-05 (log-plot).

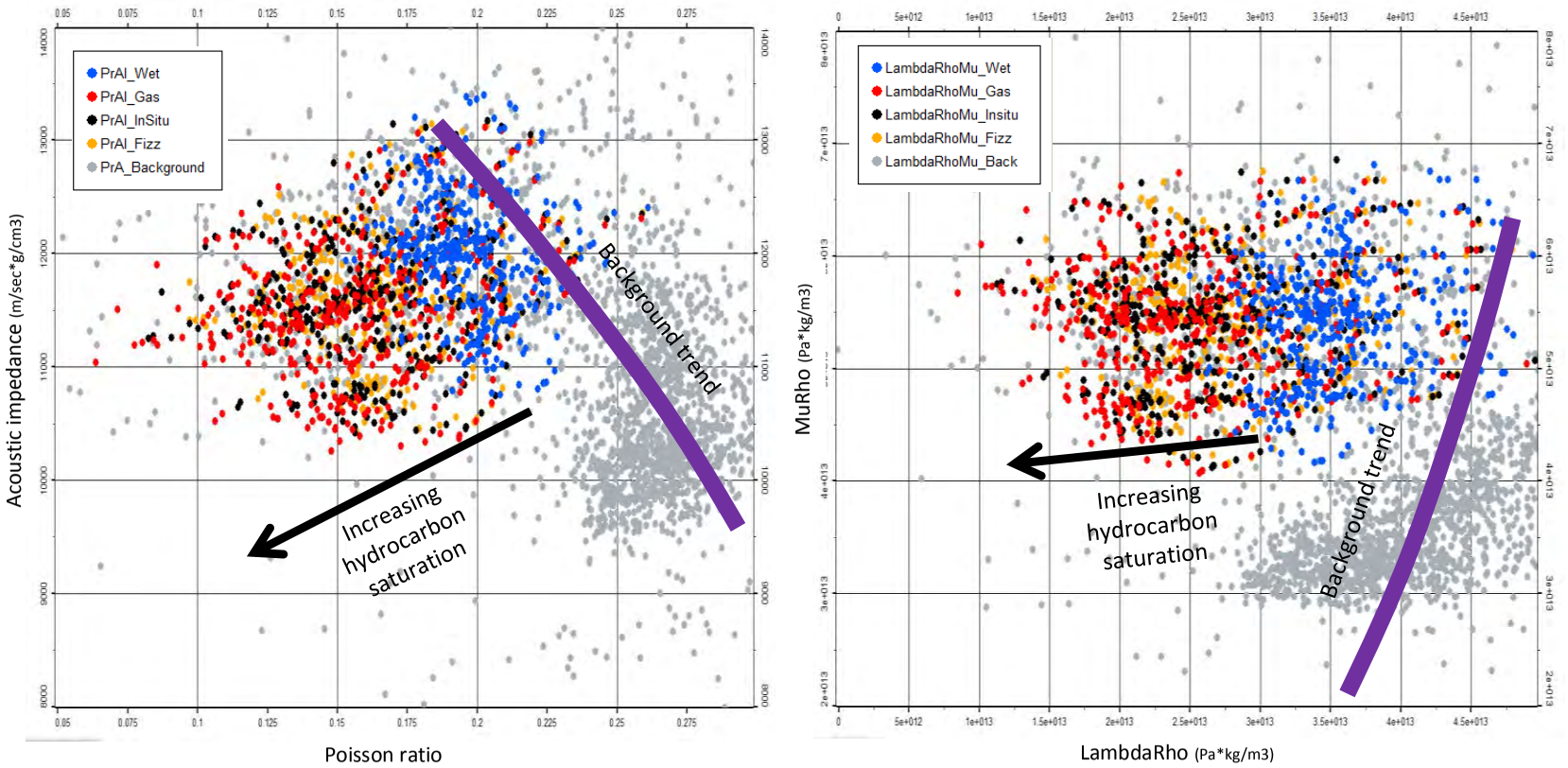

Fig. 4.4.1.6: Fluid Substitution_F-O3 (log-cross-plot).

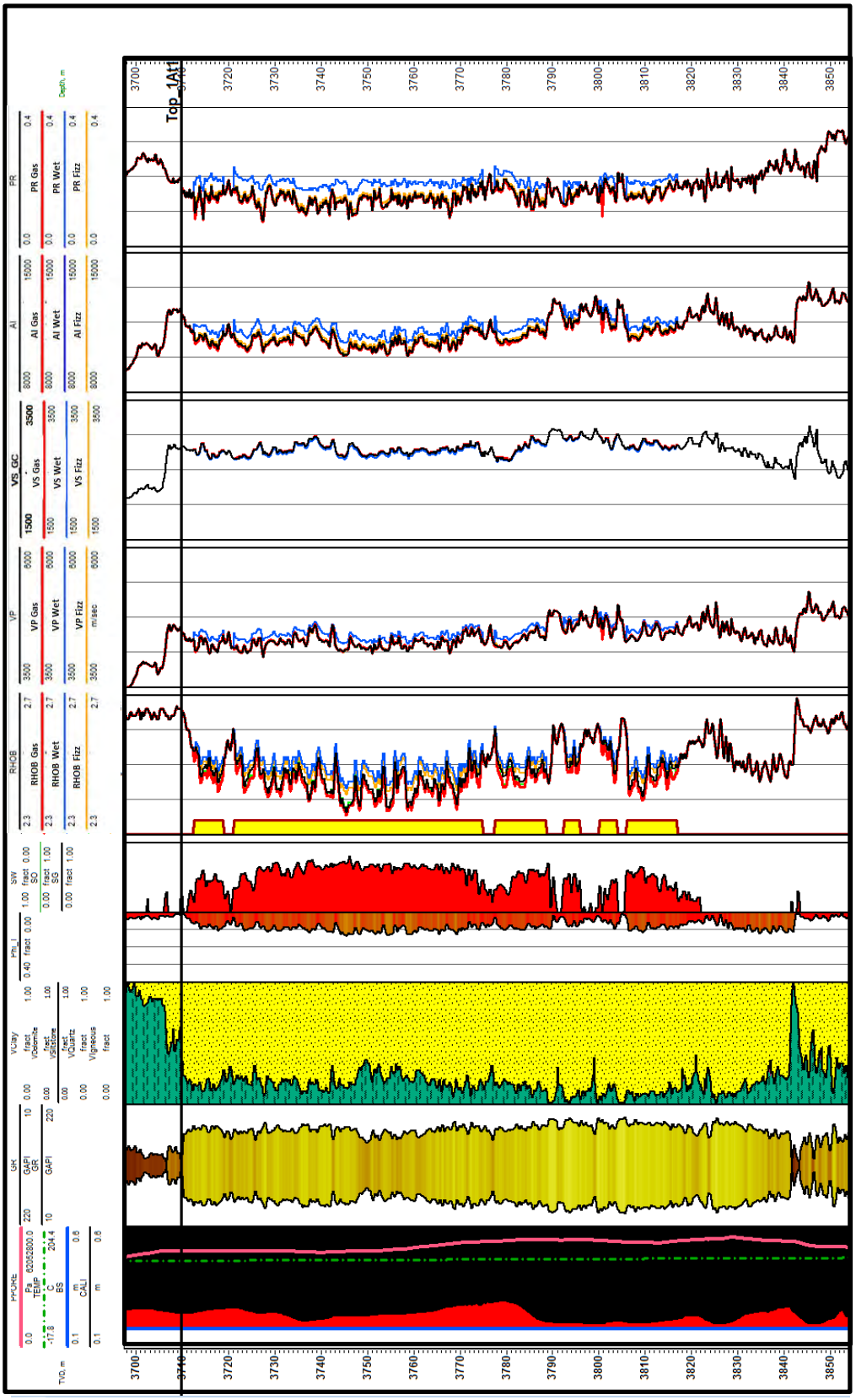

Fig. 4.4.1.7: Fluid Substitution_F-O4 (log-plot).

Acoustic Imp-Poisson ratio Plot

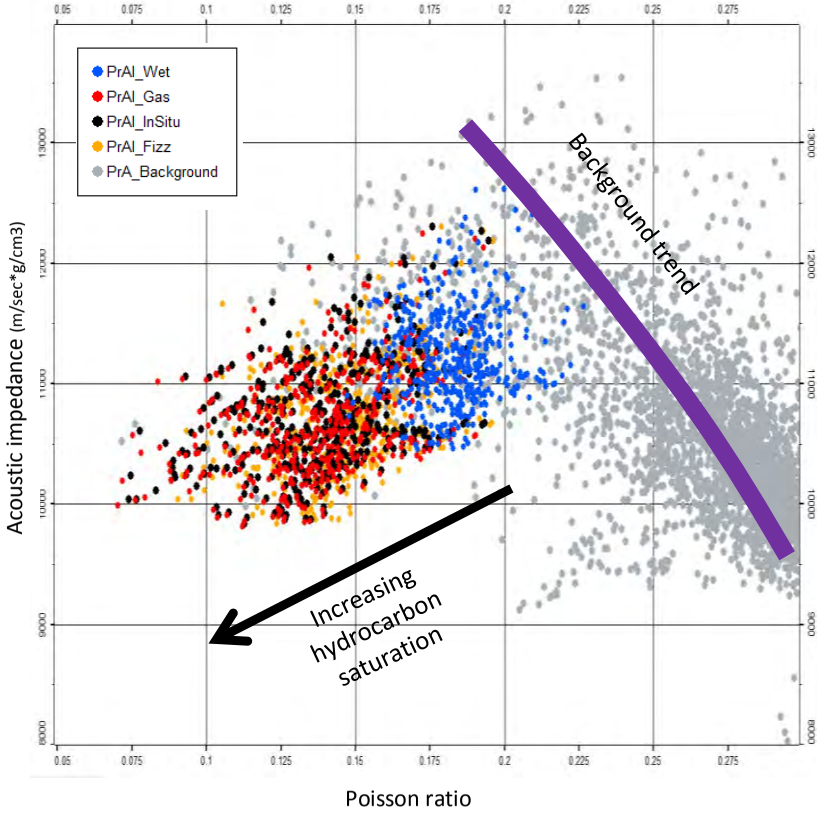

Lambda-Mu-Rho Plot

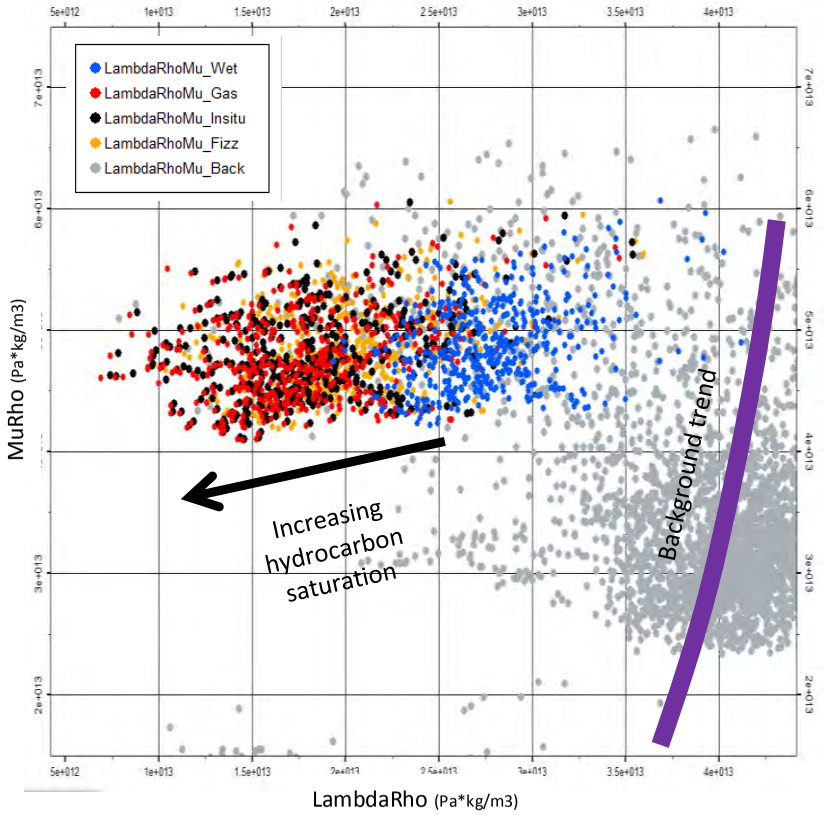

Fig. 4.4.1.8: Fluid Substitution_F-O4 (log-cross-plot).

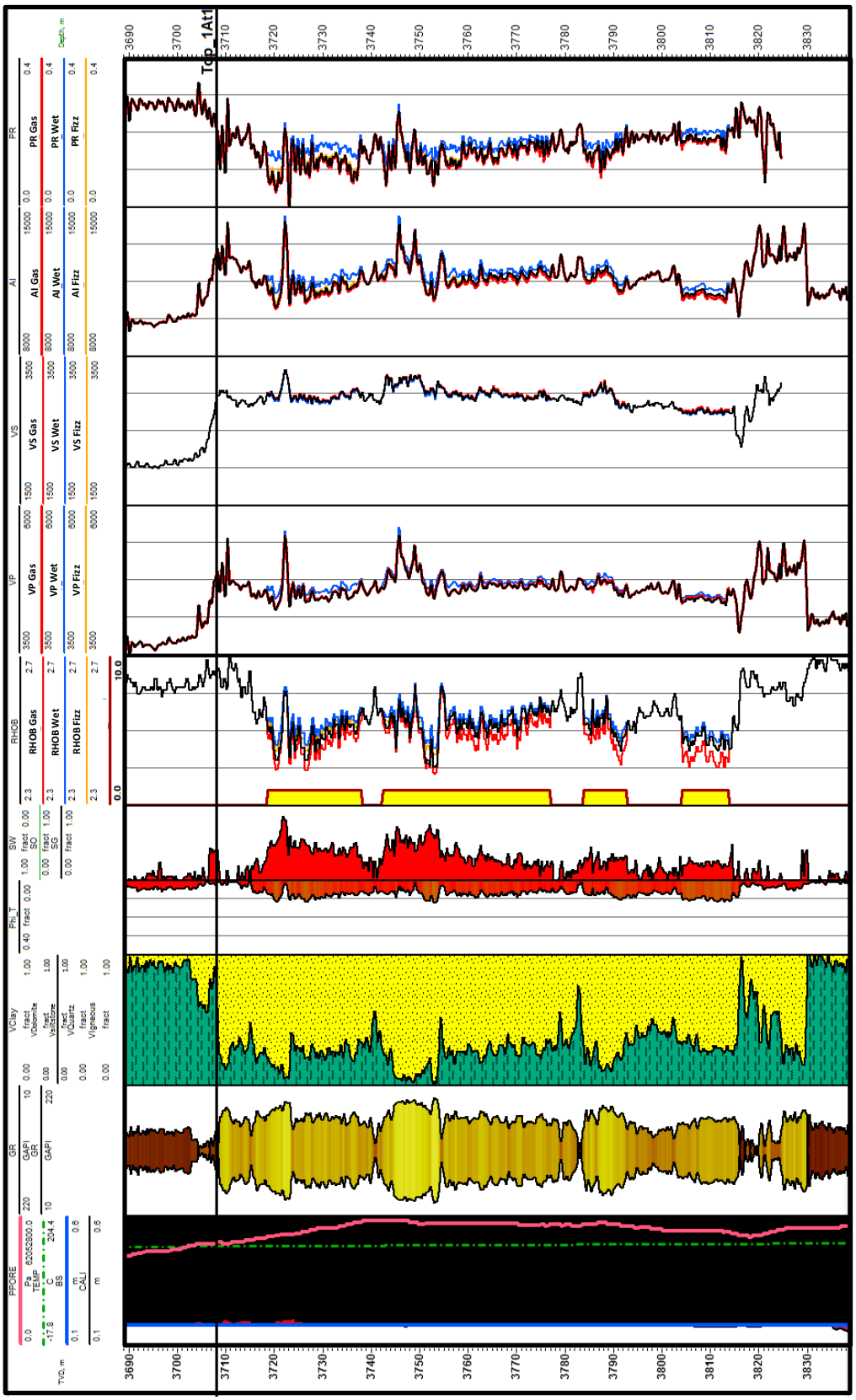

Fig. 4.4.1.9: Fluid Substitution_F-O6 (log-plot).

Acoustic Imp-Poisson ratio Plot

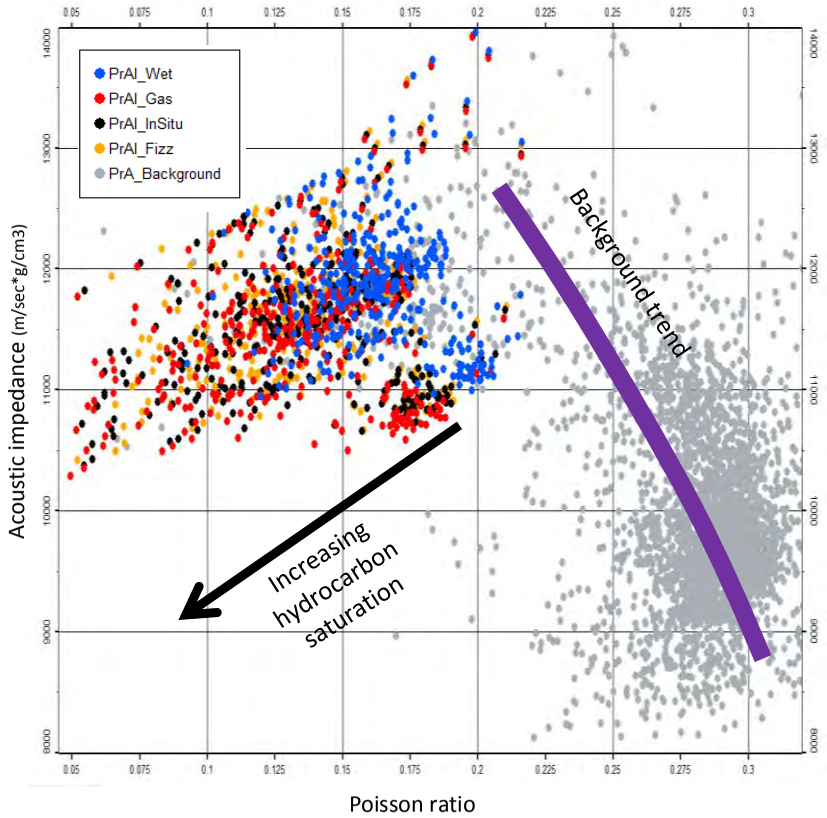

Lambda-Mu-Rho Plot

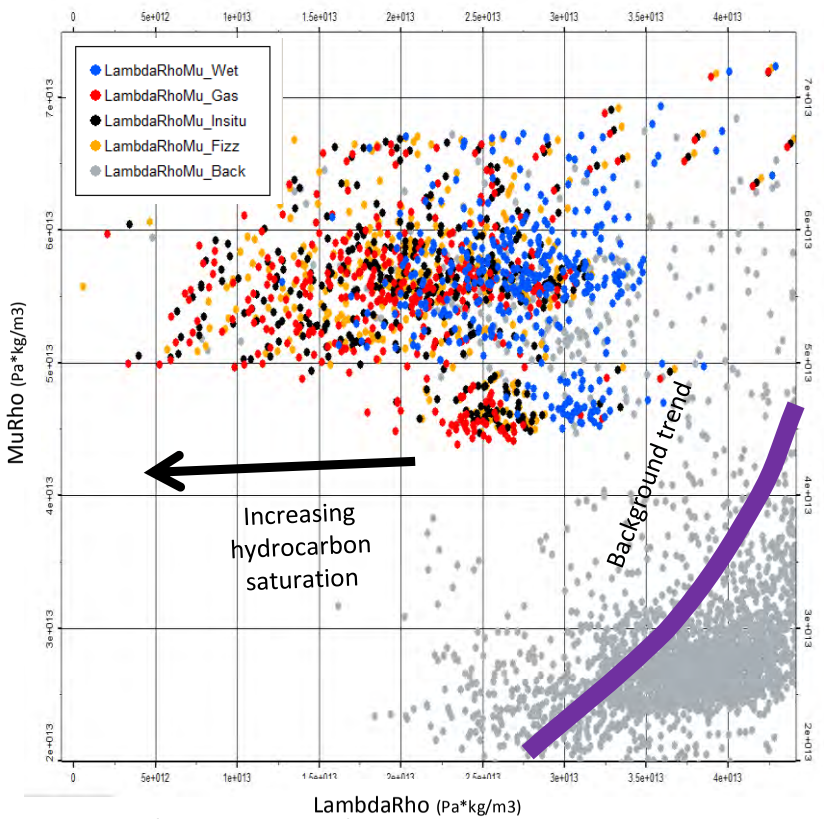

Fig. 4.4.1.10: Fluid Substitution_F-O6 (log-cross-plot).

4.4.2 Porosity models

Porosity (Phi) and fluid variation effects were examined by combining the rock physics model and Biot-Gassmann in the reservoir sandstones. The mineral properties themselves do not change in these scenarios, only the percentage of pore volume. The main reason for not changing mineral properties (Vclay) is to allow isolation of the porosity effects.

The values from the in situ case were perturbed to create "pseudo-wells" to account for possible inter-well differences (delta well modelling). The delta well modelling consisted of four porosity and fluid combinations. The in situ porosity and fluid were substituted to 1) reduced Phi, 80% gas, 20% water; 2) reduced Phi, 20% gas, 80% water; 3) increased Phi, 100% water; 4) increased Phi, 80% gas, 20% water. An optimal factor of 35% was defined to increment and reduce the in situ porosity to reasonable values according to the geological and sedimentary conceptual model. An example of how porosity at different scenarios is calculated is given below.

"-35% Phi" indicates [(in situ Phi*-0.35) + in situ Phi] (reduce case) and "35% Phi" indicates [(in situ Phi*0.35) + in situ Phi] (increment case).

These substitution models represent the spectrum of variation of possible porosity and hydrocarbon saturation conditions that are likely to be found in the reservoir.

A cut-off point to define the reservoir sands to be perturbed varied from well to well. In wells with a not so well developed in situ porosity (F-O3), a more conservative porosity cut-off of 0.05 is used to guarantee that a representative interval is included for the purpose of the exercise. However, on wells with better average porosities, such as F-O1 and F-O2, a classic cut-off of 0.06 is used.

Elastic curves (Vp, Vs and density) and derived properties (AI and PR) for the in situ case, superimposed with each porosity model, are displayed as a log curves to analyse the elastic response to porosity changes. For the purpose of this exercise, the in situ case is in black, reduce Phi with 80% gas and 20% water is in brown, reduce Phi with 20% gas and 80% water in orange, increase Phi with 100% water in blue and increase Phi with 80% gas and 20% water in red (see figures 4.4.2.1,3,5,7,9).

A more distinct separation between gas and water Poisson's ratio curves is observed when the model is perturbed with the increased porosity case than when only fluid content is perturbed. Also, in the impedance domain porosity has a greater effect on the response than the fluid content substitution exercise does. When porosity increases, acoustic impedance decreases and when porosity decreases acoustic impedance increases dramatically.

In the acoustic impedance (AI) vs Poisson's ratio (PR) cross-plot, the porosity models show that porosity has a strong effect in both acoustic impedance and Poisson's ratio response. There is good discrimination between the gas and water cases for the increased porosity case in the Poisson's ratio domain and fair discrimination in the acoustic impedance domain.

On the contrary, a negligible discrimination between gas and non-commercial gas (fizz) case when porosity is reduced.

In the cross-plot space both Lambda*Rho vs. Mu*Rho and AI vs. PR show equivalent separation between different perturbational model cases. Aside from a gentle rotation of data set from one cross-plot domain to another and consistent in all wells, neither Lambda*Rho vs. Mu*Rho nor AI vs. PR could for instance provide a better discrimination between one porosity-fluid case and another at seismic resolution. Any relative improvement could be only attributed to a scale effect (see figures 4.4.2.2, 4, 6, 8, and 10).

4.4.3 Mineralogy models

The effect of mineralogical variation is examined by varying the clay volume at the expense of quartz, any other mineral volumes remaining unchanged. Using a similar methodology, clay models were designed to analyse the effect of clay content combined with fluid in the reservoir sandstones.

The values from the in situ case were perturbed to create “pseudo-wells” to account for possible inter-well differences (delta well modelling). The delta well modelling consisted of four clay and fluid combinations. The in situ clay and fluid were changed to: 1) +20% clay volume, 100% water; 2) +20% clay volume, 80% gas, 20% water; 3) +40% clay volume, 20% gas, 80% water; 4) +40% clay volume, 80% gas, 20% water. Typically, porosity and clay volume change simultaneously; nevertheless, the porosity is not changed in these scenarios in order to isolate the different effects. When porosity and clay change simultaneously, the underlying reason for a shift in seismic response can be difficult to interpret.

These substitution models represent the spectrum of variation of possible clay and hydrocarbon saturation conditions that are likely to be found in the reservoir.

The values for perturbing the Vclay composition were generated based on typical clay values for the interval of interest and considering the range of probable Vclay values based on the geological and sedimentary conceptual model. First, an optimal value (clay factor) to be applied to the Vclay curve and restricted to the reservoir sandstones is computed, in which clay factor$_{20}$=Vclay + 0.2 and clay factor$_{40}$=Vclay + 0.4 are defined.

Then, the new Vclay (20% VClay or 40% VClay) is calculated:

20% VClay = Vclay + Clay factor$_{20}$ and

40% VClay = Vclay + Clay factor$_{40}$

The equations above are applicable when the Vclay + clay factor$_{20}$‹=1 and Vclay + clay factor$_{40}$ ‹=1 respectively. If (Vclay + clay factor >=1, new Vclay=1)

Then,

new VQz = 1 – new Vclay

where:

VQz = volume quartz and Vclay = volume clay

new Vclay = referred to the perturbed Vclay and is called 20% VClay or 40% VClay depending on the perturbation case.

Vclay and fluid variation effects on velocity and density response are examined by combining the rock physics model (intermediate stiff and soft model respectively) and Biot-Gassmann equations (see section 4.2).

In order to differentiate each clay case and for the sake of simplicity, the term “intermediate clay volume” has been coined for models in which Vclay has been increased by 20% at the expense of quartz and “high clay volume” to models in which Vclay is increased by 40% at the expense of quartz volume. In order to facilitate the visualization of different display formats (log-plot and cross-plot), elastic curves for each clay case are displayed in different colours: a) Insitu case: black, b) intermediate clay, 100% water: blue; c) intermediate clay, 80% gas, 20% water: red; d) high clay, 20% gas, 80% water: orange and e) high clay, 80% gas, 20% water: purple.

Figures 4.4.3.1,3,5,7 and 9 show the effect of the elastic response on log curves. The intermediate clay volume cases show a slightly smaller effect on the fluid content response than the in situ case, but still a decent discrimination between fluids (gas and water); however, if Vclay is increased more (high clay volume) , the discrimination between gas and water is poor and negligible between gas and non-commercial gas (fizz case).

Increasing clay leads to a decrease in acoustic impedance and an increase in Poisson’s ratio. Acoustic impedance decreases greatly when the system is initially perturbed with 20% clay (intermediate clay) and less when 20% more Vclay is added (high clay), whereas a dramatic increase in Poisson’s ratio occurs once the Vclay is incremented by 40% vs a subtle increased when only 20% is added.

Different scenarios could share the same response in any particular elastic log, as was confirmed during porosity perturbation exercises. In this respect, a similar acoustic impedance response between in situ and intermediate water case was noted. In order to separate the two responses, it is necessary to move from a log-plot to a cross-plot display, combining such variable (acoustic impedance) with Poisson’s ratio. See figures from 4.4.3.2, 4, 6, 8, and 10.

Data is plotted as P-impedance vs. Poisson’s ratio (left) and lambda*rho vs. mu*rho (right). 20% and 40% clay cases are overlaid on the in situ data (black). The clay background trend is coloured grey. The response of the increased clay models on Poisson’s ratio is the opposite to that observed in the porosity models: when porosity increases, Poisson’s ratio decreases, but when clay increases Poisson’s ratio increases. Acoustic impedance discriminates better between vclay cases, while Poisson’s ratio shows a good separation between fluid cases.

The lambda*mu*rho cross-plot shows a good discrimination on lambda*rho between cases in general and even a decent separation between high clay volume-gas and fizz case. However there is a poor to negligible separation between scenarios on mu*rho.

Overall, Vclay influencing mu*rho and fluid influencing lambda*rho is quite neat. Again acoustic impedance versus Poisson's ratio or mu*rho vs lambda*rho show similar separation of different Vclay-fluid cases.

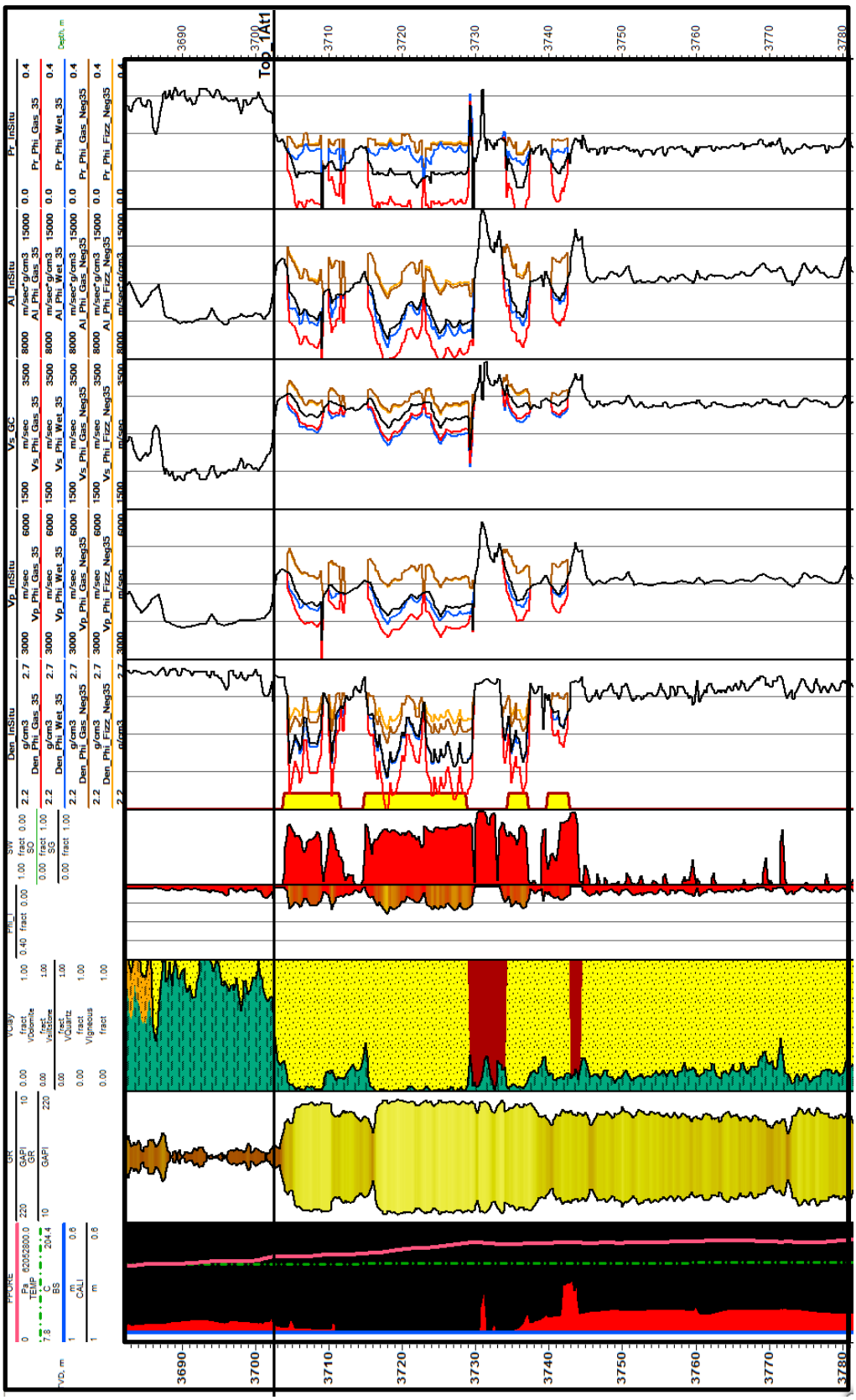

Fig. 4.4.2.1: Porosity perturbation_F-O1 (log-plot).

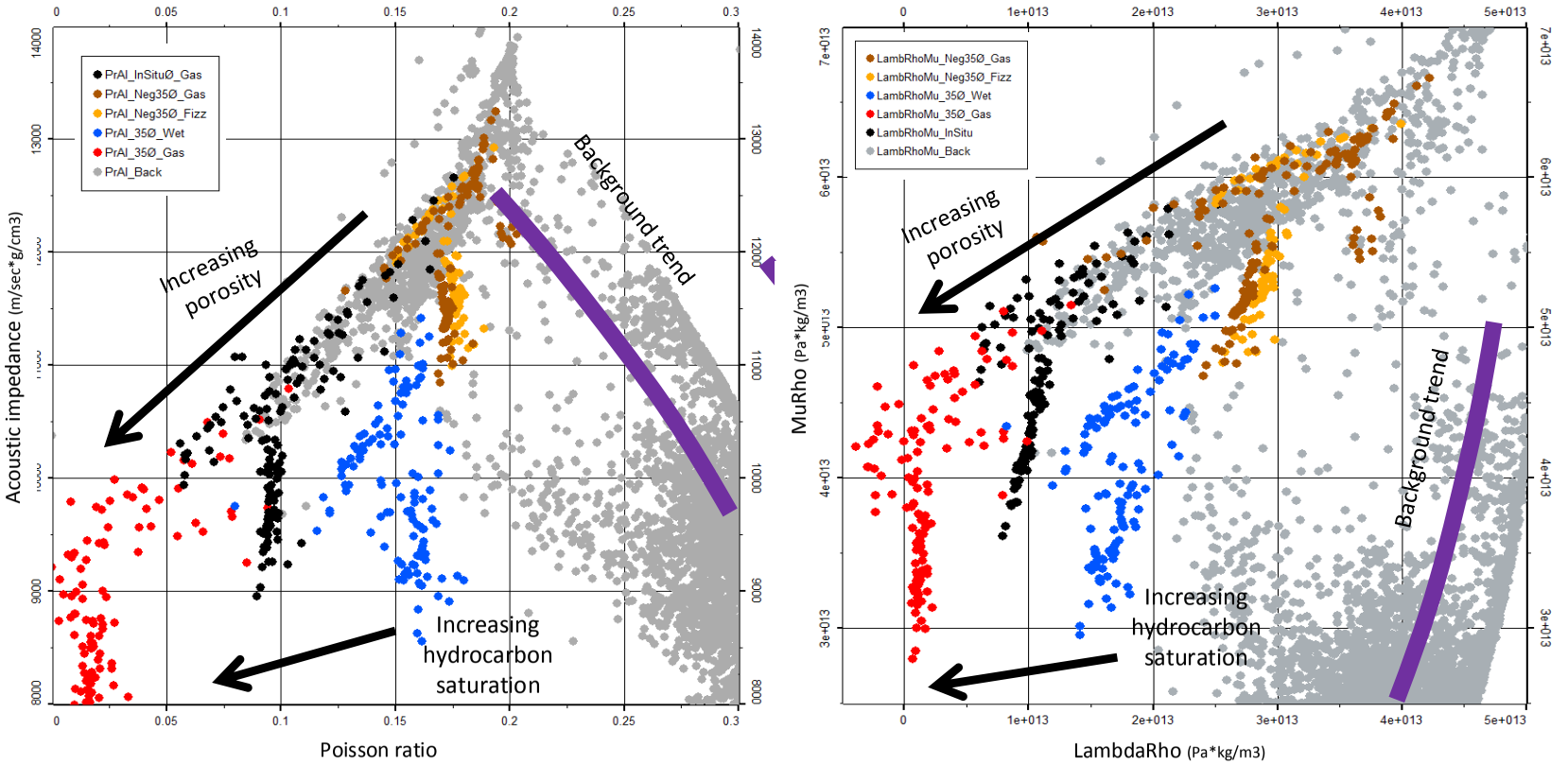

Fig. 4.4.2.2: Porosity perturbation_F-O1 (logs-cross-plot).

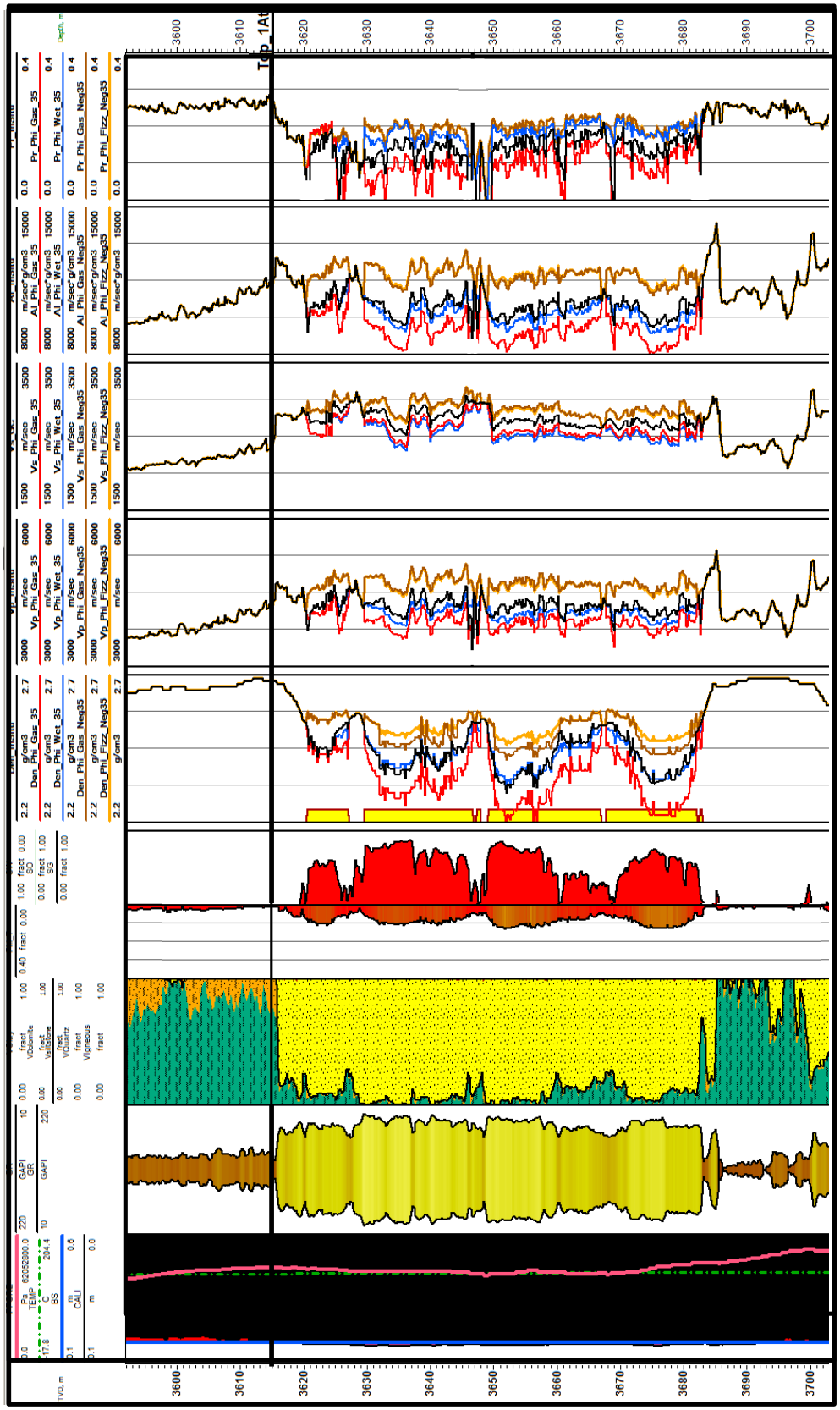

Fig. 4.4.2.3: Porosity perturbation_F-O2 (logs-plot).

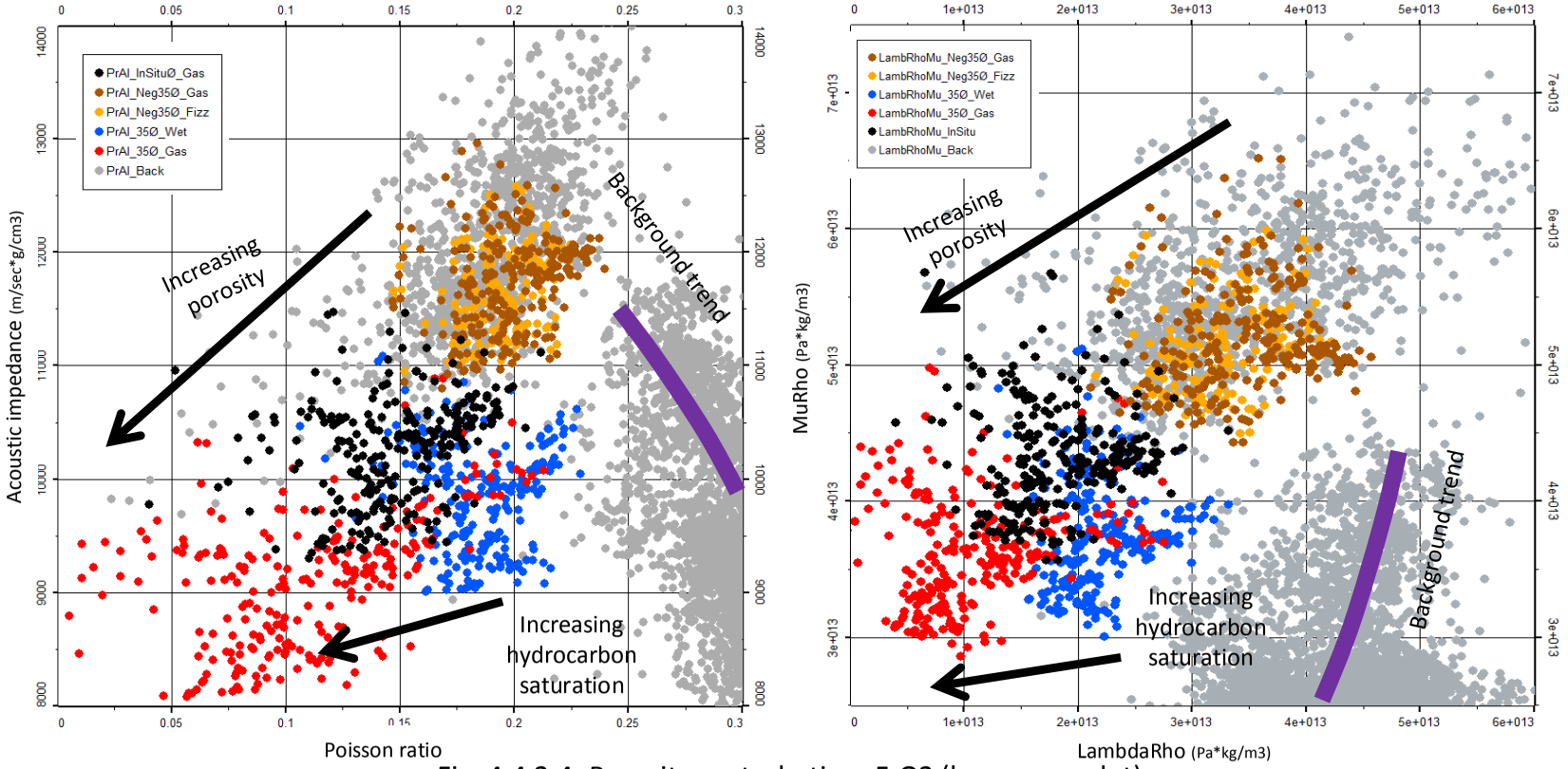

Fig. 4.4.2.4: Porosity perturbation_F-O2 (logs-cross-plot).

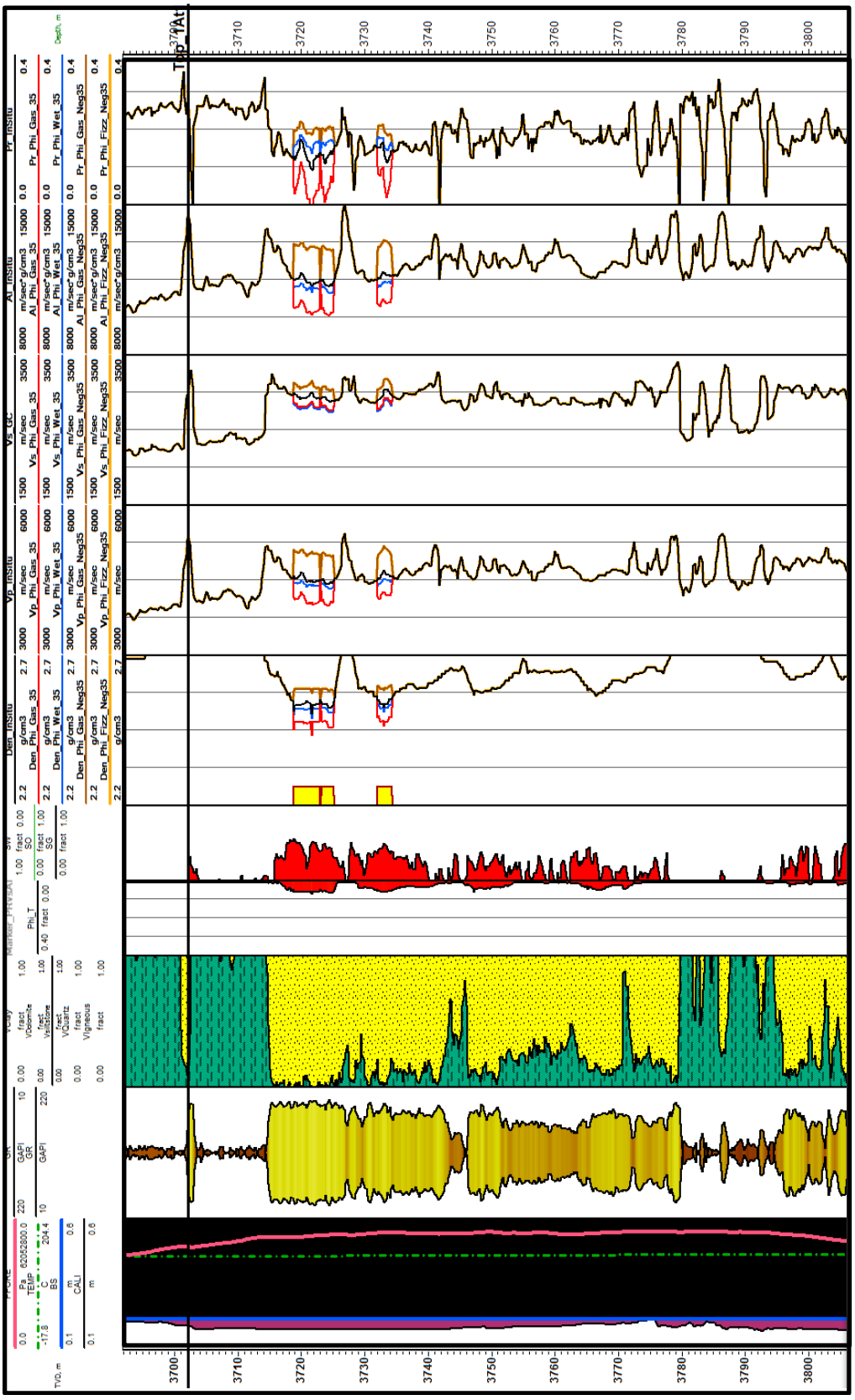

Fig. 4.4.2.5: Porosity perturbation_F-O3 (logs-plot).

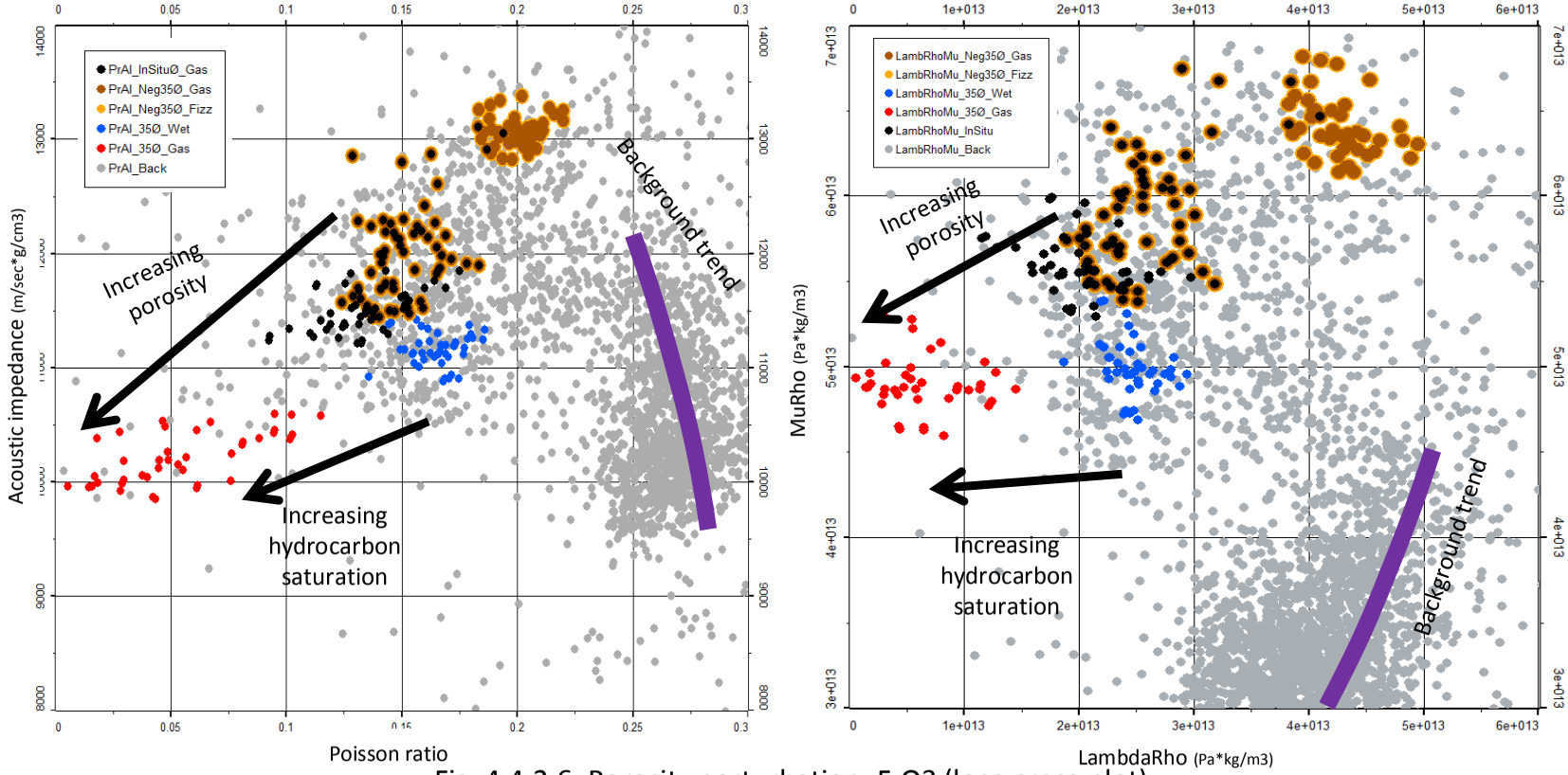

Fig. 4.4.2.6: Porosity perturbation_F-O3 (logs-cross-plot).

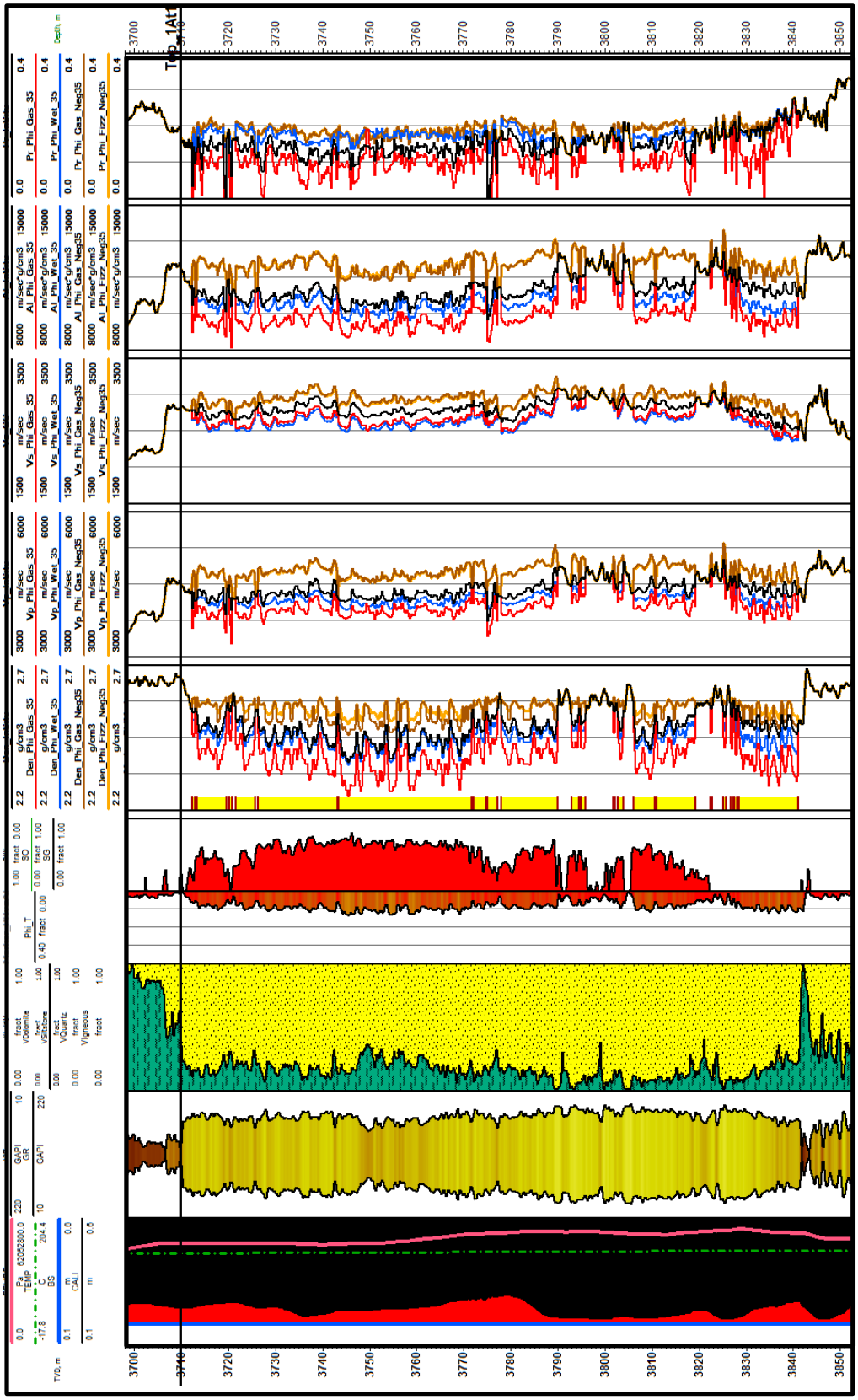

Fig. 4.4.2.7: Porosity perturbation_F-O4 (logs-plot).

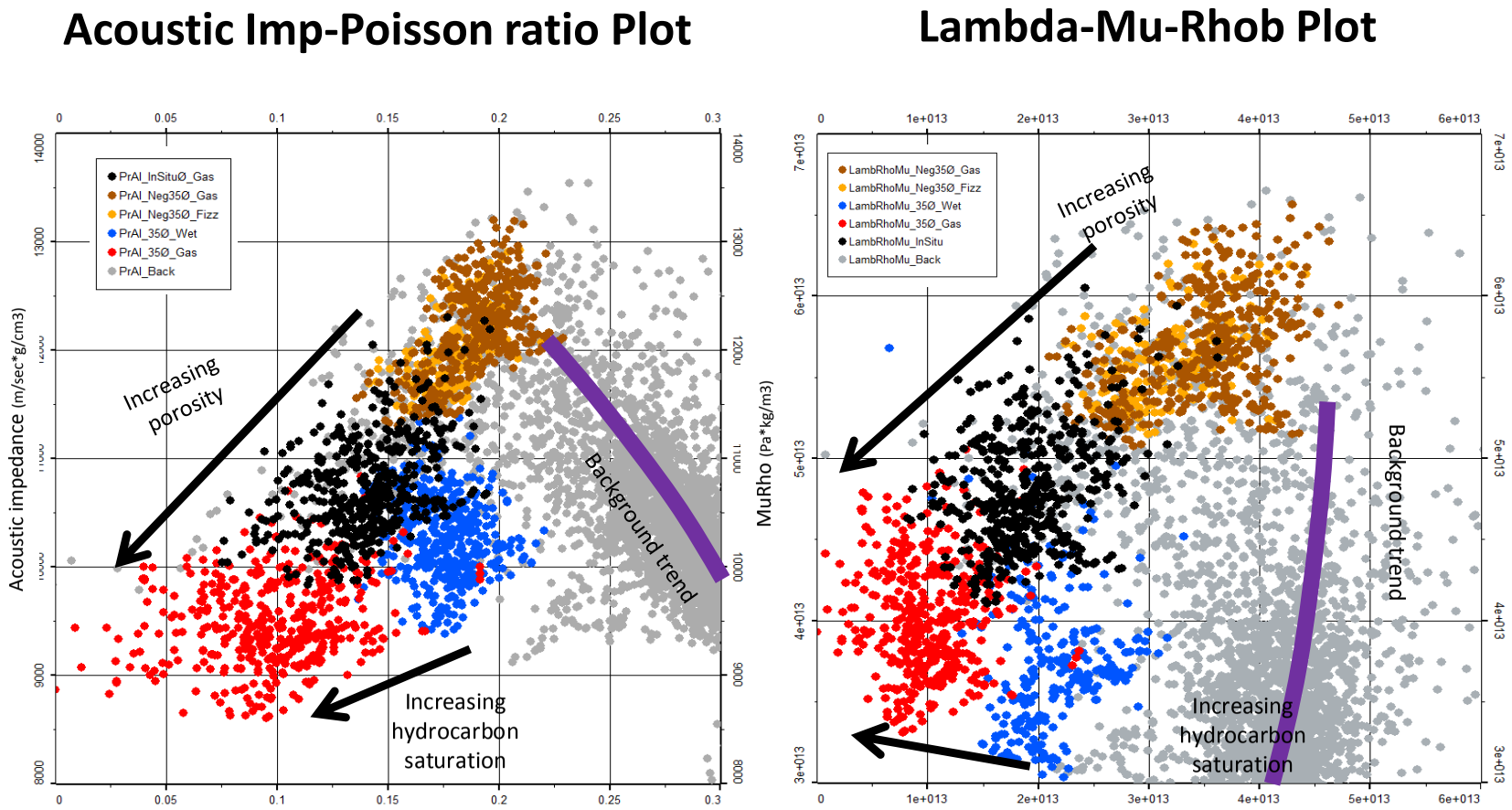

Fig. 4.4.2.8: Porosity perturbation_F-O4 (logs-cross-plot).

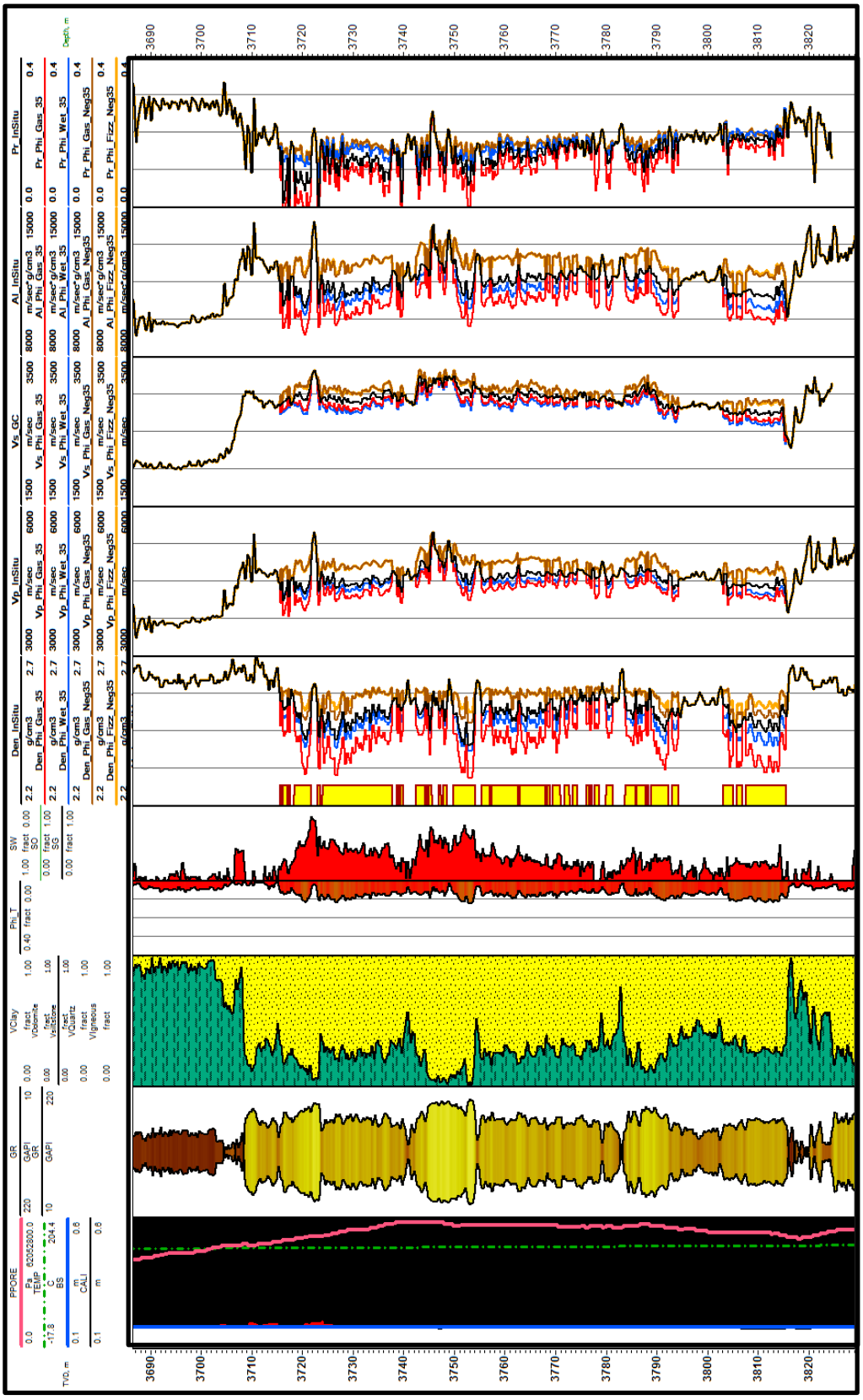

Fig. 4.4.2.9: Porosity perturbation_F-O6 (logs-plot).

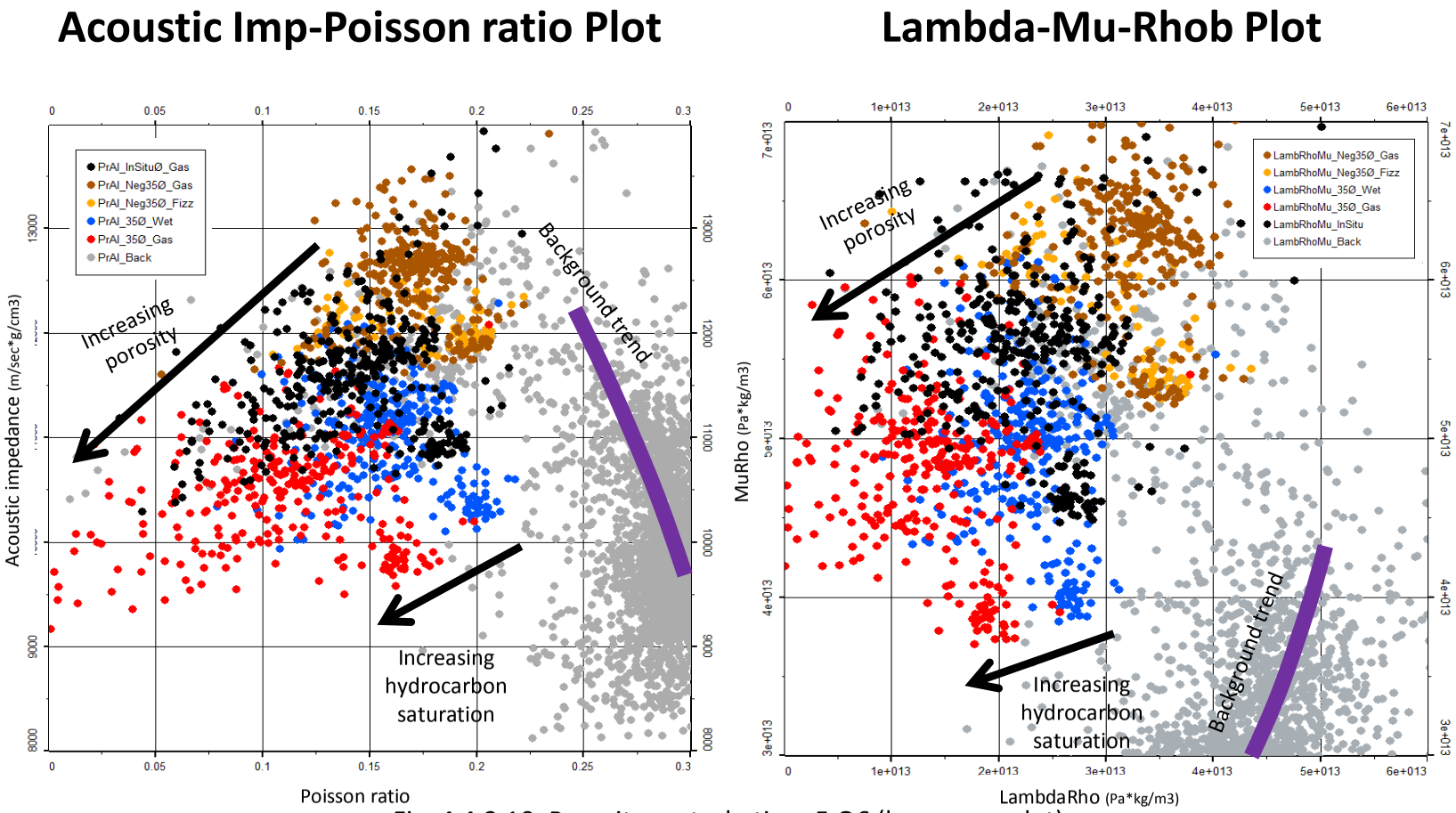

Fig. 4.4.2.10: Porosity perturbation_F-O6 (logs-cross-plot).

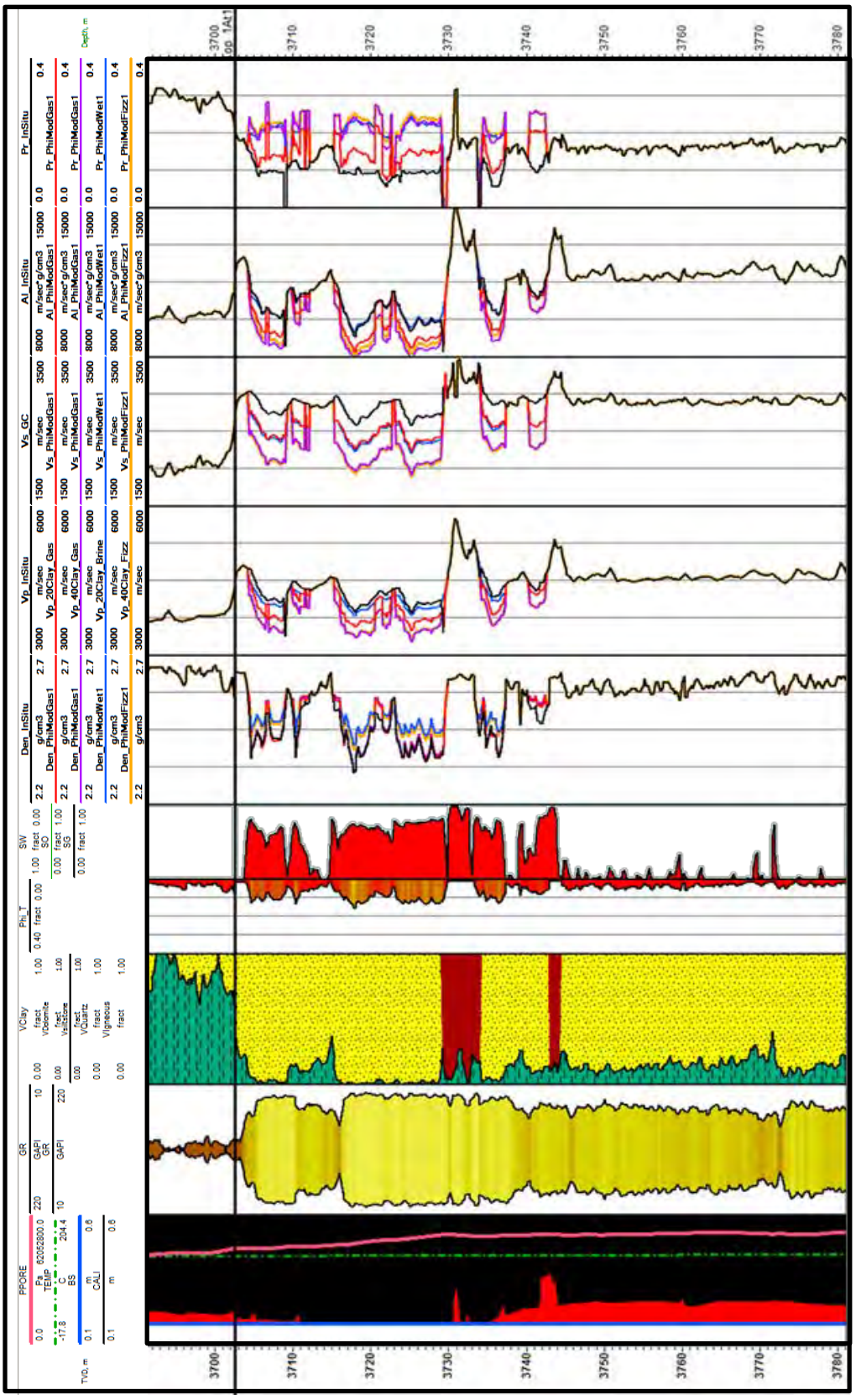

Fig. 4.4.3.1: Mineralogy perturbation_F-O1 (logs-plot).

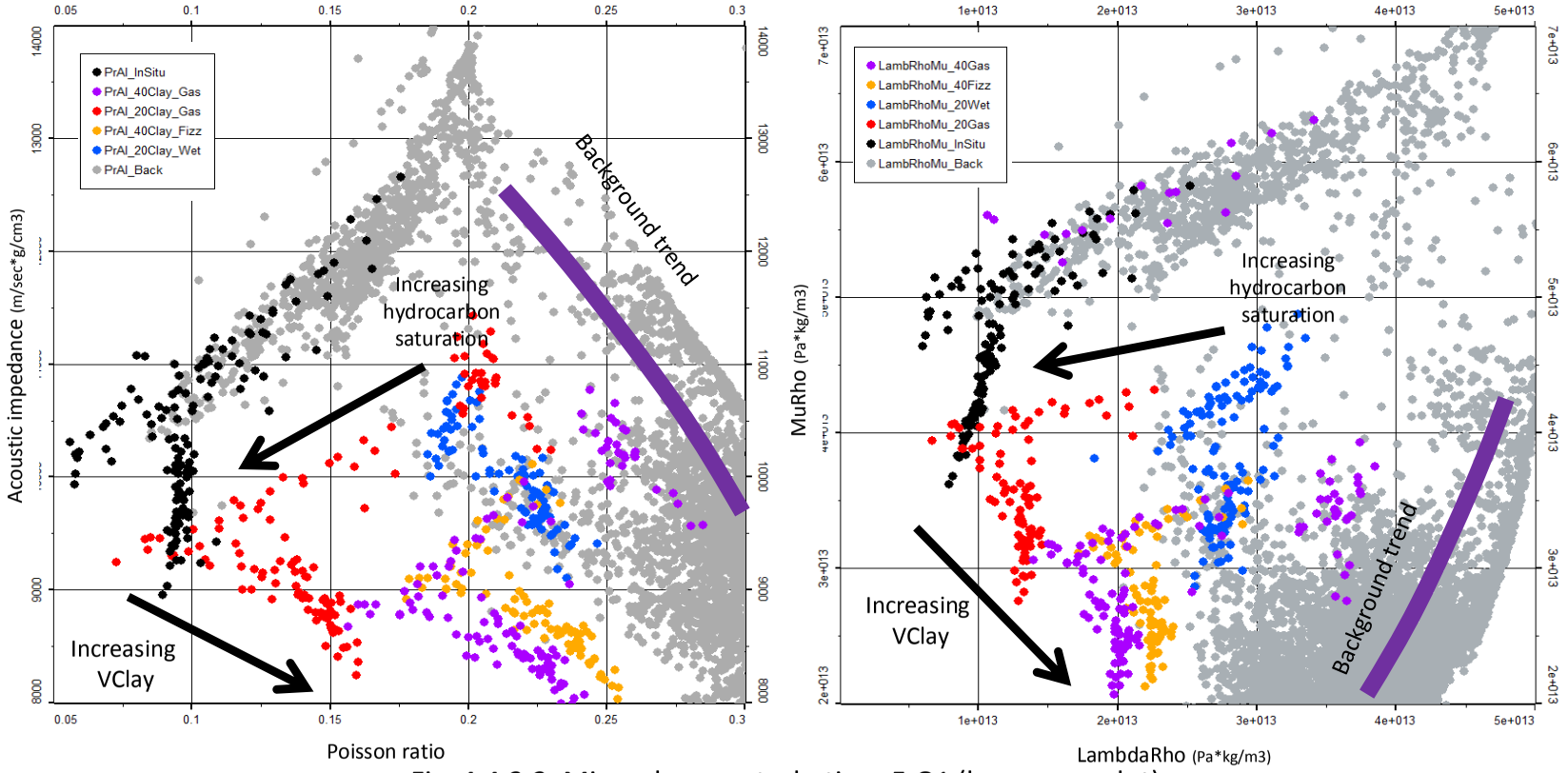

Fig. 4.4.3.2: Mineralogy perturbation_F-O1 (logs-cross-plot).

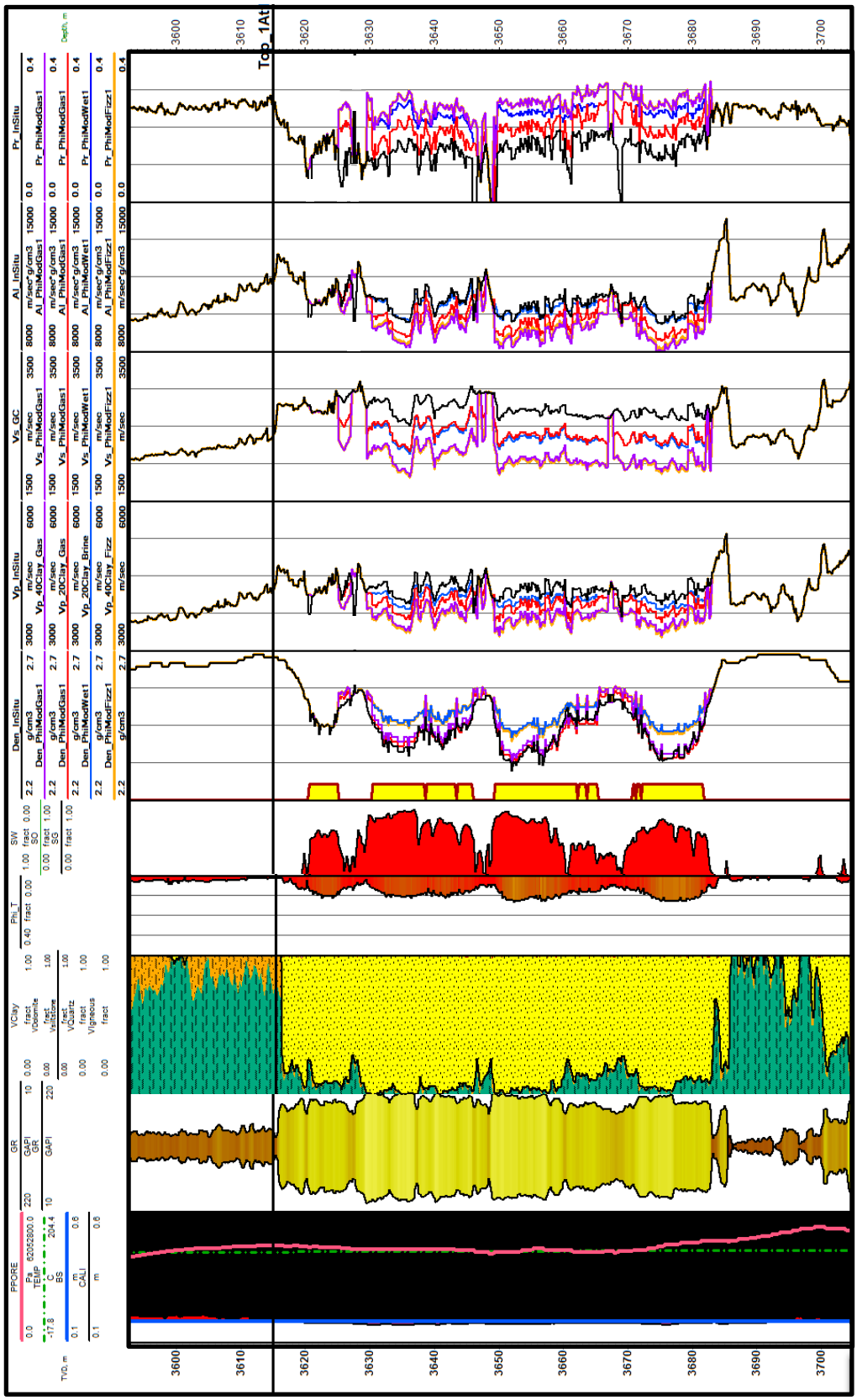

Fig. 4.4.3.3: Mineralogy perturbation_F-O2 (logs-plot).

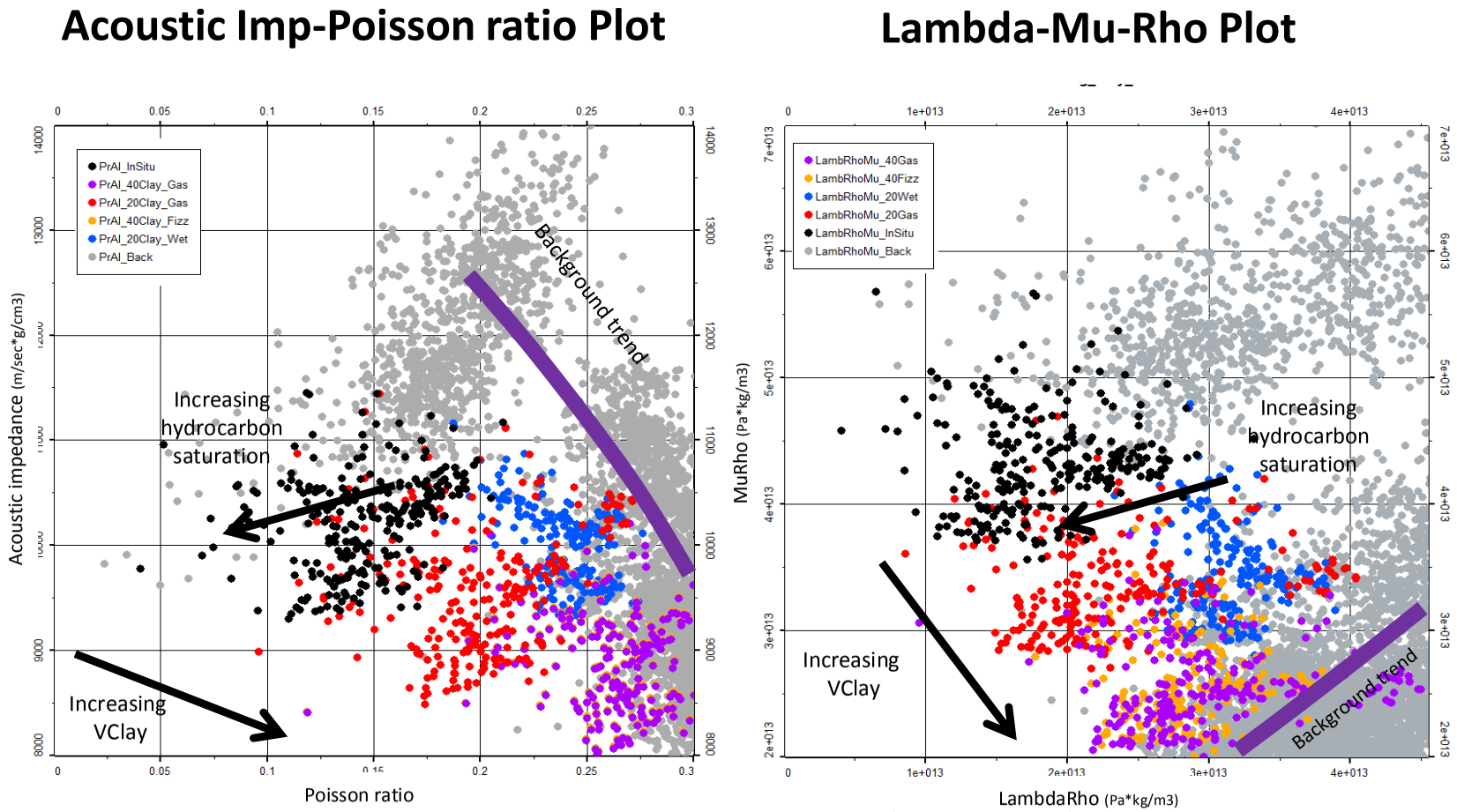

Fig. 4.4.3.4: Mineralogy perturbation_F-O2 (logs-cross-plot).

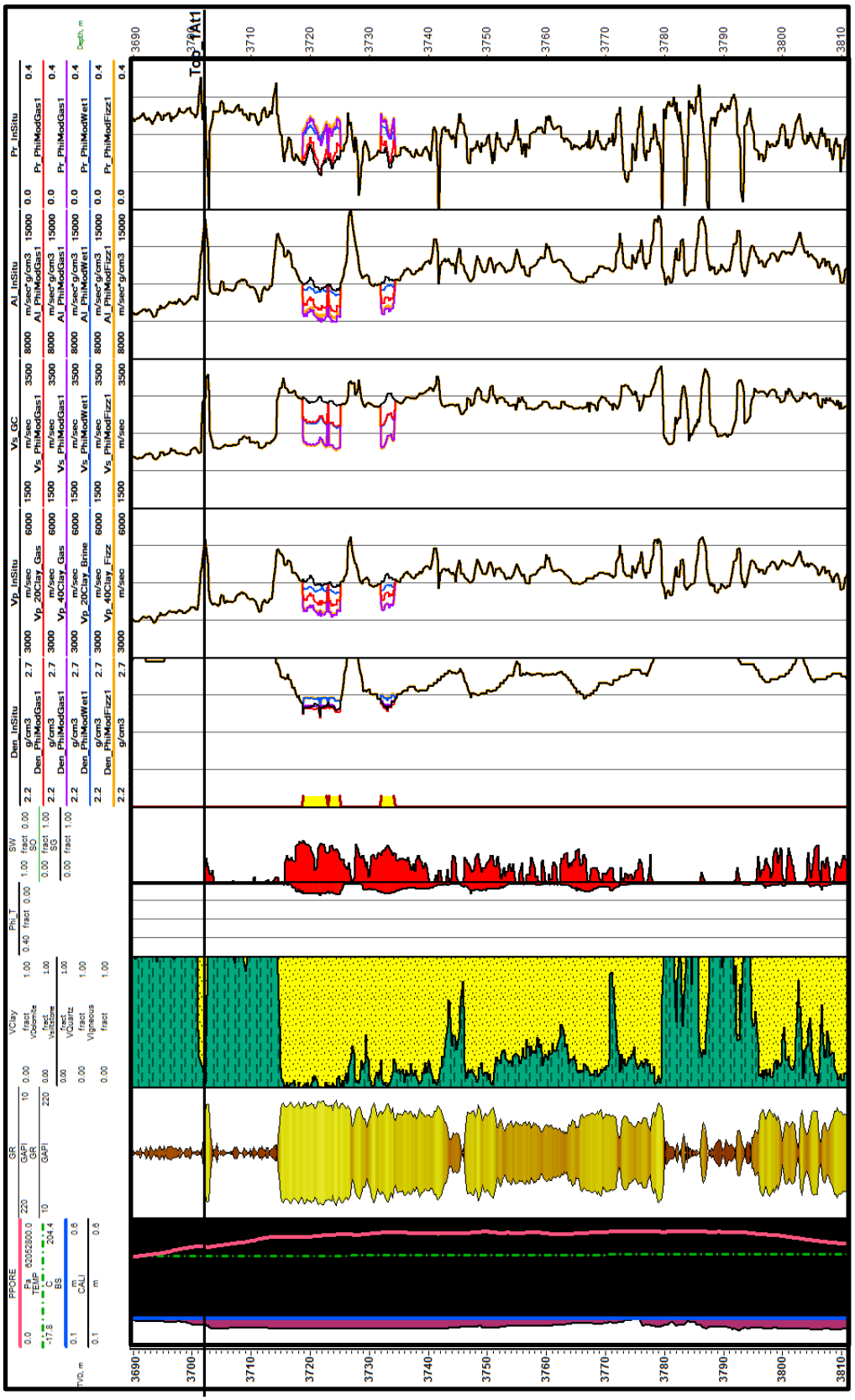

Fig. 4.4.3.5: Mineralogy perturbation_F-O3 (logs-plot).

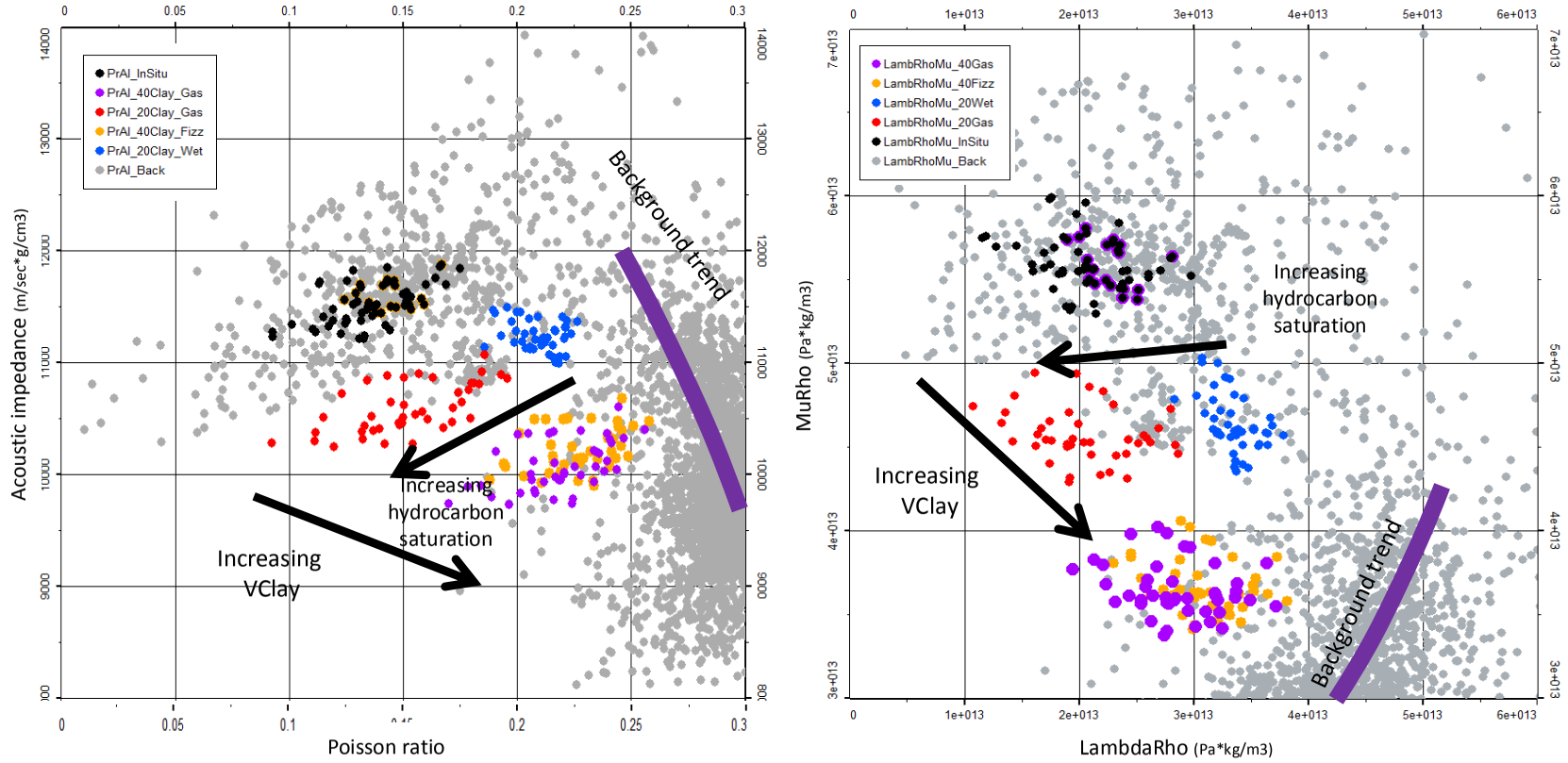

Fig. 4.4.3.6: Mineralogy perturbation_F-O3 (logs-cross-plot).

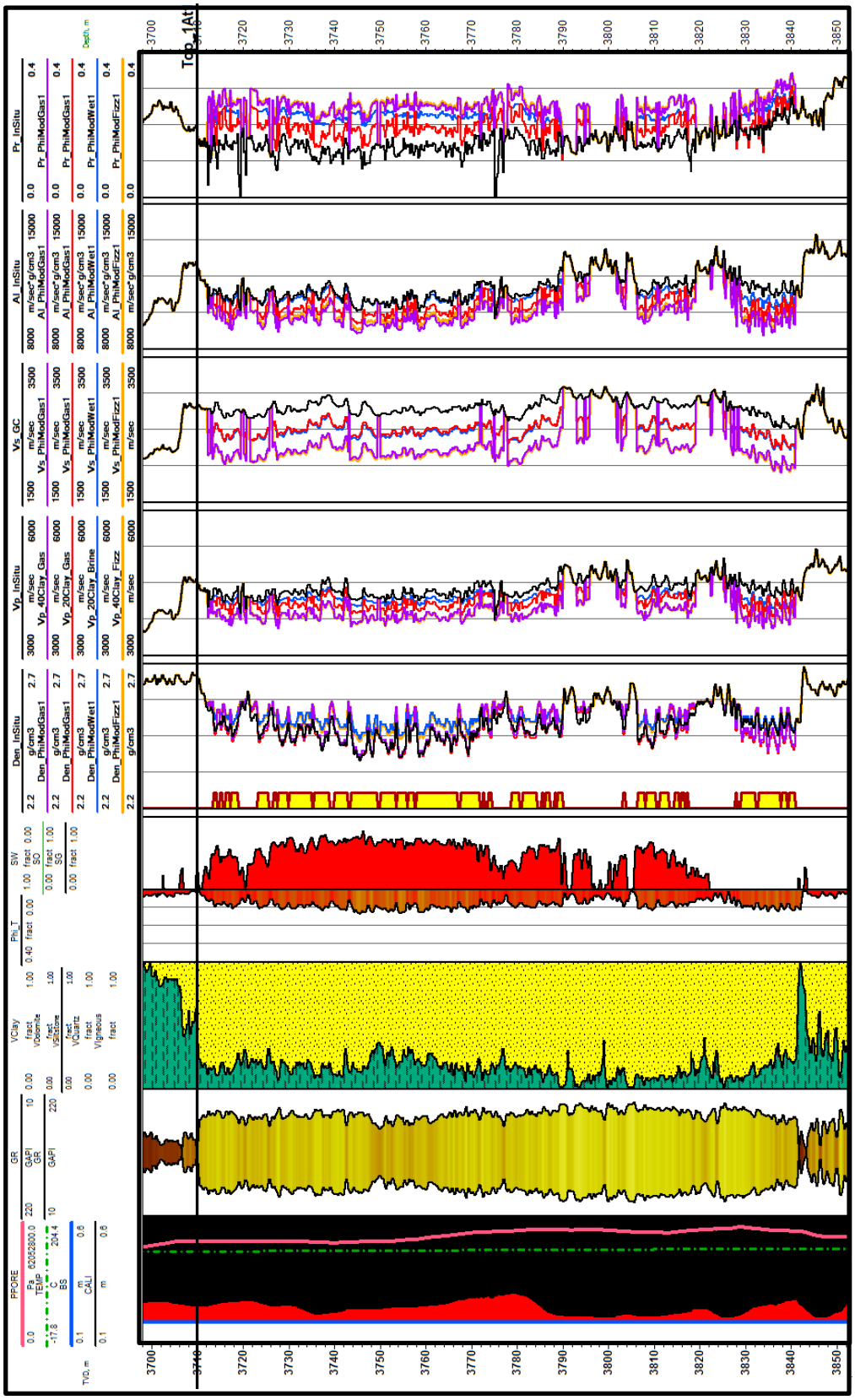

Fig. 4.4.3.7: Mineralogy perturbation_F-O4 (logs-plot).

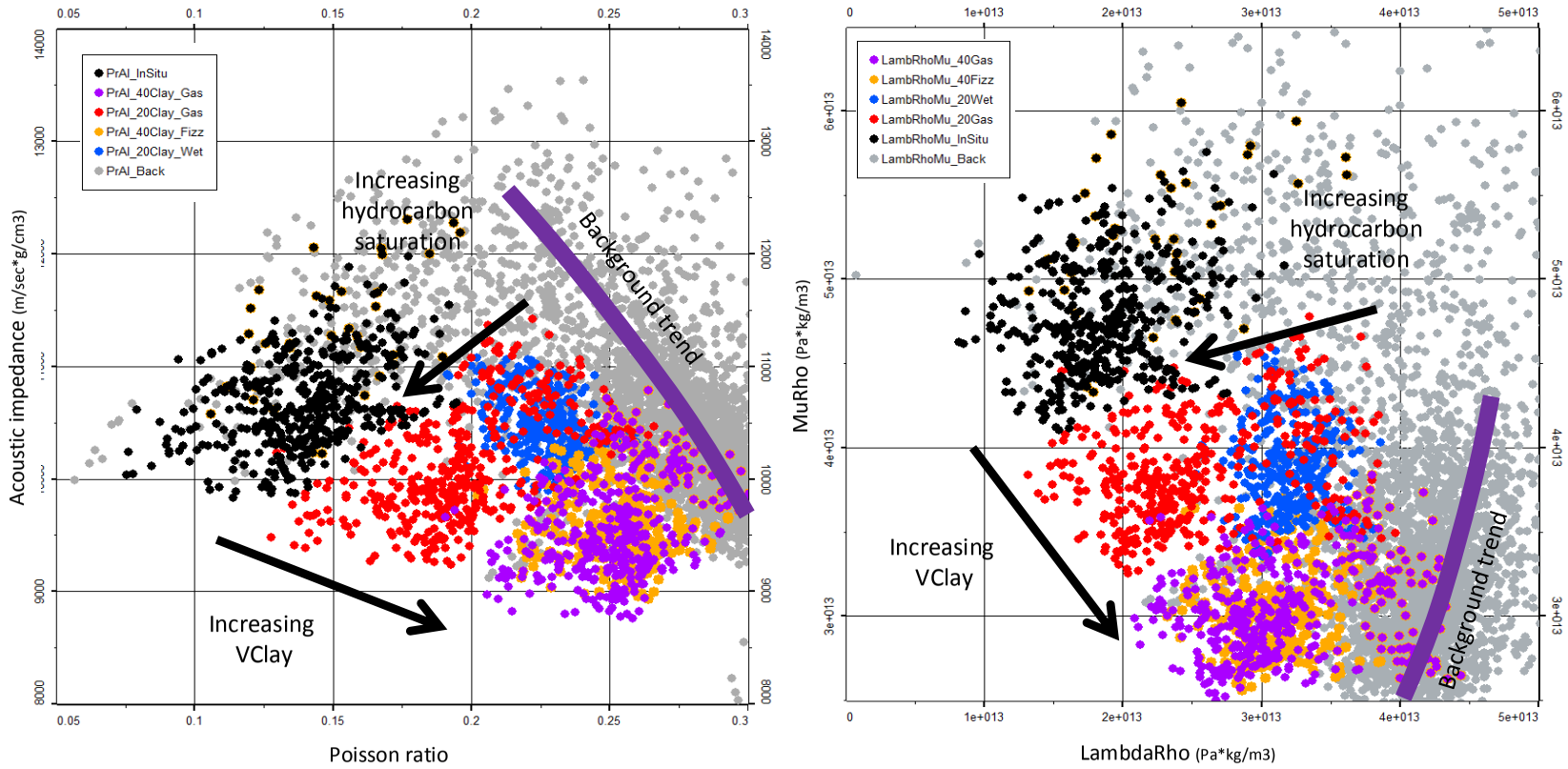

Fig. 4.4.3.8: Mineralogy perturbation_F-O4 (logs-cross-plot).

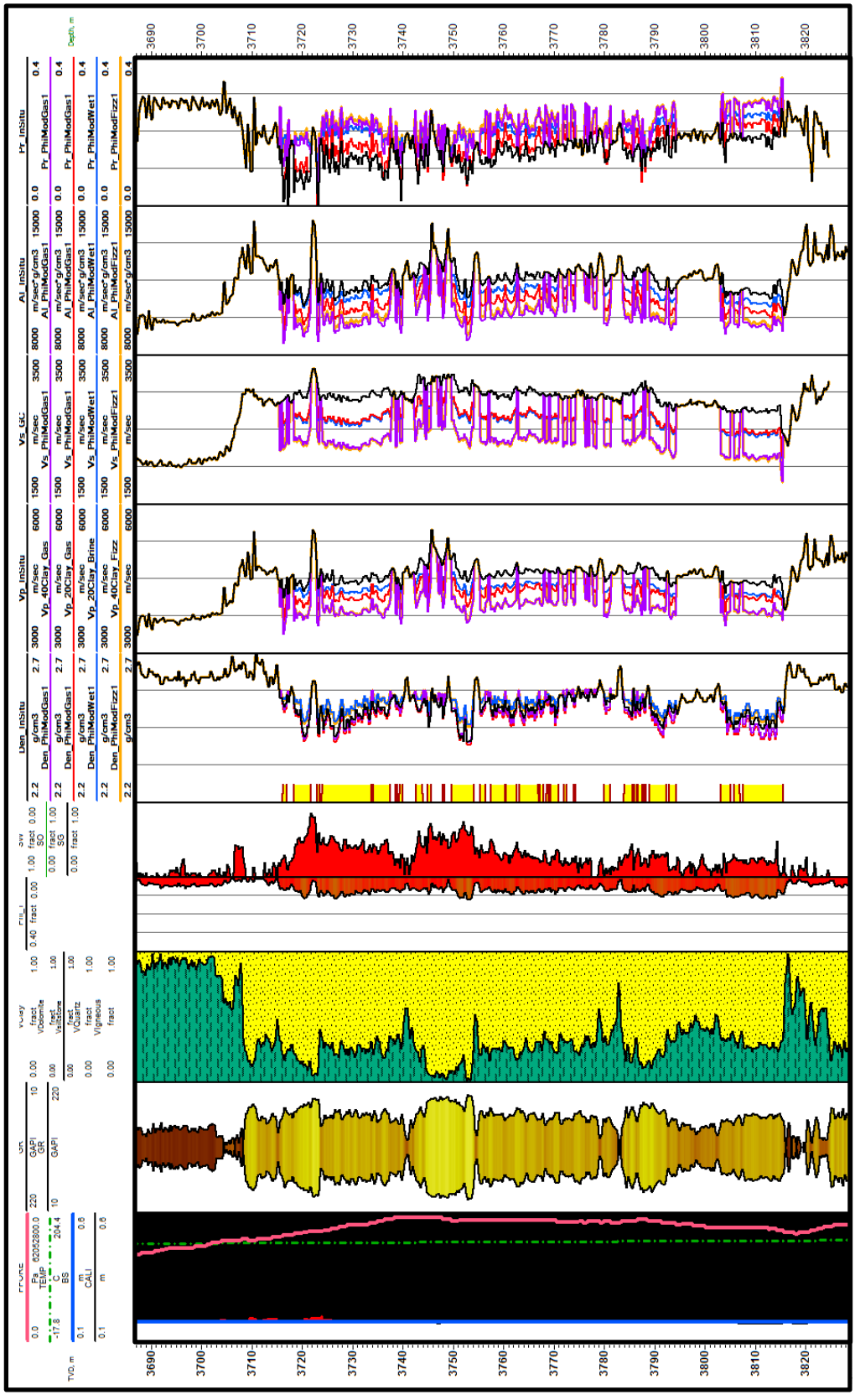

Fig. 4.4.3.9: Mineralogy perturbation_F-06 (logs-plot).

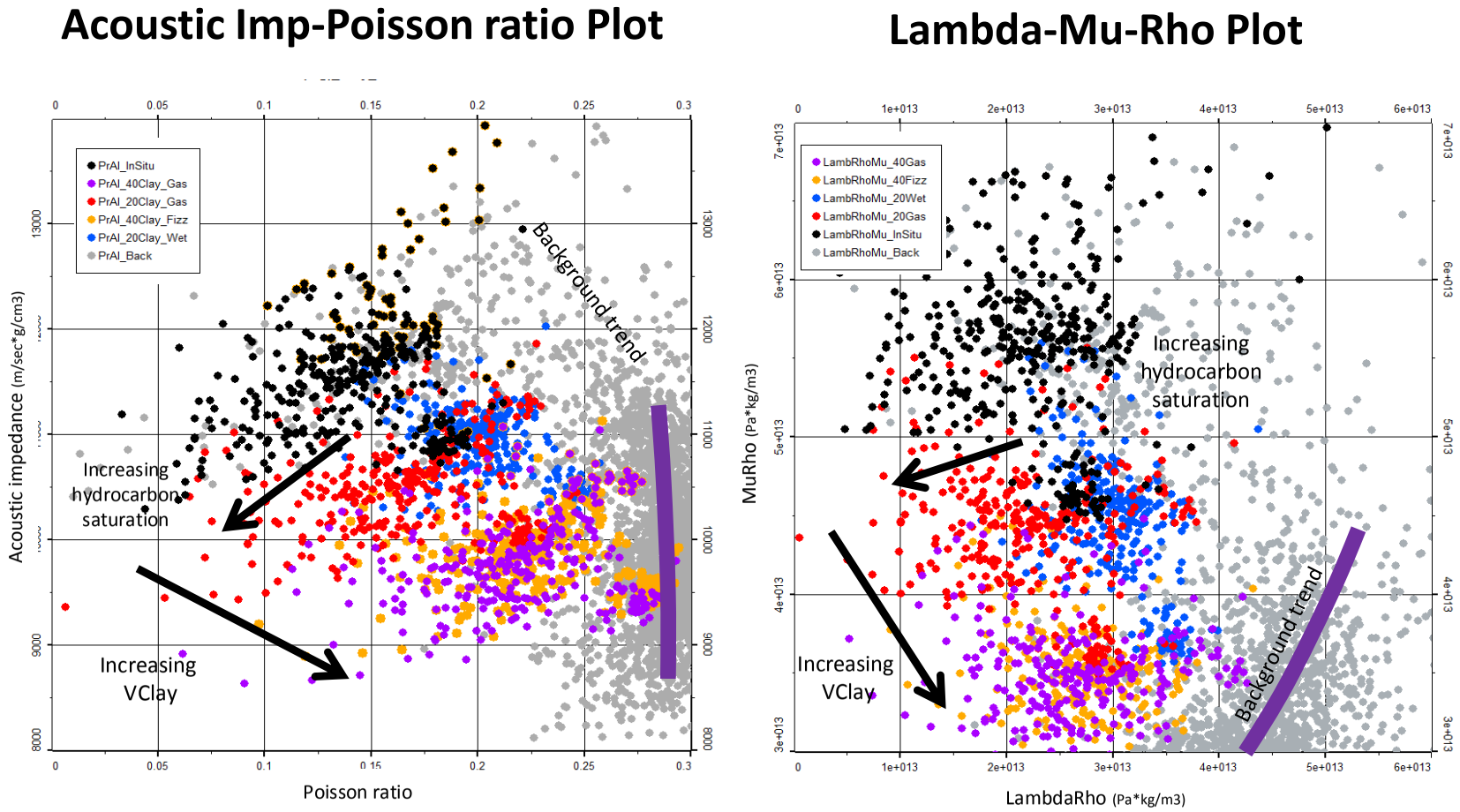

Fig. 4.4.3.10: Mineralogy perturbation_F-O6 (logs-cross-plot).

4.4.4 Thickness models

To examine the effect of variations in thickness and fluid in the reservoir sandstones, thickness modelling was performed. Curves in a select zone of the reservoir were repeated or were removed in order to achieve the desired thickness effect. The values from the in situ case were perturbed to create “pseudo-wells” to account for possible inter-well differences (delta well modeling). To design the optimal thickness scenarios, the author took note of two concepts postulated in previous studies on the field (F-O) to define the criterion to build the thickness cases:

a) The top of the reservoir (1At1) is interpreted here as a time transgressive or diachronous flooding surface resulting from near-shore marine and shoreline erosion associated with a sea-level rise, rather than a widely supposed 1At1 unconformity. The overall "swelling and pinching" gamma ray (GR) profile of the USM, partly comprising coarsening-up intervals interpretable as one or more parasequences, suggests that the USM and the overlying shale interval together represent two or more Vail-type depositional sequences. In the F-O Field, the Vail sequences are erosionally truncated by a shale-on-shale angular unconformity at the base of a low-velocity shale unit LVS (Higgs, 2007).

b) Enhanced poro-perm (EPP) values are confined to the upper part of Upper Shallow Marine (USM). Thin-section evidence shows that the enhanced porosity is secondary. Oversize pores and pores bordered by micro-indented quartz overgrowths suggests that it is telodiagenetic porosity (Schmidt & McDonald 1979), formed by dissolution of carbonate cement and feldspar-replacing carbonate (hence oversize pores), due to meteoric (rain/river) water percolating to shallow depths (metres to tens of metres) under the land surface that existed before the deposition of this low-velocity shale. Similarly, according to PGS (2001, p. 10), the EPP "has previously been attributed to leaching of calcareous material where the unit occurs near the 1At1 unconformity “, a feature in common with other USM reservoirs in the Bredasdorp Basin. Poro-perm values typically <12% and <1mD, are locally enhanced to 12-16% and 1-250mD.

Two main thickness scenarios were simulated: (a) partial to complete erosion of the upper facies susceptible to poro-perm enhancement (F-O1) and poro-perm unenhanced (F-O4), and (b) a thickening of upper poro-perm enhanced facies (F-O1). This exercise was confined to F-O1 and F-O4 wells.

The delta well modelling in F-O1 consisted of one thinning and two thickening models. The in situ clay and fluid were substituted to 1) -45% sand thinning (-45 metres): in situ; 2) +28% sand thickening (+28 metres): 80% gas, 20% water; 3) +28% sand thickening (+28 metres): 100% water. The thinning model represents what might occur if the enhanced sequence (USM) is uplifted and the enhanced unit is completely eroded, leaving a tighter bottom unit underlying the low-velocity shale. In this case gas-charged low-porosity sandstone can hardly be expected, so the in situ fluid condition remains for modelling purposes. The two

thickening models explore what might occur if the USM is preserved and additionally becomes 28 metres thicker. This scenario was modelled for gas and water cases.

Figure 4.4.4.1 shows log curves with elastic curves (Vp, Vs & density) and derived properties, (AI & PR) in F-O1 and thickness versions modelled as described above. The thinning model was produced by removing 45 metres from the top of the upper USM section (3702-3747 mTVD) and the thickening model by repeating 14 metres of the best poro-perm USM section (3714-3728 m TVD) twice (28 metres).

The section repeated in the thickening case does not add information to the acoustic impedance versus Poisson's ratio cross-plot. On the other hand, the 45 metres of enhanced unit was removed (in the thinning case), so the remainder is tighter plotting at high AI and high PR compared with the in situ case in the same cross-plot. For this exercise, the thickening-gas case is red, thickening-water is blue, thinning-in situ light green and in situ is black (see figure 4.4.4.2).

The delta well modelling in F-O4 consisted of four thinning models. The in situ clay and fluid were substituted to 1) -44% sand thickness (-67 metres): 80% gas, 20% water; 2) -44% sand thickness (-67 metres): 100% water; 3) -63% sand thickness (-96 metres): 80% gas, 20% water; 4) -63% sand thickness (-96 metres): 100% water. These models investigate the idea of gradually thinning USM sand that is not so poro-perm enhanced and modelling the tuning effect at different fluid content (gas and water). A thickening exercise was not considered because F-O4 already has a well-preserved thicker section.

An intermediate thinning model was generated by removing 67 metres from the top of the USM section (3710-3777 TVD) and substituting in situ fluid with gas and water. Then an exaggerated reduction of USM sand was simulated, this time by removing 96 metres from top of the upper USM section (3710-3806 TVD) and substituting in situ fluid with gas and water. Figure 4.4.4.3 shows log curves with different cases modelled on F-O4.

Both intermediate and exaggerated thinning cases show a good discrimination between gas and water, but cases overlay each other in the acoustic impedance space. Moreover, when thickness is reduced, acoustic impedance is decreased, because the bottom sand section has slightly better porosities. The in situ case is coloured black, intermediate thinning-gas red, intermediate thinning-water light blue, exaggerated thinning-gas purple and exaggerated thinning-water blue in figure 4.4.4.4.

These thickness models represent the spectrum of variation of possible thickness and hydrocarbon saturation conditions that are likely to be found in the reservoir.

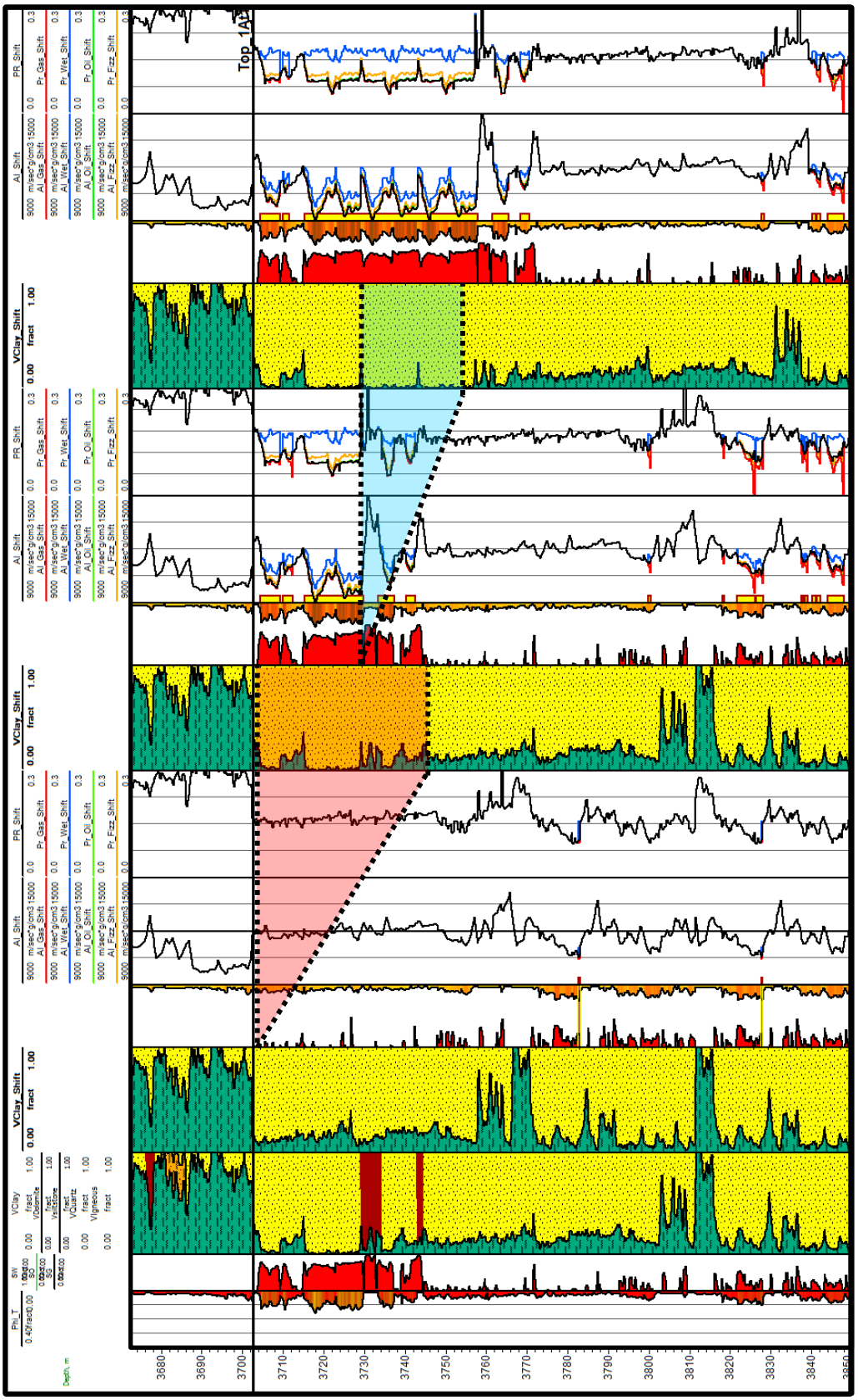

Fig. 4.4.4.1: Thickness perturbation_F-O1 (logs-plot).

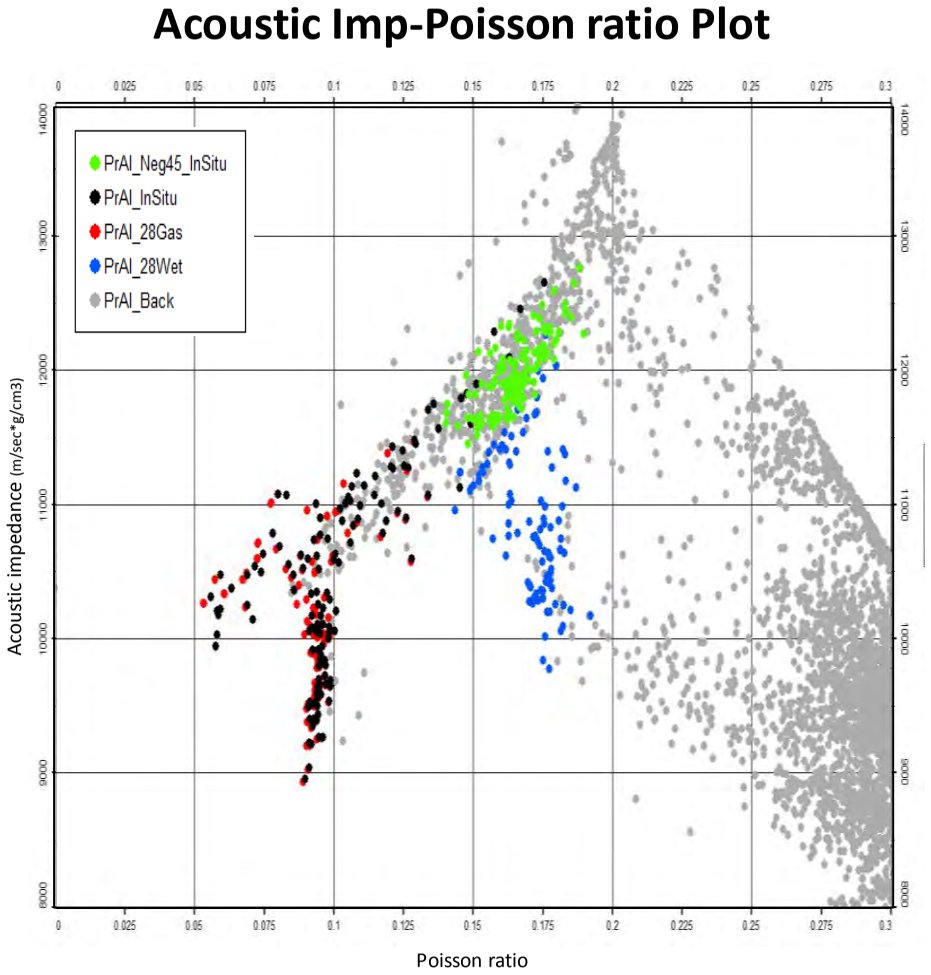

Fig. 4.4.4.2: Thickness perturbation_F-O1 (logs-cross-plot).

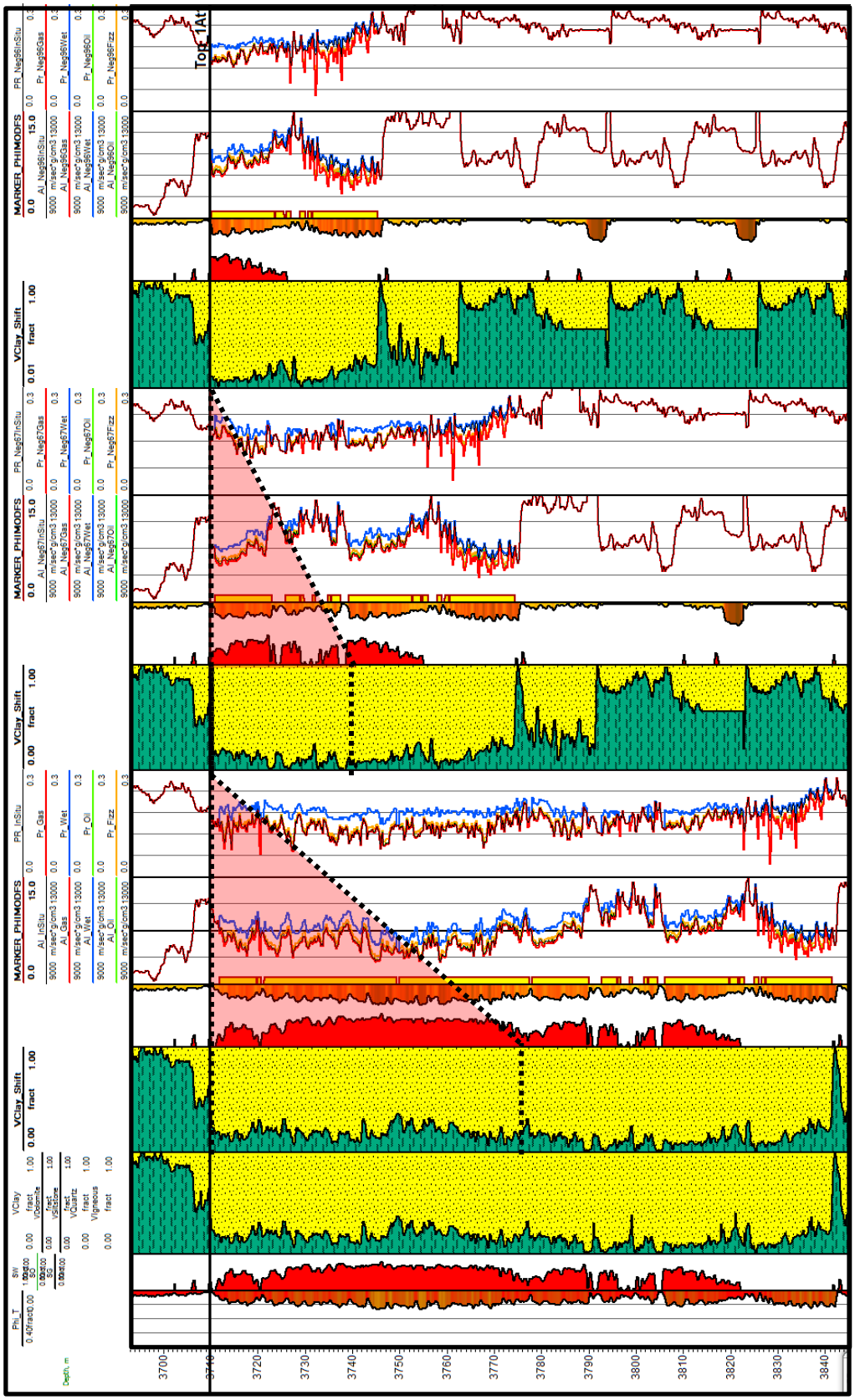

Fig. 4.4.4.3: Thickness perturbation_F-O4 (logs-plot).

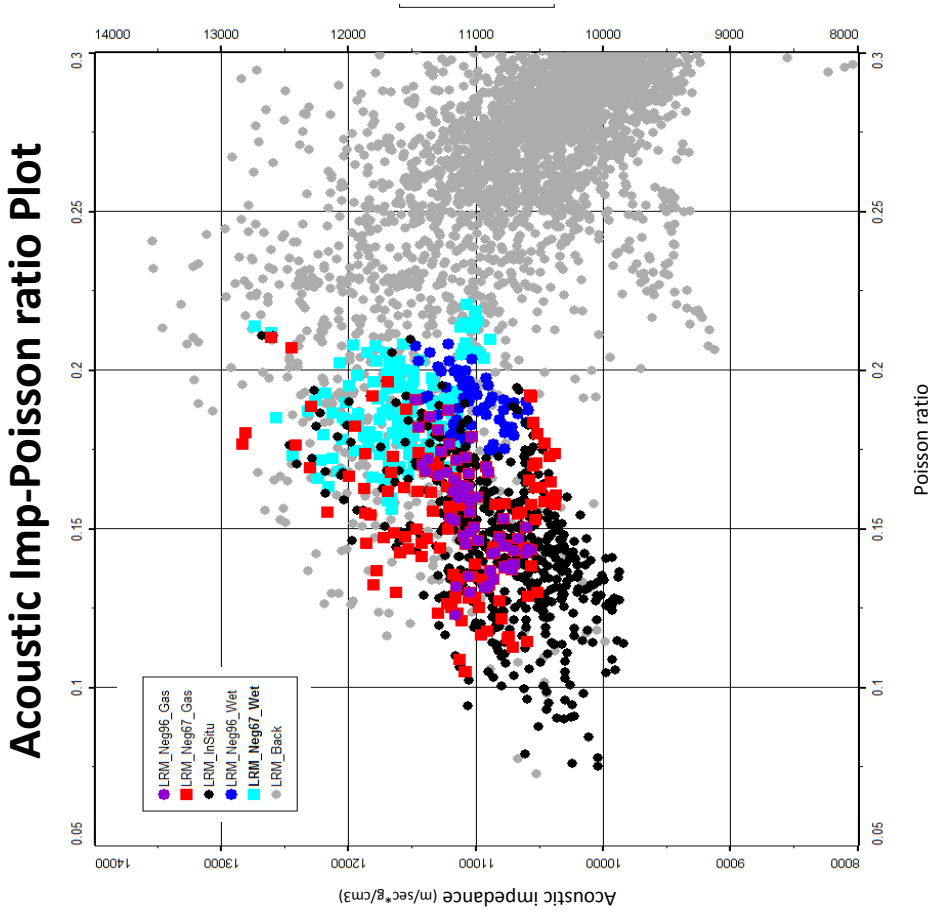

Fig. 4.4.4.4: Thickness perturbation_F-O4 (logs-cross-plot).

4.5 Synthetic seismogram modelling and AVA modelling

The modelling described so far in this chapter has been defined in the well-log domain of high resolution. However, the principal goal of a rock physics analysis is to understand and classify the elastic response due to variations in reservoir properties such as fluid content, porosity and mineralogy, and then to predict reservoir characteristics in between wells based on the seismic signature.

At this stage it is relevant to examine the sensitivity of seismic data to these variations, therefore synthetic seismic modelling is performed.

Up-scaled model cases were analysed at seismic scale, using a ray trace model, that does not include multiples or mode conversions. Seismic parameters used in the modelling are:

- 25 Hz Ricker wavelet
- 0° Phase rotation
- Offset range: 0-5000 m
- 100 m trace spacing
- 50° mute
- The increase in impedance is a peak

This section shows the results of the synthetic seismic (normal move-out (NMO) corrected gathers) generation in the five wells location using in situ curve values as well as the delta well results from section 4.4.1 to 4.4.4.

Synthetic seismograms for earth models consisting of horizontal plane layers were computed using ray tracing.

The uncorrected gather was produced by convolving the well-known Ricker wavelet with the offset-dependent reflectivities located at ray-traced travel times. The zero-offset traces of the synthetic gather have the same length as the normal-incidence synthetics.

Then NMO-corrected gather is computed by applying NMO correction to the uncorrected gather.

This method assumed that the source and receiver are located at TVDSS=0 (i.e. they are located at the depth of the datum). The method does not account for the following effects: multiples of any kind, transmission loss, converted waves or geometric spreading.

To examine the effect of the modelled scenarios on the reflection at a single interface two cross-plots were generated: reflectivity vs. angle and normal reflectivity vs. gradient. In this analysis the trace amplitude is extracted from each synthetic gather at the 1At1 marker time.

4.5.1 Fluid modelling

Fluid content has a subtle effect on seismic response. All hydrocarbon (gas and fizz) cases share a similar seismic signature, so the response is unlikely to distinguish between commercial and non- commercial at seismic resolution.

The synthetic gather behaviour on wells F-O3, F-O4 and F-O6 shows moderate positive amplitude at zero offset response for any hydrocarbon case and moderate to high when water. F-O2 and F-O1 show a weaker signal than the other wells for all fluid cases at zero offset. Fluid content changes have a little effect on the synthetic gather offset response (see figures 4.5.1, 3, 5, 7, 9).

Cross-plots of the zero offset reflection coefficient versus gradient and the incident angle versus reflection coefficient at the top of 1At1 sand showing fluid substitution results of the AVA analysis can be seen on figures 4.5.2, 4, 6, 8, and 10.

These curves (amplitude vs angle) show the similarity between hydrocarbon cases. This behaviour was consistent in all wells. Only the water case plotted away from the other cases at zero-offset.

A well pattern based exclusively on zero offset amplitude was evident. In a first pattern, F-O1 showed a near-zero (+/-) amplitude for hydrocarbon cases and 0.035 for the water case; a second pattern, which include F-O2 and F-O4, showed moderate amplitudes around 0.04 and 0.065 for hydrocarbon and the water case respectively, and a third pattern (F-O3 and F-O6) showed higher amplitudes in general, with 0.075 for hydrocarbon cases and near to 0.1 for the water case.

AVA classes for fluid models are summarized by well groups below:

Group I (F-O1):

In situ, and gas shows a Class II

The fizz case shows a Class IIP

The water case shows a Class I weak (moderate reflection coefficient <0.05)

Group II (F-O2-F-O4):

In situ, fizz and gas show a Class I weak (moderate reflection coefficient <0.05)

The water case shows a Class I (high reflection coefficient)

Group III (F-O3-F-O6):

All cases show a Class I (high impedance)

The intercept versus gradient cross-plot shows that with the exception of F-O1, for which cases are plotted in the class II area, all wells are plotted in the class I area. When 100% water- saturated rock is substituted with any gas mixture, the values move down and to the left, evidencing a fluid effect by more negative at zero offset and increasing the value of negative gradient.

There is a relationship between the AVA gradient values and wells. F-O3 shows the lower absolute gradient (>-0.02), then F-O1, F-O2 and F-O4 with gradient rounded between -0.03>G>-0.02. Lastly, F-O6 displayed higher absolute gradient values <-0.03.

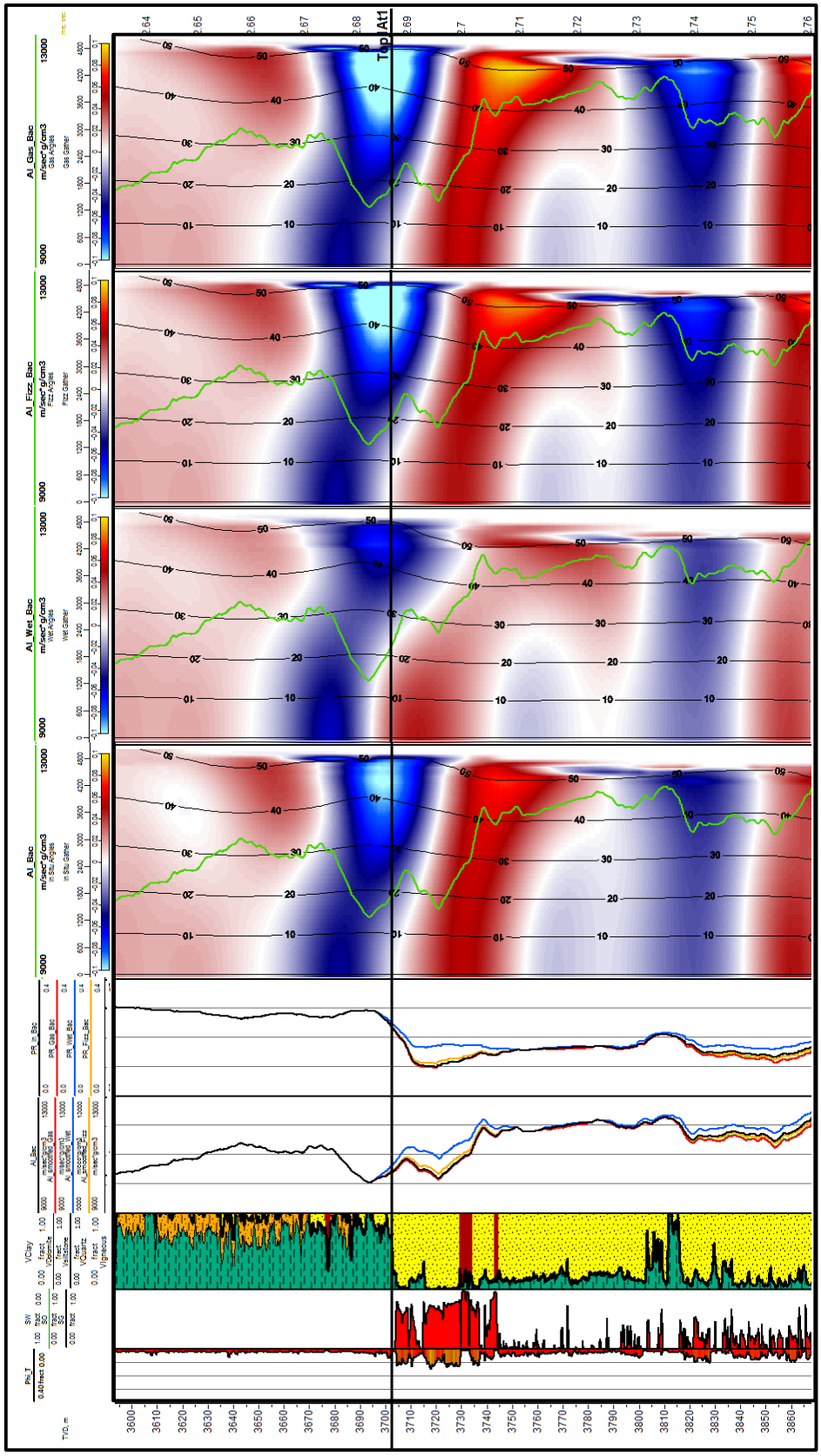

Fig. 4.5.1: AVA analysis-Fluid Models (1At1) :F-O1 Seismic Gather

Amplitude vs Angle Plot

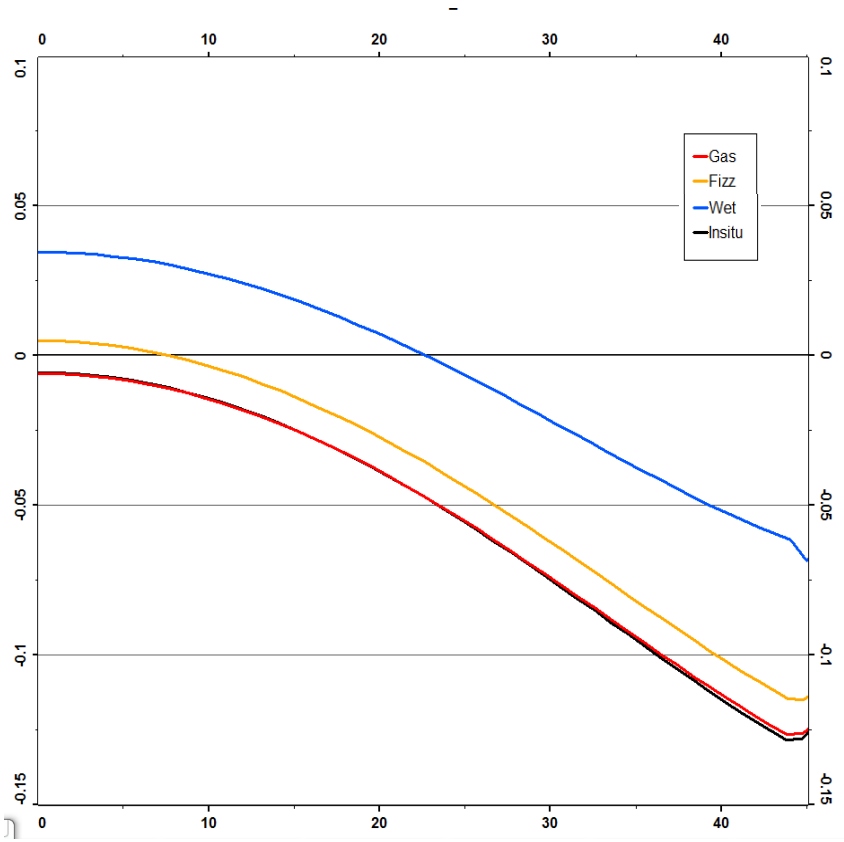

Intercept-Gradient Plot

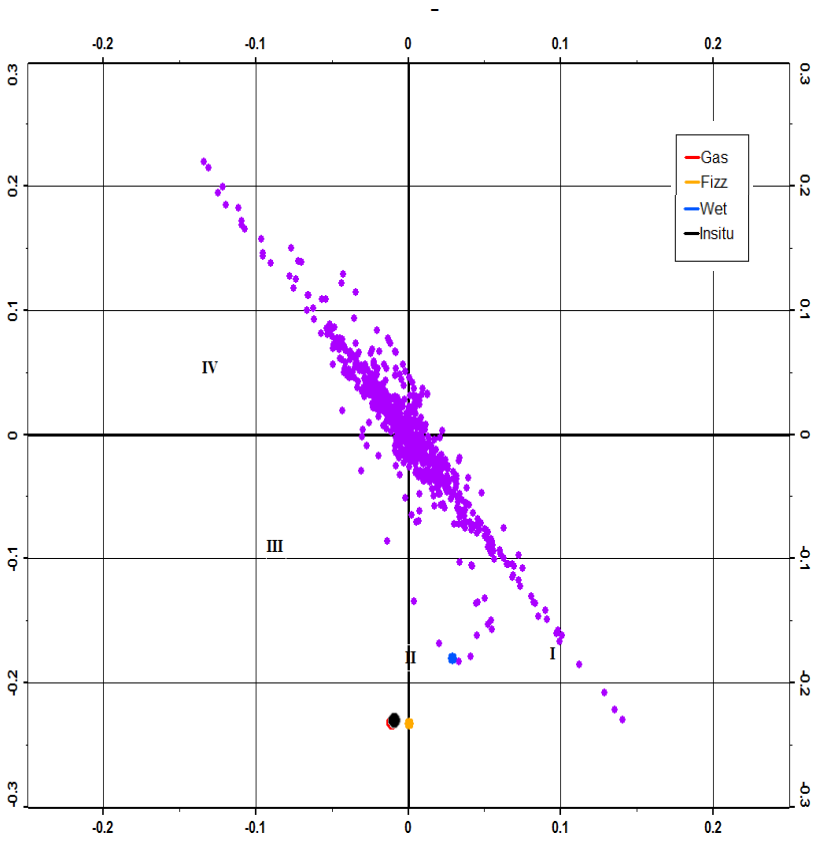

Fig. 4.5.2: AVA analysis-Fluid Models (1At1) :F-O1 AVA and IG cross-plot.

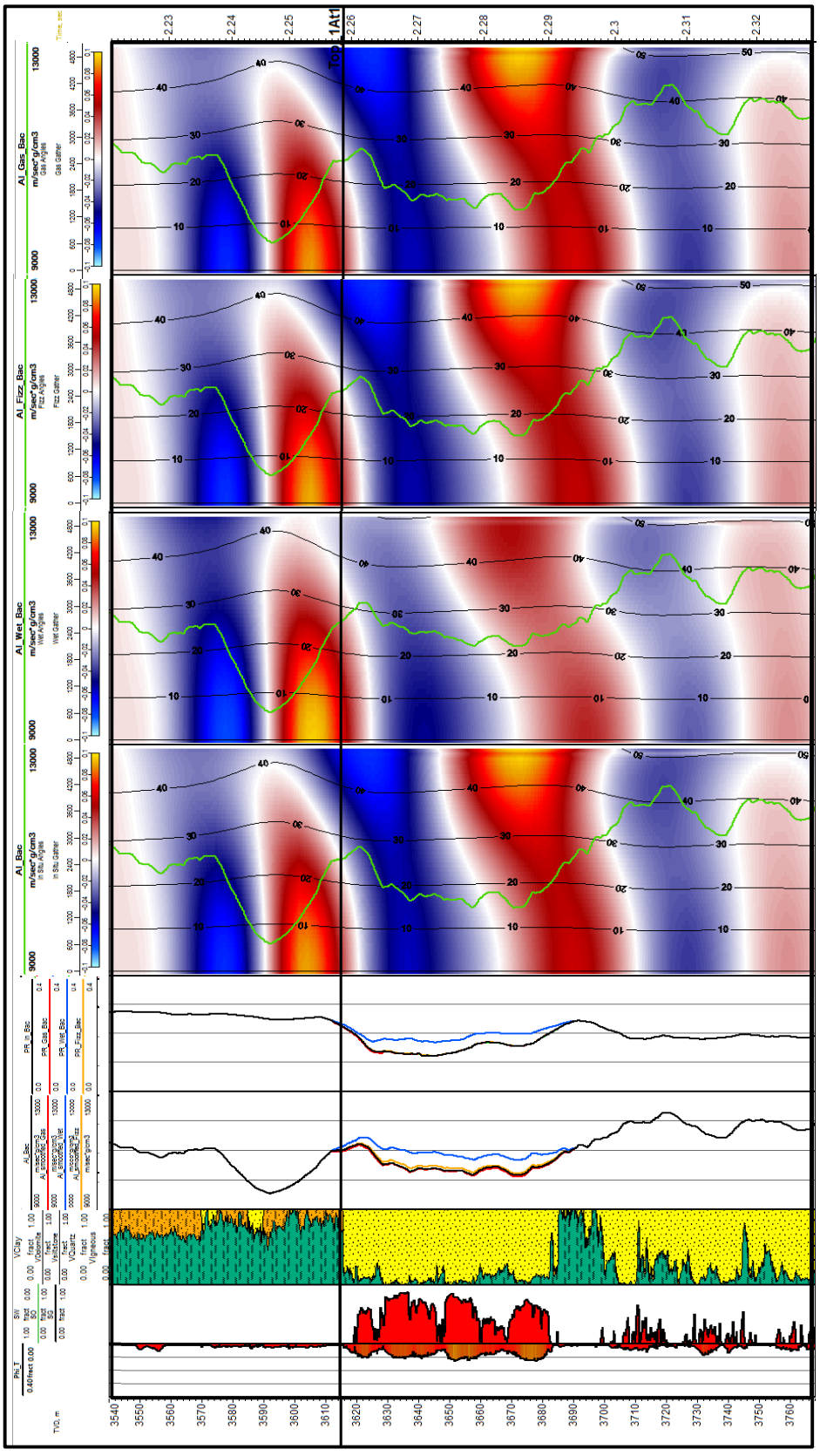

Fig. 4.5.3: AVA analysis-Fluid Models (1At1) :F-O2 Seismic Gather

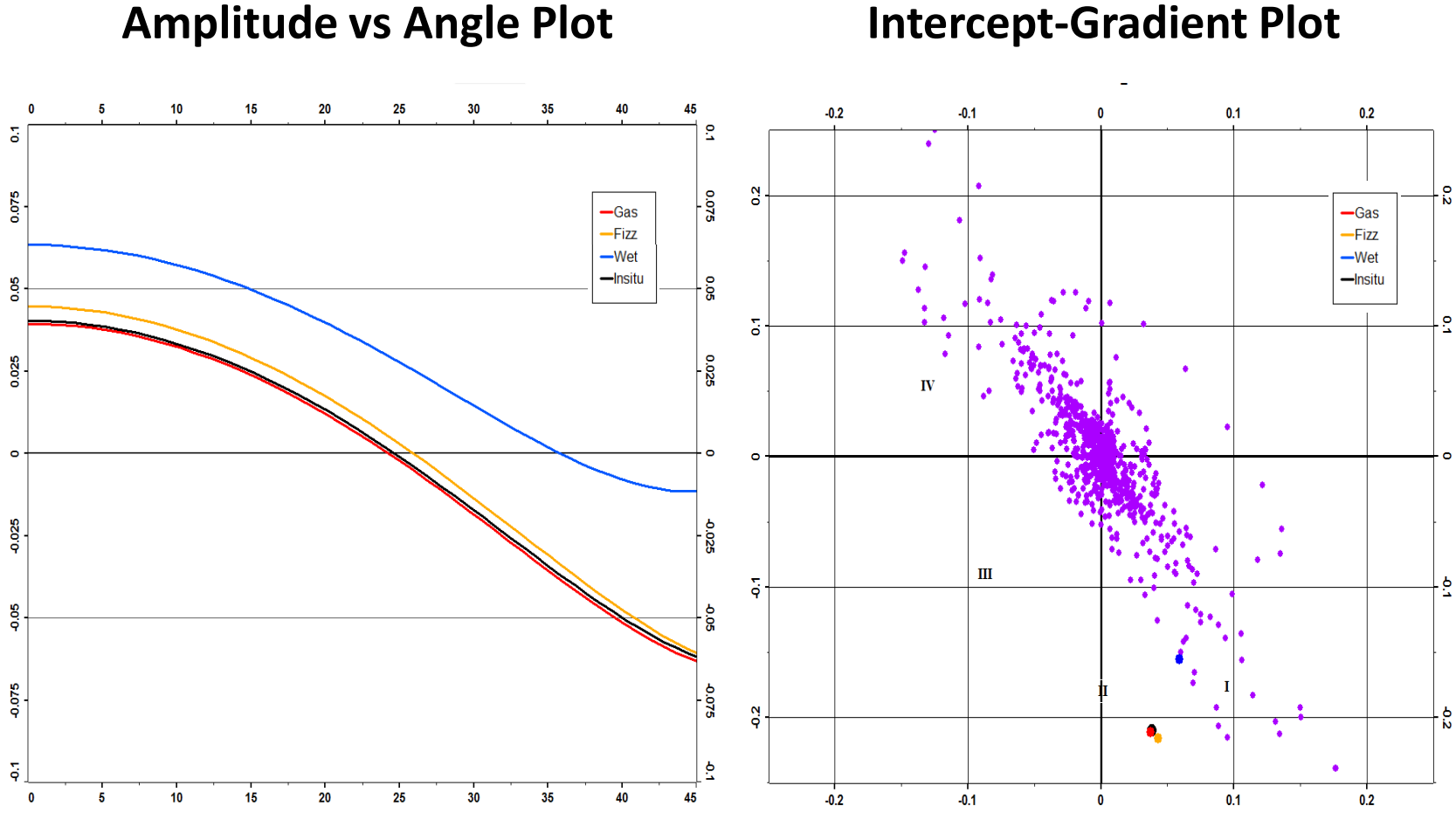

Fig. 4.5.4: AVA analysis-Fluid Models (1At1) :F-O2 AVA and IG cross-plot.

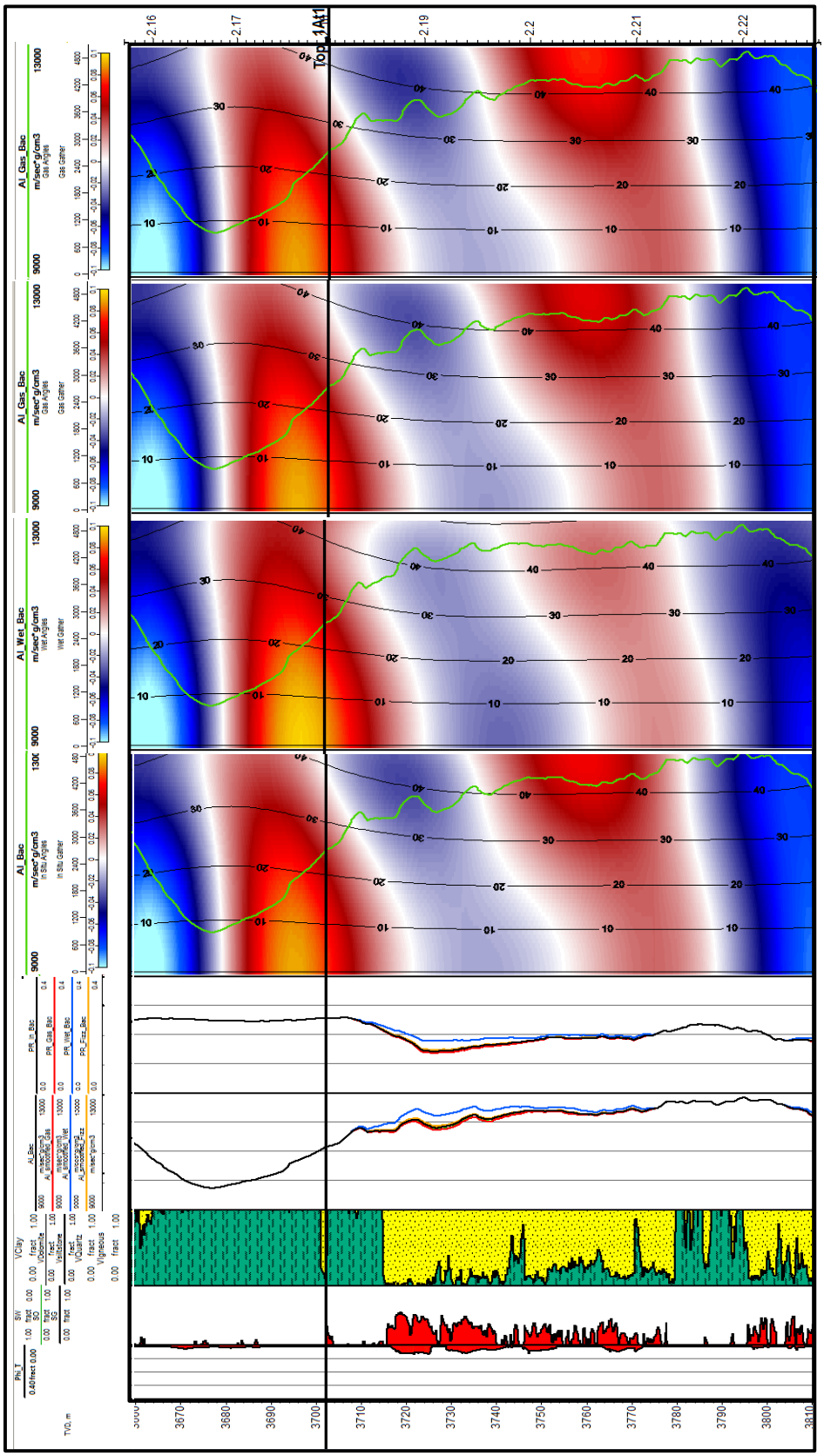

Fig. 4.5.5: AVA analysis-Fluid Models (1At1) :F-O3 Seismic Gather

Amplitude vs Angle Plot

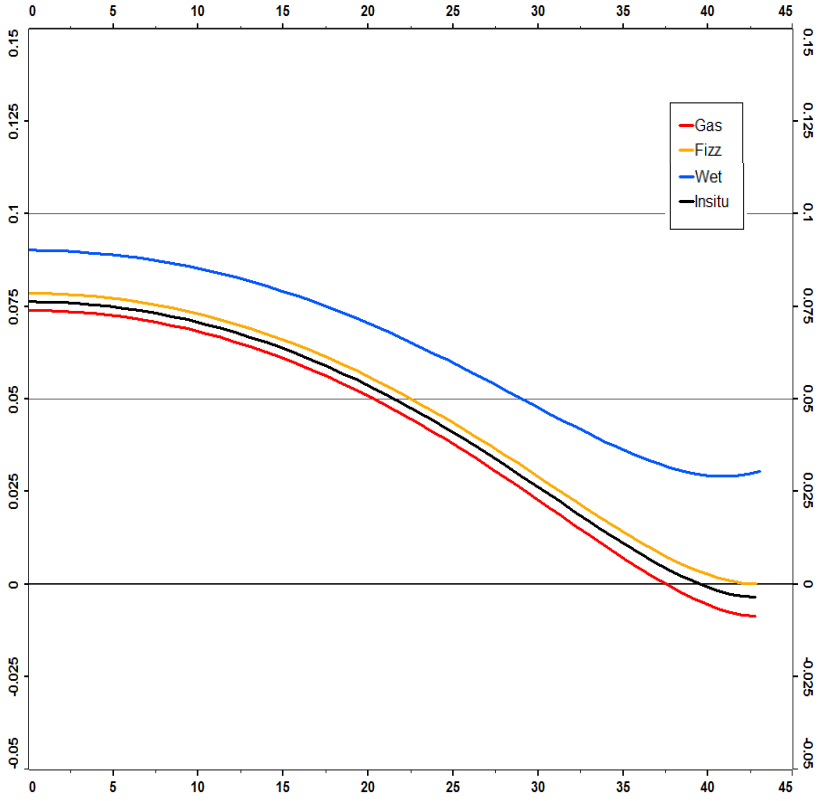

Intercept-Gradient Plot

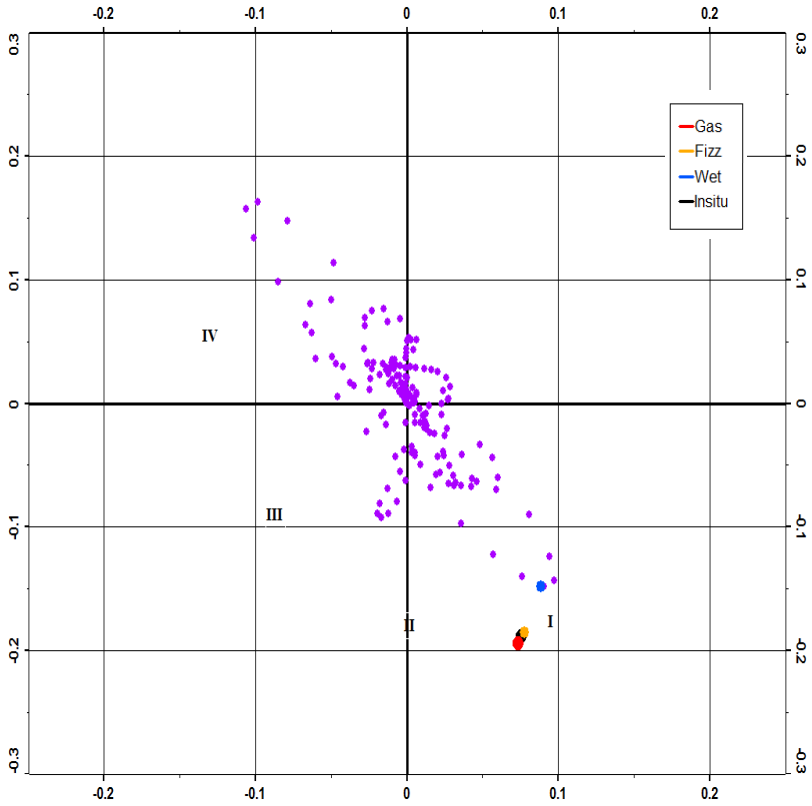

Fig. 4.5.6: AVA analysis-Fluid Models (1At1) :F-O3 AVA and IG cross-plot.

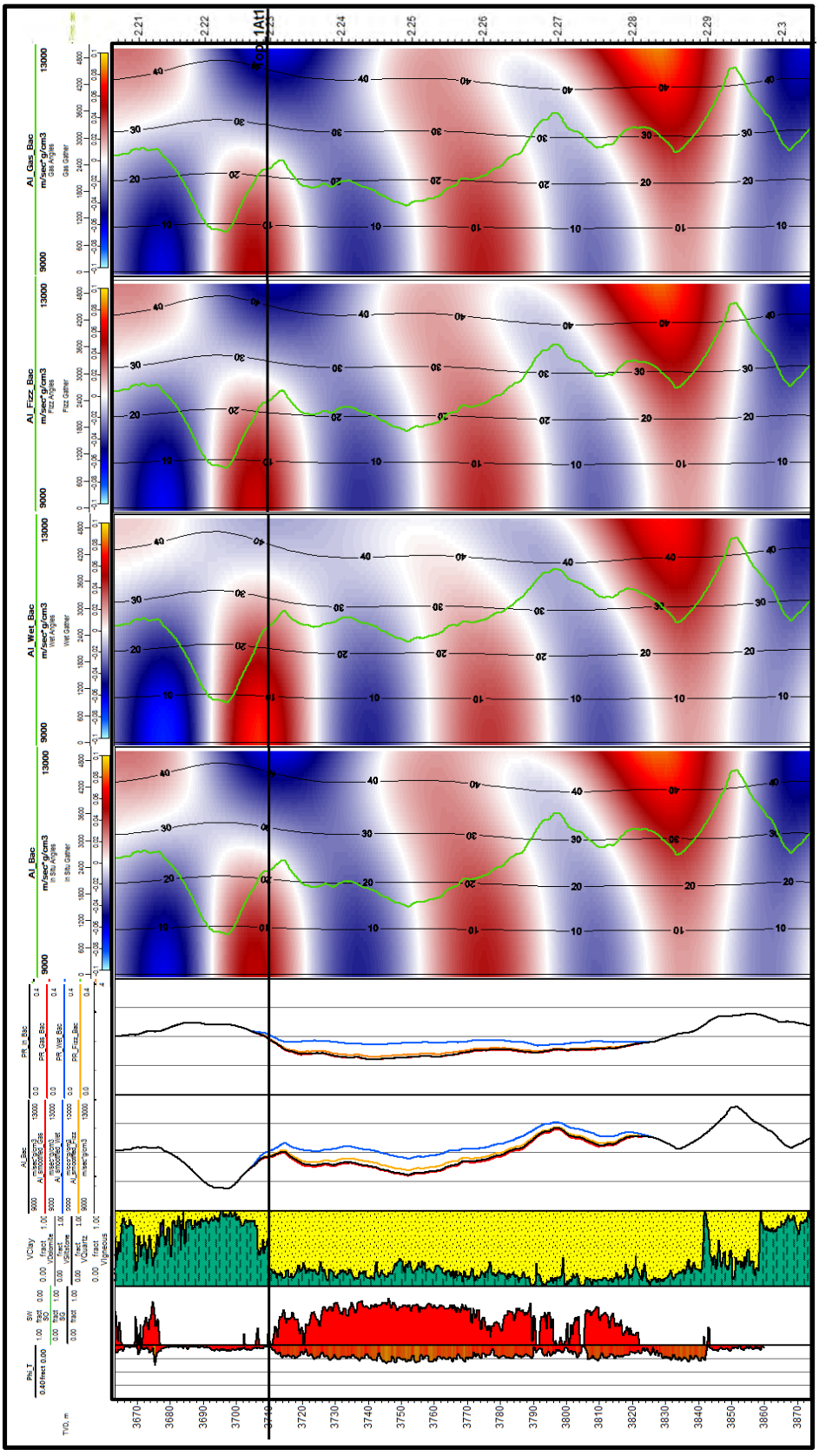

Fig. 4.5.7: AVA analysis-Fluid Models (1At1) :F-O4 Seismic Gather

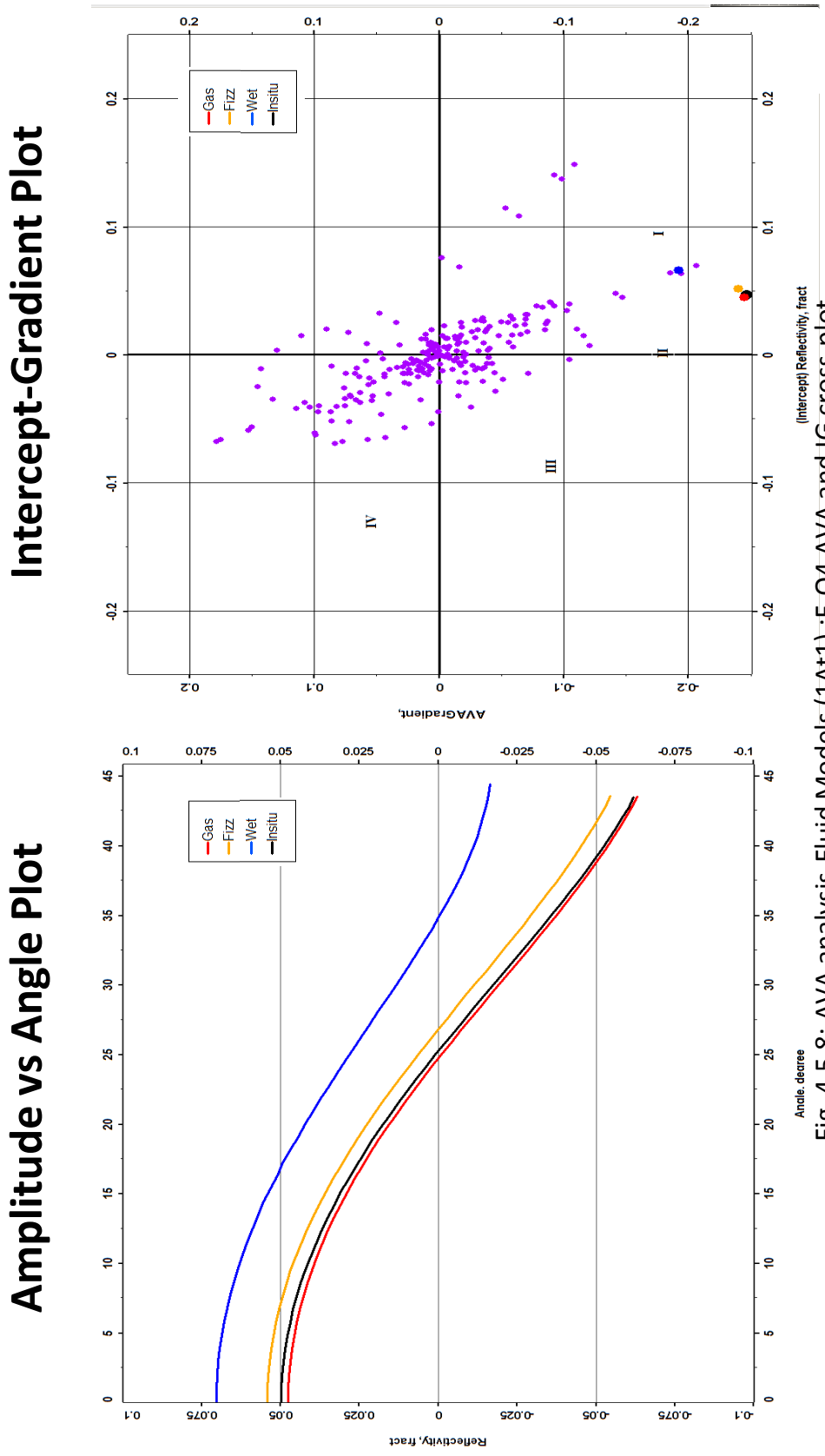

Fig. 4.5.8: AVA analysis-Fluid Models (1At1) :F-O4 AVA and IG cross-plot.

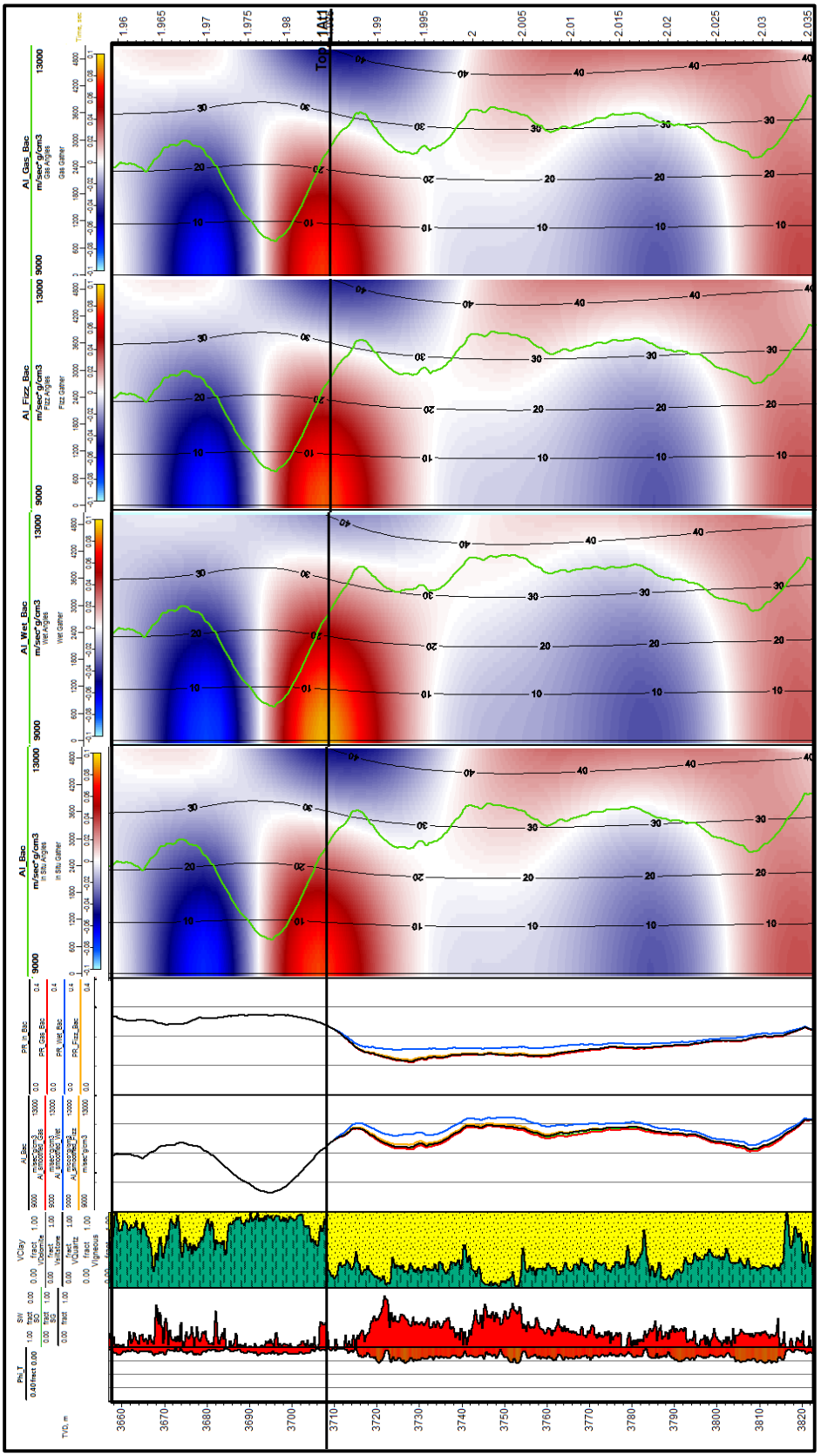

Fig. 4.5.9: AVA analysis-Fluid Models (1At1) :F-O6 Seismic Gather

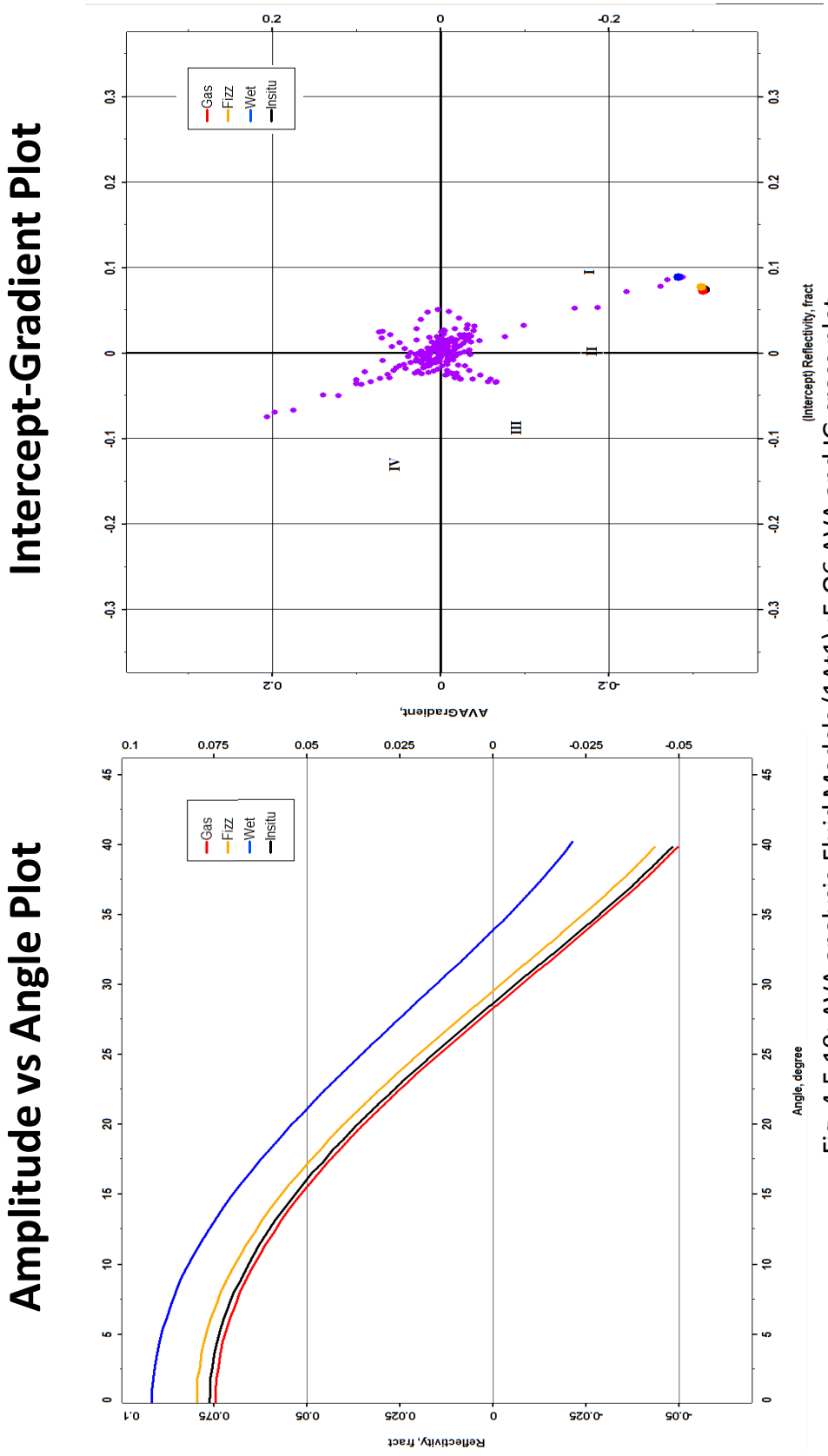

Fig. 4.5.10: AVA analysis-Fluid Models (1At1) :F-O6 AVA and IG cross-plot.

4.5.2 Porosity modelling

Increased impedance is represented by a peak in these models. For the sake of simplicity, the increased porosity case is referred to as higher Ø and decreased porosity as lower Ø.

Porosity produces a strong effect on seismic response. Elastic properties in general are very sensitive to increases and decreases in porosity, so there is good discrimination between in situ and higher Ø-gas and between in situ and lower Ø-gas. When the rock pore space (porosity) increases, the fluid effect is amplified, and vice versa. This leads to a better discrimination between gas and water cases.

From synthetic gather observations, interesting features can be extracted at the 1At1 interface. For example, the reflection coefficient magnitude at zero offset for all wells for all cases in which porosity is reduced (gas and fizz) are substantially increased compared to the in situ porosity due mainly to an increase in acoustic impedance. Conversely, the reflection coefficient magnitude decreases to very low amplitude when porosity is increased; even a polarity reversal can be expected. This effect is reflected in decreased acoustic impedance and Poisson's ratio. Thus, the effect of porosity on the pay target reservoir is expressed in the brightness and polarity of the seismic response.

The reflectivity decreases in magnitude with offset/angle (offset response) when porosity is increased or decreased alike. Therefore, the main difference in synthetic gathers is in the zero offset response. In the higher Ø scenarios the amplitude decreases and in the lower Ø scenarios increases compared with the in situ porosity. In the higher Ø scenarios the response can even change polarity, for which there may be 2 plausible reasons: the zero offset amplitude is close to zero or there is a steep negative gradient, as happens with F-O1 and F-O6 respectively (figures 4.5.11, 13, 15, 17, and 19).

Different cross-plots (amplitude vs angle and intercept vs gradient) were generated for the 1At1 interface to demonstrate porosity perturbation. AVA results can be seen in figures 4.5.12, 14, 16, 18 and 20. In both plots higher Ø-gas, in situ and lower Ø-gas curves or points lie distinctly far apart at the zero amplitude.

The great effect of porosity on the amplitude response is evident when the gas versus water cases, before and after porosity perturbation is compared. When porosity is increased, the zero-offset amplitude gap between gas and water cases becomes wider than when in situ porosity case is considered.

As in the fluid models, wells show a certain zero offset response pattern that is associated with different porosity scenarios. A first pattern is exemplified by F-O1, with amplitude near to zero (+/-) for the in situ case and -0.075 and 0.075 for higher Ø-gas and lower Ø-gas respectively; a second pattern has moderate amplitudes around 0.04 for in situ case, near-zero (+/-) for higher Ø-gas and around 0.1 for lower Ø-gas. This pattern can be seen in F-O2 and F-O4. The third pattern (F-O3 and F-O6) shows amplitudes higher than 0.075 for in situ and lower Ø-gas and moderate amplitudes around 0.045 for higher Ø-gas.

An additional indicator of the effect of porosity in the amplitude vs angle domain is the slope of curves: a less steep slope for lower Ø-gas curve than for in situ and higher Ø-gas curves overall, implies a gentler offset response when porosity is reduced. In the intercept vs gradient plot this effect is interpreted as a decrease in the gradient value.

For the same cross-plot, all porosity scenarios for all wells except F-O1 are plotted in the class I area. On well F-O1, in situ and higher Ø cases are plotted in the class III area and decreased porosity cases in the class I area.

The intercept (reflectivity) behaviour when porosity is perturbed can be analysed based on the effects of the acoustic impedance changes on the interface; when porosity increases, the rock matrix becomes softer, causing a velocity and density reduction and consequently a more negative zero-offset reflectivity response. The opposite effect is seen when porosity is decreased.

The gradient response is more complex to predict because it is affected by a combination of variables. The first variable is the changes in the solid rock fraction once porosity is perturbed and the effect of fluid content (hydrocarbon) on the pore space, which is amplified or diminished depending on the magnitude of the matrix changes.

Some observations can be made on the basis of the intercept gradient plot: (a) when porosity increases, the intercept decreases, and vice versa; (b) when higher Ø-gas and lower Ø-gas cases with the same fluid content are compared, the gradient slightly increases when porosity is higher, because more fluid content is present in the rock-frame system. Conversely, the gradient becomes gentle when porosity is lower, as less fluid content affects the rock-frame response. Again, the gradient has to be read keeping in mind that it responds to changes in the composition of the rock (porosity) and the fluid. An additional consideration is that none of the effects are necessarily linear and each well has a different in situ porosity before the perturbation.

The AVA classes for porosity models are summarized below.

<u>Group I (F-O1):</u>

In situ and higher Ø-water cases fall in Class IIP

Higher Ø-gas case fall in Class III

Lower Ø-gas and lower Ø-fizz cases fall in Class I (high reflection coefficient)

<u>Group II (F-O2, F-O4):</u>

In situ and higher Ø-water cases fall in Class I weak (moderate reflection coefficient <0.05)

Higher Ø-gas case fall in a Class IIP

Lower Ø-gas and lower Ø-fizz cases fall in Class I (high reflection coefficient)

<u>Group III (F-O3, F-O6):</u>

In situ, higher Ø-wet, lower Ø-gas and lower Ø-fizz cases fall in Class I (high reflection coefficient)

Higher Ø-gas case fall in Class I weak (moderate reflection coefficient <0.05)

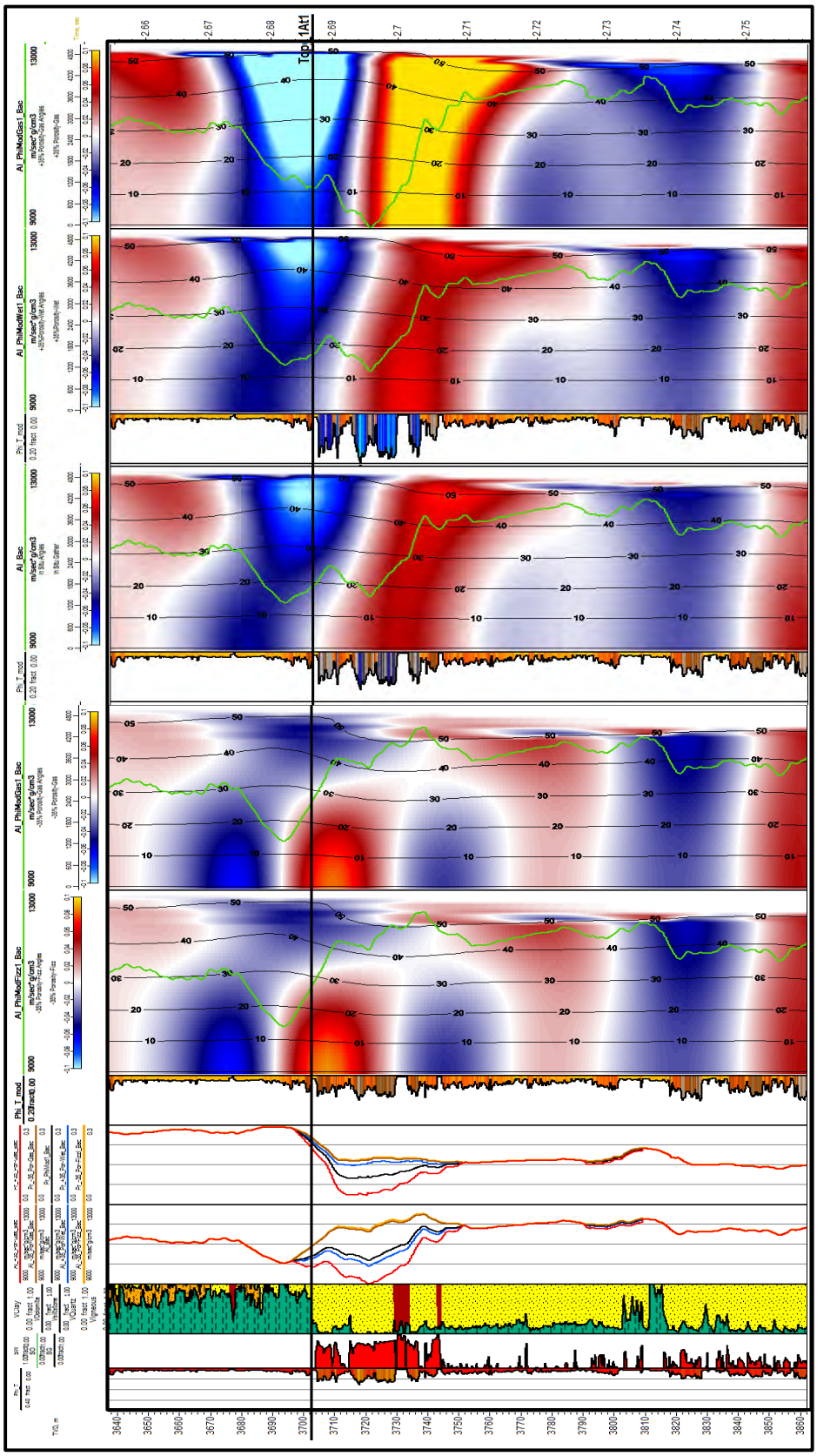

Fig. 4.5.11: AVA analysis-Porosity Models (1At1) :F-O1 Seismic Gather.

Amplitude vs Angle Plot

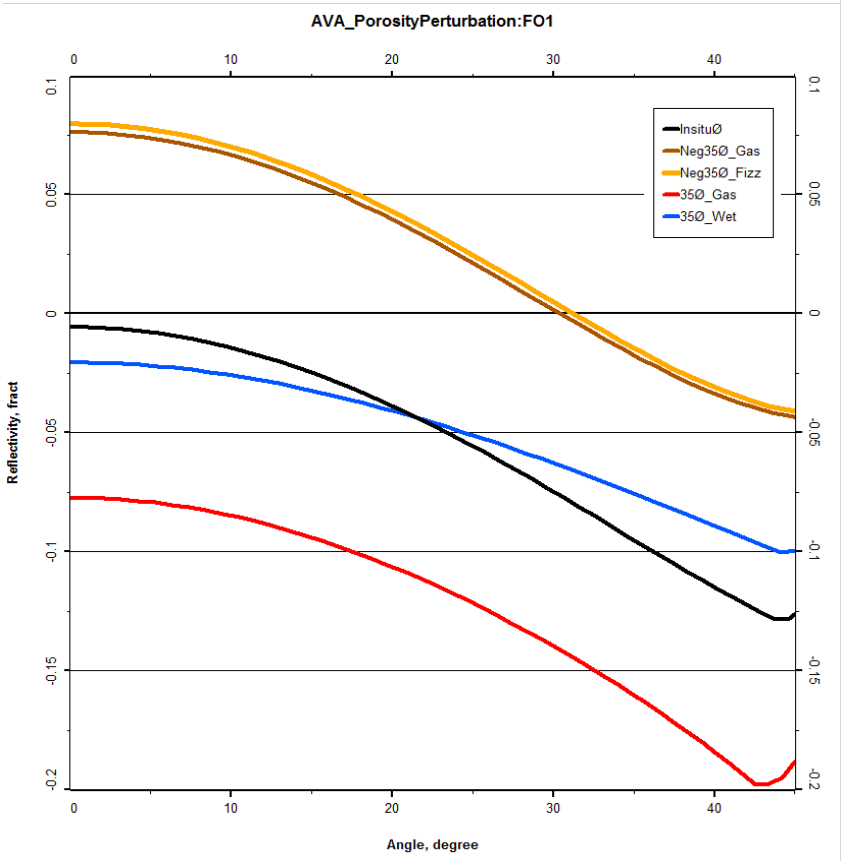

Intercept-Gradient Plot

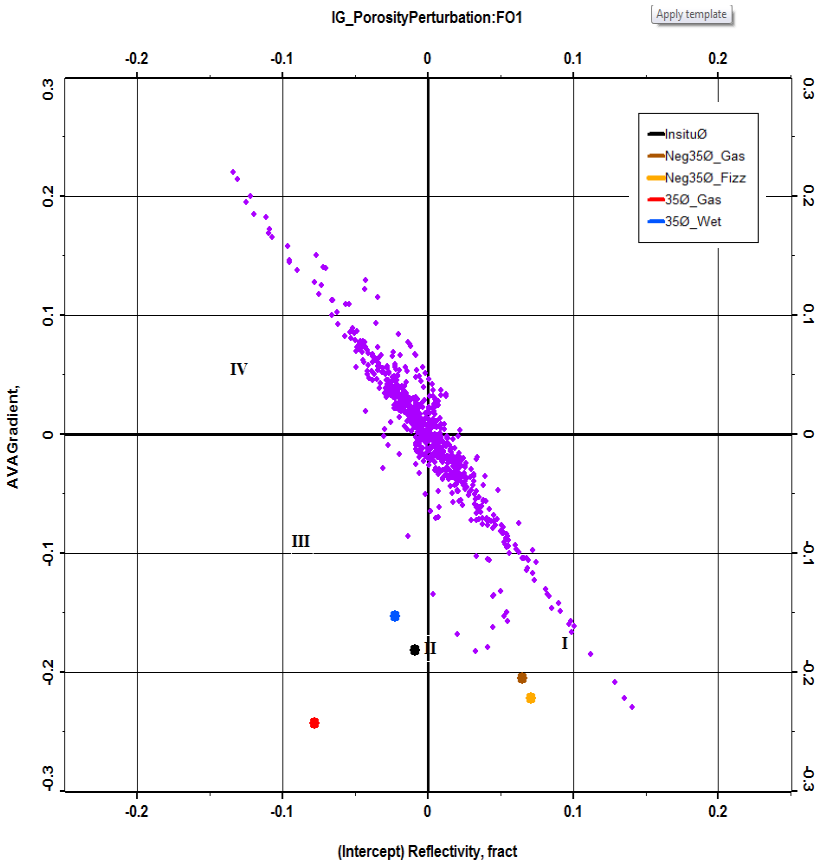

Fig. 4.5.12: AVA analysis-Porosity Models (1At1) :F-O1 AVA and IG cross-plot .

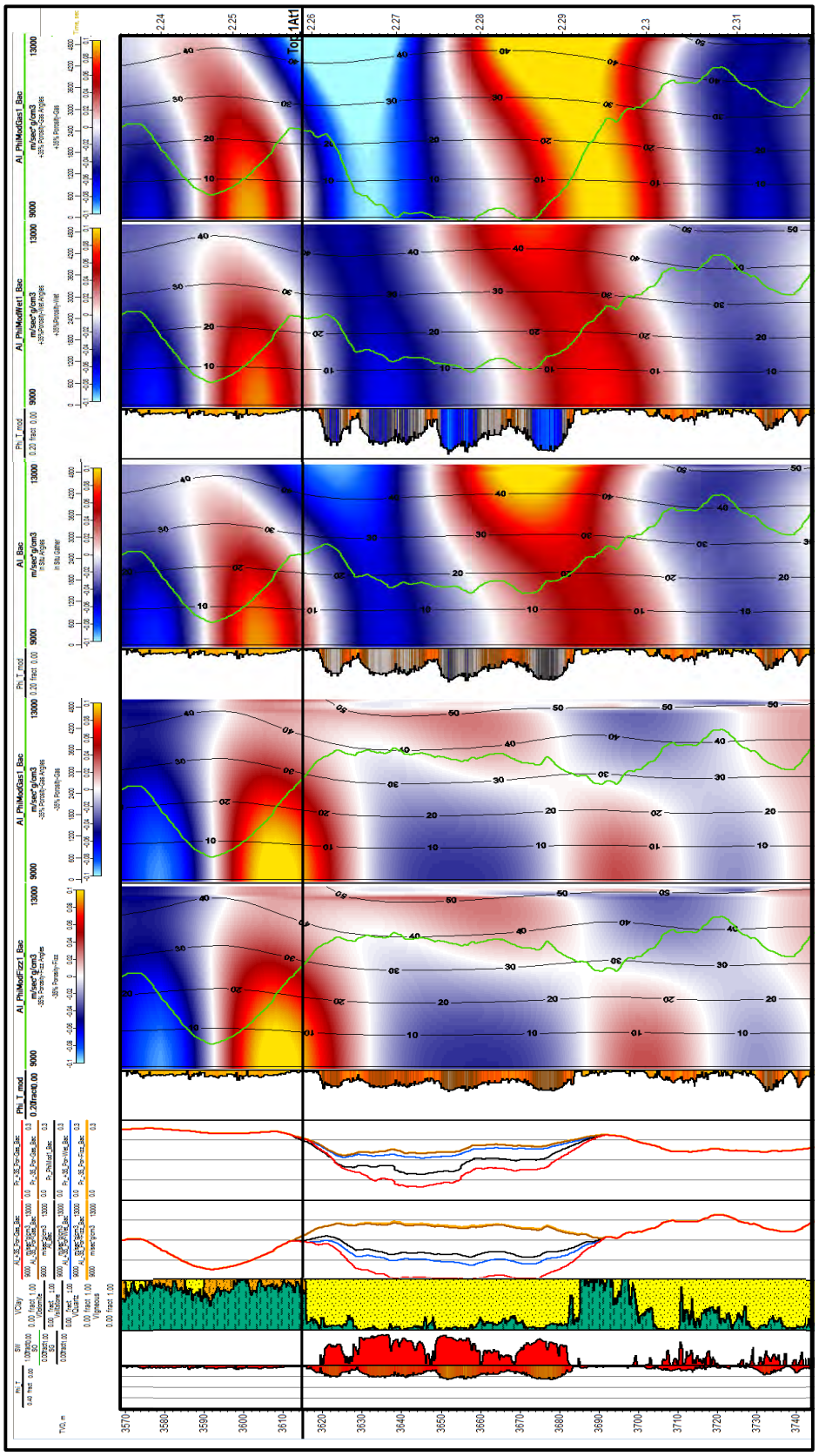

Fig. 4.5.13: AVA analysis-Porosity Models (1At1) :F-O2 Seismic Gather.

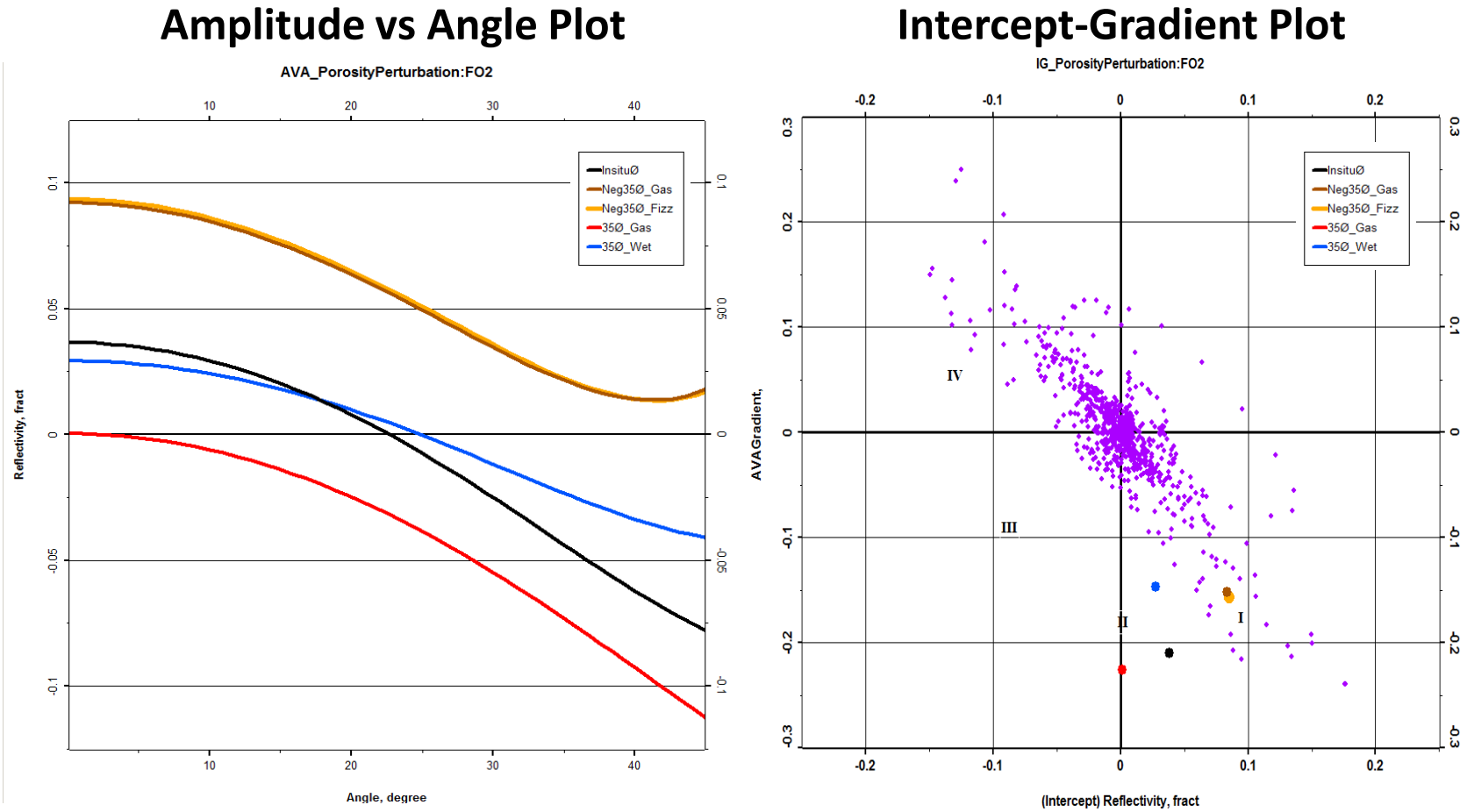

Fig. 4.5.14: AVA analysis-Porosity Models (1At1) :F-O2 AVA and IG cross-plot .

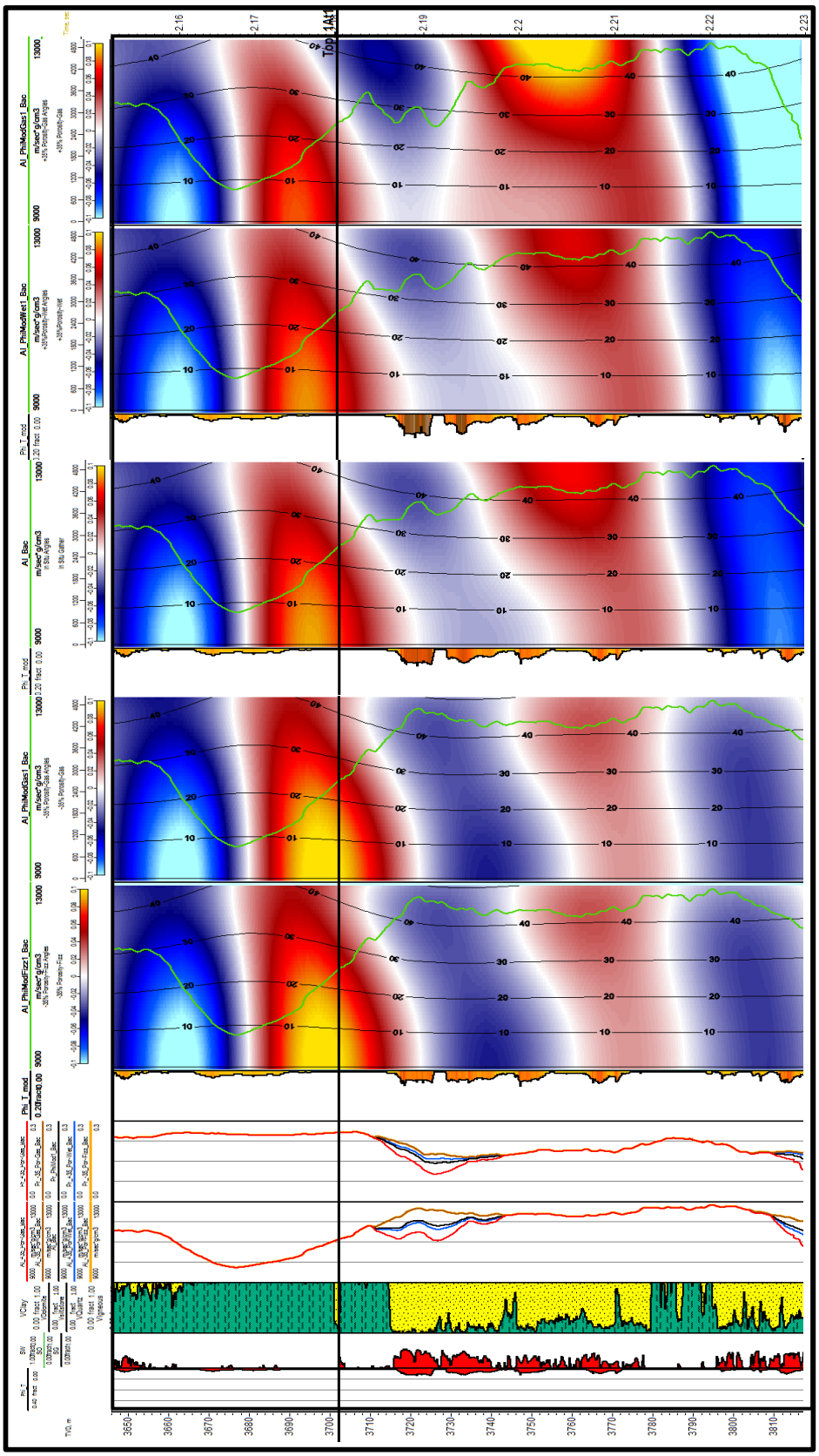

Fig. 4.5.15: AVA analysis-Porosity Models (1At1) :F-O3 Seismic Gather.

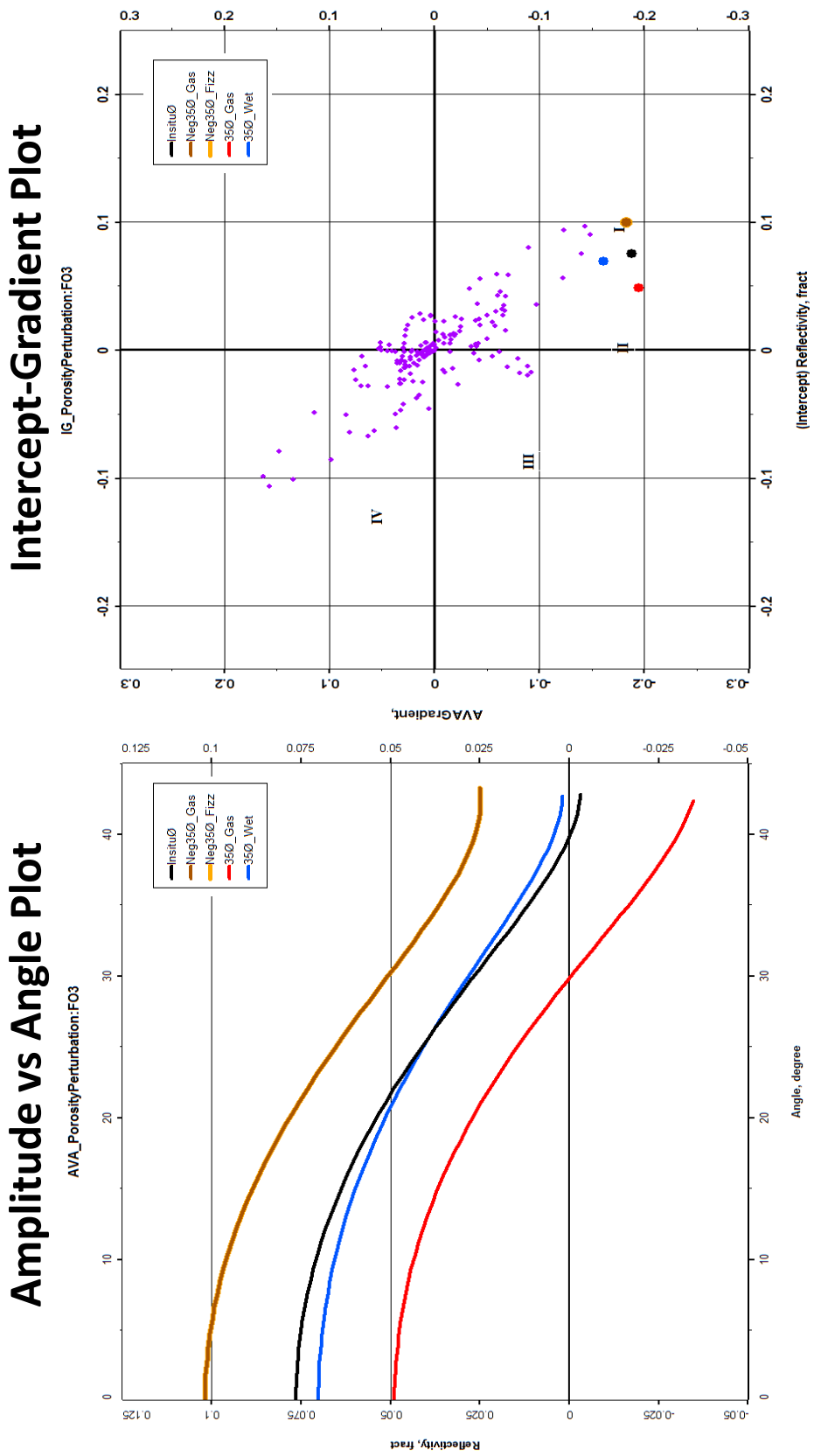

Fig. 4.5.16: AVA analysis-Porosity Models (1At1) :F-O3 AVA and IG cross-plot .

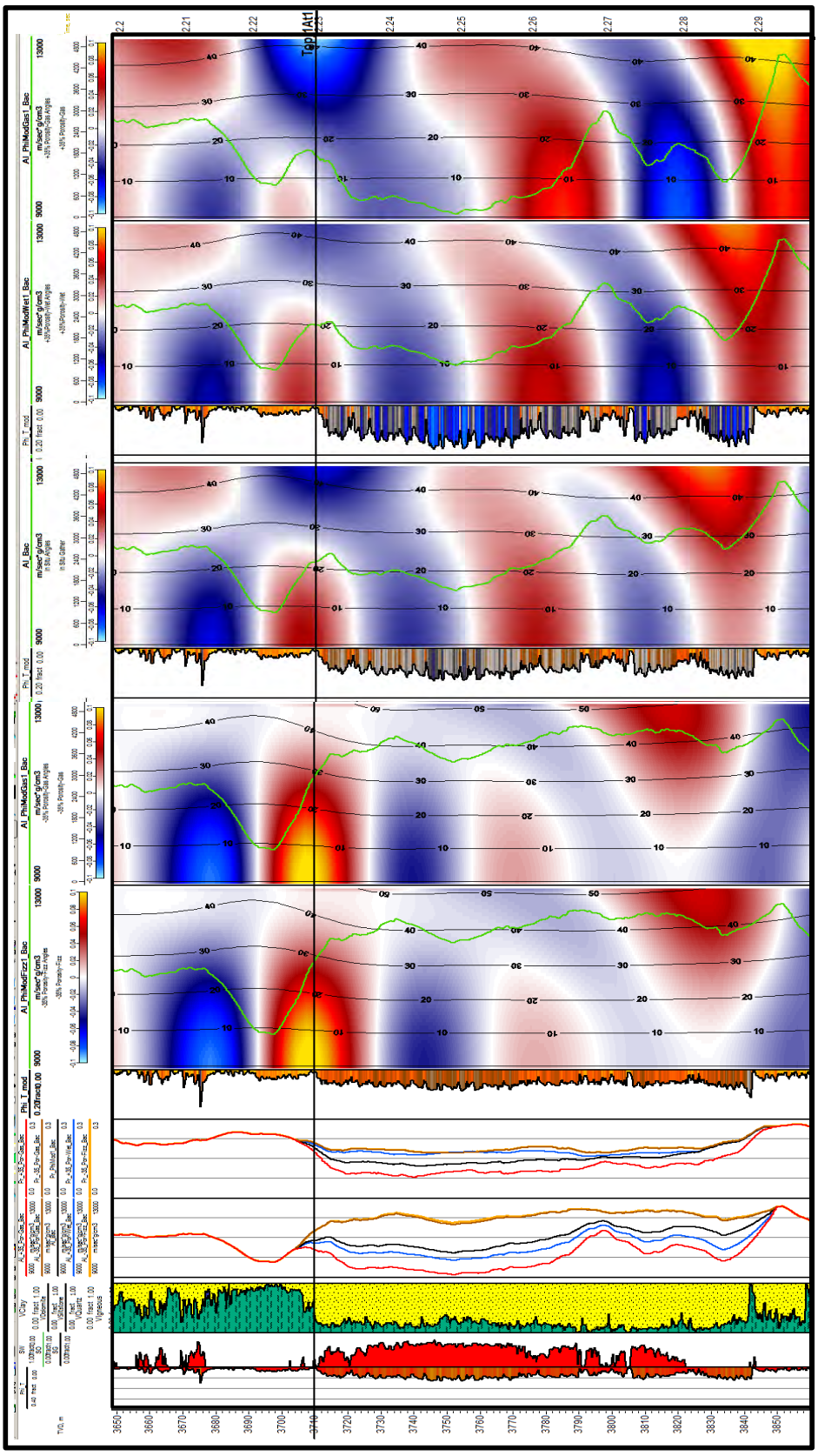

Fig. 4.5.17: AVA analysis-Porosity Models (1At1) :F-O4 Seismic Gather.

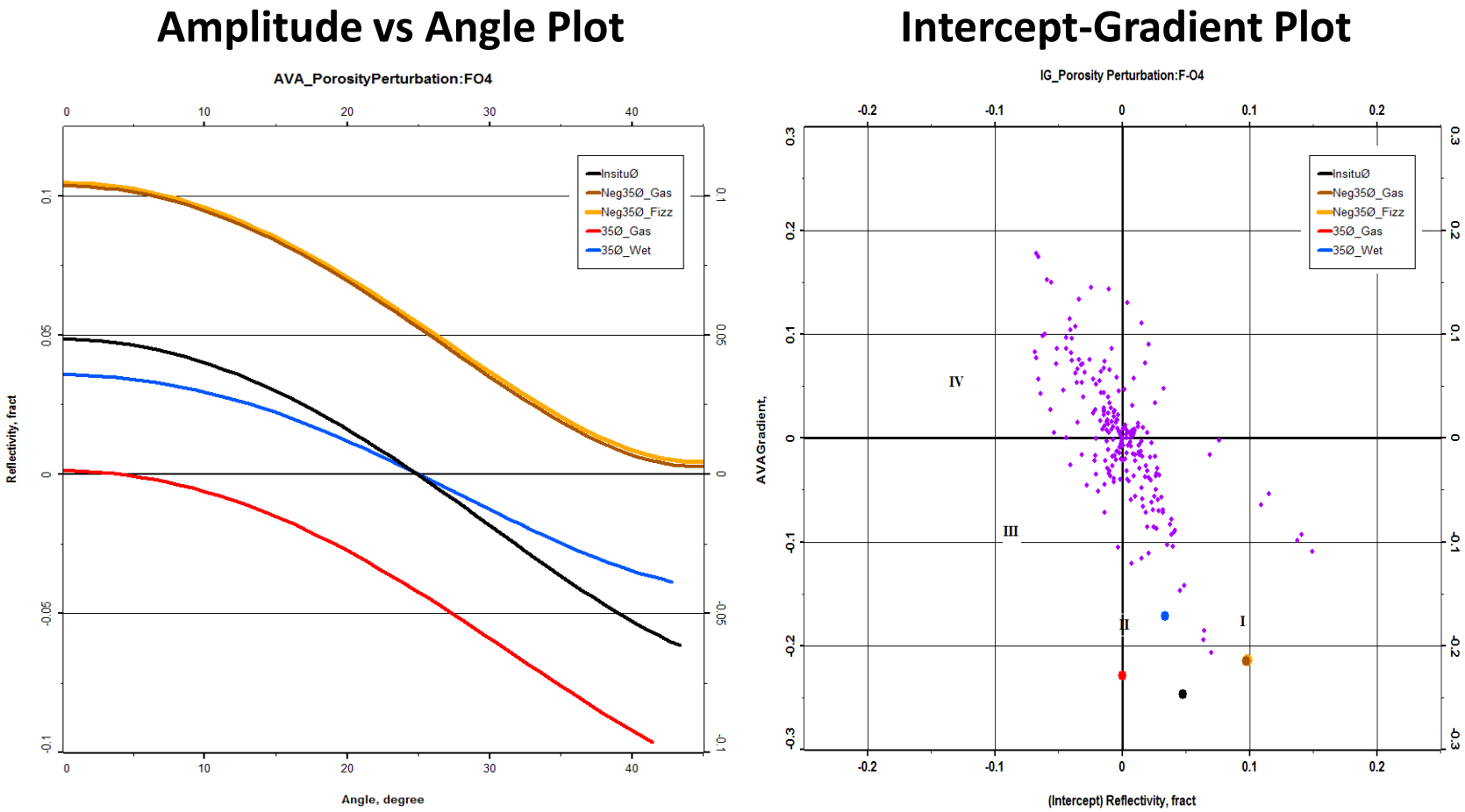

Fig. 4.5.18: AVA analysis-Porosity Models (1At1) :F-O4 AVA and IG cross-plot .

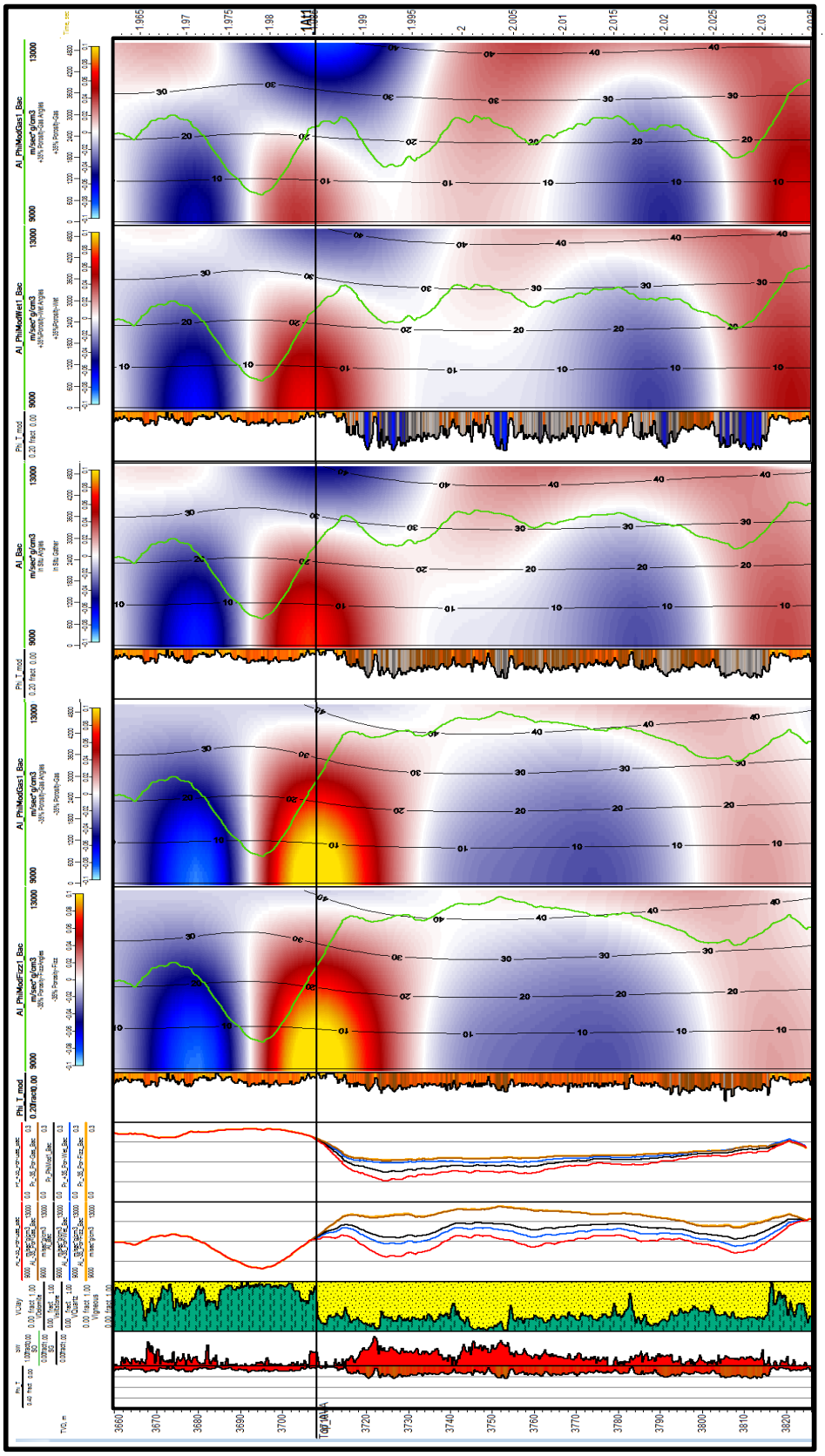

Fig. 4.5.19: AVA analysis-Porosity Models (1At1) :F-O6 Seismic Gather.

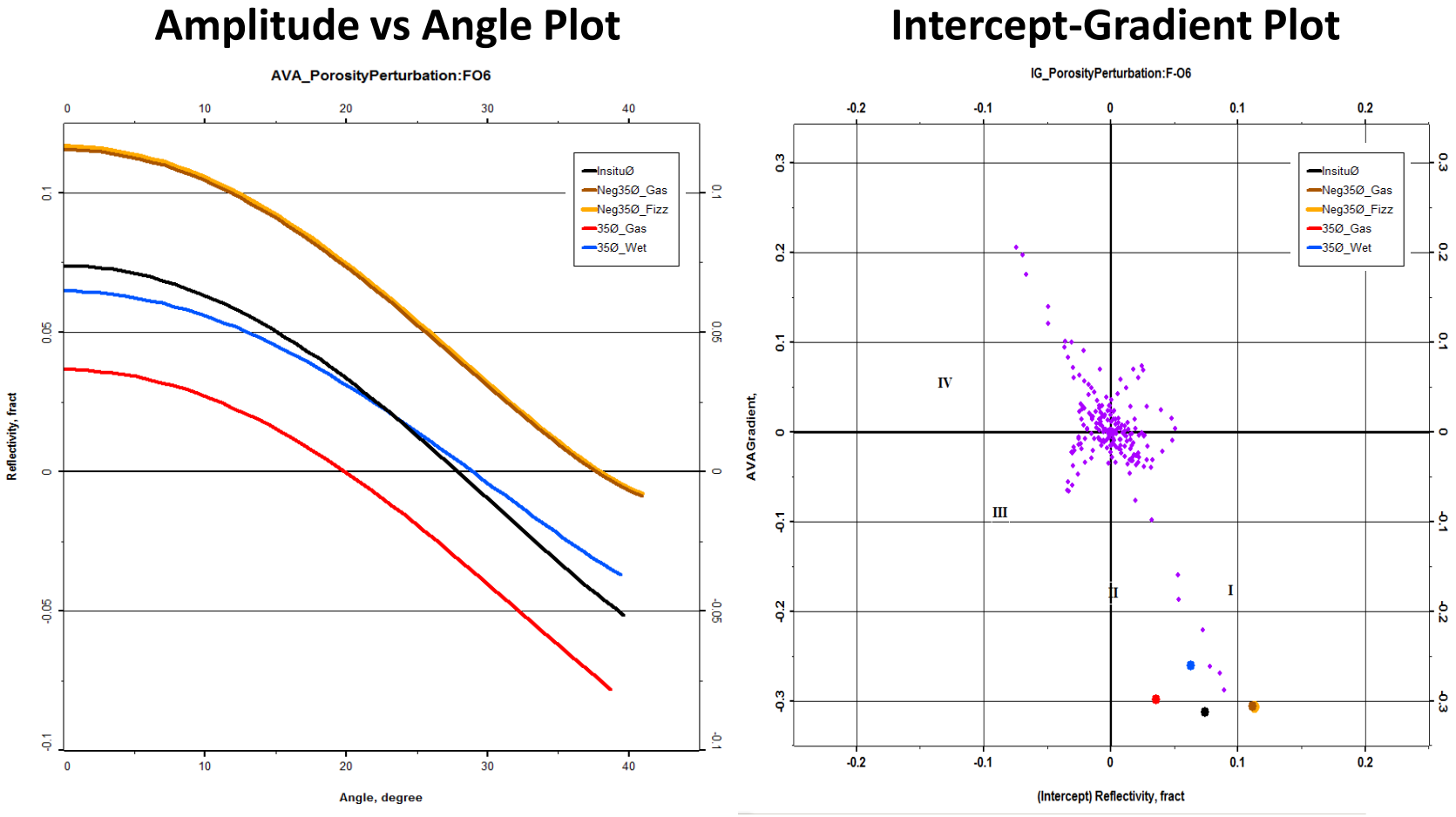

Fig. 4.5.20: AVA analysis-Porosity Models (1At1) :F-O6 AVA and IG cross-plot .

4.5.3 Clay modelling

The zero offset amplitude in gathers tends to decrease due to an important decrease in acoustic impedance if clay is introduced gradually. Wells F-O3, F-O4 and F-O6 are good examples of this behaviour. Moreover, the offset response or AVA effect is diminished. This effect is attributed to an increase in Poisson's ratio and leads to less separation between fluid cases once Vclay is increased at the expense of quartz at seismic resolution.

The seismic gather signature when an exaggerated Vclay is perturbed (high Vclay cases) shows a very similar response, regardless of fluid content. Even more, for an intermediate clay volume the seismic response is slightly different between gas and water cases, but not enough to be considered predictable (see figures 4.5.21, 23, 25, 27, and 29).

Some observations on amplitude versus angle cross-plots are (a) a continuous decay in amplitude at zero offset/angle once Vclay is increased from in situ Vclay to intermediate and high clay volume, and (b) the slope of the AVA curve becomes gentler with the angle (up to 45°) when Vclay is increased. That means a deterioration of the AVA effect or off-set response as the clay content of the rock increases.

The AVA class for mineralogy models is summarized by wells below:

F-O1:

In situ and intermediate clay volume water fall in Class II

The other cases fall in Class III

F-O2 and F-O4:

In situ, intermediate clay volume gas and intermediate clay volume water fall in Class I weak (moderate reflection coefficient <0.05)

High clay volume gas and high clay volume fizz fall in Class IIP

F-O3:

All cases fall in Class I (high reflection coefficient)

F-O6:

In situ and intermediate clay volume water fall in Class I (high reflection coefficient >0.05)

Intermediate clay volume gas and high clay volume fizz fall in Class I weak (moderate reflection coefficient <0.05)

High clay volume gas falls in Class IIP

The AVA gradient is more sensitive to Vclay perturbation than the intercept reflectivity. All mineralogy scenarios, with the exception of F-O1, fall in the class I area. F-O1 scenarios move to the class III area and some cases (high clay volume gas and water) are plotted in the vicinity of the class IV area. The results of the AVA analysis can be seen in each even figure from 4.5.22 to 4.5.30.

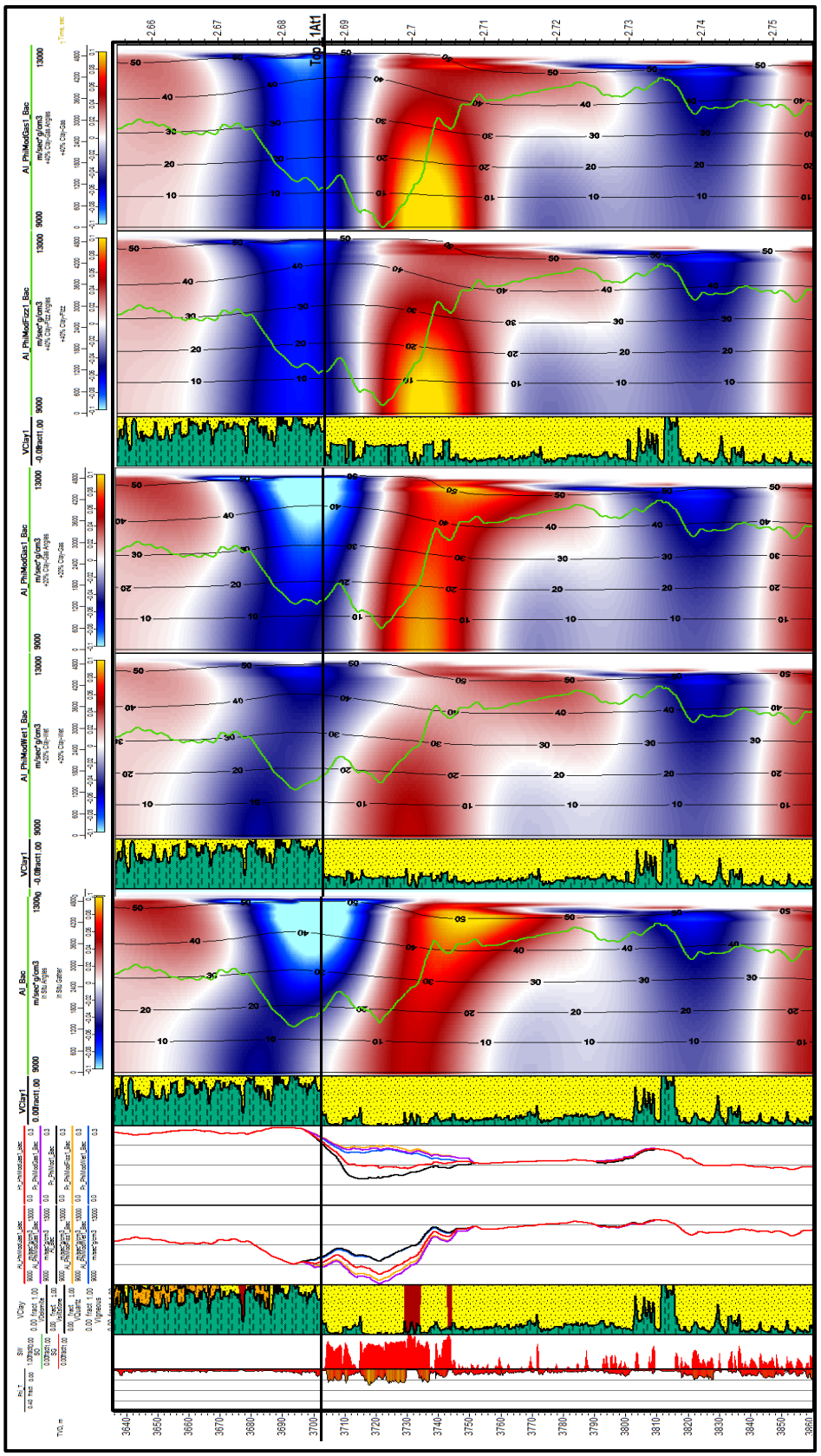

Fig. 4.5.21: AVA analysis-Mineralogy Models (1At1) :F-O1 Seismic Gathers.

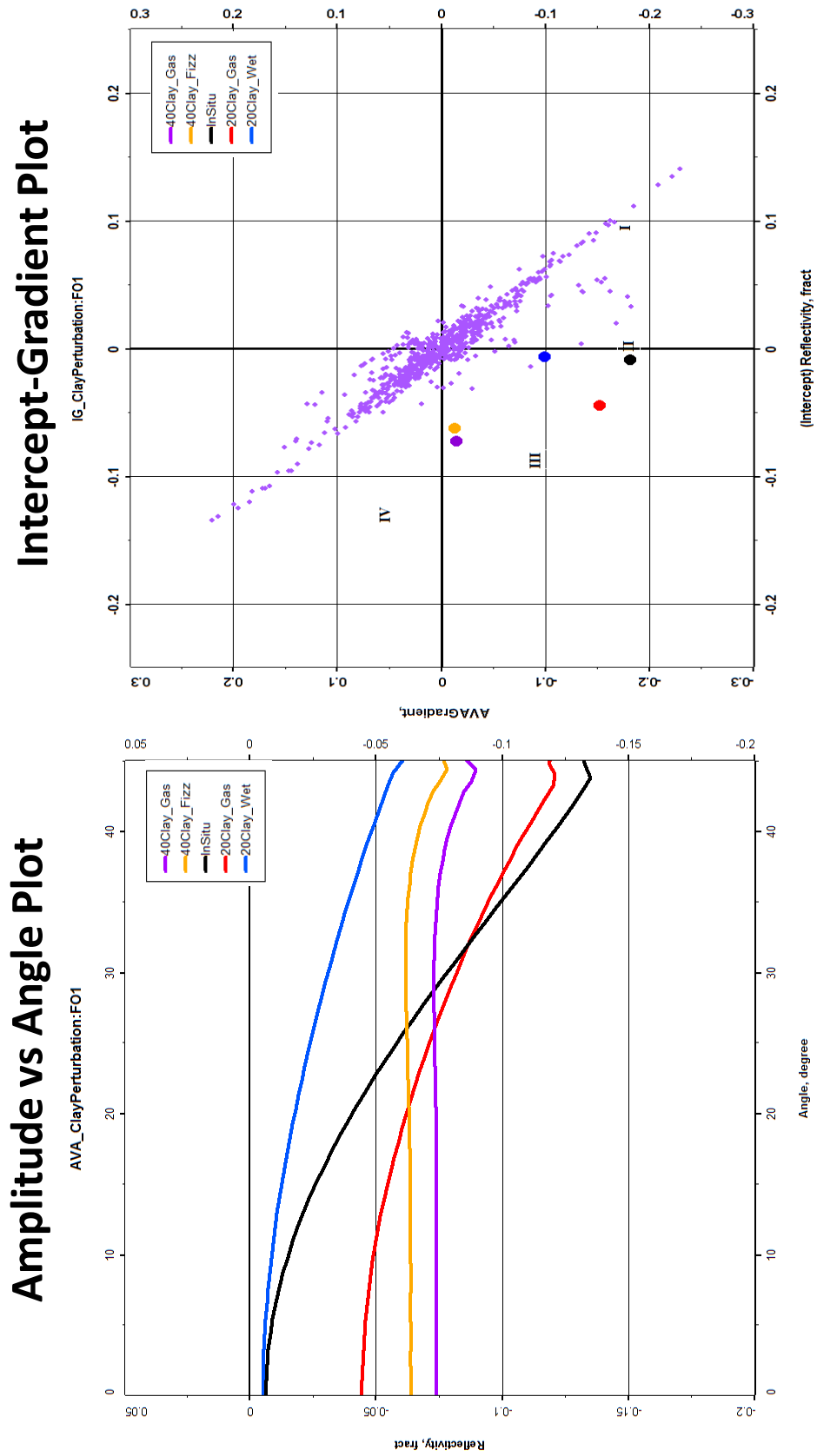

Fig. 4.5.22: AVA analysis-Mineralogy Models (1At1) :F-O1 AVA and IG cross-plot .

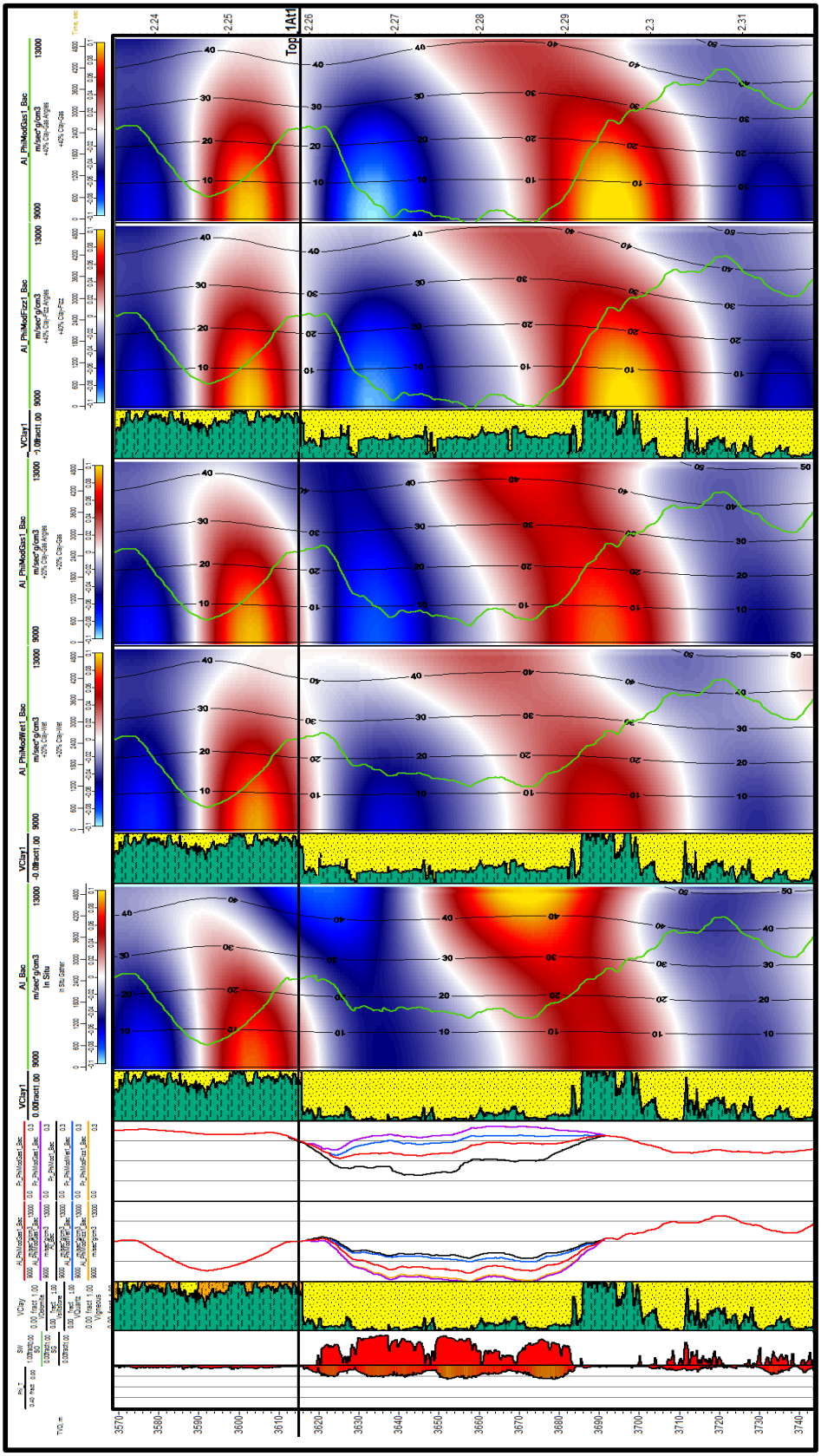

Fig. 4.5.23: AVA analysis-Mineralogy Models (1At1) :F-O2 Seismic Gathers.

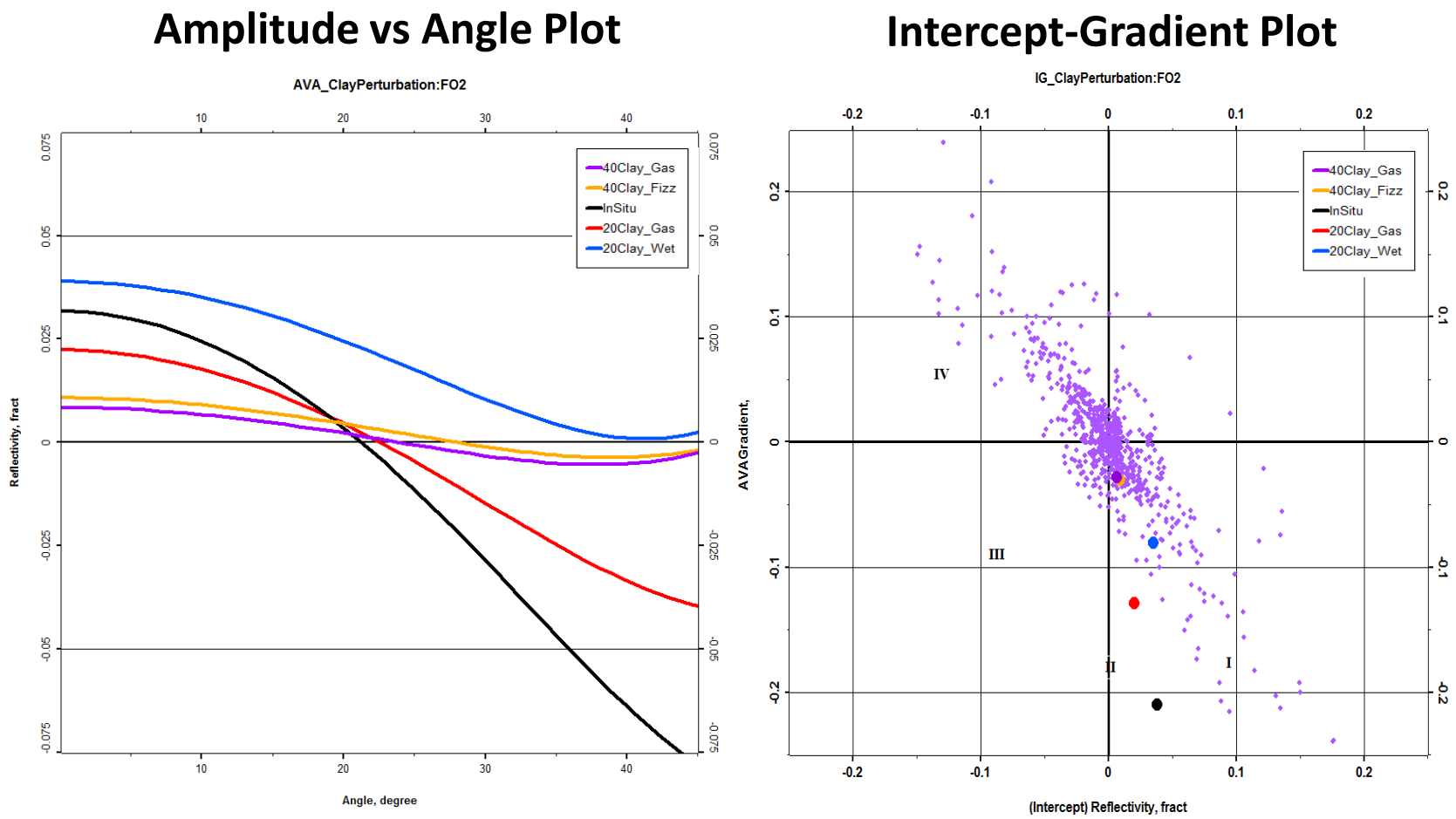

Fig. 4.5.24: AVA analysis-Mineralogy Models (1At1) :F-O2 AVA and IG cross-plot .

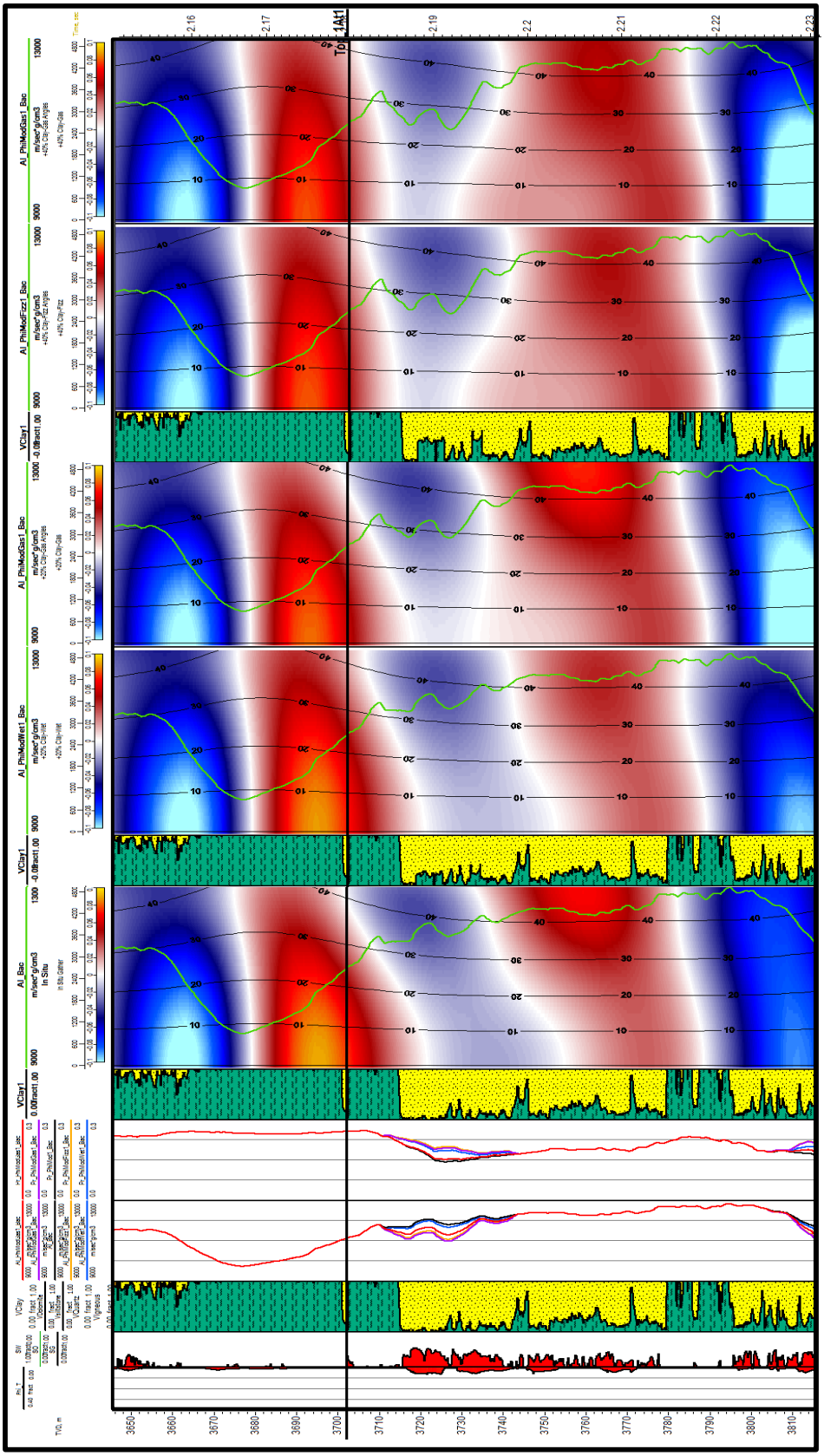

Fig. 4.5.25: AVA analysis-Mineralogy Models (1At1) :F-O3 Seismic Gathers.

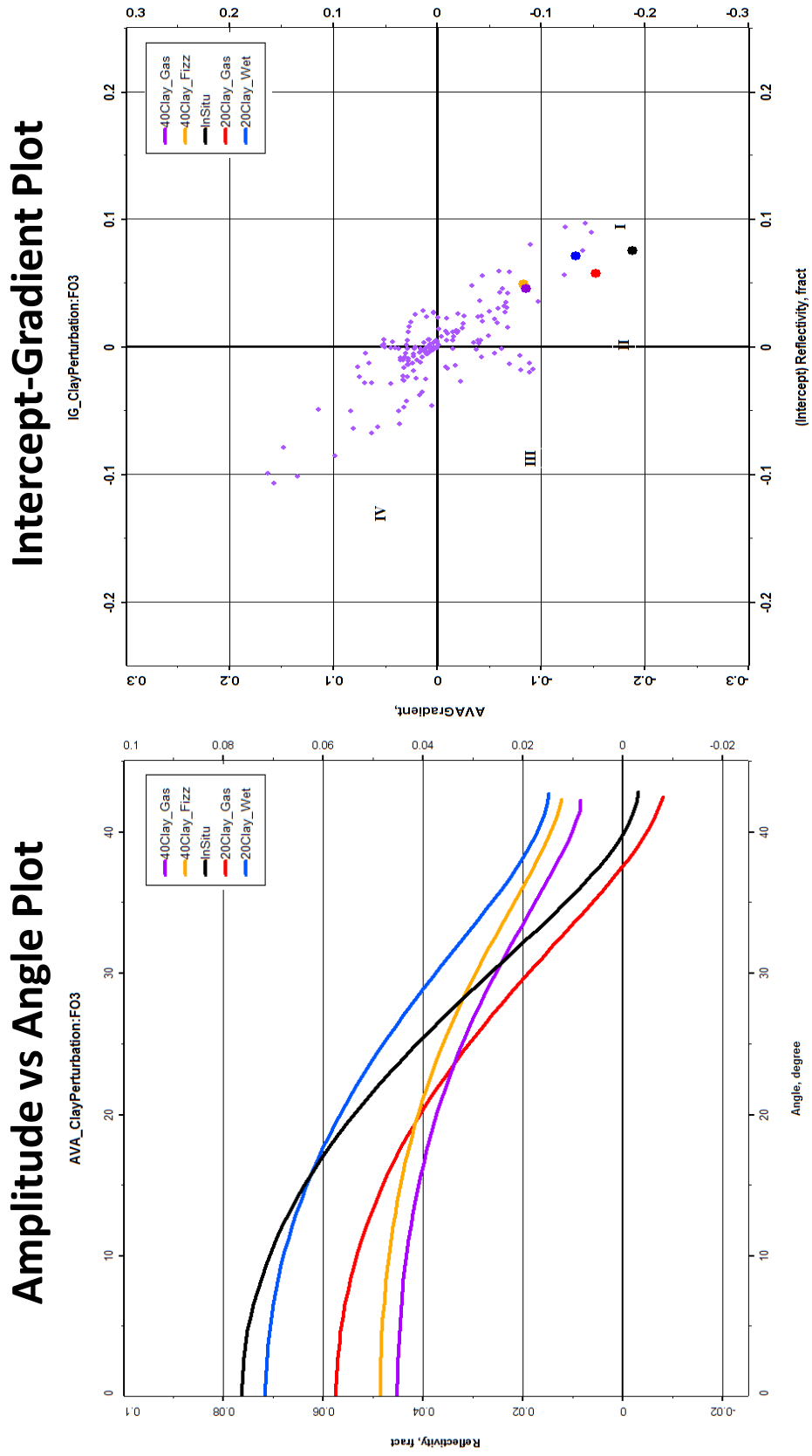

Fig. 4.5.26: AVA analysis-Mineralogy Models (1At1) :F-O3 AVA and IG cross-plot .

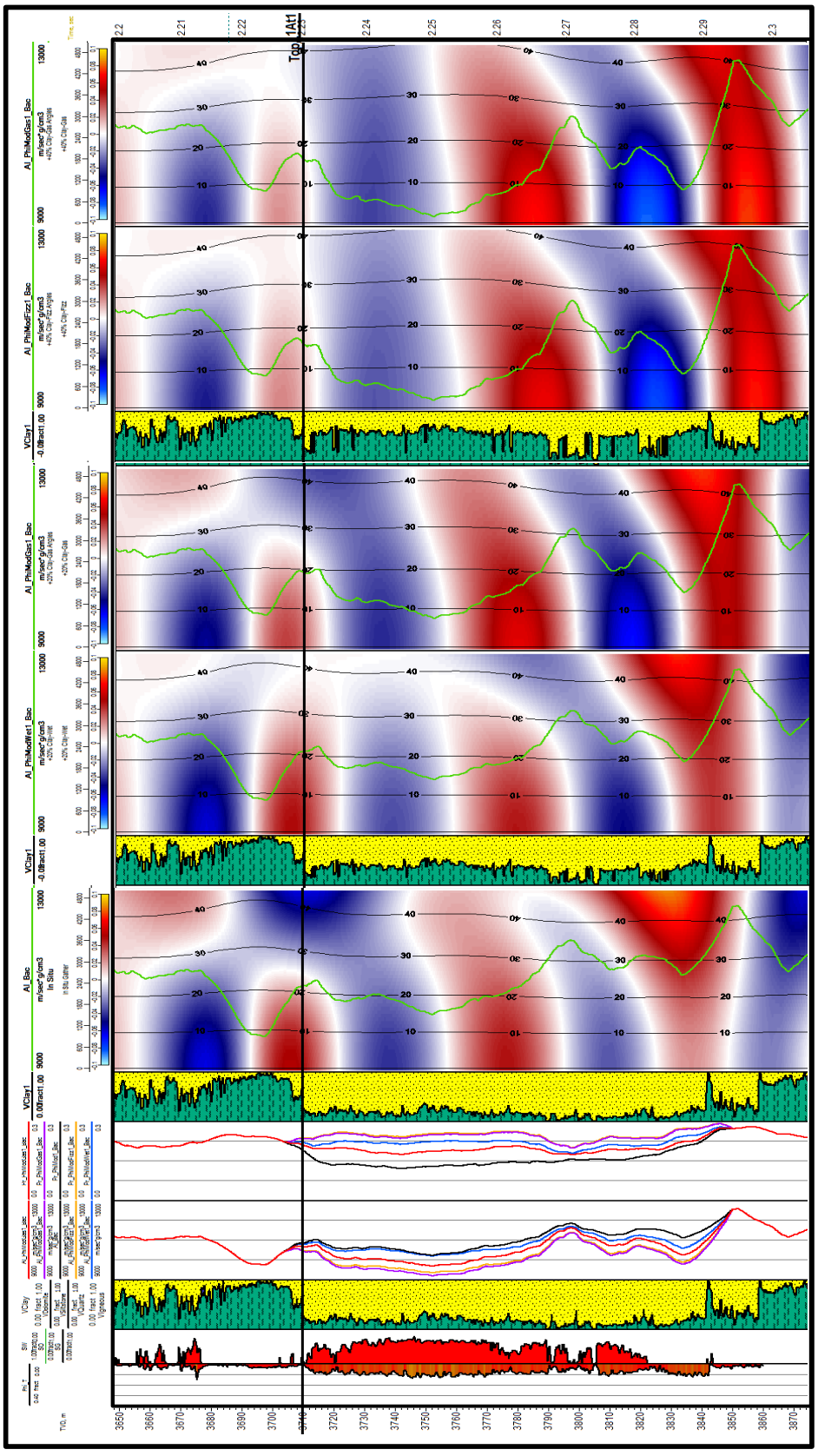

Fig. 4.5.27: AVA analysis-Mineralogy Models (1At1) :F-O4 Seismic Gathers.

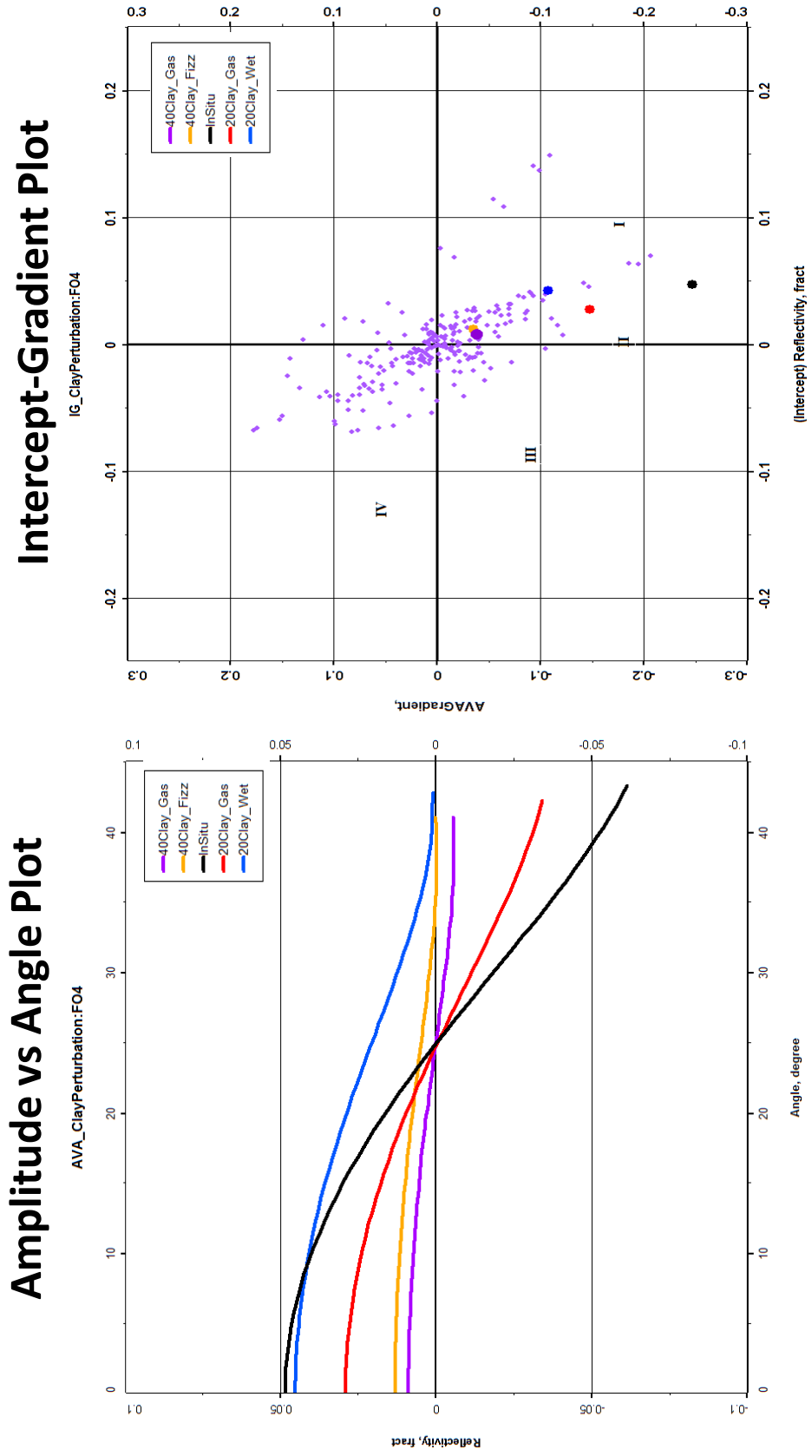

Fig. 4.5.28: AVA analysis-Mineralogy Models (1At1) :F-O4 AVA and IG cross-plot .

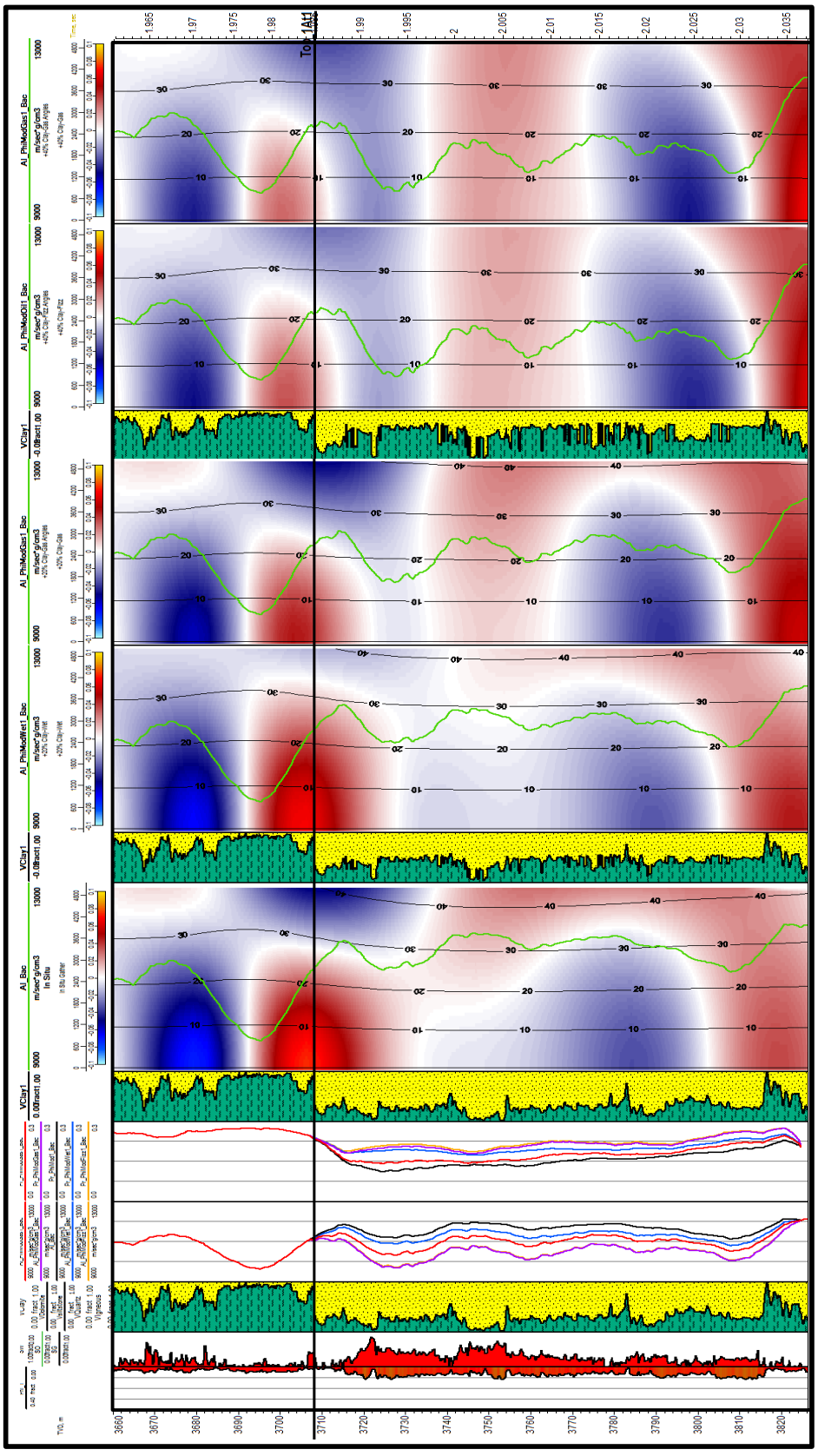

Fig. 4.5.29: AVA analysis-Mineralogy Models (1At1) :F-O6 Seismic Gathers.

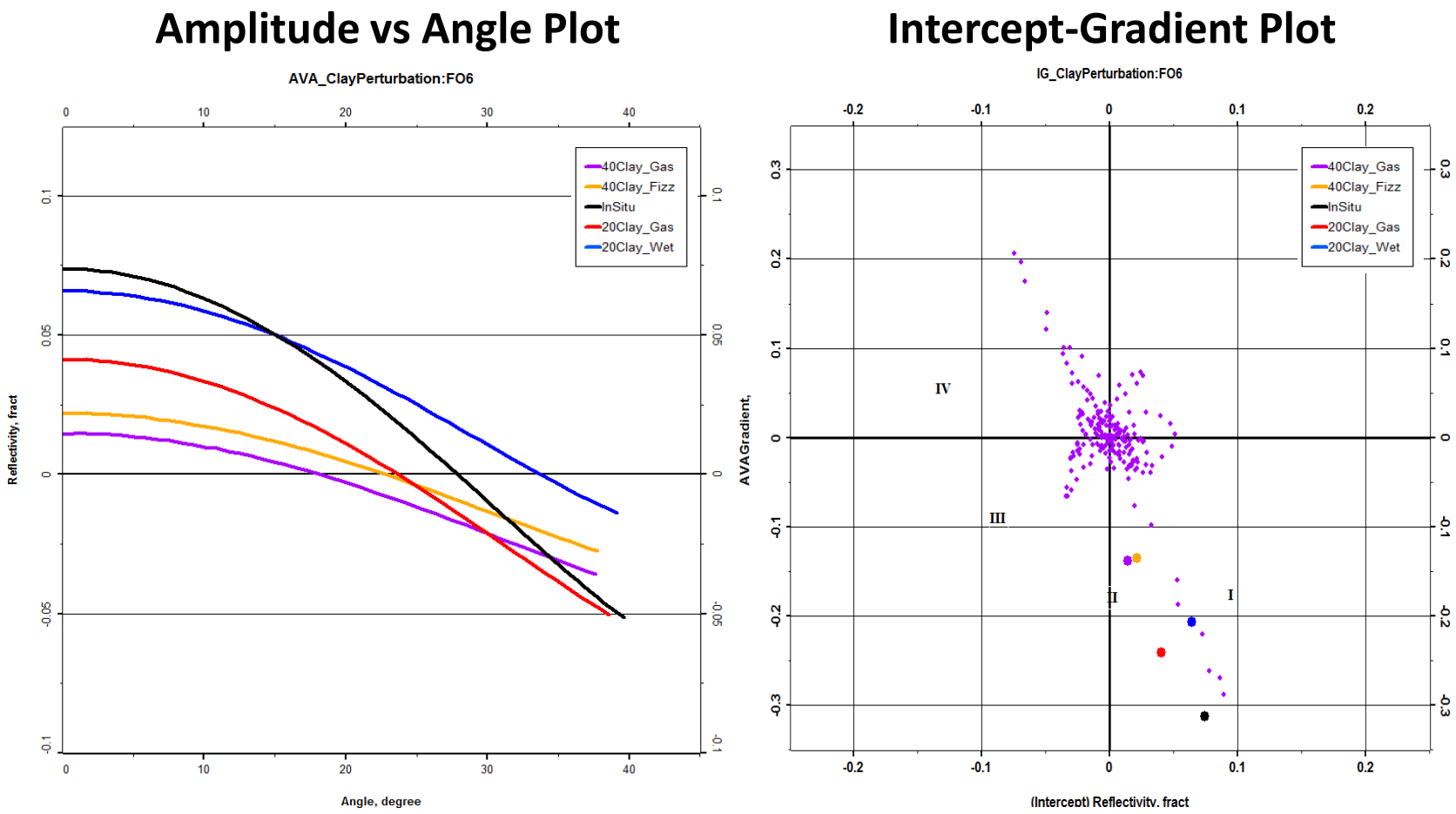

Fig. 4.5.30: AVA analysis-Mineralogy Models (1At1) :F-O6 AVA and IG cross-plot .

4.5.4 Thickness modelling

The seismic responses of gathers are driven by one or a combination of the factors: thickness and porosity. Some cases are highlighted below:

Thinning section porosity: An example of thickness and porosity competing is the exaggerated thinning gas case in F-O4. This scenario shows slightly better porosities than the intermediate thinning case, i.e. higher sensitivity to fluid (gas). However, the exaggerated case lies below the tuning thickness (<40 metres), so the brightening in the far offsets is not as high as expected for an interference effect.

Porosity: In the intermediate thinning gas case (F-O4) the porosity was not as well developed as in situ, i.e. less fluid (gas) effect and higher acoustic impedance, causing higher zero offset amplitude.

Thickening section: the thickening gas case in F-O1 shows a strong sensitivity to fluids compared with the in situ case, which is expressed in the high degree of brightening in the far offset. The amplified AVA effect is attributed to blocky (70 metres) enhanced porosity sand with less of the transition effects causing interference.

AVA Class

Thickness cases (F-O1):

In situ case: Class II

-45% sand thickness/ in situ: Class I (high reflection coefficient)

+28% sand thickness/ 80% gas, 20% water: Class II

+28% sand thickness/100% water: Class I (moderate reflection coefficient)

Thickness cases (F-O4):

In situ case: Class I

-44% sand thickness/80% gas, 20% water: Class I

-44% sand thickness/ 100% water: Class I

-63% sand thickness/80% gas, 20% water: Class I

-63% sand thickness/100% water: Class I

See figures 4.5.31 to 4.5.34

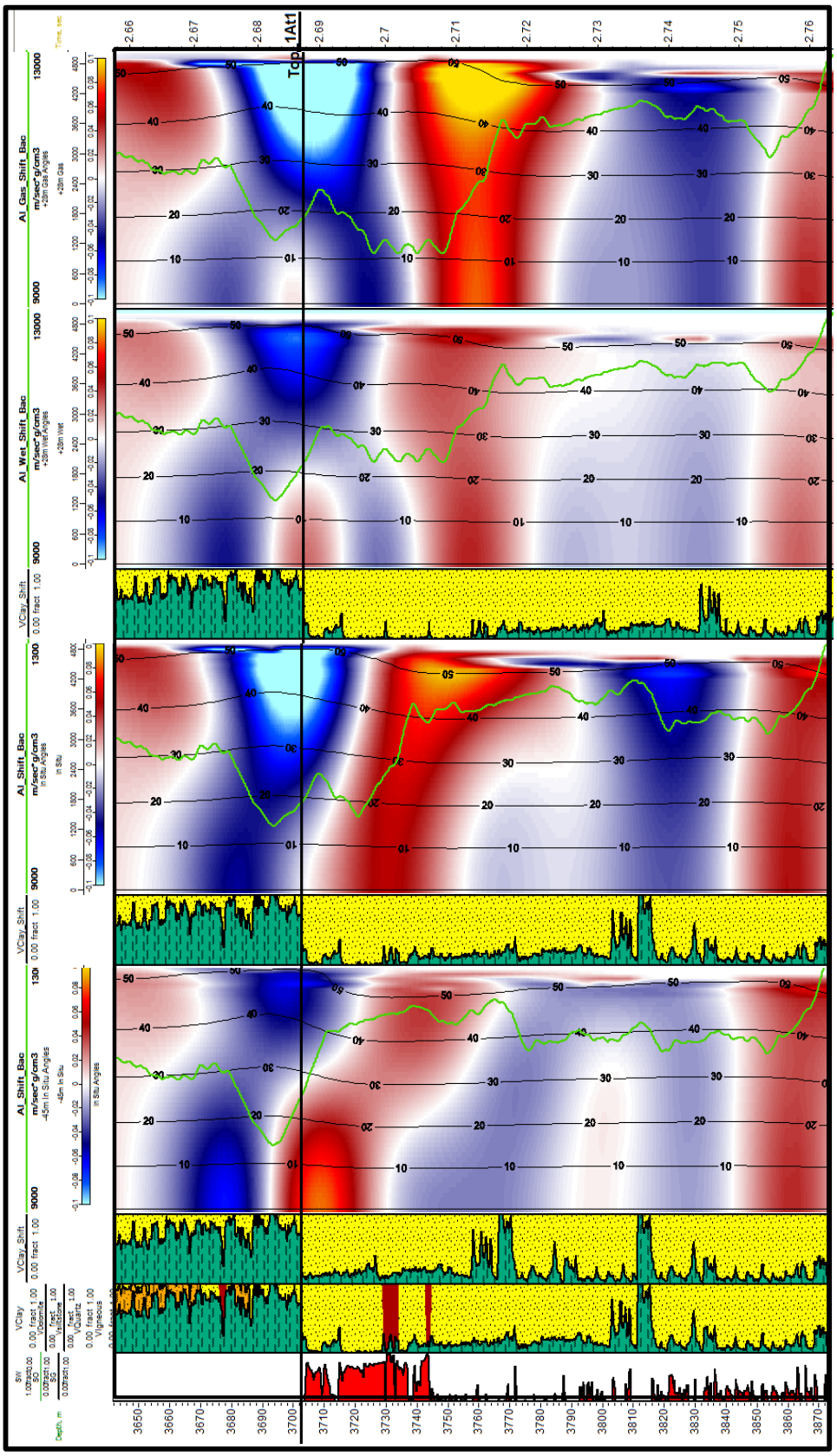

Fig. 4.5.31: AVA analysis-Thickness Models (1At1) :F-O1 Seismic Gathers.

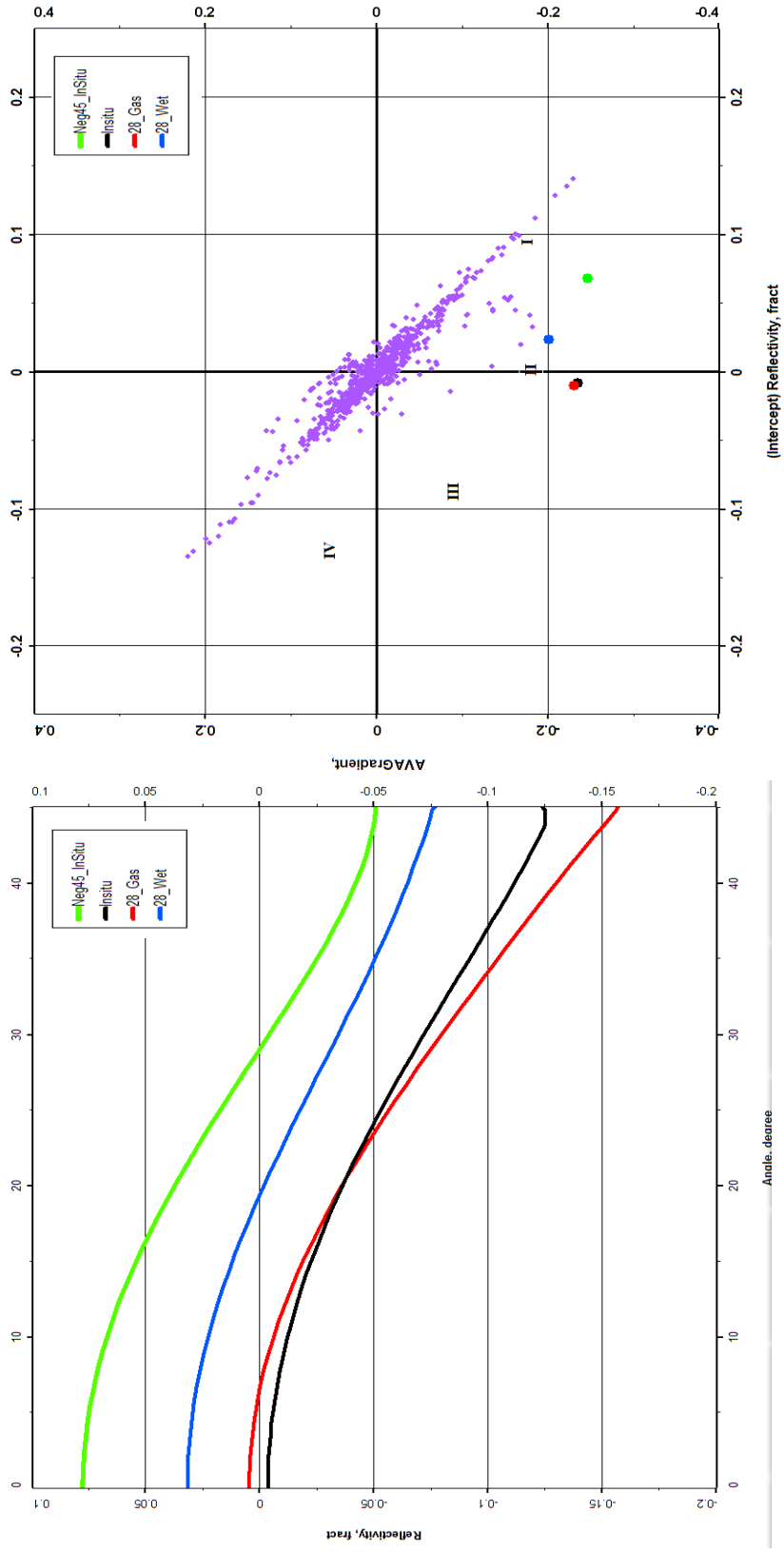

Fig. 4.5.3.32: AVA analysis-Thickness Models (1At1) :F-O1 AVA and IG cross-plot.

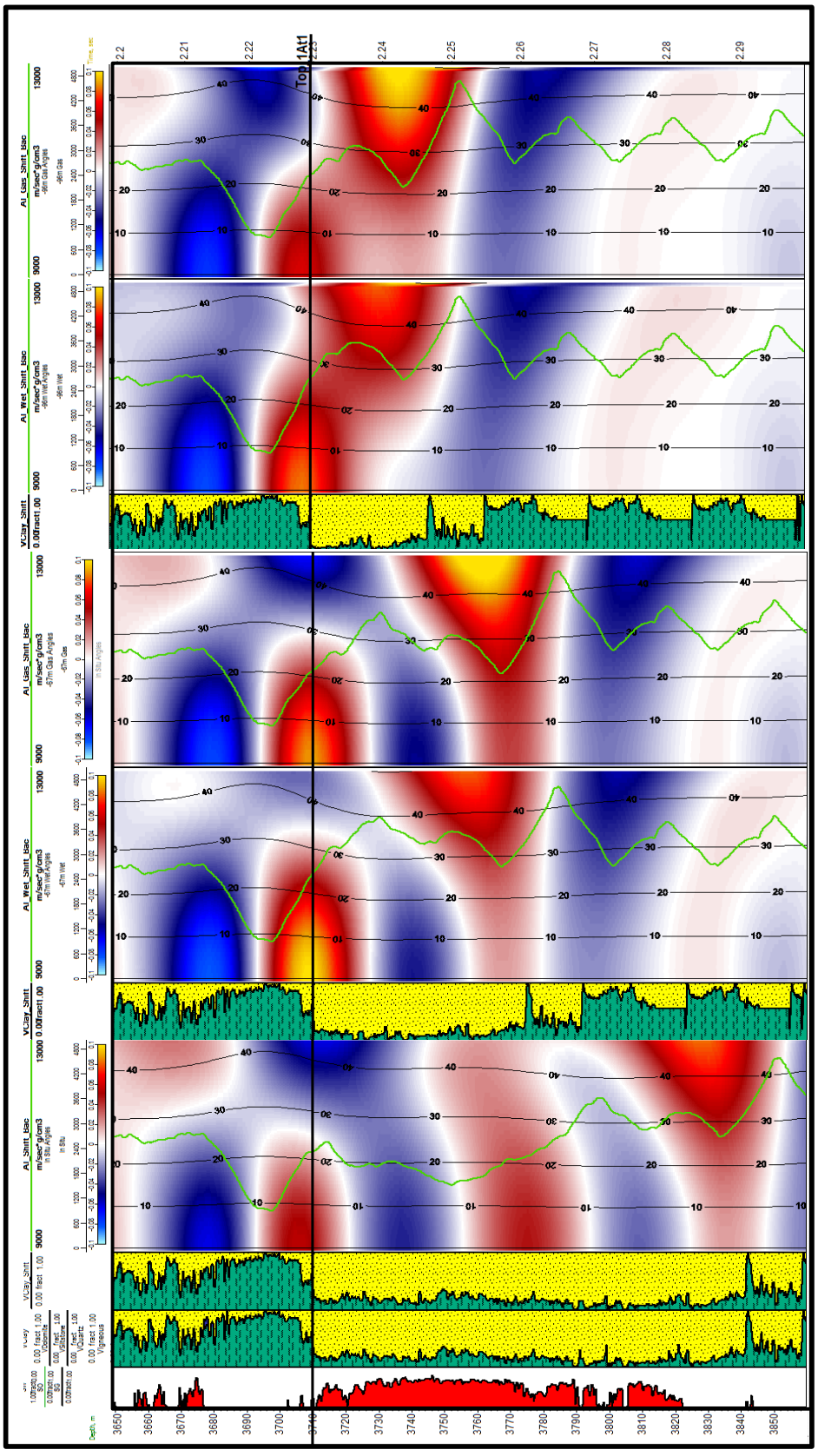

Fig. 4.5.33: AVA analysis-Thickness Models (1At1) :F-O4 Seismic Gathers.

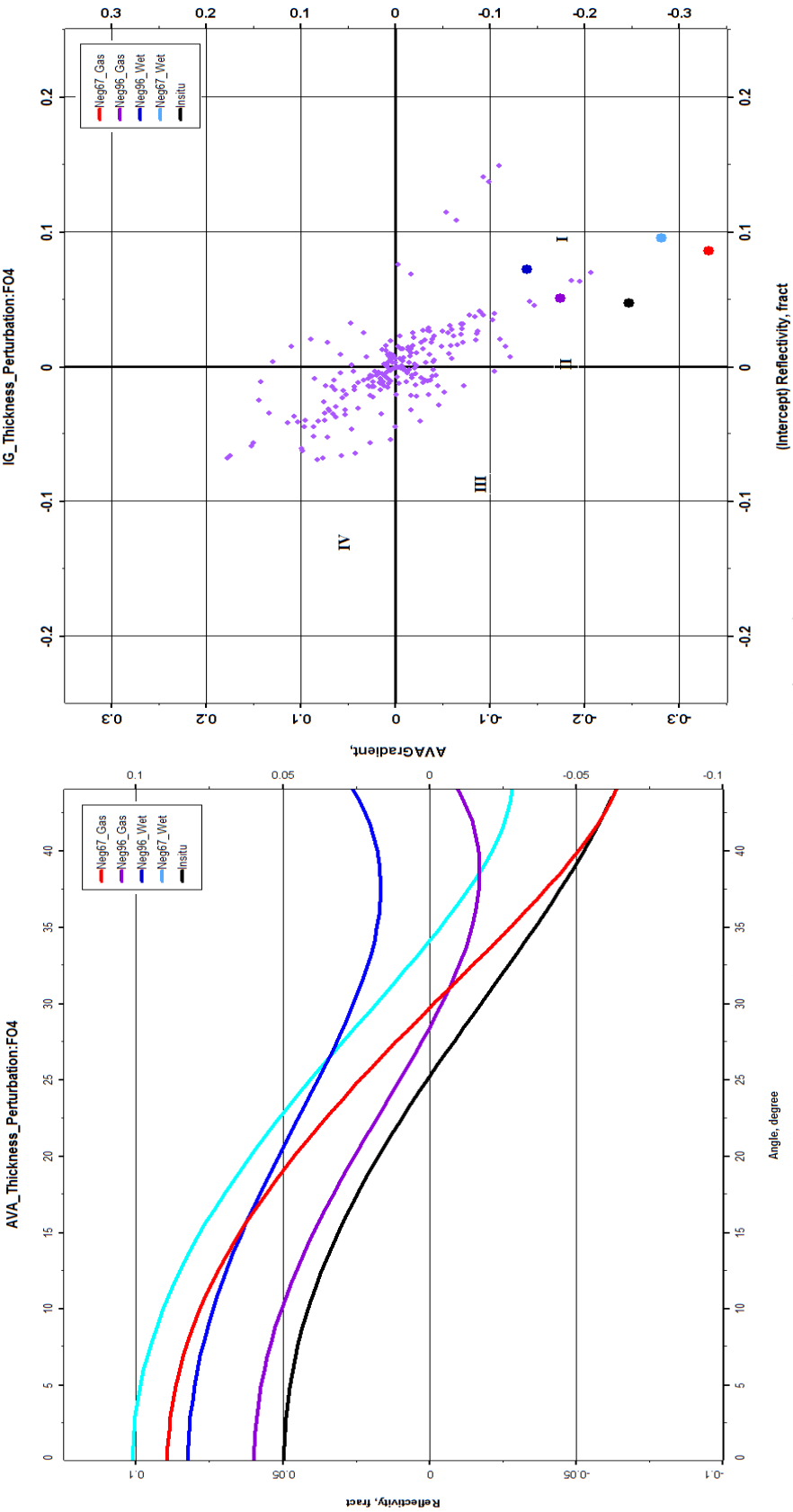

Fig. 4.5.3.34: AVA analysis-Thickness Models (1At1) :F-O1 AVA and IG cross-plot.

4.6 Discussion and conclusions

Rock physics models were used in an attempt to uncover the link between seismic observables (density, Vp and Vs) and reservoir parameters such as fluid content, porosity and mineralogy. Understanding the various effects on the seismic response is crucial to answering questions such as: Is a rock-physics model suitable for conditioning well data? Is the AVA seismic response sensitive to the presence of commercial gas? Are differences between commercial and non-commercial gas distinguishable in a seismic response? How robust would the AVA seismic response be in a situation of varying porosity, mineralogy and thickness? Can rock physics models help to understand well tie uncertainties? And if any trend is observed, can it be used as a predictive tool?

This dissertation covers five wells in an upper shallow marine synrift sequence offshore South Africa. One of the early tasks of rock physics analysis in this workflow was to guarantee consistent advanced well data conditioning for geophysical purposes across the entire well database. Overall, the data does not present dramatic measurement problems. The most significant corrections to the data were for mud invasion in the gas reservoirs, some wash-out (particularly in the 16At1 sequence) and missing shear-velocity logs, which are essential for a project of this nature.

Mud invasion was more pronounced in the zone with higher permeabilities in the reservoir. F-O1 and F-O2 showed greater invasion than the remaining wells, as higher enhanced poro-perm development took place in nearby areas. Mud invasion corrections were performed via Gassmann fluid substitution.

An intermediate stiff rock-physics model for sands and an unconsolidated “soft model” for shale were computed to generate the synthetic density, Vp and Vs curves used to edit the misread measurements, produced mainly by wash-out issues. This sand model (intermediate) was an interesting and successful variant of the soft sand model for simulating the different rock property scenarios in tight gas sands. On the other hand, the Greenberg-Castagna model fits the shear sonic compaction trend in the F-O1 well satisfactorily.

Overall, the effect of fluid fill for example, replacing relatively incompressible water with highly compressible gas, is to reduce the P-Velocity and density of the rock, while a negligent effect on Vs can be expected, since liquids have no rigidity (Simm and Bacon, 2014). Consequently, both acoustic impedance and Poisson ratio decrease. However, how much of the seismic amplitude of a rock buried at 3700 m is sensitive to fluid effect? In most cases, a sand rock exposed to such a compaction trend should be developing porosities of no more than 6-7%. However, the overpressure counteracts this trend, partially preserving the porosities in the field. This variable allowed the seismic amplitude response to be more sensitive to rock property changes, such as fluid content.

Fluid substitution modelling shows generally good discrimination between gas and water where the reservoir has a better developed porosity (F-O1 and F-O2), whereas there is more

overlap between the cases where the reservoir is thinner and less porous (F-O3 and F-O6). On the other hand, a seismic response cannot discriminate between commercial gas (80% gas) and non-commercial "fizz" (20% gas), whatever the porosity.

As mentioned-above, the role of compaction is crucial to the expected seismic response. During burial, rocks undergo both mechanical and chemical changes which may cause a general decrease in porosity (and increase in density) with depth. The F-O field stiffness has a key influence on the rock frame and is critical to porosity. The rock-physics porosity models have a greater effect on the acoustic impedance response, and consequently on Poisson's ratio, than the fluids.

The zero offset response was dramatically affected by changes in porosity. Furthermore, the higher the porosity, the greater the sensitivity to fluid changes, which implies a higher Poisson's ratio contrast. This leads to a stronger offset response, generally expressed as a brighter seismic response in far offsets. The key to explain the seismic response due to porosity changes lies in the bulk rock. When porosity is increased, i.e. a higher percentage of the bulk rock is occupied by a given fluid, porosity works as an amplifier of the fluid effect on the seismic response. Conversely, when porosity is decreased, porosity works as an attenuator of the fluid effect on the seismic response.

Shale content was an important element to be analysed in the elastic properties perturbation. The F-O reservoir consists of alternating layers sand and shale. The presence of clays derived in-situ from the breakdown of feldspars (authigenic) is limited in the sandstones. The clay volume was modelled at the expense of quartz.

The effect of increasing the clay content was a reduction of the bulk and shear velocities (Vp and Vs) and a slight increase in the density of the rock. Consequently, increasing clay leads to a dramatic decrease in acoustic impedance and a moderate increase in Poisson's ratio.

An increase in the clay volume reduces the fluid sensitivity, due to less reservoir-quality rock to store the fluid. Therefore, there is less reservoir rock available for substitution.

One consequence of the band-limited nature of seismic is that below tuning thickness different combinations of impedance and thickness can give rise to the same seismic signature (Simm and Bacon, 2014).

It is difficult to interpret the seismic response in terms of thickness when the sand reservoir (pay sand) was close to the tuning thickness (40 metres). In addition, there are other factors playing a role in the signature of seismic, such as porosity, fluid content and mineralogy. However, it is considered probable that in a scenario where the pay sand thickness is greater than the tuning thickness, a more significant AVA response can be expected, because there is less destructive interference effect (wave propagation) that can alter the amplitude as modelled in the thickening thickness scenario (F-O1). On the other hand, in the event of a partial reduction of the pay sand thickness by an erosion mechanism, an increase of zero-response might be expected, as observed in the "intermediate thinning model" on F-

O4. Nevertheless, at a greater reduction a smaller AVA effect (zero and offset response) might be expected, as observed in the “exaggerated thinning model” on F-O4.

The effect of thickness on the seismic signature might be hidden in the case of combinations of other factors that contribute more to the seismic response generation than porosity.

The F-O field is highly complex in terms of seismic amplitude response. Among the wells there are similarities, but also differences, which make it difficult to observe a defined pattern over the whole field. A good example to understand such seismic complexities is the behaviour in the well-seismic tie at the top of reservoir (1At1).

Figure 4.6 illustrates three wells in the F-O field, and they all show different responses at 1At1 top. The key to understanding this disparity lies in how various factors and/or events influence the seismic signature in different ways.

The acoustic impedance response at the top of the reservoir interface (light green curve in figure 4.6) starts with (1) a decrease in shale (LVS) directly above the 1At1 marker, followed by (2) increasing rock velocity in the transition zone, from shale to sand, which complicates the reflection, and ending (3) with the velocity decreasing again because of gas effect in the reservoir section. And because all these events occur in a condensed section, it is likely that different seismic responses will be obtained just by varying one or more of these factors, due to an interference effect.

Hence several seismic responses emerge from the combination of these factors. For instance, if the more typical fast shale sat directly above the cleanest gas reservoir, then a traditional Class III response would be observed. Conversely, if thicker slow shale overlay the gas sand reservoir, then a traditional Class I response would be expected. Accordingly, the slow shale (LVS) above the fast transition makes a significant contribution to the seismic response (peak) at the top of the reservoir (1At1). On the other hand, F-O1 has an additional element not present in any other well: an intrusive streak. This geological event shows a new increase in impedance which compromises the fast transition reflection.

A purpose of this forward modelling study was to understand the seismic response for each relevant rock property. Such seismic modelling seeks in the first instance to provide the interpreter with some seismic signature trend/pattern to facilitate the stratigraphic correlation, interpretation and prediction of reservoir facies. However, as mentioned above the degree of heterogeneity makes it difficult to reliably define such patterns in the seismic response, considering that various elements compete in the seismic signature.

Based on those observations, it is now known that (1) seismic is not sensitive enough to changes between hydrocarbon fluids, and only a pay sand charge with gas (80% - 20% gas) might be discriminated from a water sand with decent certainty; (2) porosity represents the greater effect on seismic response, and even more it amplifies or attenuates the effects of other properties (fluids). The variability in seismic response due to porosity changes is such that one might expect a top of gas reflection to go through a Class I (low Ø) to Class II (in situ Ø) to a Class III (high Ø) in some cases (F-O1). In conclusion, porosity determines the seismic

response and must be given more attention. (3) Shale content perturbation shows a consistent pattern in all wells; there is a dramatic reduction in gradient response when shale content is increased at the expense of quartz. (4) The low-velocity shale (LVS) above the fast transition is the most significant contribution to the seismic response at 1At1.

The non-uniqueness of the seismic patterns is associated with the heterogeneity of the field and makes it unlikely that reservoir properties between wells can be predicted based on seismic response with certainty. The strategy for achieving this goal with more reliability is to use rock-physics forward modelling as an input for some reservoir characterization techniques, such as AVO cross-plotting and rock physics templates (RPTs).

These various effects of porosity, mineral clay and fluid content can alternatively be visualized in the rock physics templates (RPTs). This subject is discussed in seismic reservoir characterization techniques in chapter VI.

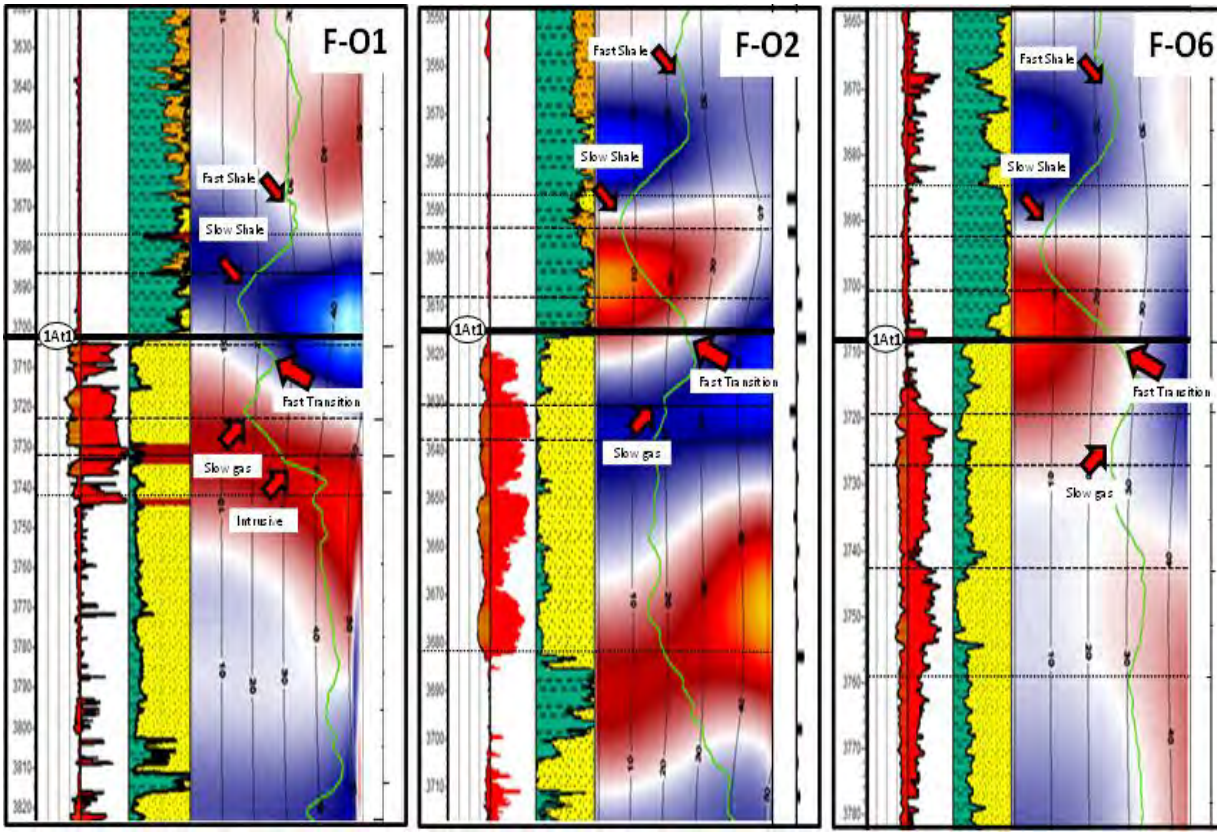

Fig. 4.6: Schematic well tie seismic response at 1At1 top.

Chapter 5: Simultaneous Seismic Inversion

There are many inversion methods. In fact, inversion methods could be classified either by the mathematical approach to the solution of the inverse problem (deterministic or probabilistic) and/or by the type of seismic data (post or pre-stack), so now the question is which is the optimum method or algorithm to provide a reliable reservoir characterization for the study area.

In many cases post-stack inversion fails to sufficiently differentiate geologic features with similar p-impedance signatures, so pre-stack inversion is then used, as that method estimates the s-impedance and density, in addition to p-impedance. While many geological features can express similar p-impedance characteristics, few will share combined p-impedance and s-impedance traits (allowing improved separation and clarity).

Rock physics analysis using well log data indicated that litho-facies cannot be isolated with p-impedance alone; s-impedance was also required. This dictated the method (pre-stack) used in this study. On the other hand, a deterministic instead of a probabilistic approach was considered because of the limited number of well data available (6 wells). The probabilistic method gives more weight to well data in the final product so a sufficient number of distributed well data is imperative, in order to ensure the reliability of the method.

This chapter addresses a detailed description of the workflow to simultaneously invert pre-stack seismic data to estimate compressional and shear impedance values. The derived elastic properties are acoustic impedance, Vp/Vs and density. These 3D properties were then used in combination with rock physics to characterize rock properties in the reservoir.

The simultaneous seismic inversion was performed in an area of 254 km² of the low poro-perm and over-pressured gas bearing sandstone. This workflow integrates a total of 6 wells (F-O1, F-O2, F-O3, F-O4, F-O6, F-R1), four seismic horizons (13At1, 1At1, BUSM and BLSM) and a suite of 3D sub-stacks seismic volumes as follows: near (5°- 15°), near-mid (15°- 25°), mid-far (25°- 35°) and far (35°- 45°). A seismic inversion depth window of investigation was defined between horizons 13At1 and a ghost BLSM surface shifted 50 milliseconds downward.

The first section of this chapter shows the method and results of a relative acoustic impedance (RAI) inversion, which served as a quick-look analysis to anticipate how sensitive the acoustic impedance response is to reservoir rock properties. The second section describes the pre-conditioning (trace mute, noise attenuation and misalignment problems) performed on the seismic data prior to inversion and some additional data preparation (partial stack definition). Wavelet extraction and the low frequency model are developed in the third and fourth sections. Section 5 includes a brief description of the simultaneous seismic inversion methodology implemented. The last section contains a discussion of the results and conclusions.

5.1 Seismic inversion (quick-look)

Before embarking on a sophisticated seismic inversion algorithm / method, it is advisable to begin with the simplest form of the inversion techniques, known as relative acoustic impedance (RAI). RAI is a simple, fast and cost effective way of inverting seismic reflection data from an interface attribute to a layer-based attribute. The reason why this method was used as a first-pass inversion before any other elaborate inversion is to anticipate apparent acoustic contrast indicative of unconformity surfaces (1At1) or also to differentiate between good and poor porosity sands.

The relative acoustic impedance (RAI) method is calculated by integrating the seismic trace, and passing the result through a high-pass Butterworth filter. This algorithm is similar to rotating the phase spectrum of a seismic trace by a constant -90 degrees.

RAI was applied to the F-O full stack seismic data. The RAI volume was used as the yard stick to measure how the seismic inversion can predict in a low poro-perm reservoir in advance.

Relative acoustic impedance logs were generated to calibrate the RAI volume at the well locations as a quality control. The logs were computed by removing their low-and-high frequency content. The procedure consisted of 5-steps:

(1) Computing acoustic impedance (AI) log as the product of P-wave velocity and density log.

(2) Estimating a polynomial regression trend-line to the AI log that represents the low frequency. For this exercise, a 5 th order polynomial satisfied that condition.

(3) Subtracting the trend-line (low frequency) from the acoustic impedance log. The outcome is a low frequency-free acoustic impedance curve (RAI).

(4) The RAI log is then normalized and calibrated to the relative acoustic impedance volume.

(5) Lastly, the RAI curve is up-scaled to seismic resolution via Backus averaging (see figure 5.1 middle and bottom). This removes the very high frequencies.

Based on lithological description, the F-O field shows a wide variability of rock properties (porosity, lithology) from one well to another. The northern area intercepted by F-O2 and F-O4 has a thicker sand interval with good porosity. In the central part of the structure, there is a transitional area (F-O3 and F-O6) with a tighter, shaly-sand sequence, further south there is a clean thin sand interval with enhanced porosity, but thinner (F-O1). All this heterogeneity is added to a complex fault setting, which is most pronounced in the central and southern part and compartmentalizes the structure into sub-blocks aligned in a north-west direction.

Figure 5.1 (top) shows a RAI attribute section between wells F-O1 and F-O2. This section cuts the main structure from south-west to north-east and is representative of the variability mentioned above. On the left of the wells is displayed the RAI log used to calibrate and check the quality of the inversion and on the right the Vclay for lithology

control. The RAI log dynamic range was normalized using the RAI seismic attribute as a reference. The color scale goes from positive to negative values (10 to -12), unlike in absolute seismic inversion methods.

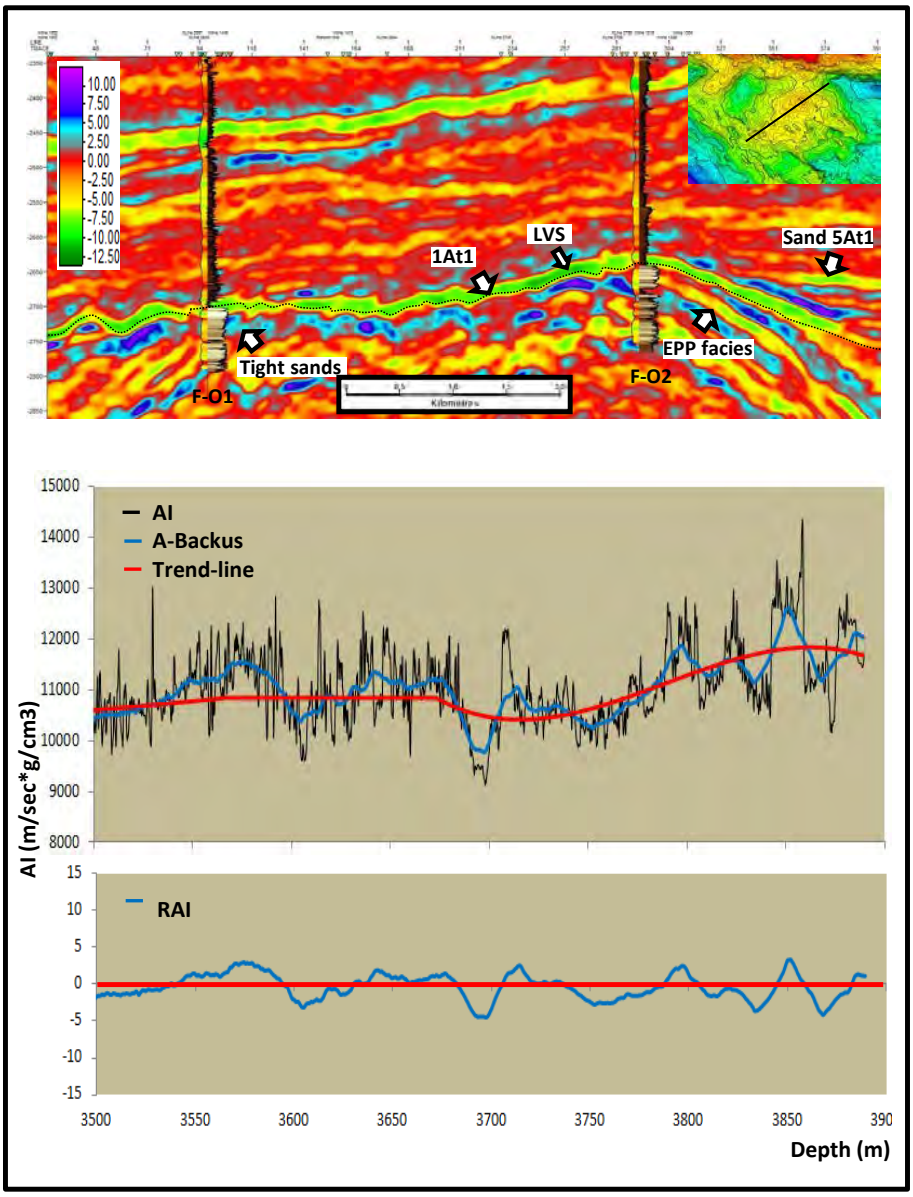

Figure 5.1. At the top, a random RAI attribute section between F-O1 and F-O2. In the middle, AI, a backus AI, and a trend-line (low frequency log) plotted versus depth. At the bottom, backus AI log with low frequency component removed.

Relative values below zero are associated with a decrease in impedance and above with an increase in impedance. For instance, high negative values (light green) represent the low-velocity shale sitting just above the 1At1 interface and clean sands in the 5At1 sequence according to the well-seismic tie. The seismic response of low-velocity is characterized by a sudden drop in the acoustic impedance. Moderate negative values in yellow delineate the continuous and enhanced poro-perm (EPP) facies of the F-O2 and F-O1 areas. However, that contrast on the relative response slightly decreases when the sand interval becomes thinner (F-O1) which might be associated to tuning effect or any kind of interference. Additionally, a

high fault compartmentalization in the southern part of the structure (F-O1) could compromise the response due to diffraction. Lastly, high positive values fit the tighter sand sequence (blue) in middle and lower USM sand units in F-O1. In summary, the attribute shows an apparent acoustic contrast indicative of a porosity response (good vs poor) (Figure 5.1).

The next sections address in detail the workflow for a deterministic inversion known as simultaneous seismic inversion including data pre-conditioning, elements that comprise it, results and quality control.

5.2 Pre-stack seismic preparation

Gather data represented a disk space and computing iteration consumption issue because of the substantial amount of information (1,2 terabytes). The available pre-stack data (773 km²) was delivered in five sub-gathers from north to south: In-lines (1039 to 1230; 1231 to 1420; 1421 to 1610; 1611 to 1800 and 1801 to 1990). All sub-gathers were merged and then cropped to an optimized area of study (254 km²) using a polygon defined by three (Inline-Xline) points: 1150, 1750; 1150, 3500; 1800, 3500 in order to deal with the storage issue and to optimize time consumption performance. The white shaded area in figure 5.2 highlight the area used for seismic inversion.

When seismic processing has not sufficiently removed noise, multiples and other data errors, gather conditioning becomes a vital part of the seismic inversion workflow.

This section addresses the conditioning process, including pre and post stack seismic data, to ensure that the ultimate inversion outcomes are not affected by any artefact, noise or mismatch on seismic data. In addition, an approach to define the optimal angle band to stack gathers is introduced.

Pre-stack seismic conditioning

The fundamental assumption made in any pre-stack AVO/A inversion study is that the data has been optimally processed. This means that the data is noise-free, with preserved amplitudes and correct time positioning for the angle range studied. However, it is often found that existing data require further conditioning in order to extract accurate reservoir properties within the zones of interest, because the standard seismic processing routine does not prepare the data sufficiently as input for a quantitative AVO/A analysis.

A step-by-step seismic conditioning workflow is introduced to reduce noise and flatten events through the seismic gathers. Consequently, this workflow improves every sub-product of the pre-stack analysis, from wavelet extraction to the estimation of the elastic properties (see figure 5.2.1.1).

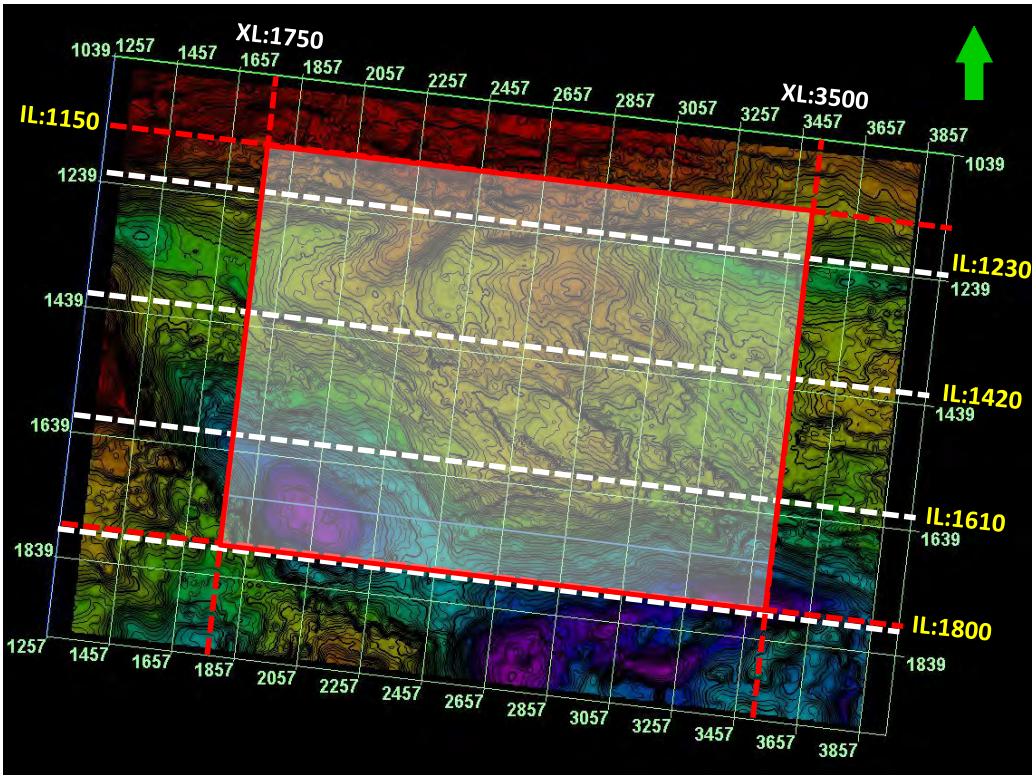

Figure 5.2: Survey area of study (254 km²) inverted in dashed red square.

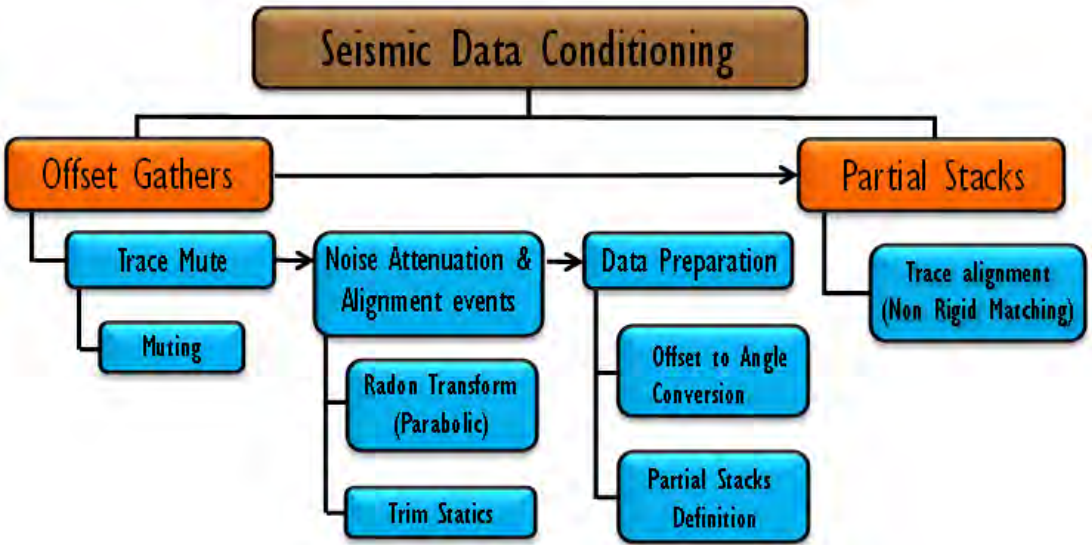

Figure 5.2.1.1: seismic data conditioning workflow.

Overall, it aims at processed seismic data that is more comparable with the theoretical AVA response. The workflow processes included in this sequence are:

(1) Mute –Trace

(2) Parabolic radon transforms

(3) Trim statics

Mute – Trace

The mute applies an offset-dependent mute (or "ramp") to a range of pre-stack gathers to remove the effects of NMO stretch (strong, coherent noise on the far offset) from a set of gathers by setting the amplitude for this data to zero, so only the reliable data is used for the gather. Therefore, the process is simply an area of data that is zeroed based on a polygon.

This polygon was built by manually picking points on the seismic gathers. The data to be zeroed is defined vertically by a zone based on the starting point to a supplied time in milliseconds and horizontally on a zone defined by offsets. The starting point depends on the type of mute. The mute in this case was an “outer trace”, where data above the mute polygon time is zeroe’d. These points were defined by screening through the seismic data (see table 5.2.1).

Figures 5.2.1.2 shows that the outer mute polygon does not reach the time at the top of reservoir (2600>time>2700 ms), so the reservoir interval is not muted. Major stretching and coherent noise occurs in a time window between 700 to 1900 ms.

The purpose of the trace mute is to remove noise without removing signal. To determine if the mute filter (quality control) has removed too much or too little of the data, the data removed is stacked. So, the undesirable noise removed from data as well as some of the coherent data can be seen. Overall, the exercise shows few coherent seismic events at the top of the seismic section (300-to-600 ms), followed by a window between 700 and 1800 msec in which the greater amount of noise coexists (figure 5.2.1.3).

Parabolic radon transform

The parabolic radon filter process either eliminates multiples or supresses random noise (see appendix 5.2.1).

The key set of parameters in this process is the number of parabolas used and their move-out range.

The delta-T parameters set the range of parabolas used in the modelling (i.e. the range of multiples used). The parabola curvature is defined by the move-out, or "Delta-T". This is the time difference for the parabola in milliseconds, from near trace to far trace at specified offset, so delta-T has a negative value for a parabola curves upward towards time zero and a positive value for a parabola that curves downwards. Low delta-T is the parameter used to distinguish between multiples and primaries. The low delta-T value handles the possibilities that some primary reflections were over-corrected. On the other hand, high delta-T represents the largest multiple move-out, usually determined by looking at the seismic data.

The criteria to define the parameters was determined by running different combinations of these parameters on a single common depth point (CDP) gather, and once a sensible

enhancement in noise reduction and signal to noise (S/N) improvement have been obtained, the selected parameters are used to apply the ultimate radon transform on the entire volume.

A number of low delta-T (-10, -30, -50) and high delta-T (50, 100, 120, 150) were examined over a number of key CDP gathers.

Looking at the difference plots (and the filtered output), all three low delta-Ts are effective. There is no significant difference in the visibility of coherent events on the difference plots. The difference being almost insignificant, the mildest filter (-50) was chosen. Similarly, high Delta-T values do not differ much from one to another. However, a 150 high delta-T better preserves the coherent events (primaries) than other cases.

In summary, delta-T of -50 msec and 150 msec for low and high delta-T respectively are the optimal and safe deltas to avoid an undesirable distortion of primary energy and to achieve multiple elimination and noise suppression. The residual (difference plot) between before and after transform application shows an important noise suppression, mainly in offsets greater than 3000 metres in a window between 1800 and 3000 metres (figures 5.2.1.4 to 5.2.1.5)

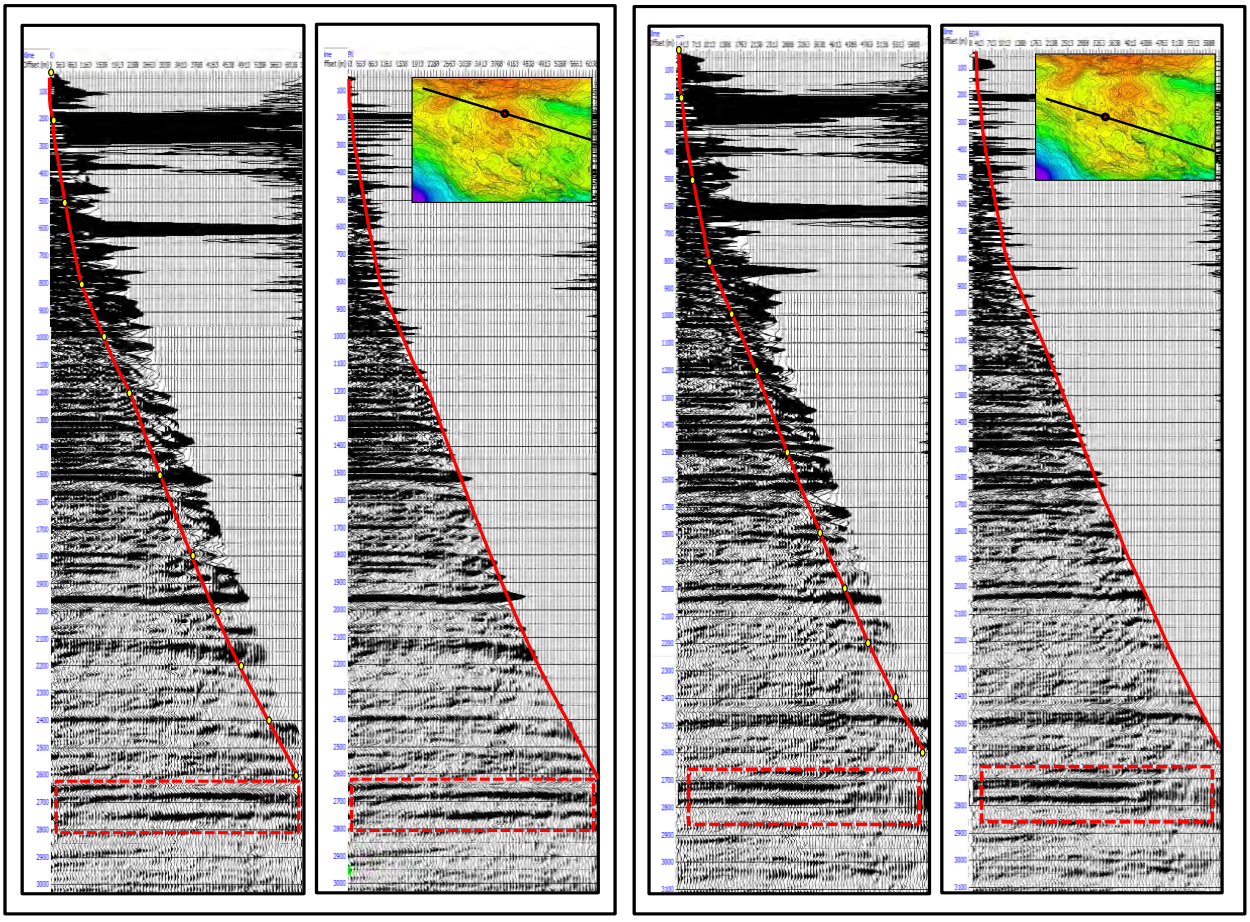

Figure 5.2.1.2: Seismic conditioning muting. On the left, F-O2 location (IN: 1315; XL: 2790) and on the right, F-O1 location(IN:1452; XL:2604).

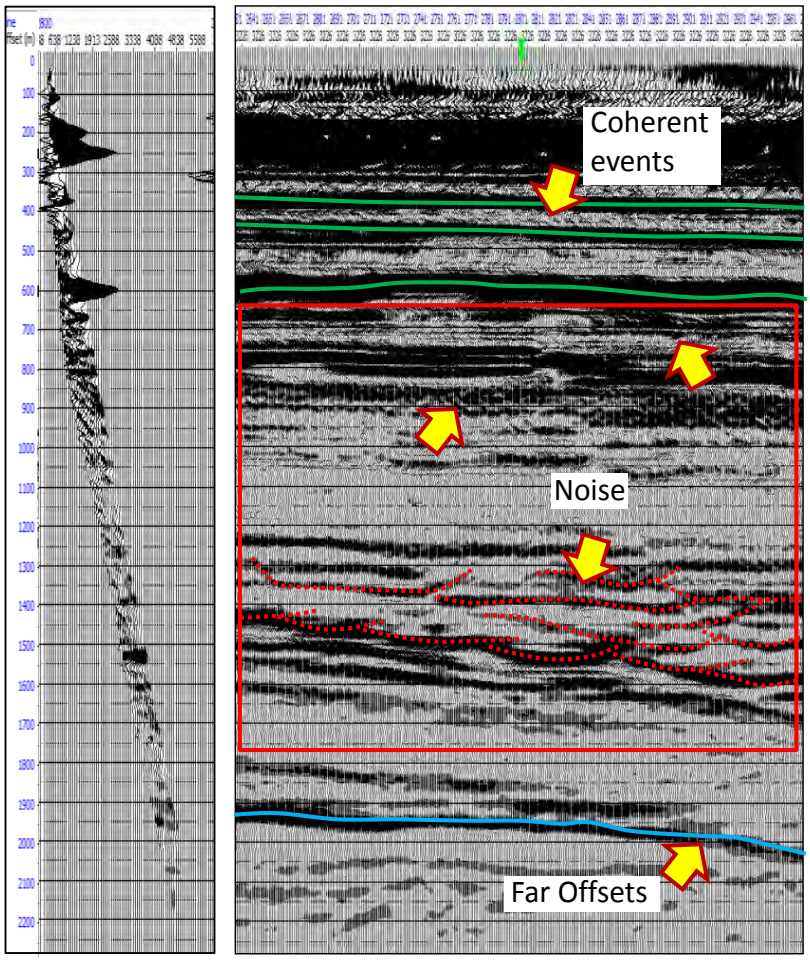

Figure 5.2.1.3: Seismic conditioning muting / Quality Control.

Trim statics

Individual traces in the gather are susceptible to small and in some cases large time shifts relative to each other. The trim statics process can fix these migration move-out problems by attempting to determine an optimal shift to apply to each trace in a gather. The shift is determined by cross-correlating each trace with a reference trace to make the input trace better match that reference trace. Usually the reference trace is the CDP stacked trace. If there is no stacked volume available, then the stacked trace is generated automatically as was the case in this analysis.

The cross-correlation was performed on a 250 msec window in a target length zone between 1200 and 3200 msec and used a multiple cross-correlation window of 10 ms. However, the critical parameter in trim statics is the maximum time shift allowed. Three different time shifts were tested: 5, 15 and 25. In the 5 msec maximum shift, the horizons are aligned with the peak of each trace in the gather. In the 15 msec case, the horizons are slightly more aligned to the peak compared with 5 msec maximum shift, and slightly move some of the overlying misaligned events as well. When a shift value of 25 msec is applied, the horizon is aligned, but some breaking occurs in the data, inside the red circles. This phenomenon indicates that some traces are wrongly displaced considerably (see figures

5.2.1.6-to-5.2.1.7).

The 15 msec was the optimum shift to flatten and align the events within the gather.

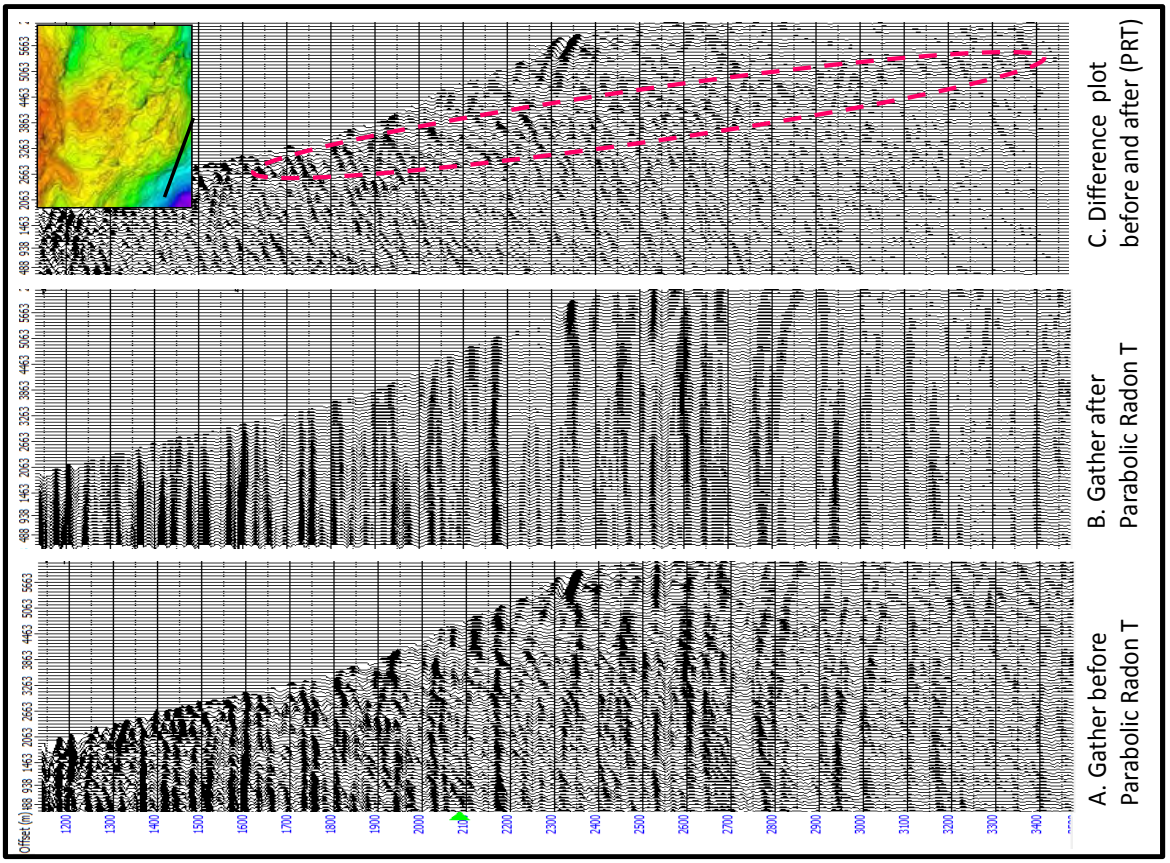

5.2.1.5: Seismic conditioning P. Radon Transform (IN:1650; XL:2740).

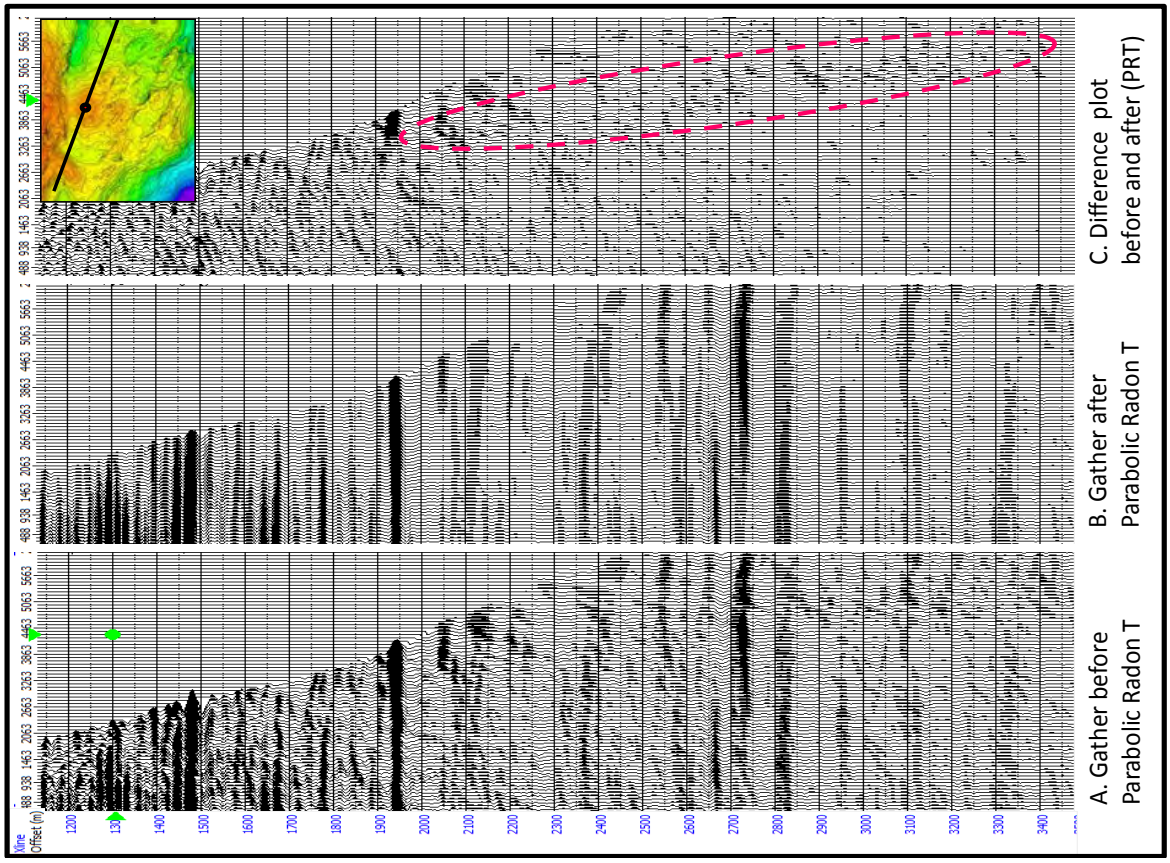

5.2.1.4: Seismic conditioning P. Radon Transform (IN:1315; XL:2790).

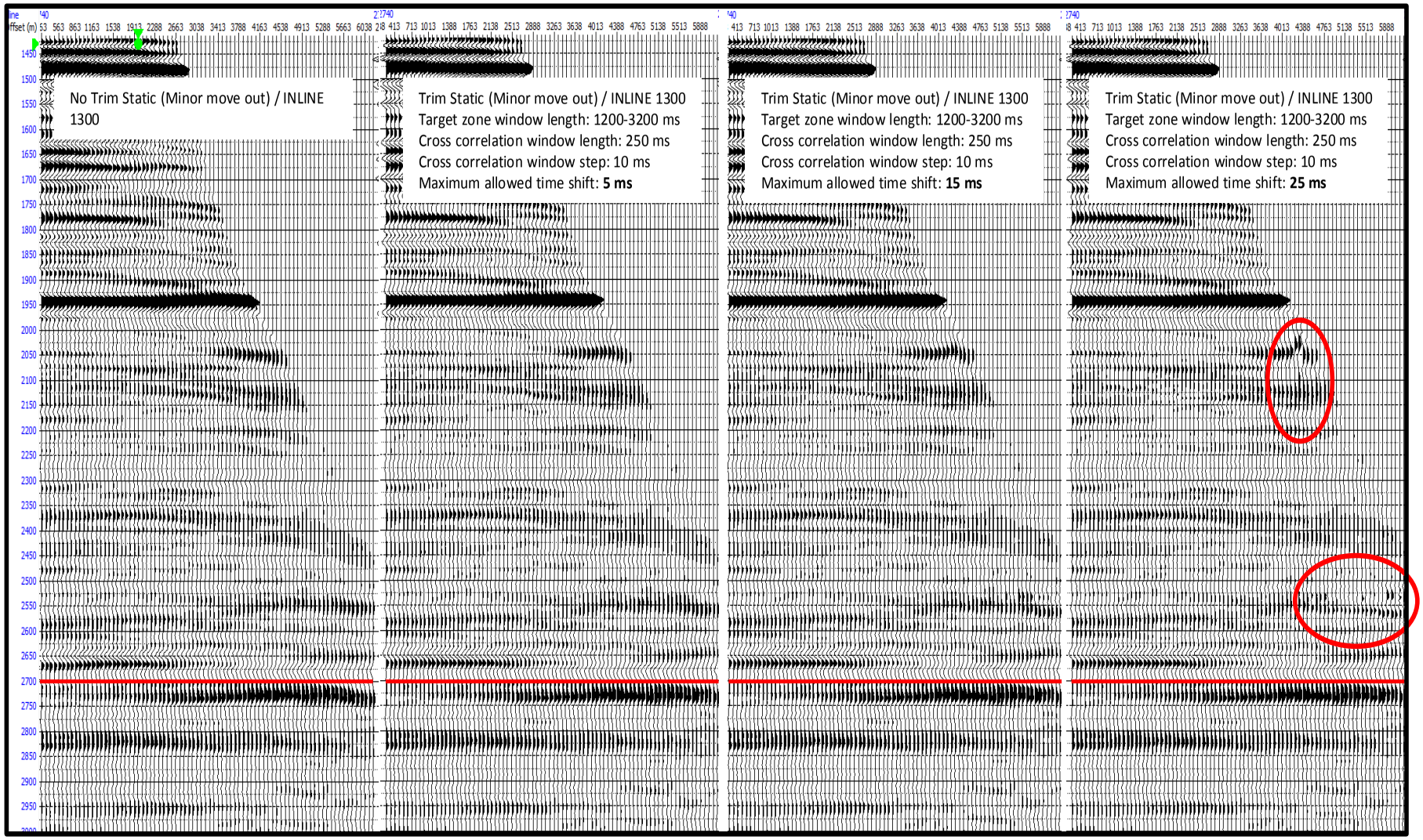

5.2.1.6: Seismic conditioning Trim static (IN:1300; XL:2740).

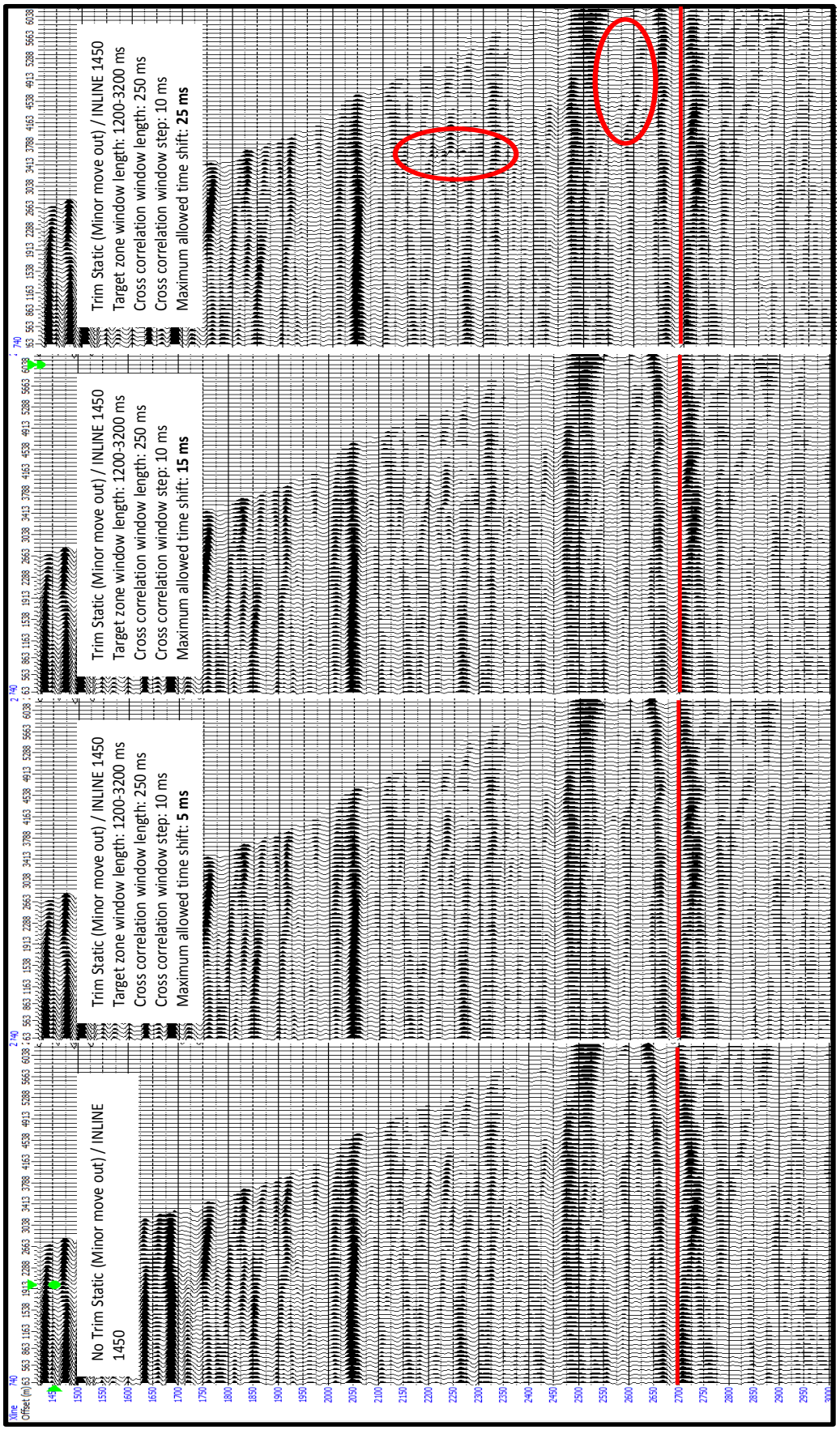

5.2.1.7: Seismic conditioning Trim static (IN:1450; XL:2740).

5.2.2 Partial stack definition

Using angle gathers for seismic inversion offers the advantage of more data constraining the process, but at the same time takes exponentially more time. However, inverting partial angles stacks gives results of comparable quality to inverting angle gathers (Kemper, 2010). In fact, there are some advantages in using partial angle stacks: (1) partial angle stacks have a higher S/N ratio due to stacking and (2) they allow estimation of wavelets per partial stack. By definition, partial stacking is the mean of a number of traces falling within a specified angle range.

The focus of this study is a simultaneous seismic inversion which involves the use of partial angle stacks. To define the optimal angle band for the partial angle stacks, some further elements were taken into account, for instance, the quality on near and far angles, the well-seismic tie correlation and seismic inversion test.

To accomplish this goal, a systematic approach was applied to a limited area around two key wells (F-O1 and F-O2) to identify the suitable partial angle stacks to enhance the final seismic inversion result (see figure 5.2.2.1).

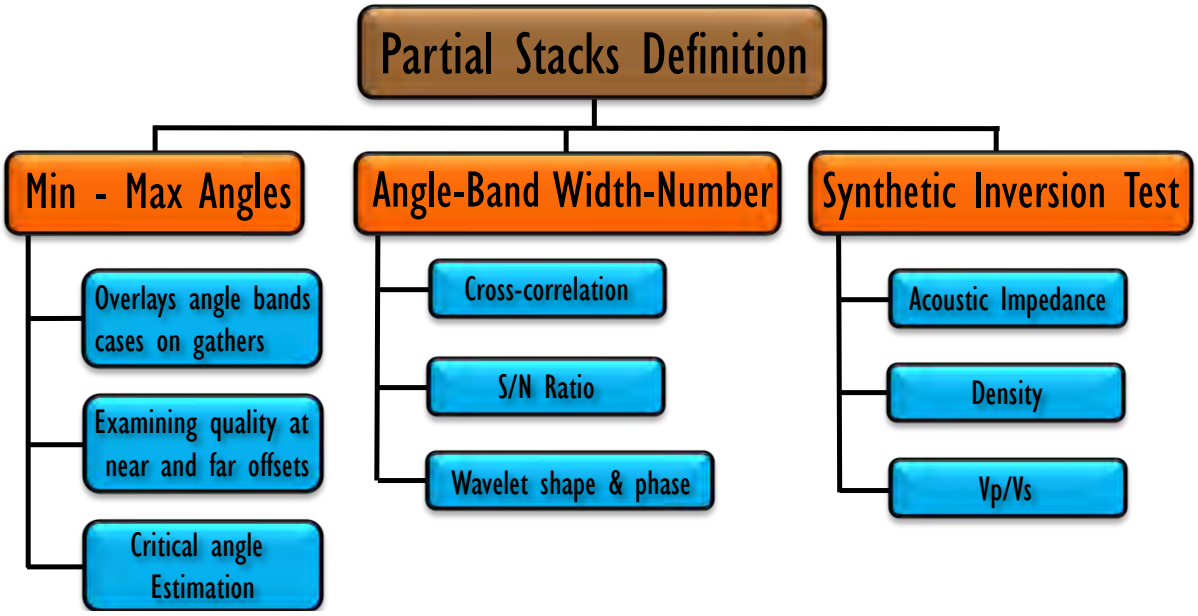

Figure 5.2.2.1: Partial angle stack workflow.

This workflow starts by defining (1) the optimal angle bands for inversion. The procedure to determine the angle band involves deciding on the parameters minimum and maximum angle, angle band width and number. (2) A useful indicator of how much each of the band cases could be affecting the seismic inversion is the goodness of the well-seismic tie. A cross-correlation (CCorr) and S/N measures were calculated in a time-window of interest to evaluate the goodness of fit. Additionally, an inspection on the wavelet phase and shape was done. (3) Lastly, a seismic inversion test was run around the key wells to measure mainly the impact of mid and far angles on Vp/Vs and density prediction.

A preliminary and necessary step before proceeding with this workflow consisted in

transforming from offset to angle domain, because both Zoeppritz's equation and/or Aki and Richard's equation are dependent upon the angle of incidence at which the seismic ray strikes the horizon of interest instead of the offset. A 3D velocity data set from the time-depth velocity model was used as input for that task.

Minimum and Maximum angles

The minimum and maximum angles were determined through a comprehensive examination of CDP offset gathers quality (from near to ultra-far). Initial estimation was done visually by using angle band overlays on gathers (see figure 5.2.2.2).

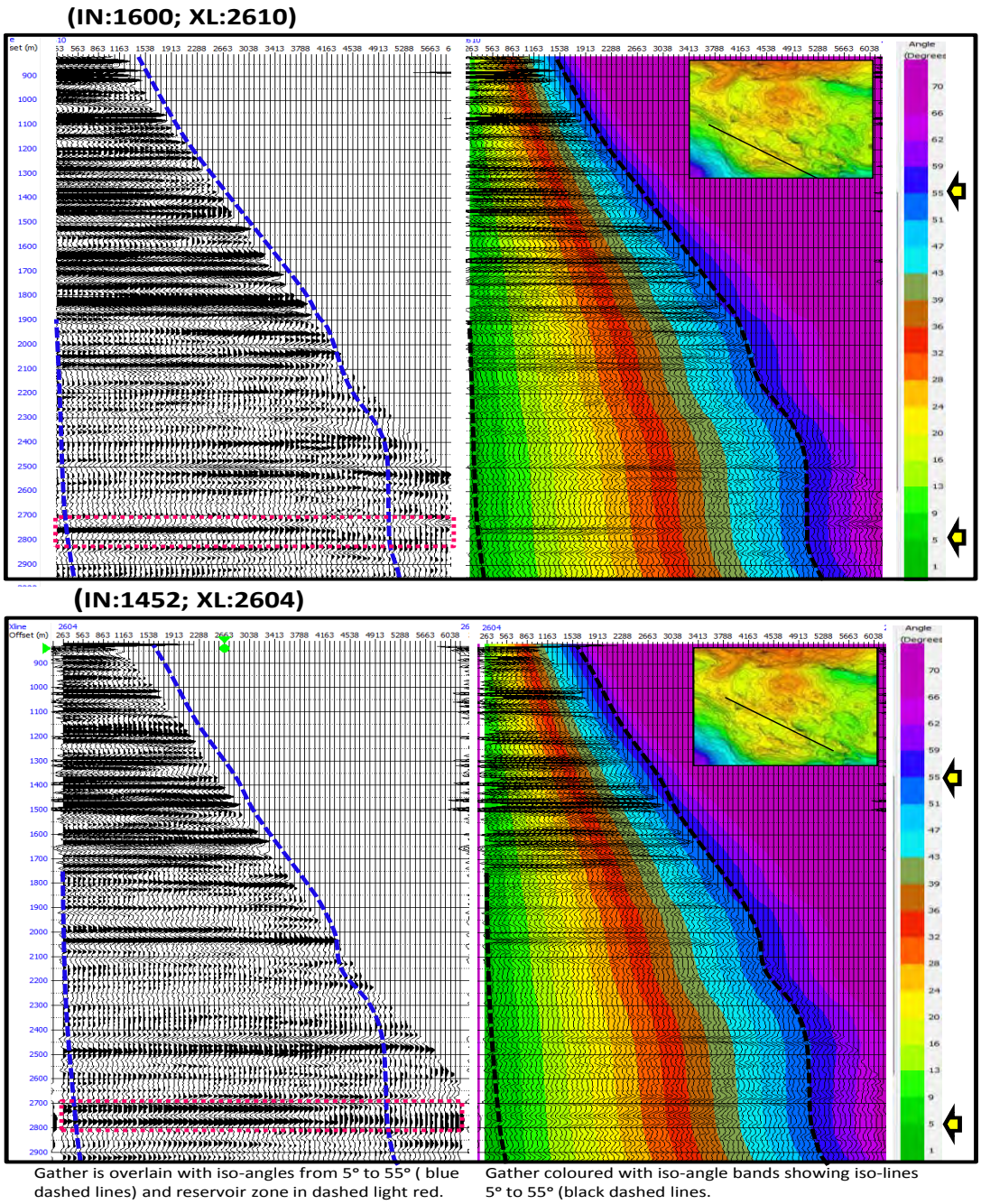

Figure 5.2.2.2: Partial Stack Definition:Min & Max Angle (Overlay angle bands on gathers).

Often very near offset traces have high noise content which cannot be fully removed at the

pre-processing stage. Even so, the CDP gathers in this data do not show a notable noise at very low angles. In fact, good enough quality is visualized at near angles, starting around 5 degrees. Even, the minimum possible angle (3 degrees) was found to qualify for consideration as part of this exercise (see figure 5.2.2.3).

In addition, the qualities of far traces (S/N) are typically contaminated by NMO stretch and therefore AVO is not dependable. Data at far offset shows a subtle distortion on amplitude versus angle (AVA) trend response beyond 43 degrees, possibly attributable to some residual stretching. On the other hand, taking into account that approximations to Zoeppritz are not valid at critical angle, and this angle being estimated around 50 degrees at the top of the reservoir interface, it was decided to use a maximum angle of 45 degrees to avoid the critical angle (figure 5.2.2.3).

See appendix 5.2.2.

(Angle gather: IN:1315, XL:2790)

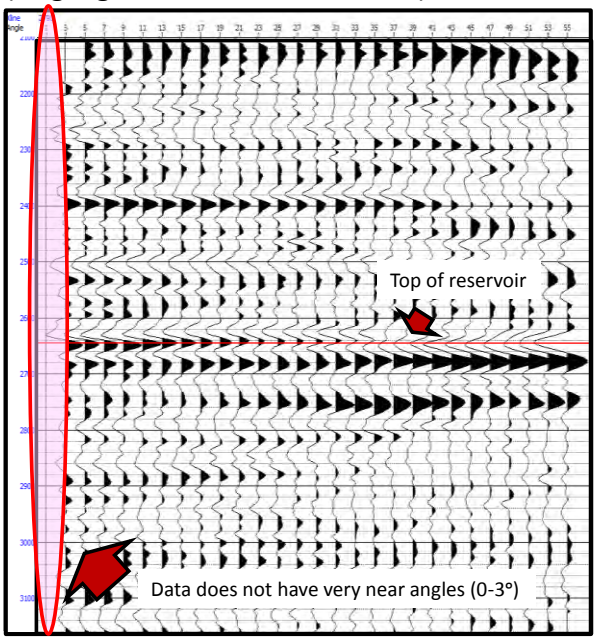

Amplitude response vs Central angle plot

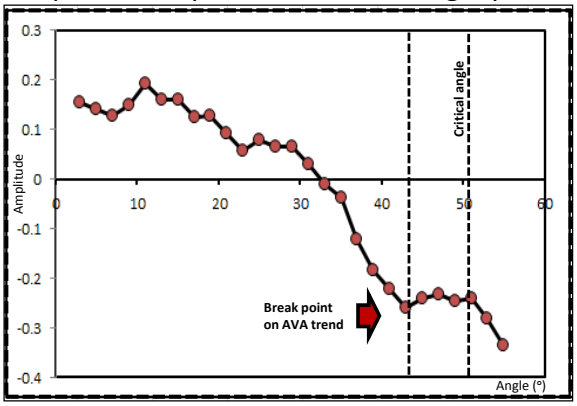

Figure: 5.2.2.3: Angle gather section at F-O1 well location and amplitude versus angle plot at top of reservoir.

Angle band width-number

Based on the definition of the minimum and maximum angles, a number of angle stacks, angle width and far angles were chosen as parameters to determine three partial angle stack cases to evaluate how sensitive the AVA signature is to the band number and range:

Case1: (4 partial angle stacks and far angle less than the critical angle (45°))

Min: 5° ; max: 45°

Number of angle bands: 4

Width angle bands: 10

Angle bands: (near) 5-15, (near-mid) 15-25, (mid-far) 25-35, (far) 35-45

Case2: (5 partial angle stacks and ultra-far angle slightly greater than the critical angle (55°))

Min: 5°; max: 55°

Number of angle bands: 5

Width angle bands: 10

Angle bands: (near) 5-15, (near-mid) 15-25, (mid-far) 25-35, (far) 35-45, (ultra-far) 45-55

Case3: (3 partial angle stacks and far angle lower than the critical angle (45°))

Min: 3°; max: 45°

Number of angle bands: 3

Width of angle bands: 14

Angle bands: (near) 3-17, (mid) 17-31, (far) 31-45

The seismic gather was then stacked using the chosen parameters. The cropped volumes or mini cubes around the vicinities of F-O1 and F-O2 cover from Inline 1442 to 1462 and Xline 2200 to 3000 and from Inline 1305 to 1325 and Xline 2400 to 3200 respectively. A smaller volume makes it possible to run several parameters in each case with more flexibility in term of computation time (figures 5.2.2.4-to-5.2.2.7).

Every partial angle stack in each case represents the average of an arrangement of seismic traces. Therefore, it could play a role in the ultimate inversion outcome, which would vary in each case. As a result, the suitability of each case is tested at this stage based on the goodness of fit of the well-seismic tie.

The well-to-seismic tie is a crucial step in seismic inversion, because it represents the relationship between the reservoir rock properties and its corresponding seismic responses. In the inversion scheme a comparison is made between the synthetic and the seismic trace at the well location.

The synthetic trace was computed from the calibrated sonic and the density logs. The sonic was converted to a velocity log for this purpose. A reflectivity trace was computed and this was convolved with the seismic wavelet to generate the synthetic trace.

The diagnosis to determine the goodness of the well-seismic tie was done by computing (1) the normalized correlation coefficient (CCorr) between seismic and synthetic trace in a time-window from the 13At1 well top to the log bottom, (2) the S/N ratio and (3) by inspecting the phase and shape of the extracted wavelet during synthetic seismogram generation (see appendix 5.2.2).

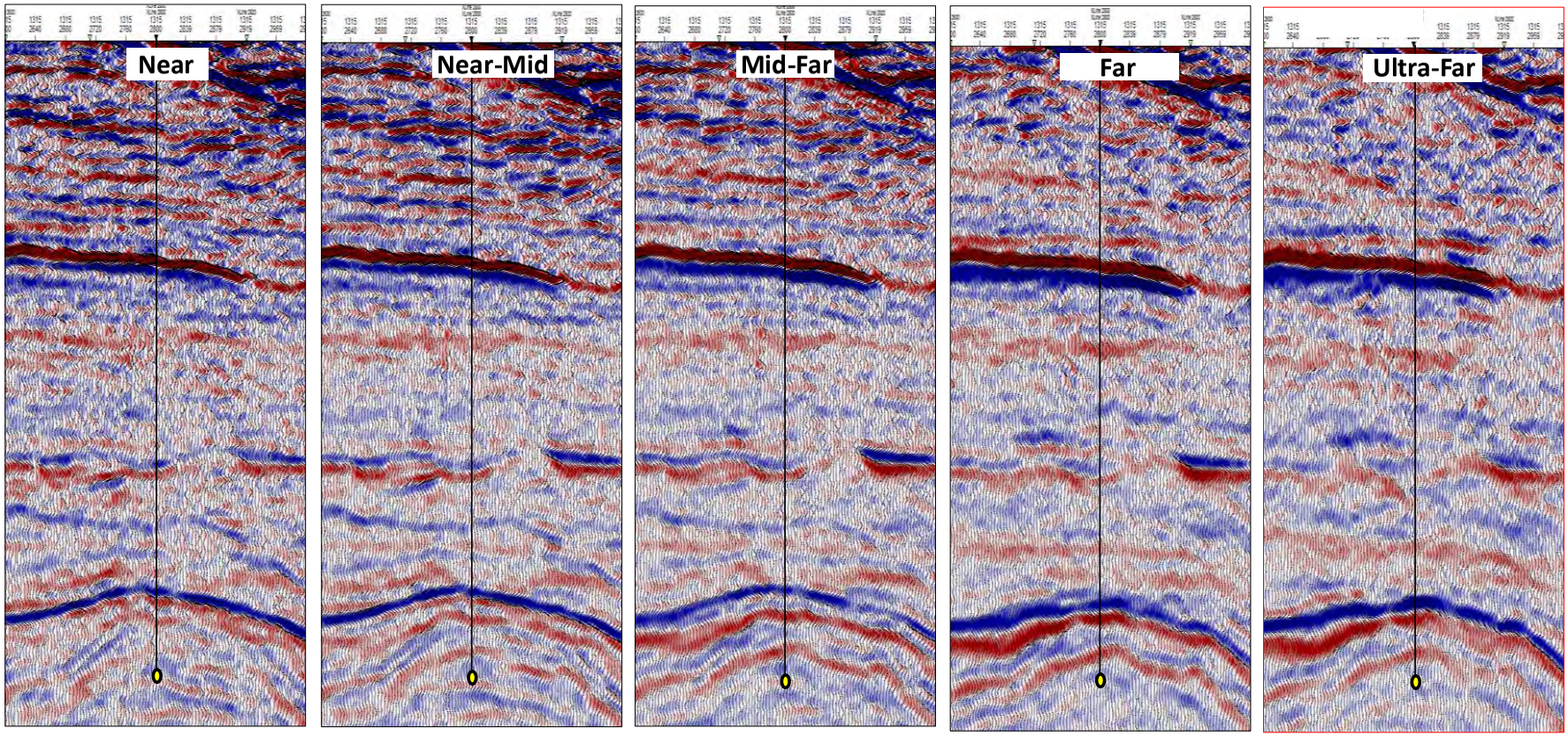

Figure 5.2.2.4: Partial angle stack (Case 1 and 2) in mini cube around well F-O2.
Ultra-far angle stack highlighted in red.

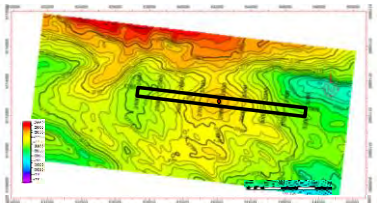

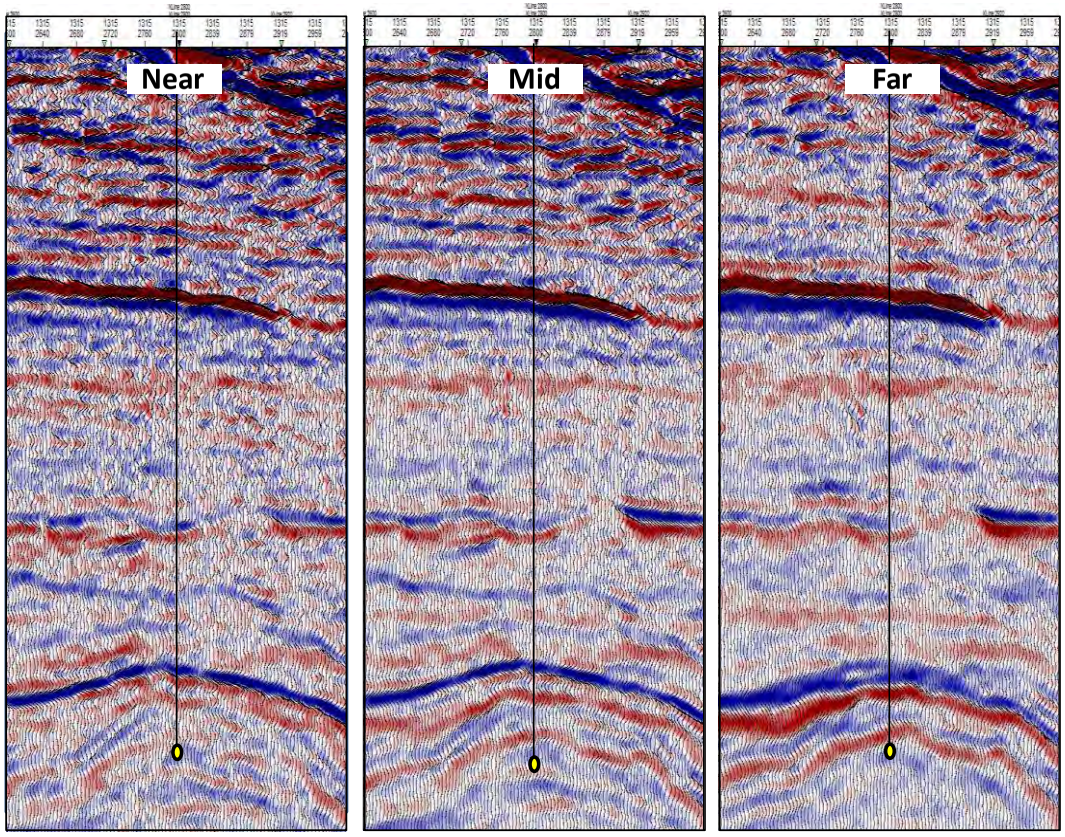

Figure 5.2.2.5: Partial angle stack (Case 3) in mini cube around well F-O2.

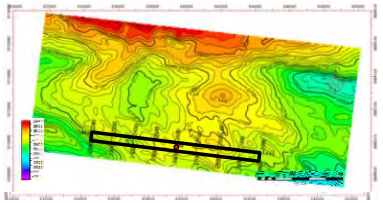

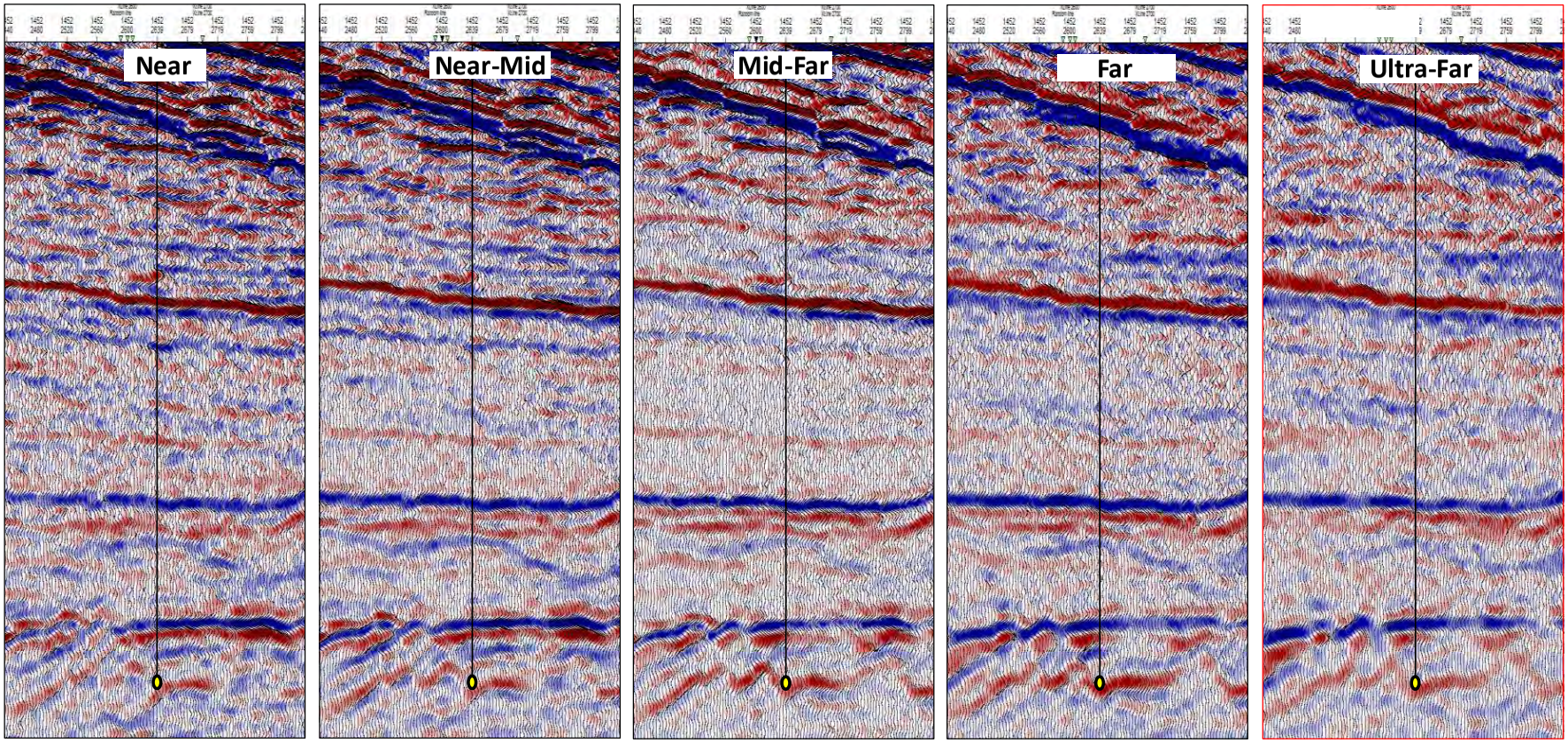

Figure 5.2.2.6: Partial angle stack (Case 1 and 2) in mini cube around well F-O1.
Ultra-far angle stack highlighted in red.

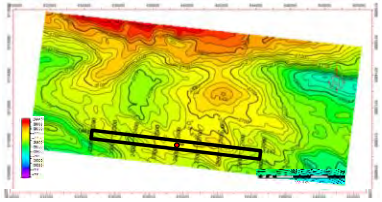

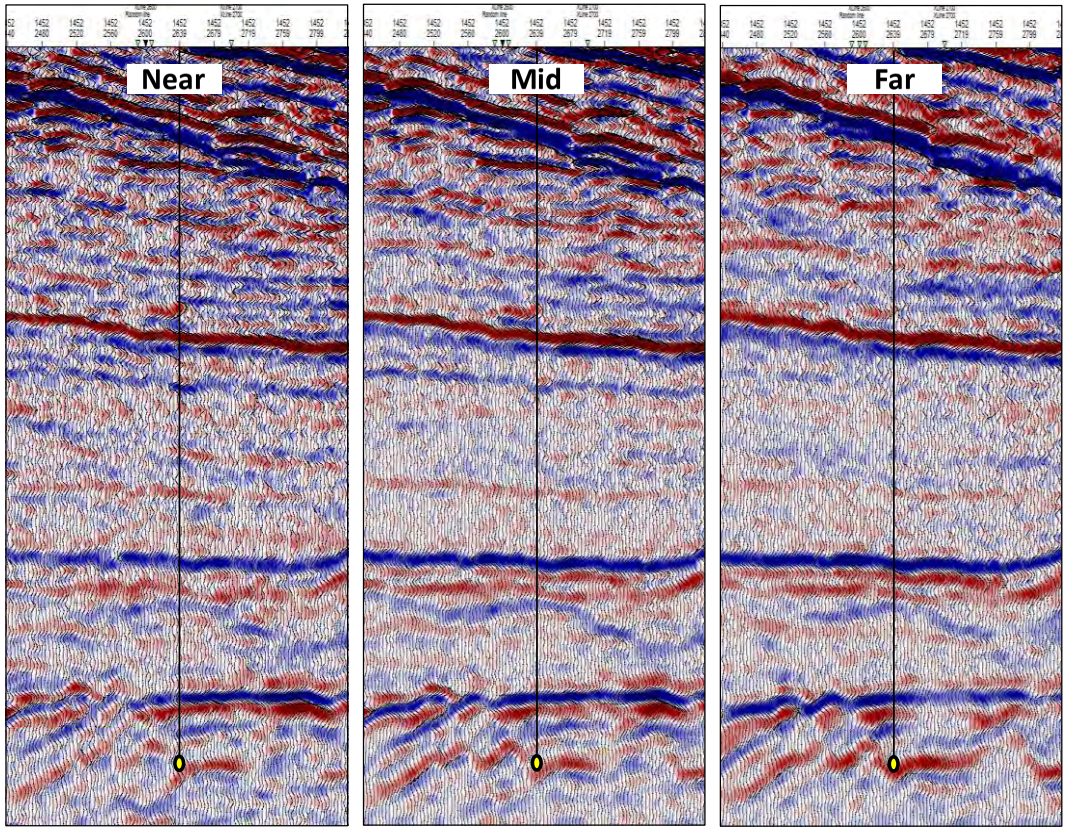

Figure 5.2.2.7 Partial angle stack (Case 3) in mini cube around well F-O1.

Figure 5.2.2.7: Partial angle stack (Case 3) in mini cube around well F-O1.

Overall, the correlation coefficient (Ccorr) between seismic and synthetic trace is good (>60%) for angles less than 45 degrees and acceptable (>55%) for angles greater than 45 degrees (ultra-far), in which some residual NMO stretching could be affecting the goodness of well-tie. The CCorr reaches its greatest value (90 – 85 %) for angles between 15 to 25 (near-mid) in cases 1-2 and corroborated on the S/N vs angle plot.

On the other hand, CCorr and S/N values for angles greater than 25 degrees in case 3 are larger than in case 1-2, but comparable in general. The CCorr and S/N decrease when angles increase. The Ccorr behavior was expected, because you are correlating with a zero angle synthetic seismic, however, the near-mid case mentioned above was the exception where CCorr and S/N are higher than the near offset case (figure 5.2.2.8).

The shape of the wavelet depends very much on the time window chosen. The wavelets were derived in a time window below 1 second TWT to ensure stability. The wavelets extracted looked symmetric and stable in both case1-2 and case3, except for the ultra-far wavelet in F-O2, which show a poor symmetry and a phase rotation greater than 40 degrees in all cases (figures 5.2.2.9-10).

In conclusion, CCorr and S/N show comparable values in all cases, hence such parameters are not conclusive to determine the optimal case to use for inversion. The match of inversion result with logs was used to make the final decision about the best partial angle stack for inversion purposes.

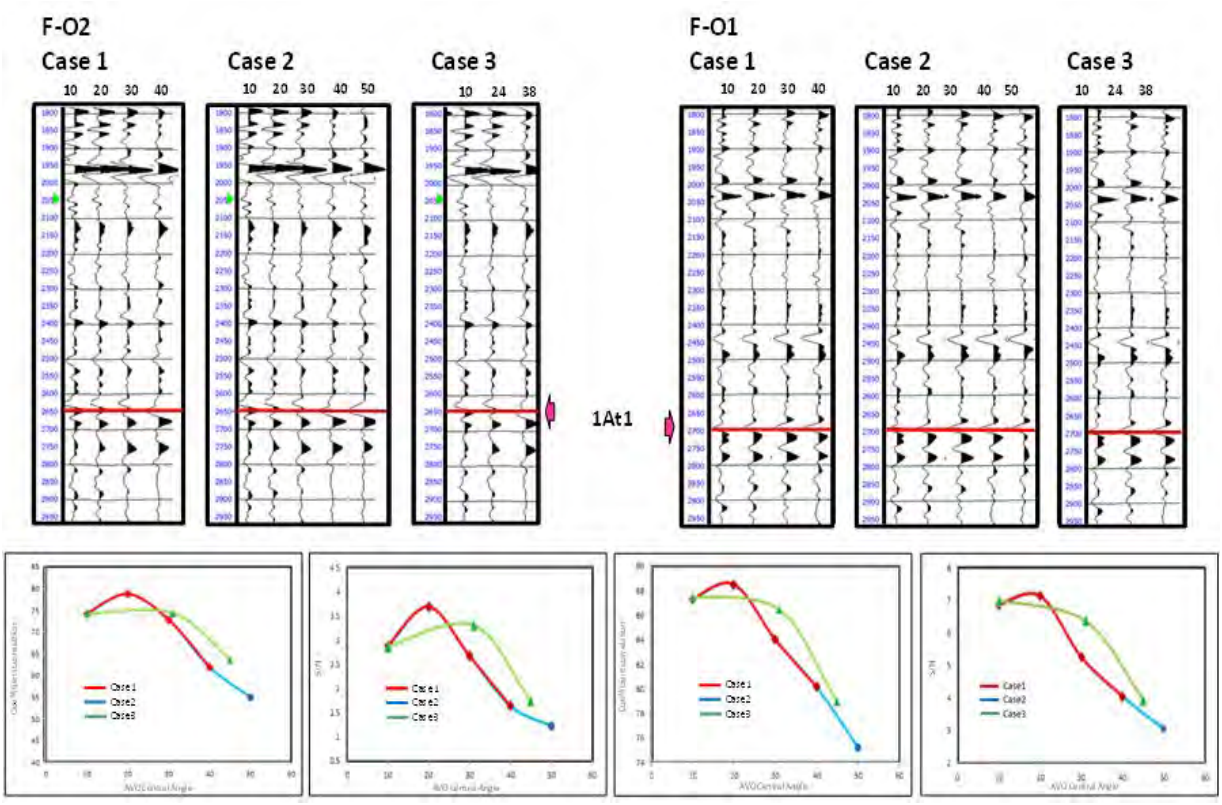

Figure 5.2.2.8: Angle gathers: well-seismic tie diagnostic (quality control)

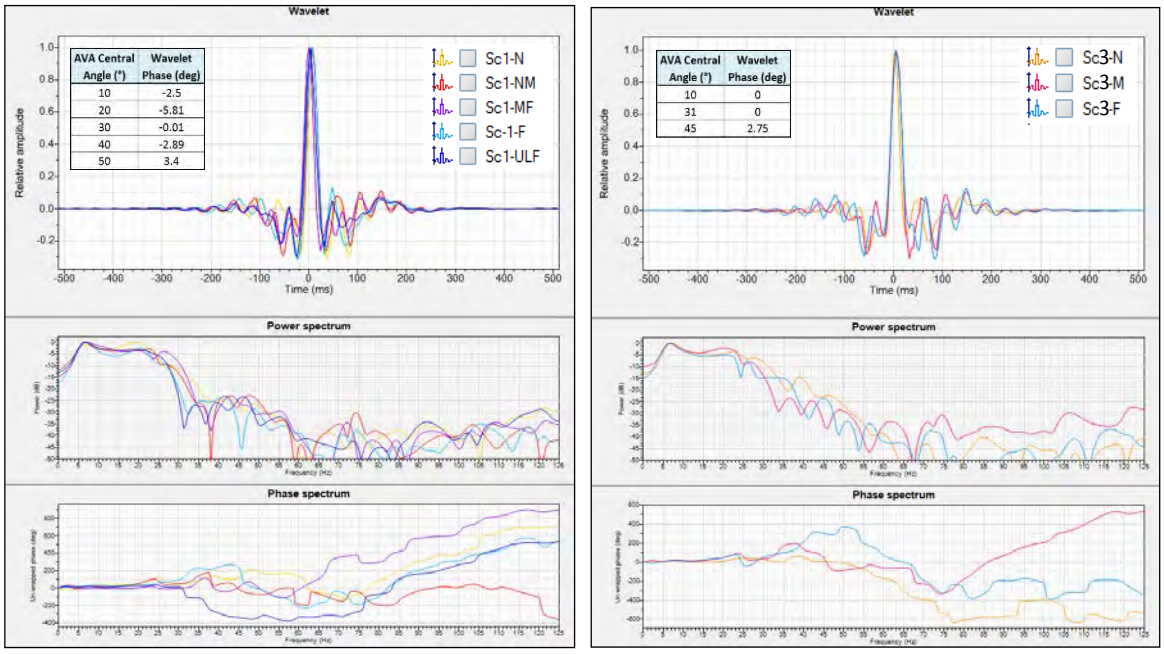

Figure 5.2.2.9: Synthetic inversion test: Wavelet extraction (wavelet shape) in mini-cube F-O1. On the left panel wavelets extracted for the 5 partial stacks that cover cases 1 and 2. A 440 ms-window from 2352 to 2792 was used for the extraction. Middle and bottom cross-plots show the amplitude and phase spectrum respectively. Right panel shows the equivalent for the case 3.

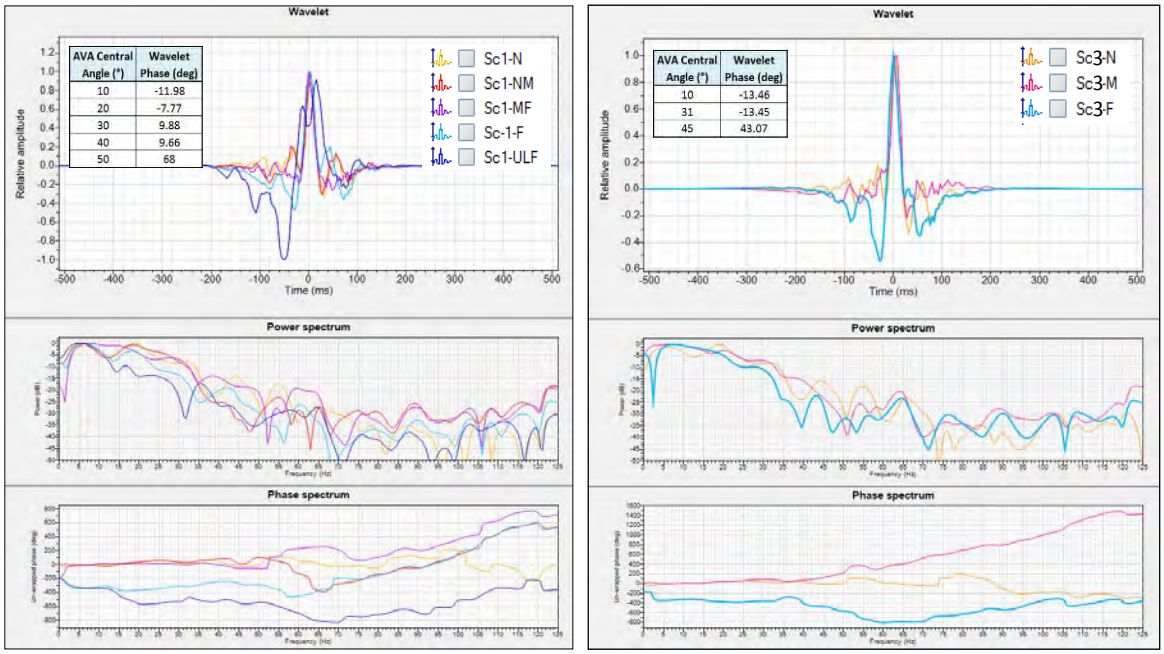

Figure 5.2.2.10: Synthetic inversion test: Wavelet extraction (wavelet shape) in mini-cube F-O2 On the left panel wavelets extracted for the 5 partial stacks that cover cases 1 and 2. A 404 ms-window from 2344 to 2748 was used for the extraction. Middle and bottom cross-plots show the amplitude and phase spectrum respectively. Right panel shows the equivalent for the case 3.

Inversion test

At this step, seismic inversions were running on the mini cubes to see the impact of band number and range in inversion.

The deterministic inversion algorithm is driven by the seismic data and is not forced to fit the wells. The prediction of elastic properties is the ultimate seismic inversion outcome.

Prior to running the absolute simultaneous AVA inversion, acoustic impedance, Vp/Vs ratio and density low-frequency models (LFM) were built by extrapolating the key well logs through the mini-volume. Inversion parameters were tested by trial and error to obtain a set of parameters that optimized the prediction.

The inversion parameters that constrain the inversion were the following:

The threshold for the reflection coefficient (R1) which controls the number of significant reflectors; all points in the estimated model with a reflection coefficient greater than R1 are interpreted as significant reflectors. An optimum value of 0.015 was used. Inversion does not vary significantly with changes of this parameter. However, when the value is less than 0.01 the shallow section above 2000 msec turns noisy in Vp/Vs and density.

The signal to noise ratio (RSNR) measures to what degree differences between the synthetic seismic and the seismic data are penalized. The greater the RSNR, the greater the penalty, so the inversion algorithm models more of the seismic energy. An initial base case using a value of 4 for all sub-angle stacks was run as a reference. Then different values were tested (trial and error) to optimize the derived synthetic properties. Higher values were used on sub-stacks (near-mid) with better quality and vice-versa. Varying the RSNR values in this way improved the Vp/Vs and density outcomes, reducing the dispersion from the LFM especially in the shallow section (above 2200 ms). The final values chosen for each angle stack were:

near: 4; near-mid: 6; mid-far: 5; far: 3

near: 4; near-mid: 6; mid-far: 5; far: 3; ultra-far: 2

near: 4; mid: 5; far: 3

The horizontal continuity parameter (RALPHA) controls to what degree horizontal variations in the impedance model are penalized. Meanwhile, the relative standard deviation of the prior model (RSIGMA) controls to what degree deviation of the estimated impedance model from the prior model was penalized. Values below 0.04 and 0.08 for RALPHA and RSIGMA respectively produced over-smoothed Vp/Vs and density. The optimum values were:

RALPHA (AI: 0.15, Vp/Vs: 0.15, density: 0.25) / RSIGMA (AI: 0.18, Vp/Vs: 0.18, density: 0.3)

Once the set of inversion parameters had been found for each case, all optimized sub-stack cases were visually examined and a measure (CC) of the degree of association between the elastic log and inversion-derived log was computed in a time-window of interest for each case (see table 5.2.2).

In wells F-O1 and F-O2, all cases are quite similar for AI. Overall, in case 1 the derived Vp/Vs has a slightly better match with the well log and even the absolute values show less deviation from the LFM trend above the target (1At1) in comparison with case 2, which includes more far angles. In case 3 the inverted Vp/Vs response is shifted upward when compared with the Vp/Vs log in F-O1 at the top of the target (1At1) and shifted down in F-

O2. In case 1 and 2 this behavior is less pronounced. On the other hand, in case 1 the inverted density shows a greater deviation from the LFM. Furthermore, case 2 and case 3 look a bit smeared: the former probably because of the ultra-far angle (45-55) and the latter because of a wider angle range (14 degrees).

See figures 5.2.2.11-12.

The results of the above inversion test on mini-cubes were inconclusive as far as AI is concerned. AI shows a very similar correlation for all cases in both wells. The Vp/Vs correlation does not increase when more angles (45-55) are included and case 3 (wider band) shows the worst correlation of all three. On the other hand, density coefficients in general were lower than previous properties regardless of the case. This result is as expected, as density information can only be separated with large angles (curvature term).Thus, in ultra-far angles (case 2) the correlation is improved slightly.

On balance, case 1 looks the most reliable for inversion purposes based on a qualitative visual inspection and quantified by the correlation coefficient (CCorr) at well location for each elastic property.

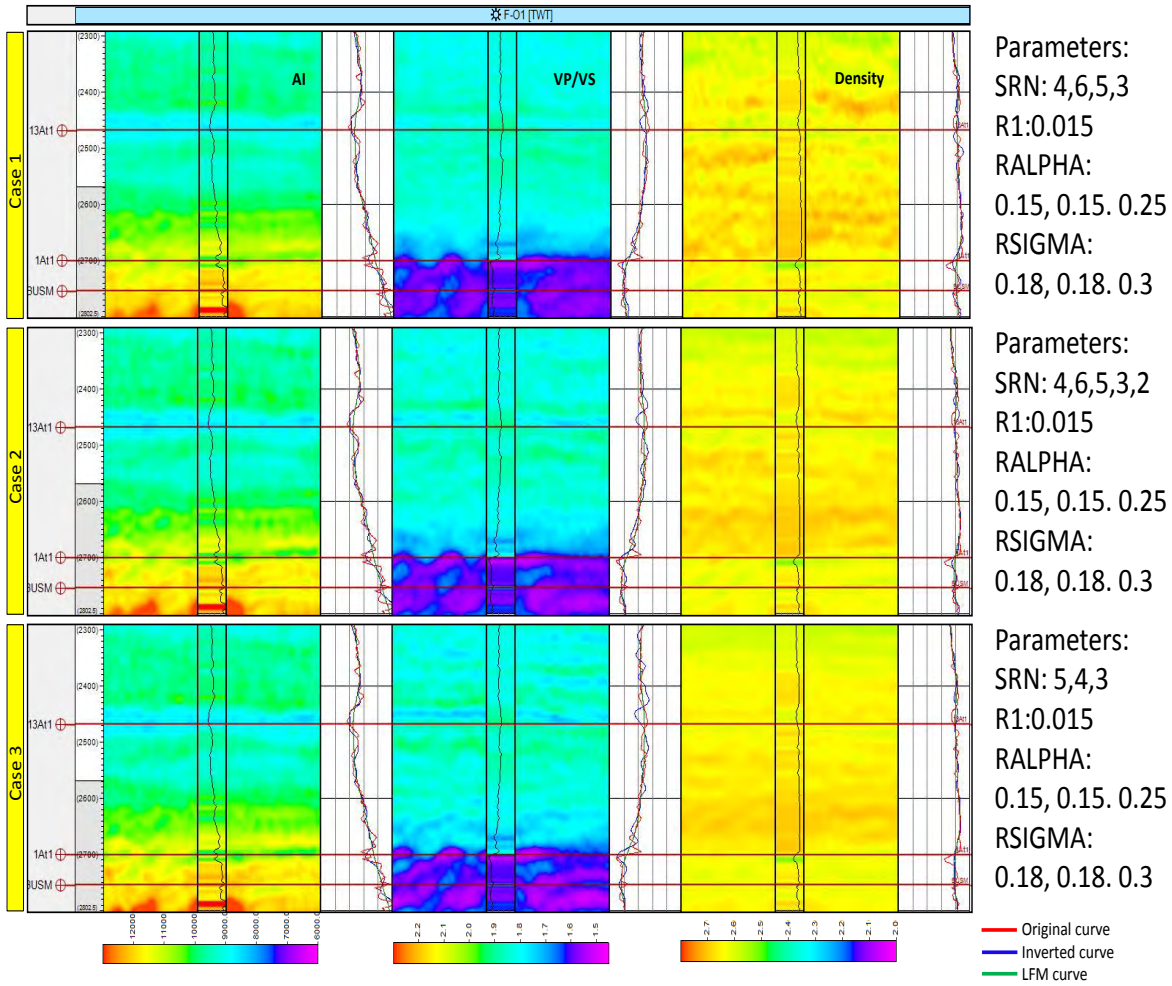

Figure 5.2.2.11: Preliminary inversion results for acoustic impedance (left), Vp/Vs ratio (middle) and density (right) on mini cube: FO1.

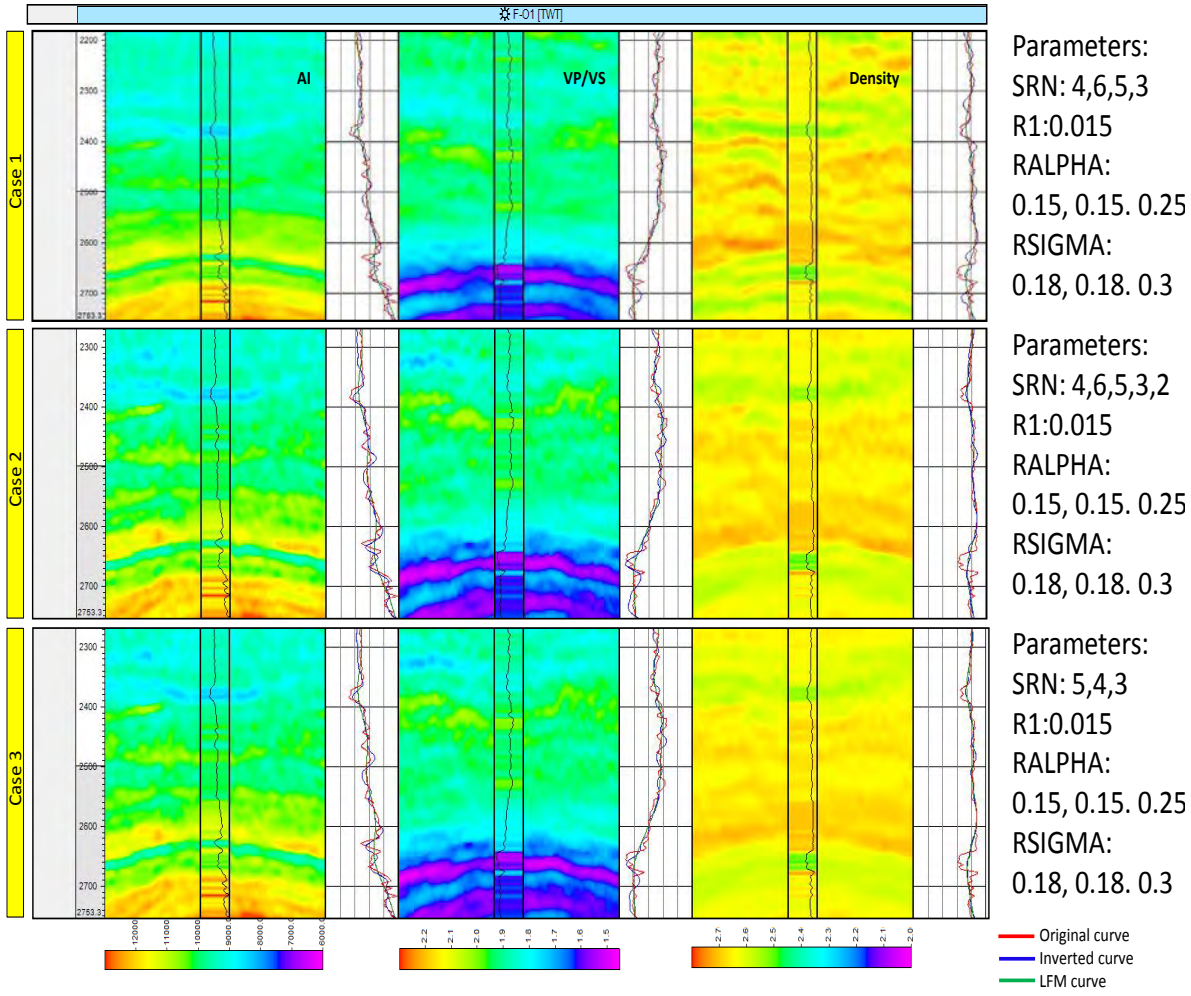

Figure 5.2.2.12: Preliminary inversion results for acoustic impedance (left), Vp/Vs ratio (middle) and density (right) on mini cube: FO2.

5.2.3 Post-stack conditioning

After gathers are stacked in partial angle stacks, it is advisable to apply an additional second-pass seismic conditioning in order to correct any residual misalignments prior to the simultaneous AVO/A inversion. All misalignment correction methods require angle stacks to be aligned with a "reference stack" that is assumed to be of better quality and move-out free. However, regardless of the method used, it could ultimately lead to a deceptive result if a careful and detailed examination of the alignment between the various angle stacks is not done to determine the optimum time shift allowed. A contingency action to mitigate under and over correction at post-stack stage is to run a move-out correction (trim stat) before stacking, because at the gathers stage this process is more intuitive and auditable.

To correct any residual move-out the algorithm "non-rigid matching" was used. The algorithm is an event registration method that uses waveform to identify local minima and maxima. The algorithm computes a sample-by-sample time variant time shift to match the

non-reference partial angle stacks to a reference partial angle stack. The reference angle stack is the volume with better resolution and quality and with the least amount of noise. The alignment sought to correct any residual misalignment not removed by trim stats.

The workflow applied to the data consisted in the following:

1. Near-mid (15-25 degrees) partial angle stack was chosen as “the reference partial angle stack”, since it was considered to have the best S/N and seismic quality in general.

2. The time shifts were computed by aligning the (35-45°) stack to the (25-35°) stack, the (25-35°) stack to the reference partial angle stack (15-25°) and so on. A minimum/maximum allowed shift of 12 msec was considered sufficient to correct any remaining misalignment.

3. Time shift cubes (cumulative displacement cubes) at each sample-to-sample were computed and a high-cut (HC) filter was applied to them to remove the waveform related artefacts in the time-shifts (high cut 10Hz and 40 dB/ octave) before being used to align the non-reference seismic cubes (“matching cubes”). These cubes represented a quality control indicator of how well trim statics performed and how much the sub-stack had to be shifted to be properly flattened.

4. The time shift cubes are applied to the original partial angle stacks as follows:

- Apply CumShift1 time shift cube to the partial stack 5-15

- Apply CumShift3 time shift cube to the partial stack 25-35

- Apply CumShift3+ CumShift4 time shift cubes to the partial stack 35-45,

where CumShift refers to cumulative shift.

Figure 5.2.3.1 shows the steps used by the seismic trace alignment to apply the cumulative shifts.

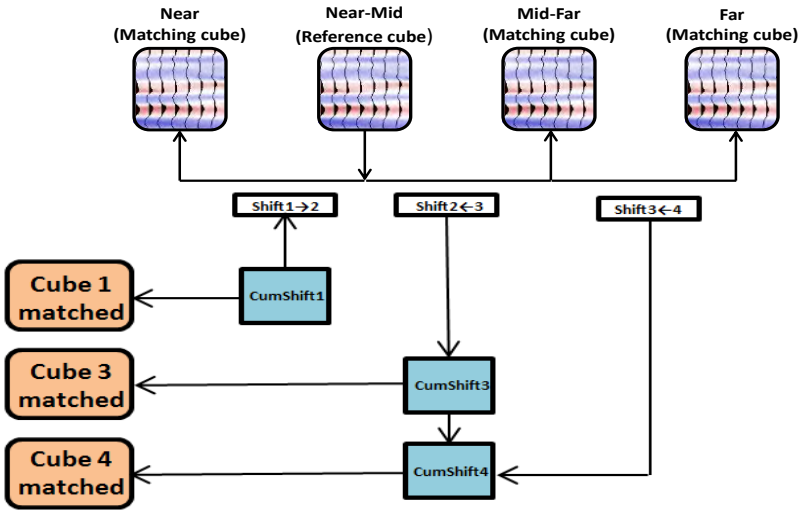

Figure 5.2.3.1: Cumulative Shift workflow used on seismic trace alignment.

5. A quality control used for seismic trace alignment was to compare cross-correlation maps between each of the angle-stack data and the reference seismic data before and

after alignments. A gate centre time (surface time) was specified for correlations based on a time window of interest. The correlation interval is the time window of the surface time to be used in the correlation surface computation. The surface time was set a 2650 msec and the correlation interval at 400 msec.

Figure 5.2.3.2 shows a multi-panel summarizing the post-alignment results. From left-to-right, data (seismic section before alignment, a displacement section and correlation maps) related to near, mid-far and far stack respectively.

Based on displacement cubes, the time variant shift calculated sample by sample was negligible (+/-3 msec) on near, small (+/-5 msec) on mid-far and around +/-8 msec for far stack. The discrete shift computed by the algorithm could be explained by the generally good quality of seismic data and the effective move-out correction at the pre-stack stage (trim statics).

5.3 Wavelet extraction

In simultaneous elastic inversion, the algorithm inverts any number of partial angle stacks with their respective wavelets. The wavelets used in the inversion process were extracted directly from the seismic data by "matching" to the reflectivity series.

A deterministic approach (extended Roy White estimation method) was implemented to perform the wavelet extraction. The procedure assumes that the drill location of the well with respect to the seismic volume may not be optimal for extracting the wavelet. The extraction was carried out for the six wells in this study and on each partial angle stack. See appendix 5.3.

The wavelet extraction and well tie method is summarized below:

(1) Edit and calibrate the sonic and density logs (Section 4.3)

(2) Construct the synthetic seismogram from the calibrated well-logs (see figures 5.3.1-to-5.3.24).

   a. For each well, the reflection coefficient series were modelled in two-way time using sonic and density logs, the depth to time conversion was done using check-shots.

   b. Convolution with the estimated seismic wavelets

(3) Perform the match, comprising:

   a. Determination of the best match location,

   b. Estimating the wavelet and its accuracy by computing goodness-of-fit parameters: (proportion of energy predicted (PEP) and coefficient of correlation (CC)).

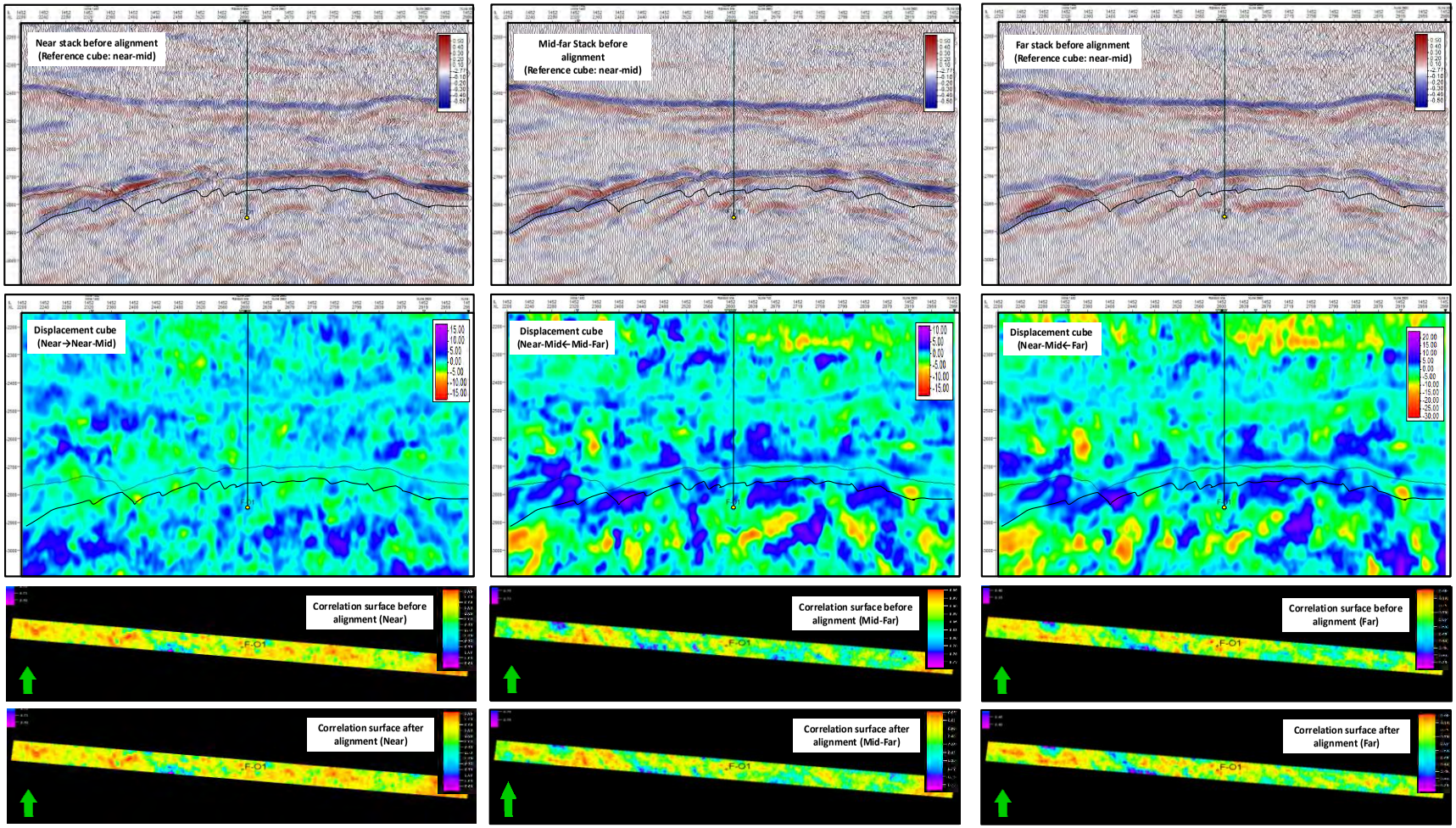

Figure 5.3.2.2.Partial Stack Conditioning (Seismic Trace Alignment results): At the top, a cross-sections of partial stacks before to be aligned to the reference partial angle stack (near-mid). In the middle the cross-section (displacement) resulted from the alignment and at the bottom correlation maps between each angle-stack cube and the reference cube before and after alignments.

PEP is a diagnostic measure calculated by the extended Roy White method to determine the reliability of the wavelet in terms of the goodness of fit (predictability) between the reflectivity calculated using the calibrated well and the seismic trace. The algorithm iteratively estimates the best time lag and shift along the x-direction and y-direction from the borehole location at which the wavelet extraction will optimize the well tie.

The global predictability (PEP) value is calculated using the following equation:

$$\text{PEP} = \frac{\sum R*S(t)^2*100}{\sum\left(RR(t)*SS(t)\right)}$$

where

RR(t) is the autocorrelation of the well data

SS(t) is the autocorrelation of the seismic data

R*S(t) is the cross-correlation computed between them

Predictability values range from 0 to 100 representing perfectly matching data

The methodology to extract the wavelet consisted of 3 steps:

1. Estimation of the (x,y) location that generates the maximum predictability value. Simultaneously a set of predictability displays and phase spectrum (shape and phase) data are generated for that location. The predictability displays are:

- Maximum predictability (top view): Calculated correlation between the RC series and the seismic around the well position (see figure 5.3.25).

- Maximum predictability (side view): Predictability for an Inline shown as a function of cross-line position and lag time (traces for 2D lines)

- Time of maximum predictability: Shows the time lag for the best predictability in map view.

- The phase of maximum predictability wavelet: Calculation of the phase rotation for a maximum predictability wavelet in each trace (see figure 5.3.26-27).

2. Then, by trial and error, the location is changed in the vicinity of the well to determine a location at which the extracted wavelet is the best to use in terms of predictability performance and wavelet characteristics (shape and phase)

3. An additional way to help improve the tie was by calculating the cross-correlation (CC) between synthetic and seismic and by calculating the time shift to be applied to the synthetic to achieve it. The degree of correlation is computed at regular time intervals, depending on the seismic sampling rate. The result is one correlation value for each position in time that the synthetic is shifted. This value is the sum of the products of the synthetic and seismic amplitudes at each time.

Wavelets were extracted in the best match location according to the PEP index using a +/- 400 msec time window length to guarantee wavelet capture of the complete seismic

bandwidth. The wavelets chosen by this method were then used to generate the final synthetic trace in each well and as input for seismic inversion (table 5.3).

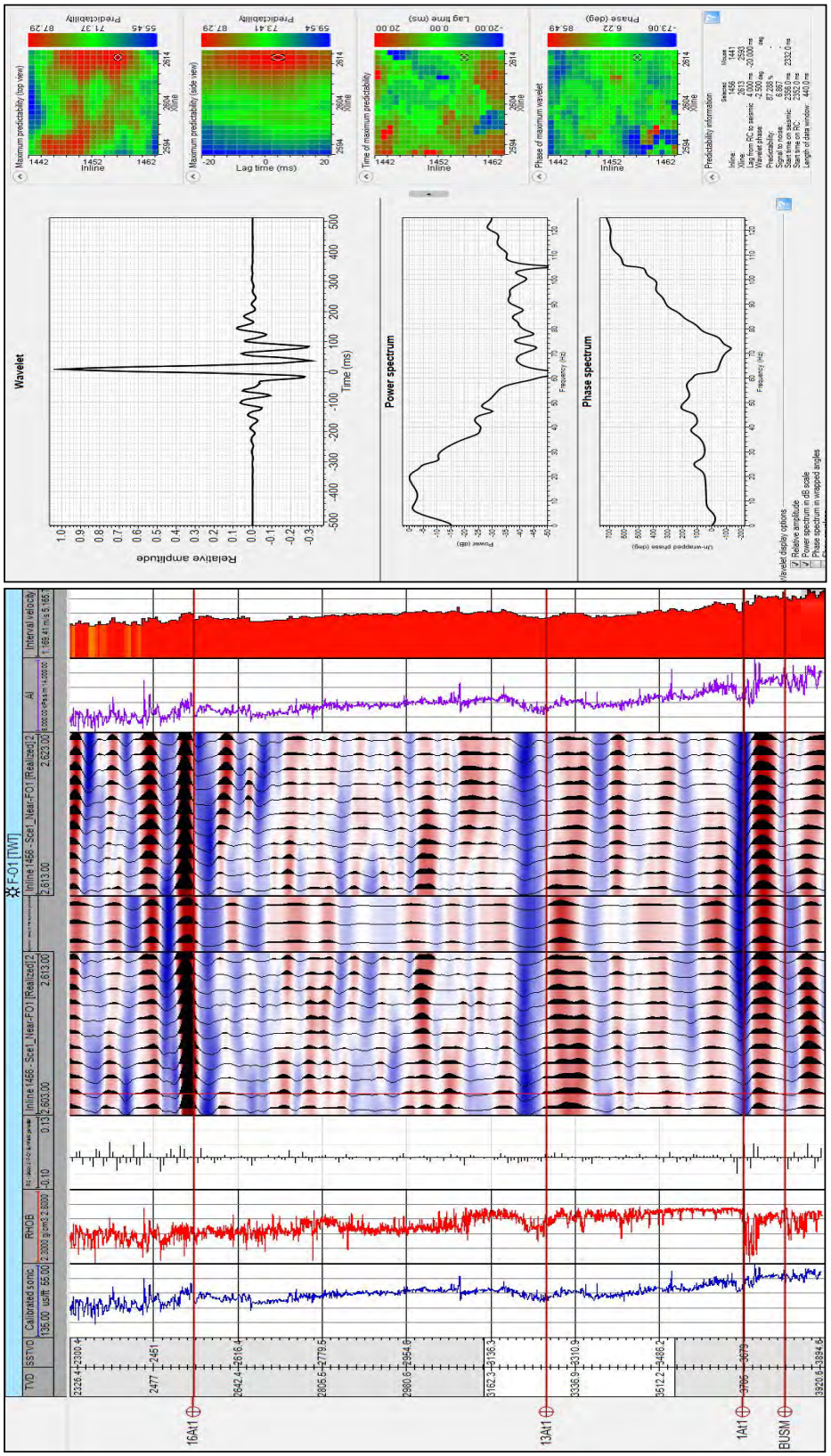

Figure 5.3.1: Well tie quality control at well F-O1 after check-shot calibration and log alignment, when necessary. The well synthetic has been generated with the wavelet extraction from the near stack. Left picture well logs, seismic panel with the well synthetic inserted. Right extracted wavelet used for the synthetic and predictability info.

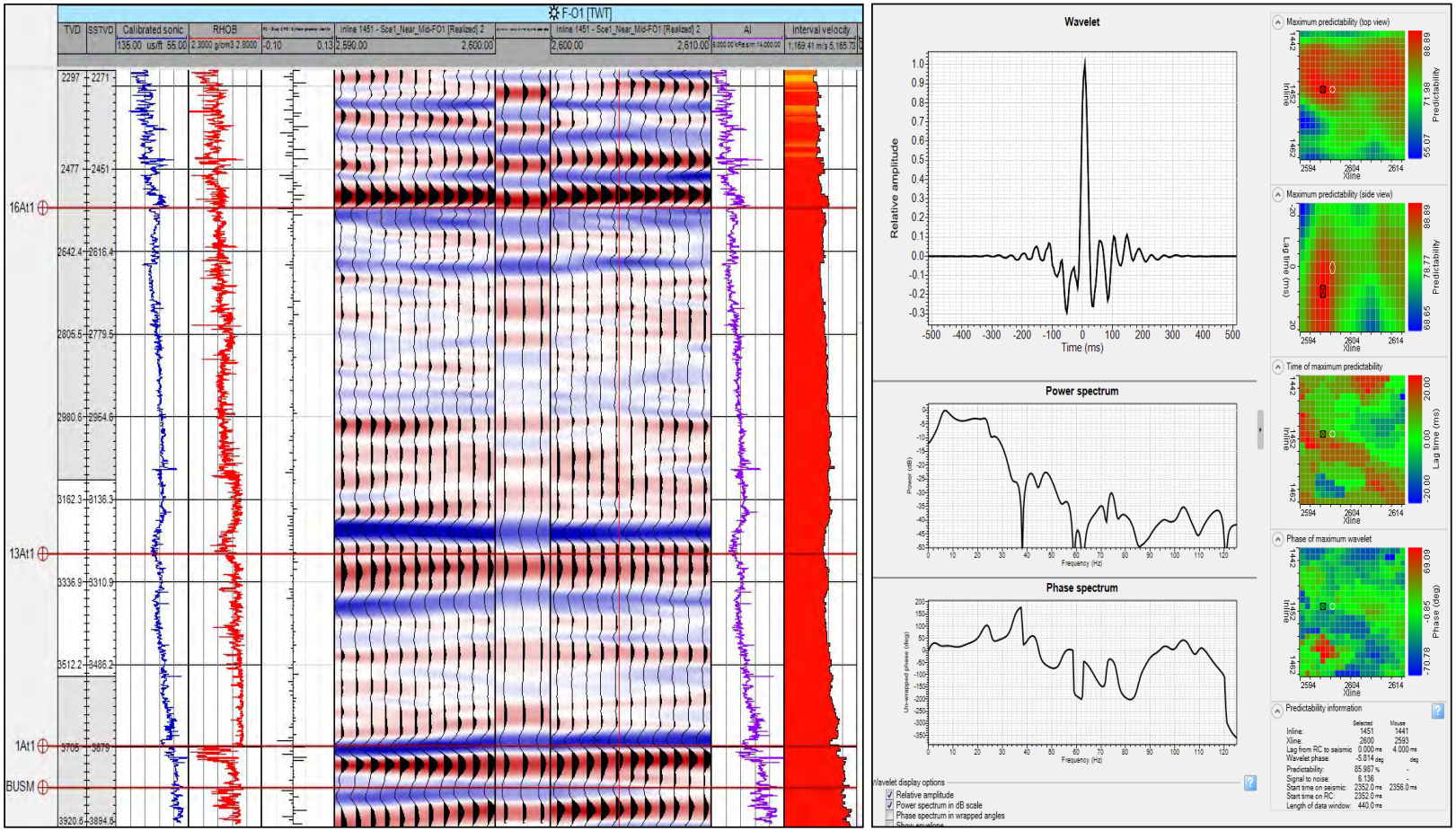

Figure 5.3.2: Well tie quality control at well F-O1 after check-shot calibration and log alignment, when necessary. The well synthetic has been generated with the wavelet extraction from the near- mid stack. Left picture well logs, seismic panel with the well synthetic inserted. Right extracted wavelet used for the synthetic and predictability info.

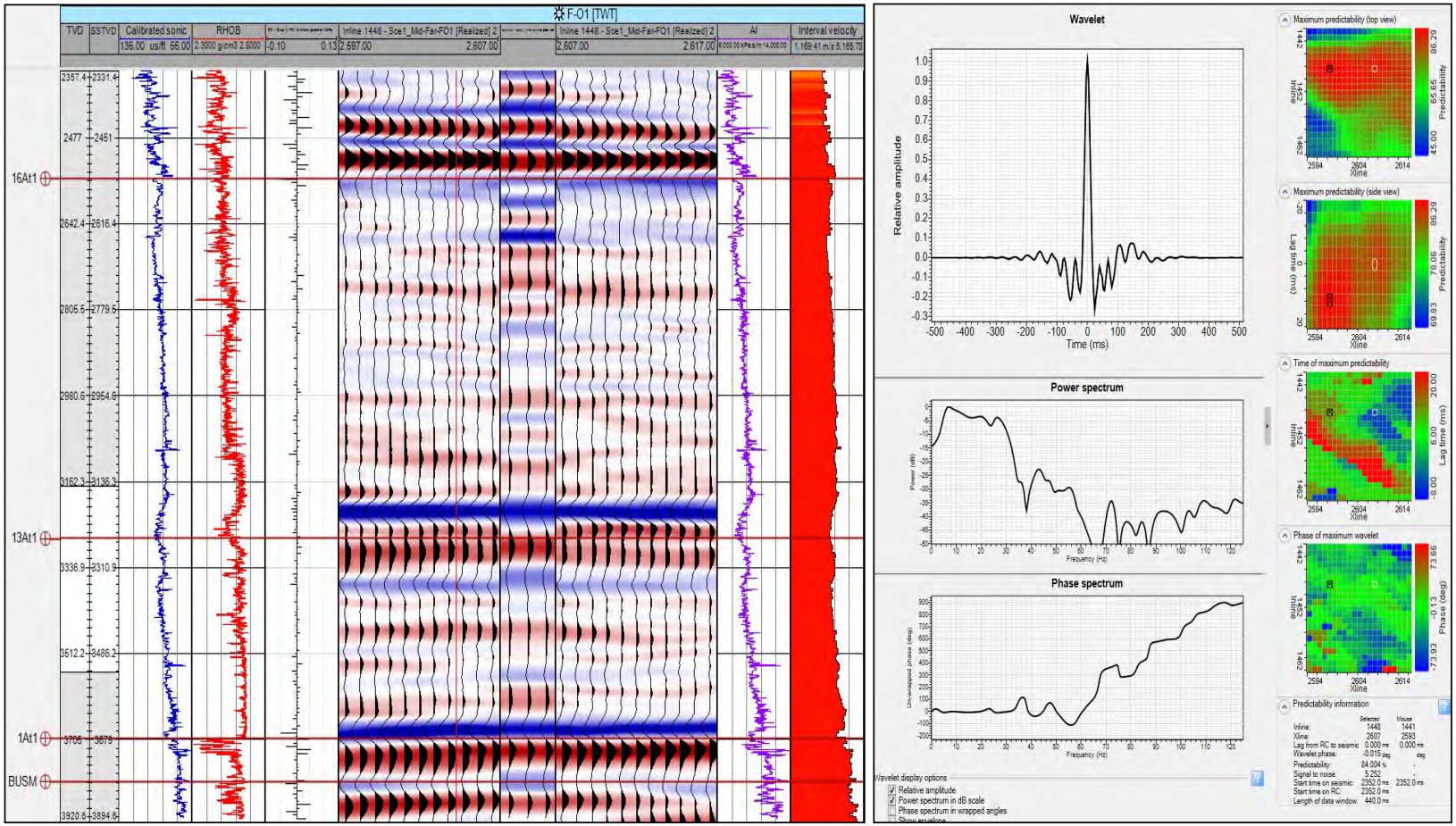

Figure 5.3.3:Well tie quality control at well F-O1 after check-shot calibration and log alignment, when necessary. The well synthetic has been generated with the wavelet extraction from the mid-far stack. Left picture well logs, seismic panel with the well synthetic inserted. Right extracted wavelet used for the synthetic and predictability info.

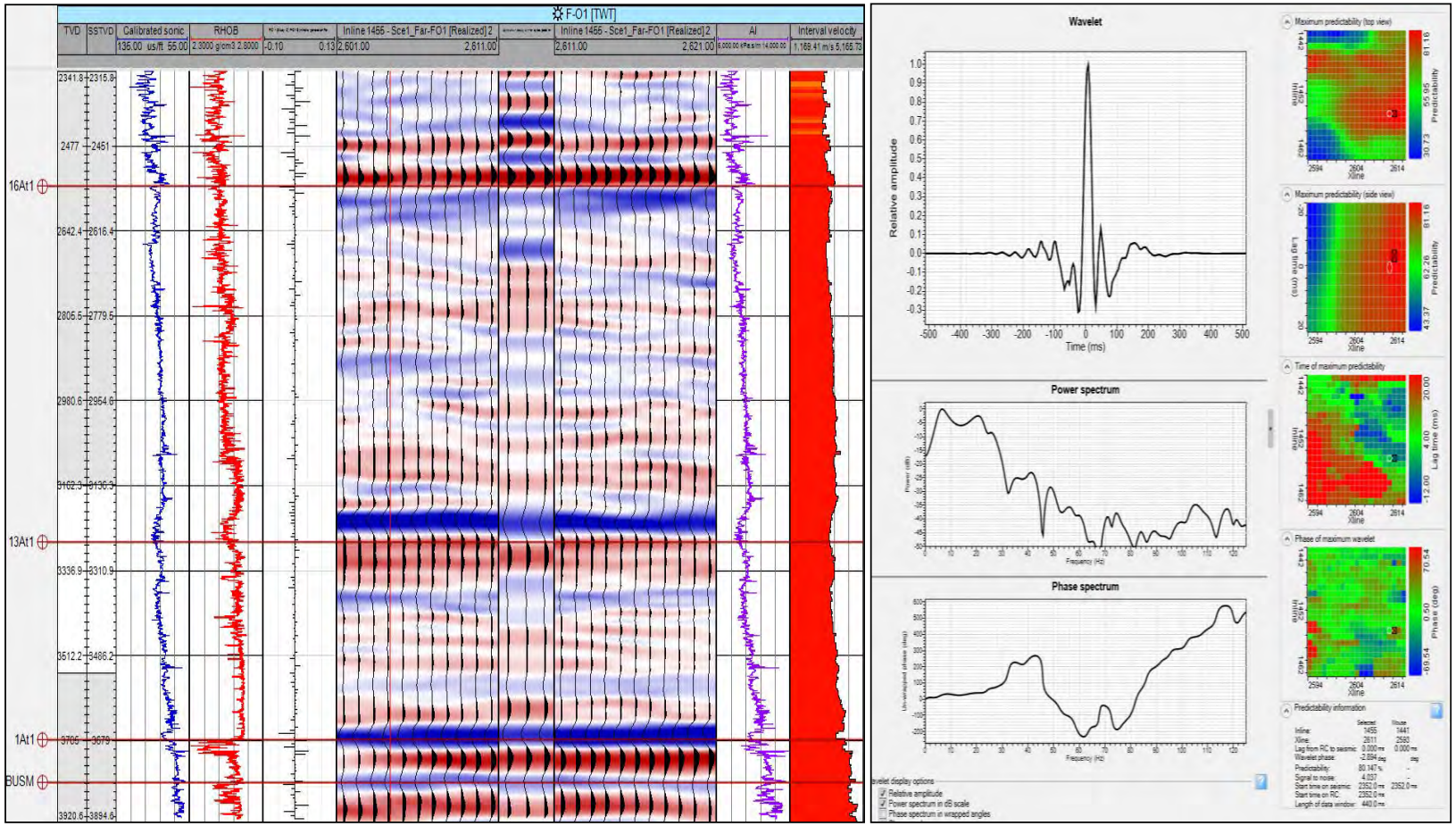

Figure 5.3.4: Well tie quality control at well F-O1 after check-shot calibration and log alignment, when necessary. The well synthetic has been generated with the wavelet extraction from the far stack. Left picture well logs, seismic panel with the well synthetic inserted. Right extracted wavelet used for the synthetic and predictability info.

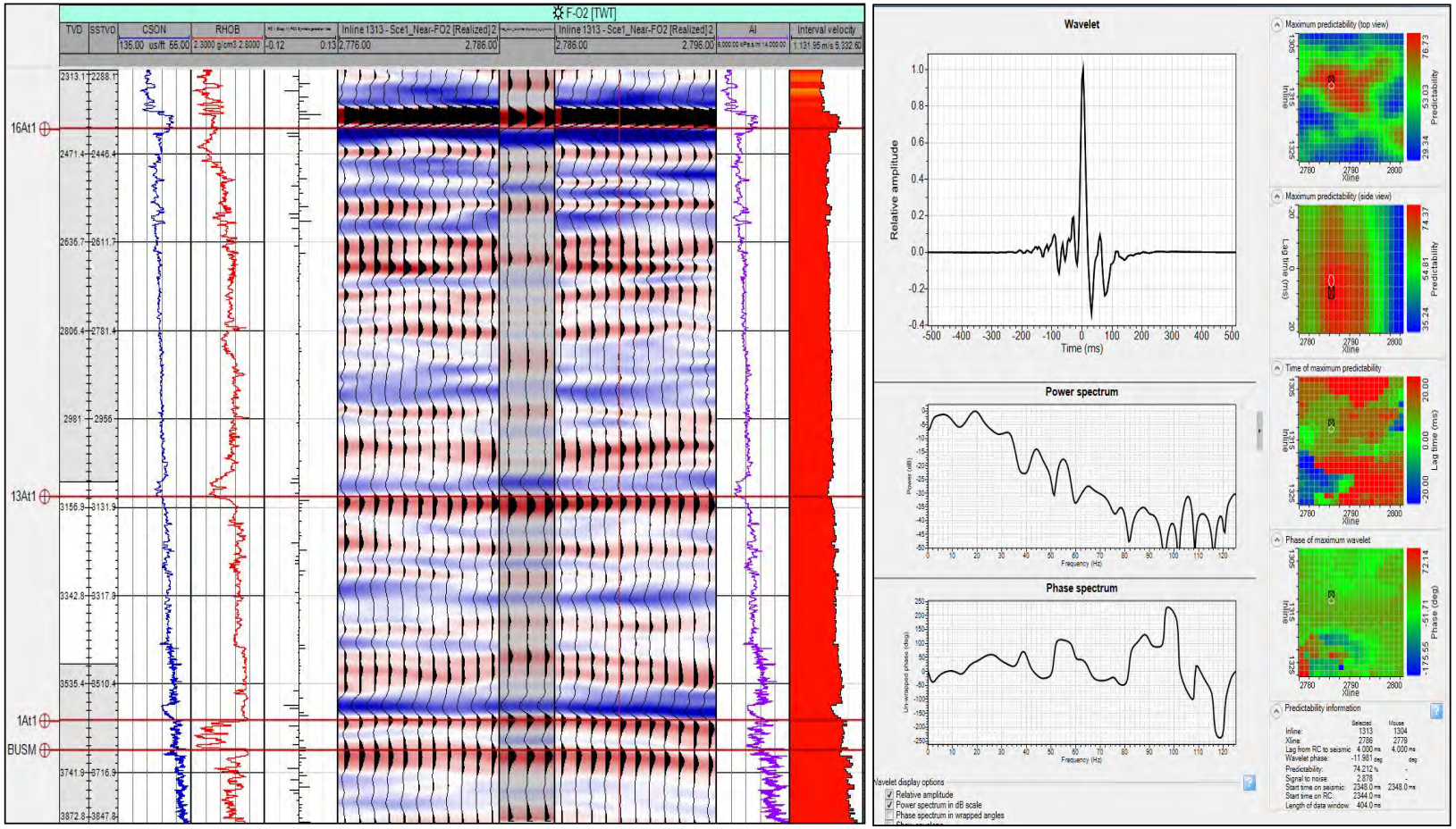

Figure 5.3.5: Well tie quality control at well F-O2 after check-shot calibration and log alignment, when necessary. The well synthetic has been generated with the wavelet extraction from the near stack. Left picture well logs, seismic panel with the well synthetic inserted. Right extracted wavelet used for the synthetic and predictability info.

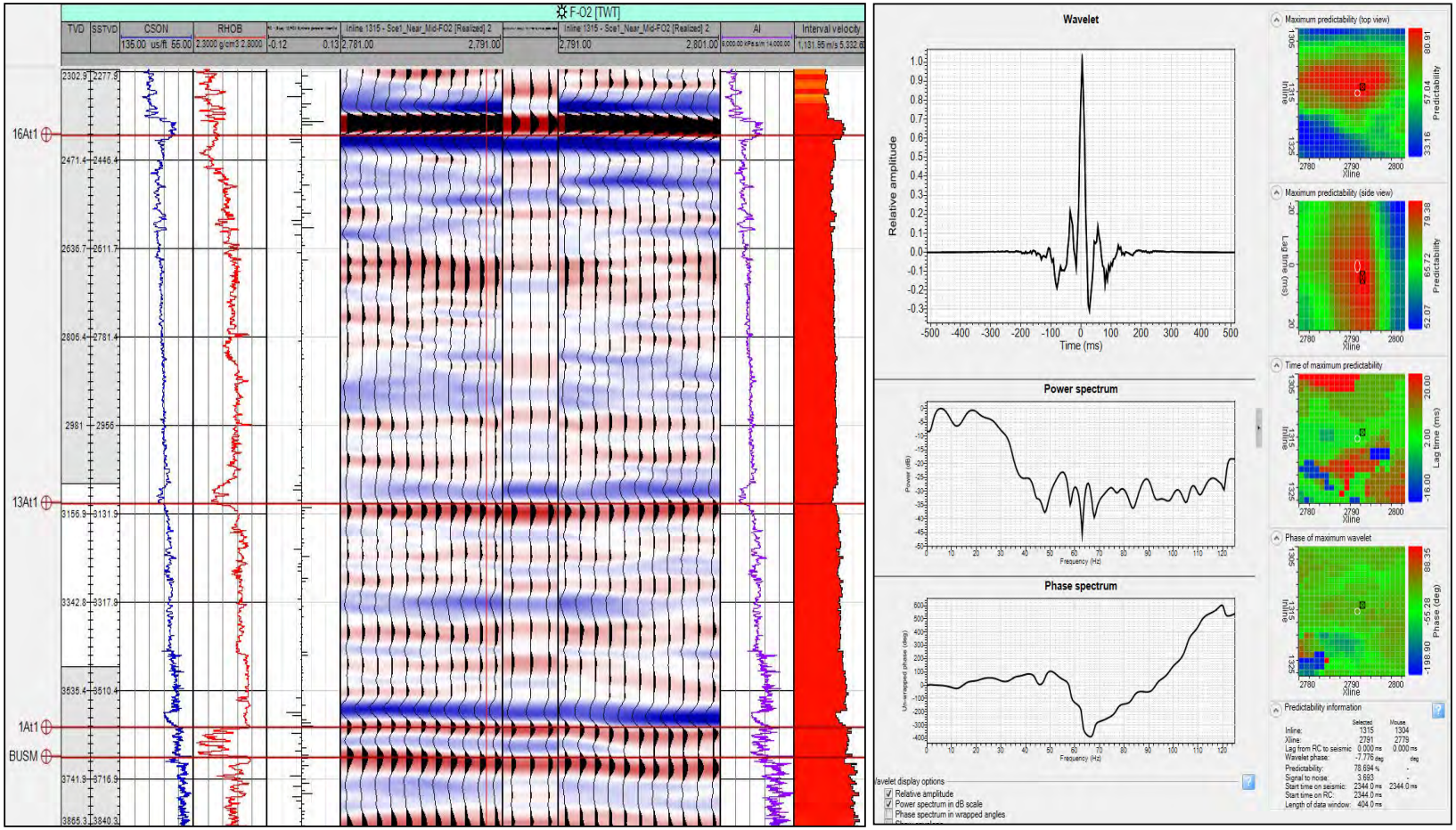

Figure 5.3.6: Well tie quality control at well F-O2 after check-shot calibration and log alignment, when necessary. The well synthetic has been generated with the wavelet extraction from the near- mid stack. Left picture well logs, seismic panel with the well synthetic inserted. Right extracted wavelet used for the synthetic and predictability info.

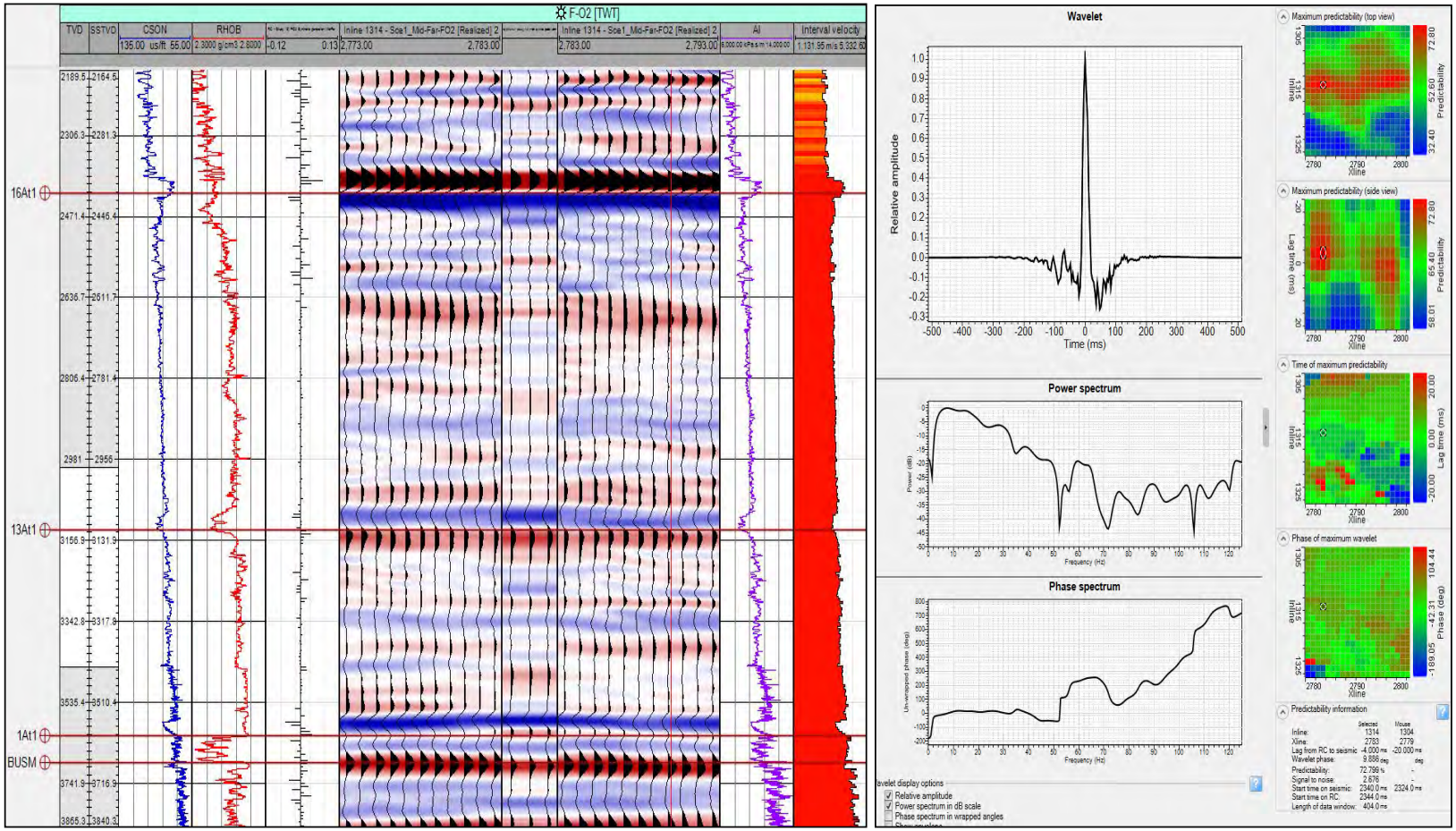

Figure 5.3.7: Well tie quality control at well F-O2 after check-shot calibration and log alignment, when necessary. The well synthetic has been generated with the wavelet extraction from the mid-far stack. Left picture well logs, seismic panel with the well synthetic inserted. Right extracted wavelet used for the synthetic and predictability info.

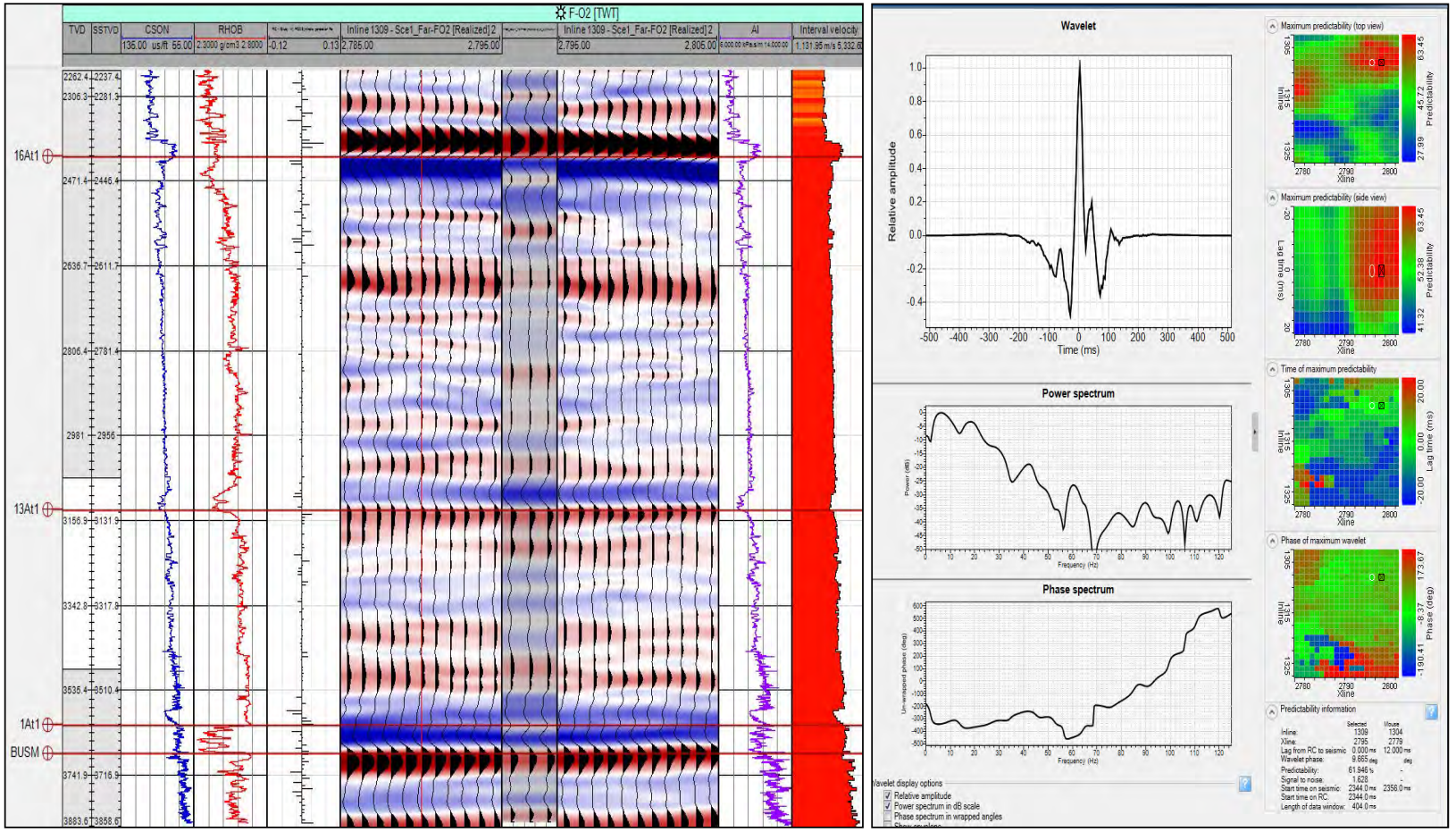

Figure 5.3.8: Well tie quality control at well F-O2 after check-shot calibration and log alignment, when necessary. The well synthetic has been generated with the wavelet extraction from the far stack. Left picture well logs, seismic panel with the well synthetic inserted. Right extracted wavelet used for the synthetic and predictability info.

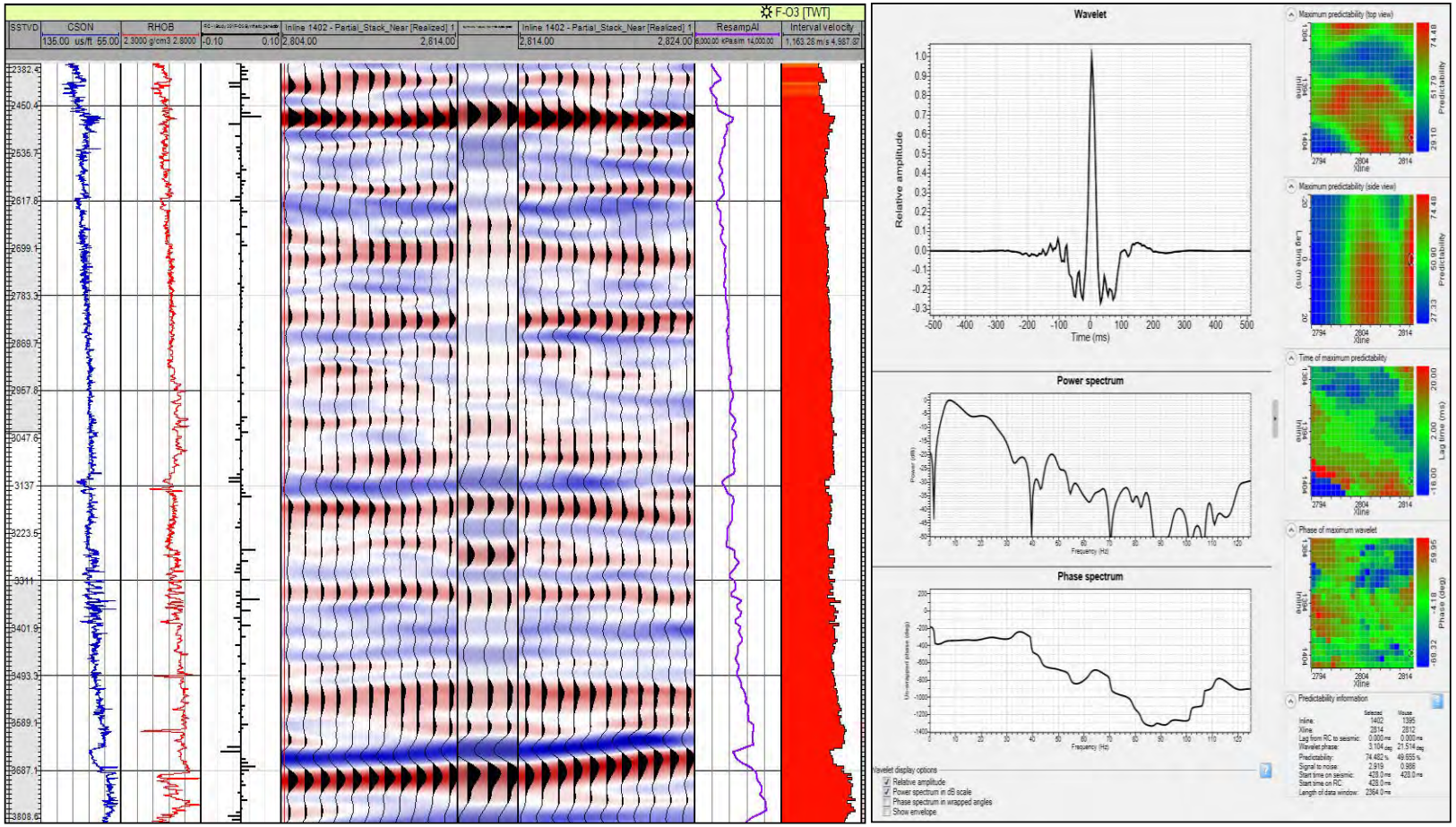

Figure 5.3.9: Well tie quality control at well F-O3 after check-shot calibration and log alignment, when necessary. The well synthetic has been generated with the wavelet extraction from the near stack. Left picture well logs, seismic panel with the well synthetic inserted. Right extracted wavelet used for the synthetic and predictability info.

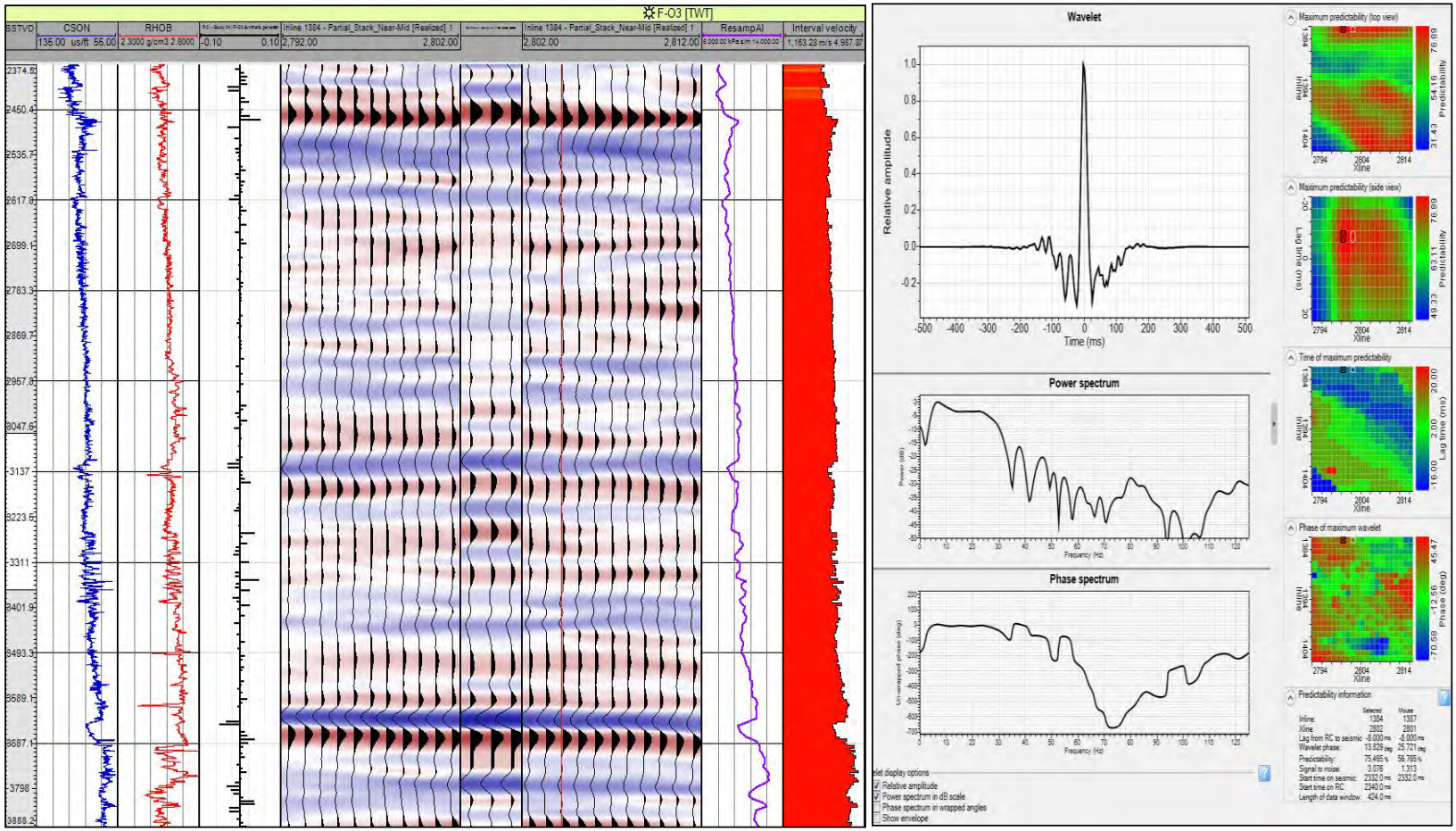

Figure 5.3.10: Well tie quality control at well F-O3 after check-shot calibration and log alignment, when necessary. The well synthetic has been generated with the wavelet extraction from the near- mid stack. Left picture well logs, seismic panel with the well synthetic inserted. Right extracted wavelet used for the synthetic and predictability info.

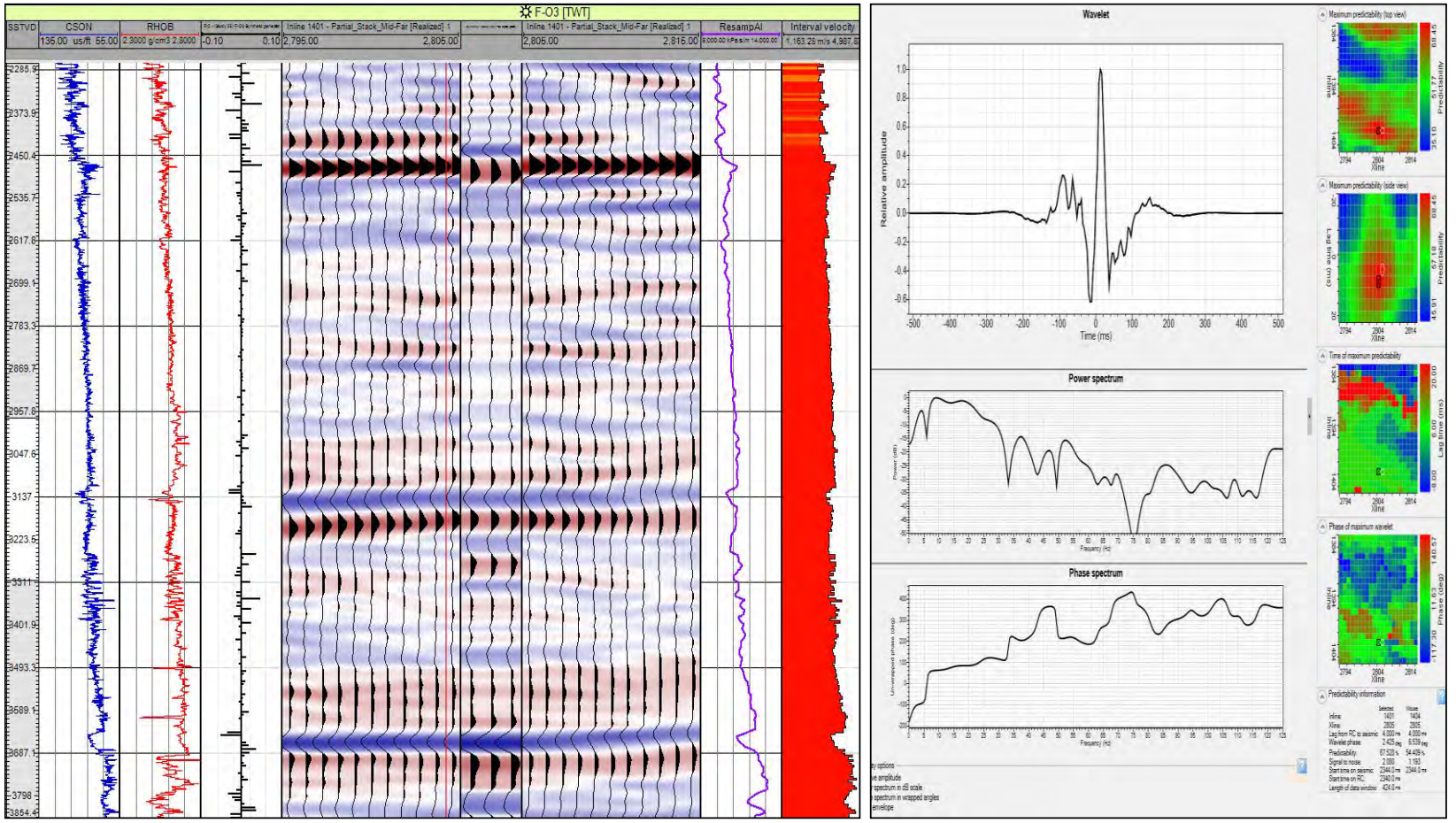

Figure 5.3.11: Well tie quality control at well F-O3 after check-shot calibration and log alignment, when necessary. The well synthetic has been generated with the wavelet extraction from the mid-far stack. Left picture well logs, seismic panel with the well synthetic inserted. Right extracted wavelet used for the synthetic and predictability info.

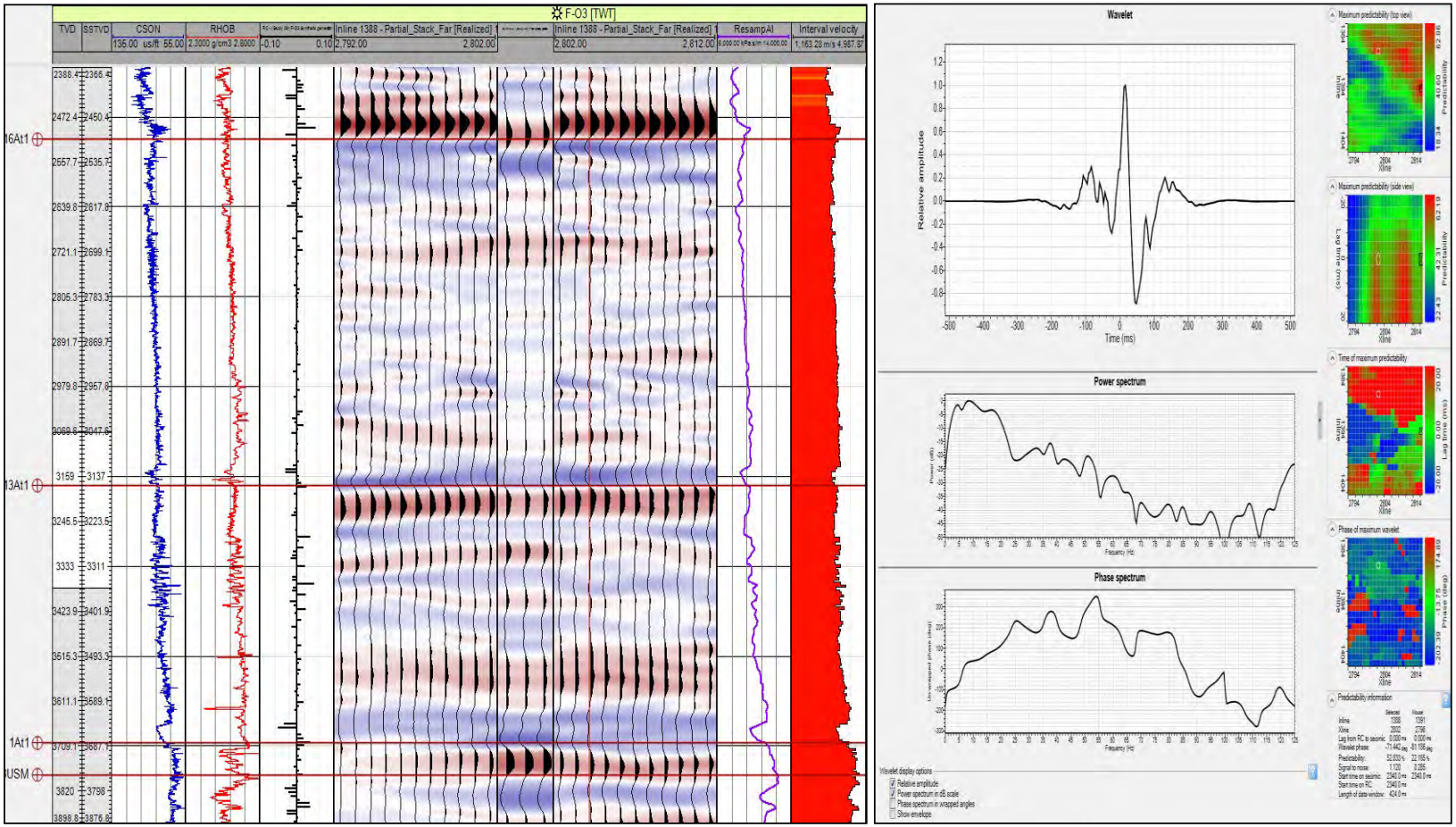

Figure 5.3.12: Well tie quality control at well F-O3 after check-shot calibration and log alignment, when necessary. The well synthetic has been generated with the wavelet extraction from the far stack. Left picture well logs, seismic panel with the well synthetic inserted. Right extracted wavelet used for the synthetic and predictability info.

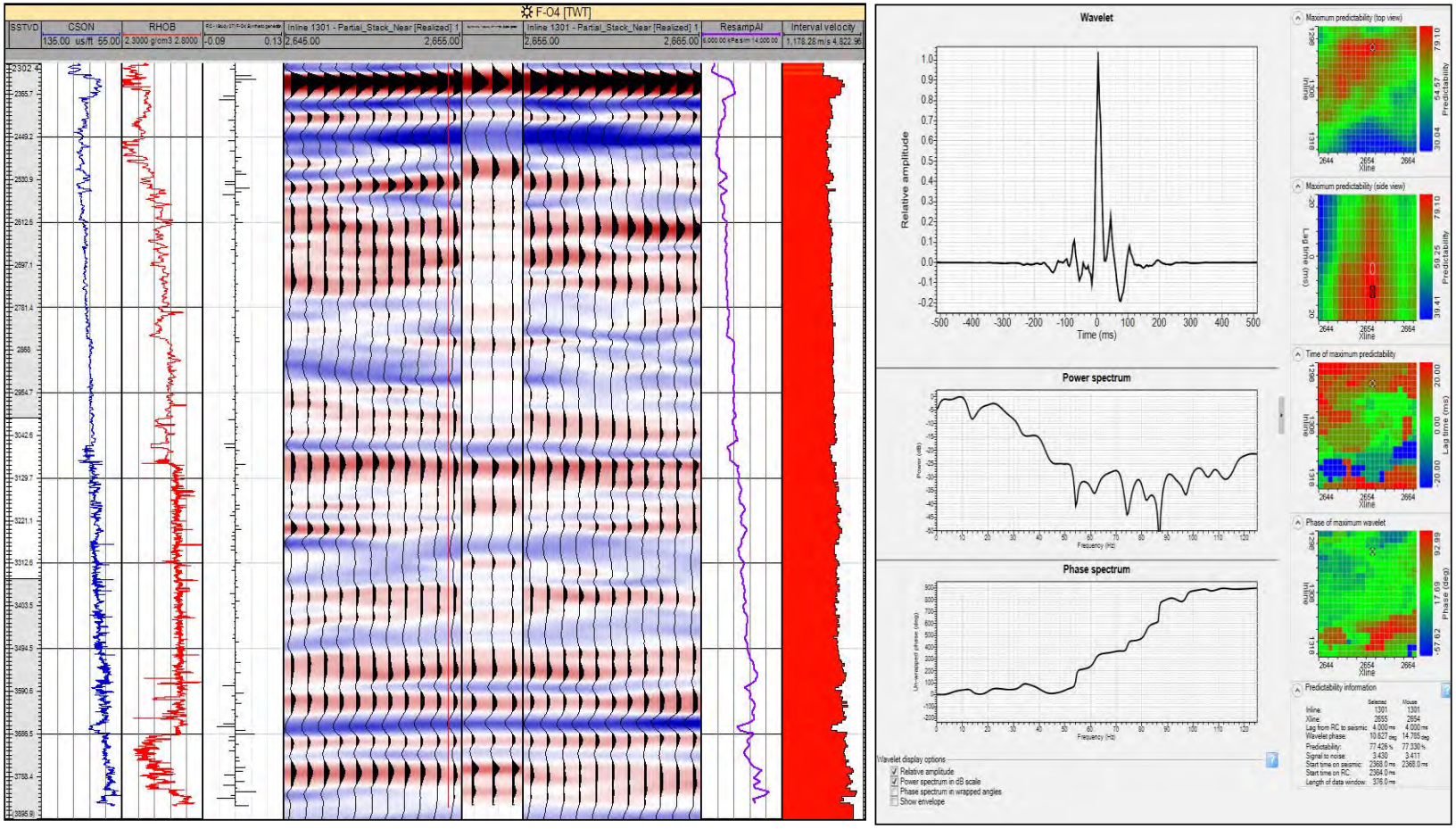

Figure 5.3.13: Well tie quality control at well F-O4 after check-shot calibration and log alignment, when necessary. The well synthetic has been generated with the wavelet extraction from the near stack. Left picture well logs, seismic panel with the well synthetic inserted. Right extracted wavelet used for the synthetic and predictability info.

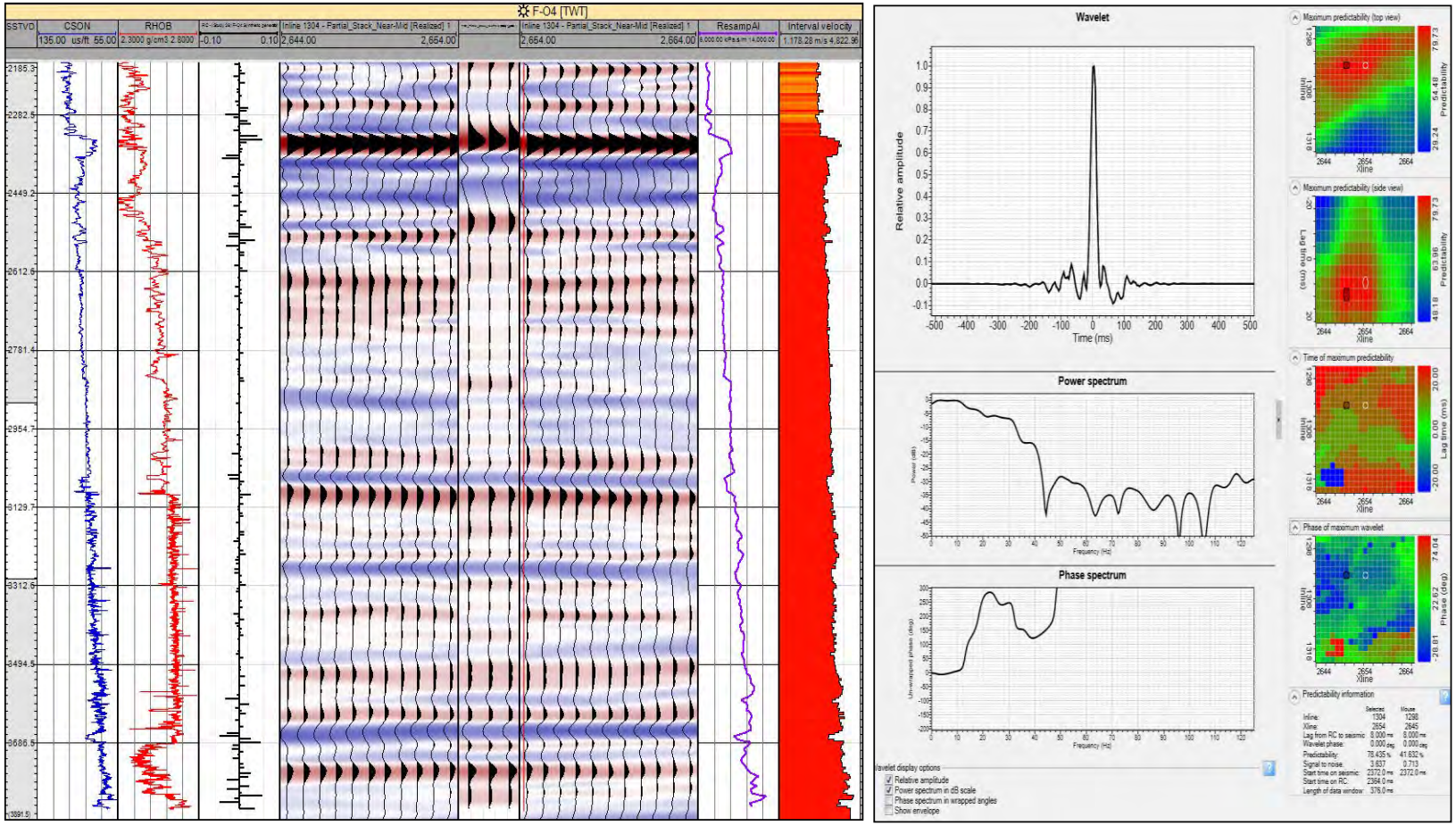

Figure 5.3.14: Well tie quality control at well F-O4 after check-shot calibration and log alignment, when necessary. The well synthetic has been generated with the wavelet extraction from the near- mid stack. Left picture well logs, seismic panel with the well synthetic inserted. Right extracted wavelet used for the synthetic and predictability info.

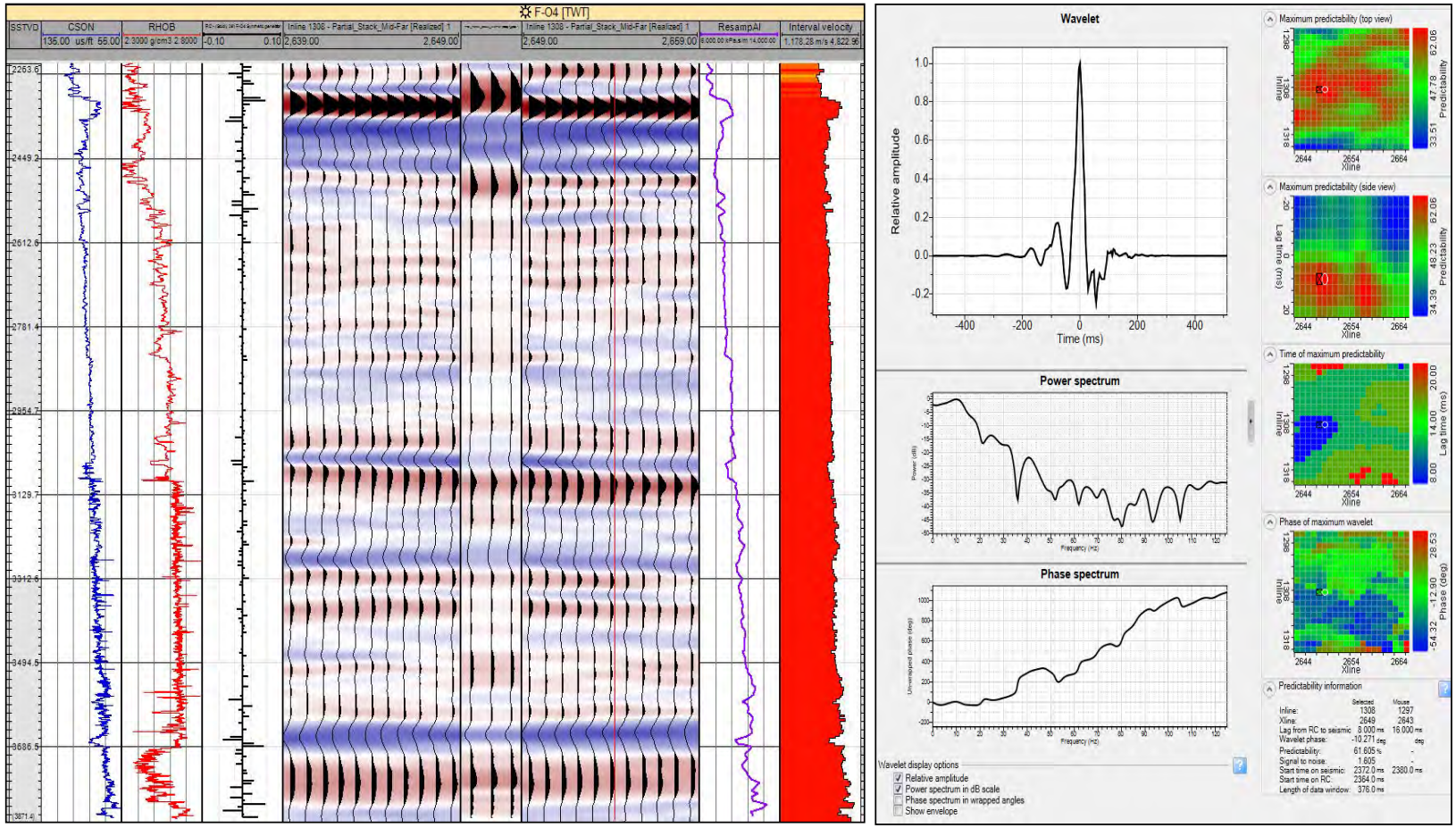

Figure 5.3.15: Well tie quality control at well F-O4 after check-shot calibration and log alignment, when necessary. The well synthetic has been generated with the wavelet extraction from the mid-far stack. Left picture well logs, seismic panel with the well synthetic inserted. Right extracted wavelet used for the synthetic and predictability info.

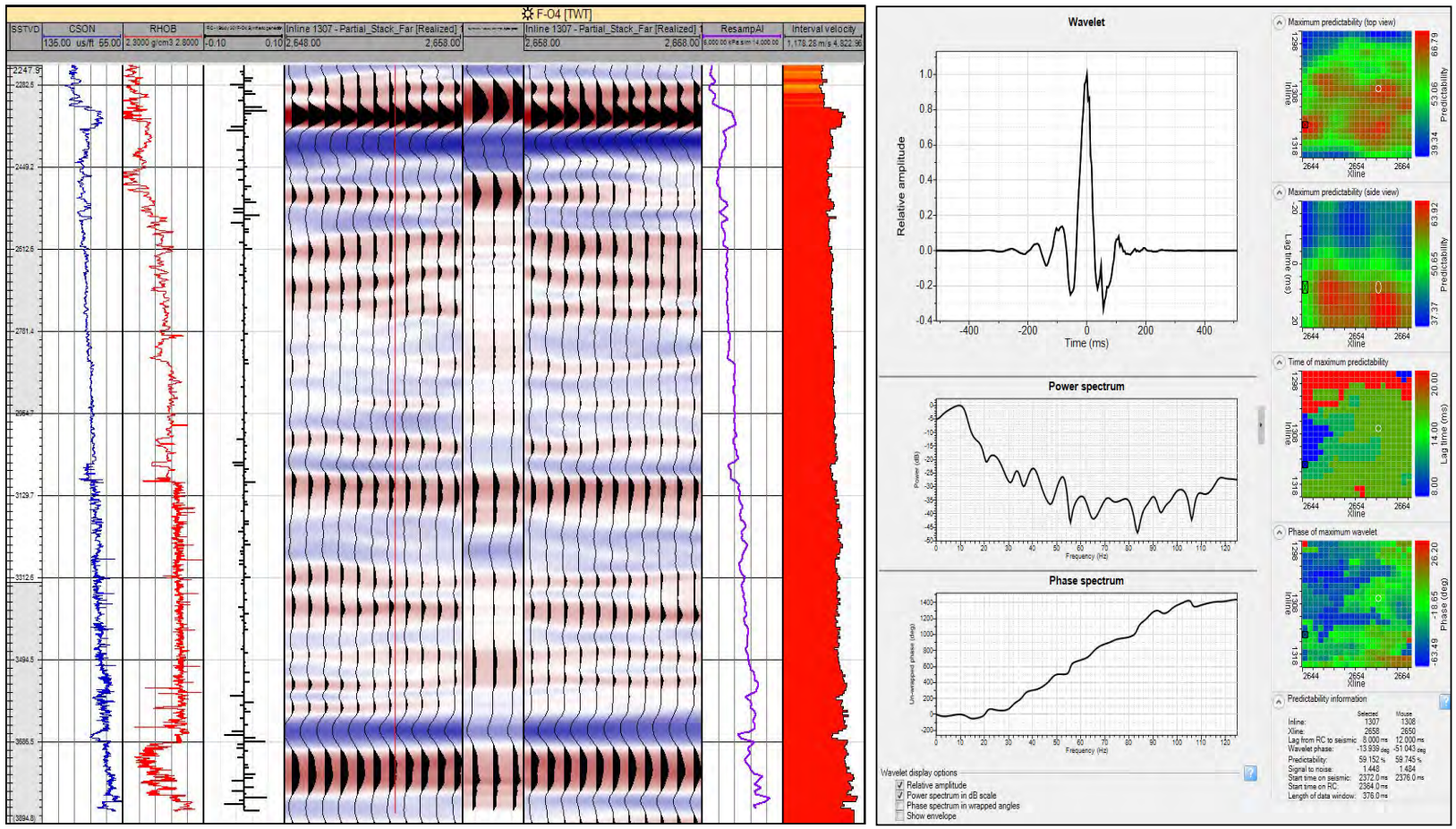

Figure 5.3.16: Well tie quality control at well F-O4 after check-shot calibration and log alignment, when necessary. The well synthetic has been generated with the wavelet extraction from the far stack. Left picture well logs, seismic panel with the well synthetic inserted. Right extracted wavelet used for the synthetic and predictability info.

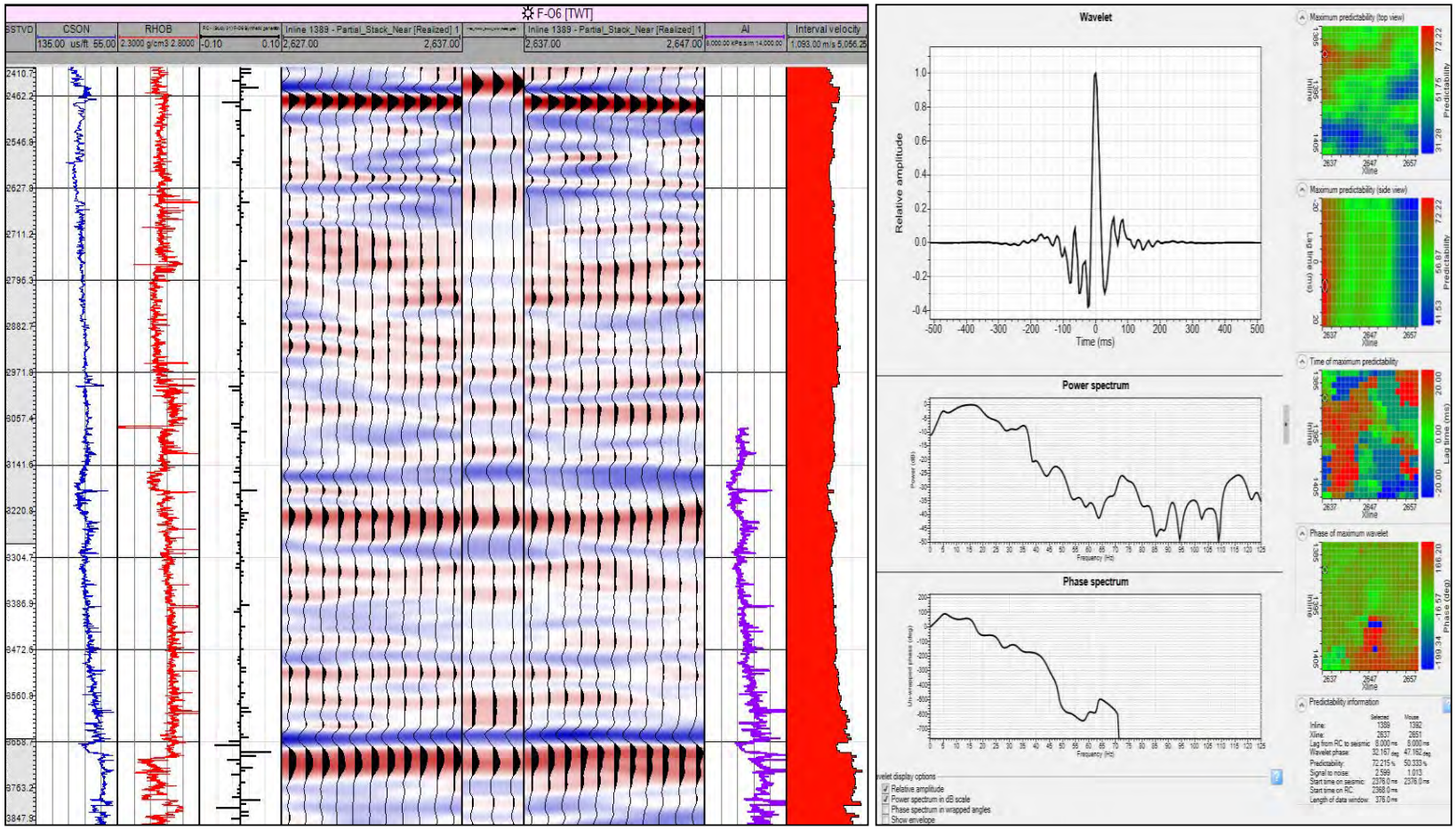

Figure 5.3.17: Well tie quality control at well F-O6 after check-shot calibration and log alignment, when necessary. The well synthetic has been generated with the wavelet extraction from the near stack. Left picture well logs, seismic panel with the well synthetic inserted. Right extracted wavelet used for the synthetic and predictability info.

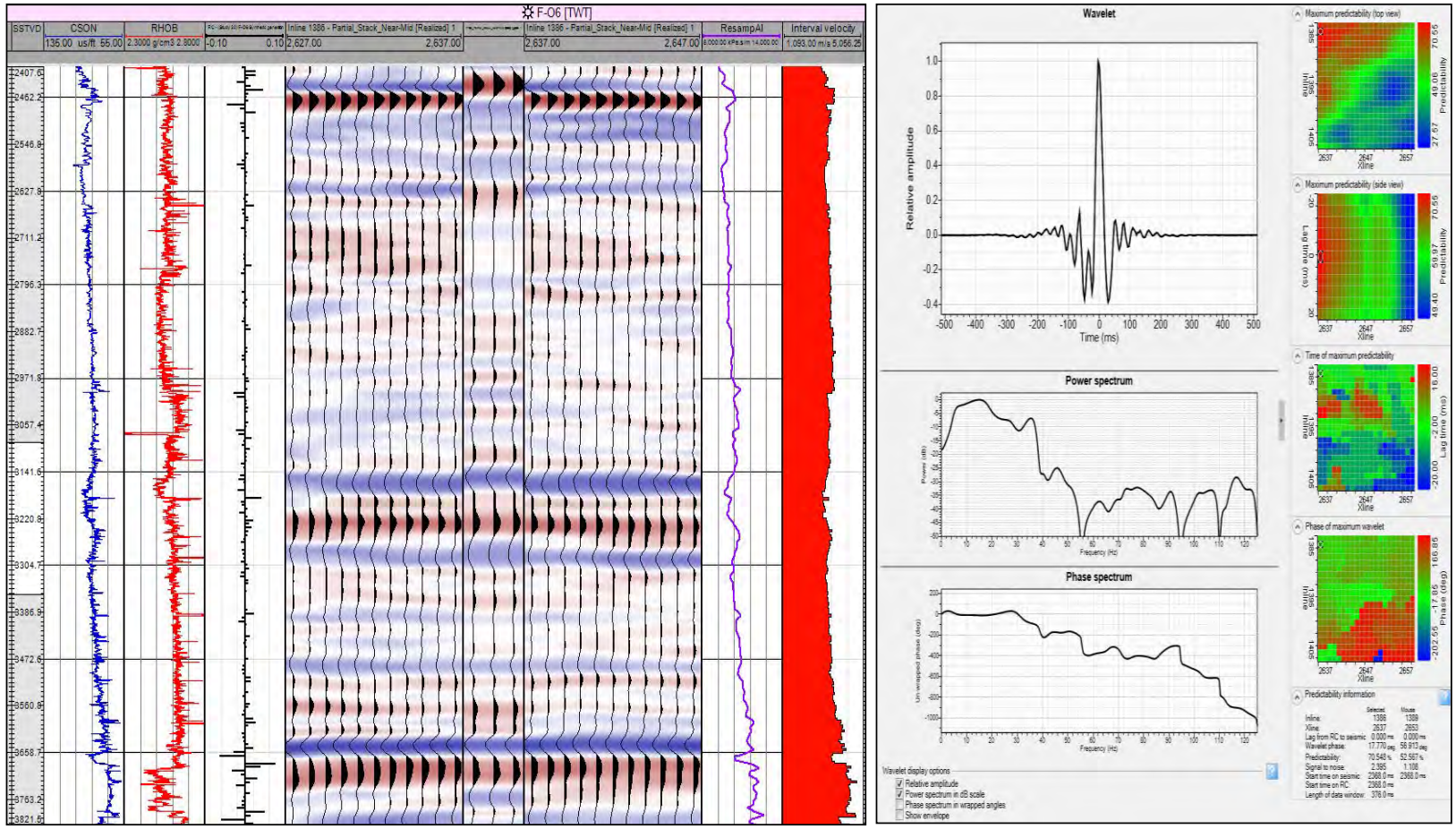

Figure 5.3.18: Well tie quality control at well F-O6 after check-shot calibration and log alignment, when necessary. The well synthetic has been generated with the wavelet extraction from the near- mid stack. Left picture well logs, seismic panel with the well synthetic inserted. Right extracted wavelet used for the synthetic and predictability info.

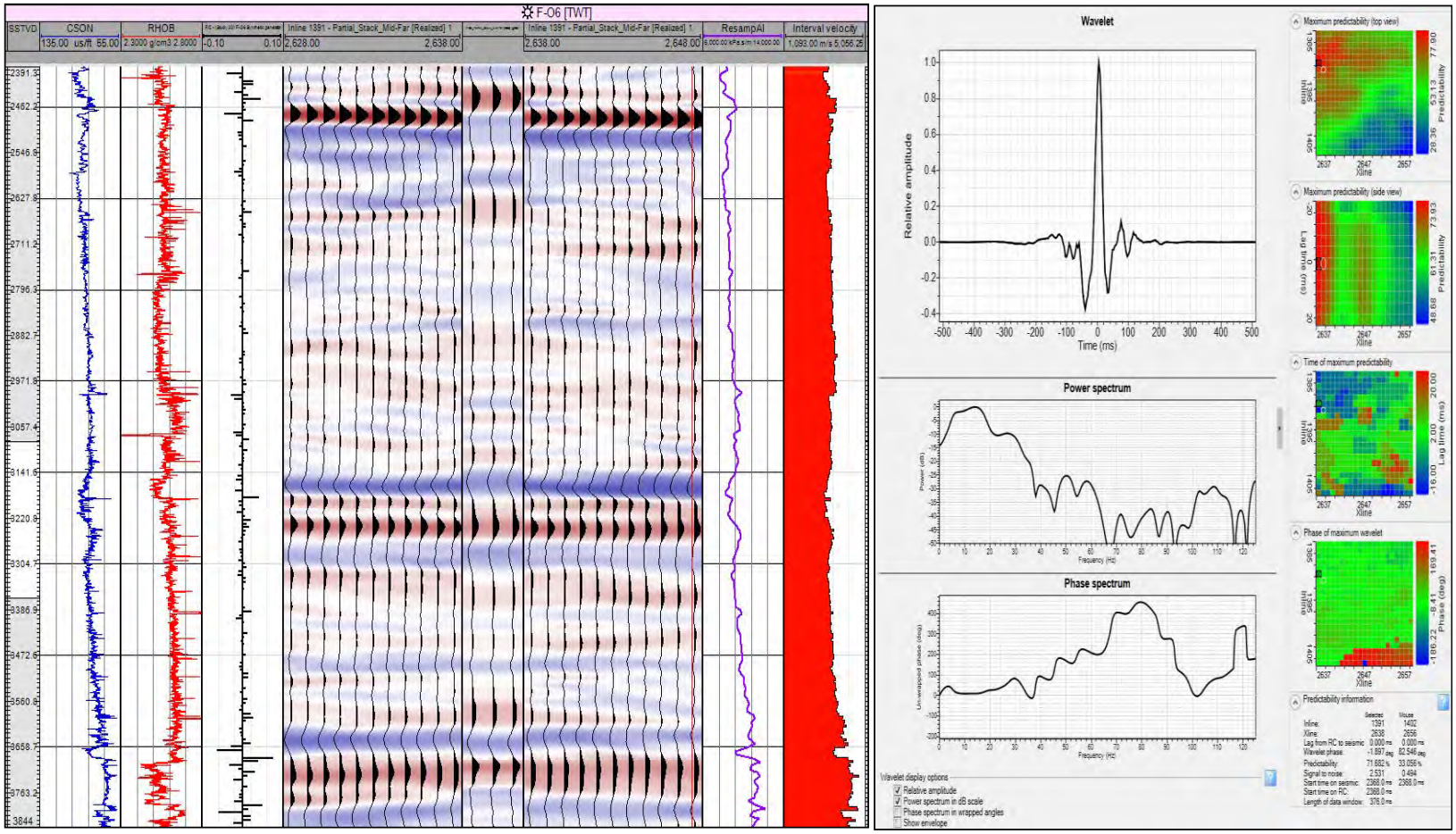

Figure 5.3.19: Well tie quality control at well F-O6 after check-shot calibration and log alignment, when necessary. The well synthetic has been generated with the wavelet extraction from the mid-far stack. Left picture well logs, seismic panel with the well synthetic inserted. Right extracted wavelet used for the synthetic and predictability info.

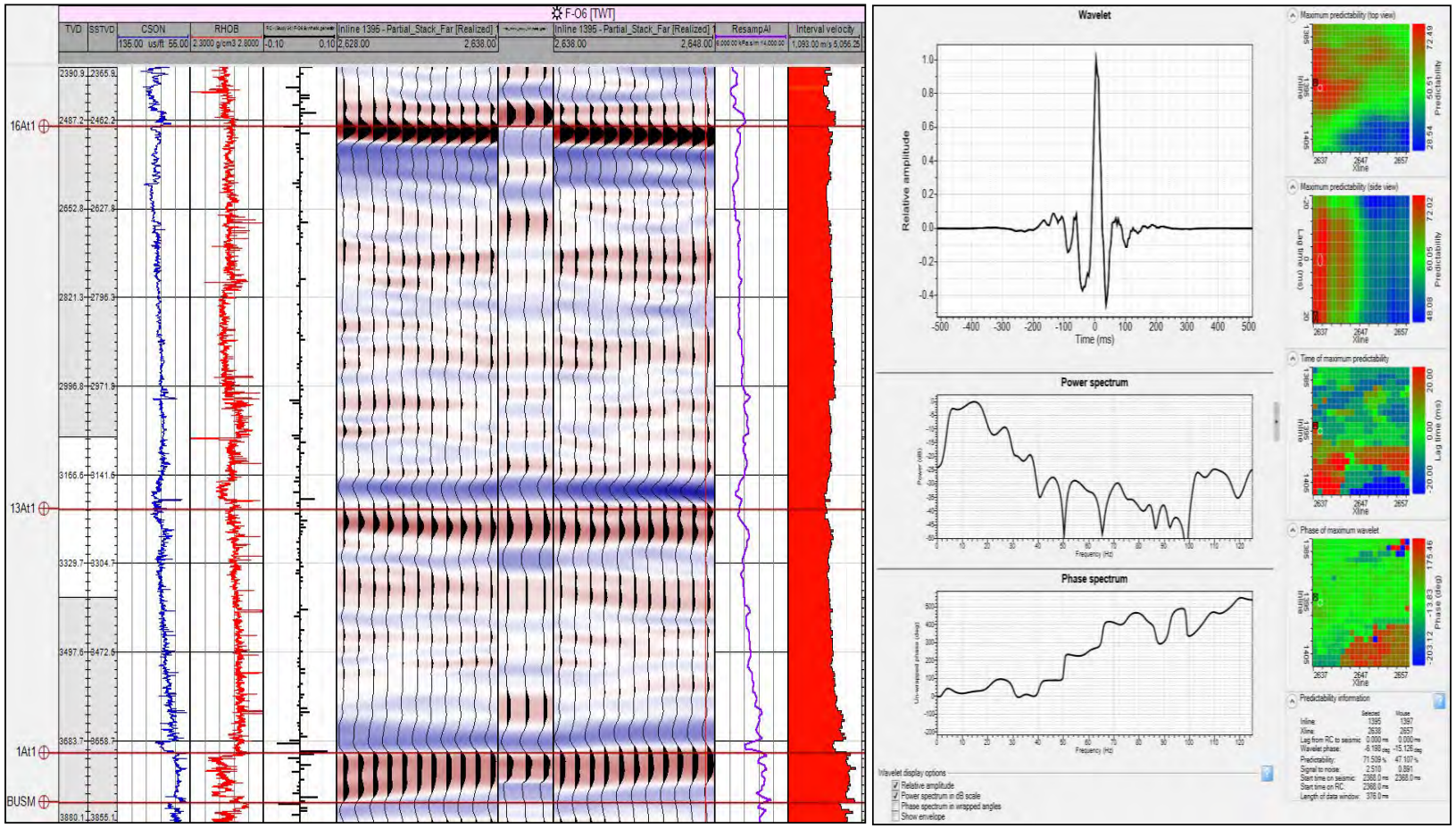

Figure 5.3.20: Well tie quality control at well F-O6 after check-shot calibration and log alignment, when necessary. The well synthetic has been generated with the wavelet extraction from the far stack. Left picture well logs, seismic panel with the well synthetic inserted. Right extracted wavelet used for the synthetic and predictability info.

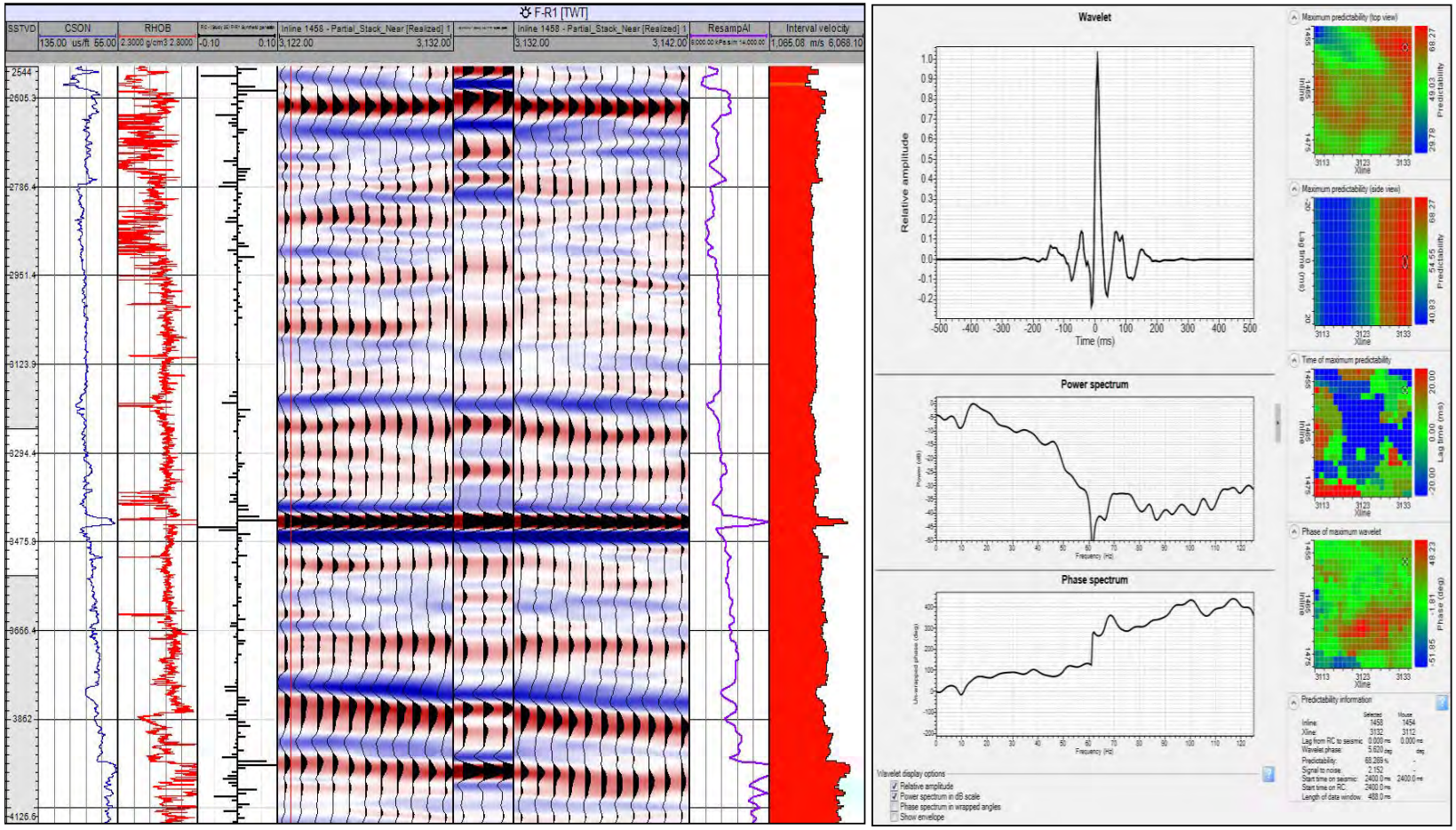

Figure 5.3.21: Well tie quality control at well F-R1 after check-shot calibration and log alignment, when necessary. The well synthetic has been generated with the wavelet extraction from the near stack. Left picture well logs, seismic panel with the well synthetic inserted. Right extracted wavelet used for the synthetic and predictability info.

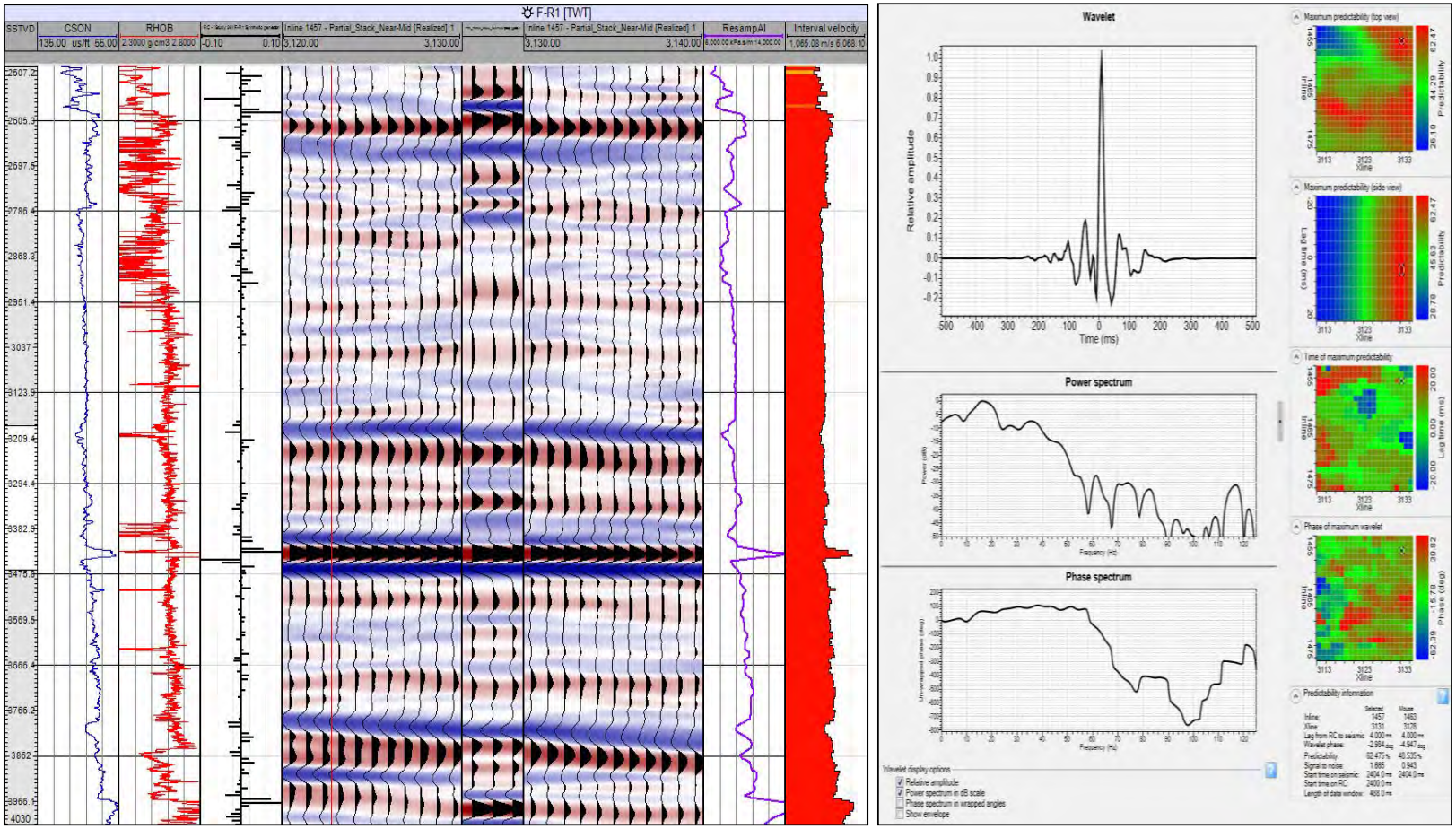

Figure 5.3.22: Well tie quality control at well F-R1 after check-shot calibration and log alignment, when necessary. The well synthetic has been generated with the wavelet extraction from the near- mid stack. Left picture well logs, seismic panel with the well synthetic inserted. Right extracted wavelet used for the synthetic and predictability info.

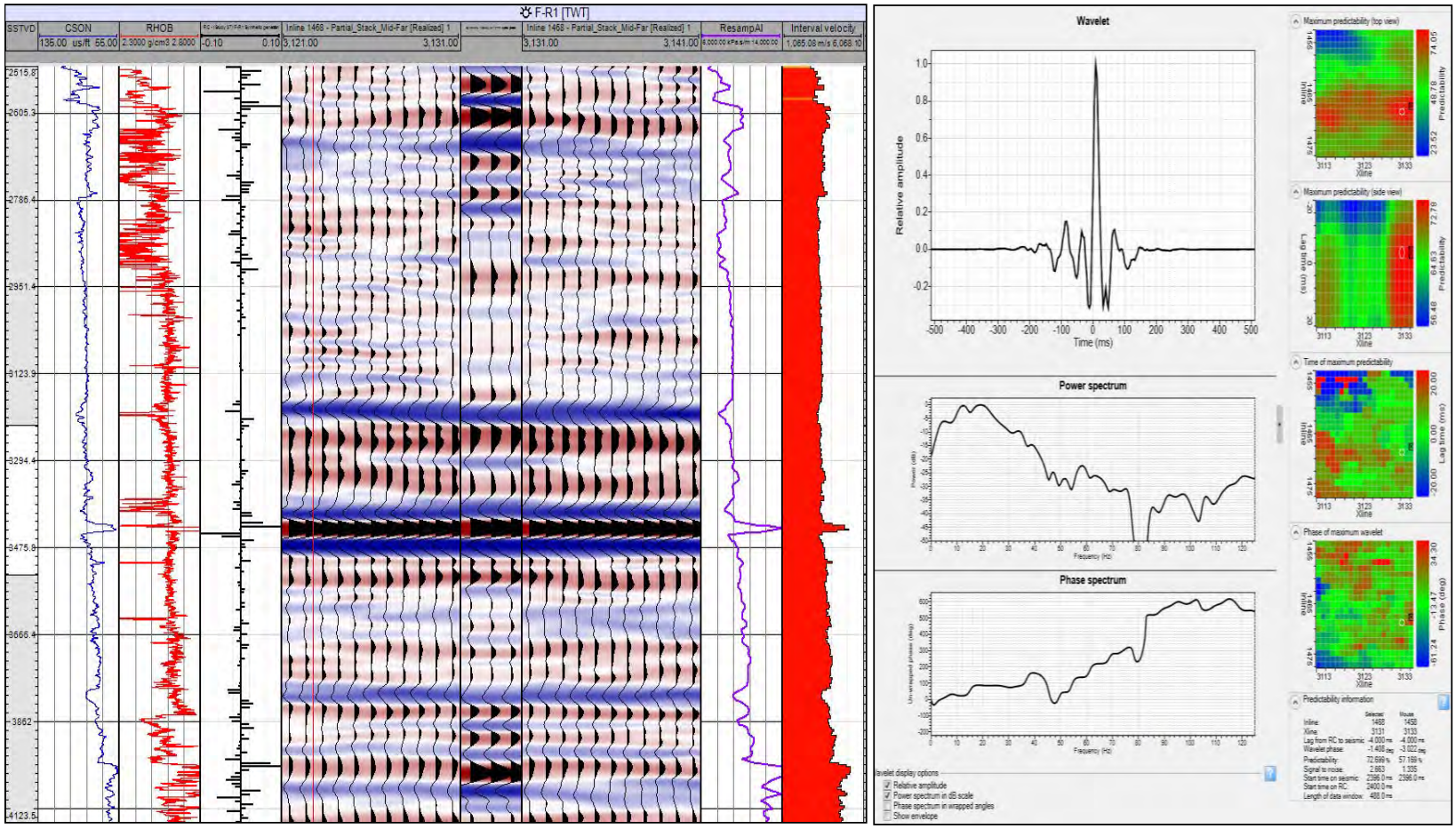

Figure 5.3.23: Well tie quality control at well F-R1 after check-shot calibration and log alignment, when necessary. The well synthetic has been generated with the wavelet extraction from the mid-far stack. Left picture well logs, seismic panel with the well synthetic inserted. Right extracted wavelet used for the synthetic and predictability info.

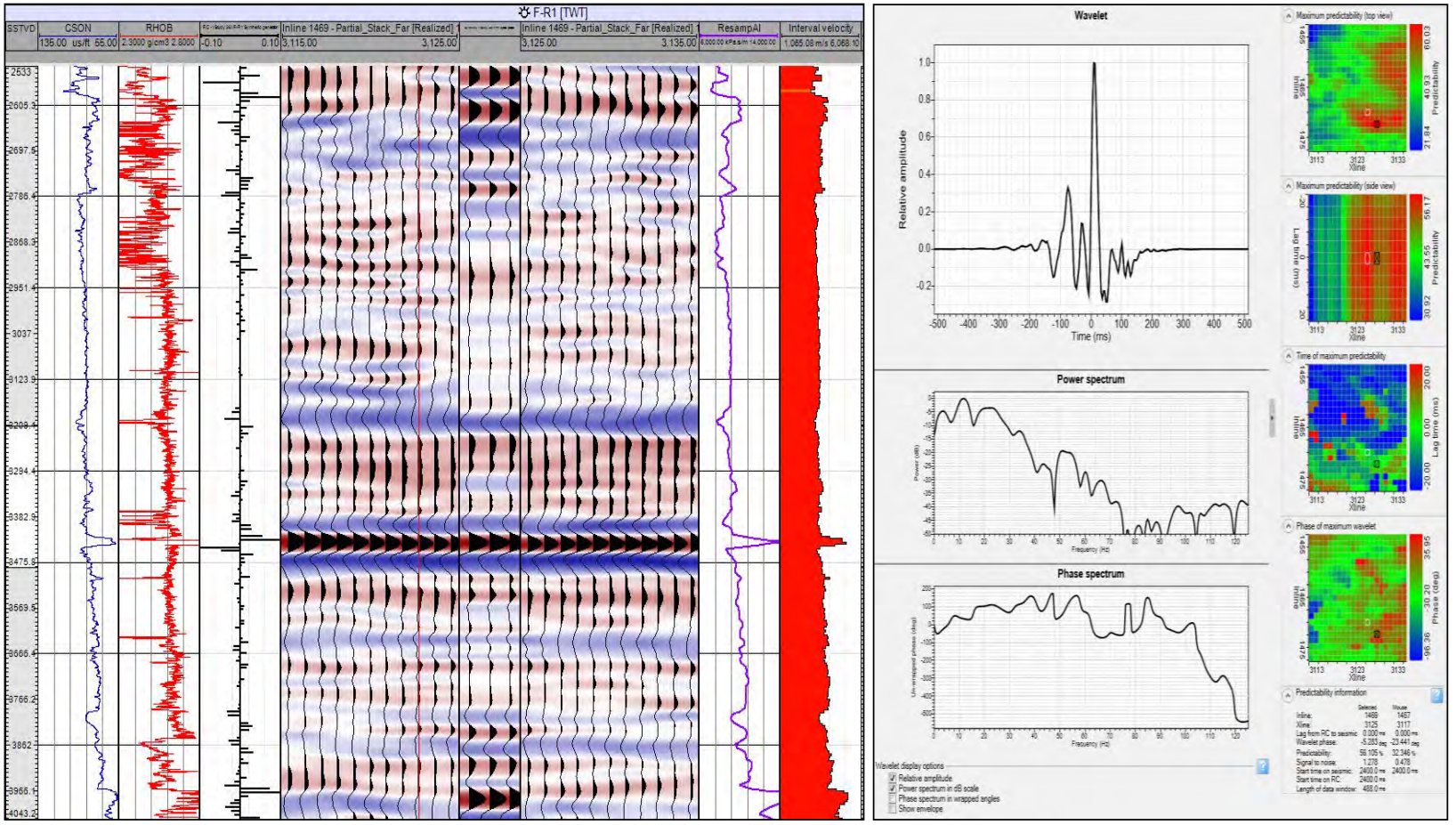

Figure 5.3.24: Well tie quality control at well F-R1 after check-shot calibration and log alignment, when necessary. The well synthetic has been generated with the wavelet extraction from the far stack. Left picture well logs, seismic panel with the well synthetic inserted. Right extracted wavelet used for the synthetic and predictability info.

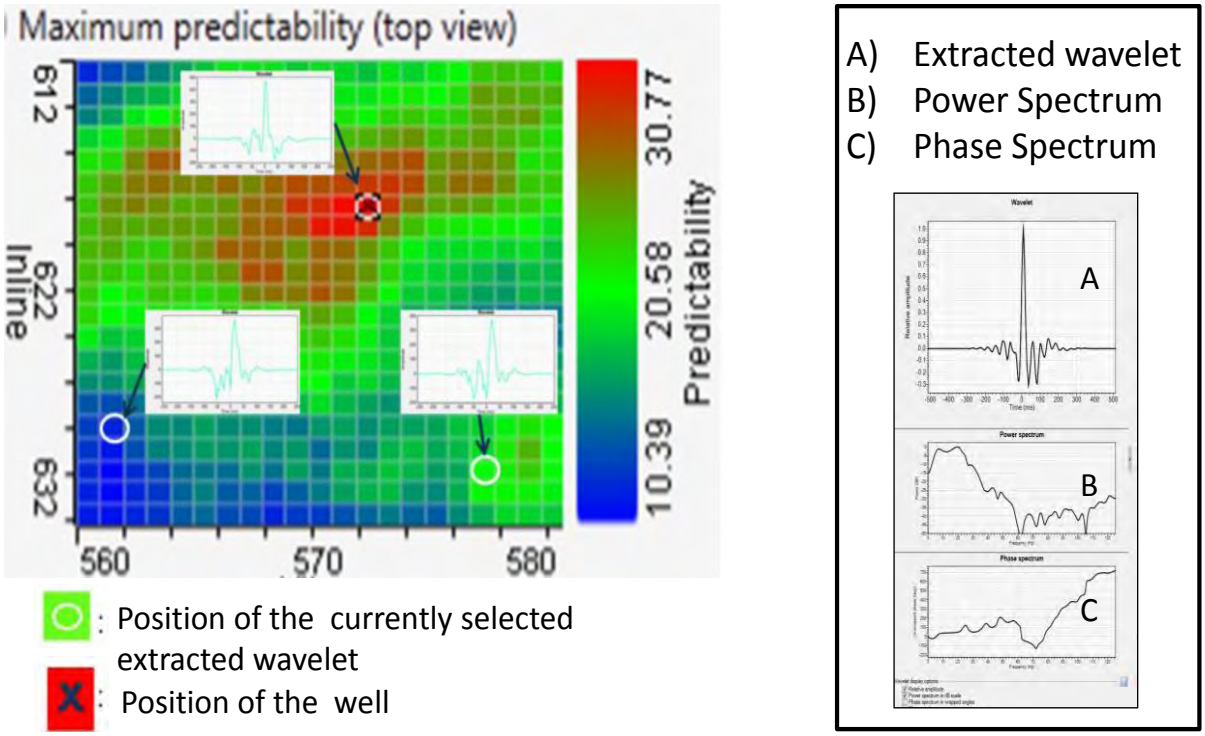

Figure 5.3.25: The white circles on map indicate the position of the currently selected extracted wavelet, which is convolved with the log reflectivity to build the synthetic. The predictability displays are interactive; by changing the location, the wavelet is re-computed to the wavelet extracted at that map location.

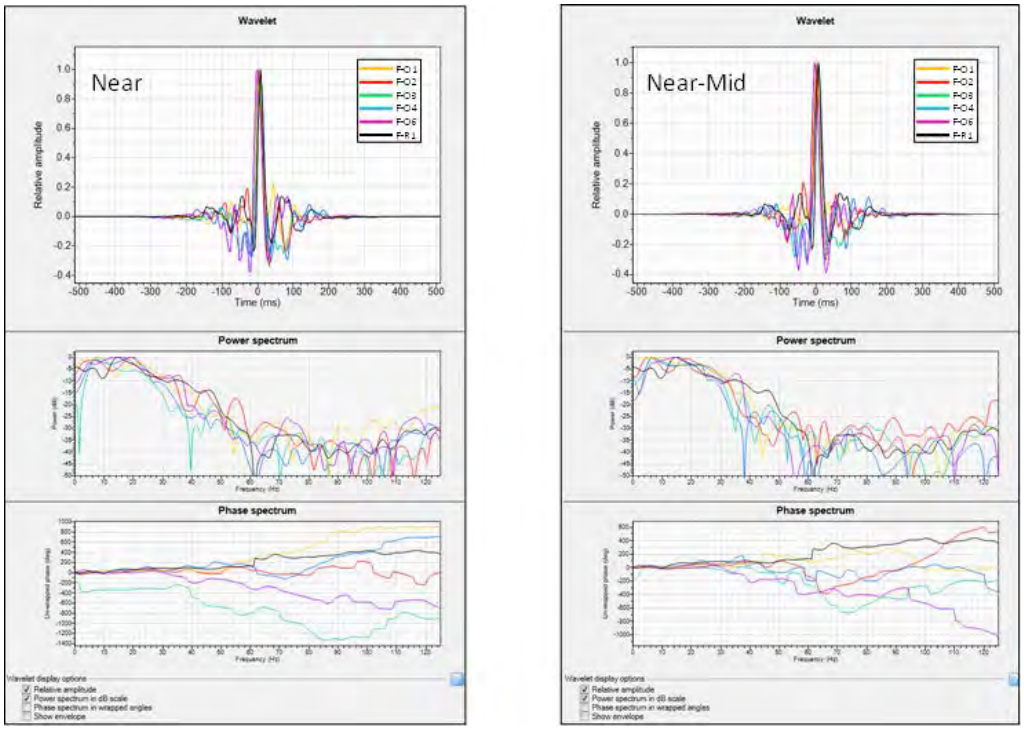

Figure 5.3.26: Near / Near-Mid extracted wavelet, power spectrum and phase spectrum. Final wavelets extracted at each well for near and near-mid partial stacks. In the bottom amplitude spectrum and phase spectrum cross-plots.

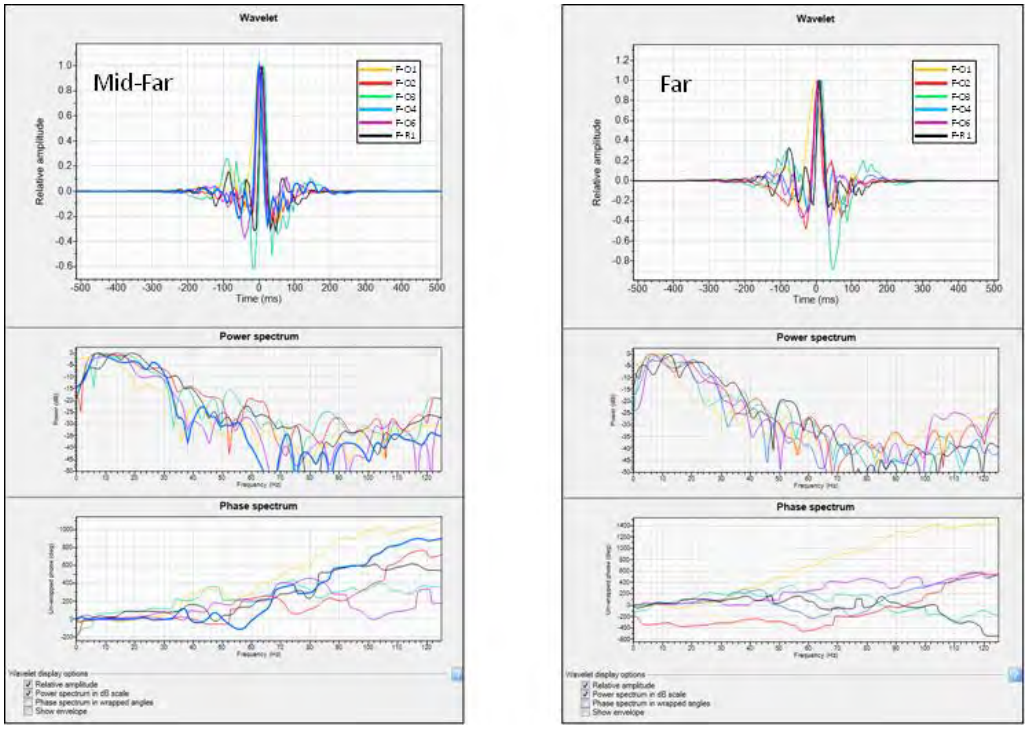

Figure 5.3.27: Mid-Far / Far extracted wavelet, power spectrum and phase spectrum. Final wavelets extracted at each well for mid-far and far partial stacks. In the bottom amplitude spectrum and phase spectrum cross-plots.

5.4 Low frequency modelling

Seismic data is band limited, causing a resolution and quality reduction. Therefore, the low frequencies missing in seismic data and so necessary for the seismic inversion are modelled using log data. Well data serves to add the low frequency below the seismic band and to constrain the inversion. Therefore, low-frequency modelling is an important aspect of obtaining absolute rock properties. Low frequencies represent the mean trend of the data and the higher frequencies the deviation from the mean trend.

The initial model shares the same area as the seismic inversion volume with in-lines from 1160 to 1710 and the cross-lines from 1920 to 3400.

The low-frequency model process is designed to generate models of acoustic impedance, Vp/Vs ratio, and density that tie in with the well data and are also representative of the underlying geology away from the wells. Full-frequency models are calculated using the well logs by extrapolating data constrained by the interpreted horizons.

The initial 3D low frequency elastic grid model was defined by using the three interpreted horizons (13At1, 1At1, BLSM ghost) and well logs up-scaled to 4 msec. The model top was the horizon 13At1. The base was created by shifting the BLSM horizon (ghost) 50 msec downward.

The layering in between horizons was determined based on each case, where layering is

defined as the internal geometry reflecting the geological deposition of a specific zone. All zones except one used “proportional layering”, in which internal layers in each zone conform to both the top and base of the zone. Zone 1At1-BLSM was the exception; taking into account that 1At1 represents an unconformity, the zone between 1At1 and BLSM used a “follow the base” layering, which means all layers are parallel to the bottom of the zone. At this target zone, the minimum layer thickness was set at 4 msec.

Well logs were first conditioned and edited (section 4.3) to ensure a suitable relationship between elastic logs and the desired properties. The logs (acoustic impedance, Vp/Vs and density) were then converted to time and filtered to extract their low-frequency component.

The full frequency well data is filtered by applying a frequency cut-off. The cut-off was determined by comparing the amplitude versus frequency spectrum of the seismic data in an 800 milliseconds TWT window of interest in an area near wells F-O1 and F-O2 and superimposing various Ormsby high cut filter scenarios. The low-cut and low-pass frequency parameters were set on 1 and 2 Hz respectively in all 4 scenarios. Then the high-pass and high cut frequency were set up as follow: 3-4, 4-6, 6-9 and 9-13 Hz (see figure 5.4.1). For a discussion of Ormsby filter refer to Appendix 5.4.

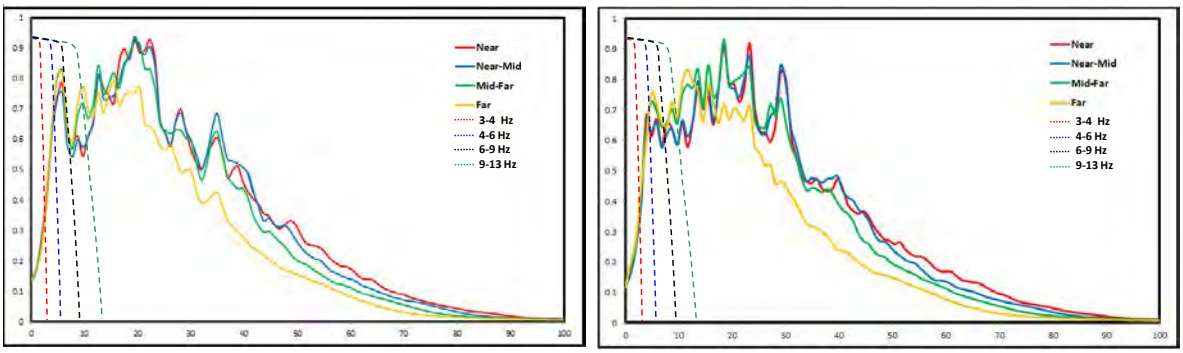

Figure 5.4.1: Amplitude spectrum for each angle stack over 800 msec window and different frequency high cut for the low frequency model. From left to right, the data from F-O1 and F-O2 respectively.

Based on plots from figure 5.4.1, the 3-4 Hz filter seems to exclude a portion of the low-frequency necessary for the inversion. Conversely, the 9-13 Hz filter includes some moderate frequencies which are not needed to build the model. The filter 4-6 Hz and 6-9 Hz filters similarly capture from one well location to other the low-frequency necessary for seismic inversion, so the 6-9 Hz filter was chosen to ensure that no low-frequency content was excluded from the model, taking into consideration that seismic inversion just adds the low frequency below the seismic band. Any frequency above it is discarded in the process.

Figure 5.4.2 shows a panel with a seismic section along F-O1 and all its 4 high-cut filtered scenarios. The display shows the seismic response at particular frequency content. Coherent information can already be seen around 6 Hz.

Once the high cut-filter had been determined, the well logs were filtered and extrapolated over the entire model using a deterministic estimation model (kriging). Figure 5.4.3 shows a comparison between the full-frequency and low-frequency models including horizon and

well logs for AI, Vp/Vs and density on a random section between F-O2 and F-O1.

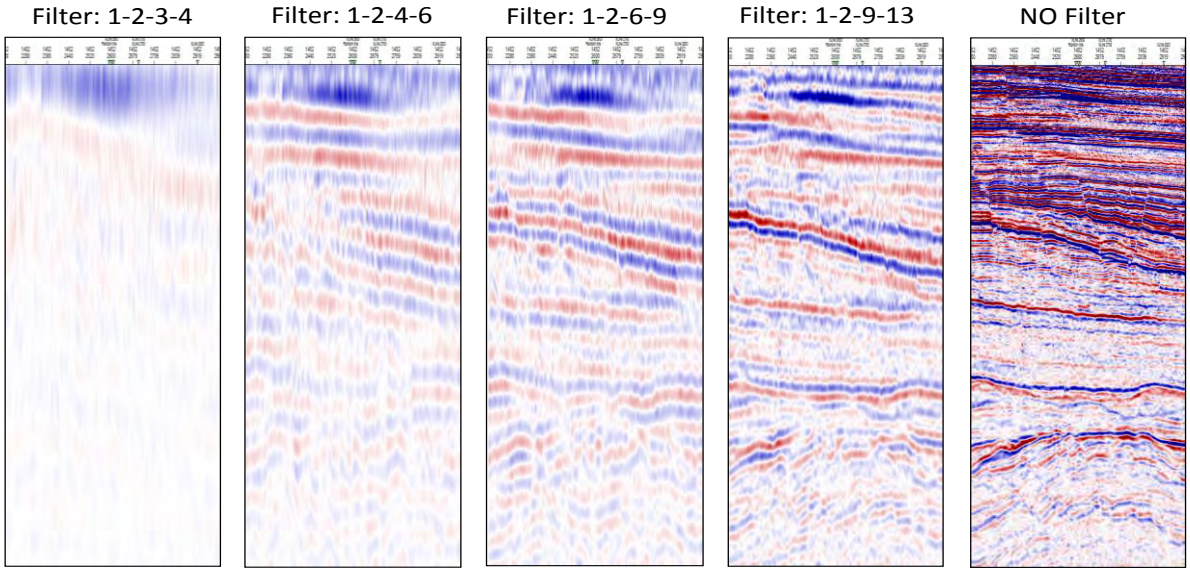

Figure 5.4.2: Multi-seismic panel showing the effect of different high-cut filter on seismic. Consistent data already down to 6 Hz.

5.5 Simultaneous seismic inversion

By definition, simultaneous seismic inversion (SSI) is a pre-stack AVO/A inversion method (Appendix 5.5) that uses multiple offset or angle seismic sub-stacks with their associated wavelets and low- frequency models as inputs in an inversion algorithm. For each partial angle stack input, a unique wavelet is estimated.

The goal of pre-stack inversion is to obtain reliable estimates of P-impedance (AI), S-impedance (SI) or Vp/Vs ratio and density as outputs to help improve discrimination between lithology, porosity and fluid effects.

SSI includes a number of steps addressed in the previous section before running the algorithm. Below is a summary of those steps:

- Seismic data conditioning (QC) at pre and post-stack if needed (section 5.2.1).

-Optimum partial angle stack definition by examining quality at near and far offsets (see section 5.2.2).

-Wavelets extraction for all partial angle stacks at each wells using a deterministic estimation method (Roy White) (see section 5.3).

-Low-frequency modelling using the well logs (acoustic impedance, Vp/Vs ratio and density), extrapolating data along the interpreted horizons (see section 5.4).

The seismic inversion algorithm used in this study is based on a combination of an advanced global search algorithm and a non-linear cost function. The simultaneous seismic inversion (SSI) algorithm uses the advanced global search algorithm to estimate the impedance subsurface model that minimizes a non-linear cost function containing the following terms: RSNR, RALPHA, RSIGMA and R1 (see section 5.2.2)

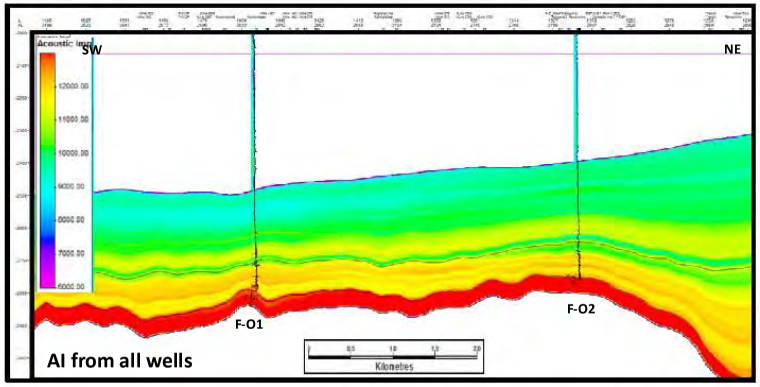

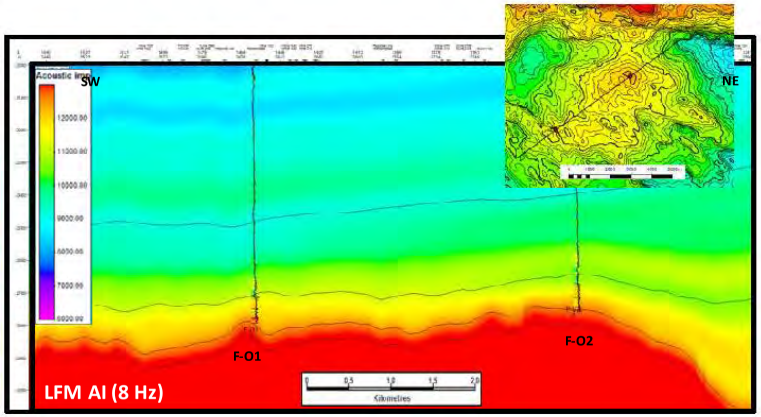

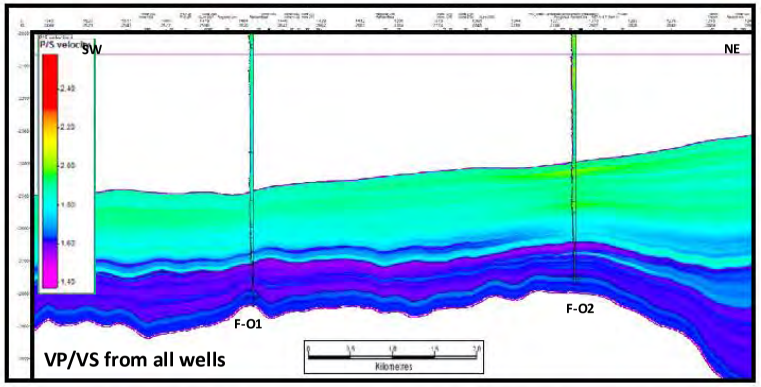

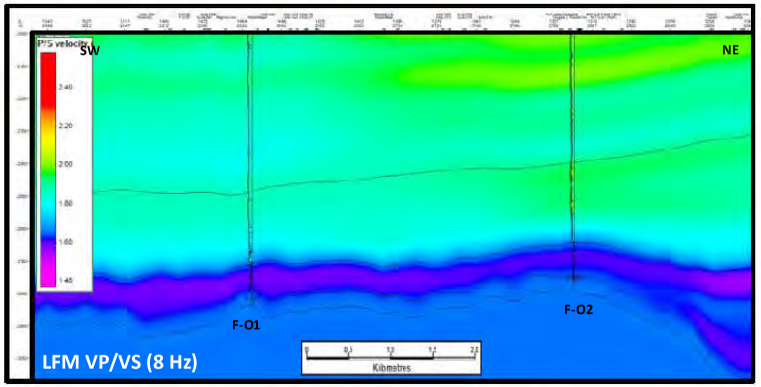

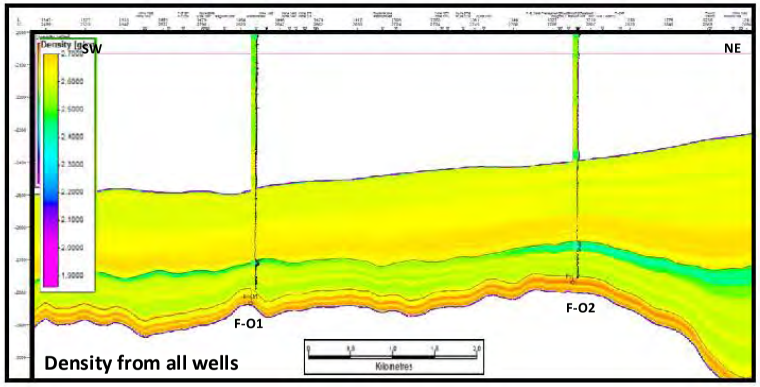

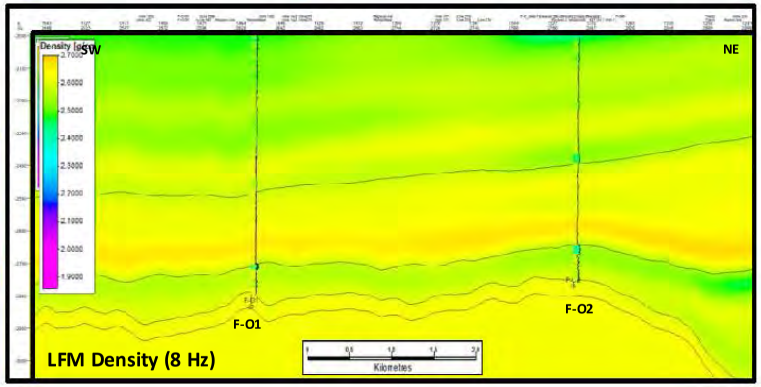

Fig. 5.4.3: Elastic Model versus Low Frequency Model

The inversion algorithm therefore finds a subsurface impedance model which produces a synthetic seismic that approximates the seismic data while also satisfying the other constraints in the cost function, which provide damping of random noise, incorporation of the prior model and correct location of significant reflectors.

The cost function is shown below:

$$E=f\left(\frac{S}{N}\right)\sum(Si-di)^2+f\left(\frac{1}{\sigma horizontal}\right)\sum Ci(Z_{i-}Z_{i+1})^2+f\left(\frac{1}{\sigma prior}\right)\sum(Zi-Zprior)^2+Rthreshold(\#reflectors)$$

where S/N is the user-defined signal-to-noise parameter (RSNR), d_i is the seismic data at sample i, S_i is the synthetic seismic at sample i, $\sigma_{horizontal}$ is the user defined horizontal standard deviation parameter (RALPHA), C_i is the continuity at sample i, Z_i is the impedance at sample i, Z_{i+-1} is the impedance of the four neighbouring samples to sample i, which may be defined using a dip, σ_{prior} is the user-defined standard deviation between the inversion result and the prior model (RSIGMA), Z_{prior} is the impedance of the prior model at sample i, $R_{threshold}$ is the user-defined threshold for significant reflectors (R1) and #reflectors is the number of significant reflectors.

The weighting of the different input partial stacks was set individually in such a way that stacks of uncertain quality, for instance far stacks, were included in the simultaneous inversion, but with a lower weight than the other input stacks. This way, the relevant elastic information in such stacks can contribute to the inversion outcome.

One of the seismic inversion dilemmas lies in the selection of the representative wavelet in each partial angle stack for inversion. Initially, each partial angle stack has six wavelets which come from the same number of wells.

A simple approach to estimate the optimum wavelet for each partial angle stack was implemented in this dissertation. The approach consists in assigning a value to each well wavelet based on a correlation coefficient between synthetic at each well and the seismic trace. The value is used to feed a weighted average expression in which the wavelet that produces the higher correlation is assigned a greater weight and vice versa.

The procedure can be listed as follows:

1.- Correlation coefficient ($CCorr_{11}$) is computed between seismic trace and synthetic using $Wavelet_1$ extracted on $well_1$. This step is repeated for $well_2$, $well_3$ up to complete all wells.

2.-Then the correlation coefficient ($CCorr_{12}$) is computed for $well_1$, which this time involves generating the synthetic trace convolving the reflectivity in $well_1$ with the wavelet (wav_2) extracted in $well_2$. This step is systematically repeated in each well permuting with each other well wavelet. For instance, $CCorr_{32}$ corresponds to the correlation coefficient at $well_3$ using wavelet extracted in $well_2$. This procedure measures how well a wavelet performs when it is used at a different location from where it was extracted.

3.-The metrics (weight) for each well using each other well wavelet and based on the CCorr outcome is defined. It is assumed that the greatest correlation comes when a well uses its own wavelet for the synthetic generation; therefore a value-weight of 1 is assigned to the

top-2 correlation coefficients computed using a wavelet extracted in a different location. If, on the other hand, the correlation coefficients fall in the bottom-2, a null (zero) value is assigned. Finally, the intermediate CCorr value is assigned a weight of 0.5.

4.- All weights estimated for a given wavelet in each well other than the well in which the wavelet was extracted are added. The value represents the weight that a particular wavelet has over all wells. This step is repeated for all wavelets. Finally, each weight is normalized to 100 and used in the equation below to determine an average-weighted wavelet that represents for each partial angle stack, the goodness of fit of each well wavelets (see figure 5.5.1):

$Wav_w = \{(Wav_1 * kw_1)+(Wav_2 * kw_2)+(Wav_3 * kw_3)+....+(Wav_n * kw_n)\}$

where:

Wav_w= wavelet average-weighted for a given partial angle stack

Wav_n= $wavelet_n$ extracted at $well_n$

kW_n= weight factor derived from the sum of all weights estimated for a given wavelet in each well other than the well in which the wavelet was extracted.

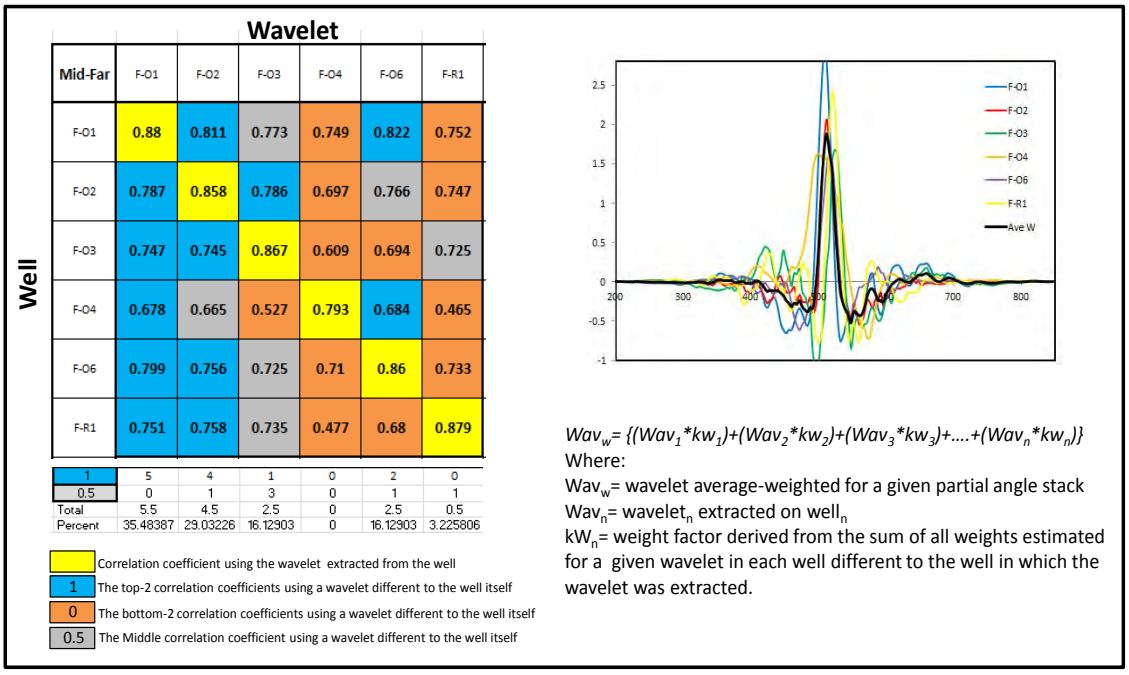

Fig. 5.5.1: Procedure to compute a weighted wavelet per partial angle stack. The mid-far stack was used as example in this figure. The rows represent the wells and the columns the wavelets extracted at each well. In yellow the CCorr value computed when a wavelet extracted from a particular well is used in that well. Blue represents the best 2 CCorr value obtained when a wavelet different than their own well is used in other wells. Conversely, in orange the worst 2 CCorr values.

Figure 5.5.2 shows the wavelets for each well on each partial angle stack overlain with the average-weighted wavelet in black.

The seismic inversion was run (AI, Vp/Vs, density) using the wavelets derived from this approach (see figure 5.5.3-8).

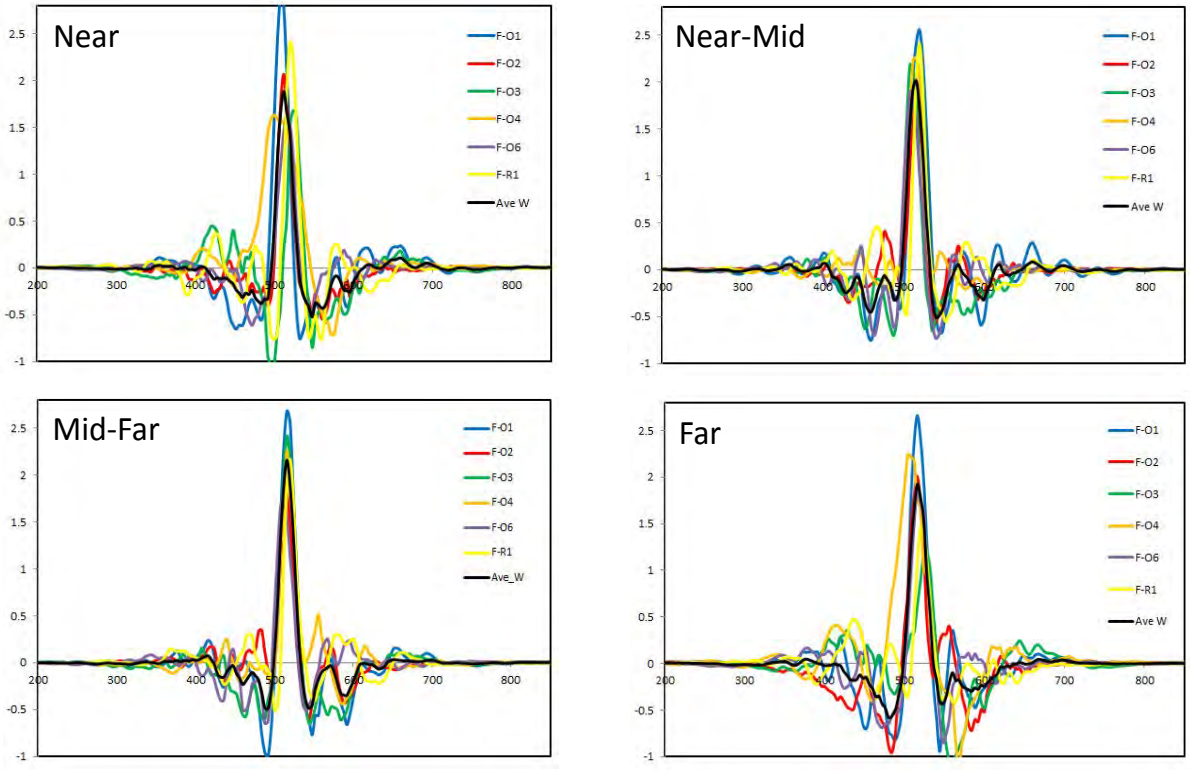

Fig. 5.5.2: Final wavelets extracted at each well for each partial stack. In black the weighted average wavelet representative for each partial stack.

Inversion quality control was performed at the well locations to ensure inversion parameters used for the computation were optimal. The inverted elastic attributes AI, Vp/Vs and density extracted at the well position were compared with the corresponding up-scaled well logs via correlation coefficient (see figure 5.5.9). Moreover, the synthetic seismic traces calculated from the inverted impedance were subtracted from the original seismic traces to quality control the inversion performance in between wells. The resulting "difference volumes" for each partial stack (Error plots) in figure 5.5.10 do not show coherent energy and have low all-over amplitude, which represent the inversion's ability to predict in between wells and in consequence is a way to validate the goodness of selected inversion parameters.

For each angle stack volume (near, near-mid, mid-far, far), traces were fully inverted and layers were computed between the top and the base of the inversion computation window.

The inversion results were also presented using the acoustic impedance (AI), the Vp/Vs ratio and density with displays of:

(a) Random lines passing through well heads (see figures 5.5.11 to 13).

(b) Maps of the attribute (AI, Vp/Vs, density) at reservoir level using a window between 1At1 horizon and a 1At1 ghost surface shifted 25 msec down and using "most of" as extracting method (see figures 5.5-14 to 16).

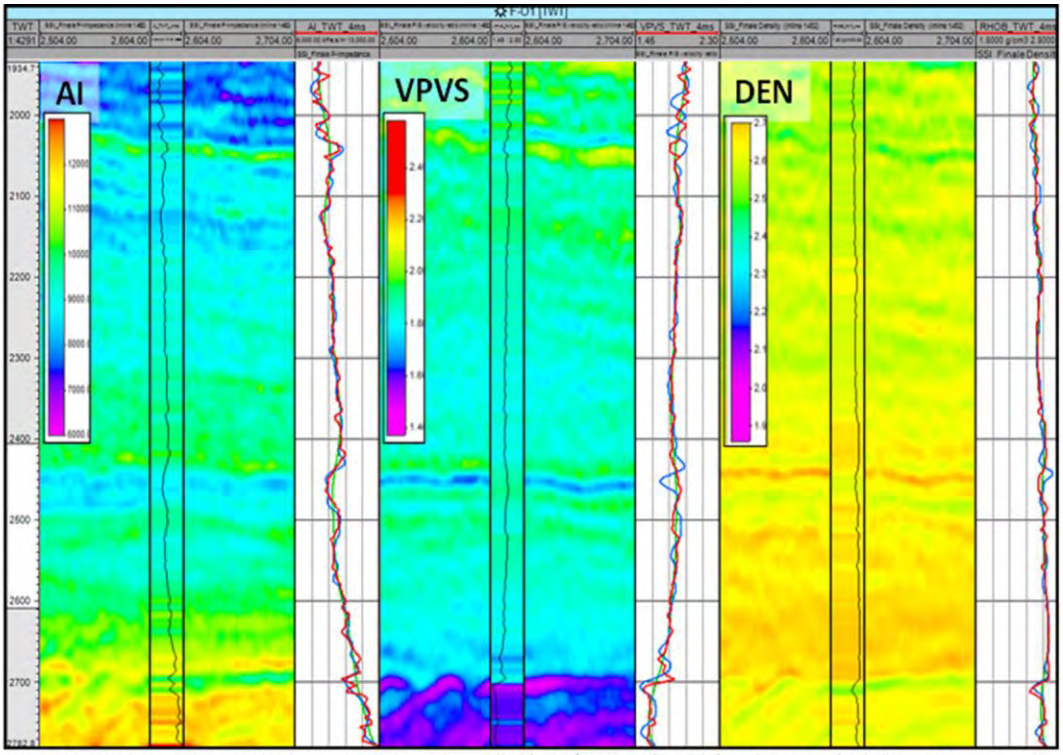

Fig. 5.5.3: Final inversion results for acoustic impedance (left), Vp/Vs ratio (middle) and density (right) on seismic panels with the well trace inserted. The well trace track shows in red the well log up-scaled to seismic resolution, in blue the inversion result and in green the low frequency model at well F-O1.

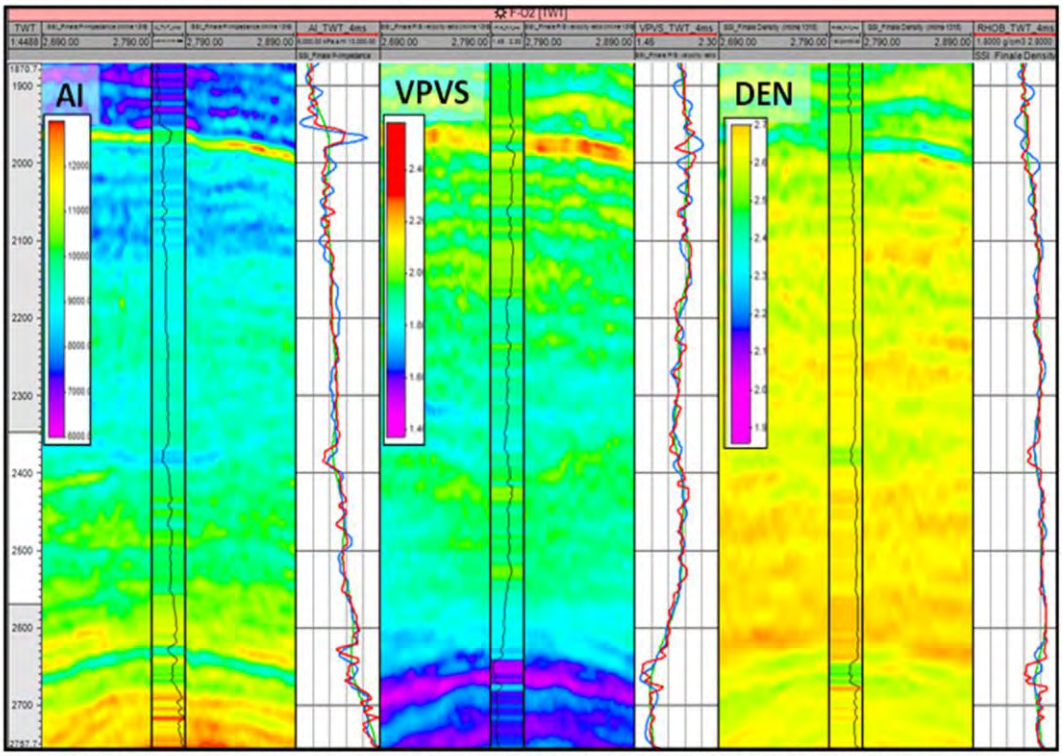

Fig. 5.5.4: Final inversion results for acoustic impedance (left), Vp/Vs ratio (middle) and density (right) on seismic panels with the well trace inserted. The well trace track shows in red the well log up-scaled to seismic resolution, in blue the inversion result and in green the low frequency model at well F-O2.

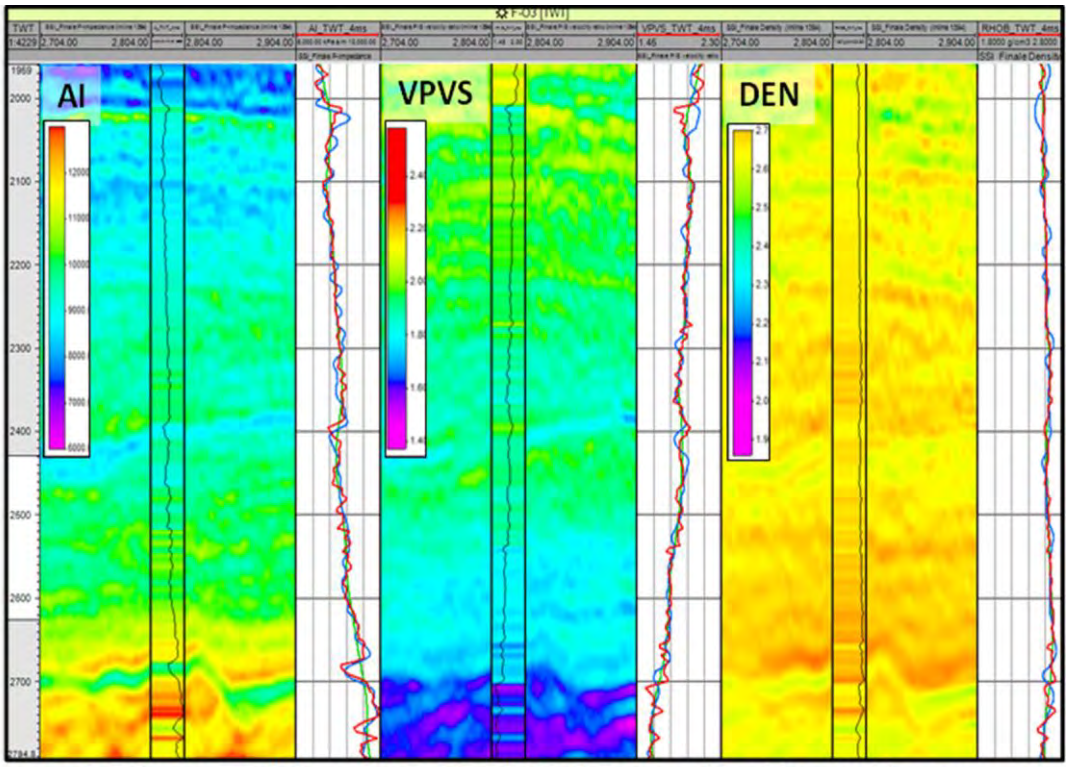

Fig. 5.5.5: Final inversion results for acoustic impedance (left), Vp/Vs ratio (middle) and density (right) on seismic panels with the well trace inserted. The well trace track shows in red the well log up-scaled to seismic resolution, in blue the inversion result and in green the low frequency model at well F-O3.

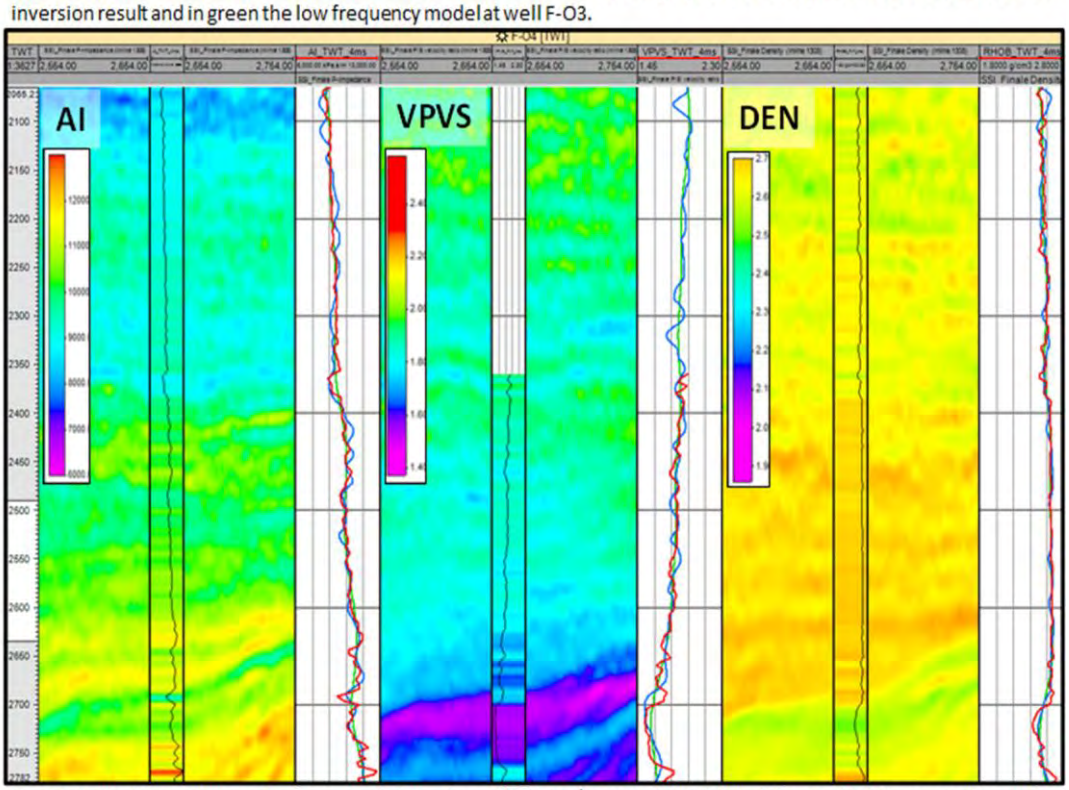

Fig. 5.5.6: Final inversion results for acoustic impedance (left), Vp/Vs ratio (middle) and density (right) on seismic panels with the well trace inserted. The well trace track shows in red the well log up-scaled to seismic resolution, in blue the inversion result and in green the low frequency model at well F-O4.

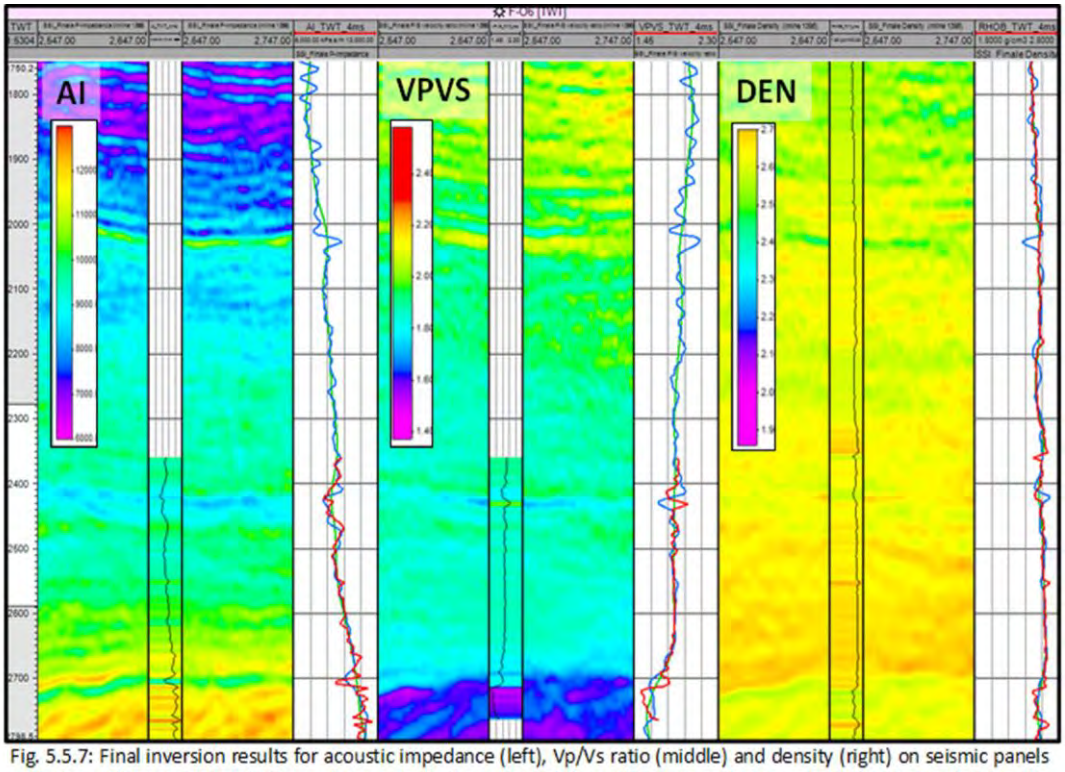

Fig. 5.5.7: Final inversion results for acoustic impedance (left), Vp/Vs ratio (middle) and density (right) on seismic panels with the well trace inserted. The well trace track shows in red the well log up-scaled to seismic resolution, in blue the inversion result and in green the low frequency model at well F-O6.

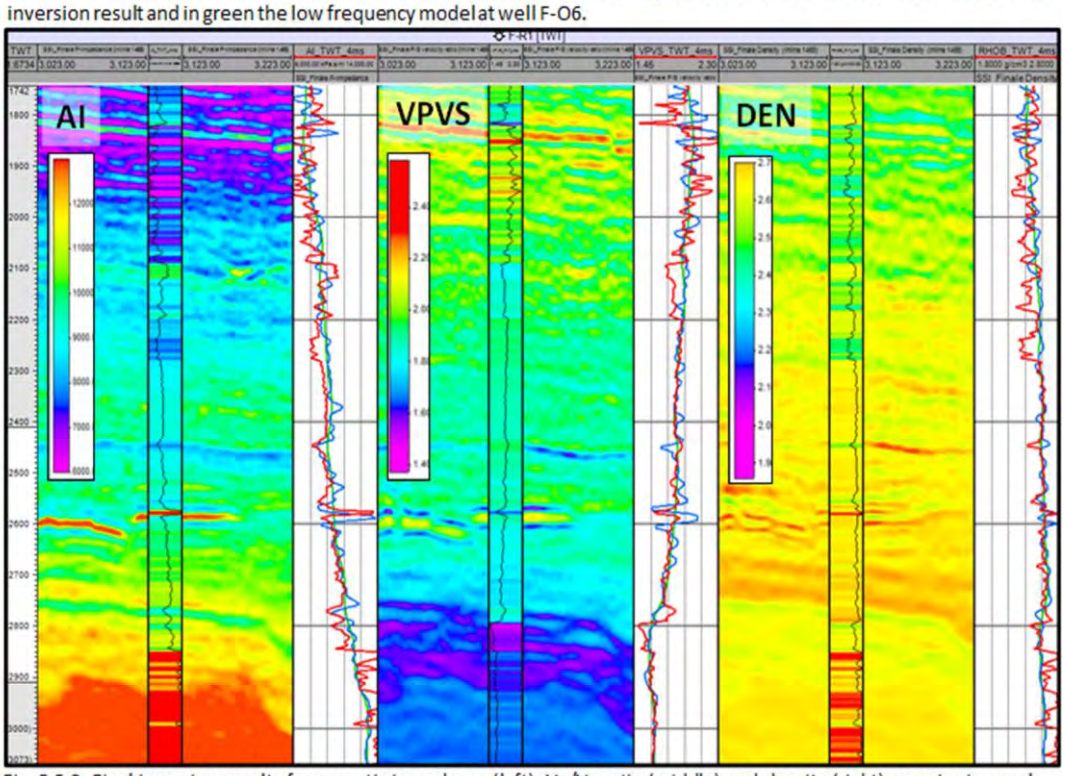

Fig. 5.5.8: Final inversion results for acoustic impedance (left), Vp/Vs ratio (middle) and density (right) on seismic panels with the well trace inserted. The well trace track shows in red the well log up-scaled to seismic resolution, in blue the inversion result and in green the low frequency model at well F-R1.

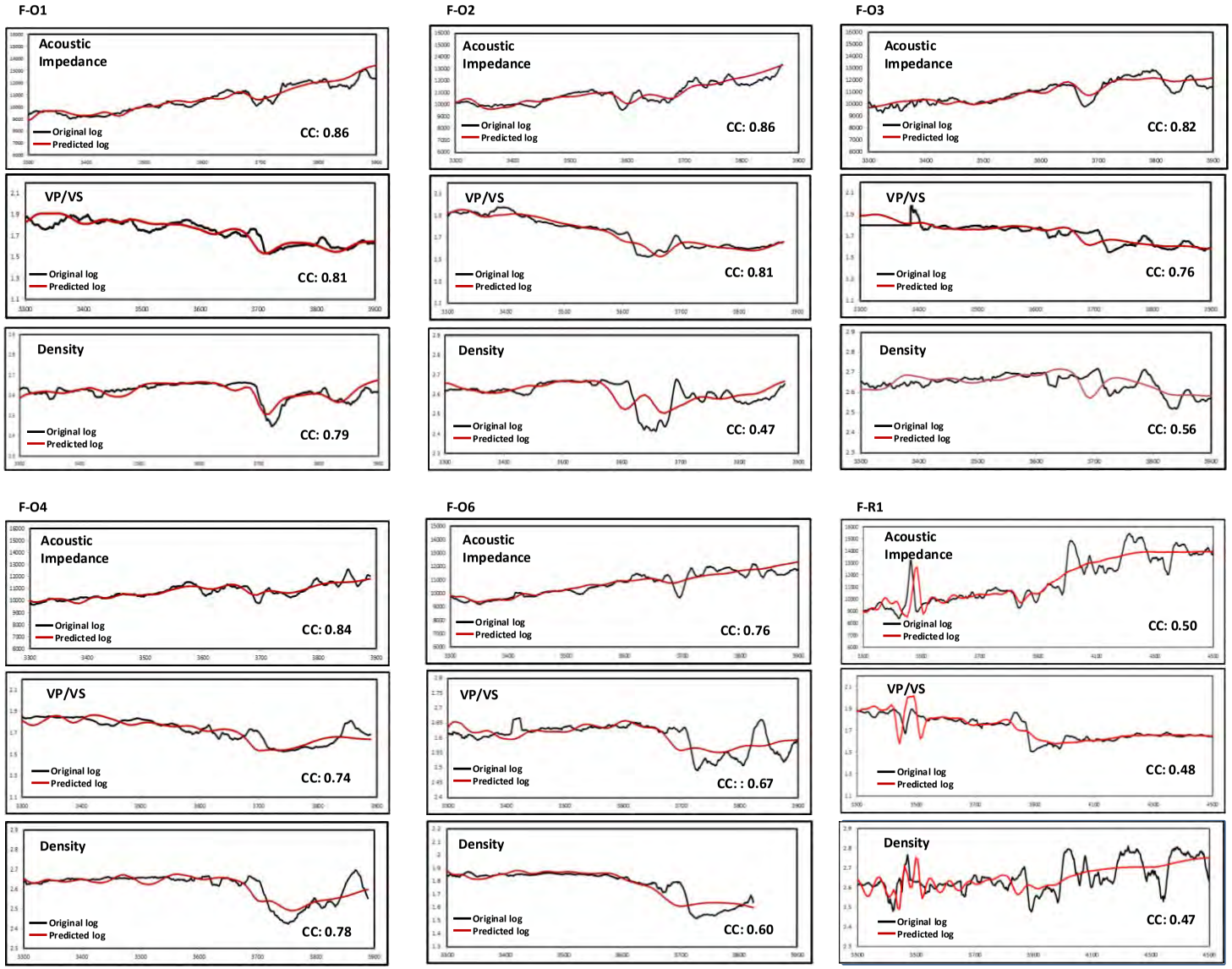

Fig. 5.5.9. Quality control (seismic inversion) / Cross-correlation.

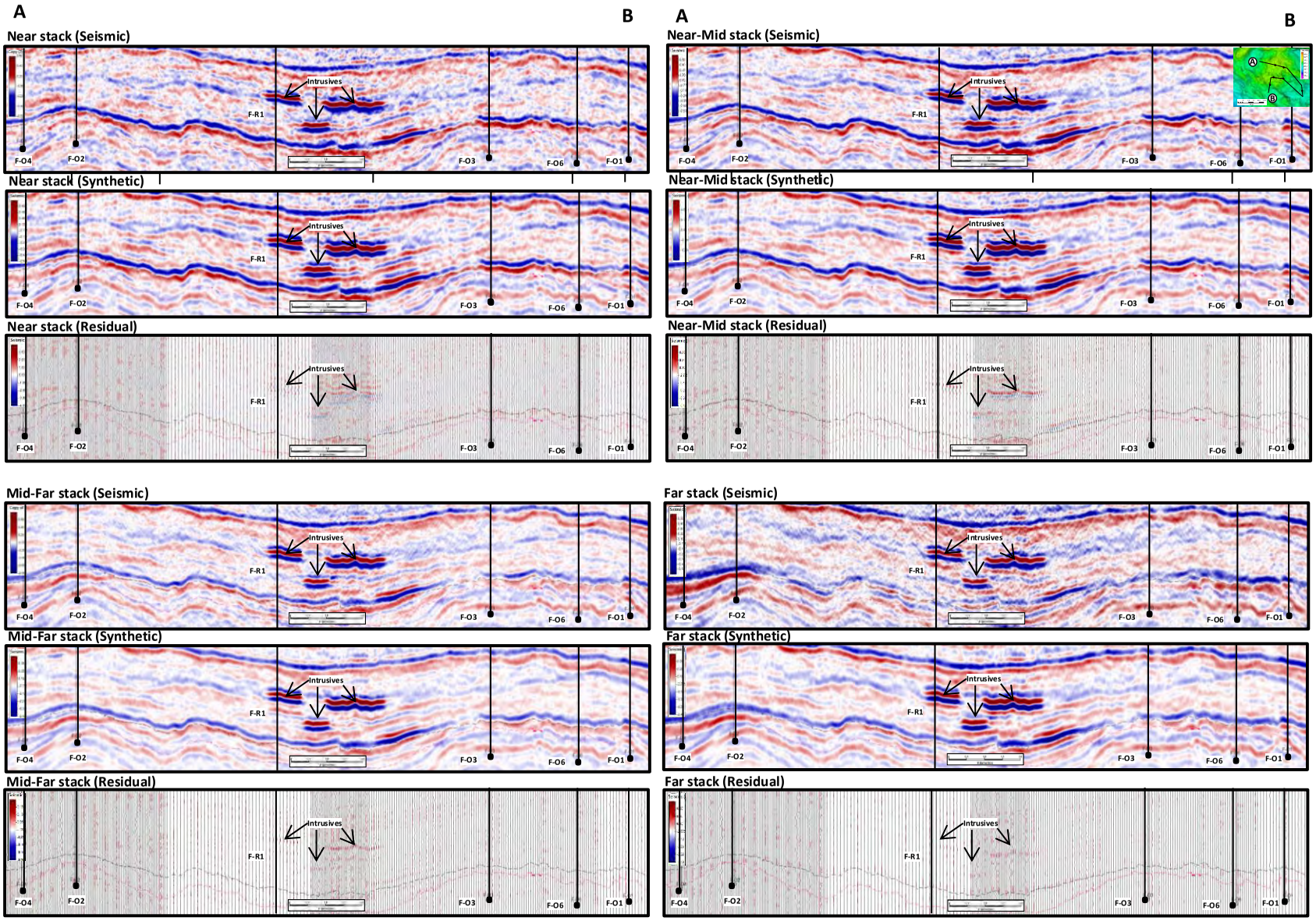

Fig. 5.5.10. Error Plot

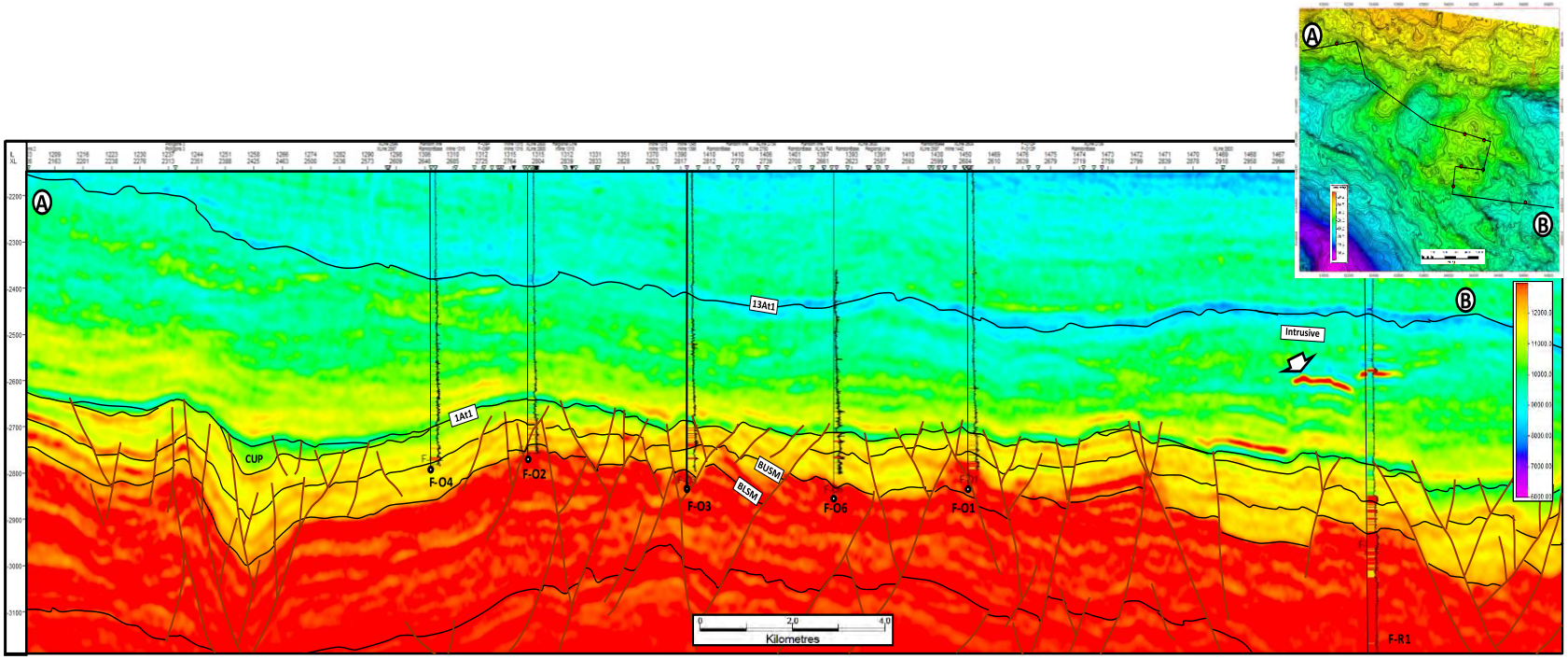

Figure 5.5.11:Random line through the AVO inversion elastic parameter: Acoustic impedance.

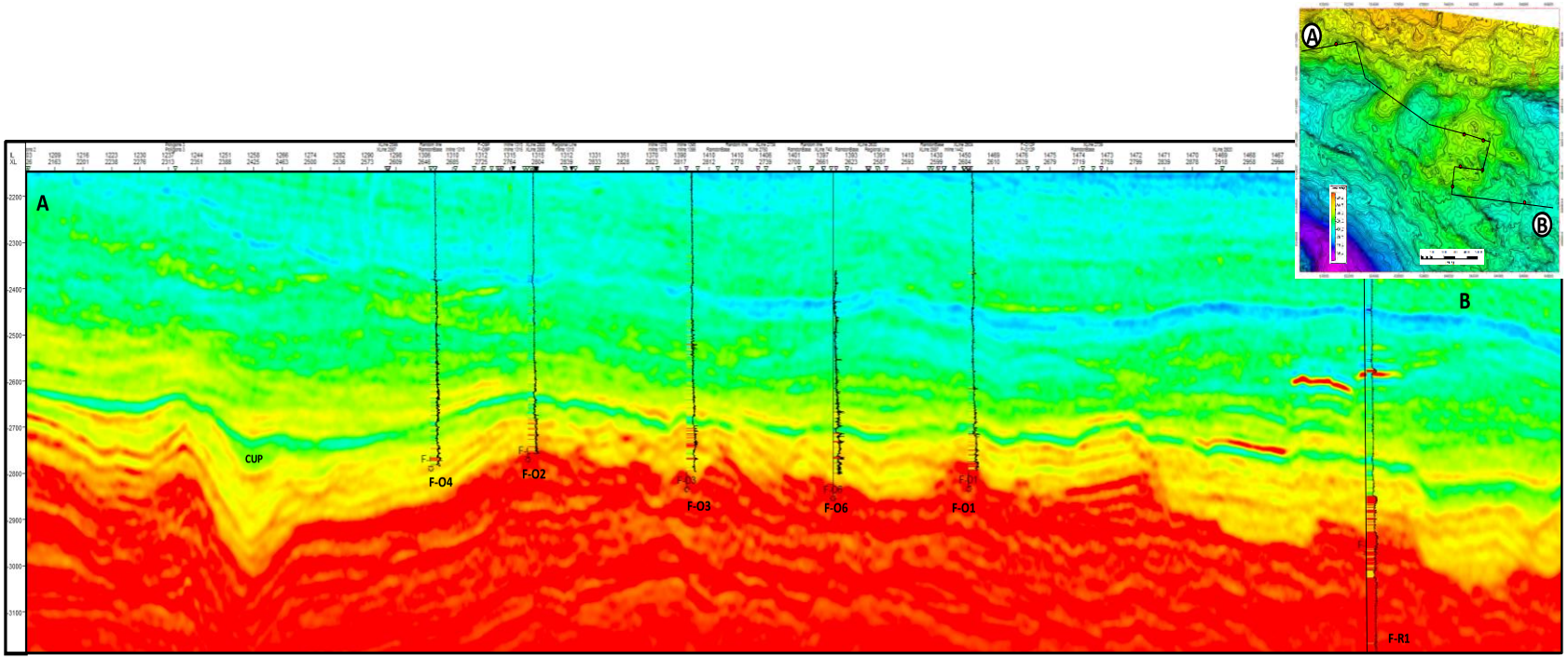

Figure 5.5.12:Random line through the AVO inversion elastic parameter: Vp/Vs

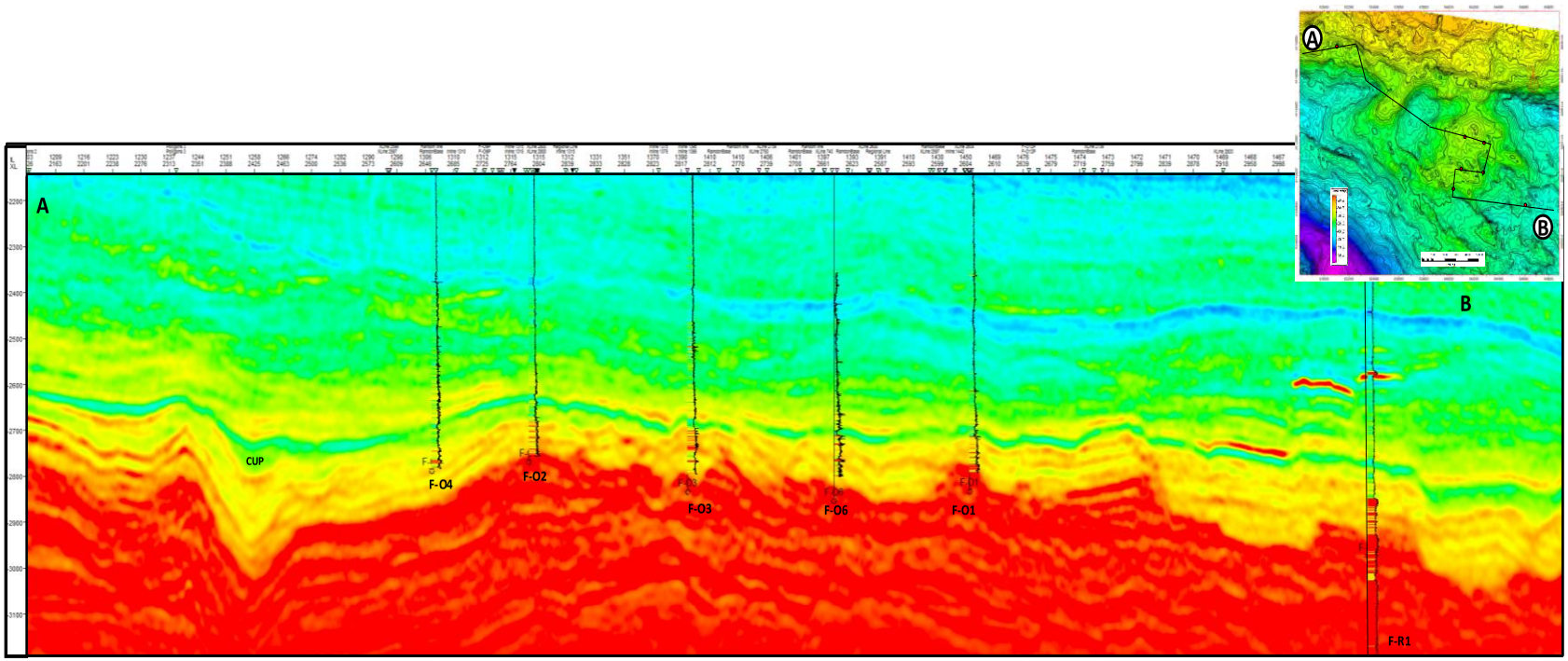

Figure 5.5.13:Random line through the AVO inversion elastic parameter: Density

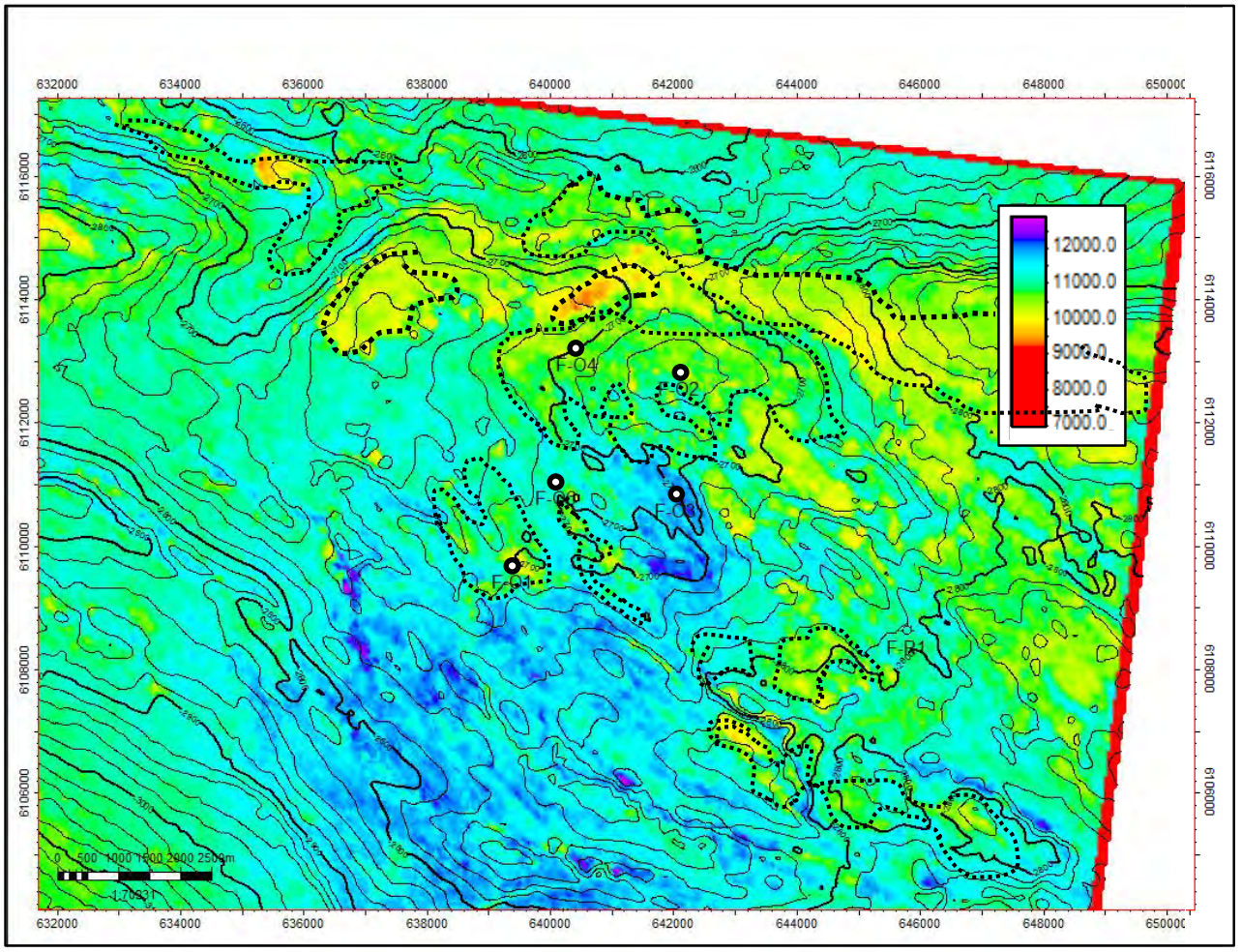

Figure 5.5.14: A. impedance map from surface extracted between top of reservoir (1At1) and a 1At1 ghost surface shifted 25ms down. The method to extract the attribute was "Most of". Dashed polygons represented the zones with attribute values (<11000 m/sec*g/cm^3) more likely to be attributed to good facies (sands with good poro-perm)

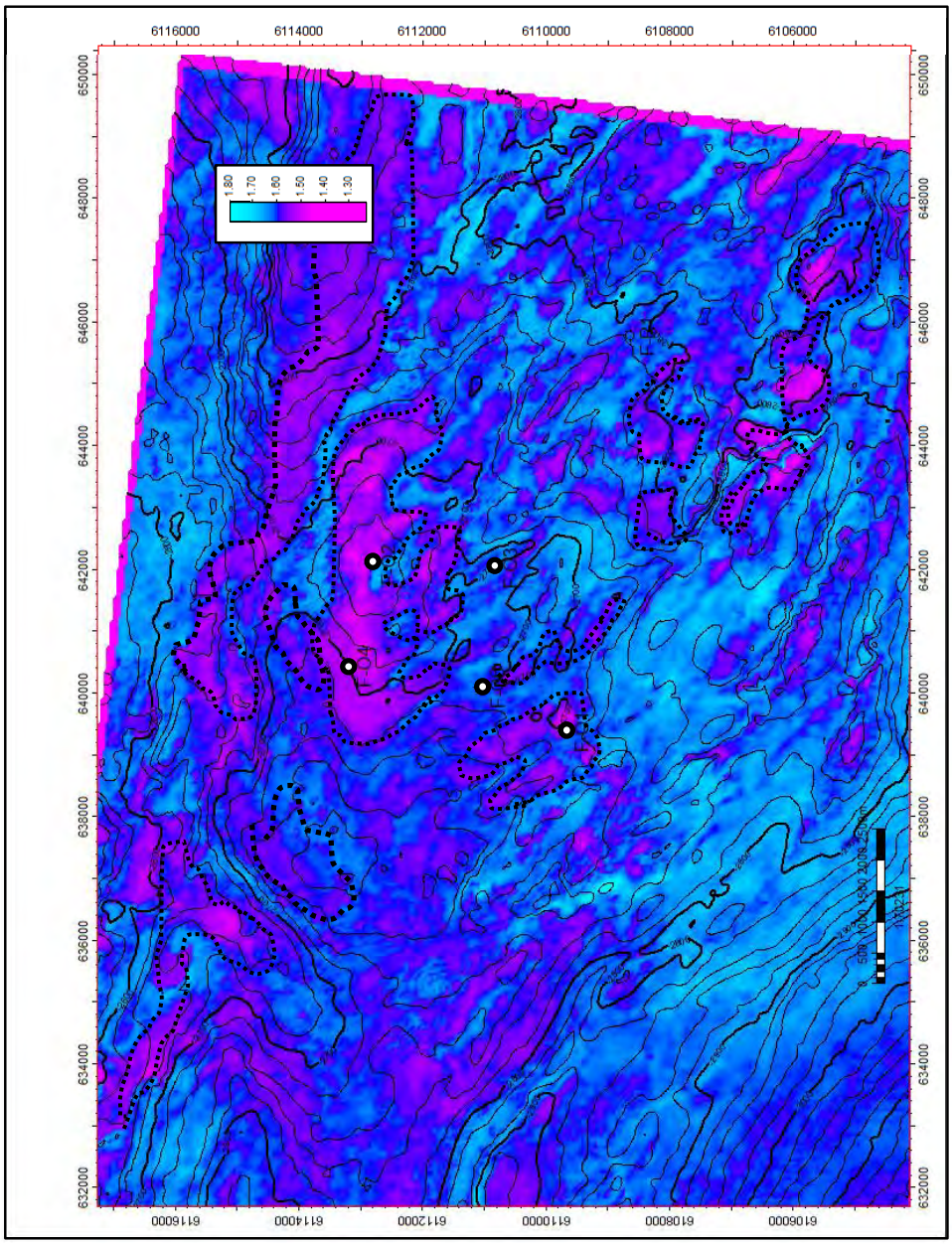

Figure 5.5.15: Vp/Vs map from surface extracted between top of reservoir (1At1) and a 1At1 ghost surface shifted 25ms down. The method to extract the attribute was "Most of". Dashed polygons represented the zones with attribute values (<1.52) more likely to be attributed to good facies (gas-sands).

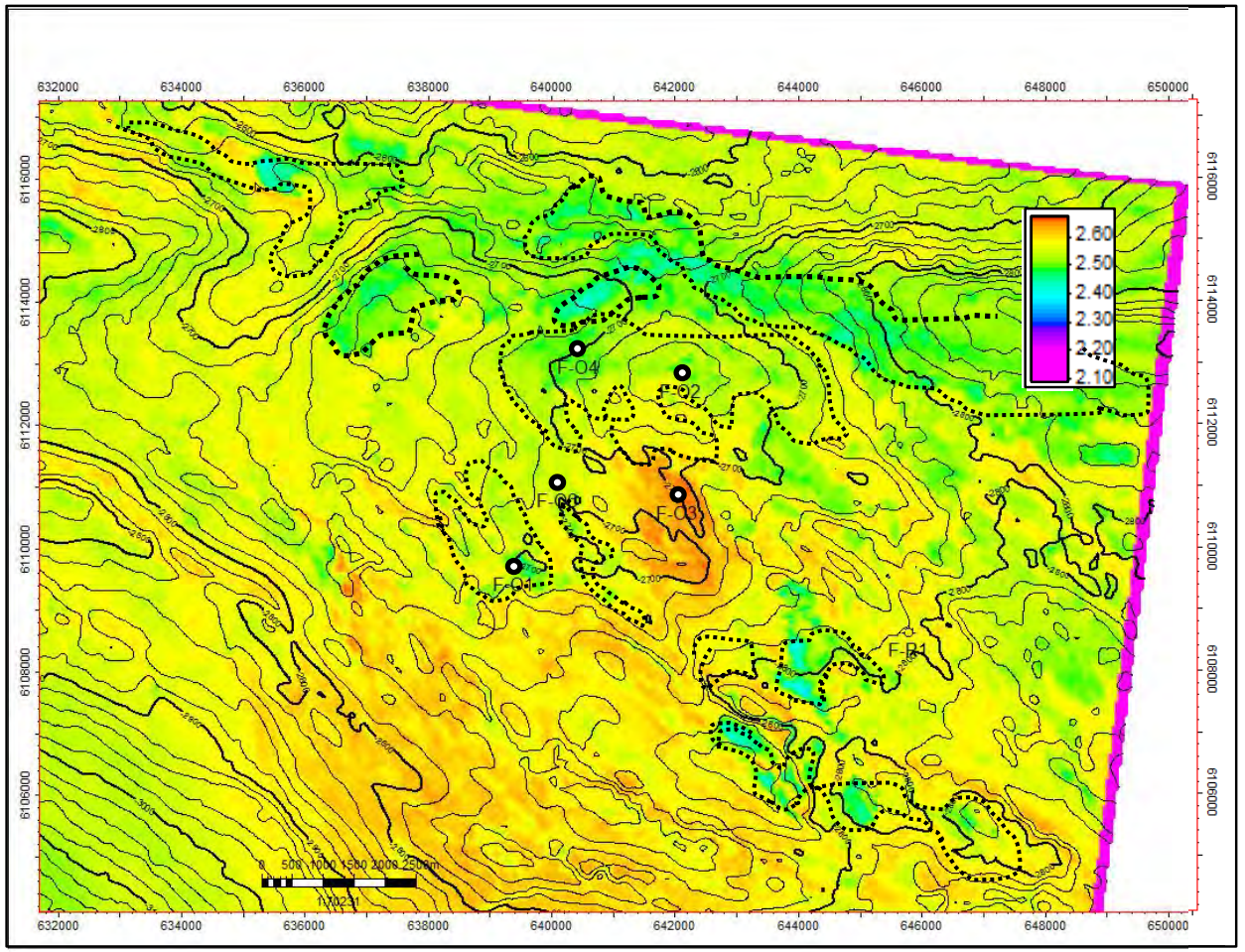

Figure 5.5.16: Density map from surface extracted between top of reservoir (1At1) and a 1At1 ghost surface shifted 25ms down. The method to extract the attribute was "Most of". Dashed polygons represented the zones with attribute values (<2.47 g/cm^3) more likely to be attributed to good facies.

5.6 Discussion and Conclusions

The most important comments, observations and conclusions from this chapter are listed below:

1) – Post-stack relative acoustic impedance inversion was an easy approach to understand how much to expect from further and more sophisticated inversion methods as a predicting tool. The method responds to the porosity variation. However, the result has to be taken with reservation taking into account that these relative seismic inversion techniques are prone to error because no account is taken of the seismic wavelet or calibration to the Earth, or offset variation.

The advantage of using RAI was to obtain a result of relative good information in a very short time, whereas a simultaneous seismic inversion for instance consumes more time.

2) The outer mute mostly worked on the shallow section above the reservoir interval, because most of the NMO stretch effect came from a shallow window (700-1900 msec). The effect of this mute on the reservoir interval was negligible to none. The parabolic radon transform represented a fine algorithm to eliminate some multiples and to suppress noise without distorting primary energy particularly at far offsets (greater than 3000 metres).

The workflow implemented in this dissertation takes care of reflector flattening in an early stage before stacking (Trim statics). The alignment process is intuitive and iterative.

3) Based on the quality of seismic data, more than 3 angle ranges could be generated. If data is good, then the more the angle ranges, the better for the inversion. However, the higher the number of angle ranges, the narrower each angle range, decreasing the S/N ratio of each.

Angles used in the gather were no more than 45 degrees, based in all evidence (CCorr, S/N values and critical angle). This was considered to the optimal cut-off to avoid affecting in a negative way the final inversion results.

Case 3 shows a better S/N ratio than case 1-2 except for the near-mid angles, which consistently show a better CCorr and S/N than any other angle band. But as all cases produce comparable CCorr and S/N values, such parameters are not conclusive when determining the optimal case to be use for inversion.

4) The RSNR is a very sensitive parameter which constrains the inversion results improving Vp/Vs and density outcomes depending on how the value is varied. A higher (6) value for a near-mid angle stack was assigned, taking into consideration the good quality of data. Conversely, a lower value was assigned to sub-stacks with relative poor quality (near and ultra-far).

All partial angle stack cases show similar results for AI in F-O1 and F-O2 regardless of the width and number of the angle bands.

The implementation of ultra-far (case 2) angles does not lead to an improvement in the

Vp/Vs prediction. Furthermore, inverted Vp/Vs in case 3 seem slightly shifted in comparison with the well log.

It was difficult to get a reliable density from inversion overall. In fact, even using 5 partial angle stacks (45-55°), does not, by visual comparison, improve the inverted density or the correlation coefficient. This result could be attributed to the quality of ultra-far stacks. The quality of the 45-55° stacks is lower than that of the other sub-stacks. Events are a bit noisy, less coherent and vary much more laterally.

So ideally, the balance sought is represented by case 1 (four angle stacks). Case 1 offers an optimal trade-off between a reasonable S/N and stacks which are not too wide or too narrow. On the other hand, the maximum stack does not include the ultra-far angles to avoid seismic artefacts and undesired noise in the results.

5) The near-mid partial angle stack (15-25°) was the optimum choice as reference stack for NRM because it had a higher S/N ratio and better resolution than that of 5-15° and 25-35° angle stacks.

The misalignments during post-stack events correction were small when far angles were corrected and negligible for the near angles.

6) The acceptable quality of gathers in general and the performance of seismic conditioning at the pre and post stack stages made the data much more time-coherent, which is well visible on well-to-seismic tie and wavelet extraction regardless of the angle stack.

Overall, the White wavelet extracted from the aligned seismic showed CCorr values higher than 60% and a good S/N ratio. On the other hand, wavelets show a subtle rotation of the phase as is evidenced in phase spectra and wavelet shape plots (see figure 5.3.1-5.3.24).

In conclusion, the wavelets chosen for all angle stacks show a reasonable stability and looked optimal as input for the seismic inversion process.

(7) As was expected, the higher-frequency content is located in the near angles and decreases when angle increases. That observation shows seismic data consistency and quality.

Seismic data lacks an important content of low-frequency, so that low-frequency models were needed in the inversion. Only around 6-7 HZ and below was effectively used from the well data. Hence, the low frequency model is considered good for the AVO/A inversion.

8) To avoid the boundary effects present within approximately 100 msec of the upper and lower edges of the volumes, the low-frequency model and inversion were run in a window from 13At1 surface to a -50 msec ghost of BLSM surface which embedded the reservoir interval sufficiently.

The seismic inversion results can be evaluated and better understood by comparing the inversion results with the seismic data. This comparison demonstrates the increased resolution in the inversion results due to the removal of the effect of the wavelet, and shows how the seismic amplitudes are explained as variations of real physical parameters.

By making a comparison between the inversion results at the well positions with the calibrated logs, it was possible to quality check the resolution improvement of the seismic inversion. Since the high-frequency information in the well logs is not used in the AVO/A simultaneous seismic inversion, this was effectively a blind test.

The predicted absolute acoustic impedance and Vp/Vs ratio from the simultaneous AVO/A inversion show a good tie with the measured data over the USM. Density results were obtained, but they remain unreliable.

Visualization of the inversion results (figures 5.5.14-16) can be used to highlight areas away from existing wells that share the same characteristics as the pay sands at the F-O wells (dashed line).

Chapter 6: Seismic Reservoir Characterization

This chapter describes some seismic reservoir characterization techniques that extensively use inverted data (AVO inversion) or AVO attributes (intercept and gradient) and/or rock physic models for an effective delineation of gas-sand zones and differentiation between gas sands and water sands.

It also highlights the value and versatility of inverted and rock physics data to characterize a low poro-perm reservoir.

Four reservoir techniques were chosen to characterize the F-O reservoir. A detailed description of each method is presented below.

6.1 3D AVO cross-plotting

Amplitude variation with offset or AVO is the general term for referring to the dependency of amplitude with the distance between the source and receiver (the offset). AVO can also be known as amplitude versus angle AVA by defining the offset as a function of the angle of incidence.

It is common practice to cross-plot AVO attributes in a two-dimensional domain in order to look for hydrocarbon anomalies, on the assumption that the attributes for water-saturated sandstones and shales follow a well-defined “back-ground” trend. The most common type of AVO cross-plotting is the intercept (A) versus gradient (B) cross-plot.

A novel approach is introduced by cross-plotting A and B in a three-dimensional domain, and isolating the expected hydrocarbon seismic response using a 3D geobody extraction and visualization technique based on opacity threshold values.

As inputs, the workflow uses the A and B AVO volume attributes and the understanding of rock behaviour, in terms of an A-B dimensional space gleaned from the rock physics forward modelling. The AVO cross-plotting technique is summarized step-by-step as follows:

1.- The linearized Aki-Richards equation is used to extract intercept (A) and gradient (B) attributes from seismic data (see appendix 6.1).

The A and B attributes computation involves converting from offset to angle and fitting a regression line to the amplitude picks as function of the sine of the angle squared. The pick amplitudes are extracted at all times and 3D velocities are used for angle calculation.

Regression curves are then calculated to give A and B values for each time sample. However, in the case where A and B are unknown, the cross-plot can even be carried out with an approximation of the dataset by using the near angle stack as the intercept volume (A) and gradient volume (B) by subtracting near angle stack from far angle stack.

2.- Data (A and B) is normalized before cross-plotting, by inspection of its ranges. For instance, the gradient is normalized by using the expression Gradient

Normalized=Gradient/SCALAR (where scalar is not necessarily the end-member, but a number that results in a histogram with about 95% of the data between -1 and 1). The procedure is repeated with the intercept volume.

3.- Once intercept and gradient volumes have been normalized, the window for cross-plotting analysis is computed. For the purpose of this exercise a horizon/surface window was chosen (see section 2.3.1). The window was calculated using volumes (A and B) and horizon 1At1 and a BLSM horizon (ghost) as top and bottom respectively to constrain the seismic (see figure 6.1.1).

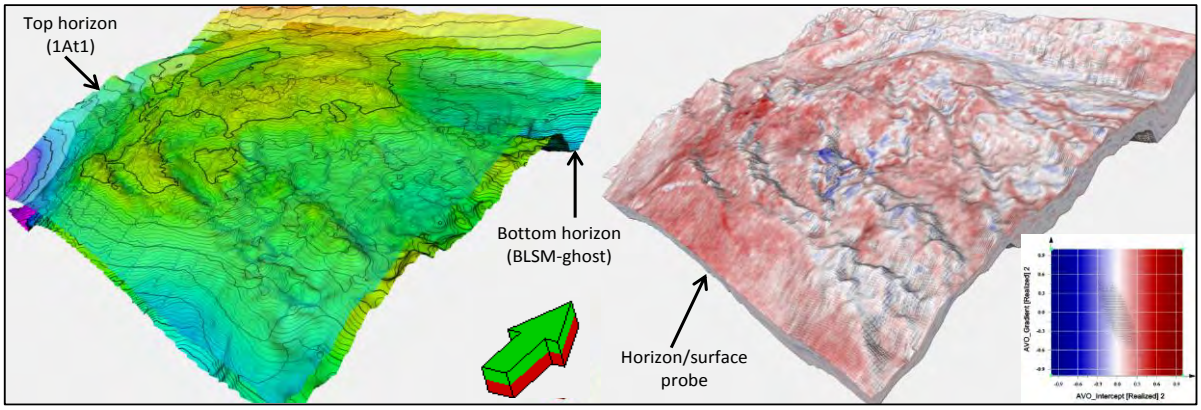

Figure 6.1.1: Horizon/surface window generated using horizons 1At1 and a 50 msec shifted down BLSM (left). The sculpted volume color-coded with the AVO intercept attribute on the right.

4.-Data contained in the window is visualized in a 2D plot to reproduce the standard A-B AVO cross-plot, using seismic data (see figure 6.1.2).

5.- An opacity filter is defined to show only the seismic data that contains the correct combination of intercept and gradient attributes equivalent to good rock-fluid sands. The filter removes or makes 100% transparent all which was outside the filter (polygon). The polygons (filter zone) corresponding to good facies were defined based on AVO classes. However, from the rock physics analysis it is known that there was not a unique AVO class that is representative of the reservoir. In fact, different AVO responses can be obtained depending how the in situ conditions are perturbed.

A colour was assigned to each filter zone to distinguish from one class to another. For instance, navy blue to class I, red to class II-IIp and yellow to class III (see figure 6.1.3).

6.- Once AVO anomalies have been isolated, the exercise is reduced to manual extraction of sample objects (voxels) from the seismic (geobody) that satisfy the prior A-B condition and converting them into a 3D grid discrete property, where the anomaly is colour-coded red and the background in grey.

The geobody extraction depends on the voxel connectivity, i.e. the continuity of the seismic anomaly throughout the 3D domain. The voxel tracking algorithm looks at all the faces, edges, or corners of the voxel cube and check the connectivity threshold condition before including a new voxel in the geobody.

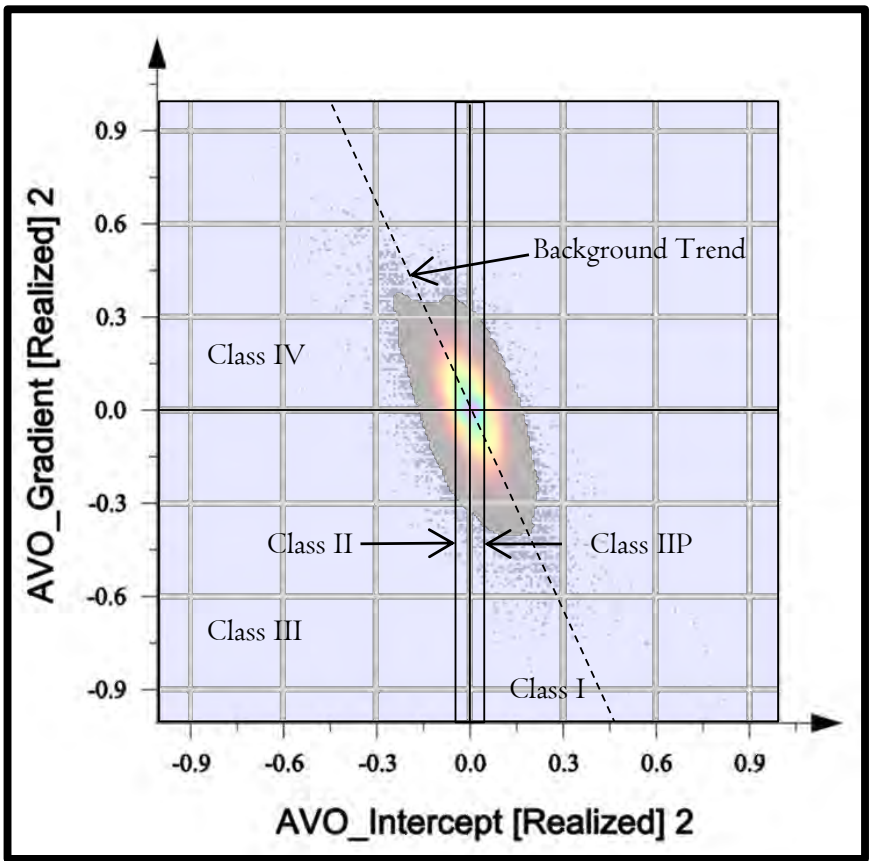

Figure 6.1.2: A-B AVO cross-plot using seismic data from the window domain. AVO classes based on the classification scheme of Rutherford and William were superimposed on the cross-plot.

Sometimes the extracted geobody is greater than expected, so trimming is required in order to clean edges on the geobodies and to remove those that have a negligent size before sampling them into a grid (see figure 6.1.4).

7.- The last step is to display the geobodies with other geological data (horizons, faults, wells, etc) so as to facilitate the identification of new prospective zones in a spatial relation with the geological framework . Figure 6.1.5 shows a random section intercepting each of the wells with the extracted geobodies in red.

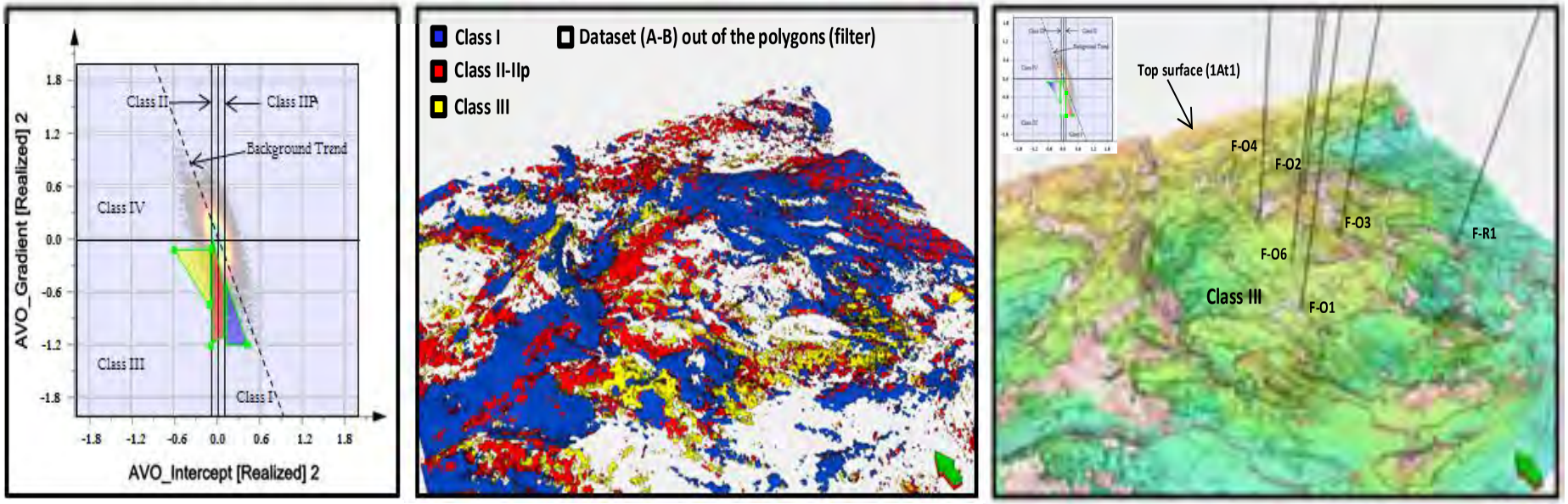

Figure 6.1.3: Polygons in the cross-plot (left) represent good reservoir facies defined based on the rock physics analysis observations. On the left, the polygons (filters) superimposed on AVO cross-plot and color-coded with a distinctive colour to differentiate between one AVO class to the another. For instance, blue for the zone associated to a class I, red for class II-IIp and yellow for a class III. In the middle a 3D view of data after filters were applied which show each AVO class distribution throught the area of interest. In the right, the 3D view with the anomalies associated to the good facies colour-coded with AVO-intercept attribute and the top of the reservoir (1At1) surface in opacity-mode and key-wells superimposed as a geographical reference.

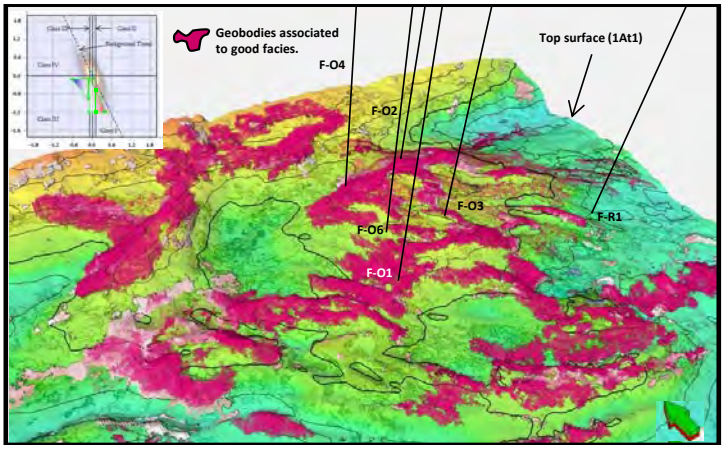

Figure 6.1.4: 3D view of window area showing seismic anomalies after the filter is applied and colour-coded with intercept (A) attribute. The seismic anomalies once extracted (geobodies) in purple and sculpted onto them.

6.2 Rock physics templates (RPTs)

Rock physics templates were first introduced by Ødegaard and Avseth (2004) as a tool-box to assist geoscientists with the interpretation of lithology and pore fluid using well log data and elastic inversion results.

Rock physics templates are based on rock physics modelling. A RPT is a collection of templates or curves that cover all possible "what if" pore fluid-lithology-porosity scenarios in one graph as a function of elastic properties.

Once RPTs have been calibrated with well-log data they can be used for direct and automated classification of any elastic property pair (for instance: acoustic impedance-Poisson's ratio) into a rock property pair (litho-porosity or litho-pore-fluids).

The procedure implemented in this dissertation for the generation and use of RPTs is described below.

1.- A rock physics model (intermediate stiff model for sand and unconsolidated (soft) model for shale) representative of the deposition and diagenetic of the study area in combination with Gassmann fluid substitution were used to calculate and compile a catalogue/atlas of templates for all the pore fluid-litho-porosity scenarios (RPTs).

Once a rock physics model had been defined, the procedure was reduced to building templates by perturbing the fluid content, porosity and mineralogy to as many possible scenarios as were expected for the area.

In accordance with cross-plot results to separate rock properties (chapter 4), neither Lambda*Rho vs. Mu*Rho nor AI vs. PR could provide a significant discrimination one over the other between rock properties cases at seismic resolution, ie, both domains provide equivalent separation. The RPTs were defined in the acoustic impedance vs Poisson's ratio domain, taking into accounts that the density volume does not have the same quality and reliability as the acoustic impedance (AI) and Vp/Vs volumes (section 4.4 & 5.5).

2.- The well log data can be used to verify the validity of the selected RPTs. RPTs can be re-calibrated by adjusting the original parameters by trial and error until an accurate theoretical rock physics model is obtained, if required.

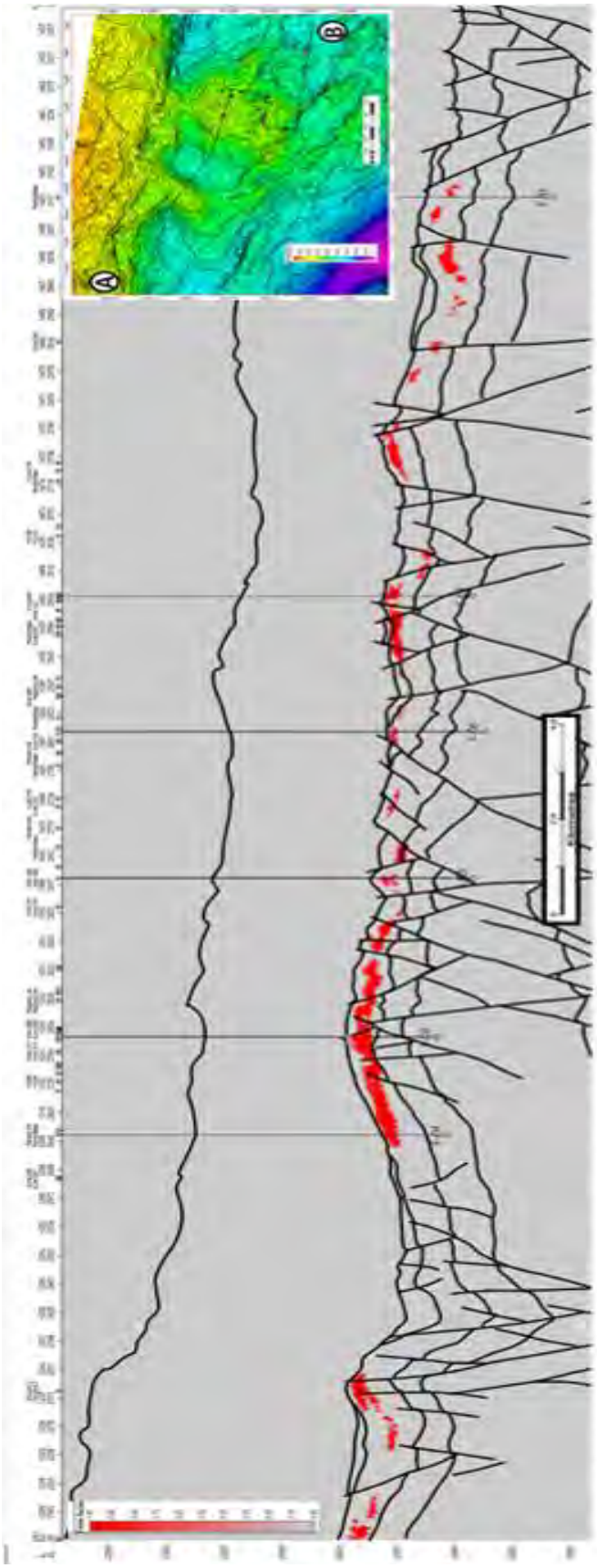

Figure 6.1.5: Random section displaying in red AVO anomalies identified in the cross-plot (intercept-vs-gradient) as good facies and converted in a 3D grid discrete property.

Figure 6.2.1 shows the cross-plot (acoustic impedance vs Poisson's ratio) for well F-O2, superimposed onto the RPT generated using the rock physics model built in section 4.2. It includes porosity trends for different lithologies in the dashed black lines. The black shale trend line represents pure shale while the blue sand trend line represents quartz sand filled with 100% water. Increasing gas saturation was simulated using Gassmann. The red line represents a clean 100% gas filled quartz sand.

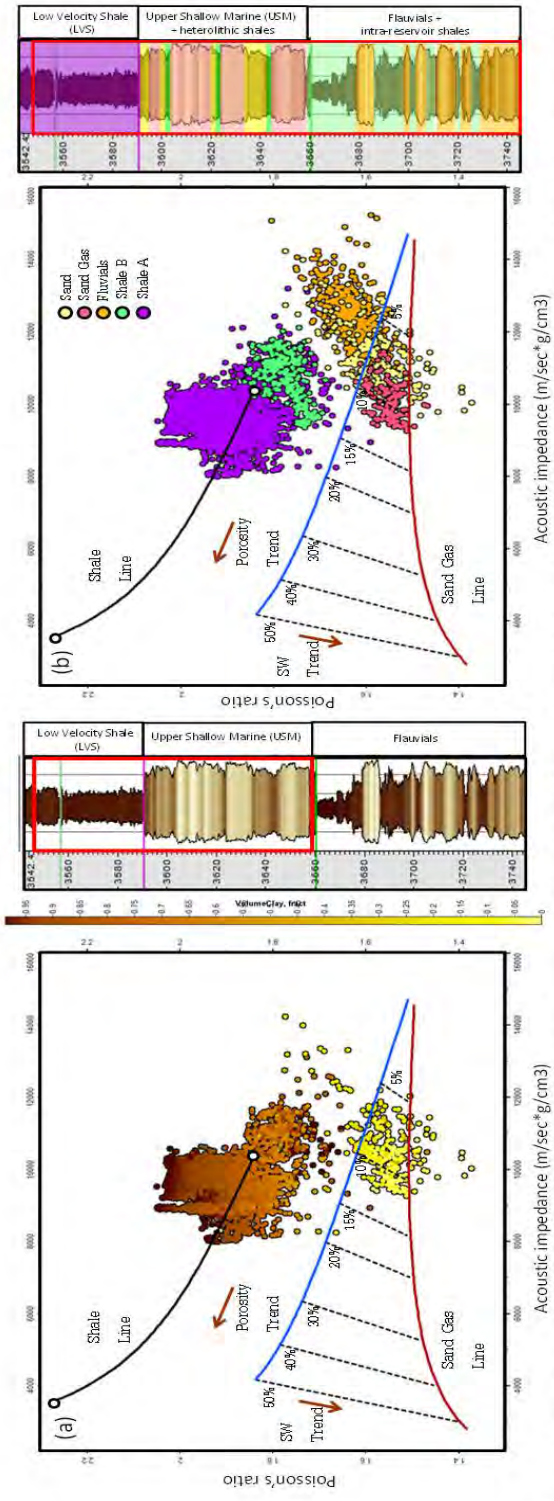

Figure 6.2.1: On the left (a), a cross-plot (acoustic impedance vs Poisson's ratio) from F-O2 well data confined to the reservoir (USM) and LVS interval (red rectangle) and colour-coded with Vclay. Rock physics templates are superimpose on it. (b) shows the cross-plot, but including the transition marine sequence (fluvials) and color-coding by facies.

3.- In order to incorporate seismic inverted data into the RPT, it was necessary first to transform the inverted Vp/Vs volume into Poisson's ratio. However, Poisson's ratio or Vp/Vs could be used interchangeably, because both elastic properties depend exclusively on p-wave and s-wave velocities and correlate perfectly. Figure 6.2.2 shows a random Poisson's ratio section intercepting each of the wells and the cross-plot (Vp/Vs vs Poisson's ratio) with the polynomial trend superimposed.

4.- A new horizon/surface window was generated, but this time populated with acoustic impedance and Poisson's ratio volumes (figures 5.5.11 and 6.2.2). The inverted data is visualized in a 2D cross-plot and the RPTs were superimposed. Inverted data is displayed in a density view mode plot (see figure 6.2.3).

5.- Facies zones were defined by manual picking in the acoustic impedance versus Poisson's ratio cross-plot using the RPTs trends lines as a guideline. The facies zones were categorized in (1) litho fluid-content and (2) litho porosity. The litho fluid-content zones were classified in 3 sub-zones: shale (brown), water-sand (blue) and gas-sand (red). The litho porosity zones were classified in 6 sub-zones depending the lithology and porosity as follows: shale(brown), poro-sands lower than 5% (blue), poro-sands between 5% and 7% (light green), poro-sands between 7% and 10% (yellow), poro-sands between 10% and 15% (orange) and poro-sands greater than 15% (red).

Logs were color-coded according with the zones defined in the cross-plot with the RPTs (see figure 6.2.4).

6.- Each zone covers a 2D population space of sample-inverted data representative of a facies. The population is colour-coded in accordance with the zones and converted into a 3D grid seismic property. The final result is 2 litho facies volumes: a litho fluid-content and litho porosity (see figure 6.2.5).

7.- The facies volumes were used to interpret/classify the observed trends and characteristics in the elastic inversion results. The facies were screened through the entire survey in conjunction with additional geological data (horizons, faults, wells, etc.) to search for new prospective zone and to validate the results. Figures 6.2.6a and 6b show random sections for each facies volume intercepting each of the wells.

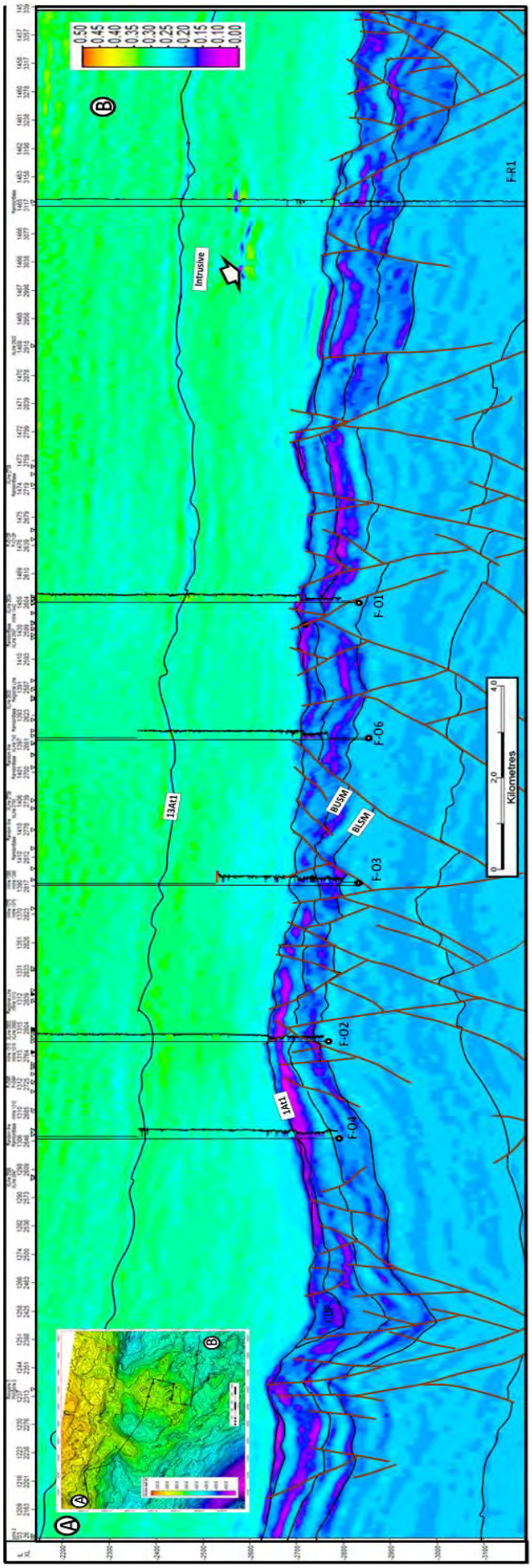

Figure 6.2.2: Random section through the Poisson's ratio property obtained from the Vp/Vs inverted volume..

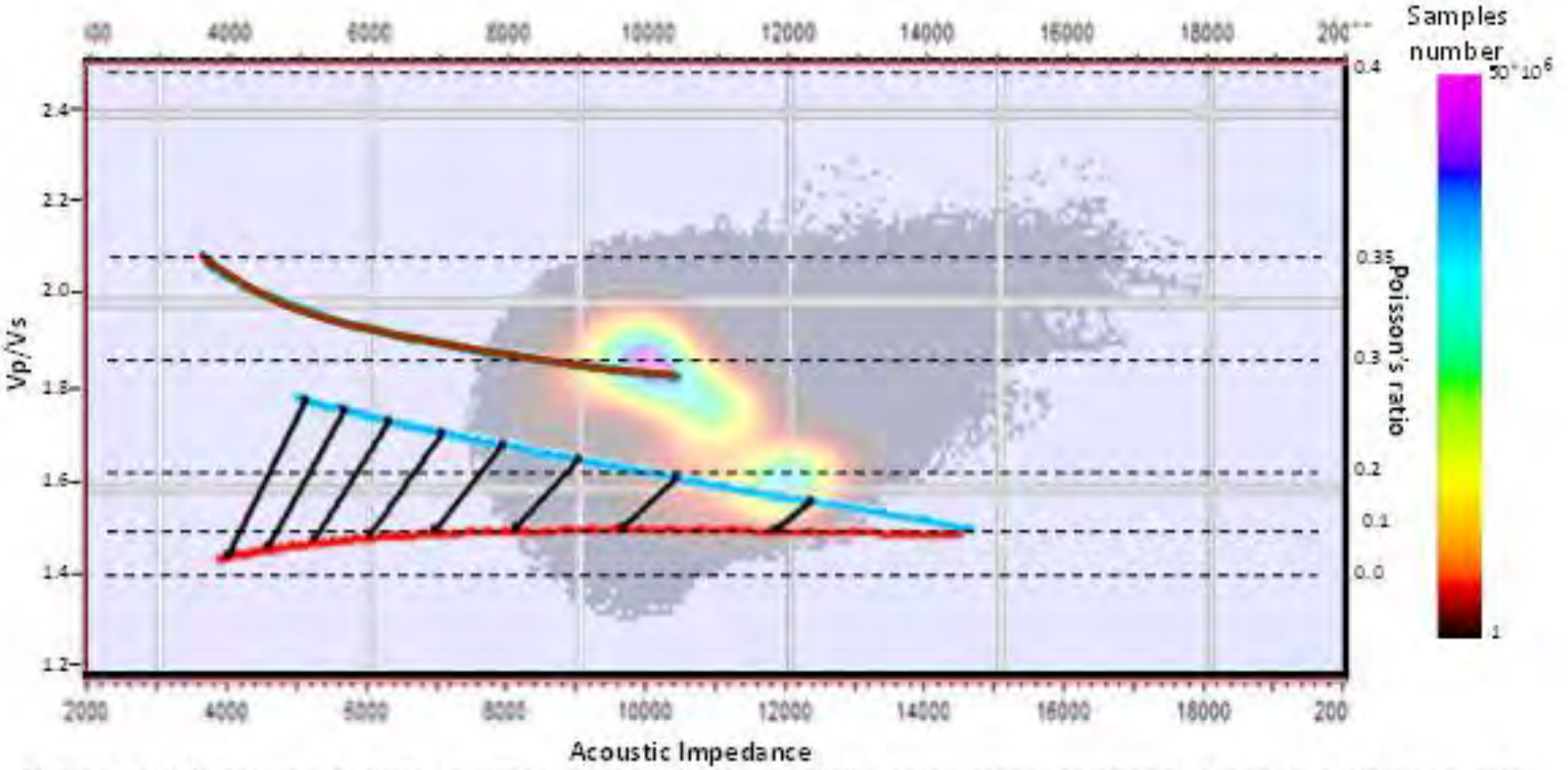

Figure 6.2.3: Inverted data is cross-plotted and the RPT were superimposed. Data is displayed in a density view mode plot

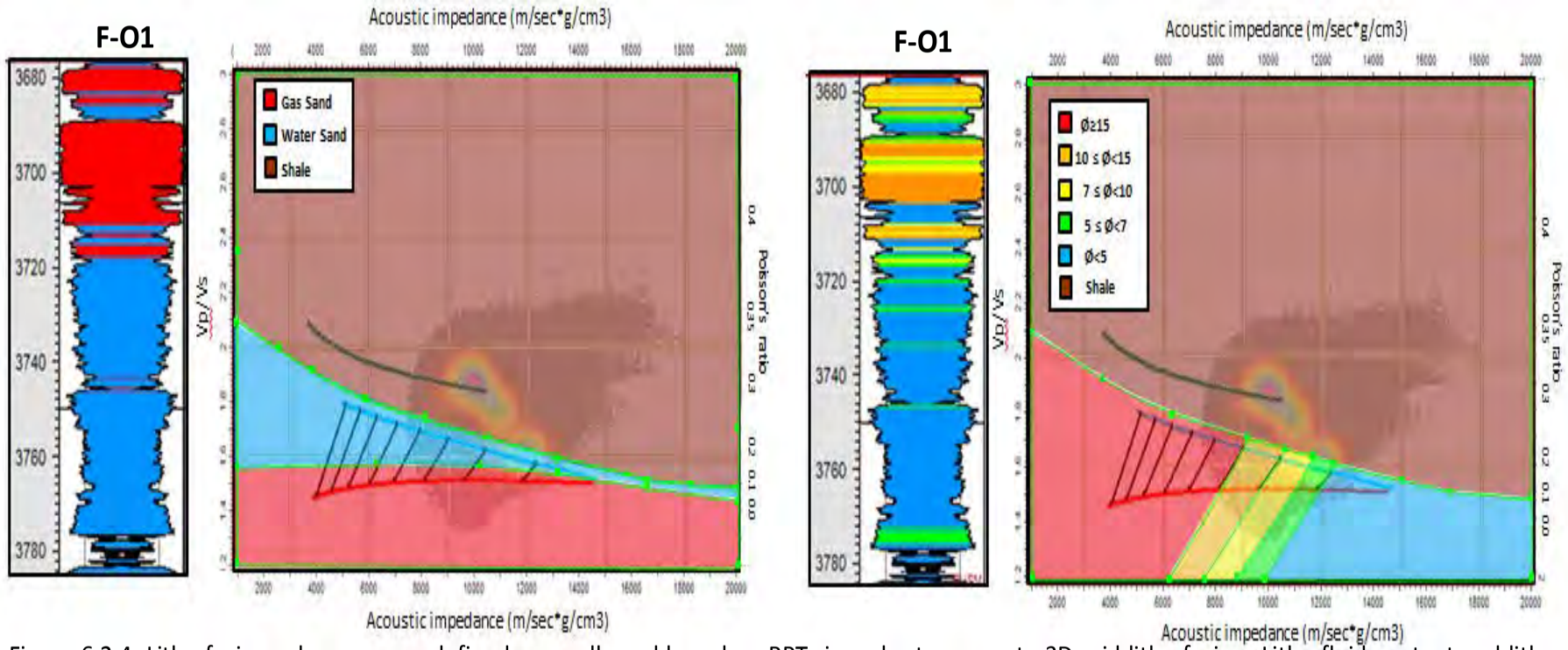

Figure 6.2.4: Litho facies polygons were defined manually and based on RPTs in order to generate 3D grid litho facies . Litho fluid content and litho porosity on the left and right respectively.

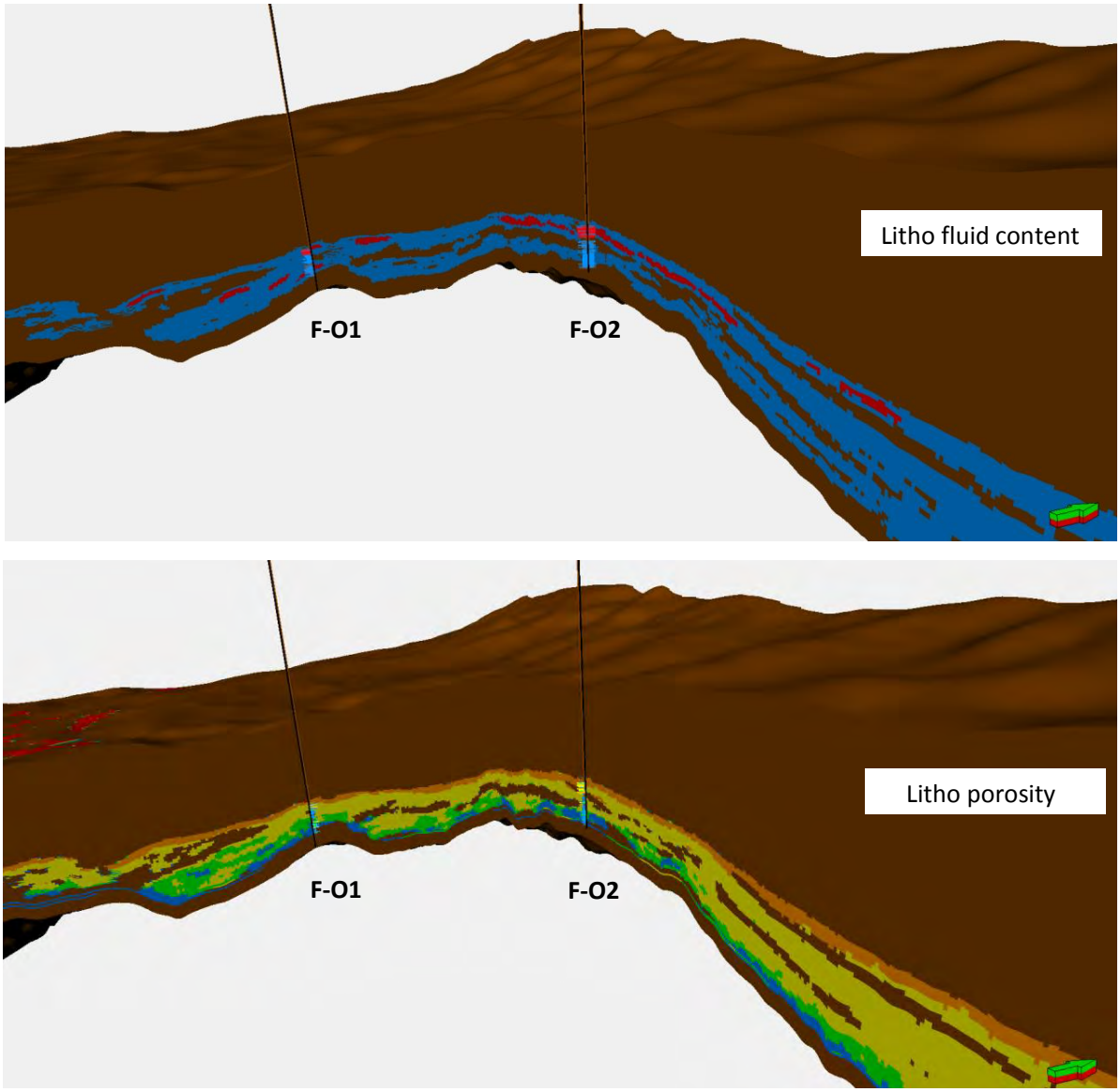

Figure 6.2.5: A 3D view of 3D grid litho property volumes.

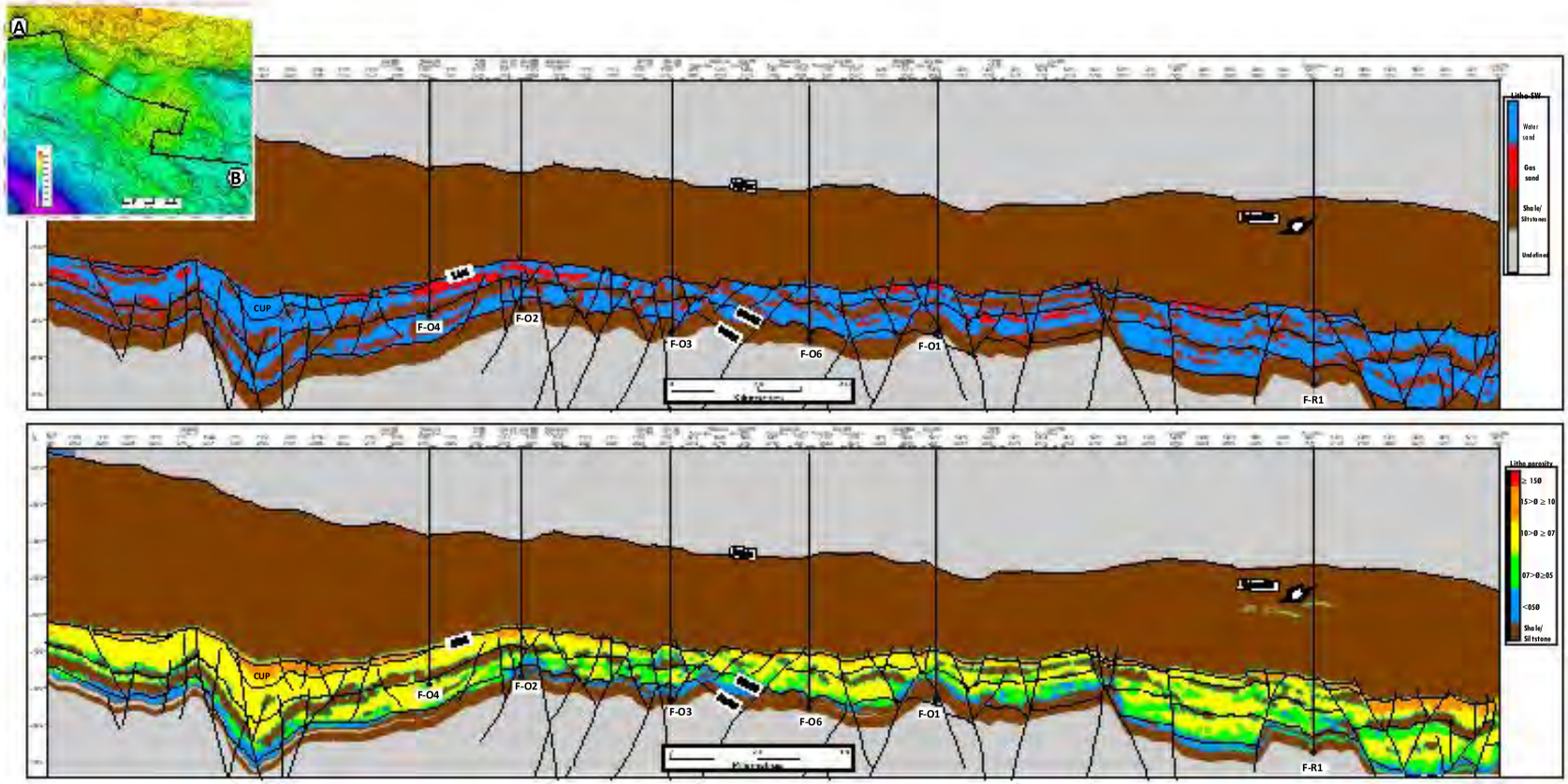
A
B
Litho SW
Water sand
Gas sand
Shale/ Siltstone
Undefined
CUP
F-O4
F-O2
F-O3
F-O6
F-O1
F-R1
Litho porosity
≥ 150
15>Ø ≥ 10
10>Ø ≥ 07
07>Ø≥05
<050
Shale/ Siltstone
CUP
F-O4
F-O2
F-O3
F-O6
F-O1
F-R1

6.3 Lithological classification

As discussed in the previous section, inverted data generated from simultaneous elastic inversion is used to interpret reservoir lithology and fluid content. To carry out this lithology interpretation, facies are classified by their characteristics. A fundamental approach to the classification problem is provided by Bayesian decision theory. In order to quantify uncertainty in the seismic lithology prediction, a supervised Bayesian classification was performed to deliver probability cubes of predicted lithology or rock property.

The technique constructs multivariate probability density functions (PDFs) of the selected inverted attributes for each of the litho-classes that must be predicted. The PDFs are then applied to elastic inversion results so as to calculate litho probability cubes that can be used for geological risk assessment when planning new wells (see figure 6.3.1).

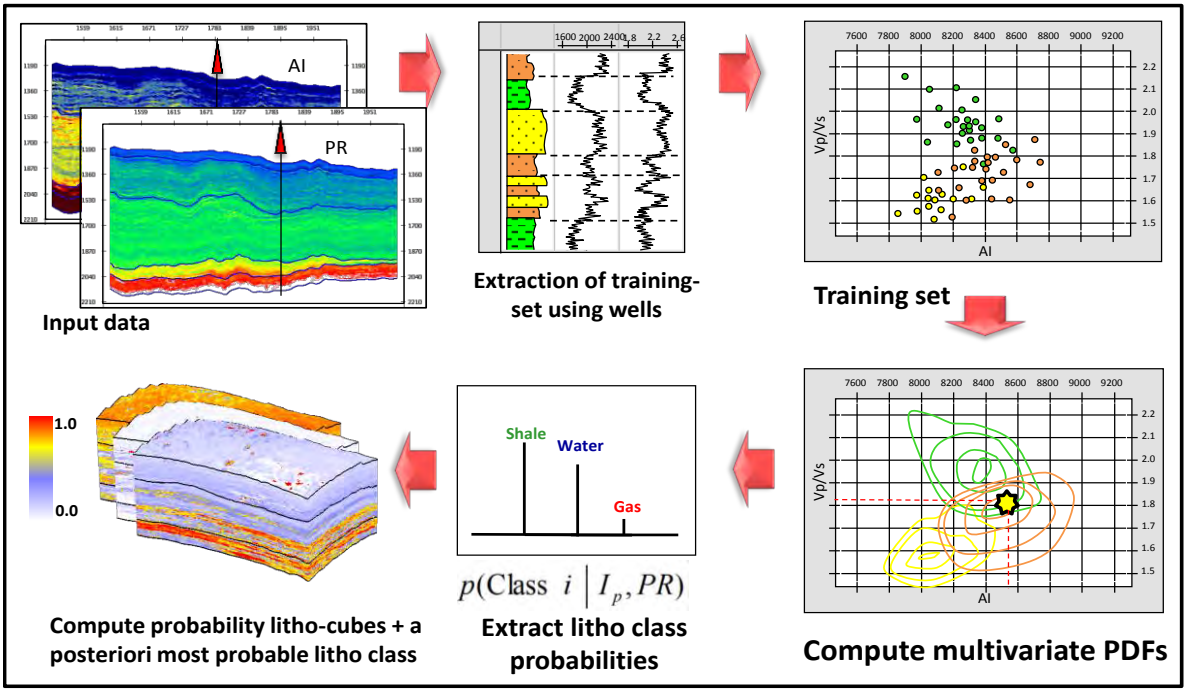

Figure 6.3.1: Lithological classification workflow.

The workflow below was adopted for this exercise.

1.- Input data (AI and Poisson's ratio) for this methodology was inverted via simultaneous seismic inversion (see figures 5.5.10, 6.2.2).

2.- Then lithology logs were generated. The litho logs were used to define a lithology classification in which 3 facies were estimated using petrophysical log cut-offs. Intervals of known lithology at well locations were used to define a training set for the classifier. The cut-offs defined in consensus with the geoscience team involved in the field were:

- Good sand: PHIE>0.065, VSH<0.3
- Tight sand: PHIE<=0.065, VSH<0.3
- Shale: VSH>=0.3

The cut-off was defined based on porosity, because the rock physics analysis concluded that the reservoir is porosity driven, so the highest porosities are implicitly linked to gas sands and vice versa. The fluid effect is limited in the seismic, and in this exercise fluid discrimination was not attempted. The five selected wells were F-O1, F-O2, F-O4, F-O6 and F-O3. An additional up scaling was applied in the time domain (see figure 6.3.2).

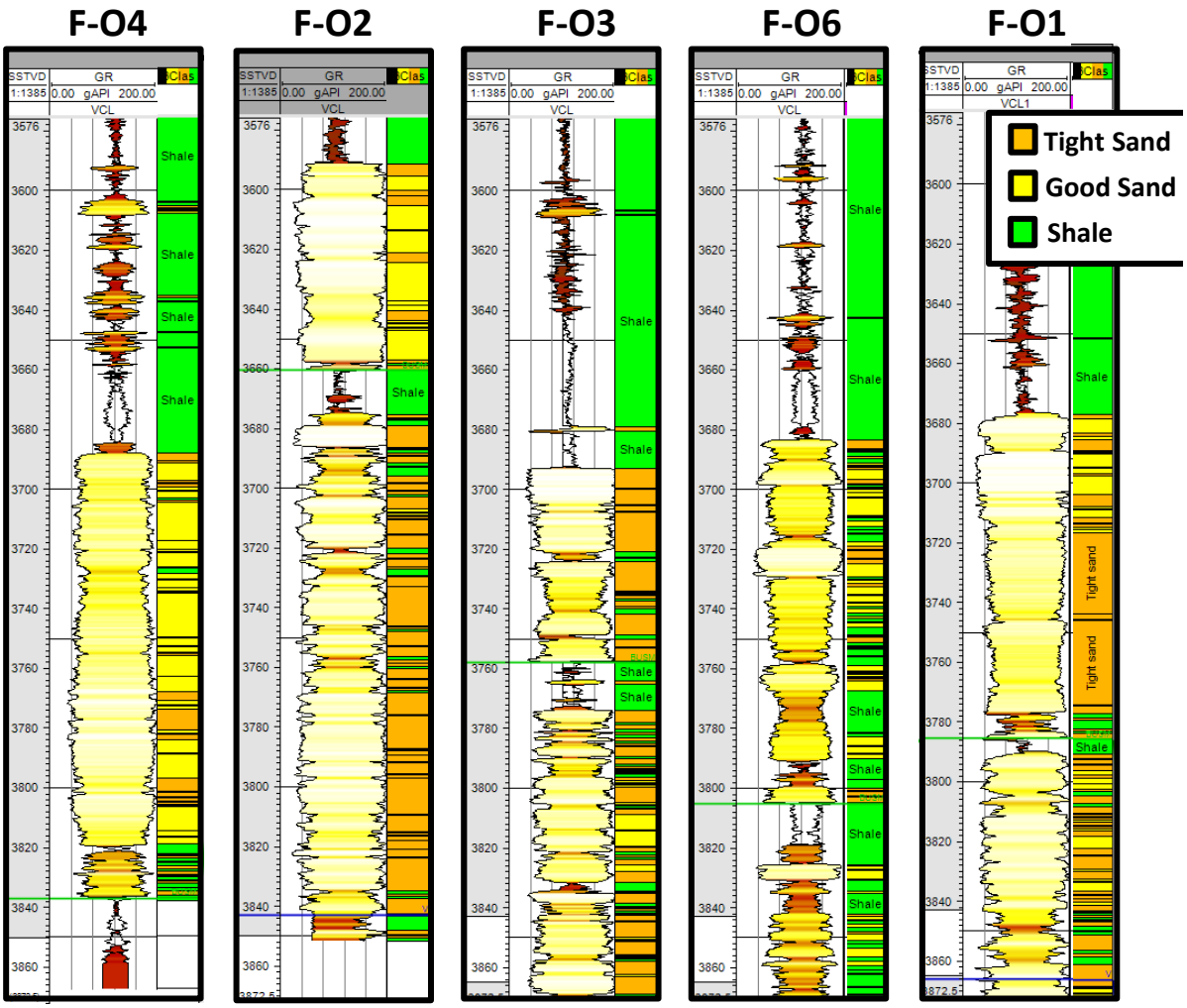

Figure 6.3.2: Litho logs computed with petrophysical data cut-offs.

3.- Log data points in the training set were displayed in 2-D cross-plots (elastic attributes). Cross-plot points are colour-coded according to each litho class to assess visually the separation between classes. The AI vs Poisson's ratio 2D domain was used to discriminate between litho facies (see figure 6.3.3).

4.- Next, a multivariate PDF was fitted to each cluster of points (lithology classes) in the training set using a non-parametric modelling technique. Non-parametric PDFs were derived from the cluster analysis as a representation of the variability in the formation properties given by the wells. Figure 6.3.4 shows the cross-plot with the contour lines (pdf) for each class .

Figure 6.3.5 summarizes the characteristics values (Vp, Vs, density) of different facies in the PDF.

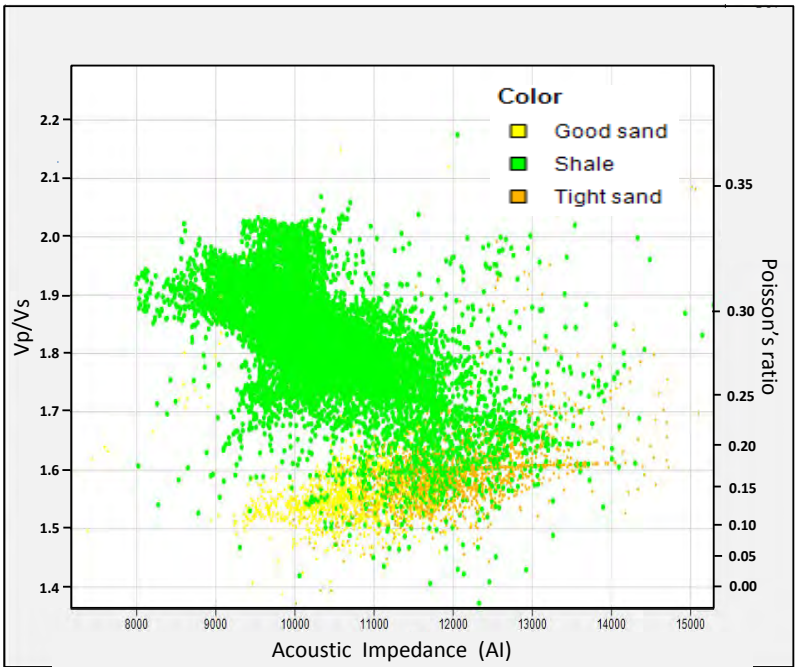

Figure 6.3.3: Acoustic impedance (AI) and Poisson's ratio (PR) cross-plot using well data from all wells and colour-coded with each litho facies calculated with the cut-off.

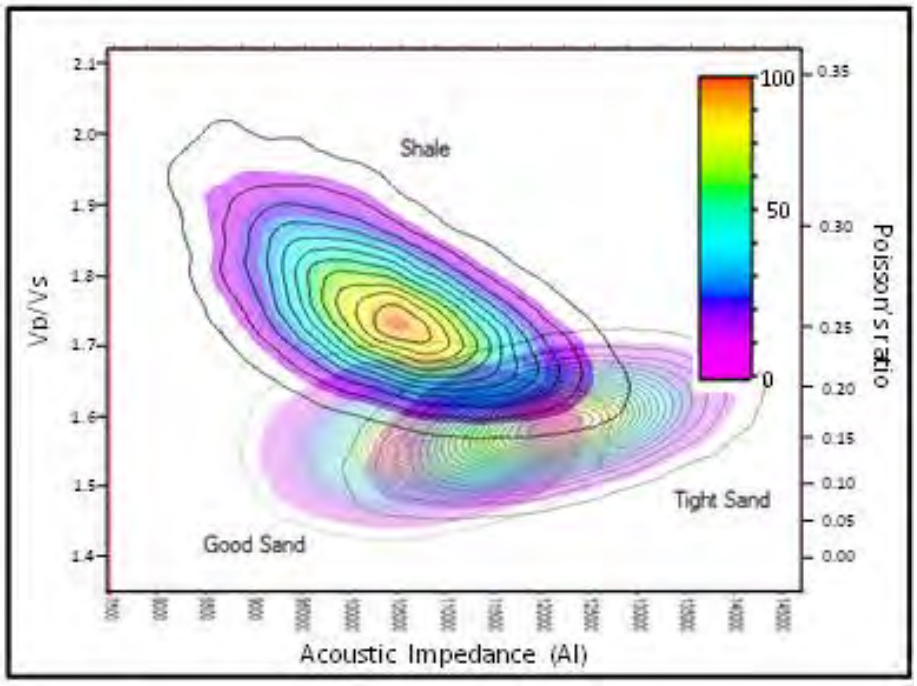

Figure 6.3.4: Probability density function (pdf) contours generated with the data from figure 6.3.3.

5.- The final step was to apply the PDF to the elastic attribute cubes (AI, PR). After the training phase, the classifier was applied sample-by-sample to the input inverted attributes cubes: the conditional PDF of each litho class given the local inverted seismic attributes, *p(litho-class | elastic attributes)*, was calculated from the computed multivariate PDFs at each sample location.

The outputs are a series of litho probability cubes per facies and a cube of the most probable facies.

QCs are shown on a 2D random section passing through the wells, with litho class logs. The attributes displayed are the probability of each facies (good sand, tight sand, shale) and most probable facies (see figure 6.3.6).

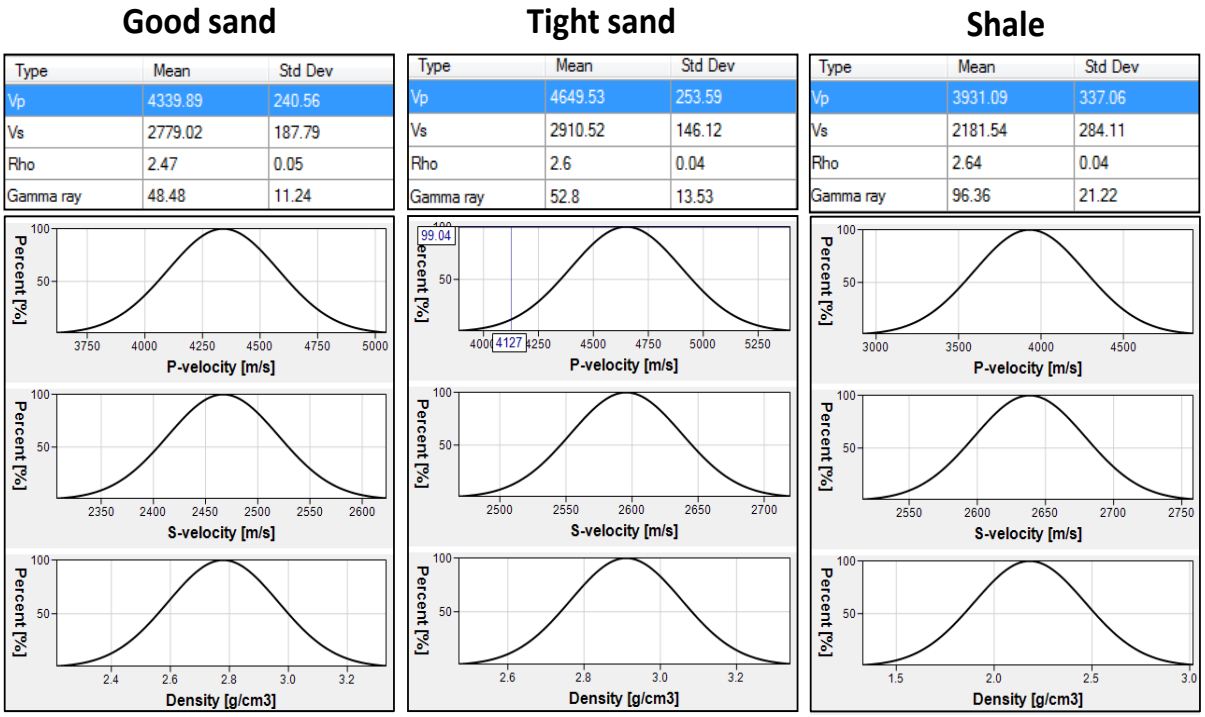

Figure 6.3.5 summarizing the characteristics values (Vp, Vs, density) of different facies in the PDF.

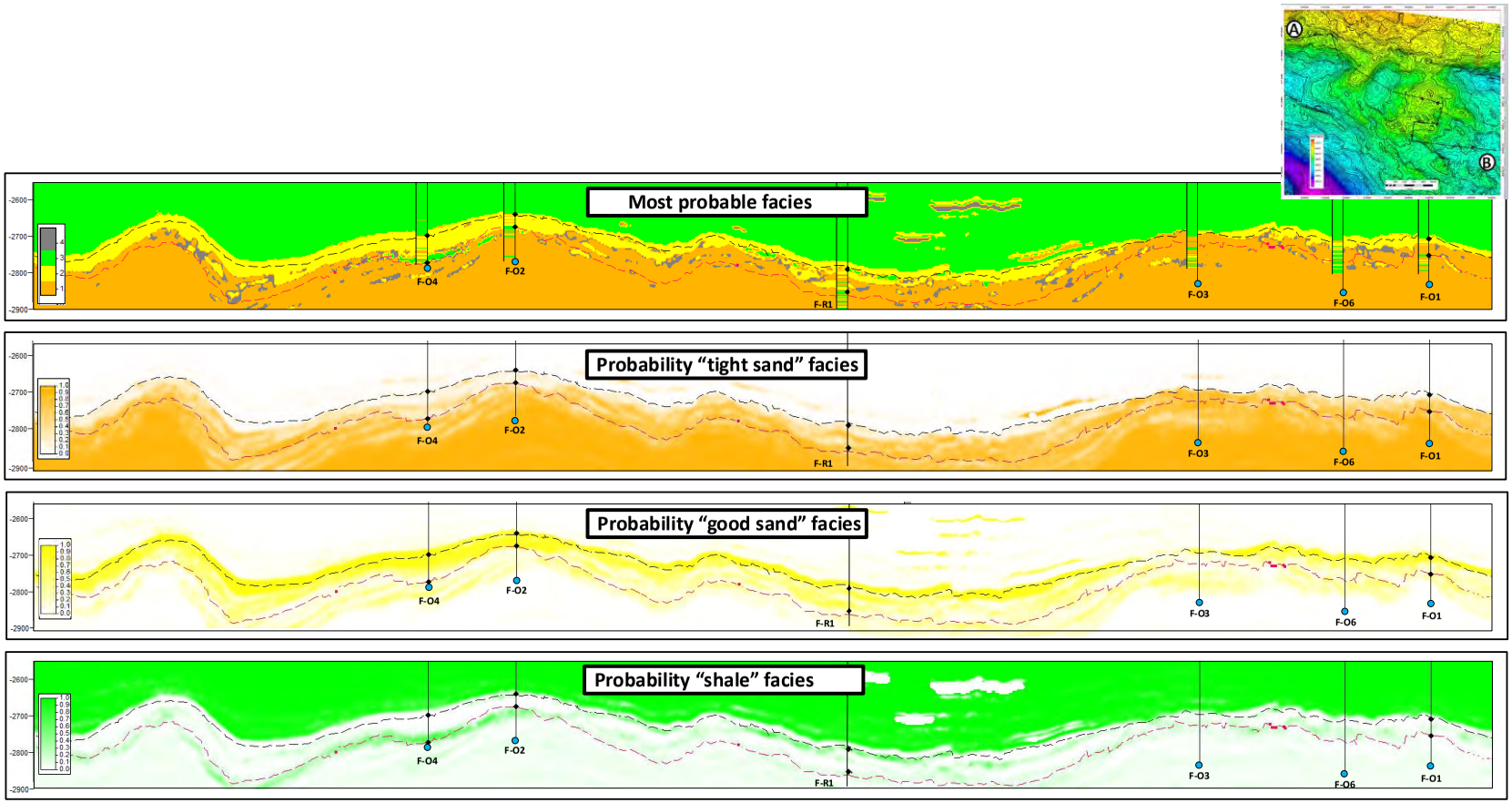

Figure 6.3.6: Random line through the probability of each facies (good sand, tight sand, shale) and most probable facies.

6.4 EEI illumination

Extended elastic impedance (EEI) is a seismic attribute that was introduced by Whitcombe et al (2000) as a method for fluid and lithology prediction. EEI is the application of angle rotation to the intercept and gradient followed by inversion under certain approximation. It essentially works by projecting intercept and gradient together with different angles which highlight different rock properties.

In this section, the concept of extended elastic impedance inversion was used to derive petrophysical properties and the distribution of reservoir facies so as to create a relationship between these attributes and well log data.

The EEI illumination workflow conducted in this section for F-O is explained in detail in figure 6.4.1. The workflow was as follows:

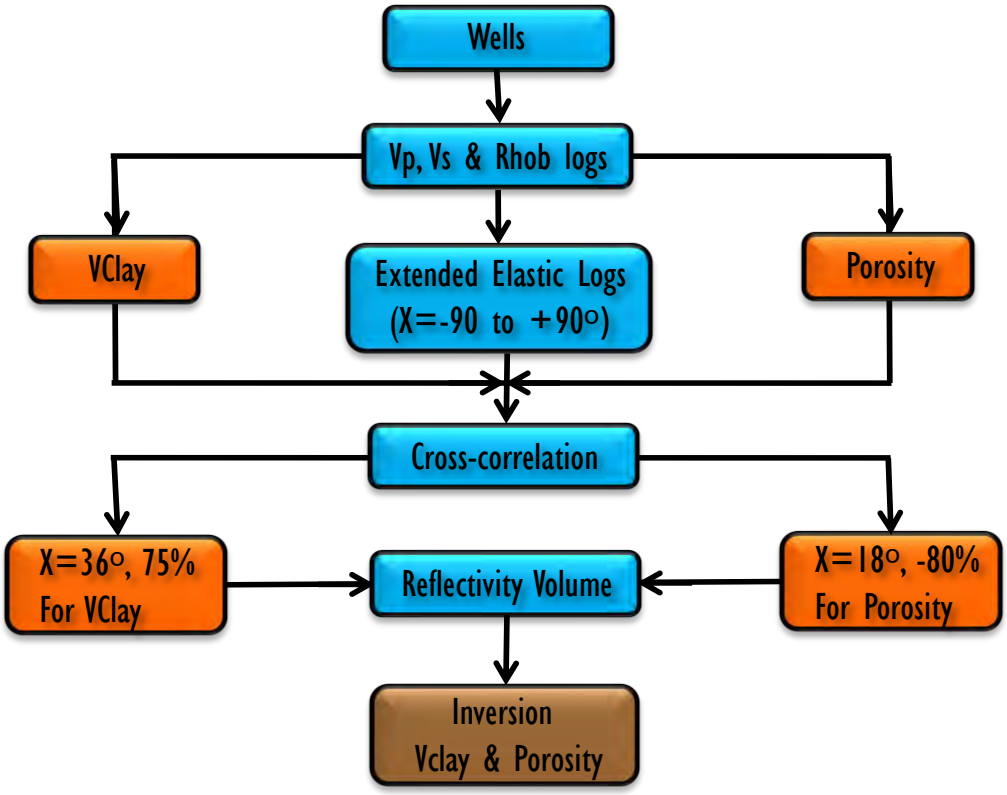

Figure 6.4.1: Extended Elastic Inversion Workflow.

1.- EEI logs for χ=-90° to χ=90° were computed using p-wave (α), s-wave(β) and density(ρ) as input in the equation below:

$$EI(\theta) = \alpha_0\rho_0 \left[\left(\frac{\alpha}{\alpha_0}\right)^p * \left(\frac{\beta}{\beta_0}\right)^q * \left(\frac{\rho}{\rho_0}\right)^r\right]$$

Figure 6.4.2 shows the EEI log spectrum for well F-O1.

2.- Then a cross-correlation between the EEI logs with the petrophysical logs (porosity, VClay and Sw) was computed.

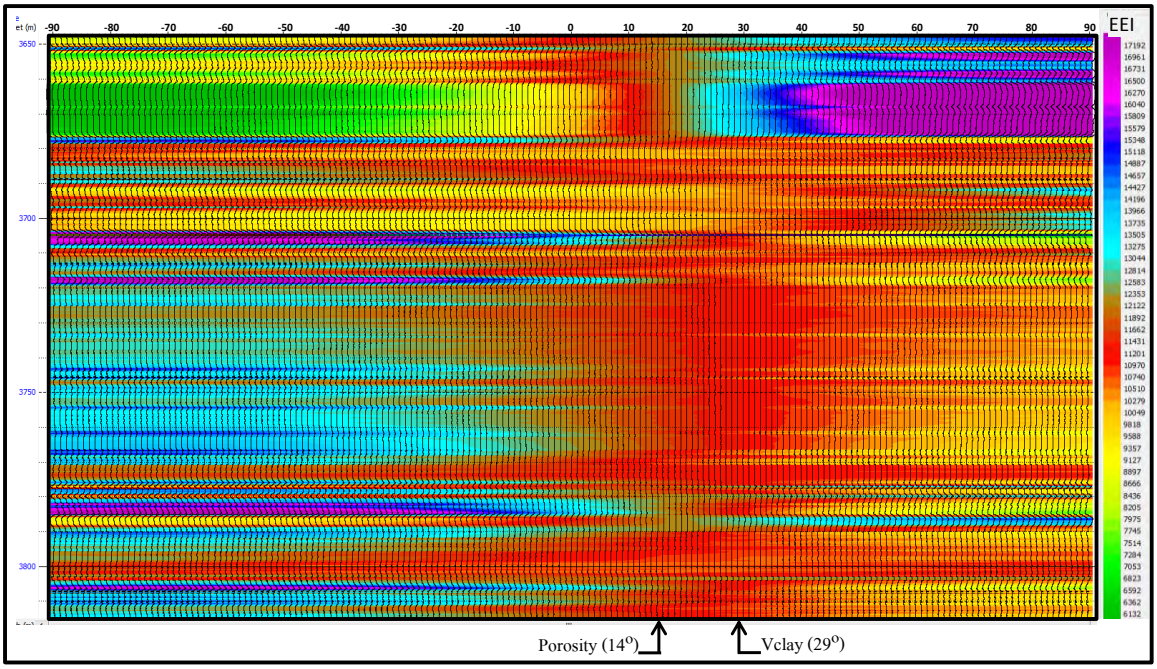

Figure 6.4.2: EEI logs spectrum (-90-to-90) plot. The spectrum plot correspond to F-O1 well. At the bottom, χ angle at which the maximum correlation is achieved for porosity and Vclay.

3.- Next, the chi angle versus cross-correlation coefficient between the targeted rock property logs and EEI logs was cross-plotted for all wells. The χ angle at which the higher correlation is obtained is commonly called the "chi angle" (see figure 6.4.3).

Figure 6.4.4 shows a well section showing the correlation between porosity and Vclay logs and respective EEI logs for wells F-O1, F-O2, F-O3, F-O4 and F-R1.

4.- The targeted reflectivity volumes were computed using as a input data the intercept (A) and gradient (B) AVO attribute volumes generated from section 6.1. The volumes were computed using the equation below at the angle of maximum correlation (χ) (see figure 6.4.5):

$$R(\chi) = A + B \tan\chi$$

The volumes created are porosity reflectivity and Vclay reflectivity. Water saturation (Sw) could not be generated, because the correlation coefficient was not acceptable (see table 6.4).

5.- These reflectivity volumes were inverted to estimate Vclay and porosity volumes. Here the procedure becomes similar to that performed in the simultaneous inversion, but instead of inverting a number of partial stacks the problem was reduced to the inversion of just one volume. This involved the following steps:

a) A well-seismic tie for each of the five wells (F-O1, F-O2, F-O3, F-O4 and F-R1) was performed and wavelets were extracted using a deterministic estimation method (Roy White). The reliability of the tie was quality controlled by computing correlation coefficients (see figure 6.4.6-7).

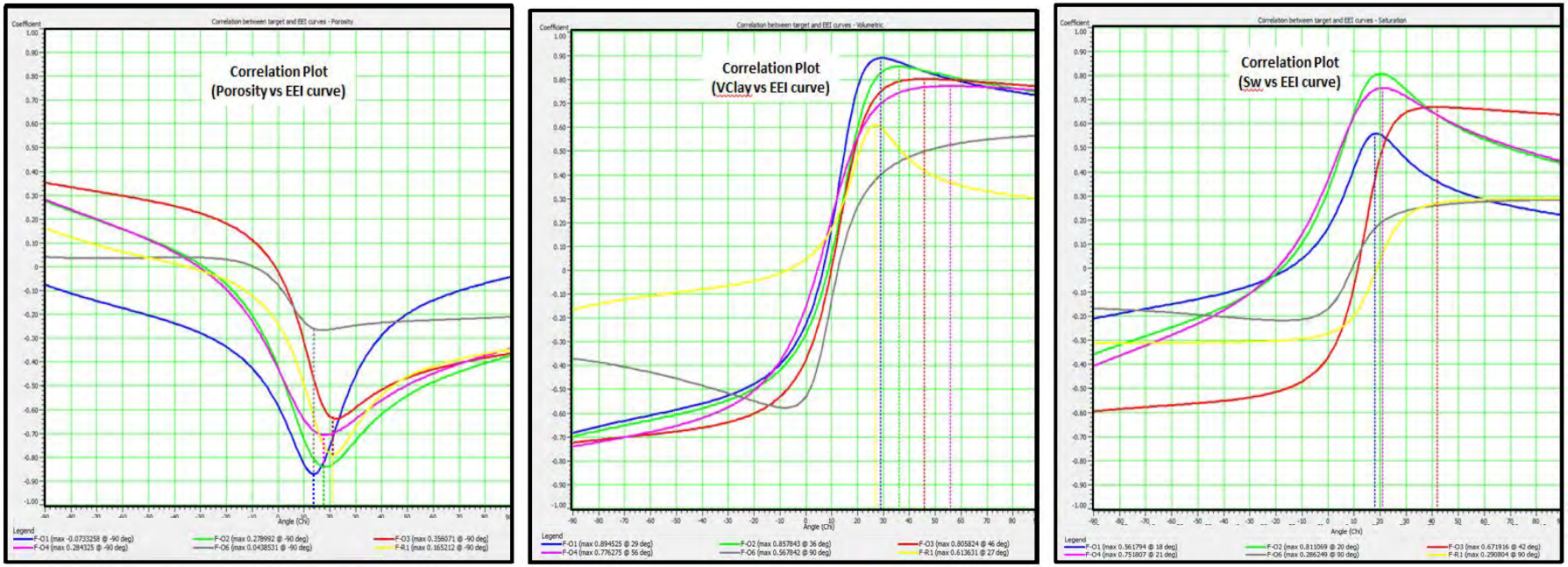

Figure 6.4.3: Correlation of logs to EEI logs as a function of angle χ

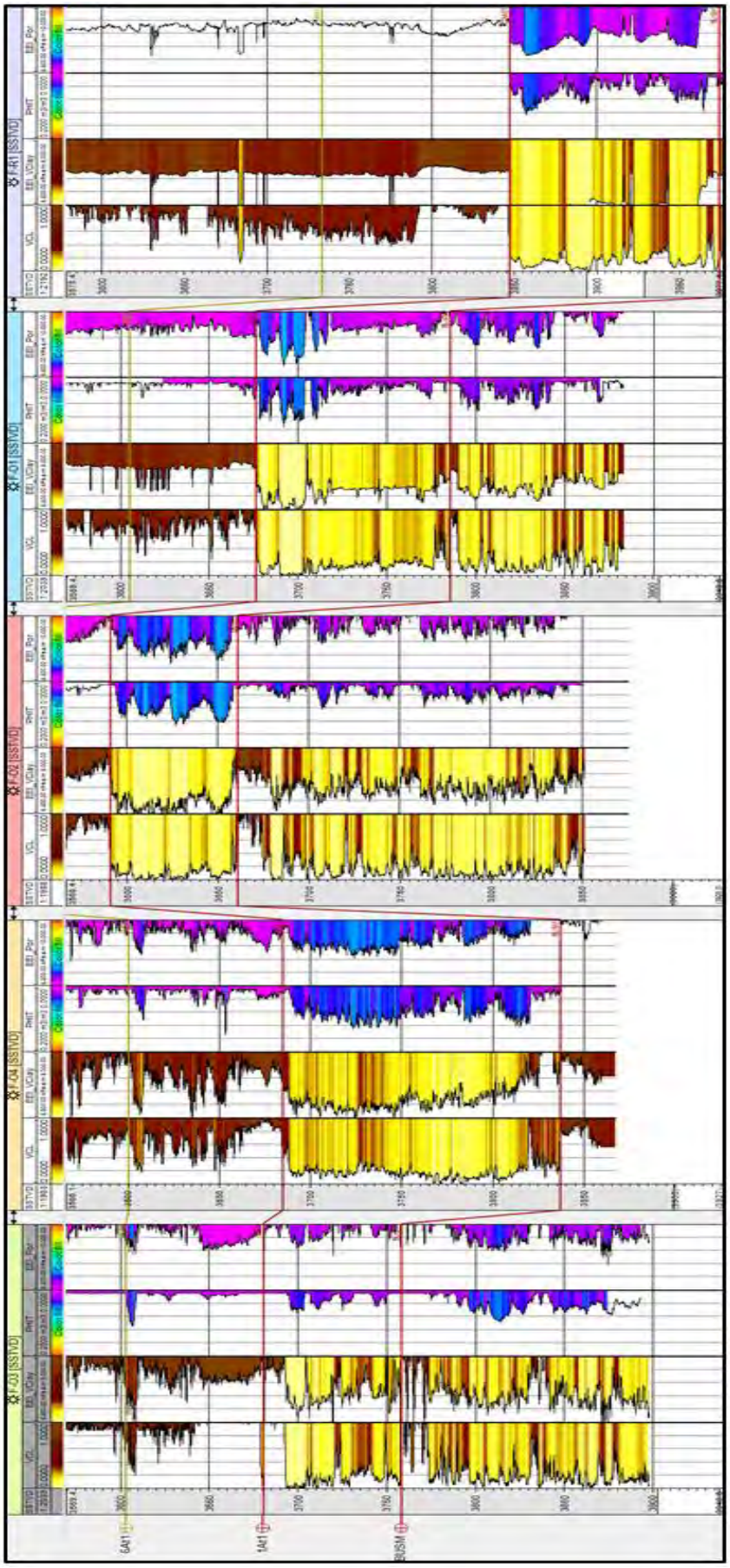

Figure 6.4.4: Well comparison section between petrophysical logs and EEI logs (vclay, porosity).

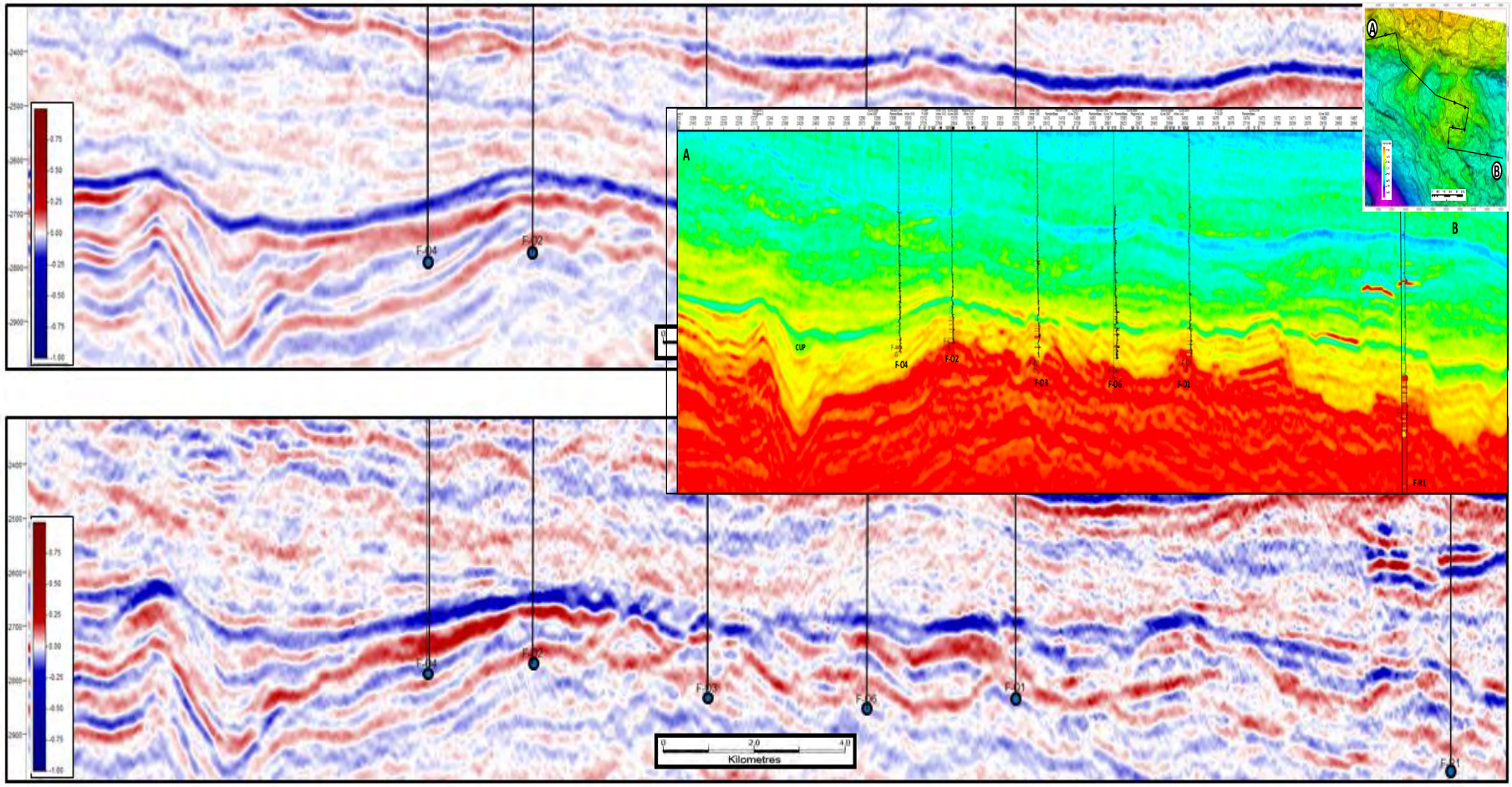

Figure 6.4.5: Random seismic section displaying the EEI reflectivity vclay (top) and porosity (bottom) generated from A and B AVO attributes.

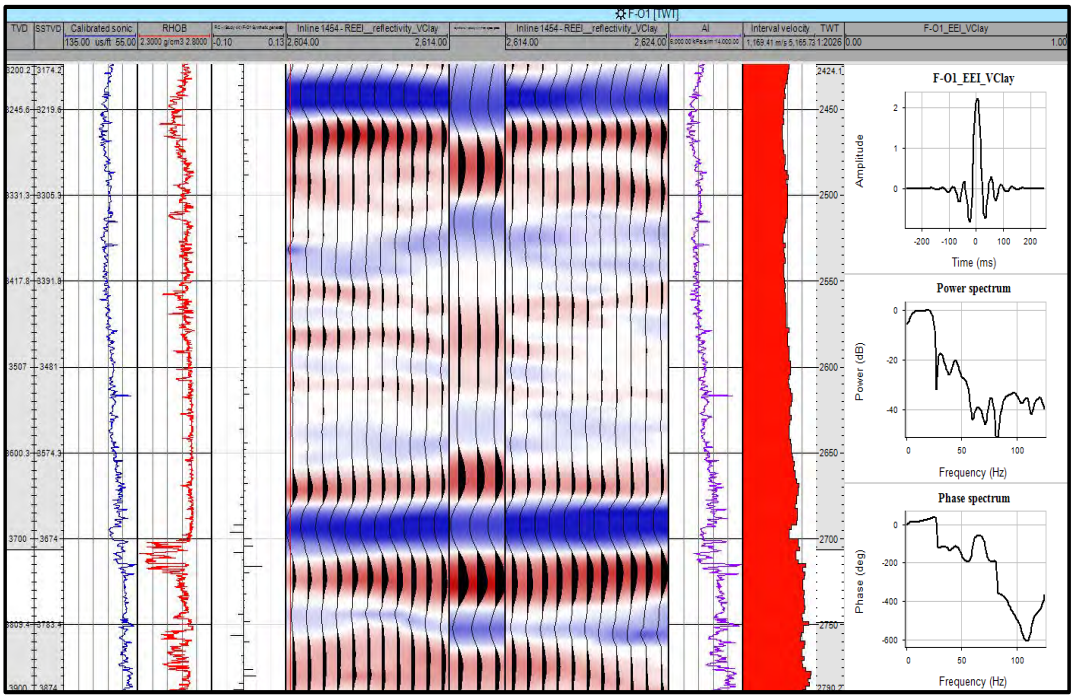

Figure 6.4.6: Well seismic tie on EEI reflectivity vclay at the F-O1 well location.

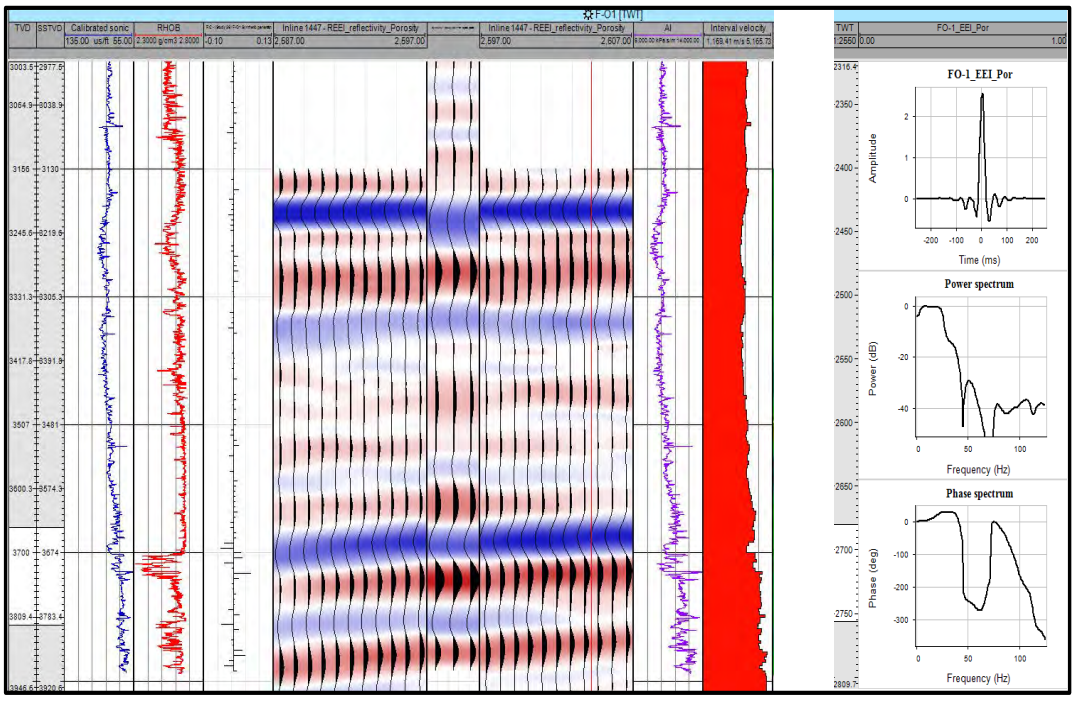

Figure 6.4.7: Well seismic tie on EEI reflectivity porosity at the F-O1 well location.

b) A low-frequency model was generated for each property. EEI logs (Vclay, porosity) and interpreted horizons (13At1, BLSM ghost) were the input data for each property. A cut-off to 8 Hz was applied to filter the well data (see figure 6.4.8-9).

c) A post-stack seismic inversion algorithm was required to invert the EEI reflectivity volumes.

The post-stack algorithm includes inversion parameters similar to the simultaneous seismic inversion (reflection threshold (R1), horizontal continuity (RALPHA) and the relative standard deviation of the prior model (RSIGMA)) (see figure 6.4.10-11).

R1 values of 0.03 and 0.015 were defined for EEI Vclay and EEI porosity respectively. RALPHA and RSIGMA were set up to 0.12 and 0.14 to obtain an optimum EEI Vclay outcome. For EEI porosity, a higher RALPHA and RSIGMA (0.2 and 0.22) values were required to achieve a satisfactory result.

6.- The inverted outcomes validation was based on the correlation of the inverted data at the well location with the up-scaled petrophysical log via correlation coefficients (CC) (see figure 6.4.12).

Additionally, error plots showing the difference between the original traces and the synthetic traces calculated using the elastic impedance inversion result were computed. Both inversions showed similar error plots, with no significant coherent energy and low all-over amplitudes (see figures 6.4.13-14).

7.- EEI volumes do not have rock property units, so a linear regression function was computed by correlation between EEI log and the targeted log at the well location to scale the data to a more appropriate units range. All wells were included to make the function more robust and accurate. Then colour-scale bars for each EEI log property were defined to make the characterization analysis more intuitive and perceptive (see figures 6.4.15-16).

The functions and CC for both EEI properties:

Vclay = 0.000416093 * (EEI Vclay) – 2.92767; CC: 0.68

Porosity = -0.000382514 * (EEI porosity) + 0.402115; CC: 0.73

The scaled properties are displayed in figures 6.4.15-16.

8.- Lastly, volumes were analysed to identify additional zones in between existing wells with encouraging properties. In addition, maps of the attributes (Vclay, porosity) at reservoir level using a window between 1At1 horizon and a 1At1 ghost surface shifted 25 msec down and using “most of” as extracting method were computed (see figures 6.4.17-18).

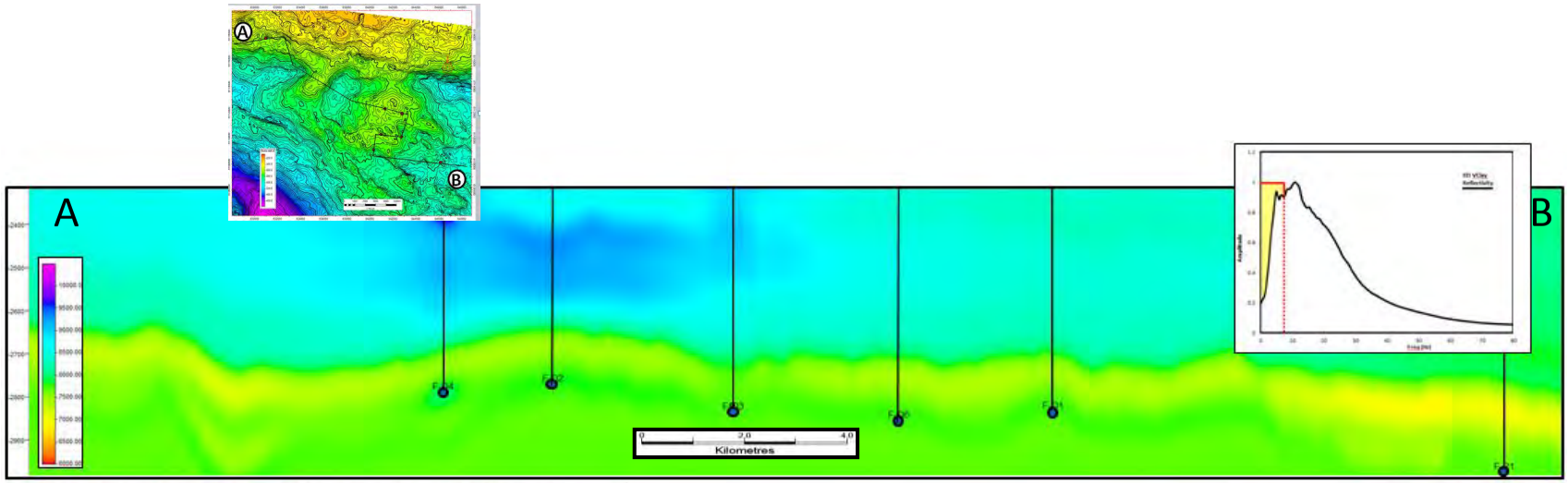

Figure 6.4.8:Random seismic section displaying the vclay low frequency model (LFM) using a 8Hz cut-off.

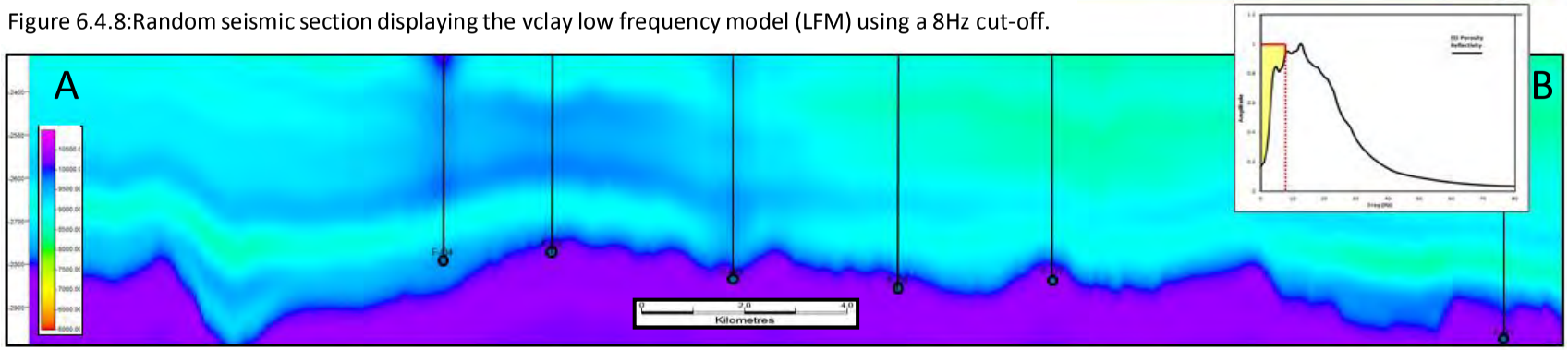

Figure 6.4.9:Random seismic section displaying the porosity low frequency model (LFM) using a 8Hz cut-off.

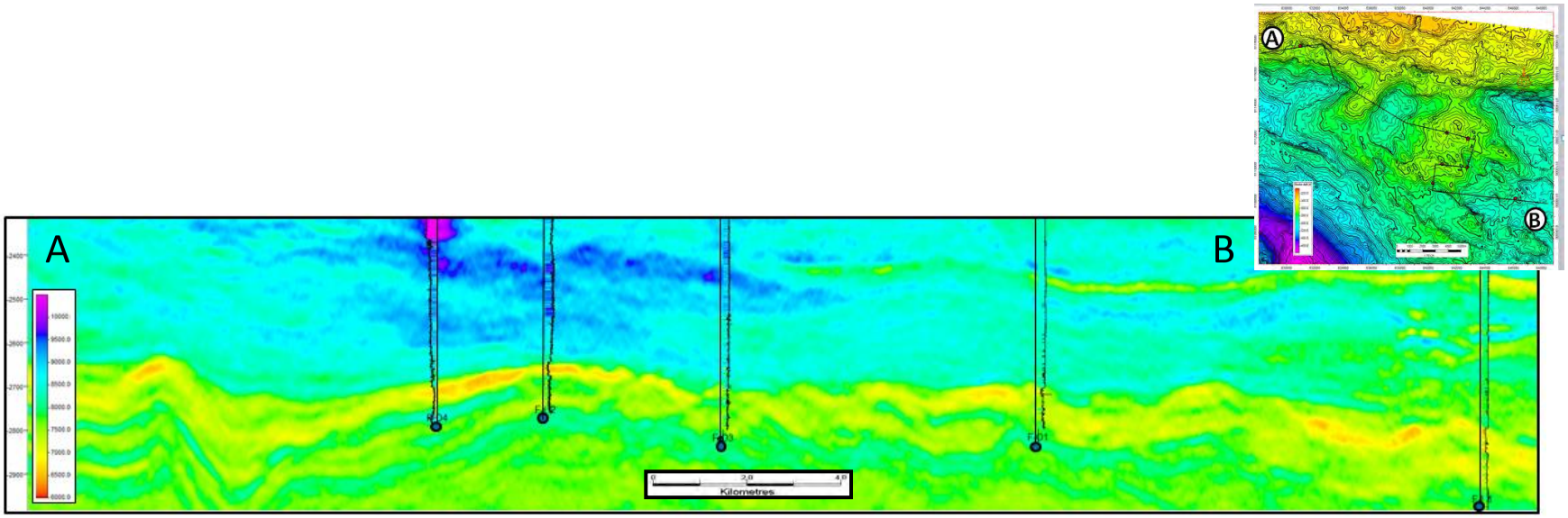

Figure 6.4.10:Random seismic section displaying the inverted vclay.

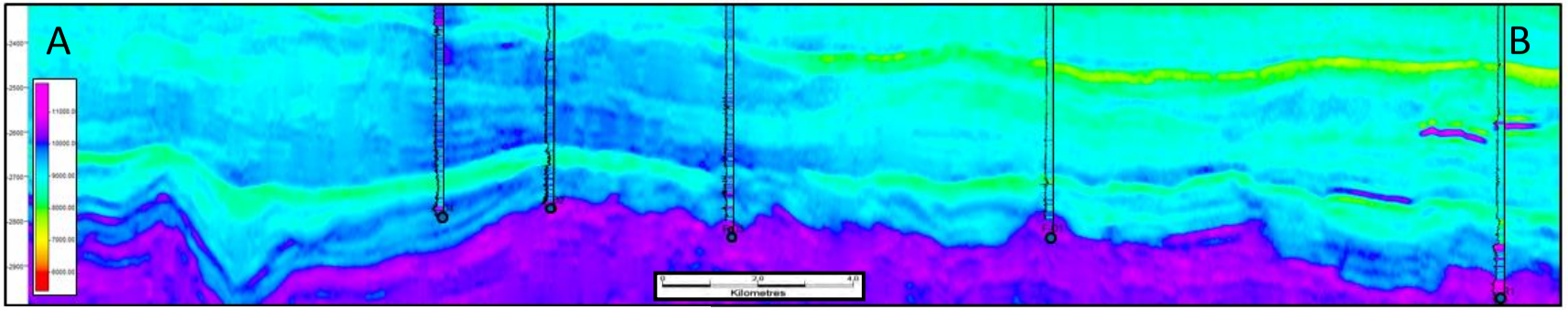

Figure 6.4.9:Random seismic section displaying the inverted porosity.

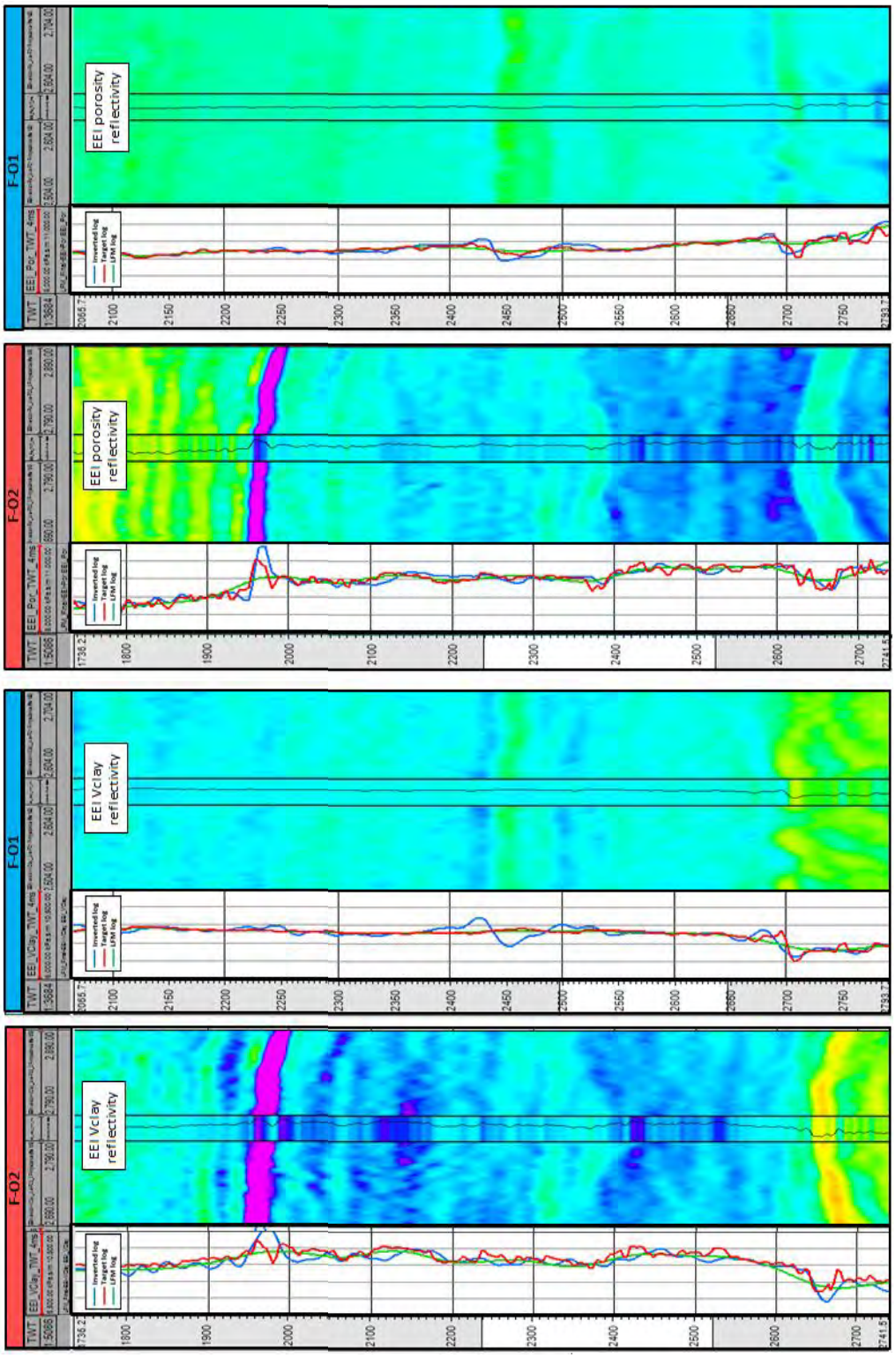

Figure 6.4.12: Correlation between inverted property (Vclay, porosity) and petrophysical logs.

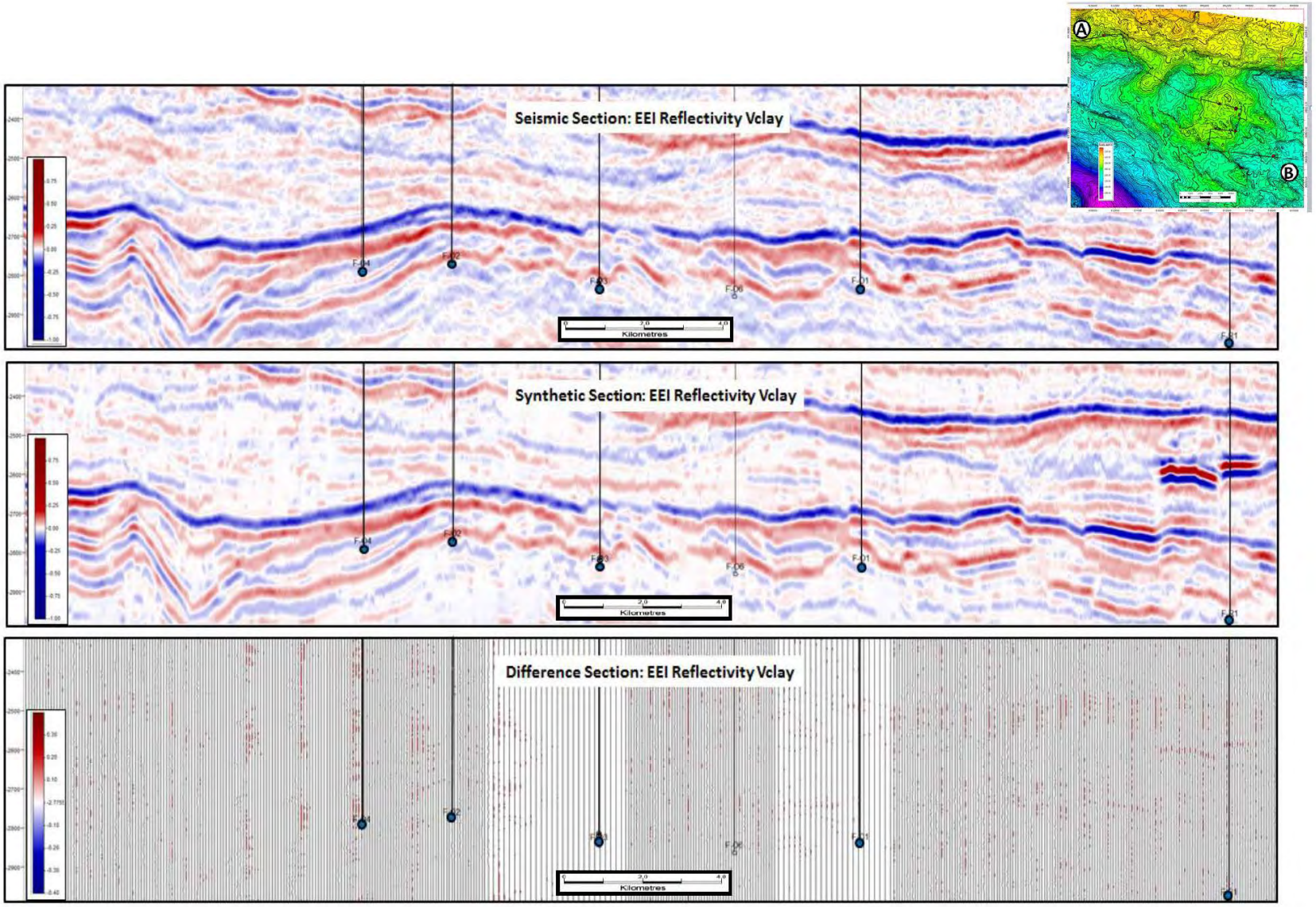

Figure 6.4.13: Random seismic section showing at the top the EEI reflectivity Vclay seismic, in the middle the EEI reflectivity Vclay synthetic generated from the inversion and at the bottom the difference between seismic and synthetic (Error plot).

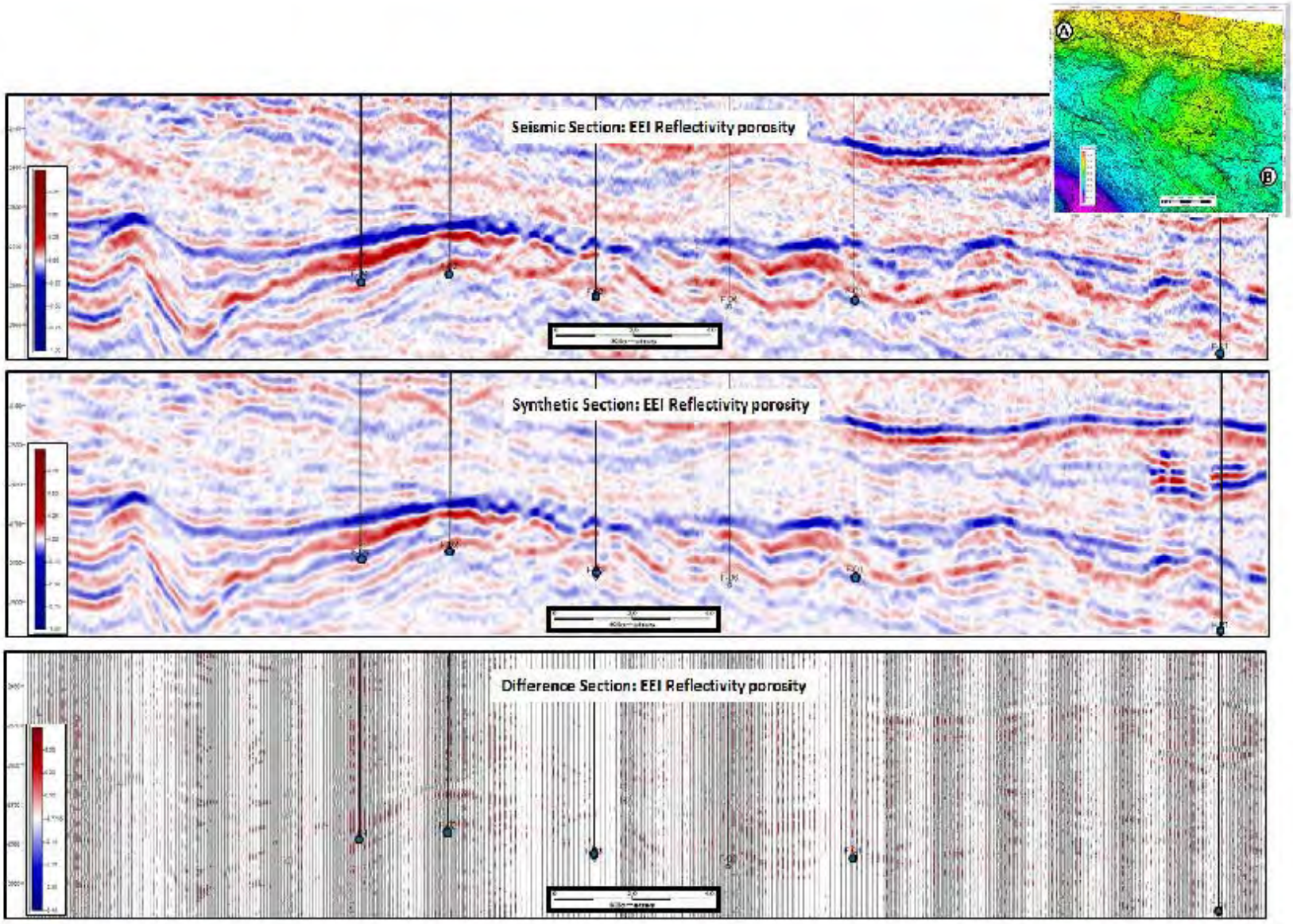

Figure 6.4.14: Random seismic section showing at the top the EEI reflectivity porosity seismic, in the middle the EEI reflectivity porosity synthetic generated from the inversion and at the bottom the difference between seismic and synthetic (Error plot).

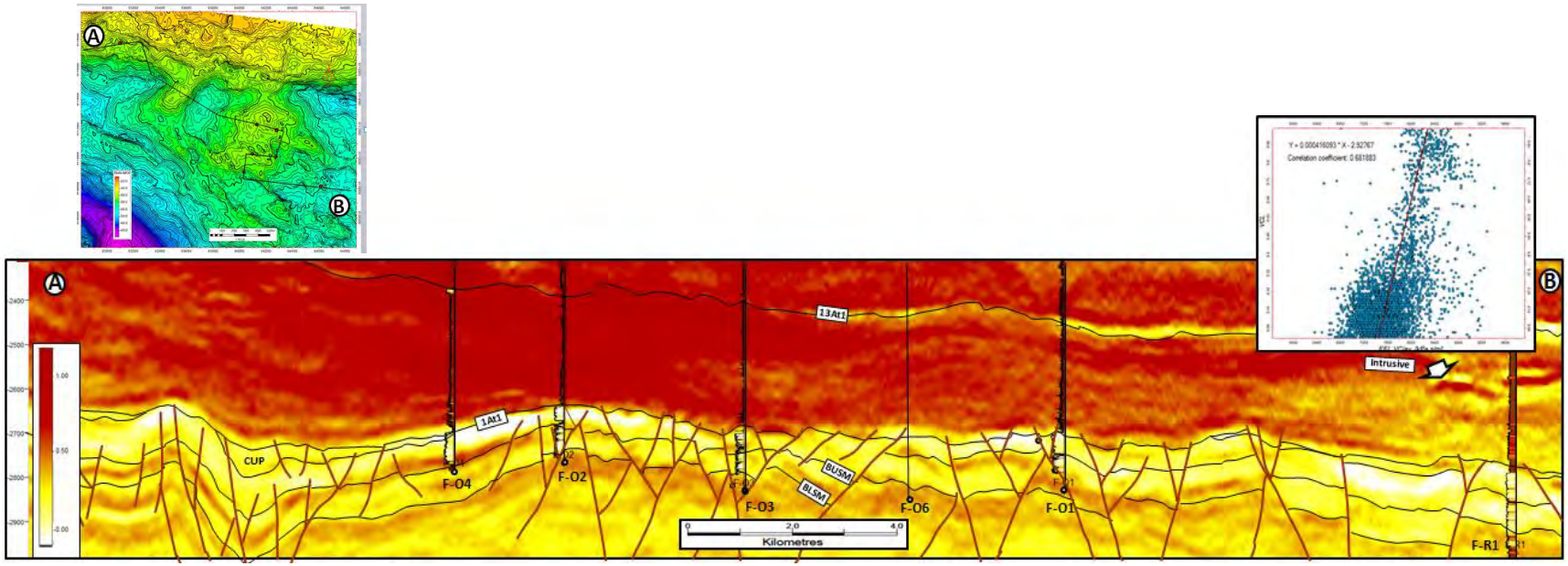

Figure 6.4.15: Random seismic section displaying the scaled inverted EEI vclay.

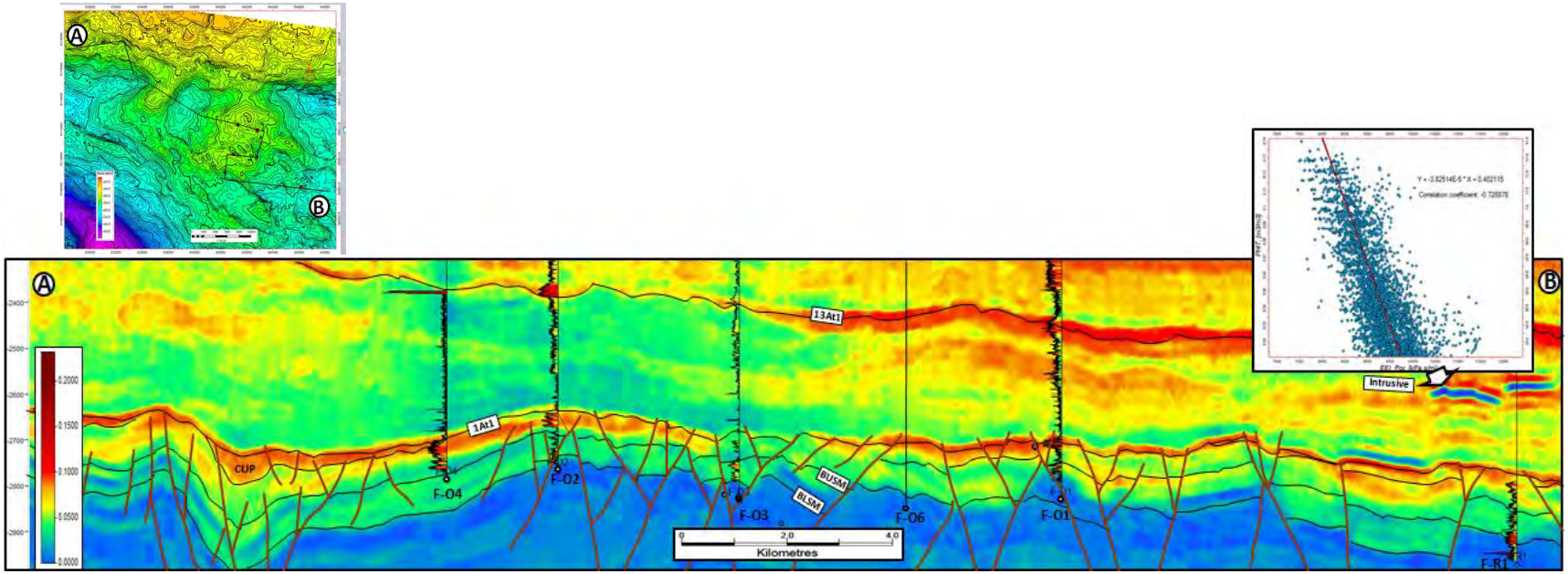

Figure 6.4.16: Random seismic section displaying the scaled inverted EEI porosity.

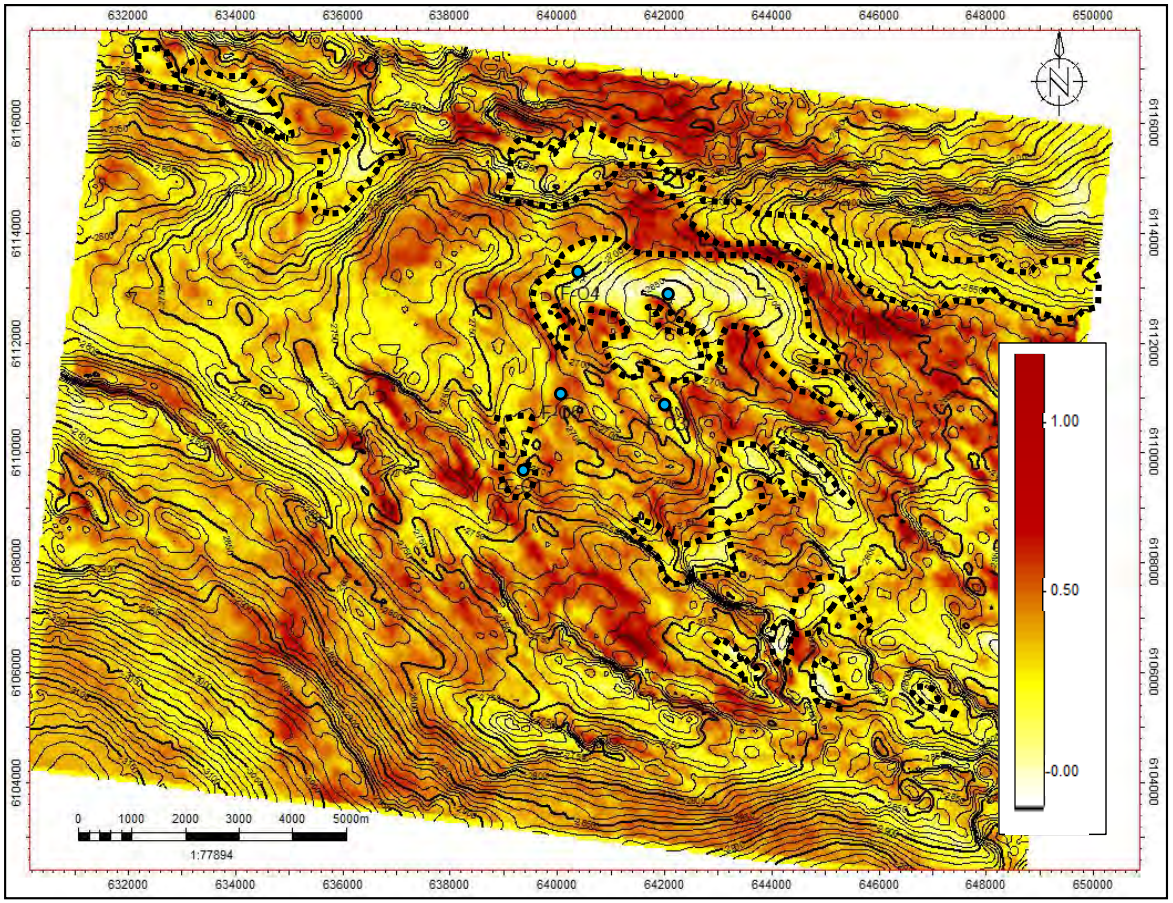

Figure 6.4.17 : EEI reflectivity Vclay map from surface extracted between top of reservoir (1At1) and a 1At1 ghost surface shifted 25ms down. The method to extract the attribute was "Most of". Dashed polygons represent the zones with low Vclay and high porosity.

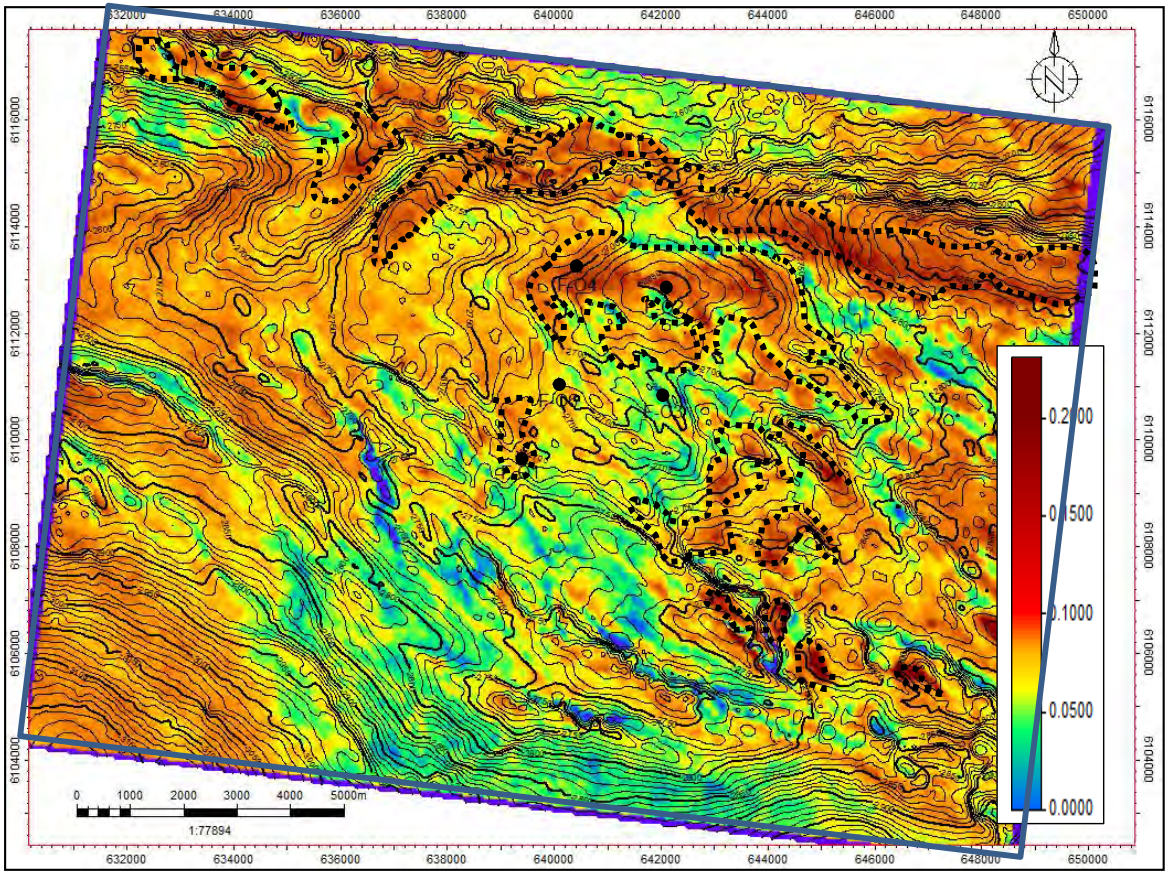

Figure 6.4.18 : EEI reflectivity porosity map from surface extracted between top of reservoir (1At1) and a 1At1 ghost surface shifted 25ms down. The method to extract the attribute was “Most of”. Dashed polygons represent the zones with high porosity and low Vclay.

6.5 Discussion and Conclusions

The main objective of the study was to image the USM reservoir, in particular to be able to distinguish between sands and shales and between water sands and gas sands. To achieve this goal four seismic reservoir characterization techniques were conducted using a vast number of results from the rock physics analysis (chapter 4) and the inverted data (chapter 5). Some remarks, observations and conclusions are presented below.

AVO cross-plotting

The technique works under the premise that the rock physics and fluid characteristics in the target reservoir exhibit a good AVO response. AVO quality responses vary depending on how those properties are combined.

By analysing AVO (intercept, gradient) behaviour over all rock-fluid perturbational scenarios, some useful conclusions that helped to define the 2D zones (opacity filters) were drawn.

a) Class I weak (moderate impedance <0.05), class II-IIP and class III weak (moderate impedance >-0.05) with a moderate to high gradient represent zones where better rock properties are plotted (see figure 6.1.3).

b) Class I (high impedance >0.05) is mostly water sands and/or low porosity sands.

c) Class I, II and III with a low gradient are associated with high Vclay content.

Only opacity filter zones for case (a) were generated, because case (a) represents the best porosity, fluid content and sand-shale ratio in the reservoir.

The accuracy with which prospective zones with good characteristic are isolated is not only subject to the AVO response, but also to the seismic quality and resolution. Negligible to subtle noise and/or slight misalignment on far offset remaining after seismic conditioning could affect the result.

These plots were a useful and intuitive way to identify AVO class distribution that are characteristics of different rock property patterns in a tight gas-sand reservoir, and provided a better understanding of the rock properties than doing an analysis of the standard AVO curves. On the other hand, this technique does not involve inverted data.

Rock physics templates

Templates were overlaid on acoustic impedance-Poisson's ratio cross-plots to read porosity, fluid content and lithology directly from the inverted modelling.

In the cross-plot on the left (figure 6.2.1) lithology can be clearly separated into 2 classes (sand-shale) colour-coded with Vclay (yellow-brown). However, for a more detailed cross-plot interpretation (right) more than a Vclay log (Sw, porosity, etc) is needed to classify different facies, and that is the typical dilemma with seismic inverted data and the main reason for using rock physics templates (figure 6.2.1).

Theoretical rock physics trends (RPTs) helped to interpret and classify facies from well and inverted data. On the other hand, well log data was a useful tool to verify the reliability of the RPTs selected, and therefore to validate the theoretical rock physics model. Some observations inferred from RPT analysis at well data domain are listed below.

a) In figure 6.2.1b both shales, shale A (overburden slow shale, in purple) and shale B (intra-reservoir shale + heterolithics, in light green) fall in the shale trend.

b) The transitional marine sequence below the USM and characterized by tight sandy-shale interbedded fluvial deposits and shallow marine facies in orange is plotted between the shale and sand trend line with porosities in the range 4-7% according with extrapolation of porosity dashed lines from the sand trend.

c) The water sand (Sw>0,3) population in yellow falls on the theoretical water sand trend, but the population shows some dispersion above the trend line. The gas-sand population plots well below the water-sand trend, but just above the gas sand trend.

Once the RPTs had been validated, well data was substituted with the seismic inverted data to interpret the outcome in terms of lithology, porosity and fluid content. A time window equivalent to the log data depth range was used.

A high density of samples clustered close to the shale trend line is related to more than 500 metres of shale column in the 13At1 sequence. A separate cluster with a lower Poisson's ratio, but high acoustic impedance represents the tighter sand-shale transitional marine facies below the reservoir (USM) (see figure 6.2.3).

As expected, the inverted data cluster shows more dispersion and less definition than the log cross-plotting. For instance, a few samples show values below zero Poisson's ratio. However, a Poisson's ratio value corresponding to porous gas sand is not less than 0.12 for this reservoir. The mismatch must be attributed to the lower depth resolution in seismic data, Vp/Vs variability and wavelet interference.

The acoustic impedance (AI) and Poisson's ratio (PR) inverted data were classified into 2 litho facies, (litho porosities, litho fluid content) and interpreted by transforming each pair AI-PR data into a pair of litho facies. Some observations in this regard are:

a) The predicted porosities match the log data fairly well with the exception of F-R1, in which porosities were over-estimated.

b) Better porosities (facies orange and yellow) were predicted in the top of the reservoir, where EPP took place. Conversely, lower porosities (facies blue and light green) were predicted in the base of USM and in the transitional zone (fluvials), with less influence of EPP and higher shaliness (cement?) respectively.

c) The bottom part of the low velocity shale (LVS) was interpreted as shaly-sand with porosities allocated on the yellow facies (7-10%). The misinterpretation could be attributed to the over-pressure, which reduces the acoustic impedance and increases the Poisson's ratio.

d) Overall, the litho fluid content RPTs distinguishes well between gas and water sands throughout the entire survey, but poorly between the gas case and fizz case.

F-O is a tight gas reservoir (stiff rock frame). This entails a limited sensitivity to fluid content, where Poisson's ratio (PR) moves down moderately with a gas saturation increment. Acoustic impedance also shows a decrease owing to the gas effect on P-velocity and density. On the other hand, the lithology is well differentiated in both domains (acoustic impedance and Poisson's ratio). In conclusion RPTs indicate that seismic response at the reservoir burial depth is more sensitive to local diagenetic changes (mineralogy, porosity) than fluid content.

Rock physics templates were validated as a tool-box for interpretation / classification of elastic inversion in low poro-perm sand. However, one should be aware of potential scale effects distorting the similarities between well log data and seismic data. So the templates are not quantitatively exact, but can be considered as a guide for enhanced qualitative interpretation of well log and seismic data. Furthermore, RPTs can be useful for quality control of elastic inversion results.

Lithological classification

From the pair AI versus Poisson's ratio it can be concluded that qualitatively, a high probability to separate between shale class and sands classes was obtained while tight sand class seems to gently overlap the good sand class.

The exercise showed that the chances of predicting sand (good, tight) in a position reserved for a shale class and vice versa were low. Also, the chances of isolating different sand classes are more reduced than previously.

When the porosity is very low, the fluid in the pore space is generally water, and there is therefore an association between gas content and porosity.

Extended Elastic Impedance (EEI)

The highest average correlation between EEI logs and targeted logs (Vclay, porosity, Sw) occurred at 0.79 and 36°,-0.76 and 18° and 0.61 and 20° respectively (see table 6.4). The strength of the correlation coefficients for Vclay and porosity confirms the effect of rock matrix on the seismic response compared with the fluid content (Sw) in a tight gas sand. While correlation for Sw was decent, a high dispersion (4-to-45) in the chi angle from one well to another was evident, downgrading the ability of EEI to predict the parameter.

On the other hand, F-O6 showed a consistently poor correlation compared with the other wells. Because of these observations, the F-O6 well was dispensed with and the exercise focused on EEI porosity and Vclay.

The correlation coefficient between petrophysical logs and inverted data at well location (F-O1, F-O2) was computed in a window from 3300m to log bottom to quality control the process. The 2 wells exhibit a correlation above 0.75 for both properties. The correlation

were of 0.904 and 0.813 for Vclay and porosity respectively in F-O2 well and 0.75 and 0.807 for F-O1 well.

The results show that EEI is worth the effort to highlight the difference between reservoir and non-reservoir using Vclay and porosity volumes.

The advantage of the EEI method was that it enables one to invert directly for an EEI volume that corresponds to a petrophysics parameter of interest (Vclay, porosity). However, although the directness of the method makes it highly efficient, the relationship between traditional AVO methods and EEI is not so intuitive.

Outcome analysis

Seismic reservoir characterization techniques, of which this chapter gives an extended review, are based on particular principles.

AVO-Cross-plotting: for a seismic event to be considered indicative of hydrocarbons in an AVO cross-plotting domain, a deviation from the background trend needs to be established.

Lithology and pore fluid prediction can be determined from elastic AVO inversion using 2 approaches.

One method used is Rock physics templates from theoretical rock models and the other Lithological classification which uses well data and probability density functions (pdfs) to define litho facies and their probability of occurrence.

EEI volumes are obtained directly from pre-stack data via linear projection in $\sin^2\theta$. This projection allows rock physics properties to be expressed in terms of impedance volumes.

Despite the principle used in each method above, all outcomes share parallels in the distribution of good and poor facies or reservoir and non-reservoir zones. Such observations were compiled below to help reduce the risk in drilling outcomes and to identify new prospective zones:

(1) In the acoustic impedance versus Poisson's ratio 2D-domain, porosity increased from right to left, hydrocarbon saturation (Sg) from top to bottom and shaliness from bottom to top.

2) Depending on the thickness and development of the low-velocity shale (LVS) and the in situ reservoir sand, different AVO classes could be expected at the top of 1At1. However, a weak Class I, in which gas sand still has higher impedance than the encasing shale, spanned a number of possible good facies cases in FO.

(3) In the (AI vs Poisson's ratio) domain at well and seismic resolution, 3 clusters can be sorted by Vclay and porosity. FO data exhibits good separation between sands and shales and moderate between gas and water sands.

(4) FO elastic interpretation was carried out taking into account the relationship between the outcomes and the geological framework (structural and depositional components).

In this regard, the F-O main structure is a high block inside a structural low zone, which could have helped to preserve the USM from erosion events during the development of the 1At1 regional unconformity. The block exhibits en-echelon faults (predominantly horst and graben structures). The area was described as a main graben divided into three block zones from north to south: (1) a half-graben (anticline) block tilted to the north and showing faults with limited extension, (2) a NNW faulted graben block and (3) a NW faulted half-graben) tilted to the south. Refer to figure 3.1.3.

Block 1 was intercepted by F-O2 and F-O4. This block shows an elongated seismic facies about 5,5 X 1,5 km long aligned to the axis of the anticline and mainly restricted to the northern flank of the structure. The facies is correlatable with a clean gas-sand with high porosities (10-12%).

Block 2 was described as a set of narrow blocks with predominantly low rock quality and poor gas facies. Two wells (F-O3, F-O6) were drilled in this zone.

Block 3 is characterized by intermittent seismic features correlated with moderate to good gas filled sands when located up the slope of the dipping blocks (F-O1).

FO is porosity-driven; therefore the predictability of seismic facies is controlled by the quality and heterogeneity of rock pores throughout the field. The quality of the reservoir (USM) is a product of a secondary enhancement poro-perm (EPP) process combined with a porosity preservation effect, owing to the over-pressure in the shales (LVS) above the reservoir. It is suggested that the enhancement is due to dissolution of carbonate cement (telodiagenesis porosity).

Regardless of the process, the EPP zone was confined to tens of metres in the upper part of USM. Simultaneously due to a rapid burial and compaction of the clay (LVS), the pressure built up and the formation became over-pressurized. The retention of high fluid pressures prevented subsequent compaction, resulting in preservation of the porosities enhanced in the crest of the structure.

F-O2 and F-O1 (block 1 and 3) were drilled in local highs of the structure and both exhibit better porosity at the top of the structure and are much tighter in the bottom interval. This behaviour was corroborated by the litho properties volumes which predicted higher porosities and better sand quality in the upper part of USM and decreasing to the base.

Another consideration concerning USM deposits is that the reservoir was interpreted as prograding marine siliciclastic sand units, where unlike block 1 and up-dip blocks in block 3, which correspond to more proximal sand deposits, sands in block 2 corresponds to a distal facies characterized by poor rock . The EPP process performed less well in block 2 than in the rest of the area. Overall, seismic litho property volumes discriminated well between good and poor litho facies.

Block 3 shows a segmented and scattered facies distribution, possibly due to the great number of tilted, faulted blocks eroded at the top of the reservoir by the 1At1 erosion

surface. This complex structure may have slightly deteriorated the image resolution, edge illumination and interpretability of otherwise masked or non-reflective events in this zone.

The northern flank of the anticline in block 1 represents a continuous area with the best rock-fluid properties in the area. On the other hand, block 3 has remaining and confined sweet spots worthy of drilling.

A coarsening upward unit outside the F-O area situated above the USM has hardly been analysed and is only recorded in a few wells outside the F-O area (E-W1 and E-M1). The sequence is only interpreted seismically in the flanks and lows in the FO structure where no wells have been drilled. This geological interval shows encouraging rock properties associated with low acoustic impedance and Poisson's ratio. Similarly, a smaller dip-fault closure (FO west structure) 5 km from FO main was interpreted as a clean gas sand with porosities greater than 10% in the crest of the structure. Refer to figure 6.4.19.

The predictability of all techniques reviewed in this dissertation depended mainly on how porous, continuous and thick the reservoir is. A good separation between lithologies (sand-shale) was exhibited, but differentiation between non-commercials to commercial gas sands is subject mainly to the rock matrix composition.

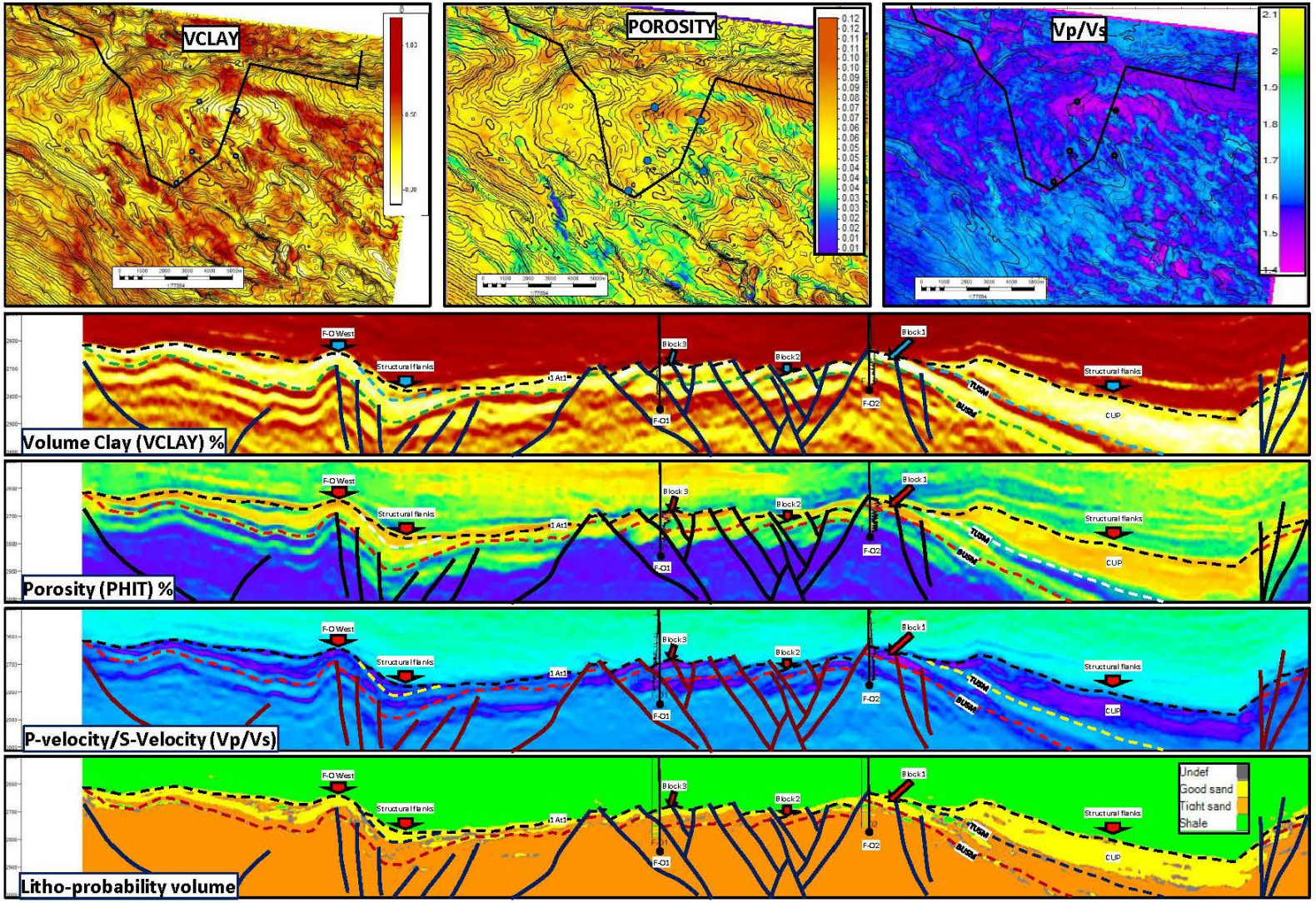

Figure 6.4.19: Sweet spots area identified using seismic rock properties volumes.

List of Tables

Table 3.1: Well results summary.

Well	Spud Year/ Location/ Details	Gross thickness (m)	Cores	Ave Porosity (%)	Permeability (mD)	DST
F-R1	. 1979 . Downdip SE of F-O structure	134	2	10	1	0.3 MMscf/d
F-O1	. 1989 . Downdip SE of F-O structure	101	2	11	5-40	No test: mechanical problem
F-O2	. 1991 . Crest of F-O structure	69.5	4	12	4	31.5 MMscf/d CGR 2
F-O3	. 1994 . Downdip S of F-O2	152	3	10.4	0.1-1	No flow
F-O4	. 2000 . West of F-O2 ? Deeper GWC	69.5	5	8	0.1	3.5 MMscf/d
F-O6	. 2008 . North-West of F-O 1	122	2	9	0.51	5.3 MMscf/d
F-O8	. 2008 . 300 m from F-O 1	110	No	10	4.2	26 MMscf/d

Table 3.1.2: Marker correlation based on gamma ray log and other interpretation.

Markers	F-O1	F-O2	F-O3	F-O4	F-O6	F-R1
1At1	3702.3	3615.7	3702.2	3706.7	3708.1	3876.9
9_RH - USM	3703.7	3617.4	3715.8	3710.3	3708.7	3882.7
8_RH	3715.8	eroded	eroded	3720.9	3715.4	3897.5
7_RH	3731.9	eroded	eroded	3748.9	3724.1	3910.2
6_RH	3737.7	eroded	eroded	3776.9	3740.7	3933.1
5_RH	3745.6	3648.7	3730.1	3798.8	3755.6	3951.9
4_RH	3771.5	3648.7	3745.8	3822.6	3783.5	3973
3_RH	3792.5	3668	3763.5	3836.9	3801.9	3991.2
2_RH	3811.5	3685.5	3780	3859	3830	4003

Table 3.3.1: Well data inventory

Well	X	Y	KB	DT	DTSM	RHOB	Petrophysical	Check-shots
F-O1	639384.6	6109719	26	YES	NO	YES	YES	YES
F-O2	642091.3	6112852	25	YES	YES	YES	YES	YES
F-O3	642035.5	6110864	22	YES	YES	YES	YES	YES
F-O4	640427	6113232	22	YES	YES	YES	YES	NO
F-O6	640087	6111072	25	YES	YES	YES	YES	YES
F-R1	645784.9	6108656	30	YES	NO	YES	YES	YES

Table 3.4.1: 3D seismic data area of interest.

Direction	Minimum	Maximum	Increment	Spacing (m)
IN-line	1160	1710	1	25
X-line	1920	3400	1	12.5

Table 3.4.2: Seismic interpretation picking coverage.

Horizon	Seabed	Ref Hor	22At1	17At1	16Bt1	16At1	13At1	1At1	BUSM	BLSM
IN-line spacing (m)	100	50	50	50	50	50	50, 25	10, 5	10	10, 5
X-line spacing (m)	100	50	50	50	50	50	50	20, 10	20	20, 10

Table 4.1.1: F-O well geothermal gradient.

	Avg Temp (Celsius C)	Depth (m)	GG (C/100m)
F-O1	141.157	3916.908	3.503
F-O2	145.533	3891.000	3.640
F-O3	149.050	3950.000	3.675
F-O4	147.800	3876.400	3.713
F-O6	158.200	3859.200	4.001

Table 4.2.1: Elastic parameters per mineral to compute the solid values (bulk modulus (K), shear modulus (G) and density).

ClayProperties		F-O1	F-O2	F-O3	F-O4	F-O6
ClayDen	(g/cc)	2.7	2.7	2.7	2.7	2.7
ClayK	Gpa	30	26	25	30	30
ClayG	GPa	11	13	13	11	11
QuartzDen	(g/cc)	2.65	2.62	2.65	2.65	2.65
QuartzK	Gpa	36.6	36.6	37.6	36.6	36.6
QuartzG	GPa	45	41	43	45	45
SiltDen	(g/cc)	2.65	2.65	2.65	2.65	2.65
SiltK	Gpa	39	39	39	39	39
SiltG	GPa	33	33	33	33	33
DolDen	(g/cc)	2.87	2.87	2.87	2.87	2.87
DolK	Gpa	76.4	76.4	76.4	76.4	76.4
DolG	GPa	49.7	49.7	49.7	49.7	49.7
IgneousDen	(g/cc)	2.62	2.62	2.62	2.62	2.62
IgneousK	Gpa	37.5	37.5	37.5	37.5	37.5

Table 4.2.2: Adjustable parameters (CN, AR and critical porosity) per each well.

Coordination number & Aspect Ratio	F-O1	F-O2	F-O3	F-O4	F-O6
Unconsolidated (Shale) / CN_Vp	15	15	9	12	15
Unconsolidated (Shale) / CN_Vs	14	14	8	11	13
Unconsolidated (Sand) / CN_Vp	18	18	11	30	18
Unconsolidated (Sand) / CN_Vs	17	17	10	28	17
HMHS (Sand) / CN_Vp	8	8	8	8	8
HMHS (Sand) / CN_Vs	7	7	7	7	0
SelfConsistent (Sand) / AR_Vp	0.04	0.04	0.04	0.04	0.04
SelfConsistent (Sand) / AR_Vs	0.04	0.04	0.04	0.04	0.04
DEM (Sand) / AR_Vp	0.9	0.9	0.9	0.9	0.9
DEM (Sand) / AR_Vs	0.6	0.6	0.6	0.6	0.6
Critical Porosity / Vp	37	37	37	37	37
Critical Porosity / Vs	35	35	35	35	35

Table 4.3.1: Greenberg and Castagna (1992) empirical coefficients versus F-O field coefficients.

Lithology	ai2	ai1	ai0
Sandstone	0	0.80416	-0.85588
Shale	0	0.76969	-0.86735
Limestone	-0.05508	1.01677	-1.03049
Dolomite	0	0.58321	-0.07775
F-O Sandstone	0	0.815	-0.845
F-O Shale	0	0.83	-1.3

Table 5.2.1: Polygon used to build the mute filter.

Muting Offset(m)	Time (ms)
340	0
350	200
600	500
1000	800
1600	1000
2150	1200
2870	1500
3663	1800
4220	2000
4800	2200
5500	2400
6150	2600

Table 5.2.2: Correlation coefficients for each partial stack cases.

F-O1	Case 1	Case 2	Case 3
AI	0.842	0.840	0.845
VPVS	0.814	0.789	0.707
Density	0.573	0.656	0.532

F-O2	Case 1	Case 2	Case 3
AI	0.805	0.789	0.779
VPVS	0.772	0.760	0.756
Density	0.273	0.353	0.290

Table 5.3: Quality control parameters computed from the best match location wavelet for each well.

Well	AVA Central Angle (°)	Partial angle stack	Predictability (%)	Coefficient correlation	Wavelet Phase (deg)	Lag from RC to seismic (ms)	Signal to noise	Top Window	Base Window	Inline	Xline
F-O1	10	Near	87.28	0.79	-2.5	4	6.86	2352	2792	1452	2604
	20	Near_Mid	85.46	0.85	-5.81	0	6.13	2352	2792	1452	2604
	30	Mid_Far	84	0.83	-0.01	0	5.25	2352	2792	1452	2604
	40	Far	80.14	0.78	-2.89	0	4.07	2352	2792	1452	2604
F-O2	10	Near	74.21	0.81	-11.98	4	2.87	2344	2748	1315	2790
	20	Near_Mid	78.69	0.89	-7.77	0	3.69	2344	2748	1315	2790
	30	Mid_Far	72.79	0.73	9.88	-4	2.67	2344	2748	1315	2790
	40	Far	61.94	0.68	9.66	0	1.72	2344	2748	1315	2790
F-O3	10	Near	74.482	0.81	3.104	0	2.91	2340	2764	1394	2804
	20	Near_Mid	75.46	0.80	13.82	-8	3.076	2340	2764	1394	2804
	30	Mid_Far	67.52	0.71	2.42	4	2.08	2340	2764	1394	2804
	40	Far	52.83	0.59	-71.4	0	1.12	2340	2764	1394	2804
F-O4	10	Near	77.42	0.70	10.62	4	3.43	2364	2740	1308	2654
	20	Near_Mid	78.43	0.80	0	8	3.63	2364	2740	1308	2654
	30	Mid_Far	61.6	0.79	-10.27	8	1.6	2364	2740	1308	2654
	40	Far	59.15	0.76	-13.9	8	1.44	2364	2740	1308	2654
F-O6	10	Near	72.21	0.59	32.16	8	2.59	2368	2744	1395	2647
	20	Near_Mid	70.54	0.56	17.7	0	2.39	2368	2744	1395	2647
	30	Mid_Far	71.6	0.73	-1.89	0	2.53	2368	2744	1395	2647
	40	Far	71.5	0.72	-6.19	0	2.51	2368	2744	1395	2647
F-R1	10	Near	68.26	0.72	5.62	0	2.15	2400	2888	1465	3123
	20	Near_Mid	62.47	0.71	-2.98	4	1.66	2400	2888	1465	3123
	30	Mid_Far	72.69	0.80	-1.4	-4	2.66	2400	2888	1465	3123
	40	Far	56.1	0.61	-5.28	0	1.27	2400	2888	1465	3123

Table 6.4: Quality control parameters computed from the best match location wavelet for each well.

	Max. Correlation Coefficient			(Chi °)		
Well	Porosity	Vclay	Saturation	Porosity	Vclay	Saturation
F-O1	-0.86	0.90	0.55	14	29	18
F-O2	-0.83	0.85	0.80	17	36	20
F-O3	-0.63	0.80	0.67	21	40	40
F-O4	-0.70	0.77	0.74	17	45	20
F-O6	-0.26	0.56	0.30	14	90	4
F-R1	-0.79	0.61	0.30	21	28	4
Average	-0.68	0.74	0.56	17	45	18
Ave w/out F-O6	-0.76	0.79	0.61	18	36	20

Appendix

2.2.1.- Theoretical models:

Contact models

The principle behind contact models is to approximate the rock as a collection of random separate grains (spherical particles). The effective elastic properties of a pack of spherical particles are determined by the deformability and normal and tangential contact stiffness of a grain-to-grain combination. The key parameters determining the stiffness of the rock are the elastic moduli of the spherical grains and the area of grain contact, which results from the deformability of the grain under pressure (Avseth et al., 2005).

The contact Hertz-Mindlin theory (Mindlin, 1949) gives a solution for the elastic behaviour of two elastic identical spherical grains in contact, subject to a hydrostatic pressure P, and lays the foundation for other contact models (Walton, 1987; Digby, 1981, etc.). Nonetheless, these contact models require extrapolation to irregular grain shapes, as all are based on idealized geometries.

Inclusion models

The inclusion models approximate the rock as a continuous elastic solid containing solid or fluid cavities (inclusions). In these models, the solid inclusions represent the grain solids and the fluid inclusions the pore spaces. Most of the inclusion models assume that both the pores and the grains are ellipsoidal inclusions in the composite material (Berryman, 1980). On the other hand, the differential effective medium (DEM) theory models a two-phase composite material by incrementally adding inclusions of one phase to the matrix phase.

Similar to contact models, inclusion models have limitations in that they idealize pore geometries that result from different depositional or diagenetic processes.

3.2.-Seismic data acquisition and processing parameters

a.- Acquisition geometry

Parameters	**Remarks**
Cable type	Q Marine Nessie 5
Number of streamers	10 (7 over and 3 under)
Group interval (m)	6.25
Streamer length (m)	6000 (active length)
Streamer depth (m)	8 and 20 m
Streamer separation (m)	100 (over streamers), 233 (under streamers)

Recording format	SegD 8036
Recording format revision	Rev 2
Recording length (binary ms)	7168
Sample rate (ms)	2
Source type	BoltGun array
Number of source arrays	2
Source array separation (m)	50
Shotpoint interval (m)	18,75
Array volume per source (in^3)	5085
Operating pressure (psi)	2000
Source depth (m)	7
Nominal bin size	12,5 X 25

b.- Processing sequence:

Subsequently, the 662 km² of 3D seismic data was processed following the offshore processing sequence below.

1. Input 6,25m enhanced DGF SEGY data; 7.164 sec record length; 80-fold
2. Spatial anti-alias K filter and trace drop

   Output 12,5 m group interval
3. Calibrated marine source designature (CMS)

   Zero phase output

   Including De-bubble
4. Resample to 4 msec (following anti-alias filter)
5. Low-cut filter (3Hz)
6. Direct arrival attenuation (Tau-p noise attenuation - applied in the common shot domain)
7. Swell noise attenuation (in the common shot and receiver domains)
8. Tidal statics.
9. Regularization of low-frequency data from under streamers to over streamer locations (including shot interpolation of the under streamer data).
10. Optimal noise weighted wavefield separation and re-datuming at aligned over/under (O/U) pairs.
11. Tau-p noise attenuation (linear) – applied in the shot domain
12. Velocity analysis at 1000 x 1000 m spacing – using as guiding function client supplied

field and Tau-P decon and Radon for multiple attenuation

13. Deterministic water demultiple (DWD)

14. 3:1-shot interpolation

15. 2D surface-related multiple elimination (SRME)

16. Directional designature – in the receiver domain

17. Direct arrival attenuation (Tau-p noise attenuation - applied in the common receiver domain)

18. Tau p noise attenuation (linear) – applied in the receiver domain

19. 3:1 K-filter in receiver domain

20. 3:1 K-filter in CMP domain

21. Weighted least squares Radon

22. Drop interpolated traces

23. 2:1 K-filter in shot domain

24. Q compensation – phase only (single average Q value)

25. Migration velocity analysis

    Iteration 1, isotropic on a 2km x 2km grid

    Iteration 2, anisotropic on a 1km grid with eta picked on a 2km grid

26. Bin regularisation using compact fourier interpolation (COMFI)

27. Fill in missing traces within offset planes

28. 3D-residual noise attenuation (RNA) on offsets planes

29. Time-variant filter (TVF)

30. Full kirchhoff pre-stack time migration

    Anisotropic, ray-traced kirchhoff migration algorithm

    Input smoothed (2km radius smoothing) velocity from migration velocity analysis step

    Input bin size : 12,5m x 25m

    Output bin size : 12,5m x 25m

    Migration aperture (radius) : 8 km

    Maximum dip limit = 80 degrees

31. Sort to 3D CMP

32. Inverse moveout correction – 2^{nd} order only

33. Output to SEGY (OUT02)

34. Post-migration velocity analysis, 2nd order on 500 m grid

35. Spatially continuous velocity analysis (SCVA)

    Automatic 2nd order velocity analysis with output on 100 m x 100m grid.

36. Normal moveout correction

37. Weighted least squares Radon

38. Post Radon remnant noise attenuation on far offsets

39. Spectral offset balancing

40. Output to SEGY (OUT03)

41. Mute

    Full, inner, mid and outer

42. 3D Angle stacks

    3 angle stacks (0-18, 18-36, 36-54 degrees)

    Output to SEGY (OUT04, OUT05, OUT06) including cable static and exponential gain

43. 3D Full stack

    Output to SEGY (OUT07) including cable static and exponential gain

44. Q compensation – amplitude only , Q=157)

45. Source static (+4.6 ms)

46. Zero phase conversion (using well match, -36,8 degrees)

47. Output angle stacks for inversion with source signature compensation filter (angles 0-8, 8-16, 16-24, 24-32, 32-40,40-48 and 48-56 degrees)

48. Output to SEGY (OUT08) – final angle stacks (0-18, 18-36, 36-54 degrees) – including exponential gain

49. Noise attenuation: layer parallel smoothing

50. Time variant spectral whitening

51. Noise attenuation: layer parallel smoothing

52. Time variant filter

53. Resolution enhancement by modulation (REM)

54. Exponential gain

55. Output to SEGY (OUT09) – final interpretation full stack

4.1.-Well data preparation

The litho-density and gamma ray curves were environmentally corrected to account for hole size and mud weight. These curves were used directly in log analysis, so it was

important to normalise them for these effects.

Core data was available for wells F-O1, F-O2, F-O3, F-O4, F-O6 and F-R1. Core analysis was largely confined to the better quality reservoir, and sufficient core was available to characterize the net reservoir sands.

Clay volume: Clay volume (Vcl) was calculated from environmentally corrected gamma ray data. However, a modification of the standard linear interpolation technique was performed to deal with the presence of small quantities of heavy radioactive minerals which, if not correctly accounted for, were misinterpreted as extra clay volume. The method, is given below:

$$\mathrm{Vcl} = \frac{\mathrm{GRlog} - \mathrm{GRmin}}{\mathrm{GRmax} - \mathrm{GRmin}}$$

If V_{cl} is less than or equal to 0.55:

$V_{cl,corr} = 0.0006078(100\ V_{cl})^{1,58527}$

If V_{cl} is greater than 0.55 but less than or equal to 0.73:

$V_{cl,corr} = (2.12\ V_{cl}) - 0.81667$

If V_{cl} is greater than 0.73:

$V_{cl,corr} = V_{cl}$

The effect of the application of this (partly) non-linear technique on clay content is a reduction with respect to the linear methodology, particularly at low to mid-clay contents. This "cleans up" the formation, decreasing the clay content and therefore increasing net sand volume. This better matches density neutron response in all wells (Lean et al., 2001).

Porosity: Porosity (ϕ) from wireline litho density (ρ_{log}) was used. This was environmentally corrected using Schlumberger Chart Por-15a (Schlumberger, 2001, Log interpretation chart) and effective porosity was generated using the conventional technique below:

$$\phi Den, eff = \frac{\rho ma - \rho log}{\rho ma - \rho fl} - Vcl\left(\frac{\rho ma - \rho cl}{\rho ma - \rho fl}\right)$$

A matrix density (ρma) of 2.67 g/cc was defined from a histogram of all core grain density data. A clay density (ρcl) of 2.65 g/cc was selected after examination of reservoir shale.

Water saturation: The Indonesia equation (Poupon and Leveaux, 1971) was used to determine S_w, allowing for the excess conductivity due to the presence of clay within the sandstone which affects the resistivity response. Though clay volumes in net sands are low, wet chemistry work on Well F-O1 core indicates significant clay conductivity (cation exchange capacity (CEC) is on average 0.1 Meq/100g). The clay resistivity (R_{cl}) for use in the Indonesia equation is taken as 7 ohm.m from examination of the resistivity response of the intra-reservoir shales.

$$\frac{1}{\sqrt{\mathrm{Rt}}} = \left(\frac{\mathrm{Vcl}^{1-\mathrm{Vcl}/2}}{\sqrt{\mathrm{Rcl}}} + \frac{\phi^{\mathrm{m}/2}}{\sqrt{\mathrm{aRw}}}\right)\mathrm{Sw}^{\mathrm{n}/2}$$

where:

Vcl and Rcl = shale volume and resistivity

Rt = deep resistivity

Rw = brine water resistivity

Ø = effective porosity

Sw= water saturation

and the electrical parameters are:

Cementation constant a = 1.00

Cementation exponent m = 2.06

Saturation exponent n = 1.81

The net to gross ratio is based on a cutoff defined by petrophysical relationships: Vcl vs θeff.

Net sand is defined as rock with a Vcl<35% and Øeff> 6%.

4.2.-Rock physics modelling

Unconsolidated sand model: The unconsolidated sand model is based on the combination of the contact Hertz-Mindlin theory and the modified Hashin-Shtrikman lower bound (Dvorkin and Nur 1996).

The Hertz-Mindlin theory gives the contact stiffnesses for two spherical grains subject to a confining pressure. The effective bulk and shear moduli of the aggregate are calculated using the assumption that all grains are spherical and are arranged in a random pack of porosity ≈ 0.36.

$$KHM = \left(\frac{n^2(1-\emptyset c)^2 G^2}{18\pi^2(1-\nu)^2} P\right)^{1/3} \qquad GHM = \frac{(5-4\nu)}{5(2-\nu)}\left(\frac{3n^2(1-\emptyset c)^2 G^2}{5\ 2\pi^2(1-\nu)^2} P\right)^{1/3}$$

where KHM and GHM are the bulk and shear moduli respectively at the high porosity end-member $\emptyset c$; P is the effective pressure; G and ν are the shear modulus of the solid phase and its Poisson ratio, respectively; and n is the coordination number (the average number of contacts per grain).

The equation for the lower modified Hashin-Shtrikman bound connects two end points. One is the critical porosity end point, where the elastic bulk and shear moduli are determined from the Hertz-Mindlin contact solution; the other is the zero point where the elastic moduli are those of the mineral phase. The effect of pore fluid is introduced by using Gassmann's (1951) equation. It is recommended for unconsolidated sands and high ranges of porosities (Figure 4.2.1).

Intermediate stiff sand model: The intermediate stiff sand model is used instead of the contact cement model (Avseth et al. 2000). The intermediate stiff sand model uses the function form of the unconsolidated sediment model as given by the equation below, but

using the high porosity end point situated on the stiff sand model curve:

$$\mathrm{KDry1} = \left[\frac{\left(\frac{\emptyset}{\emptyset o}\right)}{\mathrm{ko}+\frac{4}{3}\mathrm{Go}} + \frac{1-\frac{\emptyset}{\emptyset o}}{\mathrm{k}+\frac{4}{3}\mathrm{Go}}\right]^{-1} - \frac{4}{3}\mathrm{Go}$$

$$\mathrm{GDry1} = \left[\frac{\left(\frac{\emptyset}{\emptyset o}\right)}{\mathrm{Go}+\mathrm{Z}} + \frac{1-\frac{\emptyset}{\emptyset o}}{\mathrm{Go}+\mathrm{Z}}\right]^{-1} - \mathrm{Z}$$

$$\mathrm{Z} = \left[\frac{\mathrm{Go}}{6}\left[\frac{(9\mathrm{ko}+8\mathrm{Go})}{\mathrm{ko}+2\mathrm{Go}}\right]\right.$$

where KDry1 and GDry1 are the dry - frame bulk and shear moduli, respectively; Øo, Ko and Go are the porosity, dry-frame bulk and shear moduli values, respectively, at the high-porosity end point; and k is the bulk modulus of the grain material (the mineral phase).

The intermediate stiff sand curves can be generated by increasing the coordination number of the unconsolidated sediment model (Mavko et al., 2009). The artificially increased coordination number may be representative of an initial contact cementation effect as described in the contact cement model.

Hertz-Mindlin / Hashin-Shtrikman (HMHS): This refers to the Hashin-Shtrikman upper bound. HMHS uses the "contact cement" sand model of Dvorkin et al. to estimate bulk modulus (*K*) and shear modulus (μ) from porosity and fluid properties. Vp and Vs are computed from *K* and μ using elasticity equations (Mavko et al., 2009).

The high porosity limit of velocity is determined from the Hertz-Mindlin unconsolidated sphere pack model. This model has an adjustable parameter known as the coordination number. This is the number of contact points per sphere in the random size sphere pack. A higher coordination number means a stiffer pack and, therefore a higher velocity at the highest porosity level. The coordination number used was 8 and the c**ritical porosity used was** 0.37.

This approach is recommended for well consolidated clastics (depths > 3000 m) and low to medium porosity ranges.

Self-consistent: An effective medium theory predicts the bulk and shear moduli of composite materials consisting of a matrix material with soft or hard ellipsoidal inclusions. Disc-shaped inclusions are most effective for softening or hardening a composite material.

The self-consistent approximation (Hill, 1965; Wu, 1966) uses a mathematical solution for the deformation of isolated inclusions, but the interaction of inclusions is approximated by replacing the background medium with the as yet unknown effective medium.

These methods were approached in different ways by different authors. O'Connell and Budiansky (1976) presented effective bulk (k_{SC}) and shear moduli (μ_{SC}) equations of a cracked medium with randomly oriented dry penny-shaped cracks. Wu's self-consistent modulus estimates the moduli for two-phase composites (m = matrix, i=inclusions),

$$K_{SC}^{*} = K_m + x_i(K_i - K_m)P^{*i}$$

$\mu_{SC}^{*} = \mu_m + x_i(\mu_i - \mu_m)Q^{*i}$

but it was Berryman (1980) who gave a more general form of the self-consistent approximations for n-phase composites:

$\sum_{i=1}^{N} x_i\,(K_i - K_{SC}^{*})P^{*i} = 0$

$\sum_{i=1}^{N} x_i\,(\mu_i - \mu_{SC}^{*})Q^{*i} = 0$

where i refers to the *ith* material, x_i is its volume fraction, and P and Q are geometric factors, and the superscript **i* on P and Q indicates that the factors are for inclusion of material *i* in a background medium with self-consistent effective moduli K_{SC}^{*} and μ_{SC}^{*}.

The use of the self-consistent model is recommended for all lithologies with low-to-medium porosities.

DEM: The purpose of the differential effective medium model (DEM) is to estimate the effective elastic moduli of a rock in terms of its constituents and pore space. DEM theory is based on a two-phase composite model in which inclusions of one phase (phase 2) are incrementally added to the matrix phase (background phase, phase 1). Starting with the matrix phase 1 (when the concentration of phase 2 is zero), a new increment of phase 2 material is added at each step. The process is continued until the desired proportion of the constituents is reached (Mavko et al., 2009).

The DEM formulation does not treat each constituent symmetrically. For multiple inclusion shapes or multiple constituents, the effective moduli depend on the final volume fractions of the constituents, but also on the order in which the incremental additions are done.

The coupled system of ordinary differential equations for the effective bulk and shear moduli, *K* and μ are:

$$(1-y)\,d/dy[K^{*}(y)] = (K2-K)P^{*2}(y)$$
$$(1-y)\,d/dy[\mu^{*}(y)] = (\mu\,2-\mu)Q^{*2}(y)$$

where the initial conditions are $K(0) = K1$, $\mu(0) = \mu1$,

*K*1, μ1 are bulk and shear moduli of the initial host material (phase1, background material), *K*2, μ2 are bulk and shear moduli of the incrementally added inclusions (phase2, inclusion material), y is the concentration of phase 2.

For fluid inclusion and voids, y equals the porosity Ø. The terms *P* and *Q* are geometric factors and the superscript *² on P and Q indicates that the factors are for an inclusion of material 2 in a background medium with effective moduli *K** and μ*.

The DEM model is recommended for all lithologies, all fluids and low porosity ranges.

A conceptual difference between the DEM and the self-consistent model to calculate effective moduli of composites is that the DEM scheme identifies one of the constituents as a host or matrix material in which inclusions of the other constituent(s) are embedded, whereas the self-consistent scheme does not identify any specific host material but treats the composite as an aggregate of all constituents (Mavko et al., 2009).

Raymer model: A relatively simple monotonic relation between velocity and porosity in sedimentary rocks can often be found according to measurements by Willie et al. (1956), if (1) they have relatively uniform mineralogy and (2) they are fluid-saturated.

An improvement on Wyllie's empirical velocity-to-travel time relations was suggested by Raymer et al. (1980) as follows:

$Vp = (1-Ø)^2\ V0 + Ø\ Vfl$ If $Ø < 37\%$

$1/M = Ø\ /Mfl + (1- Ø)/M0$ If $Ø > 47\%$

where $Ø$ is the porosity; Vp, $V0$, and Vfl are the P-wave velocities of the saturated rocks, the mineral material and the pore fluids, respectively. M, Mfl, and $M0$ are the P-wave moduli ($= \rho Vp^2$) in the rock, the pore fluid and the minerals, respectively.

An expression for intermediate porosities is derived as a linear interpolation of the first two expressions at Phi=37% and Phi=47%.

This model may not yield accurate estimates in all situations, because it only an empirical formula. However, it may work better than Wyllie's relation in high-porosity, poorly consolidated sands.

4.3 Well log conditioning

Cycle skips are an instrumental phenomenon occurring in acoustic velocity logs and, consist of intervals where the velocity recorded drops sharply to very low values and equally sharply returns to a normal scale figure. Such a log is spiky.

4.4.1 Fluid substitution

Gassmann's equations relate the bulk modulus of a rock to its pore, frame and fluid properties. The bulk modulus of a saturated rock is given by the low-frequency Gassmann theory (Gassmann, 1951) as:

$$\mathrm{Ksat} = \mathrm{Kframe} + \frac{\left(1-\frac{\mathrm{Kframe}}{\mathrm{Kmatrix}}\right)^2}{\frac{Ø}{\mathrm{Kfl}}+\frac{(1-Ø)}{\mathrm{Kmatrix}}-\frac{\mathrm{Kframe}}{\mathrm{K^2matrix}}}$$

where Ksat, Kframe, Kmatrix and Kfl are the bulk moduli of the saturated rock, porous rock frame (drained of any pore-filling fluid), mineral matrix, and pore fluid respectively and ϕ is porosity (as a fraction).

5.2.1 Pre-stack seismic conditioning

Radon transform background

The Radon transform is a mathematical technique developed by Johan Radon in 1917. This application of the technique is based on the moveout difference, which usually involves a transformation of the data from the space and time (x and t) domains to zero offset time and moveout velocity domain (also known as Tau-P space) to separate primary and multiple events. The primaries can then be muted and the multiples can then be transformed back and subtracted from the input data.

In seismic data processing, there are typically 2 different implementations of the Radon transform, linear and parabolic τ-p. The correct choice for pre-stack data depends on the goal of the process.

This is because events which are imperfectly NMO corrected appear as parabolas. Also, events which are correctly NMO-corrected, but have amplitude variation, can be modelled as a superposition of closely spaced parabolas. The only logical case for linear is to attenuate linear noise on pre-stack or post-stack data.

Figure below illustrates the principles behind the Radon transform in a more intuitive way. This process assumes that all the coherent data within a gather can be modelled as a linear combination of a series of parabolic shapes of constant amplitude. While the algorithm is actually performed in the frequency domain, it can be thought of as a set of parabolas (e.g. 20) located at each time sample. Each parabola is defined by its (constant) amplitude and its moveout. The moveout is the curvature of the parabola, measured as the difference in time (ms) between the parabola at the far offset and the parabola at the near offset. The set of parabolas typically spans the range of moveouts, from -10 ms to 200 ms. Once the model is created, the Radon transform then subtracts the model of these multiples or noise from the data, leaving you with a data set that is greatly reduced in noise and optimizes the traces. The waveform is also better preserved at both near and far offset.

5.2.2 Partial angle stack definition

Critical angle

The largest possible angle of incidence which still results in a refracted ray is called the critical angle; in this case the refracted ray travels along the boundary between the two media. From the Snell's law:

$$\text{Sin}\ (\theta_{cr}) = \frac{Vp1}{Vp2}$$

where θcr is the critical angle, Vp1 is the velocity in the upper layer, and Vp2 is the velocity in the lower media.

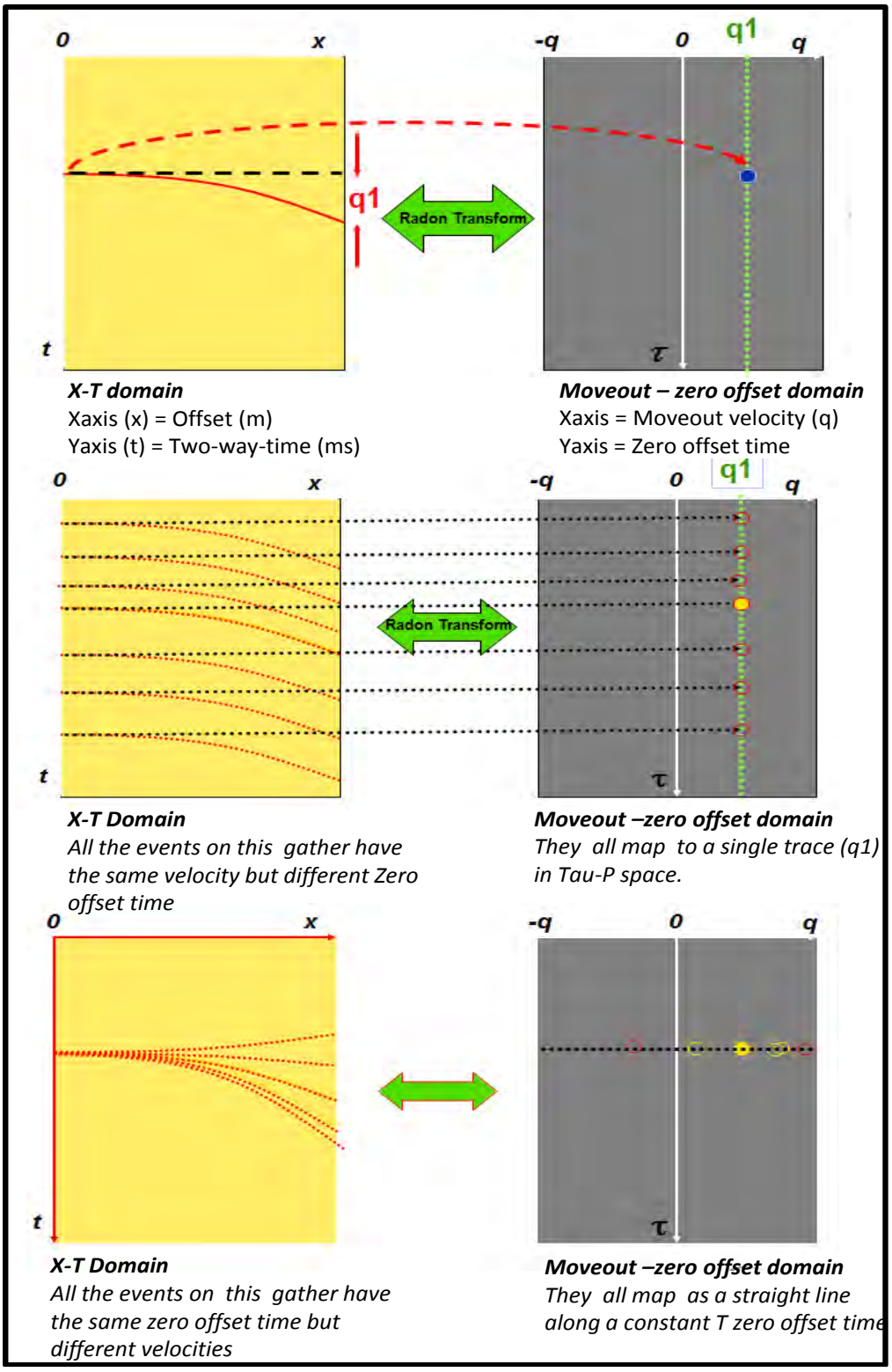

Events with the same move-out velocity but different zero offset times map to a single trace, q1 in Tau-P space and events with different velocities but the same zero offset time map to different P traces along the same Tau line in Tau-P space.

Correlation coefficient

The correlation coefficient measures the degree of association between two or more variables. In the two-variables case, the simple linear correlation coefficient for a set of

sample observations is given by:

$$\text{Correl}(X, Y) = \frac{\sum(x-\bar{x})(y-\bar{y})}{\sqrt{\sum(x-\bar{x})^2 \sum(y-\bar{y})^2}}$$

Where

$\bar{x}$ and $\bar{y}$ are the sample means average

A normalized cross-correlation, or a correlation coefficient, equal to unity indicates a perfect match, whereas a poor match will yield a value close to zero.

Signal to noise

The energy (or sometimes amplitude) of the signal divided by all remaining energy (noise) at the time. Signal to noise ratio is difficult to determine because of the difficulty in isolating the signal.

5.3 Roy White wavelet method

The Roy White wavelet algorithm estimates the seismic wavelet by calibrating well log data and seismic data. The procedure comprises three steps; (a) best match location, (b) wavelet extraction and (c) parameter diagnostic.

Roy White assumes that the well location may not be optimal for wavelet extraction, so the algorithm searches for an optimal new location within the user-specified vicinity of the existing well. (White and Simm, 2003).

Scanning the best location

The algorithm searches for the best match time location by scanning within a specified vicinity of the posted well location. From well logs (sonic and density) a reflectivity R (t) is calculated. Then, for each frequency *f* the spectral coherence function is defined as the normalized magnitude-squared cross-spectrum between the reflectivity R and the seismic trace S:

$$\Upsilon^2(f) = \frac{|\phi RS(f)|^2}{\phi RR(f)\phi SS(f)} \quad (1)$$

where

$\phi_{RS}(f)$= Cross-correlation spectrum of the reflectivity and the seismic trace in the frequency domain

$\phi_{RR}(f)$= Auto-correlation of the reflectivity in the frequency domain

$\phi_{SS}(f)$= Auto-correlation of the seismic trace in the frequency domain

The spectral coherence measures the proportion of energy in the seismic trace that can be predicted from well-log reflectivity in the bandwidth b centred at frequency *f* and by analogy the proportion PEP ("Proportion of Energy Predicted") of the total energy in the

seismic trace that can be predicted from the well log reflectivity over the whole seismic bandwidth is defined. PEP can be measured directly from the seismic trace and the optimally matched (filtered) well-log reflectivity.

$$\text{PEP} = \frac{\text{Output Energy} - \text{Residual Energy}}{\text{Out Energy}} = \frac{|S|^2 - |S - R * W|^2}{|S|^2}$$

$$\text{PEP} = \frac{\text{Energy in the Residuals}}{\text{Trace Energy}} \quad (2)$$

where the residuals are the difference between the seismic trace and its matched or filtered reflectivity and the energy of a segment of a time series is its sum of squares. The predictability PEP is a single scalar between O and I which measures the goodness of fit between the reflectivity calculated using the calibrated well and the seismic trace at the well location.

To search for the optimal location in the vicinity of the well in order to get the best fit, three parameters are introduced:

Lag = time shift in ms by which the reflectivity R is shifted before calculating the predictability,

XSHIFT = shift along the x-direction from the borehole by which the match location is moved,

YSHIFT = shift along the y-direction from the borehole by which the match location is moved.

PEP = PEP (Lag, XSHIFT, YSHIFT) (3)

The goal is to look for the three values which maximize PEP. This is done in two stages. For any given value of XSHIFT and YSHIFT, the algorithm calculates the optimum time shift, bestLag. The result is a set of maps (predictability) with values as a function of deviation from the original well location:

$PEP_{bestlag}$ = $PEP_{bestlag}$ (XSHIFT, YSHIFT) (4)

Each pair of PEP values (XSHIFT, YSHIFT) has already been optimized with respect to lag. By examining the maps, the optimum location for the subsequent wavelet extraction is selected visually.

Wavelet extraction: Once the optimal location is chosen, the wavelet spectrum is extracted by the algorithm described in White and Simm (2003). In the case where the computed reflectivity r is error-free, the wavelet spectrum is:

$$W(f) = \frac{[R(\text{bestLag}) * S](f)}{[R(\text{bestLag}) * R(\text{bestLag})(f) + \text{WNOISERRmax}(f)} \quad (5)$$

where:

R(bestLag) = the reflectivity shifted by the lag which optimizes the value at the location

R*S = the cross-correlation between R and S

R*R = the autocorrelation of R

[R*S](f) = the frequency domain version of cross-correlation R*S (a complex function)

WNOISE = noise factor added for stability

5.4 Ormsby filter

The bandpass of an Ormsby filter can be described by using up to 4 corner frequencies:

1. the low-cut frequency, where all lower frequencies are filtered out and not used;
2. the low-pass frequency after which 100% of all higher frequencies will be used until point 3;
3. the high-pass frequency beyond which frequencies will be linearly tapered until point 4;
4. the high-cut frequency beyond which any frequencies will be filtered out and not used.

Frequencies below the **low cut** or above **high cut** are rejected. Between low pass and high pass the filter is flat at amplitude of 1.

5.5 Simultaneous seismic inversion

A brief summary of the foundations on which the method is based is given below.

When incident P-waves propagate through an interface with different medium properties on both sides, the seismic wave energy of the ray is partitioned so that P-waves and converted S-waves reflect and transmit (refract) off an interface at non-normal incidence. The incident angle, reflection angles, and transmitted angles, together with P and S velocities on both sides of the medium obey Snell's law as:

$$\frac{\sin(\vartheta 1)}{\alpha 1} = \frac{\sin(\vartheta 2)}{\alpha 2} = \frac{\sin(\phi 1)}{\beta 1} = \frac{\sin(\phi 2)}{\beta 2} = p$$

where p is the ray parameter and $\vartheta 1$ and $\vartheta 2$ are the incident/reflected P-wave angle and transmitted P-wave angle respectively, $\phi 1$ and $\phi 2$ are the reflected and transmitted S-wave angle respectively, α1 and β1 are the P and S wave velocities of medium 1 and α2 and β2 are the P and S wave velocities for medium 2.

Zoeppritz equations were developed and published in 1919 to describe the partitioning of seismic wave energy at an interface, typically between two different layers of rocks. They are relevant to the scope of seismic characterization because they relate the amplitude of P-waves incident upon a plane interface and the amplitude of reflected and refracted P- and S-waves to the angle of incidence, and that is the basis for investigating the factors affecting the amplitude of a returning seismic wave when the angle of incidence is altered, also known as amplitude versus offset analysis.

However, although Zoeppritz equations represent the exact theoretical solution for reflection coefficients they are not so intuitive and easy to apply to seismic data because of

the high number of unknowns about the subsurface and the complexities of the earth. Therefore, in order to provide simpler solutions to reflection coefficients, an approximation of the Zoeppritz equations was introduced by Aki and Richards (1980). Aki and Richards introduced a first-order Zoeppritz approximations for the P-P (incident P-wave and reflected P-wave) reflection coefficient (Rpp) as:

$$\mathrm{Rpp}\,(\vartheta) \approx \frac{1}{2}(1 - 4\left(\frac{\beta}{\alpha}\right)^2 \sin^2\vartheta)\frac{\Delta\rho}{\rho} + \frac{1}{2}(1 + \tan^2\vartheta)\frac{\Delta\alpha}{\alpha} - 4\left(\frac{\beta}{\alpha}\right)^2 \sin^2\vartheta\frac{\Delta\beta}{\beta}$$

where α is the average of the two P-wave velocities on both sides of the reflector. β is the average of the two S-wave velocities on both sides of the reflector, ρ is the average of the two densities on both sides of the reflector, and θ is the average of the incident and transmitted P-wave angles. $\Delta\alpha = \alpha 2 - \alpha 1$, $\Delta\beta = \beta 2 - \beta 1$ and $\Delta\rho = \rho 2 - \rho 1$.

Additional approximations of Zoeppritz equations were postulated by Shuey (1985), Smith and Gidlow (1987) and Fatti, et al., (1994). Simultaneous AVO inversion was performed using two possible model parameterizations: Aki and Richards approximation to the Zoeppritz equations and the Fatti approximation to the Zoeppritz equations.

6.1 Estimation of intercept, gradient and curvature

A totally equivalent form of the Aki-Richards equation was derived by Wiggins et al. (1983). They separated the previous equation into three reflection terms, each weaker than the previous term:

$$\mathrm{R}(\theta) = \mathrm{A} + \mathrm{B}\sin^2\theta + \mathrm{C}\sin^2\theta\tan^2\theta$$

Where: $\mathrm{A} = \frac{1}{2}\left[\frac{\Delta \mathrm{Vp}}{\mathrm{Vp}} + \frac{\Delta\rho}{\rho}\right]$ = intercept,

$$\mathrm{B} = \frac{1}{2}\frac{\Delta \mathrm{Vp}}{\mathrm{Vp}} - 4\left[\frac{\mathrm{Vs}}{\mathrm{Vp}}\right]^2\frac{\Delta \mathrm{Vs}}{\mathrm{Vs}} - 2\left[\frac{\mathrm{Vs}}{\mathrm{Vp}}\right]^2\frac{\Delta\rho}{\rho}$$ = gradient,

$$\mathrm{C} = \frac{1}{2}\left[\frac{\Delta Vp}{Vp}\right]$$ = curvature

This is often considered to be the AVO equation or ABC equation.

References

Aki, K. and Richards, P. G., 1980, Quantitative seismology: Theory and methods, v.1 : W.H. Freeman and Co.

Avseth, P., Dvorkin, J., Mavko, G,and Rykkje,J., 2000, Rock physics diagnostic Of North Sea sands: Link between microstructure and seismic properties. Geophys. Res. Lett, 27, 2761-2764.

Avseth, P., Mukerji, T., Mavko, G, 2005, Quantitative Seismic Interpretation. Applying Rock Physics Tools to Reduce Interpretation Risk: Cambridge University Press.

Avseth, P. and Skjei, N., 2011. ”Rock physics modeling of static and dynamic reservoir properties—a heuristic approach for cemented sandstone reservoirs.” The Leading Edge. Volume 30, Issue 1, 90-96.

Bayes, T., and Price, R., 1763. "An Essay towards solving a Problem in the Doctrine of Chance. By the late Rev. Mr. Bayes, communicated by Mr. Price, in a letter to John Canton, A. M. F. R. S.". Philosophical Transactions of the Royal Society of London 53 (0): 370–418.

Berryman, J.G., 1980; Long-wavelength propagation in composite elastic media 1. Spherical

inclusions. Journal of the Acoustical Society of America, 68, 1809-1819.

Biot, M.A., 1956. Theory of propagation of elastic waves in a fluid-saturated porous solid.The journal of the acoustic society of America, Vol. 28, No. 2, pp. 168-178, March.

Budiansky,B., 1965. On the elastic moduli of some heterogeneous materials. J. Mech. Phys. Solids, 13, 223-227.

Castagna, J., Batzle, M.L.. and Eastwood, R.L., 1985. Relationships between compressional-wave and shear-wave velocities in clastic silicate rocks: Geophysics, 50, 571-581.

Castagna, J., Batzle, M.L. and Kan, T.K., 1993. Rock physics – The link between rock properties and AVO response, Geophysics 8, 135-171.

Castagna, J.; Swan, H., 1997, Principles of AVO cross-plotting, The leading Edge, April

Castagna, J.P., Swan, J.G., and Foster, D.J., 1998. Framework for AVO gradient and intercept interpretation. Geophysics 63, 948-956.

Connolly, P, 1999, Elastic Impedance, The Leading Edge 18 (4), 438-352.

Cooke, D. and Cant, J.; 2010, Model-based Seismic Inversion: Comparing deterministic and probabilistic approaches, Santos, Ltd. Adelaide, SA, Australia; Makaira Geotechnical, Perth WA, Australia.

Digby, P.J., 1981. The effective elastic moduli of porous granular rocks, J. Appl. Mech, 48, 803-808.

Dvorkin, J., Nur, A., and Yin, H., 1994; Effective properties of cemented granular materials, Mechanics of Materials, 18, 351-366.

Dvorkin, J., Nur, A., 1996; Elasticity of high-porosity sandstones: Theory for two North Sea datasets, Geophysics, 61, 1363-1370.

Eaton, B., 1975: The equation for geopressure prediction from well logs, Society of

petroleum engineers, paper number SPE 5544, pag. 1-11.

Fatti, J.L., Vail P.J., Smith G.C., Strauss P.J., and Levitt P.R., 1994 : Detection of gas in sandstone reservoir using AVO analysis: A 3D seismic case history using the Geostack technique: Geophysics 59, 1362-1376.

Filippova, K., Kozhenkov, A., and Alabushin, A., 2011; Seismic inversion techniques: choice and benefits, First break, volume 29, 103-114.

Gassmann, F., 1951. Űber die elastizität poröser medien: Vierteljahrss-chrift der Naturforschenden Gesellschaft in Zurich, 96, 1-23.

Gidlow, P.M., Smith, G.C., 1987: Weighted stacking for rock property estimation and detection of gas, Geophysical Prospecting, volume 35, issue 9, pages 993-1014.

Greenberg, M.L. and Castagna, J.P., 1992. Shear wave velocity estimation in porous rocks: Theoretical formulation, preliminary verification and applications, Geophysical Prospecting, 40, 195-209.

Higgs, R., 2007. Sedimentology of the F-O Gas field, Bredasdorp basin, offshore South Africa: Interpreted depositional environments, sequence stratigraphy & diagenetic history, and therir bearing on Poro-Perm prediction. Internal report.

Hill, R., 1965. A self-consistent mechanic of composite materials. J. Mech. Phys. Solids, 13, 213-222.

Hill, S., 1994: Petrographic appraisal of the F-O reservoir sandstones. Report/Document number: SOE-PET-RPT-051.

Jungslager, E.H.A., 1996, Geological Evaluation of the Remaining Prospectivity for Oil and Gas of the Pre-1At1 “Synrift”Succession in Block 9, Republic of South Africa: Soekor (PTY) LTD.

Kemper, M.; 2010, Rock physics driven inversion: the importance of workflow, first break, volume 28, October 2010, 69-81.

Krief, M., J. Garat, 1990. A petrophysical interpretation using the velocities of P and S waves. The Log Analyst, 31, 355-369.

Lean, J., Regan, T., Bardwell, K. and Storer, A.,2001: F-O Field Evaluation, PGS Reservoir (UK) Limited

Mavko, G., Mukerji, T., and Dvorkin, J., 2009, The Rock Physics Handbook. Cambridge: Cambridge University Press.

Mindlin, R.D., 1949. Compliance of elastic bodies in contact. Trans. Transaction of the American Society of Mechanical Engineers, 71, A-259.

Norris, A.N., 1985. A differential scheme for the effective moduli of composities. Mechanisc of Material, 4, 1-16.

O'Connell, R.J. and Budiansky, B., 1976. Elastic moduli of a cracked solid. Int. J. Solids and Structures, 12, 81-97.

Ødegaard, E.; Avseth, P., 2004. Well log and seismic data analysis using rock physics templates, First Break, volume22.

PennState, Eberly College of Science, Probability Theory and Mathematical Statistics, (STAT 414/415)

PGS, 2001. F-O Field evaluation, Revision 1. PGS Reservoir Consultants (UK) Limited, for Mossgas. August 2001.

Poupon, A., Leveaux, J., 1971: Evaluation of water saturation in shaly formations, The Log Analyst, August-September,1971, pag. 3-8.

Radon, J.,1917: "Über die Bestimmung von Funktionen durch ihre Integralwerte längs gewisser Mannigfaltigkeiten", [Reports on the proceedings of the Royal Saxonian Academy of Sciences at Leipzig, mathematical and physical section] (Leipzig: Teubner) (69): 262–277; Translation: Radon, J.; Parks, P.C. (translator) (1986), "On the determination of functions from their integral values along certain manifolds", IEEE Transactions on Medical Imaging **5** (4): 170–176

Raymer, L. L., Hunt, E. R., and Gardner, J. S., 1980, An improved sonic transit time-to-porosity transform. Soc. Professional Well Log Analysts (SPWLA), 21st Ann. Logg. Symp., Paper P July 1980

Robles, G. 2009. Updating of the F-O Static Model, Block 9, Bredasdorp Basin. Project 185. PETSA-TEC-RPT-0659

Ruiz, F., 2009, Porous Grain Model and Equivalent Elastic Medium Approach for Predicting Effective Elastic Properties of Sedimentary Rocks: Stanford University.

Russell,B.; 2004, Introduction to seismic inversion methods, Course Notes Series, No 2, S.N. Domenico, Series Editor, Hampson-Russell Software Services, Ltd. Calgary, Alberta.

Rutherford, S., Williams, R., 1989: Amplitude-versus-offset variations in a gas sand, Geophysics, Vol. 54, No. 6, Pag: 680-688.

Schlumberger, 2001, Log interpretation chart, 242.

Schmidt, V. & McDonald, D.A., 1979, Texture and recognition of secondary porosity in sandstones. Pp.209-225 in: Aspects of Diagenesis (P.A. Scholle and P.R. Schluger, editors). SEPM Spec. Pub. 26.

Shuey, R. T. (April 1985). "A simplification of the Zoeppritz equations". *Geophysics* 50 (9): 609–614.

Simm, R., White, R., and Uden, R., 2000, The anatomy of AVO crossplots: The Leading Edge, 19, No 2, 150-155.

Simm, R., Bacon, M., 2014: Seismic Amplitude: An Interpreter's Handbook. Cambridge University Press, 279 pages.

Vernik, L., and Liu, X., 1997, Velocity anisotropy in shales: A petrophysical study, Geophysicis, 62, 521-532.

Walls, J.D., 2001; The use of Fluid Substitution for Correction of Mud Filtrate Invasion in Sandstone reservoirs: SEG.

Walton, K., 1987. The effective elastic moduli of a random packing of spheres. J. Mech. Phys. Solids, 35, 213-226.

Wiggins, R., Kenny, G.S., and McClure, C.D., 1983, A method for determining and displaying the shear-velocity reflectivities of a geologic formation. European Patent Application 0113944.

Whitcombe, D.N., Connolly, P.A., Reagan, R.L. and Redshaw, T.L., 2000, Extended elastic impedance for fluid and lithology prediction: 70th Ann. Internt. Mtg., Soc. Expl. Geophys., Expanded Abstracts.

Whitcombe, D.N., 2002, Normalization Elastic Impedance: Geophysics 67, 59-61.

White, R.E., 1980. Partial coherence matching of synthetic seismograms with seismic traces: Geophysical Prospecting 28, 333-358.

White, R.E, and Simm,R, 2003, Tutorial: Good practice in well ties: First Break:21, 75-83.

Wu, T.T., 1966. The effect of inclusion shape on the elastic moduli of a two phase material. Int. J. Solids Structures, 2, 1-8.

Wyllie, M.R, Gregory, A.R., Gardner, L.W., 1956. Elastic wave velocities in heterogeneous and porous media. Geophysicis 21, 41-70.

Zoback, M., 2008: Reservoir Geomechanics, Cambridge University Press, pag.7-10.

Zoeppritz, K.,1919: Erdbebenwellen VII. VIIb. Über Reflexion und Durchgang seismischer Wellen durch Unstetigkeitsflächen. Nachrichten von der Königlichen Gesellschaft der Wissenschaften zu Göttingen, Mathematisch-physikalische Klasse, 66-84.